Lecture Notes in Networks and Systems 554

Sanyog Rawat
Sandeep Kumar
Pramod Kumar
Jaume Anguera *Editors*

Proceedings of Second International Conference on Computational Electronics for Wireless Communications

ICCWC 2022

Springer

Lecture Notes in Networks and Systems

Volume 554

The series "Lecture Notes in Networks and Systems" publishes the latest developments in Networks and Systems—quickly, informally and with high quality. Original research reported in proceedings and post-proceedings represents the core of LNNS.

Volumes published in LNNS embrace all aspects and subfields of, as well as new challenges in, Networks and Systems.

The series contains proceedings and edited volumes in systems and networks, spanning the areas of Cyber-Physical Systems, Autonomous Systems, Sensor Networks, Control Systems, Energy Systems, Automotive Systems, Biological Systems, Vehicular Networking and Connected Vehicles, Aerospace Systems, Automation, Manufacturing, Smart Grids, Nonlinear Systems, Power Systems, Robotics, Social Systems, Economic Systems and other. Of particular value to both the contributors and the readership are the short publication timeframe and the worldwide distribution and exposure which enable both a wide and rapid dissemination of research output.

The series covers the theory, applications, and perspectives on the state of the art and future developments relevant to systems and networks, decision making, control, complex processes and related areas, as embedded in the fields of interdisciplinary and applied sciences, engineering, computer science, physics, economics, social, and life sciences, as well as the paradigms and methodologies behind them.

Indexed by SCOPUS, INSPEC, WTI Frankfurt eG, zbMATH, SCImago.

All books published in the series are submitted for consideration in Web of Science.

For proposals from Asia please contact Aninda Bose (aninda.bose@springer.com).

Sanyog Rawat · Sandeep Kumar · Pramod Kumar · Jaume Anguera
Editors

Proceedings of Second International Conference on Computational Electronics for Wireless Communications

ICCWC 2022

Springer

Editors
Sanyog Rawat
Department of Electronics
and Communication Engineering
Central University of Rajasthan
Ajmer, Rajasthan, India

Sandeep Kumar
Department of Electronics
and Communication Engineering
National Institute of Technology Karnataka
Surathkal, India

Pramod Kumar
Department of Electronics
and Communication Engineering
Manipal Institute of Technology
Manipal Academy of Higher Education
Manipal, India

Jaume Anguera
Department of Telecommunication
Engineering
Universitat Ramon Llull
Barcelona, Spain

ISSN 2367-3370 ISSN 2367-3389 (electronic)
Lecture Notes in Networks and Systems
ISBN 978-981-19-6660-6 ISBN 978-981-19-6661-3 (eBook)
https://doi.org/10.1007/978-981-19-6661-3

Preface

It is a matter of great pleasure to bring out the volume containing the papers from the International Conference on Computational Electronics for Wireless Communications, ICCWC-2022, held at the Department of Electronics and Communication Engineering, National Institute of Technology Karnataka, Surathkal, India, during June 9–10, 2022. The conference was attended by faculty members, students, and researchers from leading institutes and universities along with industry professionals. The papers presented in the conference focused on the recent developments in the field of computational electronics and wireless communication. Out of nearly 250 research papers received, about 60 quality research papers were selected for presentation in the conference. The deliberations covered many upcoming technologies such as electronic warfare communications, sprintronics material and devices, and photonics devices for 5G/6G wireless communications that hold great promise in achieving the objective of performance enhancement of future networks. Technical program was rich and varied with keynote speeches, invited talks, and multiple technical sessions. It provided a good platform for the scholars to enhance their knowledge by holding interaction with the experts and scholars. The conference started with opening addresses by Dr. Ashvini Chaturvedi, Professor and Head, Department of Electronics and Communication Engineering, NITK Surathkal, Guest of Honor Dr. Anupam Sharma, Outstanding Scientist and Associate Director, Directorate of Special Projects (DSP) DRDO, Ministry of Defense, Hyderabad, India, Chief Guest Dr. Aloknath De, Corporate Vice President of Samsung Electronics and Chief Technology Officer of Samsung R&D Institute, Bangalore, India, and Prof. G. C. Mohan, Director in Charge and Dean Faculty Welfare, NITK Surathkal. The keynote addresses were delivered on the topics of "Electronics Warfare and its Applications", "Spintronics Material and Devices", "Piezoelectric and Ferroelectric Devices for Wireless Communications", and "Medical Imaging Research toward Wireless Monitoring" by Dr. Anupam Sharma, Outstanding Scientist and Associate Director, DRDO, Ministry of Defense, Hyderabad, Prof. Ajay Gupta, University of Petroleum and Energy Studies, Dehradun, Prof. T. S. Kalkur, Department of Electrical and Computer Engineering, University of Colorado, Colorado, and Prof. Luciano Oliveira, Department of Computer Science, Federal University

of Bahia (UFBA), Brazil, respectively. There were five technical sessions, spread over two days, to facilitate paper presentations. With a wide range of quality papers, this volume will be of interest to researchers in both industry and academia. We express our gratitude to the invited speakers for enriching this conference through their outstanding presentations. It is our pleasure to acknowledge the help we received in finalizing the technical contents of this conference. We wish to thank all reviewers and program committee members who helped us in completing the review process in a timely manner. We thank all the authors and participants for their contributions in the conference. We also gratefully acknowledge the guidance and support from the advisory and program committee members of ICCWC-2022. We hope this volume will be a valuable addition to the literature on computational electronics and wireless communication.

Ajmer, India — Dr. Sanyog Rawat
Mangalore, India — Dr. Sandeep Kumar
Manipal, India — Dr. Pramod Kumar
Barcelona, Spain — Dr. Jaume Anguera

Contents

Editors and Contributors

About the Editors

Dr. Sanyog Rawat is Associate Professor in the Department of Electronics and Communication Engineering (ECE) at Central University of Rajasthan. He graduated with Bachelor of Engineering (B.E.) in Electronics and Communication, Master of Technology (M.Tech.) in Microwave Engineering and Ph.D. in the field of Planar Antennas. He has been into teaching and research for more than eighteen years. He has published more than 100 research papers in reputed journals and conferences and several book chapters. He has supervised five Ph.D.s till date and currently six are underway. He has supervised 31 M.Tech. dissertations work and nearly 44 UG projects. He has been Member of the Technical Program Committee of many IEEE/Springer conferences and Reviewer of reputed journals like IEEE/Elsevier/Wiley/Springer. He has also edited the books on proceedings of the International Conference on Soft Computing Theories and Applications (SoCTA-2016, 2017), proceedings of International Conference on Smart Systems, Innovations and Computing (SSIC-2017) and International Conference on Engineering Vibrations, Communication, Information Processing (ICoEVCI, 2018) and International Conference for Wireless Communications (ICCWC-2021, 2022) for Springer publication. He has extensively traveled to countries like Japan, Singapore, Malaysia, Vietnam, Indonesia, Thailand, and UAE, to deliver talks, present research papers or in connection with other research/academic activities. He is Life Fellow of the Institution of Electronics and Telecommunication Engineers (IETE), India, and Life Member of Institution of Engineers (India), Indian Society for Technical Education (ISTE) and Indian Society of Lighting Engineers (ISLE). His current research interests include RF and microwave devices, microstrip and smart antennas and reconfigurable antennas.

Dr. Sandeep Kumar is Assistant Professor in the Department of Electronics and Communication Engineering at NIT Surathkal, Karnataka. Prior to joining this institute, he was Research Professor in Nano Circuit design lab, Inje University, South Korea. He received his Ph.D. in Electronics Engineering from Indian Institute of

Technology (IIT), Dhanbad, Jharkhand, in 2016. He has a keen research interest in analog RF and mixed integrated circuit for wireless communication. He has published more than 50 publications including 32 international SCI journals, 22 international conferences and several book chapters in IEEE, IET publishers, etc. Dr. Kumar had successfully executed 02 research projects sponsored by agencies of Government of Korea. Currently, he is handling three research projects sponsored from SERB-DST and International Division, Indo-Korea Ministry of Science. He signed two MoUs with Prof. Hanjung Song, Inje University South Korea, and Prof. Zhi-gong Wang, Prof. Lu Xiaoying, Southeast University China, for academic and research collaboration.

Dr. Pramod Kumar received his B.E. degree in Electronics and Communication Engineering from Visvesvaraya Technological University in 2002 and M.Tech. degree in Microwave Engineering from Madhav Institute of Technology and Science, Gwalior, India, in 2007. He obtained Ph.D. from National Institute of Technology Karnataka, Mangalore, India. Currently, he is working as Professor in the Department of Electronics and Communication Engineering at Manipal Institute of Technology, Manipal, India. He has published more than 50 papers in reputed peer-reviewed international journals and conferences. His current areas of research are wireless sensor networks, design of antennas and microwave components for wireless communications. He is on the board of reviewers of journals like the *IEEE Transactions on Antennas and Propagation*, *IET Networks*, *AEU International Journal of Electronics and Communications*, *Wireless Personal Communication* (WPC), *International Journal of Microwave and Wireless Technologies*, *International Journal of Communications*, etc.

Dr. Jaume Anguera is IEEE Fellow, Founder and CTO of the technology company Ignion. He is Associate Professor at Ramon Llull University. He is Inventor of more than 150 granted patents and licensed to Telecommunication companies. He is Inventor of Antenna Booster Technology, which fostered the creation of Ignion. Many of antenna booster products have been adopted by the wireless industry worldwide, to allow connectivity to IoT devices through a miniature multiband/radio and off-the-shelf components ten times smaller than conventional antennas. He is Author of +250 scientific papers and international conferences (h-index 50) and 7 books. He has participated in +22 competitive research projects financed by the Spanish Ministry, Generalitat de Catalunya, and the European Commission exceeding € 6 M, and Principal Researcher in most of them. He has taught +20 antenna courses worldwide. He has 22 years of R&D experience and has developed part of his professional experience with Fractus in South Korea in the design of miniature antennas for large Korean companies. He has received several national and international awards. He has directed the master/doctorate thesis to +140 students. His biography appears in Who's Who in the World and Who's Who in Science and Engineering. He is Associate Editor of the *IEEE Open Journal Antennas and Propagation*, *Electronics Letters*. He is IEEE Antennas Prop. Distinguished Lecturer and Vice-Chair of the working group "Software and Modeling" at EurAAP.

Contributors

U. Shripathi Acharya Department of Electronics and Communication Engineering, National Institute of Technology Karnataka, Surathkal, Karnataka, India

Vaibhav Aggarwal School of Electronics and Communication Engineering, Vellore Institute of Technology, Vellore, India

Samarth Agrawal Department of CSE, Ajay Kumar Garg Engineering College, Ghaziabad, Uttar Pradesh, India

AlaaDdin Al-Shidaifat Department of Electronics and Communication Engineering, NITK, Surathkal, Mangaluru, India;
Department of Nano Science and Engineering, Inje University, Gimhae, Korea

Basim Alhadidi Department of Computer Information Systems, Prince Abullah Bin Ghazi Faculty of Information and Communication Technology, Al-Balqa Applied University, Salt, Jordan

Aditya Aman Department of Electronics and Communication Engineering, Dr. B R Ambedkar National Institute of Technology, Jalandhar, India

Prakasa Rao Amara Department of Electronics and Communication Engineering, National Institute of Technology Warangal, Hanamkonda, Telangana, India

B. S. Anjana Department of Communication Engineering, School of Electronics Engineering, Vellore Institute of Technology, Vellore, Tamil Nadu, India

J. A. Ansari University of Allahabad, Prayagraj, Uttar Pradesh, India

S. Anuradha Department of Electronics and Communication Engineering, National Institute of Technology, Warangal, India

E. Aparna National Institute of Technology Warangal, Hanamkonda, Telangana, India

M. Arokiasamy LRDE, DRDO, Radar III, Bangalore, India

Rajeev Kumar Arya Department of Electronics and Communication Engineering, National Institute of Technology, Patna, India

MD. Ataur Safi Rahaman Laskar Antenna Research Laboratory, Department of Electronics and Communication Engineering, Aliah University, Kolkata, India

Varun Bajaj PDPM-Indian Institute of Information Technology Design and Manufacturing, Jabalpur, Madhya Pradesh, India

L. K. Balyan PDPM-Indian Institute of Information Technology Design and Manufacturing, Jabalpur, Madhya Pradesh, India

Bharani Bandi Department of Electronics and Communication Engineering, Vignan's Institute of Information Technology (A), Visakhapatnam, India

Yashas Bharadwaj Electronics and Communication Engineering, Manipal Institute of Technology, Manipal Academy of Higher Education, Manipal, India

L. Bhargava Kumar Department of Electronics and Communication Engineering, National Institute of Technology Karnataka, Surathkal, Karnataka, India

Saumyata Bhargava ABES Institute of Technology, Ghaziabad, India

Ketan Bhujange Wireless Information Networking Group (WiNG), Department of Computer Science and Engineering, National Institute of Technology Karnataka, Surathkal, Mangalore, India

Yaswanth Chalamalasetti Wireless Communication Lab, School of Electrical Sciences, Indian Institute of Technology Bhubaneswar, Jatani, Khordha, Odisha, India

B. R. Chandavarkar Wireless Information Networking Group (WiNG), Department of Computer Science and Engineering, National Institute of Technology Karnataka, Surathkal, Mangalore, India

Lakshay Chauhan ABES Institute of Technology, Ghaziabad, India

Priyanka Chawla Lovely Professional University, Phagwara Jalandhar, Punjab, India

Sakshi Chhabra Vellore Institute of Technology, Vellore, Tamil Nadu, India

Wan Young Chung Department of Electronic Engineering, Pukyong National University, Busan, Republic of Korea

Nikhil Danthamala Department of Electronics and Communications Engineering, National Institute of Technology, Goa, India

Anusha P. Das Wireless Information Networking Group (WiNG), Department of Computer Science and Engineering, National Institute of Technology Karnataka, Surathkal, Mangalore, India

Vijitaa Das Department of Electronics Design Technology, National Institute of Electronics and Information Technology, Calicut, India

Pallepogu Divya Vignan's Foundation for Science Technology and Research, Vadlamudi, Andhra Pradesh, India

Tarun Kumar Dubey Department of Electronics and Communication Engineering, Manipal University Jaipur, Jaipur, Rajasthan, India

Vivek K. Dwivedi Department of Electronics and Communication, Jaypee Institute of Information Technology Noida, Noida, Uttar Pradesh, India

C. Elavarasi Department of ECE, National Institute of Technology, Tiruchirappalli, India

Kasu Pravachana Evangelin Karunya Institute of Technology and Sciences, Coimbatore, India

Suganthi Evangeline Karunya Institute of Technology and Sciences, Coimbatore, India

Sameer Farooq Lovely Professional University, Phagwara Jalandhar, Punjab, India

Akhilraj V. Gadagkar Wireless Information Networking Group (WiNG), Department of Computer Science and Engineering, National Institute of Technology Karnataka, Surathkal, Mangalore, India

Shilpa Garg Department of Electronics and Communication Engineering, IGDTUW, Delhi, New Delhi, India;
Department of Electronics and Communication Engineering, JIMSEMTC, Greater Noida, Uttar Pradesh, India

Abhishek Gaur USICT, Guru Gobind Singh Indraprastha University, New Delhi, India

Tarun Gautam Chandigarh University, Gharuan, Punjab, India

Ramandeep Gill Department of Electronics and Communication Engineering, Manipal University Jaipur, Jaipur, Rajasthan, India

Pradeep Gorre Department of Electronics and Communication Engineering, National Institute of Technology Karnataka, Surathkal, Mangaluru, India

Tattukolla Gowthami Vignan's Foundation for Science Technology and Research, Vadlamudi, Andhra Pradesh, India

Kiran Gunde National Institute of Technology Warangal, Warangal, Telangana, India

Juhi Gupta Department of Electronics and Communication, Jaypee Institute of Information Technology Noida, Noida, Uttar Pradesh, India

Kapil Gupta PDPM-Indian Institute of Information Technology Design and Manufacturing, Jabalpur, Madhya Pradesh, India

Meenu Gupta Chandigarh University, Gharuan, Punjab, India

Saptarshi Gupta Department of Electronics and Communication Engineering, Faculty of Engineering and Technology, SRM Institute of Science and Technology, NCR campus, Delhi-NCR Campus, Modinagar, U. P, India

Sugandh Gupta Department of Electronics and Communication Engineering, Faculty of Engineering and Technology, SRM Institute of Science and Technology, NCR campus, Delhi-NCR Campus, Modinagar, U. P, India

Tarun Kumar Gupta Maulana Azad National Institute of Technology, Bhopal, Madhya Pradesh, India

Vishwnatha Hanchinal Design Engineer, NXP Semiconductors, Austin, USA

Md. Nazmul Haque Department of Nanoscience and Engineering, Inje University, Gimhae, Korea

K. Harshitha Electronics and Communication Engineering, Manipal Institute of Technology, Manipal Academy of Higher Education, Manipal, India

Md. Tarikul Islam Department of Nanoscience and Engineering, Inje University, Gimhae, Korea;
Department of Electronics and Communication Engineering, NITK, Surathkal, Mangaluru, India

Hindavi Jadhav Department of Communication Engineering, School of Electronics Engineering, Vellore Institute of Technology, Vellore, Tamil Nadu, India

P. V. Y. Jayasree Department of EECE, GITAM Deemed to Be University, Visakhapatnam, India

Sumit Kumar Jindal School of Electronics Engineering, Vellore Institute of Technology, Vellore, Tamil Nadu, India

Nitesh Kashyap Department of Electronics and Communication Engineering, Dr. B R Ambedkar National Institute of Technology, Jalandhar, India

Sapna Katiyar Electronics and Communication Engineering, ABES Institute of Technology, Ghaziabad, U. P, India

Ranbirjeet Kaur Department of Electronics and Communication, National Institute of Technical Teacher's Training and Research Chandigarh, Chandigarh, India

Sudhansh Kesharwani School of Electronics and Communication Engineering, Vellore Institute of Technology, Vellore, India

Samiur Rahman Khan Department of Nanoscience and Engineering, Inje University, Gimhae, Korea

Sagar Khatri National Institute of Technology Karnataka, Surathkal, India

Aditya Khosla School of Electronics and Communication Engineering, Vellore Institute of Technology, Vellore, India

Tulasi Naga Jyothi Kolanti B.M.S. College of Engineering, Bengaluru, India

Venkata Kishore Kothapudi Center of Excellence Advanced RF Microwave and Wireless Communications, Department of Electronics and Communication Engineering, Vignan's Foundation for Science, Technology, and Research (VFSTR), Vadlamudi, Guntur District, Andhra Pradesh, India

Prabu Krishnan Department of Electronics and Communication Engineering, National Institute of Technology Karnataka, Surathkal, Karnataka, India

M. Kulkarni National Institute of Technology Karnataka Surathkal, Mangaluru, India

Vinoth Babu Kumaravelu Department of Communication Engineering, School of Electronics Engineering, Vellore Institute of Technology, Vellore, Tamil Nadu, India

Arvind Kumar School of Electronics and Communication Engineering, Vellore Institute of Technology, Vellore, India;
Department of Electronics and Communication Engineering, Visvesvaraya National Institute of Technology, Nagpur, India

A. Kumar PDPM-Indian Institute of Information Technology Design and Manufacturing, Jabalpur, Madhya Pradesh, India

Ashok Kumar National Institute of Technology, Srinagar, India

D. Sriram Kumar Department of Electronics and Communication Engineering, National Institute of Technology, Tiruchirappalli, India

G. Arun Kumar National Institute of Technology Warangal, Hanamkonda, Telangana, India

Manjeet Kumar Department of Electronics and Communication Engineering, DTU, Delhi, New Delhi, India

Narander Kumar Department of Computer Science, Babasaheb Bhimrao Ambedkar University (A Central University), Lucknow, India

Pramod Kumar Electronics and Communication Engineering, Manipal Institute of Technology, Manipal Academy of Higher Education, Manipal, India

Rakesh Kumar Chandigarh University, Gharuan, Punjab, India

Sandeep Kumar Department of Electronics and Communication Engineering, National Institute of Technology Karnataka, Surathkal, Mangaluru, India

Thadagoni Pranay Kumar Vardhaman College of Engineering, Hyderabad, India

Ajay Kumar Kushwaha Bharati Vidyapeeth (Deemed to be University) College of Engineering, Pune, India

Vinay Kushwaha National Institute of Technology, Surathkal, Karnataka, India

Kirankumar H. Lad Department of Electronics and Communication Engineering, National Institute of Technology Karnataka, Surathkal, India

Chhagan Lal Department of Intelligent Systems, Cybersecurity Group, TU Delft, Delft, South Holland, The Netherlands

T. Laxminidhi Department of Electronics and Communication Engineering, National Institute of Technology Karnataka, Surathkal, India

Lakshay Lohumi ABES Institute of Technology, Ghaziabad, India

Chinmay Malkhandi National Institute of Technology, Surathkal, Karnataka, India

Belcy D. Mathews Puducherry Technological University, Puducherry, India

Ankit Kumar Maurya Department of Electronics and Communication Engineering, Dr. B R Ambedkar National Institute of Technology, Jalandhar, India

Ashish Mishra Bharati Vidyapeeth (Deemed to be University) College of Engineering, Pune, India

Poornima Mittal Delhi Technological University, Delhi, India

SK. Moinul Haque Antenna Research Laboratory, Department of Electronics and Communication Engineering, Aliah University, Kolkata, India

Krishnay Mudgal Department of CSE, Ajay Kumar Garg Engineering College, Ghaziabad, Uttar Pradesh, India

Apeksha Murdeshwar Electronics and Communication Engineering, Manipal Institute of Technology, Manipal Academy of Higher Education, Manipal, India

Arthi Murugadass Department of Computer Science and Engineering (AI and ML), Sreenivasa Institute of Technology and Management Studies, Chittoor, Andhra Pradesh, India

Sarada Musala Vignan's Foundation for Science Technology and Research, Vadlamudi, Andhra Pradesh, India

Srikalyani Nageti Department of Electronics and Communication Engineering, Vignan's Institute of Information Technology (A), Visakhapatnam, India

Ramavath Prasad Naik Research Institute of Artificial Intelligence Convergence, Pukyong National University, Busan, Republic of Korea

Jatoth Deepak Naik Department of Nanoscience and Engineering, Inje University, Gimhae, Korea;
Department of Electronics and Communication Engineering, NITK, Surathkal, Mangaluru, India

Afrah Nayeem Wireless Information Networking Group (WiNG), Department of Computer Science and Engineering, National Institute of Technology Karnataka, Surathkal, Mangalore, India

Pradeep Nazareth Wireless Information Networking Group (WiNG), Department of Computer Science and Engineering, National Institute of Technology Karnataka, Surathkal, Mangalore, India

Bala Ankaiah Nunna Center of Excellence Advanced RF Microwave and Wireless Communications, Department of Electronics and Communication Engineering, Vignan's Foundation for Science, Technology, and Research (VFSTR), Vadlamudi, Guntur District, Andhra Pradesh, India

Krishna Pandey Department of Electronics and Communication Engineering, National Institute of Technology, Patna, India

Binayak Parashar Department of CSE, Ajay Kumar Garg Engineering College, Ghaziabad, Uttar Pradesh, India

Khan Masood Parvez Antenna Research Laboratory, Department of Electronics and Communication Engineering, Aliah University, Kolkata, India

K. S. Vasundara Patel B.M.S. College of Engineering, Bengaluru, India

Rachit Patel ABES Institute of Technology, Ghaziabad, India

P. Prarthana School of Electronics Engineering, Vellore Institute of Technology, Vellore, Tamil Nadu, India

Sai Spandana Pudipeddi Department of EECE, GITAM Deemed to Be University, Visakhapatnam, India

S. Radhakrishnan Department of Electronics and Communication Engineering, National Institute of Technology, Tiruchirappalli, India

G. Thavasi Raja Department of Electronics and Communication Engineering, National Institute of Technology, Tiruchirappalli, India

Tanisha Rakshit Vellore Institute of Technology, Vellore, Tamil Nadu, India

Gopi Ram National Institute of Technology Warangal, Hanamkonda, Telangana, India

CH. Ramakrishna Vardhaman College of Engineering, Hyderabad, India

Barathram Ramkumar Wireless Communication Lab, School of Electrical Sciences, Indian Institute of Technology Bhubaneswar, Jatani, Khordha, Odisha, India

Rathnamala Rao National Institute of Technology, Surathkal, Karnataka, India

Bhawna Rawat Delhi Technological University, Delhi, India

Jinugu Harsha Vardhan Reddy Karunya Institute of Technology and Sciences, Coimbatore, India

MD. Rehana Vardhaman College of Engineering, Hyderabad, India

S. Rekha Department of Electronics and Communication Engineering, National Institute of Technology Karnataka, Surathkal, India

Gunjan Mittal Roy Institute of Innovation in Technology and Management, Janakpuri, New Delhi, India

Subham Roy Department of Electronics and Communication Engineering, National Institute of Technology Karnataka, Surathkal, India

Eshan Sabhapandit School of Electronics Engineering, Vellore Institute of Technology, Vellore, Tamil Nadu, India

Garima Saini Department of Electronics and Communication, National Institute of Technical Teacher's Training and Research Chandigarh, Chandigarh, India

Parul Saini PDPM-Indian Institute of Information Technology Design and Manufacturing, Jabalpur, Madhya Pradesh, India

SD. Sairam Department of Electronics and Communication Engineering, National Institute of Technology, Tiruchirappalli, India

M. Sandeep National Institute of Technology Karnataka, Surathkal, India

R. K. Sarin Department of Electronics and Communication Engineering, Dr. B R Ambedkar National Institute of Technology, Jalandhar, India

Vishal Narain Saxena Department of Electronics and Communication, Jaypee Institute of Information Technology Noida, Noida, Uttar Pradesh, India

Md. Shohel Sayeed Faculty of Information Science and Technology (FIST), Multimedia University, Melaka, Malaysia

Bhawana Sharma Department of Information Technology, Manipal University Jaipur, Jaipur, Rajasthan, India

Dolly Sharma Department of Mechatronics, Manipal Institute of Technology Manipal Academy of Higher Education, Manipal, India

K. K. Sharma Department of Electronics and Communication, Malaviya National Institute of Technology, Jaipur, Rajasthan, India

Lokesh Sharma Department of Information Technology, Manipal University Jaipur, Jaipur, Rajasthan, India

Mamta Devi Sharma Global Institute of Technology, Jaipur, Rajasthan, India; Malaviya National Institute of Technology, Jaipur, Rajasthan, India

Ranjana Sharma ABES Institute of Technology, Ghaziabad, India

Ritu Sharma Department of Electronics and Communication, Malaviya National Institute of Technology, Jaipur, Rajasthan, India

Vipin Sharma Department of Electronics and Communication Engineering, National Institute of Technology, Patna, India

Yashaswini Sharma Department of Electronics and Communication, Malaviya National Institute of Technology, Jaipur, Rajasthan, India

Aayush Shrestha Vellore Institute of Technology, Vellore, Tamil Nadu, India

Vibhakar Shrimali ECE Department, GB Pant Government Engineering College, Government of NCT of Delhi, New Delhi, India

Yogesh Shrivastava Maulana Azad National Institute of Technology, Bhopal, Madhya Pradesh, India

H. M. Shwetha Department of Electronics and Communication Engineering, National Institute of Technology, Warangal, India

Sarthak Singhal Malaviya National Institute of Technology, Jaipur, Rajasthan, India

Abhishek Singh PDPM-Indian Institute of Information Technology Design and Manufacturing, Jabalpur, Madhya Pradesh, India

Aditya Kumar Singh University of Allahabad, Prayagraj, Uttar Pradesh, India

Ashutosh Singh Bharati Vidyapeeth (Deemed to be University) College of Engineering, Pune, India

G. K. Singh Department of Electrical Engineering, Indian Institute of Technology Roorkee, Roorkee, India

Pranjali Singh Department of CSE, Banasthali University, Rajasthan, India

Pratima Singh Department of CSE, Ajay Kumar Garg Engineering College, Ghaziabad, Uttar Pradesh, India

Sweta Singh University of Allahabad, Prayagraj, Uttar Pradesh, India

Mukesh Kumar Sinha Department of Physiotherapy, Manipal College of Health Professions, Manipal Academy of Higher Education, Manipal, India

Hanjung Song Department of Nano Science and Engineering, Inje University, Gimhae, Korea

N. B. Srinivasulu Wireless Communication Lab, School of Electrical Sciences, Indian Institute of Technology Bhubaneswar, Jatani, Khordha, Odisha, India

Ankita Srivastava Department of Computer Science, Babasaheb Bhimrao Ambedkar University (A Central University), Lucknow, India

Balapanur Julian Deva Sundar Karunya Institute of Technology and Sciences, Coimbatore, India

Anuradha Sundru National Institute of Technology Warangal, Warangal, Telangana, India

Soumya Suresh School of Electronics Engineering, Vellore Institute of Technology, Vellore, Tamil Nadu, India

M. Tamilarasi Puducherry Technological University, Puducherry, India

Catherine Protas Tarimo National Institute of Technology Karnataka Surathkal, Mangaluru, India

Nageswar Rao Thadikamalla Department of Electronics and Communication Engineering, National Institute of Technology Warangal, Hanamkonda, Telangana, India

Prashant Upadhyay Department of ECE, Madanapalle Institute of Technology and Science, Madanapalle, Andhra Pradesh, India

K. Vaishali Department of Physiotherapy, Manipal College of Health Professions, Manipal Academy of Higher Education, Manipal, India

A. R. Vandana LRDE, DRDO, Radar III, Bangalore, India

Ajay Yadav Jaipur Engineering College and Research Center, Jaipur, Rajasthan, India

Prakhar Yadav University of Allahabad, Prayagraj, Uttar Pradesh, India

Ram Suchit Yadav University of Allahabad, Prayagraj, Uttar Pradesh, India

Richa Yadav Department of Electronics and Communication Engineering, IGDTUW, Delhi, New Delhi, India

Shubham Yadav Electronics and Communication Engineering, Manipal Institute of Technology, Manipal Academy of Higher Education, Manipal, India

Voltage-Mode and Current-Mode Universal Filter Using IC LT1228

Ajay Kumar Kushwaha, Ashok Kumar, Ashish Mishra, and Ashutosh Singh

Abstract The novelty of the paper is an electronically tunable second-order voltage-mode and current-mode universal filter employing commercially available IC LT1228 and passive components. The low-pass (LP), high-pass (HP), band-pass (BP), notch, and all-pass (AP) responses are realized using voltage-mode and current-mode second-order universal filters. The DC bias currents can be electronically modified to change the natural frequency of the presented arrangement. Furthermore, the voltage and current gain of filters can be adjusted. The Cadence OrCAD PSpice simulation is used to verify the theoretically described performance of the proposed filters.

Keywords Universal filter · LT1228 IC · Voltage mode (VM) · Current mode (CM) · Active building block (ABB)

1 Introduction

The realization of a filter using the externally tunable active building block (ABB) has been mainly focused on the research topic due to its advantages such as greater linearity, higher bandwidth, higher dynamic range, and lower power consumption [1–4]. Its key components are analog signal processing, automatic control, and instrumentation systems including phones, crossover networks, television communication,

A. K. Kushwaha (✉) · A. Mishra · A. Singh
Bharati Vidyapeeth (Deemed to be University) College of Engineering, Pune, India
e-mail: akkushwaha@bvucoep.edu.in

A. Mishra
e-mail: ashish.mishra2-coep@bvucoep.edu.in

A. Singh
e-mail: ashutosh.singh1-coep@bvucoep.edu.in

A. Kumar
National Institute of Technology, Srinagar, India
e-mail: ashok.kumar@nitsri.ac.in

S. Rawat et al. (eds.), *Proceedings of Second International Conference on Computational Electronics for Wireless Communications*, Lecture Notes in Networks and Systems 554,
https://doi.org/10.1007/978-981-19-6661-3_1

sound systems, instrumentation, control systems, and phase-locked loop circuits. An analog filter [5–8] is a standard research topic in current-mode circuit design. In the world of electrical and electronics engineering, a circuit that concurrently supplies all the filter responses is most useful. The different output filter responses can be realized by suitable combinations of inputs.

In this paper, the four-input, two-output voltage-mode universal filter and the single-input, five-output current-mode filter are proposed using a commercially available IC, LT1228 from Linear Technology Inc. [6]. The proposed VM and CM filters comprise two ICs, one or two resistors, and two capacitors, which are appropriate for off-the-shelf usage. The natural frequency and quality factor can be electronically tuned. The simulation and theoretical results have both been verified.

2 Circuit Description

2.1 IC Description

The Linear Technology Corporation's LT1228 IC [6], which combines a current feedback amplifier and an OTA, Fig. 1, depicts the symbolic picture of the IC.

The relationship is given below:

$$\left\{\begin{array}{c} I_{V+} = I_{V-} = 0 \\ I_Y = g_m V_+ - g_m V_- \\ V_X = V_Y \\ V_W = R_T I_X \end{array}\right\} \tag{1}$$

Ideally, R_T is infinite resistance, and it represents the transresistance gain of the IC. Hence, LT1228 would have an infinite open-loop voltage gain.

$$g_m = 10.I_{\text{set}} \tag{2}$$

The g_m is the transconductance gain, and it is controlled by DC bias current (I_{set}).

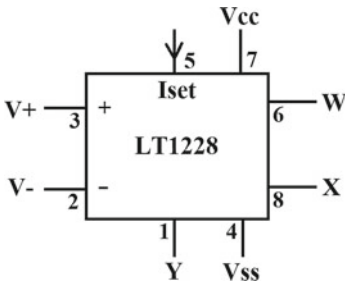

Fig. 1 LT1228 IC

2.2 Proposed Voltage-Mode Universal Filter

Figure 2 shows the structure of a four-input, two-output voltage-mode universal filter made from a commercially available IC LT1228, a single resistor, and two capacitors. In Table 1, the combinations of the input voltages and output voltages are mentioned.

In the analysis of the VM filter circuit, the output voltages (V_{out1} and V_{out2}) can be written as

$$V_{Out1} = \frac{-sR_1g_{m2}C_2V_{in1} + s^2C_1C_2R_1V_{in2} + R_1g_{m1}g_{m2}V_{in3} + sR_1g_{m2}C_2V_{in4}}{s^2C_1C_2R_1 + sC_2 + g_{m1}g_{m2}R_1} \quad (3)$$

$$V_{Out2} = \frac{\begin{array}{l} g_{m1}g_{m2}R_1V_{in1} - sC_1R_1g_{m1}V_{in2} + (sC_1R_1g_{m1} + g_{m1})V_{in3} \\ +(s^2C_1C_2R_1 + sC_2)V_{in4} \end{array}}{s^2C_1C_2R_1 + sC_2 + g_{m1}g_{m2}R_1} \quad (4)$$

From Eqs. (3) and (4), the filter parameters are obtained as

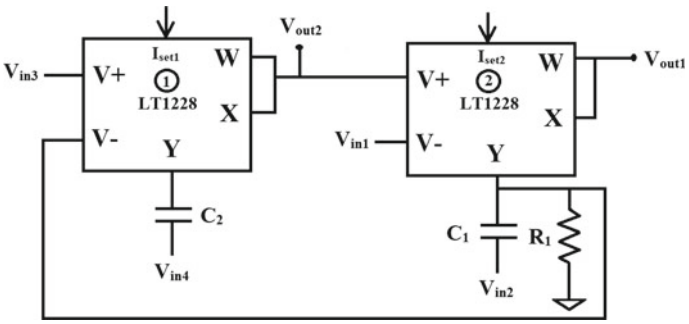

Fig. 2 Voltage-mode universal filter

Table 1 Combination of input and output voltages

S. No.	V_{in1}	V_{in2}	V_{in3}	V_{in4}	V_{out1}	V_{out2}
1	1	0	0	0	BP	LP
2	0	1	0	0	HP	BP
3	0	0	1	0	LPF	–
4	0	0	0	1	BP	–
5	0	1	1	0	BS	–
6	1	1	1	0	AP	LP
7	1	1	1	1	BS	LP

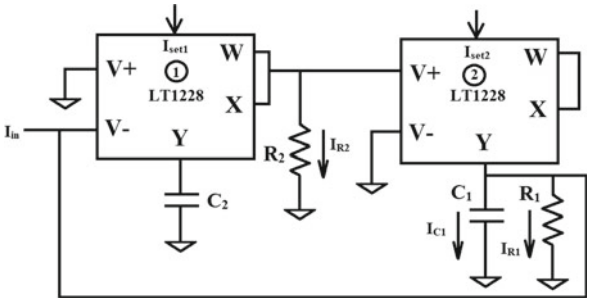

Fig. 3 CM universal filter

$$\omega_0 = \left(\frac{g_{m1}g_{m2}}{C_1C_2}\right)^{1/2},\ B.w. = \frac{1}{C_1R_1},\ Q = R_1\left(\frac{g_{m1}g_{m2}C_1}{C_2}\right)^{1/2} \tag{5}$$

Analysis of Eq. (5) shows that frequency and quality factor are the function of g_m and that can be easily controlled by DC bias current (I_{set}).

2.3 Proposed Current-Mode Universal Filter

Figure 3 shows the circuit of a current-mode filter made from a commercially available IC LT1228, two resistors, and two capacitors.

In the analysis of the CM filter circuit, the output currents (I_{out}) can be written as

$$\frac{I_{\text{LP}}}{I_{\text{in}}} = \frac{I(R_2)}{I_{\text{in}}} = -\frac{g_{m1}R_1/R_2}{s^2C_1C_2R_1 + sC_2 + g_{m1}g_{m2}R_1} \tag{6}$$

$$\frac{I_{\text{BP}}}{I_{\text{in}}} = \frac{I(R_1)}{I_{\text{in}}} = \frac{sC_2}{s^2C_1C_2R_1 + sC_2 + g_{m1}g_{m2}R_1} \tag{7}$$

$$\frac{I_{\text{HP}}}{I_{\text{in}}} = \frac{I(C_1)}{I_{\text{in}}} = \frac{s^2C_1C_2R_1}{s^2C_1C_2R_1 + sC_2 + g_{m1}g_{m2}R_1} \tag{8}$$

$$\frac{I_{\text{BS}}}{I_{\text{in}}} = \frac{I_{\text{HP}} - I_{\text{LP}}}{I_{\text{in}}} = \frac{s^2C_1C_2R_1 + g_{m1}g_{m2}R_1}{s^2C_1C_2R_1 + sC_2 + g_{m1}g_{m2}R_1} \tag{9}$$

$$\frac{I_{\text{AP}}}{I_{\text{in}}} = \frac{I_{\text{HP}} - I_{\text{BP}} - I_{\text{LP}}}{I_{\text{in}}} = \frac{s^2C_1C_2R_1 + g_{m1}g_{m2}R_1}{s^2C_1C_2R_1 + sC_2 + g_{m1}g_{m2}R_1} \tag{10}$$

The current outputs of LP, BP, and HP responses are through R_2, R_1, and C_1, respectively. The band-stop response is obtained by the difference between the high-pass and low-pass current output currents. The all-pass response is obtained by the difference between the high-pass, band-pass, and low-pass current output currents.

3 Simulation and Theoretical Result

The VM universal filter in Fig. 2 is simulated with Cadence OrCAD PSpice. The main analog building block is the commercially available IC LT1228, which is a combination of a current feedback amplifier and transconductance. The supply voltage is $\pm$ 5 V, and there is a DC bias current (I_{set}) which is externally controlled by the user.

To design the voltage-mode filter for a cutoff frequency of $f_0 = 1.59$ MHz and a quality factor $Q = 1$, the values of the components are taken as $C_1 = C_2 = 100$ pF and $R_1 = 1$ KΩ. The DC bias current is used as $I_{set1} = I_{set2} = 100$ μA, which can be externally electronically tunable without changing the other component. The input and output combinations of the voltage-mode filter realization are mentioned in Table 1. In the figures, the dashed line is the theoretical result, and the solid line is the simulation result. As shown in Fig. 4, the output responses V_{out1} and V_{out2} with respect to V_{in1} are band pass and low pass. Figure 5 depicts the high-pass and band-pass responses of V_{out1} and V_{out2} to V_{in2}. As shown in Figs. 6 and 7, the output responses V_{out1} to V_{in3} and V_{in4} are low pass and band pass, respectively. Figure 8 shows the band-stop response V_{out1} with respect to a combination of the inputs V_{in2} and V_{in3}. The all-pass and low-pass responses at V_{out1} and V_{out2} with respect to the combination of the inputs V_{in1}, V_{in2}, and V_{in3} are shown in Fig. 9. Figure 10 shows the band-stop and low-pass responses V_{out1} and V_{out2} with respect to a combination of the inputs V_{in1}, V_{in2}, V_{in3}, and V_{in4}. The gain and phase response of all-pass filter is shown in Fig. 11. The frequency of the filter can be electronically tunable by DC bias currents (I_{set1} and I_{set2}) as shown in Fig. 12.

The CM universal filter in Fig. 3 is simulated with Cadence OrCAD PSpice. To design the current-mode filter for a pole frequency of $f_0 = 1.59$ MHz and $Q = 1$, the values of the components are taken as $C_1 = C_2 = 100$ pF and $R_1 = R_2 = 1$ KΩ. The DC bias current is used as $I_{set1} = I_{set2} = 100$ μA which can be electronically tunable. The simulated (solid line) and theoretical (dashed line) LP, HP, BP, and BS responses are shown in Fig. 13. Figure 14 shows the all-pass output response.

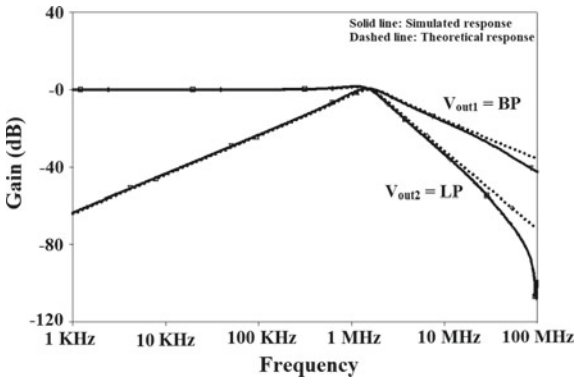

Fig. 4 Band-pass and low-pass responses (V_{out1} and V_{out2} versus V_{in1})

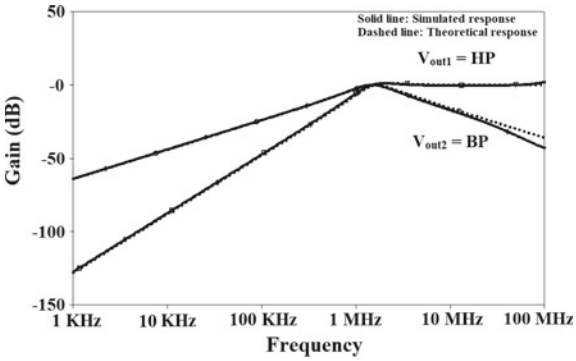

Fig. 5 High-pass and band-pass responses (V_{out1} and V_{out2} versus V_{in2})

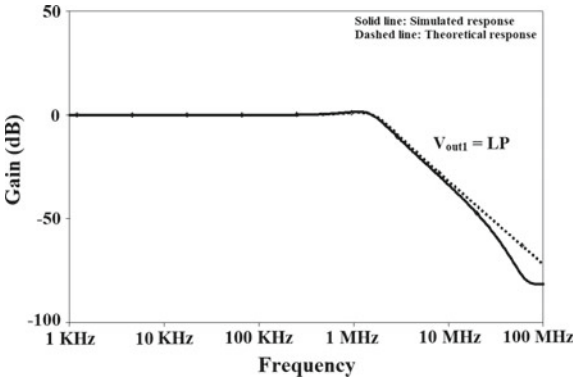

Fig. 6 Low-pass response (V_{out1} versus V_{in3})

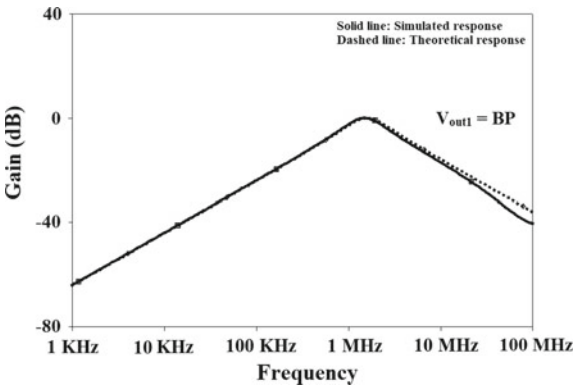

Fig. 7 Band-pass response (V_{out1} versus V_{in4})

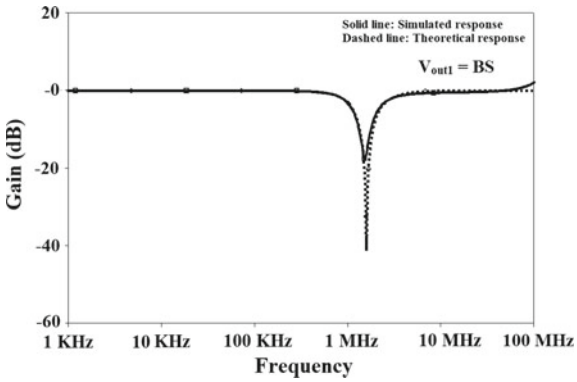

Fig. 8 Band-stop response

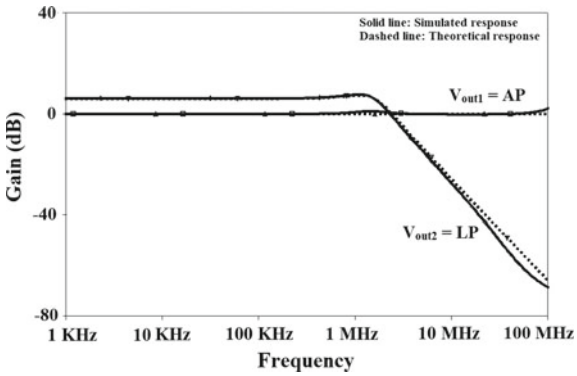

Fig. 9 All-pass and low-pass responses

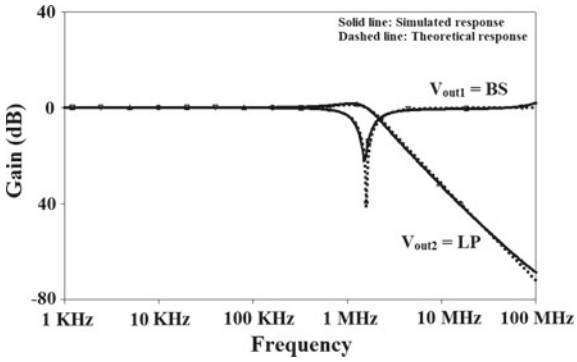

Fig. 10 Band-stop and low-pass response

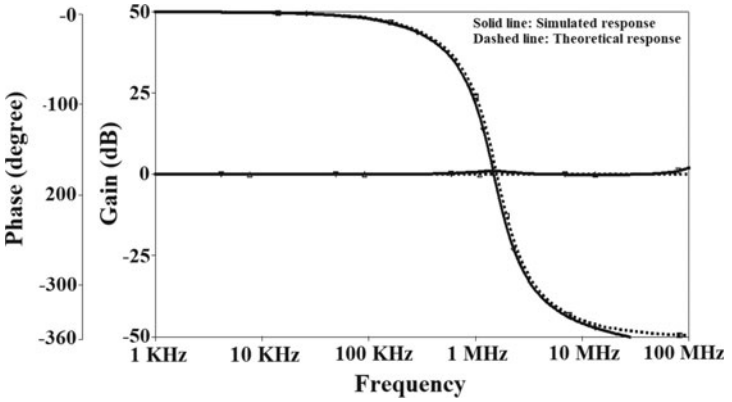

Fig. 11 Gain and phase response of all pass

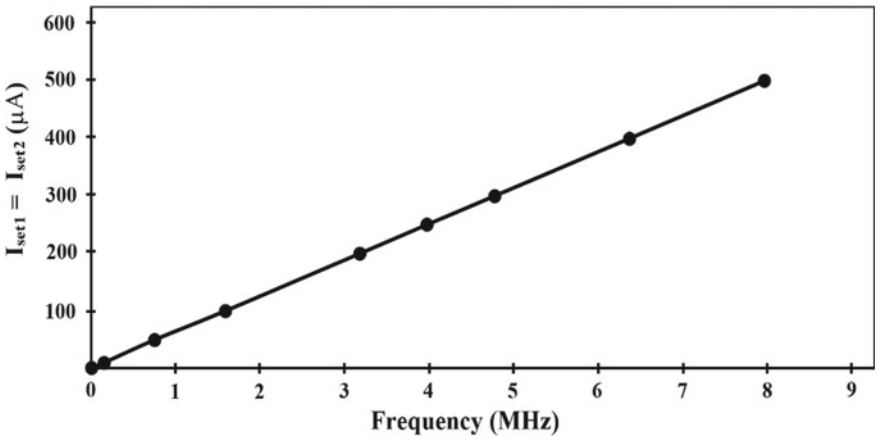

Fig. 12 Frequency versus DC bias current (I_{set})

4 Conclusion

VM and CM filters have been presented using IC LT1228, capacitors, and resistors. VM and CM filters can realize the high-pass, low-pass, band-pass, band-stop, and all-pass responses from the different combinations of the inputs. Bias currents can be used to electronically adjust the filter parameters. PSpice simulation results authenticate the theoretical results.

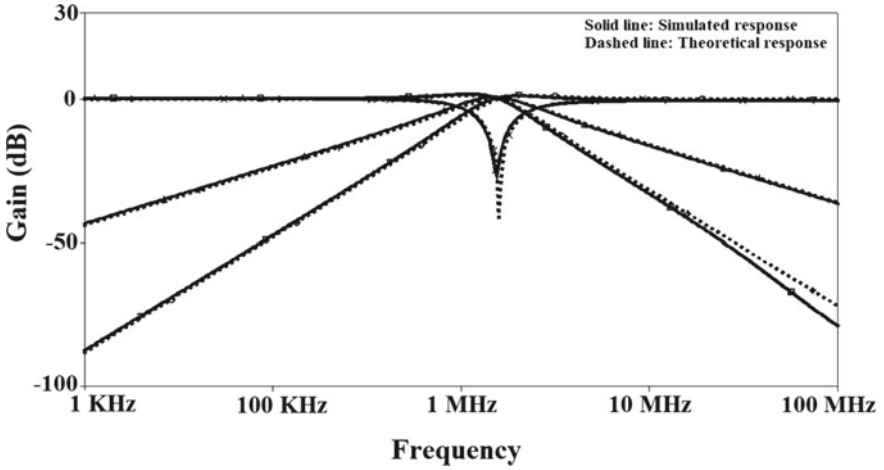

Fig. 13 LP, HP, BP, and BS responses

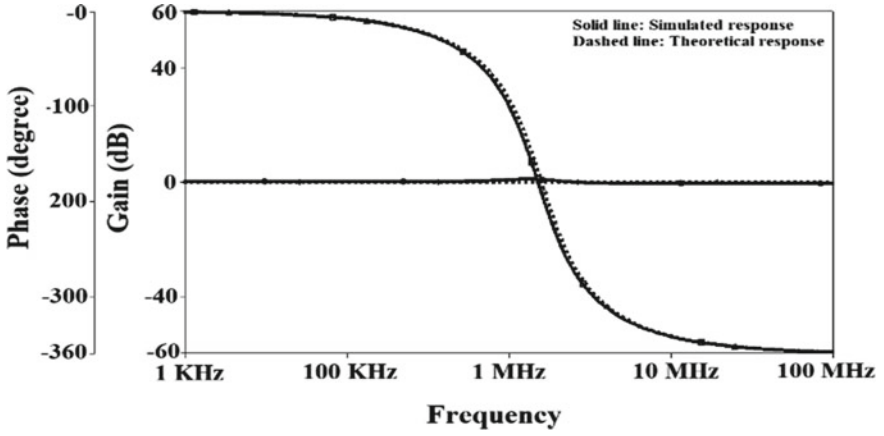

Fig. 14 Gain and phase response of AP

References

1. Siripongdee S, Jaikla W (2017) Electronically controllable grounded inductance simulators using single commercially available IC: LT1228. AEU-Int J Electron Commun 76:1–10
2. Angkun K, Kaew-on R, Silapan P (2021) A square wave and sinusoidal quadrature Oscillator based-on LT1228. In: 18th international conference on electrical engineering/electronics, computer, telecommunications and information technology (ECTI-CON), pp 833–836
3. Kushwaha AK, Kumar A (2019) Sinusoidal oscillator realization using band pass filter. J Inst Eng (India) Series B Springer 100:499–508
4. Chanapromma C, Worachak T (2012) Electronically controlable gain and dynamic range positive/negative half-wave rectifier using FD and SE OTAs based on commercially available ICs. In: International symposium on communications and information technologies (ISCIT), pp 38–41

5. Siripongdee S, Jaikla W (2017) Universal filter using single commercially available IC: LT1228. In: MATEC web of conferences vol 95, pp 1–4
6. LT1228–100 MHz Current Feedback Amplifier with DC Gain Control, Linear Technology Corporation. http://www.linear.com/product/LT1228.pdf
7. Klungtong S, Thanapatay D, Jaikla W (2017) Three-input single output voltage-mode multi-function filter with electronic controllability based on single commercially available IC. Active Passive Electron Compon, pp 1–10
8. Wang SF, Chen HP, Ku Y, Yang CM (2019) Independently tunable voltage-mode OTA-C biquadratic filter with five inputs and three outputs and its fully uncoupled quadrature sinusoidal oscillator application. AEU-Int J Electron Commun, vol 110

Detection of Hovering Helicopter Using Ground-Based Radars

A. R. Vandana and M. Arokiasamy

Abstract Detection of hovering helicopters is of prime importance to the military sector given the destructive capabilities of them. A method is described to detect the hovering helicopter using conventional radar waveforms. This method is suitable for radars where dwell time is very crucial. The method described in this paper identifies the existence of the helicopter using search beam and then computes blade flash frequency using confirmation beam.

Keywords Hovering helicopter · Even bladed · Odd bladed · Blade flash frequency · Dwell time · Conventional radar waveform

1 Introduction

The main radar subsystem consists of antenna, transmitter, receiver, signal processor and display. The transmitter transmits the signal, while the receiver receives the reflected echo from the target. Processing of reflected echo is done at signal processor. Processed output from signal processor is presented at display. The antenna system referred in this algorithm is active phased array antenna. This paper discusses the method/algorithm to detect the hovering helicopter which needs to be implemented at signal processor subsystem of the radar. The reflected echo signal from the helicopter consists of the returns from the body, main and tail rotors of a hovering helicopter [1]. The type of the hovering helicopter can be determined by the processed output such as blade flash width and blade flash frequency. These parameters give us information regarding the blade length, frequency of rotation of the blades and parity of the blades. To differentiate the helicopter from the cluttered environment, the proposed algorithm uses the Doppler shift generated due to the rotation rate of the blades that are utilized [2]. The reflection from the rotors gives rise to both positive and negative Doppler shifts depending upon the orientation of the blades with respect to the radar.

A. R. Vandana (✉) · M. Arokiasamy
LRDE, DRDO, Radar III, Bangalore, India
e-mail: vandana.ar.lrde@gov.in

S. Rawat et al. (eds.), *Proceedings of Second International Conference on Computational Electronics for Wireless Communications*, Lecture Notes in Networks and Systems 554,
https://doi.org/10.1007/978-981-19-6661-3_2

2 Radar Echo of a Hovering Helicopter

Radar echo can be modelled as a combination of reflections from three parts of the helicopter, namely hub echo, main rotors and tail rotors. The reflections from the main rotor are very useful in the detection of a hovering helicopter [3]. The amplitude of reflections from the tail rotor is of almost negligible [4, 5]. To see the complete radar echo of a hovering helicopter, one needs to look for a dwell time of 0.05 to 0.1 s and PRF of 20 to 40 kHz. The expected Doppler is spread across Doppler bins. But in conventional radar, such a dwell time and PRF are not used. Hence, detection of hovering helicopter becomes difficult or nearly impossible. In this paper, an approach is discussed for detection of helicopter using conventional radar waveform. Radar waveform in this paper refers to the operational PRF and dwell time. Figure 1 shows the time domain plot of even bladed hovering helicopter. Figure 2 shows the time domain response of odd bladed helicopter. The difference in plot is due to the symmetric and asymmetric placement of the blades. The even bladed helicopter consists of rotors that are diametrically opposite to each other with an angular spacing of.

$$\alpha = 2\pi/N \tag{1}$$

where N is the number of blades. The blade flashes occur when the front end of one blade and the rear end of its diametrically opposite blade are orthogonal to the radar radial vector.

Thus, the blade flashes will be a combination of the flashes from both the blades. For an even bladed helicopter, the overall blade flash pattern will be spikes of equal amplitude occurring in equal time intervals as shown in Fig. 1. The blade flashes frequency is given by $B = N * \text{Ro}$, where N is the number of blades. The duration of blade flash (t) is given by

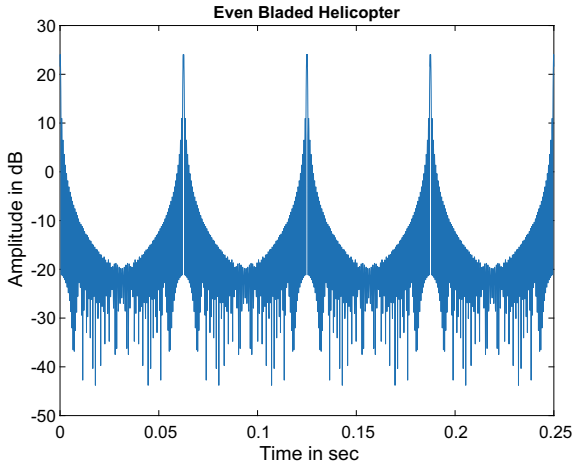

Fig. 1 Time domain response for even bladed helicopter

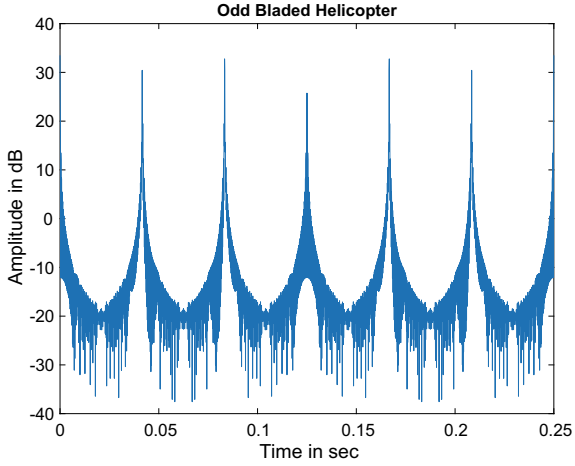

Fig. 2 Time domain response for odd bladed helicopter

$$t = \lambda/(2 * \text{pi} * \text{Ro} * L) \tag{2}$$

where Ro is rotation rate (Hz), L is blade length, and λ is wavelength.

The odd bladed helicopters consist of rotors that are not diametrically opposite to each other with an angular spacing as given by Eq. (1).

The blade flashes for an odd bladed helicopter differ as compared to an even bladed helicopter. Each blade of an odd bladed helicopter accounts for two sets of blade flashes with different amplitudes, one of higher amplitude than the other. For an odd bladed helicopter, the overall blade flash pattern will be spikes of different amplitudes symmetrically as shown in Fig. 2. Given the number of blades and the rotation rate Ro (Hz), the blade flash frequency for an odd bladed helicopter is given by $B = 2 * N * R_{o.}$ The time duration of each blade flash is given by Eq. (2). Figures 3 and 4 show the frequency domain response for even bladed and odd bladed helicopter. The amplitude variations in Figs. 1 and 2 are due to the fluctuating radar cross section (RCS) of the rotating blades (Figs. 3 and 4).

3 Recognition of Hovering Helicopter Using Conventional Radar Waveform

Figures 5 and 6 show the time domain and frequency domain response of even bladed helicopter using conventional radar waveform with PRF of 1 kHz and dwell time of 64 ms. Figures 7 and 8 show the time domain and frequency domain response of odd bladed helicopter for PRF of 1 kHz and dwell time of 32 ms. Figures 9 and 11 show the range Doppler response of helicopter and aircraft, respectively. It can be seen from Fig. 9 that there is a spread in Doppler due to the rotation of helicopter blades. The Doppler spread is circled for visibility. 3D view of Fig. 9 is shown in Fig. 10 for

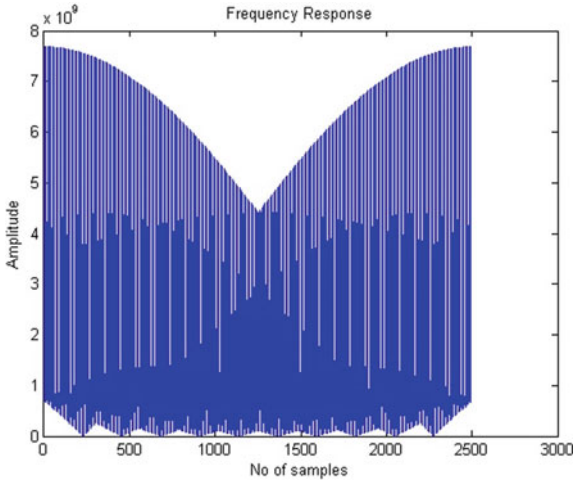

Fig. 3 Frequency domain response for even bladed helicopter

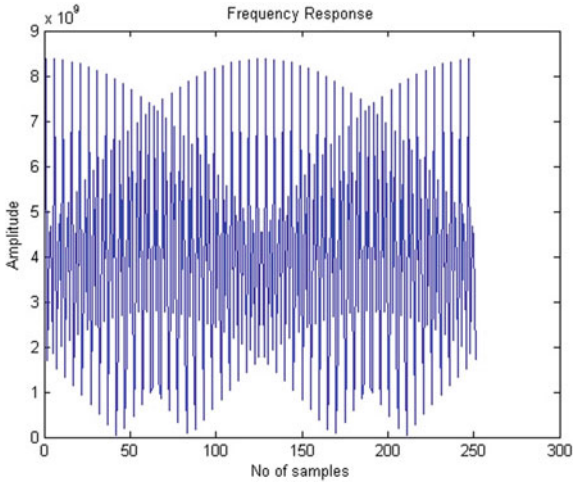

Fig. 4 Frequency domain response for odd bladed helicopter

better clarity on Doppler domain response. 3D view of Fig. 11 is shown in Fig. 12 for better clarity on Doppler domain response.

Many literatures have discussed methods for helicopter detection. In [10], STFT and tunable Q-factor wavelet transform are used. In [11], algorithm which differentiates periodic signal by correlation function is presented. In [12], knowledge of antenna beam shape, hub echo and fuselage echo allows detection of helicopter with short time on target. In this paper, a method is discussed to detect the hovering helicopter using conventional radar waveform. Figure 13 shows the flow chart of the same, which uses search beam and confirmation beam.

The proposed method checks for Doppler spread using predefined threshold. If there is a Doppler spread, a confirmation beam is played with the PRF of 10 kHz and

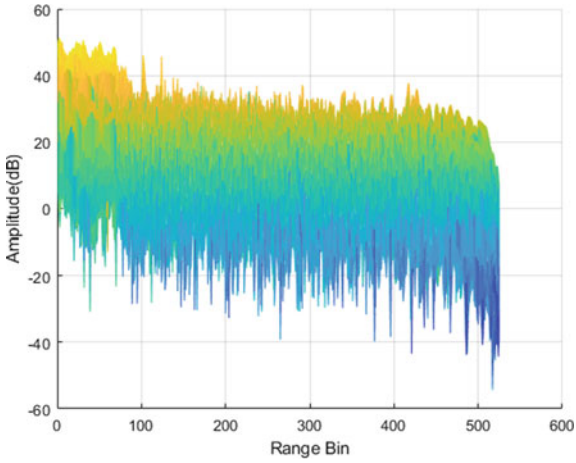

Fig. 5 Time domain response for even bladed helicopter

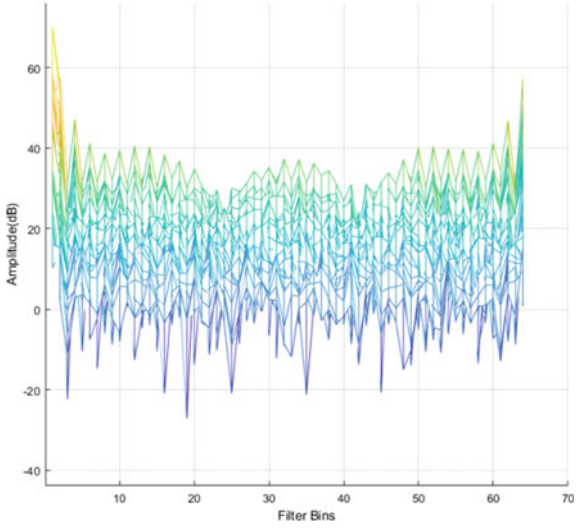

Fig. 6 Frequency domain response for even bladed helicopter

dwell time of 128 ms. The dwell data obtained from confirmation beam is used to compute the blade flash duration. Figures 14 and 15 show the time domain plot for a confirmation beam with dwell time of 128 ms and PRF of 10 kHz of even bladed and odd bladed helicopter, respectively. FFT output is compared with plots shown in Figs. 3 and 4 to declare the presence of even or odd bladed hovering helicopter.

By comparing the above computed information (i.e. odd or even bladed helicopter and blade flash duration) with the database of the available helicopter, one can detect the rate of rotation, blade length and number of blades. This detection algorithm was successfully tested using real test data. Table 1 shows the comparison between

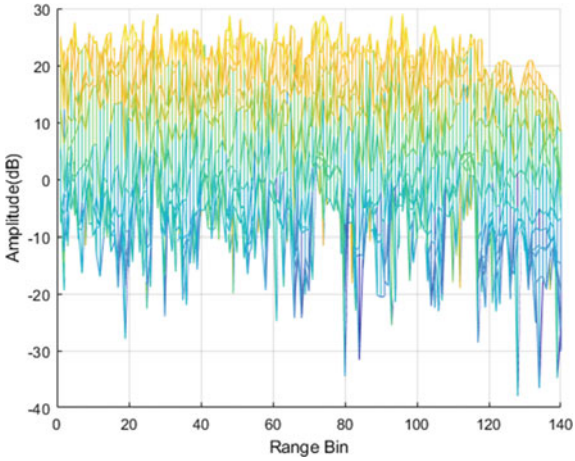

Fig. 7 Time domain response for odd bladed helicopter

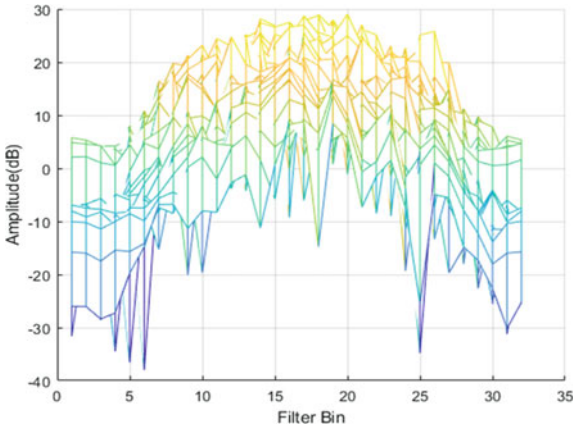

Fig. 8 Frequency domain response for odd bladed helicopter

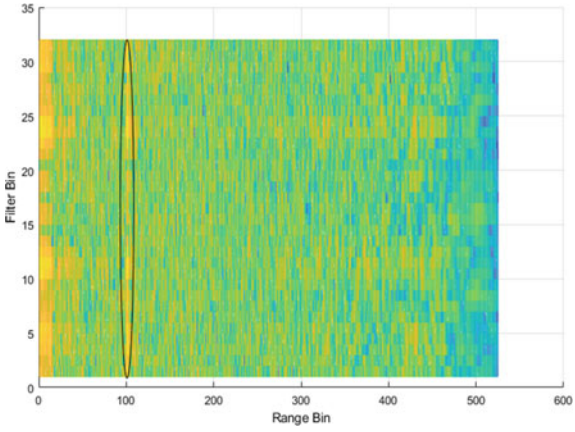

Fig. 9 Range Doppler response of helicopter

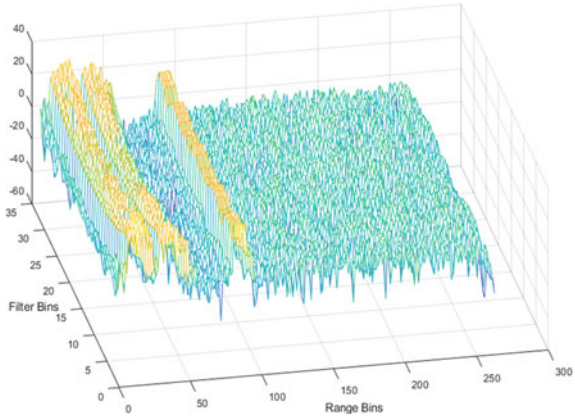

Fig. 10 3D view of Fig. 9

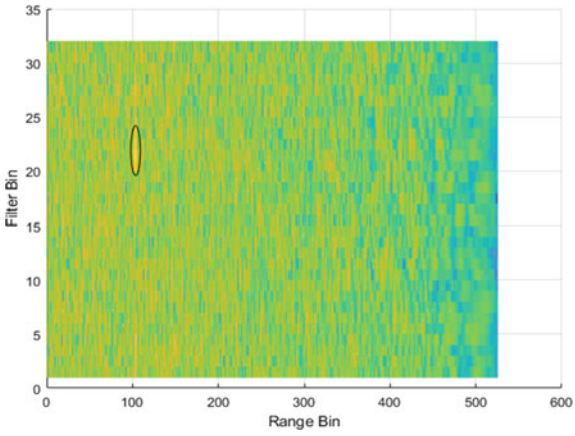

Fig. 11 Range Doppler response of aircraft

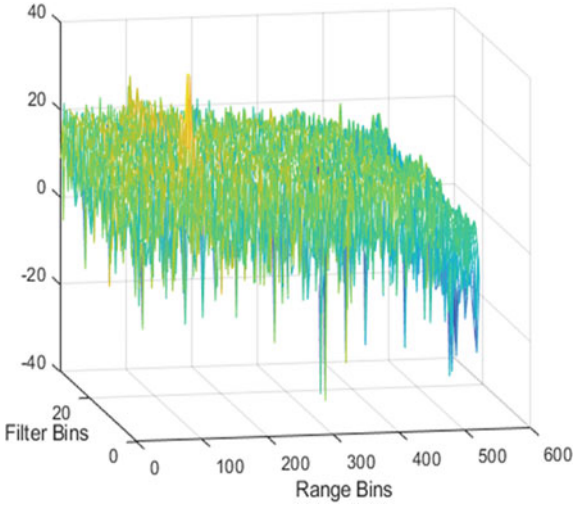

Fig. 12 3D view of Fig. 11

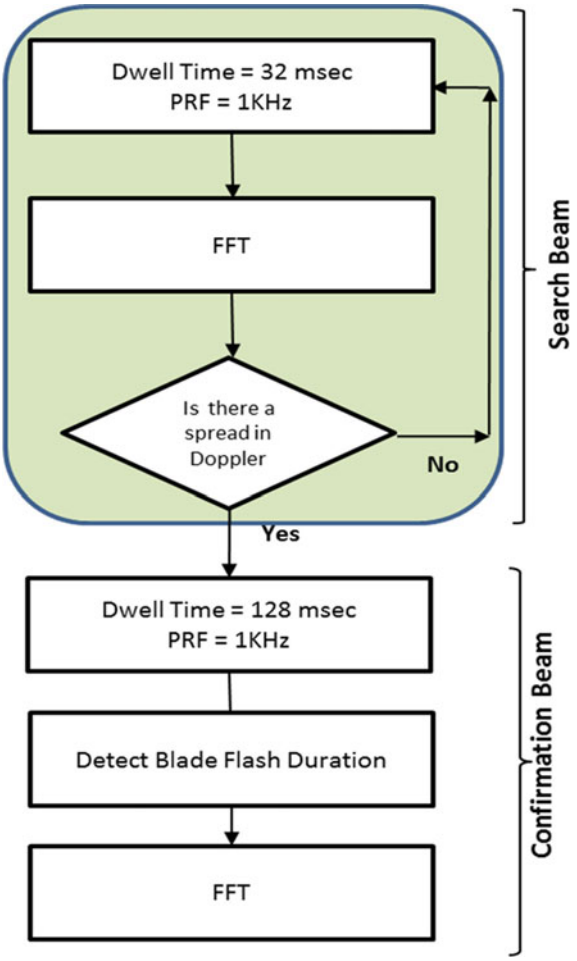

Fig. 13 Flow chart of hovering helicopter detection method

calculated value and expected value of some major parameters using test helicopter data.

4 Conclusion

The above-mentioned detection scheme using time and frequency domain analysis has good performance over a wide range of allowable noise values and different helicopter parameters. The previous algorithms [6–9] for detection of hovering helicopters are probabilistic in nature which may lead to faulty conclusions. This paper provides a method for the successful detection of blade flash of a hovering helicopter using conventional radar waveforms.

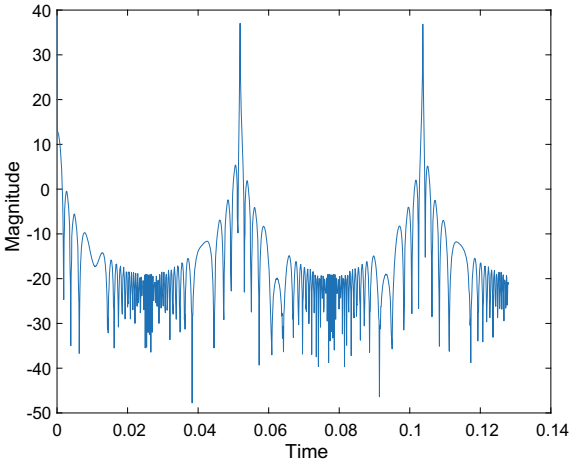

Fig. 14 Time domain response for even bladed helicopter

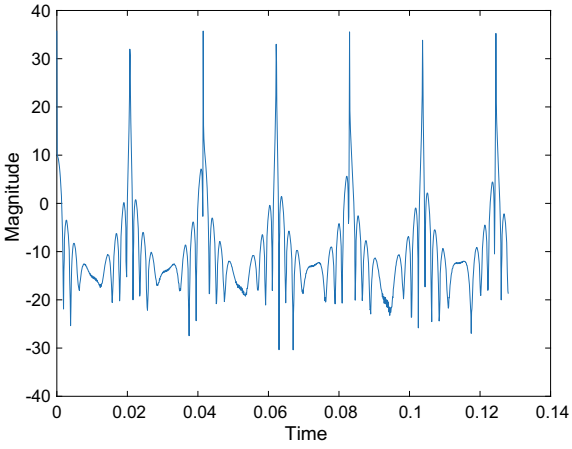

Fig. 15 Time domain response for odd bladed helicopter

Table 1 Comparison between calculated value and expected value of various parameters

	Rate of rotation (Hz)	Blade length (m)	Number of blades
Calculated value	5.40	15	4
Expected value	5.24	15	4

References

1. Tait P (2005) Introduction to radar target detection, 3rd edn. IET 2005 technology and engineering
2. Skolnik MI (2001) Introduction to Radar Systems, 3rd edn. Mc Graw Hill
3. Melino R, Bourne C, Tran HT (2011) Modeling helicopter radar backscatter, DSTO-TR-2547, DSTO Australia-formal Reports, June 2011
4. Johnsen T, Olsen KE, Gundersen R (2003) Hovering helicopter measured by bi/multi static CW radar, Detection and classification Issues, Defence Norwegian Research Establishment, Radar Conference, 5–8th May 2003. In: Proceedings of 2003 IEEE, pp 165–170
5. Cilliers A (2010) Helicopter blade parameter extraction for purposes of radar target identification. Thesis to department of electrical engineering University of Cape Town-May 2010
6. Gini F, Farina A (1999) Matched subspace CFAR detection of hovering helicopters. IEEE Trans Aerosp Electron Syst vol 35, No 4 October 1999.
7. Ziyue T, Yongliang W, Zhiwen W (2000) STAP scheme to detection of hovering helicopters. In: Proceedings of ICSP 2000
8. www.boeing.com/defense
9. www.bellhelicopter.com/military.
10. Nguyen DD, Nguyen STN, Melino R, Kodituwakku S, Tran H-T (2018) Radar detection of helicopter at low SNR using time-frequency transforms. DST-Group-TR-3481, April 2018, Australian government department of defence science and technology
11. Monakov AA (2021) Radar detection and recognition of a hovering helicopter. In: WECONF-2021
12. Point G, Degurse JF, Savy L, Milin JL, Montecot M (2019) Parametric modelling of the radar signature of helicopter. In: International radar conference 2019

A Low Profile Double Notched UWB Antenna with Asymmetric Coplanar Strip for Wireless Applications

Thadagoni Pranay Kumar, MD. Rehana, and CH. Ramakrishna

Abstract In this research, a low profile double notched UWB antenna with an asymmetric coplanar strip is proposed for wireless applications. A compact high isolation ACS fed UWB antenna has a semi-circle shaped radiating patch with a semi-circle shaped slot and U-shaped slots are used for coverage of the entire UWB band with double notch. The total dimension of the proposed antenna is 40 × 40 × 3.2 mm^3. It has good radiation characteristics over entire frequency band. The UWB antenna has a frequency range of 2.9 to 11.8 GHz and a 121% impedance bandwidth. The proposed ACS fed double notched antenna achieved notch bands at WiMAX (2.9–3.6 GHz) and WLAN (5.5–6.5 GHz). By etching semi-circle slot on the patch and U-slot on the micro-strip line are realized correspondingly. The fabricated MIMO UWB antenna has a low envelop correlation coefficient of ≤0.20.015 channel capacity loss of ≤ 0.2 bits/sec/Hz, high isolation ≥0.215 dB and good impedance match.

Keywords ACS fed · Band notch · High isolation · MIMO antenna · UWB antenna

1 Introduction

Everyday life wireless technology devices have been developing into an integral part of human's. Wireless technology facilitates consumer's right to use wide frequency band of services. Consecutively to accomplish high data rate with inadequate resources and limitations, to achieve these issue one of the promising wireless technology was the UWB communication. The printed UWB monopole antenna is more appropriate intended for smaller hand held devices. In such devices, smallest amount distortion and protect the shape of the pulse are main requirements. It has been designed a UWB antenna with band notched features. To avoid interference between UWB system with WiMAX and WLAN, filters are needed. As per FCC

T. P. Kumar (✉) · MD. Rehana · CH. Ramakrishna
Vardhaman College of Engineering, Hyderabad, India
e-mail: thadagonipranaykumar@gmail.com

S. Rawat et al. (eds.), *Proceedings of Second International Conference on Computational Electronics for Wireless Communications*, Lecture Notes in Networks and Systems 554,
https://doi.org/10.1007/978-981-19-6661-3_3

regulations [1], UWB antenna should be attain at least 500 MHz bandwidth or at least 20% fractional bandwidth. UWB antenna wants designate serviceable from 3.1 to 10.6 GHz band. UWB antenna with dual and triple notch band characteristics is discussed [2–5]. Two planar antennas are placed perpendicular to each other to improve the isolation and impedance bandwidth of the UWB antenna. [6]. CLFS surface employed to accomplish broadband radiation characteristics with circular arc decoupling structures [7]. High isolation was accomplished nearly placed antennas [8], from the linear UWB-MIMO antenna array, polarization diversity and high isolation are realized due to radiators are 90° to each other [9]. A novel UWB quasi-self-complementary antenna polarization diversity characteristics, anti-interference and high isolation achieved without additional decoupling technique [10].

A four elements frequency reconfigurable UWB antenna is achieved using PIN diodes [11] and stepped slot for band rejection [12]. The compact MIMO UWB antenna has a low coupling of ≤ -20 dB over the UWB range. The dual polarized eight port MIMO antenna achieved a UWB band used looping structure [13]. High isolation dual bands are notched due to T-shaped stub, L-shaped stub [12] and J-shaped slits are used to reject band [14] and L-shaped slits. Low correlation due to the orthogonal arrangement of elements in the compact planar printed wideband MIMO antenna [15]. Eight port antenna array realized with zero envelope correlation coefficient and 100% efficiency [16] due to the square loop radiating strips are asymmetrically placed at the corners. UWB antenna fed by a coplanar waveguide with three notch bands were achieved by a π and T-shaped slits embedded on to the split ring patch [17]. This paper describes an ACS fed UWB monopole antenna with double band characteristics are presented. The propose MIMO UWB antennas are symmetrical and identical. The presented four-element UWB antenna is fabricated on FR4 substrate. The antenna parameters are S-parameters, diversity gain, ECC, MEG, radiation pattern and gain are simulated and measured. Remaining paper describes as follows. The structure of the MIMO UWB antenna and return loss and isolation characteristics are illustrated in Sect. 2.

2 ACS Fed MIMO UWB Antenna Structure

This proposed antenna was designed on a substrate with a thickness of 3.2 mm and a dielectric constant of 4.4, as shown in Fig. 1a. From the antenna 1, the semi-circle radiating patch is fed with 50Ω impedance micro-strip line, beside Asymmetric coplanar strip to accomplish an impedance bandwidth from 2.9 GHz to 11.8 GHz. From Fig. 1b, the presented antenna with single band notched by WiMAX (2.9–3.6 GHz) be attained with the semi-circle slot on the semi-circle radiating patch. From Fig. 1c, the proposed antenna among single band notched at WLAN (5.5–6.5 GHz) be attained with the U-shaped slot on the micro-strip line. From Fig. 1d,

the presented antenna with dual band notches at WiMAX (2.9–3.6 GHz) and WLAN (5.5–6.5 GHz) are achieved with the semi-circle slot and U-shaped slot, respectively. Table 1 illustrates the geometry specifications of the proposed antenna.

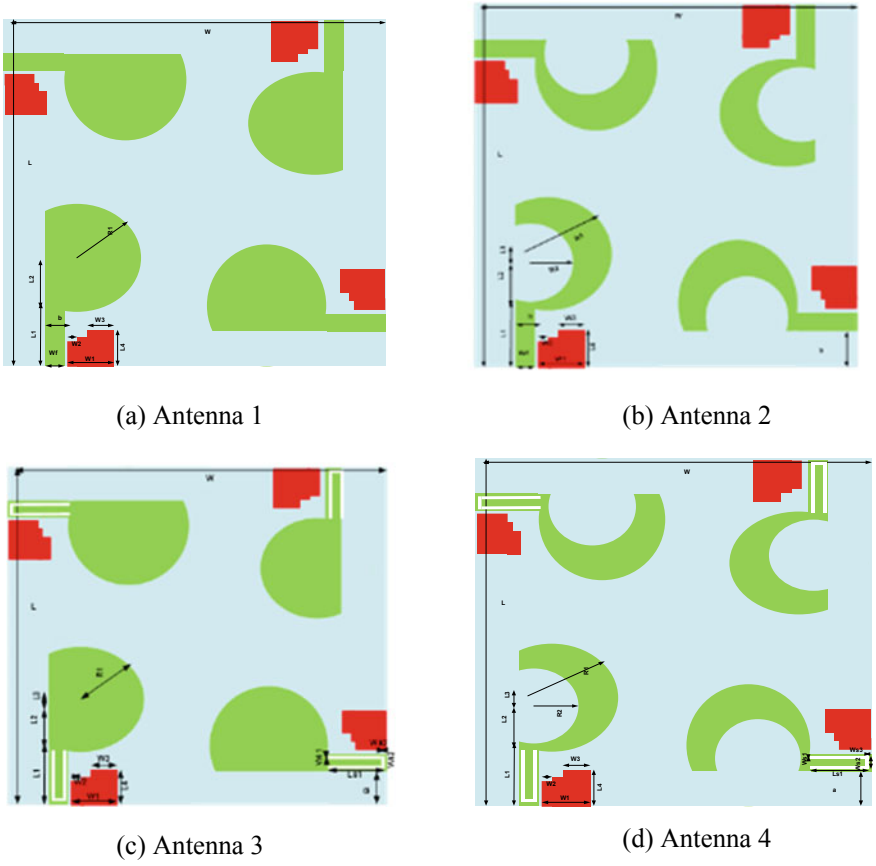

(a) Antenna 1 (b) Antenna 2

(c) Antenna 3 (d) Antenna 4

Fig. 1 Structure of proposed antenna

Table 1 Antenna optimized dimensions

L	*W*	*L*1	*L*2	*R*1	Wf	*B*	Ws1	Ws
40	40	9.4	5.9	8.1	1.45	2.15	0.2	1.45
*W*2	*W*3	*L*4	Ls1	L3	*a*	*W*1	Ws3	*R*2
0.5	3.4	6	6.5	2.8	2.15	4.6	0.45	5.2

3 Proposed Antenna Performance Parameters and Antenna Characteristic

Figure 2 shows that the antennas covers an UWB frequency band (2.9–11.8 GHz), to remove existing frequency bands WiMAX (2.9–3.6 GHz) and WLAN (5.5–6.5 GHz) from the UWB band. Semi-circle slot and U-slots are etched from the patch and micro-strip line, respectively. Similarly, for this entire frequency band maintains VSWR $\leq$2, except at notched frequency bands and realized isolation is less than $-$ 15 dB. Figures 3 and 4 show the measured and simulated results of two dimensional radiation patterns in xy plane, yz plane and xz planes at 5 GHz and 10 GHz. So, the gain-theta is cross polarization and gain-phi is the co-polarization. The major beam radiation from the xy plane is along the end-fire direction, with maximum radiation at the 150° and 210°. The simulated values are in line with the measured results, it will demonstrate the accuracy of the design. The presented antenna simulated and measured gain characteristics with port1 (M1) excitation are shown in Fig. 7b. And peak gain achieved by the presented antenna is 6.9 dB. It can be seen that at notch frequencies, the gain drops dramatically. From Fig. 5a, the proposed MIMO UWB monopole antenna realized above 80% except at band notch frequencies. From Fig. 6, it is observed that for MEG1 with respect to MEG2, MEG3 and MEG4 are identical and the value of mean effective gain (MEG) of the designed antenna is less than 3 dB. So it satisfies the equality criterion for the two antennas.

ECC is used to find diversity between elements of presented MIMO antenna. For good diversity, any MIMO antenna envelop correlation coefficient should be below 0.5. Figure 5b, envelop correlation coefficient of MIMO UWB antenna with $M1$ and $M2$, $M1$ and $M3$, $M1$ and $M4$ can be measured. The proposed MIMO UWB simulated and measured value is $\leq$ 0.015 in the entire UWB frequency band except notch band frequency. So fine diversity achieved by the proposed ACS fed MIMO UWB antenna. The signal-to-noise ratio is improved by increasing the diversity gain. The proposed antenna diversity gain was derived using Eq. (1). From Fig. 7a, the simulated and experimental results are correctly inline. And it is observed that

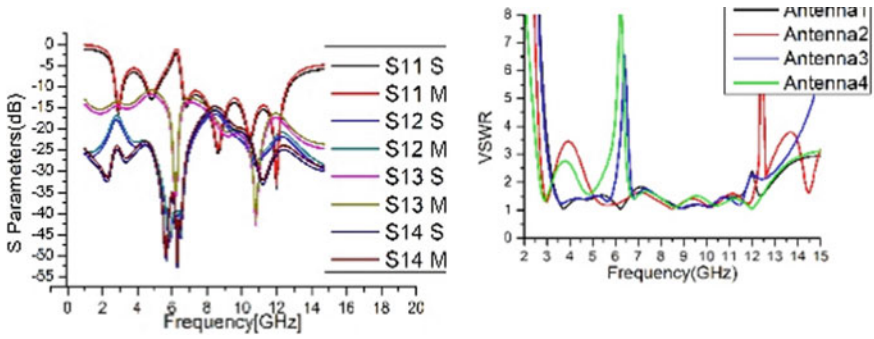

Fig. 2 Proposed MIMO UWB monopole antenna return loss and VSWR

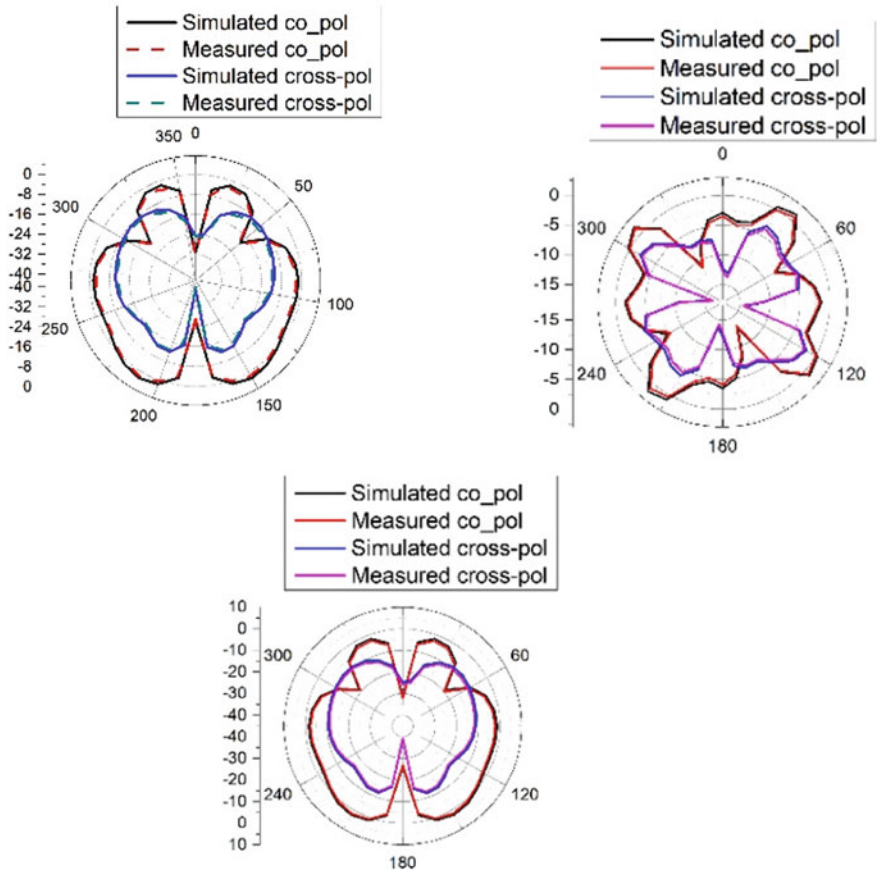

Fig. 3 MIMO UWB monopole antenna radiation characteristics at 10 GHz

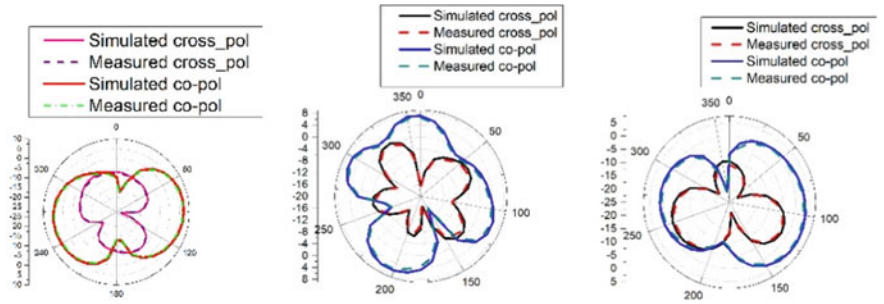

Fig. 4 MIMO UWB monopole antenna radiation characteristics at 5 GHz

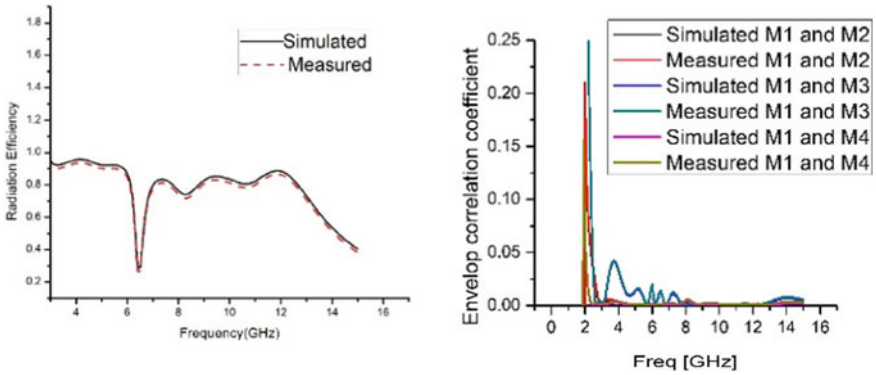

Fig. 5 Radiation efficiency and ECC of the designed antenna

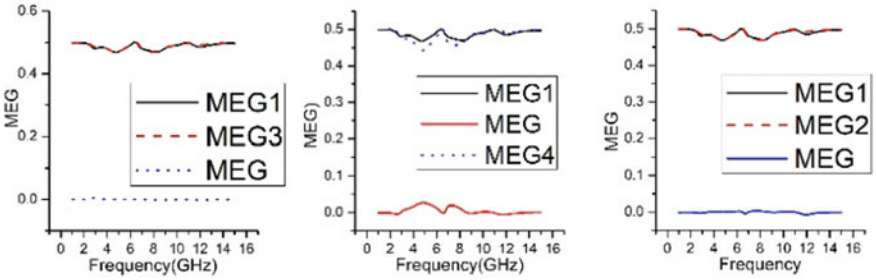

Fig. 6 Mean effective gain of the presented MIMO UWB monopole antenna

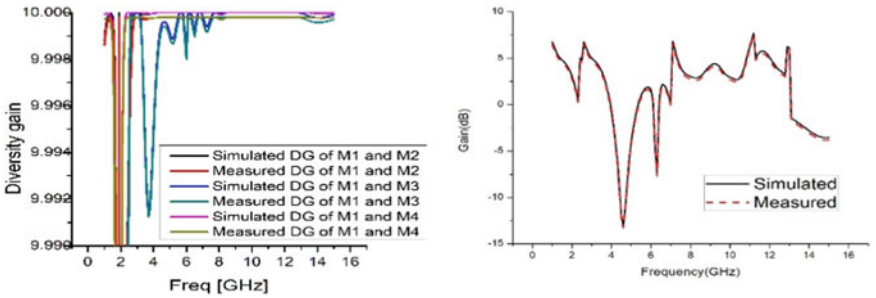

Fig. 7 Proposed MIMO UWB monopole antenna diversity gain. And the peak gain proposed MIMO UWB monopole antenna

diversity gain fluctuations at notch bands. For all four elements, diversity gain is greater than 9.99.

$$\mathrm{DG} = 10 * \sqrt{1 - \mathrm{ECC}^2} \tag{1}$$

From Fig. 8a, TARC is the performance constraint of the MIMO antenna. It relates input power to the total outgoing power in and two-port. It is directly computed from the scattering matrix. From Fig. 8b, the overall group delay values are $\leq$ 2 ns. The delay between port1 and port1 is given by group delay (1, 1). Correspondingly for group delay (1, 2), group delay (1, 3) and group delay (1, 4). And also observed that group delays are symmetrical and identical. For MIMO antenna, channel capacity loss [4] is performance parameter. It is observed from Fig. 9a that CCL is $\leq$ 0.2bits/sec/Hz except at notches.

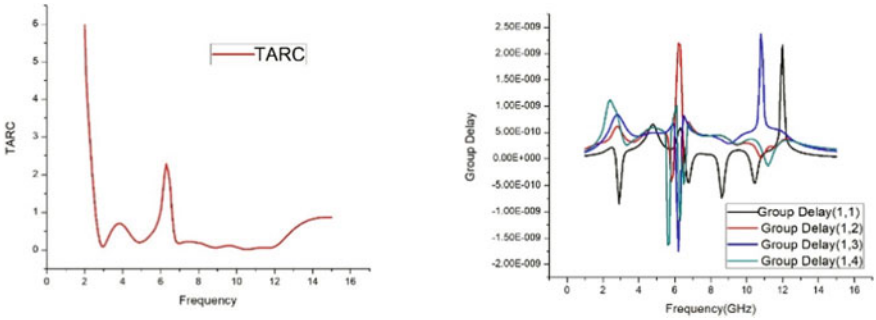

Fig. 8 TARC of the designed monopole antenna and group delay of the designed MIMO UWB monopole antenna

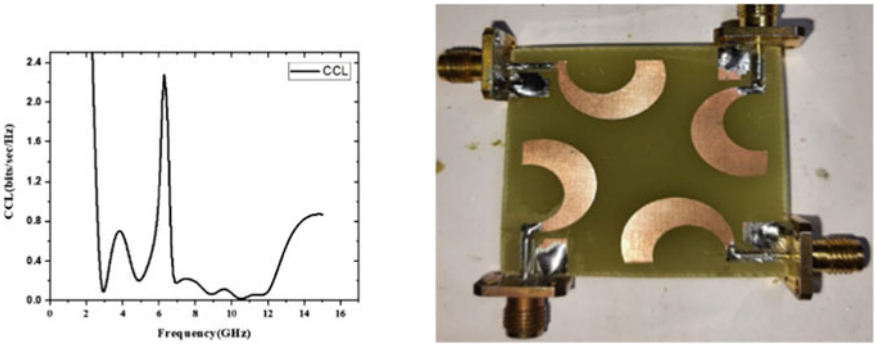

Fig. 9 Channel capacity loss of the proposed antenna and the fabricated proposed antenna

Table 2 Comparison between proposed antennas with existing systems

References	Size (mm^3)	Ports	Operating band (GHz)	Notch bands (GHz)	MEG	ECC	CLL	Gain (dBi)	Isolation (dB)
[18]	27 × 30 × 0.8	2	3–11	3.3–3.7, 5.15–5.18	NA	≤0.015	NA	NA	>20
[12]	50 × 39.8 × 1.524	4	2.7–12	4.8–6.2	NA	≤0.025	NA	5.5	>17
[15]	48 × 48 × 1.6	2	3.1–10.6	4.7–5.4	NA	≤0.03	NA	5.2	>20
[17]	31 × 43.4 × 0.8	2	2.93–20	5.1–5.8, 6.7–7.1	NA	≤0.01	NA	6.5	>22
[19]	18 × 34 × 1.6	2	2.9–11.6	5.3–5.8, 7.85–8.55	NA	≤0.02	NA	4.2	>16
[20]	60 × 60 × 1.6	4	2.3–13.7	3.25–3.75, 5.08–5.95, 7.06–7.95	NA	≤0.02	NA	3.2	>22
[21]	26 × 26 × 0.762	4	3–16.2	5.1–5.6, 7.3–9.1	NA	≤0.3	NA	8.4	>17.4
[2]	39 × 39 × 1.6	4	2.7–12	5.1–5.9	NA	NA	NA	5.5	>17
[3]	80 × 80 × 1.6	4	2.1–20	3.3–4.1, 8.2–8.6	NA	≤0.02	NA	5.8	>25
Proposed work	40 × 40 × 3.2	4	2.9–11.8	2.9–3.6,5.125–6.25	≤0.05	≤0.015	≤0.2	6.9	>17

4 Conclusion

In this paper, ACS fed UWB monopole antenna for ultra-wideband applications is presented. The proposed antenna has achieved a dual notch bands with a fractional bandwidth of 10.7 and 8.3% and operates throughout 2.9 to 11.8 GHz with 121% of a fractional impedance bandwidth. Its performance has been obtained by experimentally. This achieves a 2:1 VSWR bandwidth from 2.9 to 11.8 GHz with a maximum radiation efficiency of 95% and the peak gain of 6.9 dB.

Acknowledgements We would like to thank the resource providers from Keysight-Advanced Vardhaman college of Engineering RF Microwave and Wireless Communications Centre of Excellence, the Ansys software company. For this work, the HFSS software is widely used to generate simulations.

References

1. Federal Communications Commission (2004) Bell Labs Tech J 9(1):1–1. https://doi.org/10.1002/bltj.20017
2. Tang Z, Wu X, Zhan J, Hu S, Xi Z, Liu Y (2019) Compact UWB-MIMO antenna with high isolation and triple band-notched characteristics. IEEE Access 7:19856–19865
3. Rekha VSD, Pardhasaradhi P, Madhav BTP, Devi YU (2020) Dual band notched orthogonal 4-element MIMO antenna with isolation for UWB applications. IEEE Access 8:145871–145880
4. Ramakrishna CH, Satish Kumar GAE, Reddy PCS (2018) A coplanar compact monopole reconfigurable UWB antenna with band notches using pin diodes. In: 2018 international conference on smart systems and inventive technology (ICSSIT), pp 110–117. IEEE
5. Ramakrishna CH, Kumar GAE, Reddy P, Sekhar C (2021) Quadruple band-notched compact monopole UWB antenna for wireless applications. J Electromagnet Eng Sci 21(5): 406–416
6. Liu L, Cheung SW, Yuk TI (2013) Compact MIMO antenna for portable devices in UWB applications. IEEE Trans Antennas Propag 18(8):4257–4264
7. Khan MS, Capobianco A-D, Asif S, Iftikhar A, Braaten BD (2015) A 4 element compact ultra-wideband MIMO antenna array. In: 2015 proceedings IEEE international symposium on antennas and propagation, pp 1–2
8. Tang T-C, Lin K-H (2014) An ultrawideband MIMO antenna with dual bandnotched function. IEEE Antennas Wirel Propag Lett 13:1076–1079
9. Saleem R, Bilal M, Bajwa KB, Shafique MF (2015) Eight-element UWB-MIMO array with three distinct isolation mechanisms. IET Elect Lett 51(4):311–313
10. Khan MS, Capobianco A-D, Naqvi A, Ijaz B, Asif SM, Braaten BD (2015) Planar compact ultra-wideband polarisation diversity antenna array. IET Microw Antennas Propag 9(15):1761–1768
11. Zhu J, Li S, Feng B, Deng L, Yin S (2016) Compact dual-polarized UWB quasiself-complementary MIMO/diversity antenna with band-rejection capability. IEEE Antennas Wirel Propag Lett 15:905–908
12. Khan SM, Iftikhar A, Asif SM, Capobianco A-D, Braaten BD (2016) A compact four elements UWBMIMO antenna with on-demand WLAN rejection. Microw Opt Technol Lett 58(2):270–276
13. Anitha R, Vinesh PV, Prakash KC, Mohanan P, Vasudevan K (2016) A compact quad element slotted ground wideband antenna for MIMO applications. IEEE Trans Antennas Propag 64(10):4550–4553

14. Li M, Xu Z, Ban Y, Sim C, Yu Z (2016) Eight-port orthogonally dual-polarised MIMO antennas using loop structures for 5G smartphone. IET Microw Antennas Propag vol 11
15. Kang SW, Chang T-S (2018) Design of a planar monopole antenna with gap sleeve by half cutting method. Int J Microw Opt Technol 12(4), pp 274–278. Electromagn Res M vol 63, pp 119–129
16. Tang Z, Wu X, Zhan J, Xi Z, Hu S (2018) A novel miniaturized antenna with multiple band-notched characteristics for UWB communication applications. J. Electromagn Waves Appl 32(15):1961–1972
17. Yadav D, Abegaonkar MP, Koul SK, Tiwari VN, Bhatnagar D (2018) Two element band-notched UWB MIMO antenna with high and uniform isolation. Prog Electromagn Res M 63, 119–129
18. Li J-F, Chu Q-X, Li Z-H, Xia X-X (2013) Compact dual band-notched UWBMIMO antenna with high isolation. IEEE Trans Antennas Propag 61(9):4759–4766
19. Chandel R, Gautam AK, Rambabu K (2018) Tapered fed compact UWB MIMO-diversity antenna with dual band-notched characteristics. IEEE Trans Antennas Propag 66(4):1677–1684
20. Wu W, Yuan B, Wu A (2018) A quad-element UWB-MIMO antenna with band-notch and reduced mutual coupling based on EBG structures. Int J Antennas Propag 2018:1–10
21. Li Z, Yin C, Zhu X (2019) Compact UWB MIMO vivaldi antenna with dual band-notched characteristics. IEEE Access 7, 38696–38701

Analysis of Antennas for IoT Environment

Sugandh Gupta, Saptarshi Gupta, and Sapna Katiyar

Abstract This paper provides an overview of various antennas proposed for Internet of Things (IoT) environment. IoT is an emerging technology in the market these days that aims to deploy numerous devices available, in a network. Antenna plays an important role in wireless technology and hence in IoT. The basic premise is to have antennas that can work efficiently in IoT applications in terms of frequency of operation, gain, radiation pattern and sensitivity. The antenna must be designed keeping in mind that IoT is expected to involve new applications in the coming years. This paper, in its initial part, provides an overview of the importance of antenna design in IoT. Then, an overview of the antennas proposed for IoT applications is given. Finally, we present detailed comparison of proposed antennas to illustrate the approach to design an IoT efficient antenna.

Keywords Internet of Things (IoT) · Microstrip · Reconfigurable antenna · Ultra-high frequency (UHF) · Linear array · RFID · Multiband antenna

1 Introduction

Internet of Things (IoT) has brought revolution in the field of wireless communication. IoT aims to connect billions of heterogeneous devices in the coming future. IoT enables the devices that are deployed in the network to detect the signals from

S. Gupta · S. Gupta (✉)
Department of Electronics and Communication Engineering, Faculty of Engineering and Technology, SRM Institute of Science and Technology, NCR campus, Delhi-NCR Campus, Delhi Meerut Road, Modinagar, U. P, India
e-mail: ece.saptarshi@gmail.com

S. Gupta
e-mail: sugandhaquarius@gmail.com

S. Katiyar
Electronics and Communication Engineering, ABES Institute of Technology, Ghaziabad, U. P, India
e-mail: sapna.katiyar@abesit.in

S. Rawat et al. (eds.), *Proceedings of Second International Conference on Computational Electronics for Wireless Communications*, Lecture Notes in Networks and Systems 554,
https://doi.org/10.1007/978-981-19-6661-3_4

each other and respond accordingly, thereby resulting in an intelligent smart decision taking system [1]. Some of the common examples of such IoT systems that are used these days are heating, ventilation, air conditioning (HVAC) and thermostats monitoring and control systems that are used for enabling smart homes. There are also many other areas and environments where IoT plays an important role and has improved the quality of our lives. These areas include agriculture, wearables, healthcare, smart grids and industrial automation.

Antenna plays a crucial role in IoT devices as it is an interface between various devices or between devices and outside world. The connection of IoT devices and range of communication depends upon the antenna. Thus, antenna has an impact on the overall performance of the system. Nowadays, the IoT devices being designed are small in size, intend to have a high communication range and long battery life, all these factors certainly affect the antenna design. Antennas to be deployed in an IoT network must be tuned to the frequency band of operation. The gain of the antenna should not suffer on the cost of its size. Directionality of the antenna should be considerable for the signal to be detected. The most important factor in antenna design that is still to be mentioned is its size. As mentioned earlier, the small size of IoT devices has always been the aim of engineers, and thus, there is a need of compact antennas. The IoT module antenna must also maintain a reasonable performance under adverse conditions like fading and noise. Some of the antennas that we all might be aware of are:

PCB Antennas: As the name itself implies, printed circuit board antennas are printed on the circuit board itself, consisting of a copper trace. The main drawback of these antennas is that they occupy space of the PCB, also they are designed to operate only on a certain frequency.

Chip Antennas: Chip antennas are better over PCB antenna as they are electric components that are mounted on the PCB along with other components. The chip antennas sometimes come with certain design restrictions like they may require to be placed at a fixed distance with other components.

Whip Antennas: Whip antennas are those which are held out of the device in the air. They could be as simple as a bare wire soldered onto the PCB or could be of plastic which is very commonly seen on the Wi-Fi routers.

An important factor that should be also considered while designing an antenna for IoT device is the structure of antenna. There are many antennas available that can be used for IoT applications like microstrip patch antenna, dipole antenna and various other antennas can be designed according to specific IoT applications with the help of software tools like HFSS and can be tested. Microstrip antennas are the most common for IoT applications due to its compact size and hence, easy integration into IoT devices is possible.

2 Related Work

The related work gives a detailed explanation of various antennas proposed.

Vamseekrishna et al. in [2] proposed an octahedron frequency reconfigurable multiband antenna by the use of an omega shaped slot in the radiating structure. This is used for microwave sensing-based IoT applications. A reconfigurable frequency tunable inverted F antenna using a digitally tuned capacitor (DTC) is proposed in [3]. The size and low power consumption of this antenna makes it suitable for IoT applications. Khalili et al. [4] proposed a dual semi-circular microstrip patch antenna which is implemented on a biodegradable substrate. It operates in 863–873 MHz and 2.4–2.5 GHz bands. Its omnidirectional coverage and low profile integration make it suitable for smart floors and smart houses.

A dual-lens millimeter wave (MMW) radar antenna is designed in [5] for a smart parking system. Here, the gain of transmitting antenna is increased by the use of a flat dielectric punch lens. This antenna operates at 2.4 GHz. Tajin et al. in [6] proposed a cheap, easy-to-fabricate and pattern reconfigurable ultra-high frequency (UHF) RFID reader antenna for ISM band which offers MHz bandwidth and a maximum gain of 8.9 dBi. Metal glasses frame antenna is proposed in [7]. Here, the prototype that has been designed is based on a pair of glasses. It has been shown that the material of lens and shape of the frame can significantly change the resonance frequency points and matching performance. This antenna operates at 5.8 GHz and hence is an efficient tool for sensing applications in IoT.

Chi et al. in [8] proposed a rugged structure linear array similar to Yagi antenna for covering both LTE and 5G bands with a moderate gain. A balun is included in the antenna to minimize the effect of unbalanced common mode currents, thereby resulting in a much higher gain and fractional bandwidth. A two antenna array is proposed in [9] to resonate at 5.8 GHz-band for IoT applications. Lin et al. in [10] proposed a small and low profile linearly polarized and circularly polarized wireless power rectennas for IoT application to operate at 915 MHz.

Compact cavity backed slot antenna using dual mode for IoT applications is proposed in [11]. The proposed antenna has stub structures, present in it for generating two polarization components orthogonal to each other and hence a circularly polarized radiation to avoid multipath fading and depolarization is generated. The antenna proposed in [11] is compact in size. A modified microstrip meander line antenna is proposed in [12] for 2.4 GHz ISM band applications. The inverse S shape, capacitive load and a parasitic element is incorporated in the antenna to increase its performance. Another dual-band meander line monopole antenna is proposed in [13] for 5G IoT applications. The combination of meander line and substrate in the antenna design improves the radiation efficiency and gain of proposed antenna. The measured gain of antenna is −10 dBi at 28 GHz and 0 dBi at 60 GHz.

Burtowy et al. in [14] proposed a low profile electronically steerable parasitic array radiator (ESPAR) antenna that can be successfully used to estimate direction-of-arrival of incoming signals on the basis of received signal strength (RSS) for wireless sensor applications. The height of the proposed antenna is a major advantage as it is approximately three times lower than other conventional ESPAR antenna. The time required for estimating direction of arrival (DoA) of signal has also been reduced in the proposed antenna due to the use of eight unique beam directions instead of 12

that are used in earlier ESPAR antennas [15]. The integration of unlicensed ultra-wideband (3.1–10.6 GHz) with the existing bands of 1.9 GHz LTE and 2.4 GHz ISM band with the design of a compact dual polarized multiband MIMO antenna for IoT applications is proposed in [16]. A two-row ESPAR antenna is proposed in [17] for the estimation of DoA in IoT application which simply relies on microcontroller oriented steering circuit that produces 18 directional radiation patterns.

An inverted six shaped coplanar waveguide fed antenna is proposed in [18]. Rounded corners have been used in the design to improve gain and bandwidth of antenna. It is suitable for IoT applications due to low back holes and low cross polarization. Another coplanar waveguide antenna with two inverted L shape elements is proposed in [19] where a defected ground structure is used to improve the bandwidth from 30 to 119%. The proposed antenna has a wide bandwidth of 1.77–6.95 GHz. Another coplanar bowtie antenna with digital tunable capacitor is proposed in [20]. This antenna design is presented in two configurations—first configuration makes use of modified ground plane arrangement and there is vertical folding for the ground plane as well as radiating arm in the second configuration. Both the antennas are designed to operate at 868 MHz. The first configuration exhibits 77% size reduction, and the second configuration exhibits 84% size reduction.

Rocio et al. in [21] proposed a quadrupole-based antenna for 5G IoT applications. The design makes use of two quadrupolar near field resonant parasitic (NFRP) elements and consists of a coax-fed-driven dipole. The total efficiency of antenna is measured to be 85% at 1.579 GHz. A chip less RFID tag to operate at UHF bands is proposed in [22] that uses microelectromechanical systems (MEMS) technology. The MEMS switches act as programmable elements for communication between tag and RFID interrogators. The tag is tested for 910 MHz with less than 1 dB insertion loss and −17 dB return loss.

Mohta et al. in [23] proposed an inset fed triple band microstrip patch antenna for ISM band. This antenna is suitable for power transmission applications. Slots are cut on the surface of proposed antenna to improve the reflection coefficient which is below −10 dB and gain is optimized to 5.50 dB.

Falkner et al. proposed a 1×3 linear array for Broadband Global Area Network in [24]. The antenna operates at L band (1.518–1.675 GHz) and generates right hand circularly polarized radiation. The structure of the proposed antenna ensures high gain and low profile. Another slot-based antenna for 5G-enabled IoT devices is proposed in [25] which has a shared radiating aperture. The proposed antenna operates in eight bands for sub-6-GHz operation.

3 Factors to Be Considered for Antenna Design

Application Environment: The application environment is a very important factor to be considered while designing an antenna. In the present paper, we are reviewing the antenna designs for IoT environment. IoT mainly aims at connecting devices for the indoor environment which is highly dense. The electromagnetic waves suffer from

multipath fading in such environment, and this can change the polarization of EM waves. Also there are other factors in such environment that can cause depolarization like scattering from walls, panels, etc [26].

Frequency bands of operation: Once we identify the application for which antenna is to be designed, we need to identify the frequency band of operation for the application. The most common frequency bands used for IoT applications is 2.4 GHz ISM band. Depending on the frequency band for which antenna is to be designed, the type of antenna should be chosen. Microstrip antenna is suitable for microwave frequencies, dipole antenna is suitable for 20 MHz to 2.2 GHz and so on.

Size and Profile: IoT devices are generally compact in size, and therefore, the antenna to be designed must fit in the device enclosure. The size of antenna designed must be such that it can be easily integrated into IoT devices and also optimal performance should be achieved from antenna. The antenna length is proportional to the square root of antenna gain. Thus, trade-off has to be maintained between both the parameters.

Heterogeneity: IoT networks connects heterogeneous devices which have different access technologies. Thus, all these devices should be well synchronized. Hence, the antenna to be designed for such IoT network must have flexible characteristics.

Overall Performance of Antenna: There are a number of parameters which indicate the performance of an antenna. It is not possible to maintain all the parameters to their best value while designing an antenna for a specific application, but it is certainly necessary to maintain a trade-off between these parameters. The important parameter that decides the antenna performance are gain, bandwidth, directivity, beam width, polarization, radiation pattern and antenna efficiency. Antenna efficiency is defined as the ratio of power that is radiated by the antenna to the input power accepted. Gain indicates the ability of an antenna to radiate in a particular direction as compared to a theoretical antenna. Antenna bandwidth is the range of frequencies over which the antenna can operate correctly. Directivity measures the degree to which the radiation emitted by the antenna is concentrated in a single direction.

4 Comparison of Proposed Designs

The present section gives a detailed comparison of some of the antennas designed for IoT applications.

Any antenna when designed for IoT application is greatly influenced by the IoT environment. A small variation in the surrounding of antenna results in the shifting of its resonant frequency, thereby resulting in mismatching of impedance at the operating frequency. Thus, an antenna with a digitally tuned capacitor (DTC) as shown in Fig. 1 is designed in [3] which results in the shifting of antenna resonant frequency over 32 different positions ranging from 600–960 MHz. The shape of antenna is inverted F type, and this structure is popularly adopted for mobile handsets. The tunability achieved by the use of DTC is used to compensate for the detuning caused by the change in the characteristics of antenna surroundings. The inverted F

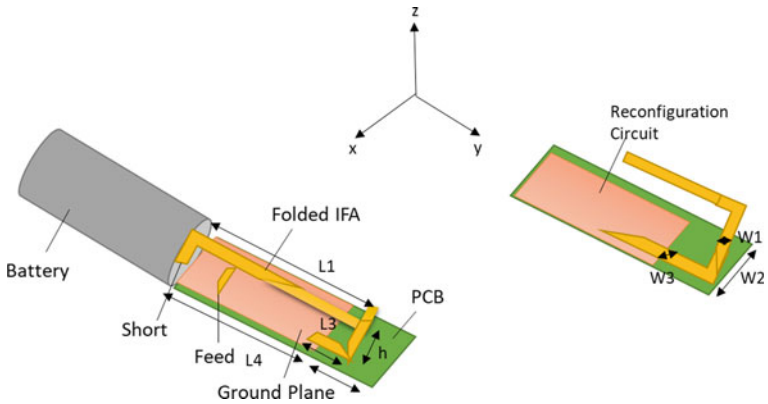

Fig. 1 Structure of DTC-enabled antenna

shape is chosen as it is low profile and can be easily integrated. In other conventional antennas like planar inverted F antenna (PIFA), the varactor diodes are used for tuning but varactor diodes are not suitable to be used in IoT because they need high voltage to be operated while the IoT devices are battery powered and cannot provide high voltage. The use of DTC maximizes the antenna total efficiency. It has been found that in comparison with passive the total efficiency of the above designed antenna over a metallic surface increases by more than 9 dB.

The frequency bands at which the designed antenna operates is also of utmost importance. IoT has applications in various frequency bands. Therefore, a multiband antenna is always recommended. A dual-band microstrip patch antenna is designed in [4] for smart floors. This antenna is implemented on a biodegradable cork tile which is used in laminate floors. The antenna radiation pattern has omnidirectional coverage. The antenna has sufficient gain and operates in the frequency bands of 2.4 GHz and 863 MHz.

The overall performance of antenna in terms of gain, fractional bandwidth is also very important and must be kept in mind while designing any antenna. A modified meander line microstrip antenna is designed in [12] for 2.4 GHz ISM band. Certain modifications have been done in the structure of a microstrip antenna like a rectangular box, parasitic element, capacitive load has been introduced in the design as can be seen in Fig. 2. The shape of antenna is inverted S. The rectangular structure increased the overall efficiency of the antenna, and the simulated gain came out to be 1.347 dB.

Parasitic patch results in higher fractional bandwidth and the gain as well as efficiency of the antenna are kept static by the use of capacitive load. The antenna has been tested with the use of IoT sensors.

A compact triband antenna has been designed in [16] which aims at integrating the unlicensed ultra-wideband (3.1–10.6 GHz) with existing bands like 1.9 GHz LTE and 2.4 GHz ISM bands which are mainly used for IoT applications. This antenna has a bandwidth of 2.9% for 1.9 GHz and 4.7% for 2.4 GHz which is sufficient to support

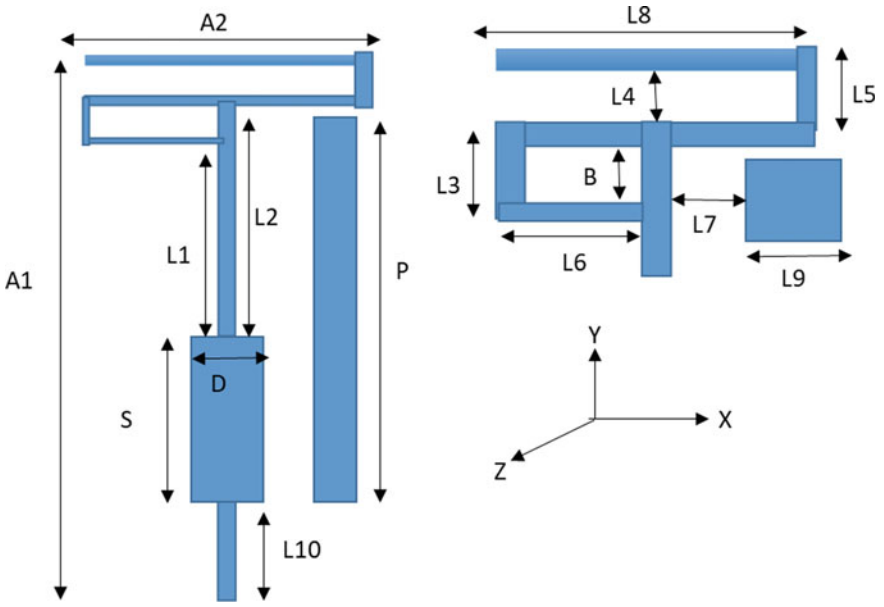

Fig. 2 Topology of modified meander line microstrip patch antenna

low data rate IoT applications. Near field simulations are carried out to find the best position of MIMO elements so as to improve port-to-port isolation. As we all know IoT aims to set up the connection in a highly dense indoor environment, this results into depolarization effects as the electromagnetic suffers from multipath fading. Thus, near field simulation is done to provide appropriate port-to-port isolation. The compact size of antenna is achieved by the use of inverted L shape.

The wireless sensor networks (WSNs) in IoT require to detect the signals and the height of antenna in such networks has to be low. For such requirement, a low profile electronically steerable parasitic array radiator (ESPAR) antenna is designed in [14] which is used to approximate the directional of arrival of incoming signals on the basis of received signal strength (RSS). The height of the antenna designed is reduced than the other ESPAR antennas designed so far. The overall time required for direction of arrival estimation is also reduced by 33% in this design as compared to other ESPAR antennas due to the use of eight unique beam directions instead of 12 beam directions in the case of others [15], with the same error levels. The designed antenna has only one active element that is surrounded by various passive elements connected to variable reactance. The radiation pattern is formed by setting the reactances to appropriate value as shown in Fig. 3. The DoA test frequency for this antenna is 2.48 GHz.

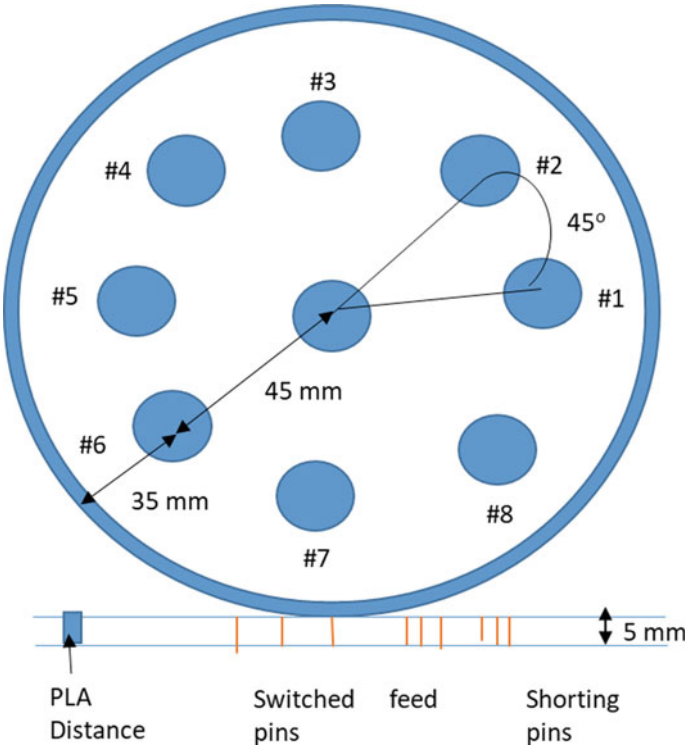

Fig. 3 Design of low profile ESPAR antenna

5 Conclusion

In this paper, the various approaches used to design an antenna for IoT applications has been presented. In the first part of the paper, the various types of antenna used in IoT has been discussed, then the factors that are to be considered for designing an antenna have been explained. In this paper, we also reviewed some antenna designs which have been proposed for IoT applications. It has been found that each design has come up with a different approach to design the antenna, thereby trying to provide an improvement in the overall performance of antenna. This paper basically specifies that while designing an antenna, first of all we need to identify the frequency of operation according to the application, then the structure of antenna must be studied properly and finally, the aim is to construct an antenna with improved performance in all respects like profile of antenna, gain and frequency response. It has been found that it is not possible to achieve all the antenna parameters to their maximum value but a balance has to maintain between all the parameters to achieve an optimal performance. Microstrip antennas are the most commonly used antennas for IoT applications. They are well suited due to their compact size and easy integration into IoT devices (Table 1).

Table 1 Comparison of designed antennas

References	Author name	Nature of antenna	Description of antenna	Advantage for IoT application	Scope of antenna	Limitations found
[3]	Houret et al. [3]	Inverted F antenna with a digitally tunable capacitor	Antenna height is 50 mm, frequency of operation is 868 MHz, fractional bandwidth is 46%, and gain is 1 dBi	Small size, low power consumption	Compensation of the detuning caused by change in surroundings	Not suitable for S and C band
[4]	Khalili et al. [4]	Semi-circular microstrip patch antenna	Frequency of operation is 863 MHz, 2.5 GHz with bandwidths of 14 MHz, 200 MHz, respectively, and gain of 0.8 dBi and 5.1 dBi, respectively	Omnidirectional coverage, stable performance, low profile integration	Excellent for smart floors and smart houses	High power consumption
[12]	Shahidul Islam et al. [12]	Meander line microstrip patch antenna	Antenna size is 40 × 10 mm^2, frequency of operation is 2.4 GHz, fractional Bandwidth is 12.5%, and fain is 1.347 dBi	Small size, high radiation efficiency of 79% at 2.4 GHz	Integration of IoT devices with wireless communication technology	Not suitable for 5G applications
[16]	Maurya et al. [16]	Compact triband antenna	Antenna size is 33 × 57.25 mm^2, operates at 1.9 GHz band, 2.4 GHz band, fractional bandwidth is 2.9 and 4.7%, respectively, and Gain is 0.75 dBi	Highly compact, high quality factor, narrowband impedance matching	Support low data rate communication in IoT	Data rate is quite low

(continued)

Table 1 (continued)

References	Author name	Nature of antenna	Description of antenna	Advantage for IoT application	Scope of antenna	Limitations found
[14]	Burtowy et al. [14]	Low profile ESPAR antenna	Antenna height is 10 mm, operates at 2.4 GHz, bandwidth is 63 MHz, and gain is 7.5 dBi	Three times lower than other ESPAR designs	DoA estimation time reduced by 33%	Not suitable for 5G applications

References

1. Al-Fuqaha A, Guizani M, Mohammadi M, Aledhari M, Ayyash M (2015) Internet of things: a survey on enabling technologies, protocols, and applications. IEEE Commun Surv Tutorials 17(4)
2. Vamseekrishna A, Madhav BTP, Anilkumar T, Reddy LSS (2017) An IoT controlled octahedron frequency reconfigurable multiband antenna for microwave sensing applications. IEEE Sensors Lett 2(3)
3. Houret T, Lizzi L, Ferrero F, Danchesi C, Boudaud S (2019) DTC enabled frequency tunable inverted-F antenna for IoT applications. IEEE Antennas Wirel Propag Lett
4. Khalili HF, Lemey S, Caytan O, Deckmyn T, Agneessens S, Ginste DV, Rogier H (2018) Biodegradable dual semi-circular patch antenna tile for smart floors. IEEE Antennas Wirel Propag Lett
5. Cai Z, Zhou Y, Zhuang W, Deng L (2020) A millimeter wave dual-lens antenna for IoT based smart parking radar system. IEEE Internet of Things J
6. Tajin MAS, Dandekar KR (2020) Pattern reconfigurable UHF RFID reader antenna array. IEEE Access
7. Wang Y, Zhang J, Peng F, Wu S (2019) A glasses frame antenna for the applications in internet of things. IEEE Internet of Things J
8. Chi L, Weng Z-B, Meng S, Qi Y, Fan J, Zhuang W, Drewniak JL (2020) Rugged linear array for IoT applications. IEEE Internet of Things J 7(6)
9. Olan-Nuñez KN, Murphy-Arteaga RS, Colin-Beltran E (2017) Miniature patch and slot microstrip arrays for IoT and ISM band Applications. IEEE Access
10. Lin W, Ziolkowski RW, Huang J (2018) Electrically small, low profile, highly efficient, huygens dipole rectennas for wirelessly powering Internet of Things (IoT) devices. IEEE Trans Antennas Propag
11. Oh J-I, Jo H-W, Kim K-S, cho H, Yu J-W (2021) A compact cavity-backed slot antenna using dual mode for IoT applications. IEEE Antenna Wirel Propag Lett 20(3)
12. Islam MS, Islam MT, Ullah MA, Beng GK, Amin N, Misran N ()2019 A modified meander line microstrip patch antenna with enhanced bandwidth for 2.4 GHz ISM-band Internet of Things (IoT) applications. IEEE Access
13. Burasa P, Djerafi T, Wu K (2021) A 28 GHz and 60 GHz dual-band on-chip antenna for 5G-compatible IoT-served sensors in standard CMOS process. IEEE Trans Antennas Propag 69(5)
14. Burtowy M, Rzymowski M, Kulas L (2017) Low-profile ESPAR antenna for RSS-based DoA estimation in IoT applications. IEEE Access
15. Santamaria L, Ferrero F, Staraj R, Lizzi L (2020) slot-based pattern reconfigurable ESPAR antenna for IoT applications. IEEE Trans Antennas Propag
16. Maurya NK, Bhattacharya R (2020) Design of compact dual-polarized multiband MIMO antenna using near-field for IoT. Int J Electron Commun
17. Rzymowski M, Kulas L (2021) Two-row ESPAR antenna with simple elevation and azimuth beam switching. IEEE Antennas Wirel Propag Lett 20(9)
18. Kumar SA, Shanmuganantham T (2020) Design of CPW-fed inverted six shaped antenna for IoT applications. Trans Electr Electron Mater
19. Abutarboush HF, Li W, Shamin A (2020) Flexible-screen-printed antenna with enhanced bandwidth by employing defected ground structure. IEEE Antennas Wirel Propag Lett
20. Fatima A. Asadallah, Aline Eid, Ghinda Shehadeh, Joseph Costantine, Youssef Tawk, Emmanouil M. Tentzeris, "Digital Reconfiguration of a Single Arm 3-D Bowtie Antenna," in IEEE Transactions on Antennas and Propagation, 2021.
21. Rodriguez-Cano R, Richard W. Ziolkowski (2021) Single-layer, unidirectional, broadside-radiating planar quadrupole antenna for 5G IoT applications. IEEE Trans Antennas Propag
22. Attaran A, Rashidzadeh R (2016) Chipless radio frequency identification tag for IoT applications. IEEE Internet of Things J

23. Mohta M, Rajawat A, Gupta SH (2018) Design of an inset-fed slotted triple band antenna. In: 2018 3rd International conference on internet of things: smart innovation and usages (IoT-SIU), 23rd–24th February 2018. IEEE. https://doi.org/10.1109/IoT-SIU.2018.8519937
24. Falkner BJ, Zhou H, Mehta A, Arampatzis T, Mirshekar-Syahkal D, Nakano H (2021) A circularly polarized low-cost flat panel antenna array with a high impedance surface meta-substrate for satellite on-the-move medical IoT applications. IEEE Trans Antennas Propag
25. Hussain R (2021) Shared-aperture slot-based sub-6-GHz and mm-wave ioT antenna for 5G applications. IEEE Internet of Things J
26. Kim T, Chae SH (2020) A novel random access framework for uplink cellular IoT: non-orthogonal preambles and multi-antennas. IEEE Commun Lett

Design and Analysis of Three-Port Patch Antenna for the X and Ku Band Applications

Prakhar Yadav, Sweta Singh, Aditya Kumar Singh, Ram Suchit Yadav, and J. A. Ansari

Abstract An innovative three-port MIMO microstrip patch antenna for X and Ku band applications is offered in this paper. Ringing phenomenon is described using coaxial and microstrip line feeding. Results of three-port microstrip patch antenna are studied with the support of gain, reflection coefficient, ECC, diversity gain and radiation pattern and efficiency.

Keywords Three port · Patch antenna · ECC · Diversity gain · Ringing phenomenon

1 Introduction

Antenna is an essential component for wireless communication system. Planar structure, low cost, easy fabrication, bulk production, compact size and integration with microwave circuits are features of microstrip patch antenna [1, 2]. Due to such advantageous features, researchers and scientists are making effort to find the antenna with high gain and bandwidth. Various feeding techniques are used to improve gain and bandwidth. Feeding effect on microstrip patch antenna is reported in [3]. Microstrip patch antenna performance also depends on shape, size and substrate type. It is gaining popularity as it can be designed for wireless communication devices along with the numerous communication systems. Miniaturization of devices is in rapid pace. Microstrip patch antenna is no different. Implementation of one microstrip patch antenna which operates over different frequency band is always be preferable in comparison with the antenna which operates for single frequency band [4–6]. The increasing demand for multiband features and wide bandwidth is striking which avoids the use of multiple antennas for different applications.

There is a lot of literature accessible for multiple input multiple output (MIMO) microstrip patch antenna systems. These antennas can exist for various applications like wireless local area network (WLAN) and word wide interoperability for

P. Yadav · S. Singh · A. K. Singh · R. S. Yadav (✉) · J. A. Ansari
University of Allahabad, Prayagraj, Uttar Pradesh, India
e-mail: rsyadav_au@rediffmail.com

S. Rawat et al. (eds.), *Proceedings of Second International Conference on Computational Electronics for Wireless Communications*, Lecture Notes in Networks and Systems 554,
https://doi.org/10.1007/978-981-19-6661-3_5

microwave access (WiMAX), long term development (LTE), etc. Faster transmission rate along with better communication signal quality enables MIMO antenna system desirable for the bands like X, Ku, K also. There are only few MIMO antennas of three port are reported in the literature. Compact size MIMO patch antenna of three is reported for WLAN applications [9]. Three-port MIMO antennas for various applications are reported in [10–13].

Three-port small size MIMO microstrip patch antenna on FR-4 substrate is designed, simulated and discussed. We also explore the performance of MIMO microstrip patch antenna by means of coaxial feeding and microstrip line feeding.

2 Antenna Design Evolution

The three-port MIMO microstrip patch antenna is shown in Figure 1a. A three step process is used to offer the three-port MIMO microstrip antenna on HFSS software. In Step-I, a primary bat-shaped microstrip patch antenna (Antenna-1) is designed and simulated on an FR-4 substrate of size ($L \times W$) mm^2 with coaxial feeding only. Two circular (radius r) and one rectangular slot (L1 $\times$ W1) mm^2 are engraved from the patch. Antenna-1 shows dual band, i.e., (11.2–12.2) GHz and (13.2–14.4) GHz. Both bands are showing "ringing effect". The ringing effect is known to be a phenomenon in which the antenna exhibits two resonant frequencies in a single band [14]. Due to which the gain in the same band is falling at particular resonance frequency (c.f.1b).

Peak gain of Antenna-1 is 3.6 dBi but dropping in gain is observed in the band (11.2–12.2) GHz at 11.7 GHz and in the band (13.2–14.4) GHz at 13.9 GHz, respectively (c.f.1b). Further, we focus in the direction of port management for the removal of this undesired ringing effect.

In Step-II, Antenna-2 is designed and simulated using microstrip line feeding on one side of a bat-shaped patch with a rectangular strip of size (L2 $\times$ W2) mm^2. We observed that the ringing effect is removed in the (13.2–14.4) GHz frequency band and the gain also increases to 4.6 dBi (c.f.1c). Antenna-3 is designed with microstrip line feeding using rectangular strip of size (L2 $\times$ W2) mm^2 on Antenna-2. After simulation ringing effect in the band (11.2–12.2) GHz is also removed and the peak gain in this third Step-III increases to 4.8 dBi. (cf 1d) (Table 1).

The gain of all three antennas is shown in Figure 1e. Antenna-1 has a maximum peak gain of 3.6 dBi, while Antenna-2 is showing a peak gain of 4.6 dBi. The proposed Antenna-3 is showing a peak gain of 4.8 dBi. The dual band characteristics (11.2–12.2) GHz and (13.2–14.4) GHz and with a maximum peak gain of 4.8 dBi enable Antenna-3 to be chosen as the proposed antenna. This three-port MIMO microstrip patch antenna will be discussed in the following results and discussion section.

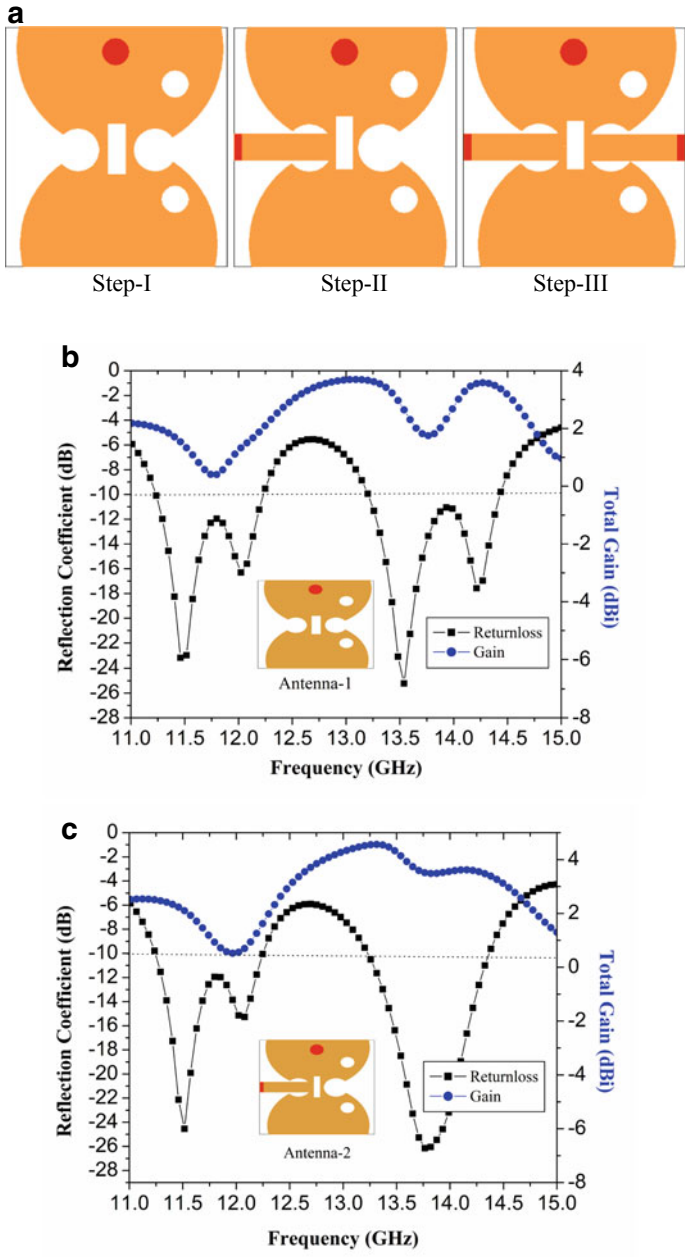

Fig. 1 **a** Evolution of the proposed three-port bat-shaped MIMO patch antenna, **b** Antenna-1 reflection coefficient and gain plot with frequency variation, **c** Antenna-2 reflection coefficient and gain plot with frequency variation, **d** Antenna-3 reflection coefficient and gain plot with frequency variation, **e** Antenna-1, Antenna-2 and Antenna-3 gain with the variation of frequency, **f** Proposed three-port bat-shaped MIMO microstrip patch Antenna-3

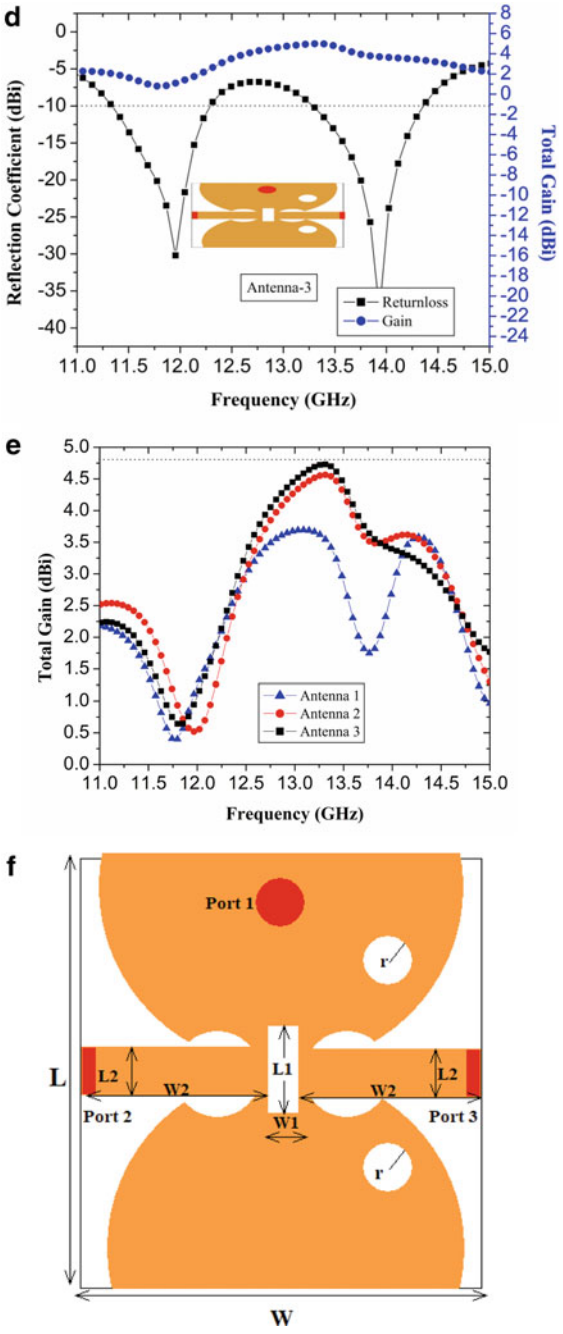

Fig. 1 (continued)

Table 1 Proposed Antenna-3 specification

Proposed Antenna-3 specifications	Units (mm)
W (Proposed antenna width)	20
L (Proposed antenna length)	20
*W*1 (Rectangular slot width)	01
*L*1 (Rectangular slot width)	05
*W*2 (Rectangular strip width)	08
*L*2 (Rectangular strip length)	1.8
r (Circular slot radius)	2

3 Results and Discussion

The results of the proposed three-port MIMO microstrip patch antenna are explored in detail in this section. The surface current circulation at the resonance frequency 11.7 GHz for φ-0° and φ-90° is shown in Fig. 2a and b. The peak value of surface current is 59.6 A/m. The surface current distribution for φ-0° and φ-90° at the resonant frequency 13.9 GHz is shown in Fig. 3a and b. The peak value of surface current is 52.5 A/m. Fig. 4 shows the reflection coefficient of all three ports for the operating frequency band (11–15) GHz. With port 1, we get two frequency bands (11.2–12.2) GHz and (13.2–14.4) GHz bandwidths of 1 GHz and 1.2 GHz, respectively. The frequency band (13.5–14.2) GHz on port 2 is achieved with bandwidth (0.7 GHz).

Antenna resonates from (11.3–12.0) GHz with port 3 and bandwidth (0.7 GHz) is obtained. Antenna gain is above zero for the entire effective band and highest gain up to 4.8 dBi is observed (c.f. 1(d) and 4). Isolation, diversity gain and envelope correlation coefficient (ECC) are used to realize MIMO microstrip patch antenna features. Isolation, ECC and diversity gain are achieved with the help of S-parameter. Antenna-3 isolation between port 1 and port 2 is below -15 dB. The isolation between

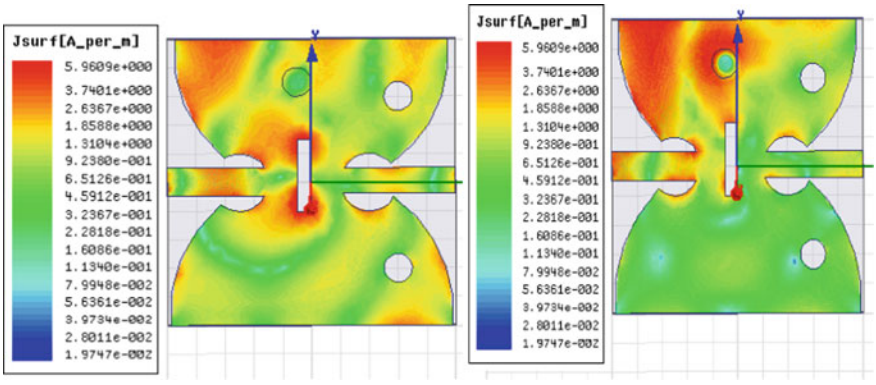

(a) (b)

Fig. 2 Surface current distribution at 11.7 GHz **a** φ-0°, **b** φ-90°

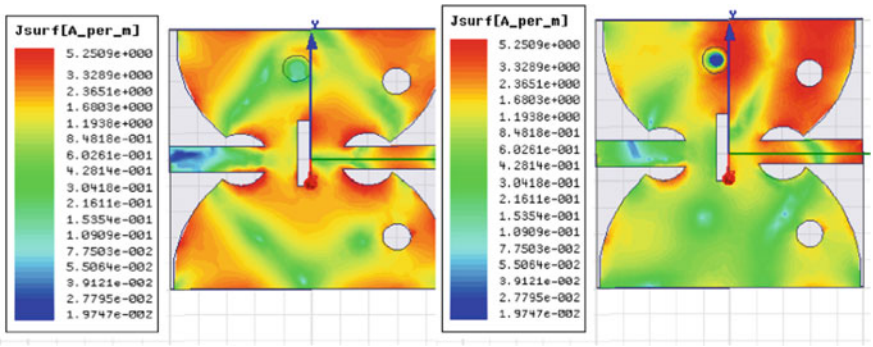

Fig. 3 Surface current distribution at 13.9 GHz **a** φ-0° **b** φ-90°

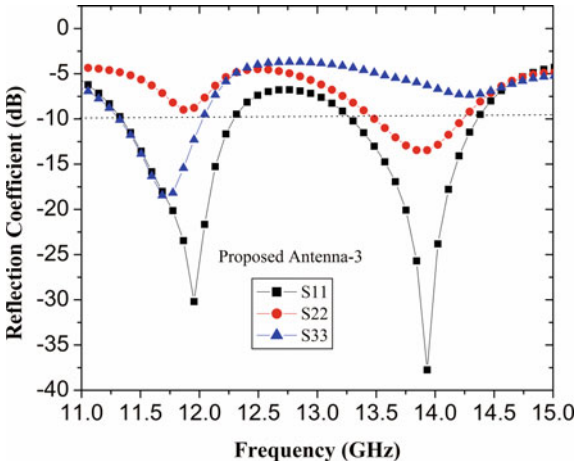

Fig. 4 Proposed Antenna-3 reflection coefficients of port 1, port 2 and port 3

port 1 and port 3 is below −20 dB. Similarly, the separation between port 2 and port 3 is below −25 dB (c.f. Fig. 5). We can conclude that there is good isolation between the three ports (Table 2).

ECC and diversity gain are achieved as shown in Eqs. (1) and (2) [15] for a three-port MIMO microstrip patch antenna. For MIMO antenna systems, the ECC value is recommended to be less than 0.5 or its value close to zero so that the coupling effect across the antenna elements is minimal. Figure 6 shows that the peak ECC for the entire operating frequency range (11–15) GHz is 0.16. Variation can be calculated using ECC as shown in the formula in Eq. (2). The variety of Antenna-3 offered varies from 9.84 to 10.

$$\mathrm{ECC} = \frac{|S_{11} * S_{12} + S_{12} * S_{22} + S_{13} * S_{32}|}{\left(1 - |S11^2| - |S21^2| - |S31^2|\right)\left(1 - |S22^2| - |S12^2| - |S32^2|\right)} \quad (1)$$

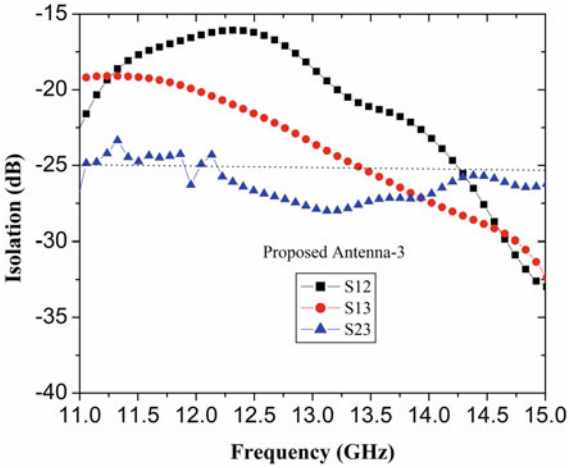

Fig. 5 Antenna-3 isolation with the variation of frequency

Table 2 Proposed Antenna-3 performance

Port name	Operating frequency (GHz)
Port1	11.2–12.2, 13.2–14.4
Port2	13.5–14.2
Port3	11.3–12.0

$$\text{Diversity Gain} = 10\sqrt{1-\text{ECC}^2} \tag{2}$$

The lower the ECC, the greater the benefit of diversity. The proposed antenna is showing good agreement of diversity. The radiation characteristics of all three antennas are shown in Figure 7 which varies between 54 and 70% for the operative frequency band. Fig. 8 is displaying the radiation pattern of Antenna-3, proposed

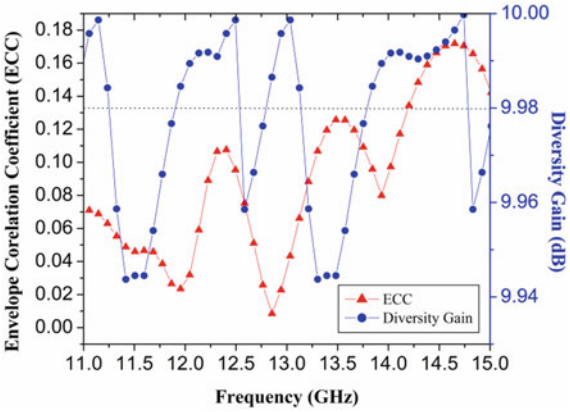

Fig. 6 ECC and diversity gain of proposed Antenna-3

to resonate frequencies 11.7 and 13.9 GHz, respectively. Both the E-plane and the H-plane are showing omni-directional radiation patterns at the resonance frequencies.

Proposed work is compared with the practically available antennas for the same application band in Table 3. Wideband characteristics is shown by antenna reported in ref. [16, 18]. Antenna reported in [17] and [19] is showing the dual band characteristics. Antenna-3 is the smallest in size among all reported antennas except antenna reported in ref. [19]. Small size antenna accommodating good gain and dual band characteristics.

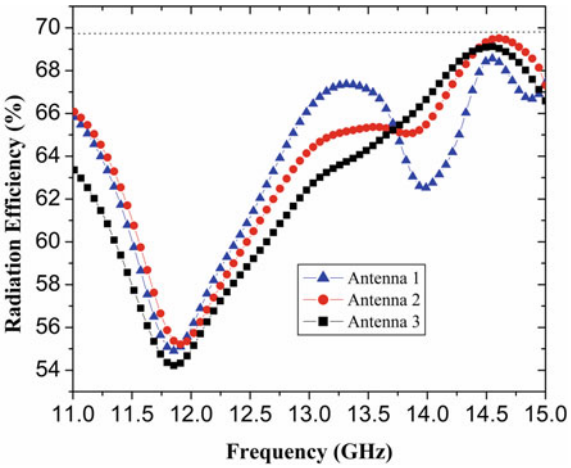

Fig. 7 Radiation efficiency of all three antenna

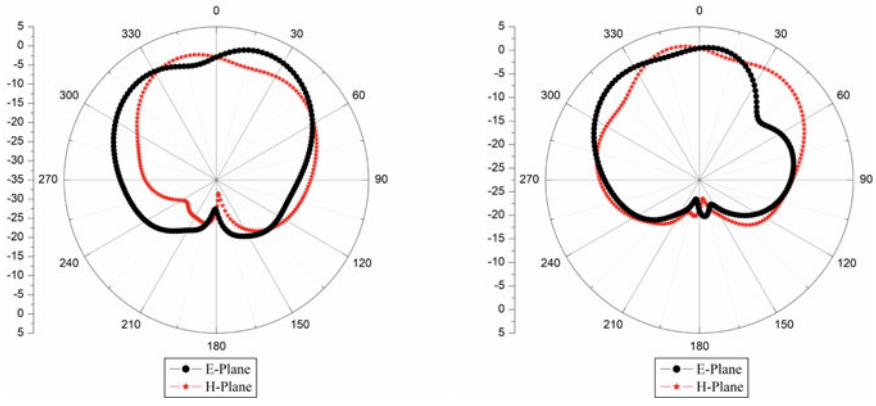

Fig. 8 Radiation pattern of proposed Antenna-3 **a** at 11.7 GHz **b** at 13.9 GHz

Table 3 Proposed antenna comparison with previous antennas

Refs.	Overall size (mm^3)	Antenna type	Operating frequency band (GHz)	BW	Impedance BW	Applications
[16]	25×23×1.6	Wideband	10.4–16.5	6.1	45.35	X and Ku band
[17]	50×50×1.52	Dual-band	11.44–12.48, 13.47–14.39	1.04 0.92	8.7 6.6	X and Ku band
[18]	36×36×0.76	Wideband	9.89–17.55	7.66	55.83	X and Ku band
[19]	20×11×1.56	Dual-band	11.13–11.82, 15.77–16.89	0.69 1.12	6.0 6.8	X and Ku band
Proposed work	20×20×1.6	Dual-band	11.2–12.2, 13.2–14.4	1.0 1.2	8.5 8.7	X and Ku band

4 Conclusion

In this paper, we find ports (coaxial and microstrip line feeding) plays a significant role on the patch antenna efficiency. Multiple resonant frequency in a single operating band is named as ringing effect which is also the causal of dropping gain. In this paper, we investigated how the port can remove this undesired effect. Proposed Antenna-3 with port 1 has increased gain shows two band (11.2–12.2) and (13.2–14.2) GHz without any ringing effect. The same antenna resonates at (13.5–14.2) GHz and (11.3–12) GHz with port 2 and port 3, respectively. Antenna-3 is a suitable applicator for the application of X and Ku band applications.

References

1. Balanis CA (2015) Antenna theory analysis and design. Wiley, New York, NY
2. GargBhartia R, Bahl PI, Ittipiboon A (2001) Microstrip antenna design handbook. Norwood, MA: Artech House
3. Singh I, Tripathi VS (2011) Microstrip patch antenna and its applications: a survey. Int J Comp Tech Appl 2(2):1595–1599
4. Kaur J, Khanna R, Kartikeyan MV (2014) Optimization and development of O-shaped triple-band microstrip patch antenna for wireless communication applications. Int J Microwave Wirel Tech. 60(2):95–105
5. Liu WC, Wu CM, Dai Y (2011) Design of triple-frequency microstripfed monopole antenna using defected ground structure. IEEE Trans Antennas Propag 59(7):2457–2463
6. Agarwal EN, Dhubkarya DC, Mittal ER (2011) Designing & testing of rectangular micro strip antenna operating at 2.0 GHz using IE3D. Global J Res Eng 11(1):44–48
7. Kaur J, Khanna R, Kartikeyan MV (2014) Novel dual-band multistrip monopole antenna with defected ground structure for WLAN/ IMT/BLUETOOTH/WiMAX applications. Int J Microwave Wirel Tech 6(2):93–100
8. Karli R, Ammor H (2015) Rectangular patch antenna for dual-band RFID and WLAN applications. Wirel Pers Commun 83(2):995–1007

9. Deng C, Shi B, Liu D (2020) Compact omnidirectional three-port MIMO antenna with the same vertical polarization for WLAN applications. Microw Opt Technol Lett 62:800–805
10. Chen, W-S, Lin, R-D (2021) Three-port MIMO antennas for laptop computers using an isolation element as a radiator. Int J RF Microw Comput Aided Eng 31
11. Martens R, Manteuffel D (2014) Systematic design method of a mobile multiple antenna system using the theory of characteristic modes. IET Microwaves Antennas Propag vol 8, pp 887–893
12. Wang H, Liu L, Zhang Z, Li Y, Feng Z (2014) Ultra-compact three-port MIMO antenna with high isolation and directional radiation patterns. IEEE Antennas Wirel Propag Lett vol 13, pp 1545–1548
13. Abdalrazik A, El-Hameed ASA, Abdel-Rahman AB (2017) A three-port MIMO dielectric resonator antenna using decoupled modes. IEEE Antennas Wirel Propag Lett 16, pp 3104-3107
14. Singh V, Mishra B, Singh R (2019) Dual-wideband semi-circular patch antenna for Ku/K band applications. Microw Opt Technol Lett. 2019(61):323–329
15. Garg P, Jain P (2020) Isolation improvement of MIMO antenna using a novel flower shaped metamaterial absorber at 5.5 GHz WiMAX band. In IEEE transactions on circuits and systems II, express briefs 67(4):675-679
16. Singh R, Singh VK (2017) Wide band and miniaturized partial ground plane microstrip antenna for X & Ku band applications. Int J Comp Tech Appl. 10(8):477–486
17. Thi TN, Hwang KC, Kim HB (2013) Dual-band circularly-polarised Spidron fractal microstrip patch antenna for Ku-band satellite communication applications. Electron Lett 49(7):444–445
18. Khandelwal MK, Dwari S, Kanaujia BK, Kumar S (2013) Design and analysis of microstrip DGS patch antenna with enhanced bandwidth for Ku band applications. In: international conference on microwave and photonics
19. Khanna RN, Kaur J (2017) Optimization of modified T-shape microstrip patch antenna using differential algorithm for X and ku band applications. Microw Opt Technol Lett 60: 219–229

An Efficient Band CMOS LNA for Satellite-Based Remote Sensing Application

Gunjan Mittal Roy, Sandeep Kumar, and Pradeep Gorre

Abstract The paper demonstrates an efficient band CMOS LNA for satellite-based remote sensing application using 45 nm CMOS technology. The designed LNA comprises of a two stage cascode amplifier with shunt resistance feedback and dual inductive peaking (SRF-DIP) technique with source and gate inductive degeneration. The received band is 35.7 GHz that ranges from 61–96.7 GHz. The maximum power gain is 22.2 dB at resonant frequency of 74.7 GHz. The minimum noise figure is 1.25 dB at 60 GHz. The noise figure and power gains are calculated theoretically as well. The DC current I_d is measured between 20–25 mA for the drain voltage of 0–1.2 V.

Keywords Two stage cascode amplifier · Shunt resistance feedback · Dual inductance peaking

1 Introduction

In the field of radio frequency receivers, the researches have adopted new methods and technology to satisfy the technical demand of human beings. In the field of satellite and space communication, the remote sensing is being adopted very frequently. The use of satellite has served various purposes including weather forecasting, military surveillance, foresting, biodiversity, and many more. The satellite sensors are able to detect the information and deliver it to the ground station for processing. To study the large areas which cannot be observed by simple modeling, the satellite-based remote sensing is adopted [1]. It also caters detailed information about continuous variations in the properties of atmosphere and climate [2]. The satellite-based remotely sensed data is processed at the base station in which the crucial role is played by RF receivers.

G. M. Roy
Institute of Innovation in Technology and Management, Janakpuri, New Delhi, India

S. Kumar · P. Gorre (✉)
National Institute of Technology Karnataka, Surathkal, Mangaluru, India
e-mail: pradeepgorre@gmail.com

S. Rawat et al. (eds.), *Proceedings of Second International Conference on Computational Electronics for Wireless Communications*, Lecture Notes in Networks and Systems 554,
https://doi.org/10.1007/978-981-19-6661-3_6

In the design of RF receivers, many components have been designed which include low noise amplifiers, filters, mixers, VCO, and frequency converters. LNA has to play a major role as it is the first active element after antenna. Thus, the designing of LNA is really very crucial and needs proper attention. In the designing of LNA, various techniques and topologies are used. CMOS technology is the most promising technique to achieve high gain, large band width, low noise factor, good impedance matching, and technological scaling with least power consumption. The distributed stages of amplifiers are most widely used for the obvious reason of offering broadband frequency response with high gain and good impedance matching. But the chip size and power requirements are the problems that still need to be entertained [3, 4]. The cascading of the amplifiers is the next basic platform of LNA designing to boost the gain parameter. The designing criteria can be based on feedback topology, inductive peaking and cascoding, and so on. In ordinary resistive feedback scheme having a resistor between input and output, the tradeoff between NF and input impedance is present. To nullify it, voltage buffers are deployed [5–7]. The benefits of negative feedback are many including impedance matching, reduced noise, insensitivity to the process and supply voltage fluctuations, and stabilized gain at the expanse of gain [8, 9]. In shunt feedback technique, highly flat wide band is achieved [10–13]. At the gate, this technique helps to attain high gain with least power consumption [14]. For input matching, one of the most popular choices is the inductive peaking that provides good gain and noise matching. The dual peaking strategy is even superior in terms of offering high gain flatness along with the improved noise performance at high frequencies [15]. For inter stage, matching transformer coupling is the traditional choice. This method not only brings to optimum impedance matching and noise figure but also enlarges the bandwidth [16]. Thus, this paper brings out the combination of all the above said techniques to come out with the benefits of all of them which include DA technique, cascode amplifier technique, shunt resistive feedback, and dual peaking technique.

Section 2 presents the circuit design of LNA, while section III yields out the results and conclusion (Fig. 1).

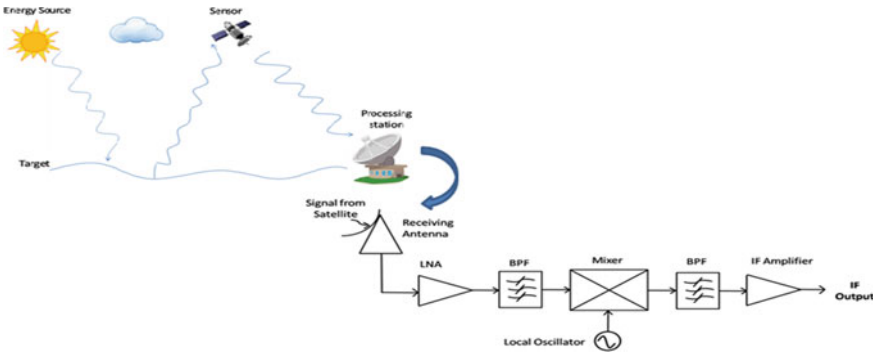

Fig. 1 Satellite communication environment in conjunction with RF frontend receiver

2 LNA Design Consideration

While designing of an RF receiver, the most considered part is the low noise amplifier. Researchers have been incorporating various technologies on day-to-day basis. It is, therefore, a complex task to take out the best solution as the tradeoff between the parameters has always been an issue. Moreover, designing complexities also occur. The effort has been made here to come to a simpler and beneficial solution in all aspects.

The proposed LNA shown in Fig. 2 caters a two stage cascode amplifier with shunt resistive feedback and dual inductive peaking technique. At the input, the filter synthesis technology has been adopted for impedance matching [17]. Cascode technology is the traditional one to achieve high gain and impedance matching. The obvious benefits of using it are the input–output isolation, higher gain but on the cost of reduced noise performance. In two stage cascode, the input and inter stage matching plays very important role. For input matching, the most popular choice is inductive peaking that provides good gain and noise matching. It makes input impedance purely resistive to limit the input noise [18]. As mentioned in upper paragraph, dual peaking strategy offers high gain flatness along with the improved noise performance at high frequencies shown by gate inductors L_1 and L_2 and source inductors L_{s1} and L_{s2}. The bandwidth is further extended by using drain inductance shunt peaking as it resonates with the capacitance offered by the MOS at drain [19]. Finally, interstage matching is done by using transformer coupling to achieve optimum impedance matching and noise figure and enlarged bandwidth. The biasing elements are used to stabilize quiescent point in order to reduce complexities in the circuit. The shunt resistance feedback is the classical way to achieve flat gain, higher stability, reduced sensitivity of CMOS devices with small voltage standing wave ratio. It is attained by deputing a resister in shunt to elevate the impedance matching of input port. It provides negative feedback to produce impedance matching of 50 Ω at input port [20]. The inductors L_{d1}, $L_{d2,}$ and L_g provide biasing, while the L_s and R_f offer stabilization of the operating point in the LNA design architecture.

The input impedance of the inductive peaking matching circuit is given by the following equation

$$Z_{\text{in}} = S\left(L_{g1} + L_{s1}\right) + \frac{1}{\text{SC}_{gs1}} + \frac{g_{m1} L_{s1}}{C_{\text{gs1}}} \tag{1}$$

whereas the output impedance can be determined from the small signal model as shown in Fig. 3. It is given by Eq. (2).

$$Z_{\text{out}} = \frac{Z_d R_{m4} R_L}{R_L R_{m4} + Z_d R_L + Z_d R_{m4}} \tag{2}$$

Here, Z_a, Z_b, Z_c, and Z_d are the impedances at nodes a, b, c, and d.

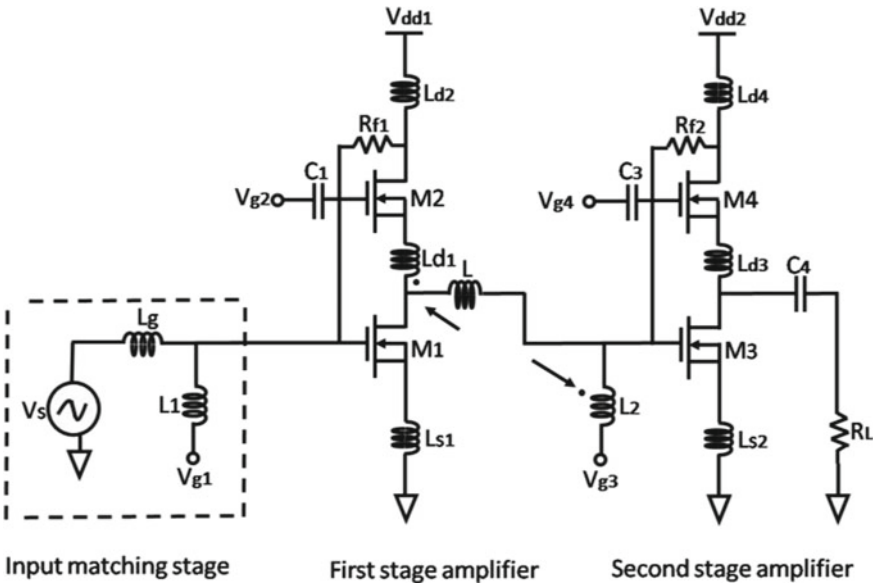

Fig. 2 Proposed low noise amplifier design architecture

$$Z_a = \frac{1}{\mathrm{SC_{gs2}}} || \left(\mathrm{SL}_{d1} + \frac{1}{\mathrm{SC_{ds1}}} || r_{\mathrm{ds1}} \right) \tag{3}$$

$$\mathrm{Z_b} = \mathrm{SL_{d2}} + \mathrm{r_{ds2}} \left\| \frac{1}{\mathrm{SC_{ds2}}} + \left[1 + \mathrm{g_{m2}} \left(\mathrm{r_{ds2}} \left\| \frac{1}{\mathrm{SC_{ds2}}} \right. \right) \right] \mathrm{Z_a} \right. \tag{4}$$

$$Z_c = \frac{1}{\mathrm{SC_{gs4}}} || \left(\mathrm{SL}_{d3} + \frac{1}{\mathrm{SC_{ds3}}} || r_{\mathrm{ds3}} \right) \tag{5}$$

$$Z_d = \mathrm{SL}_{d4} + r_{\mathrm{ds4}} \left\| \frac{1}{\mathrm{SC_{ds4}}} + \left[1 + g_{m4} \left(r_{\mathrm{ds4}} \left\| \frac{1}{\mathrm{SC_{ds4}}} \right. \right) \right] Z_a \right. \tag{6}$$

Figure 3 presents the $|\mathrm{Z_R}|$ with respect to frequency band. The variation in the inductance value L_1 brings out to almost identical curves ranges from 42 to 58 Ω. The worth noting point is that the increment in inductance results into the proportionate increment in impedance.

The most general expression of NF can be estimated from the Frii's equation [21]

$$F = F_1 + \frac{F_2 - 1}{G_1} + \frac{F_3 - 1}{G_1 G_2} + \cdots \frac{F_N - 1}{\Pi_{n=1}^{N-1} G_n} \tag{7}$$

The noise of a cascode cell is given as

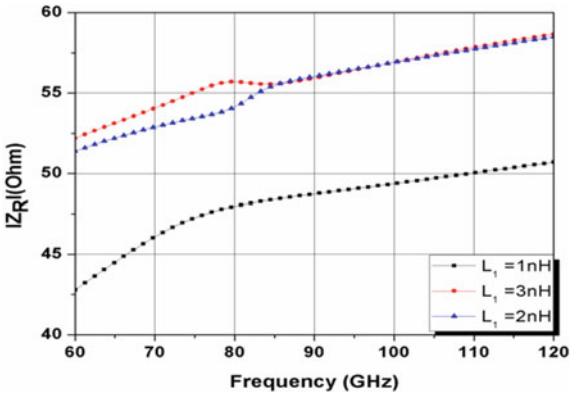

Fig. 3 Impedance response for different inductance values

$$F = 1 + \frac{v_{n1}^2 + i_{n1}^2 R_s}{4\mathrm{KTR}_s} + 4R_s\gamma_2 g_{\mathrm{do2}}\left(\omega_{\mathrm{o}}/\omega_{T1}\right)^2\left(\frac{\omega_{\mathrm{o}}^2 \mathrm{C}_{\mathrm{x}}^2}{g_{m2}^2}\right) \tag{8}$$

where V_{n1} and i_{n1} are the input noise voltage and current, Rs is the internal source resistance, and γ_2 is parameter depending on bias of M_2. g_{do2} and g_{m2} are zero bias drain conductance and transconductance of M_2. The total parasitic capacitance is given as $c_x = c_{\mathrm{po}} + c_{p1}$. Here, c_{po} and c_{p1} are parasitic capacitance of M_1 and M_2 [22]. The measured and simulated noise performance is shown in Fig. 4.

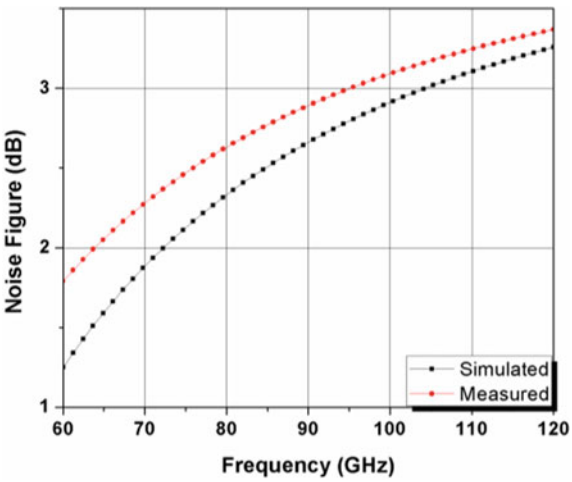

Fig. 4 Noise performance of the proposed LNA

2.1 S-parameter Analysis

The basic S-parameter theory can be given as

$$S_{11} = \frac{m_1}{l_1}|l_2 = 0 \tag{9}$$

$$S_{21} = \frac{m_2}{m_1}|l_2 = 0 \tag{10}$$

Assuming that $V_{in} = l_1 + m_1$ and $V_{out} = l_2 + m_2$
To find S_{21}, l_2 is kept at zero. Therefore,

$$V_{out} = b_2 = -g_m v_{gs}.SL_d \tag{11}$$

$V_{in} = v_g = l_1 + m_1$ Since $m_1 = l_1 s_{11}$, therefore,

$$l_1 = \frac{v_g}{1 + s_{11}} \tag{12}$$

To get $S_{21,}$ we divide equation by l_1. Thus,

$$S_{21} = \frac{m_2}{m_1} = \frac{SL_d g_m (1 + S_{11})}{1 + S^2 C_{gs} L_s + SL_s g_m} \tag{13}$$

From Eq. (13), it can be concluded that S_{21} and C_{gs} are reciprocal of each other. Finally, S_{11} can be given by the below mentioned equation [19].

$$S_{11} = \frac{SL_g\left(1 + S^2 C_{gs} L_s + SL_s g_m\right) - SL_d\left(1 + S^2 C_{gs} L_s + SL_s g_m + S^2 C_{gs} L_g\right)}{SL_g\left(1 + S^2 C_{gs} L_s + SL_s g_m\right) + SL_d\left(1 + S^2 C_{gs} L_s + SL_s g_m + S^2 C_{gs} L_g\right)} \tag{14}$$

Figure 5 depicts the bandwidth versus return loss characteristics. The inductive peaking technology at the gate can be used to modify the bandwidth parameter. By keeping the gate inductance values at 1, 2 and 3 nH, slight deviation in the bands is achieved. The best bandwidth ranging from 61 to 96.7 GHz is obtained for L_g = 1nH for the obvious reason of being reciprocal of bandwidth. Also it yields best return loss of -31 dB. Looking at the other S –parameters that are S_{12} and S_{22} the band is narrow and slightly shifted from the original band. S_{12} band lies between 72 to 82 GHz, while S_{22} falls in the range of 82–92 GHz making both bands of 10 GHz (Fig. 6).

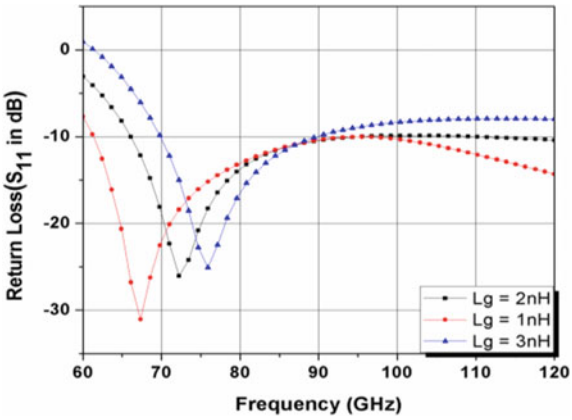

Fig. 5 Band performance for different values of inductance

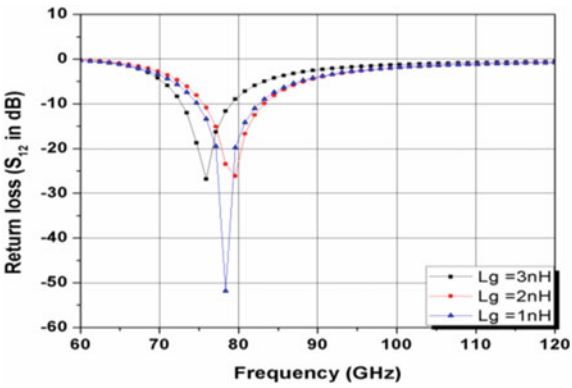

Fig. 6 S_{12} for different values of gate inductance

2.2 Drain Characteristic

Figure 7 illustrates the drain characteristic of MOS device. It is clear that it follows the desired basic rules of characteristics. The current varies with the change in drain voltage by keeping gate voltage fixed at 0.4 V, 0.8 V, and 1.2 V. It should be noted that for maximum V_{gs} the maximum drain current is attained.

2.3 Linearity

The linearity of an amplifier model is given as [23]

$$V_{out} = a_1 v_{in} + a_2 v_{in}^2 + a_3 v_{in}^3 \tag{15}$$

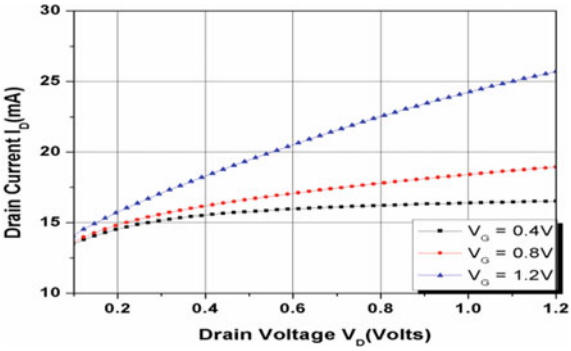

Fig. 7 Drain current at different gate voltages

By incorporating negative feedback, the linearity is enhanced in the following manner

$$\frac{\text{IP3}|_{\text{CL}}}{\text{IP3}|_{\text{OL}}} = (1 + a_1 f)^2 \sqrt{\frac{a_2}{a_2(1 + a_1 f) - 2\text{fa}_2^2}} \tag{16}$$

Here, IP3|CL is the IP3 when close loop and IP3|OL is IP3 when open loop. Both open and close loop gain are inter dependent. The open loop gain of the amplifier causes reduced linearity of close loop gain. Conventional feedback loop does not help to elevate the factor especially when the high frequency roll off occurs in open loop gain. In the cascode amplifier of the circuit presented in this paper is having the MOS transistors M_1 and M_2. The transconductance of the two MOS devices comes in series so that their sum boosts the overall transconductance (g_m) at the input stage (Table 1)

Table 1 Comparisons of LNA performance with other reported papers

Design parameters	[24]	[25]	[26]	[27]	Present work
Technology	90 nm CMOS	200/240 SiGe HBT	200/290 SiGe HBT	200/290 SiGe HBT	45 nm CMOS
Peak gain (dB)	14.6	18	17	16.1	22.2
NF (dB)	<5.5	10.5	4.5	8.8	1.25
B.W (GHz)	58	60	77	77	61–96.7
Power (mW)	24	34	10.8	54	1.8
Area (mm^2)	0.35 × 0.4	0.3 × 0.4	0.6 × 0.9	1.3 × 1.0	–

3 Result and Discussion

Voltage gain for first and second stage can be calculated by the below mentioned equations [19].

$$G_1 = \left(\frac{g_{m1}}{1 + \mathrm{SZ}_{s2}C_{\mathrm{db1}}}\right)\left(\frac{g_{m2}Z_{L2}}{g_{m2} + \mathrm{SC}_{\mathrm{sb2}} + \mathrm{SC}_{\mathrm{gs2}}}\right) \tag{17}$$

$$G_2 = \left(\frac{g_{m3}}{1 + \mathrm{SZ}_{s4}C_{\mathrm{db3}}}\right)\left(\frac{g_{m4}Z_{L4}}{g_{m4} + \mathrm{SC}_{sb4} + \mathrm{SC}_{\mathrm{gs4}}}\right) \tag{18}$$

Here, $Z_{s2} = \mathrm{SL}_{d1} + \frac{1}{(\mathrm{SC}_{\mathrm{sb2}}+\mathrm{SC}_{\mathrm{gs2}}+g_{m2})}$

$$\text{and } Z_{L2} = (R_{d2} + \mathrm{SL}_{d2}) \left\| \left(\frac{1}{\mathrm{SC}_{\mathrm{db3}}}\right) \right\| Z_L \tag{19}$$

Here , g_{m1}, g_{m2}, g_{m3}, and g_{m4} are transconductance of CMOS devices, R_{m2} and R_{m4} are the effective input impedances of the M_2 and M_4 appearing at the input ports. C_{ds2}, C_{ds4}, r_{ds2}, and r_{ds4} are the parasitic capacitances and resistances of the devices. Finally, $R_L^{'}$ is the effective resistance of second stage appearing in parallel to the output impedance of first stage where as R_L is the load resistance. Figure 8 depicts that the gain obtained both theoretically and practically is quite correlated with each other with the desired flatness. The circuit resonates at 75 GHz giving rise to a spike with the gain above 22 dB. For rest of the band, it is maintained at nearly 21 dB. The shunt resistance feedback technique is the key method for obtaining such flat gain. The value of R_f is kept at 280Ω.

The paper demonstrated an efficient band converted CMOS LNA for satellite-based remote sensing application. The designed LNA comprised of a two stage cascode amplifier with shunt resistance feedback and dual inductive peaking (SRF-DIP) technique using both source and gate inductive degeneration. The received band was 35.7 GHz that ranges from 61 to 96.7 GHz. The maximum power gain is attained to be 22.2 dB at resonant frequency of 74.7 GHz. It got a peak near the

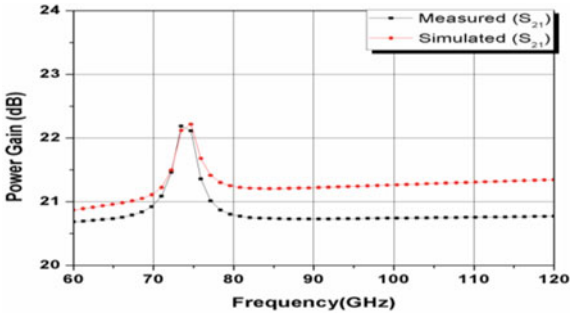

Fig. 8 Power gain of the proposed LNA

resonance while for rest of the frequency range turned out to be almost flat with the maximum value of about 21 dB. The minimum noise figure of 1.25 dB at 60 GHz with impedance matching has been achieved. The maximum value of I_d came between 20 to 25 mA for the drain voltage of 0–1.2 V. The designing platform is Agilent's ADS with 45 nm CMOS technology.

References

1. Venevsky S (2018) Emergence of climate change ecology. Elsevier's reference module in earth systems and environmental sciences, remote sensing
2. Unninayar S, Olsen LM (2015) Monitoring, observations, and remote sensing—global dimensions. Elsevier's reference module in earth systems and environmental sciences
3. Liu R, Lin C, Deng K, Wang H (2003) A 0.5–14-GHz 10.6-dB CMOS cascode distributed amplifier. VLSI Circuits Symp Dig 17:139–140
4. Zhang F, Kinget PR (2006) Low-power programmable gain CMOS distributed LNA. IEEE J Solid-State Circuits 41(6):1333–1343
5. Chang T, Chen J, Rigge LA, Lin J (2008) ESD-protected wideband CMOS LNAs 56(8):1817–1826
6. Zhan JHC, Taylor SS (2006) A 5 GHz resistive-feedback CMOS LNA for low-cost multi-standard applications. In Proc IEEE Int Solid-StateCircuits Conf, San Francisco, CA, USA, pp 721–722
7. Im D, Kim H, Lee K (2009) A CMOS resistive feedback differential low-noise amplifier with enhanced loop gain for digital TV tuner applications. IEEE Trans Microw Theory Techn 57(11):2633–2642
8. Li X, Serdijn WA (2012) On the design of broadband power-to-current low noise amplifiers. IEEE Trans Circuits Syst I, Reg Papers 59(3):493–504
9. Fu CT, Kuo CN (2007) A 3–11 GHz CMOS UWB LNA using dualfeedback for broadband matching. In: Proceedings IEEE radio frequency integrated circuits (RFIC) symposium, pp 67–70
10. Kim C-W, Kang M-S, Anh PT, Kim H-T, Lee S-G (2005) An ultra-wide-band CMOS low-noise amplifier for 3–5-GHz UWB system. IEEE J Solid-State Circuits 40(2):544–547
11. Chang C-P, Chuang H-R (2005) 0.18-um 3–6 GHz CMOS broad-band LNA for UWB radio. Electron Lett 41(12):696–698
12. Pavio AM (1982) A network modeling and design method for a 2–18-GHz feedback amplifier. IEEE Trans Microw Theory Tech MTT-30(12):2212–2216
13. Perez F, Ortega V (1982) A 0.15–12-GHz matched feedback amplifier using commercially available FET's. IEEE Trans Microw Theory Tech MTT-30(8):1289–1290
14. Lo, C.-M. Lin, C.-S. and Wang, H.: A miniature V band 3-stage cascode LNA in 0.13μmCMOS. In Proc. IEEE Int. Solid-State Circuits Conf. Tech. Dig., pp. 402–403, 2006
15. Hu J, Ma K, Mou S, Meng F (2018) A seven-octave broadband LNA MMIC using bandwidth extension techniques and improved active load. IEEE Trans Circuits Syst–I: Regular Papers, pp 1549–8328
16. Huang CY, Liu, JYC (2018) 62–92 GHz low-noise transformer-coupled LNA in 90-nm CMOS. Electron Lett 17th 54(10), pp 634–636
17. Sapone G, Palmisano G (2011) A 3–10-GHz low-power CMOS low noiseamplifier for ultra-wideband communication. IEEE Trans Microw Theory Techn 59(3):678–686
18. Low Noise Amplifier Design and Optimization Thesis.
19. Kumar ARA, Sahoo BD, Dutta A (2018) A wideband 2–5 GHz noise canceling subthreshold low noise amplifier. Trans Circuits Syst II: Express Briefs. 65(7). https://ieeexplore.ieee.org/xpl/RecentIssue.jsp?punumber=8920Vol.

20. Molavi R The design of wideband Cmos low-noise amplifiers. Thesis
21. Huang ZY, Huang CC, Chen CC, Hung C.C, Chen CM (2009) An inductor coupling resonated CMOS low noise amplifier for 3.1–10.6GHz ultra-wideband system. In: IEEE international symposium on circuits and systems
22. Huang B-J, Lin K-Y, Wang H (2009) Millimeter-wave low power and miniature CMOS multicascode low-noise amplifiers with noise reduction topology. IEEE Trans Microw Theory Tech 57(12)
23. Perumana BG, Zhan JHC, Taylor SS, Carlton BR, Laskar J (2008) Resistive-feedback CMOS low-noise amplifiers for multiband applications. IEEE Trans Microw Theory Tech 56(5)
24. Yao T, Gordon MQ, Tang KKW et al (2007) Algorithmic design of CMOS LNAs and PAs for 60-GHz radio. IEEE J Solıd-State Circuıts 42(5)
25. Pfeiffer U (2006) A 20 dBm fully-integrated 60 GHz SiGe power amplifier with automatic level control. In Proceedings ESSCIRC, pp 356–359
26. Komijani A, Hajimiri A (2005) A wideband 77 GHz, 17.5 dBm power amplifier in silicon. In: Proceedings custom integrated circuits conference (CICC), pp 571–574
27. Pfeiffer UR, Reynolds SK, Floyd BA (2004) A 77 GHz SiGe power amplifier for potential applications in automotive radar systems. In: Radio frequency integrated circuits (RFIC) system. Digest of paper, pp 91–94

SRR Loaded Oxalis Triangularis Leaf-Shaped Fractal Antenna for Multiple Band Resonance

C. Elavarasi and D. Sriram Kumar

Abstract Triangularis Oxalis leaf-shaped snowflake fractal patch antenna with tri-leaf has been designed for appropriate wireless communication applications and capable of exhibiting S, C and X-band behavior. The proposed structure is created by introducing meander-snowflake curve on ground with a triangular shaped CPW fed patch exhibiting multiband behavior. The tri-Oxalis antenna has dimensions of 14 mm × 12 mm × 1.6 mm with defected Koch ground structure. The values of return loss of the proposed antenna are − 28.684 dB, − 20.29 dB, − 15.76 dB, − 23.34 dB, − 28.05 dB, − 21.39 dB and − 26.91 dB at resonating frequencies 2.94 GHz, 3.88 GHz, 7.04 GHz, 8.9 GHz, 9.72 GHz and 11.38 GHz, respectively. VSWR parameter for the Oxalis antenna is lying under 2. It has satisfactory production for E and H-planes in all the ideal existence bands and produce greater performance compare to the obtainable antenna. The loaded SRR creation concert is authenticated all the way thru negative permeability removal and mixed parametric study.

Keywords CPW · SRR · Fractal antenna · SRR monopole antenna · Oxalis triangularis leaf · Multi-resonant band · Koch snowflake fractal

1 Introduction

A fractal is a figure that the laws of nature reiterated at diverse scales. Samples are universally in the forest. Trees are usual fractals, patterns that reappears slighter and smaller copies of themselves to generate the biodiversity of a forest. Individually, tree branch, since the trunk to the tips, is a reproduction of the one that came previously [1]. This is a basic belief that we see over and over again in the fractal assembly of organic life procedures all over the natural world. The most communal species grown as a houseplant is Oxalis triangularis which has three common names, purple and false shamrock and love plant. It has three [customarily] purple heart-shaped

C. Elavarasi (✉) · D. S. Kumar
Department of ECE, National Institute of Technology, Tiruchirappalli, India
e-mail: celavarasi@nitt.edu

S. Rawat et al. (eds.), *Proceedings of Second International Conference on Computational Electronics for Wireless Communications*, Lecture Notes in Networks and Systems 554,
https://doi.org/10.1007/978-981-19-6661-3_7

Fig. 1 Oxalis triangularis leaf

leaves, which each leaf has three sides that sit equally to one another at the end of every stem [or "petiole"].

It has three [customarily] purple heart-shaped leaves, which each leaf has three sides that sit equally to one another at the end of every stem [or "petiole"]. The global effect is that they end up viewing like a trio of butterflies combined together by their noses [2] (Fig. 1).

Meander-Koch snowflake fractal has been implemented on CPW fed patch to enhance its characteristics of multiple frequency resonances. The structure of antenna ground is shaped by an iterative mathematical process referred to an iterative function system (IFS) exploiting geometry like Koch curve. A primary baseline is exchanged with a series of four reduced same size line segments, two finish segments lying on the first line and input its termination points and two other line segments forming a spike that protrudes removed from this baseline [3, 4]. For the Koch curve iteration, angle is 55°. So, work for Koch curve is truly an efficient step. For every iteration, the length of a plane decreases by an element of three. It was initial delineate by Helge von Koch in 1904. The options of the Koch curve will overcome to the drawbacks of little antenna. The expected good thing about employing a shape as an antenna is to miniaturize the full height of antenna at resonance [5]. This is often achieved by modifying oxalis triangular leaf and snowflake curve.

In this manuscript, a CPW feed SRR Oxalis triangularis leaf-shaped fractal monopoly patch with the several band frequency is executed. The Oxalis antenna has two circular SRR imprinted reverse side of the FR4 and Oxalis tri-leaf is placed on the top patch radiator with constraints of 14×12 mm^2 with thickness of 1.6 mm. With this flattened design, the SRR Oxalis patch antenna realizes the operational S band at 2.94 GHz and 3.88 GHz/C band at 7.04 GHz/X band at 8.9 GHz, 9.72 GHz and 11.38 GHz. Particulars of the SRR loaded Oxalis leaf-shaped fractal antenna is explained and S11, far- field pattern with gain and VSWR are deliberated in the consequent segment.

2 Iterative Function System (IFS)

IFS is a widely used mathematical tool used for the design of fractal geometries. The affine transformation of proposed antenna is following: (Fig. 2)

$$W\begin{pmatrix} x \\ y \end{pmatrix} = \begin{pmatrix} a_f & c_f \\ b_f & d_f \end{pmatrix}\begin{pmatrix} x \\ y \end{pmatrix} + \begin{pmatrix} e_f \\ f_f \end{pmatrix} \tag{1}$$

where a_f, b_f, d_f, cf, e_f and f_f are real numbers of the fractals. a_f, b_f, c_f and d_f control the turning and scaling while e_f and f_f control linear shift or translation [6]. Assume $W_1, W_2, \ldots, W_n$ are series of direct affine transformations. The first iteration for the Koch curve consists of taking four copies of the horizontal line phase, each is scaled by $r = 1/3$. Two segments should be turned to 55°, one clockwise and one anti-clockwise as shown in Fig. 2. In conjunction with the specified translations, this yields the subsequent IFS. The iterative function system (IFS) is used to concept the fractal generator. This method is useful to create a number of fractal geometries [7, 8]. Using IFS, the meander-Koch curve fractal antenna is designed after a sequence geometric operation which encompasses scaling, rotation and translation is known as transformation. The transformations for getting generator structure are uttered by the subsequent function:

$$W_1\begin{pmatrix} x \\ y \end{pmatrix} = \begin{pmatrix} 0.25 & 0.00 \\ 0.00 & 0.25 \end{pmatrix}\begin{pmatrix} x \\ y \end{pmatrix} + \begin{pmatrix} 0.00 \\ 0.00 \end{pmatrix} \tag{2}$$

$$W_2\begin{pmatrix} x \\ y \end{pmatrix} = \begin{pmatrix} 0.25 & -0.55 \\ 0.55 & 0.25 \end{pmatrix}\begin{pmatrix} x \\ y \end{pmatrix} + \begin{pmatrix} 0.25 \\ 0.00 \end{pmatrix} \tag{3}$$

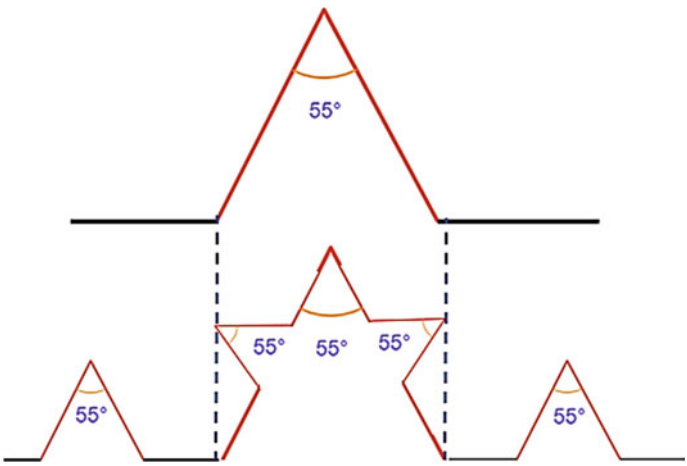

Fig. 2 Meander-Koch fractal with modified 55° angle

$$W_3\begin{pmatrix} x \\ y \end{pmatrix} = \begin{pmatrix} 0.25 & 0.55 \\ -0.55 & 0.25 \end{pmatrix}\begin{pmatrix} x \\ y \end{pmatrix} + \begin{pmatrix} 0.50 \\ 0.55 \end{pmatrix} \tag{4}$$

$$W_4\begin{pmatrix} x \\ y \end{pmatrix} = \begin{pmatrix} 0.25 & 0.00 \\ 0.00 & 0.25 \end{pmatrix}\begin{pmatrix} x \\ y \end{pmatrix} + \begin{pmatrix} 0.75 \\ 0.00 \end{pmatrix} \tag{5}$$

where the Wx is termed Hutchinson operator. W_1, W_2, W_3 and W_4 are set of affine linear transformations [9]. The transformations to gain the segments of the originator of our proposed geometry are as follows:

$$W(A) = \mathrm{UW}_n(A) \tag{6}$$

The ground is designed with snowflake iterations. The modified angle in Koch curve patch is 55°. The construction of iteration from simple patch is shown with various iteration stages to construct modified ground of the Oxalis geometry [10].

3 Oxalis Triangularis Leaf Antenna Pattern

3.1 Construction

Meander-Koch curve ground with CPW fed patch is designed to achieve multiple band resonance. Oxalis leaves are also designed to introducing the flower shaped fractal patch as revealed in Fig. 3. The advantage of the leaf during this proposed antenna is to get more numbers of upper, lower and middle frequency resonance bands and improvement in gain. The proposed structure of strip design is shown with tri-shaped leaves for good results which is engraved on an FR4 substrate through dielectric constant εr = 4.4 whose dimensions are WFR4 X LFR4 X h mm^3 and the ground is tailored as snowflake. The snowflake iterations are wrapped up to third level of iteration. Structural calculations are described in Tables 1 and 2 with proper dimensions of parameters of design antenna. The cleft 'g' among the center strip plus snowflake ground plane is 0.2 mm. The circular split-ring resonator is positioned back-side of the substrate as exposed in Fig. 4.

3.2 Antenna Dimensions

See (Tables 1 and 2)

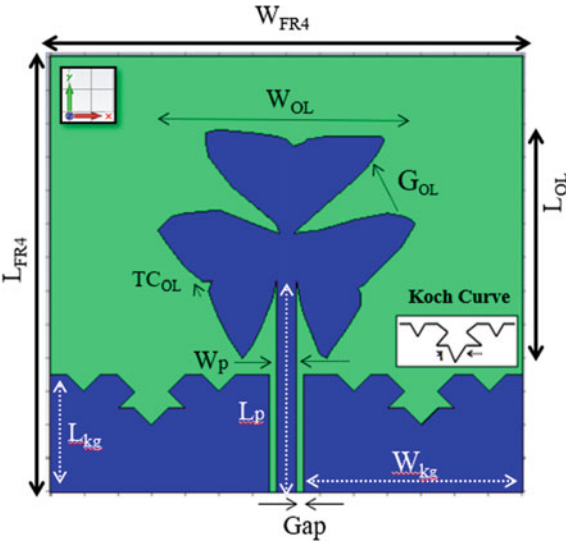

Fig. 3 CPW fed Oxalis triangularis leaf shape patch antenna

Table 1 Optimized constraints

Parameters	Explanation	Values (mm)
W_{FR4}	Width of the flame retardant-G4	14
L_{FR4}	Length of the flame retardant-G4	12
Gap	Gap b/w the patch and ground	0.2
W_{kg}	Width of the Koch ground	6.5
L_{kg}	Length of the Koch ground	2.5
W_p	Width of the patch	0.6
L_p	Length of the patch	6.0
H	Thickness of the substrate	1.6
r1	Radius of the outer ring	4.0
r2	Radius of the inner ring	3.0
S	Splits between the ring	0.4
W	Width of the ring	0.4

Table 2 Optimized constraints of Oxalis triangularis leaf

Parameters	Explanation	Values (mm)
L_{OL}	Length of the Oxalis leaf	6.5
W_{OL}	Width of the Oxalis leaf	6.5
G_{OL}	Gap of the Oxalis leaf	1.5
TC_{OL}	Triangular cut of the Oxalis leaf	0.2

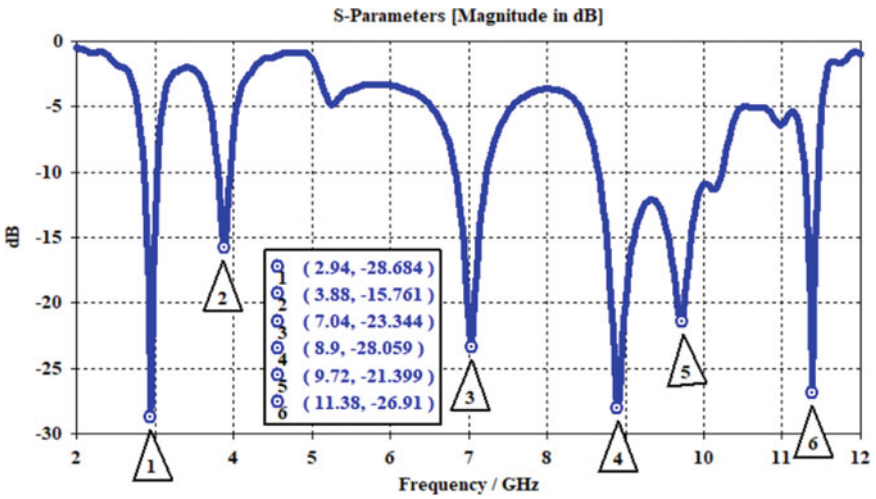

Fig. 4 S_{11} versus freq. of oxalis leaf shape antenna

4 Results and Discussion

The antenna illustrations the resonances at 2.94 GHz at −28.684 dB and 3.88 GHz at −15.761 dB casing S band, 7.04 GHz at −23.344 casing C band and 8.9 GHz at −28.059 dB, 9.72 GHz at −21.399 dB and 11.38 GHz at −26.91 dB casing X band as show in Fig. 5. The ground is modified as snowflake and also iterated to achieve multiple frequency band. Comparison of iterated meander snowflake fractal with customized ground is shown in Fig. 10.

VSWR for Oxalis antenna is shown in Fig. 6 that is lying below 2. VSWR parameter basically describes the ohmic resistance of antenna. It matched to the magnitude relation of the cable connected to that. Simulated outcomes satisfy the condition of VSWR for all deep frequencies and conform the ohmic resistance matching's for proposed antenna.

In broad, the SRR acquires unusual property like −ve permeability and −ve permittivity. To authorize the incidence of −ve permeability features in the SRR structure, wave-guide technique is used to designate. The Oxalis circular split-ring structure is positioned inside wave-guide on the FR4 as revealed in Fig. 7a. Here, PMC is allotted to together the top/bottom of the wave-guide, and PEC is allotted to X and Z-axis. The attained real permeability standards are categorized in Fig. 7b, which signifies the negative permeability characteristics at 5.6 and 10 GHz and these properties are the root for recital improvement of the Oxalis triangular leaf-shaped antenna.

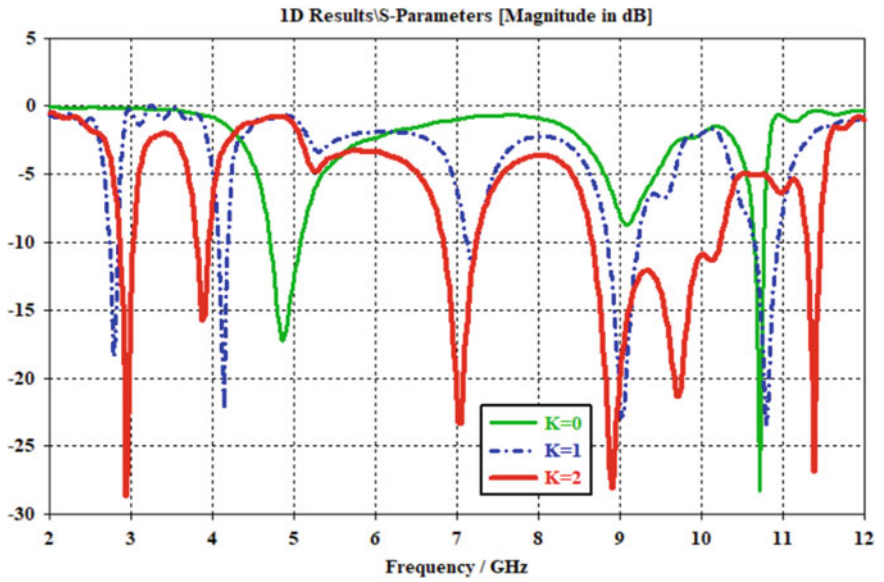

Fig. 5 Snowflake iterations of S_{11} versus Freq. of $K = 0, 1, 2$

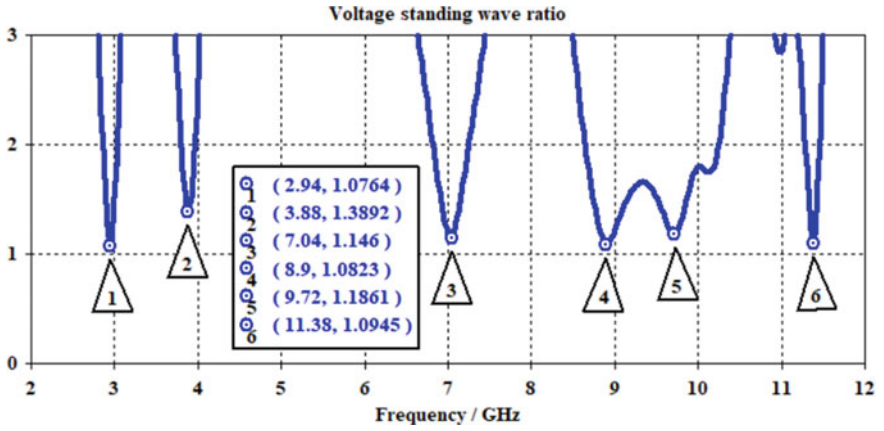

Fig. 6 VSWR versus frequency

Figure 8 displays the simulated 3D outline of SRR overloaded Oxalis triangularis leaf fractal antenna for 4 and 9 GHz, which shows the signs of omnidirectional energy sketch at H-plane with bi-directional energy mold at E-plane and the gain is realized beyond 2 dBi and has maximum peak gain as 6.685 dBi, routinely as revealed in Fig. 9.

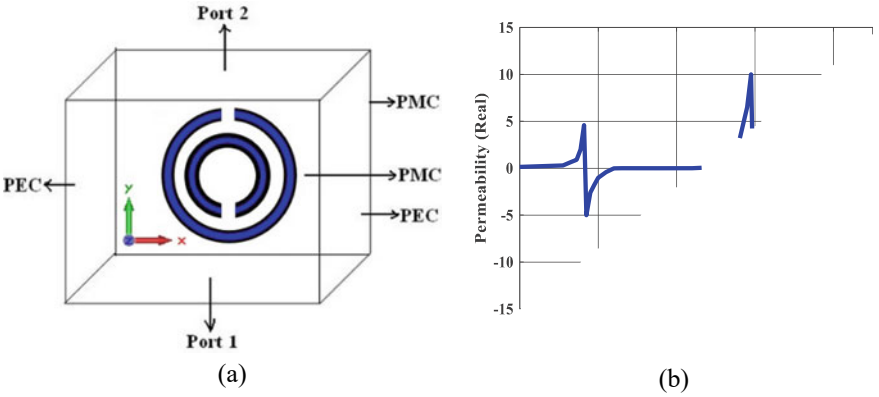

Fig. 7 Wave-guide setup for SRR and extracted negative permeability of SRR

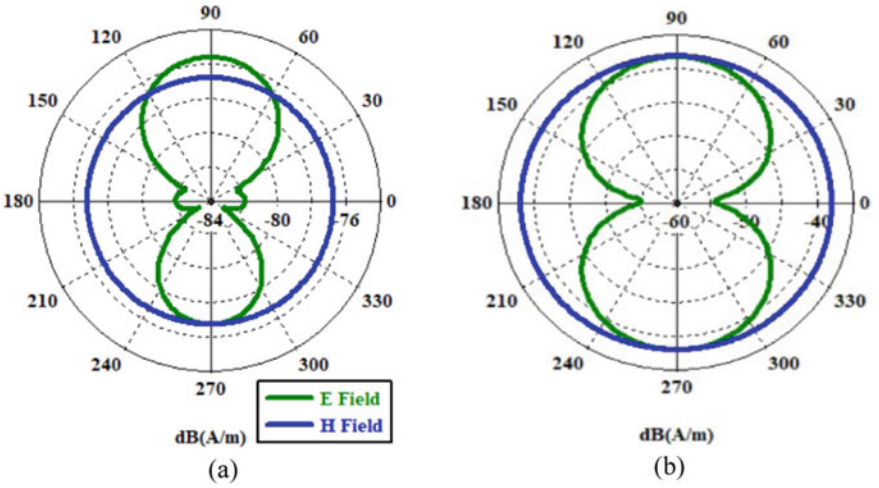

Fig. 8 Far-field patterns **a** 4 GHz **b** 9 GHz

5 Conclusion

A Oxalis triangularis leaf-shaped CPW fed patch antenna supported by Koch curve has been simulated and designed on FR4 substrate and outcomes are investigated. The Oxalis structure has compacted dimensions of 14 mm × 12 mm × 1.6 mm and exhibits S/C/X-band operation by resonating at six various frequencies. Acceptable values of return loss 2.94, 3.88, 7.04, 8.9, 9.72 and 11.38 GHz, capable of be utilize in assorted communication systems in LTE2300, wireless comm., fixed satellite, Wi-Fi and WiMAX, The maximum peak gain is 6.685 dB at 12 GHz and VSWR (less than 2) are achieved. The 2D far-field radiation pattern is incredibly uniform in all directions.

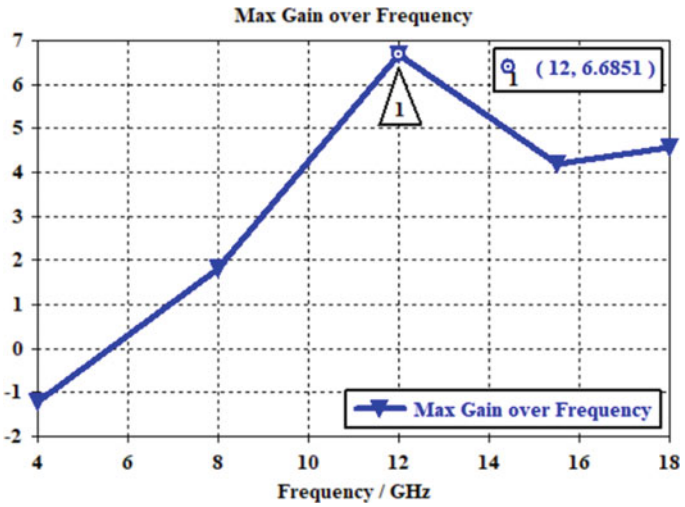

Fig. 9 Gain versus frequency

References

1. Kaboutari K, Zabihi B, Virdee B, Salmasi MP (2019) Microstrip patch antenna array with cosecant-squared radiation pattern profile. AEU—Int J Electron Commun 106:82–88. https://doi.org/10.1016/j.aeue.2019.05.003
2. Arif A, Zubair M, Ali M, Khan MU, Mehmood MQ (2019) A compact, low-profile fractal antenna for wearable on-body WBAN applications. IEEE Antennas Wirel Propag Lett 18(5):981–985
3. Paracha KN, Rahim SKA, Chattha HT, Aljaafreh SS, Rehman S, Lo YC (2018) Low cost printed flexible antenna by using an office printer for conformal applications. Int J Antennas Propag, 1–7
4. Elavarasi C, Shanmuganantham T (2018) Multiband SRR loaded leaf shaped Koch fractal with a modified CPW-fed antenna. Int J Electron Lett 6(2):137–145. https://doi.org/10.1080/21681724.2017.1329942
5. Shi Y, Fan Y, Jing J, Yang L, Li Y, Wang M (2018) An efficient fractal rectenna for RF energy harvest at 2.45 GHz ISM band. Int J RF Microw Comput Eng 28(9):e21424
6. Darimireddy NK, Reddy RR, Prasad AM (2018) A miniaturized hexagonal-triangular fractal antenna for wide-band applications. IEEE Antennas Propag Magazine, 104–110
7. Hong W, Baek KH, Ko S (2017) Millimeter-wave 5G antennas for smartphones: overview and experimental demonstration. IEEE Trans Antennas Propag 65(12):6250–6261
8. Choukiker YK, Behera SK (2017) Wideband frequency reconfigurable Koch snowflake fractal antenna. IET Microwaves Antennas Propag 11(2):203–208
9. Farswan A, Gautam AK, Kanaujia BK, Rambabu K (2016) Design of Koch fractal circularly polarized antenna for handheld UHF RFID reader applications. IEEE Trans Antennas Propag 64(2):771–775. https://doi.org/10.1109/TAP.2015.2505001
10. Gonzalez MC, Kumar BSP, Branner GR (2016) Generalised design method of broadband array antennas using curved geometry. IET Microwaves Antennas Propag 10(14):1553–1562
11. Singhal S, Singh AK (2016) Cpw-fed hexagonal sierpinski super wideband fractal antenna. IET Microwaves Antennas Propag 10(15):1701–1707

12. Choukiker YK, Sharma SK, Behera SK (2014) Hybrid fractal shape planar monopole antenna covering multiband wireless communications with MIMO implementation for handheld mobile devices. IEEE Trans Antennas Propag 62(3):1483–1488
13. Yurduseven O, Smith D, Elsdon M (2013) Printed slot loaded bow-tie antenna with super wideband radiation characteristics for imaging applications. IEEE Trans Antennas Propag 61(12):6206–6210
14. Behera S, Vinoy KJ (2012) Multi-port network approach for the analysis of dual band fractal microstrip antennas. IEEE Trans Antennas Propag 60(11):5100–5106
15. Puente C, Romeu J, Pous R, Ramis J, Hijazo A (1998) Small but long Koch fractal monopole. Electron Lett 34(1):9–10

Computation of SAR Variation with Oblique Angle of Incidence for Human Head Exposed to Mobile Phone Using Transparent Shield

Sai Spandana Pudipeddi and P. V. Y. Jayasree

Abstract In the proposed work, a mathematical analysis of specific absorption rate (SAR) deduction using transmission line method is performed in adult and child head by considering a planar four-layer head model at lower and mid 5G mobile frequencies. The change in the SAR with the oblique incidence of EM wave (0 to 90°) is observed utilizing the shielding effectiveness (SE) variable of transparent silver nanowire/poly (diallyldimethylammonium chloride) (PDDA) with nickel coating on top. The simulations were performed for SE with the angle of incidence, and results are tabulated for the same. It is found from the results that the child model has absorbed more radiation levels than an adult head model at 6 GHz without a shield, but with transparent AgNW/PDDA/Ni laminated shield, the SAR has reduced to 0.000779 mW/kg at 89° TE polarization in a four-layered child head model than in TM polarization. The SAR absorption by the brain layer of the head is less in the TE polarization in the adult than in the child head model.

Keywords Four-layer human head model · Transmission line method · Silver nanowire (AgNW) · Transparent laminated shield · Mobile smartphone exposure · Specific absorption rate (SAR)

1 Introduction

A labyrinthine protection and safety of human health and electrical equipment against the undesirable electromagnetic fields should meet the electromagnetic compatibility (EMC) essentialiaties and the bio-standards specifying the acceptable limits [1]. With the enormous rapid development of wireless communication devices, the health hazards are also increasing at a rapid pace. Dosimetry is essential to study

S. S. Pudipeddi (✉) · P. V. Y. Jayasree
Department of EECE, GITAM Deemed to Be University, Visakhapatnam, India
e-mail: psspandana26@gmail.com

P. V. Y. Jayasree
e-mail: jpappu@gitam.edu

S. Rawat et al. (eds.), *Proceedings of Second International Conference on Computational Electronics for Wireless Communications*, Lecture Notes in Networks and Systems 554,
https://doi.org/10.1007/978-981-19-6661-3_8

the tissue interaction in human beings with EMF and health hazards caused by EMF by understanding the safety of radiation from mobile phones. The thermal effects of non-ionizing radiation increase the temperature of human tissues to the maximum of 4 °C due to neuron damage in the brain. Many health disorders are caused by mobile phone radiation exposure, including insomnia, headache, fatigue, cardiovascular symptoms, and an increased risk of developing cancer and leukemia [1].

The interaction of human tissues with electromagnetic field (EMF) with variable sizes in a tissue multi-layer structure shows variation in dielectric properties with frequency. Thus, the distribution of EMF absorbed by the human bodies depend on the geometry, dielectric tissue properties, frequency, and polarization of the incident EM wave. Researchers have implemented the SAR as a metric for EMF exposure from wireless devices based on the distribution of absorbed mobile phone radiation in living beings. The human head is a vulnerable part that is most affected when a user is speaking over the mobile phone for a long time. With a combination of two or three layers called laminated shield, the EMF between head and the mobile device can be limited.

In the proposed work, the SAR variation with the oblique angle of incidence at four lower and mid-band frequencies of 5G when a user's head (adult or a child) is exposed to mobile RF radiation considering a planar four-layered head structure using the shielding effectiveness (SE) property of the transparent thin film by the transmission line method.

1.1 Specific Absorption Rate (SAR)

The local (head, limbs, etc.) and whole-body values of SAR depend on including the distance between the human head and the mobile device frequency and polarization of radiated wave, grounding, etc. It is the dosimetry value, which measures the energy absorbed per unit mass of the head tissue (Wkg^{-1}). Some international guidelines provide recommended worldwide SAR limit that determine the main EMF exposure conditions. India has adopted the guidelines coined by International Commission for Non-Ionizing Radiation Protection (ICNIRP) regulatory body [2]. According to ICNIRP, the recommended SAR limit for local exposure or energy absorbed by head, limbs, etc., by the general public is 2 Wkg^{-1} [3]. The SAR is calculated from the induced electric field in general:

$$\mathrm{SAR} = \frac{\sigma |E|^2}{\rho} \tag{1}$$

where σ is tissue conductivity (S/m), E is the tissue induced electric field (V/m), and ρ is tissue density ($\mathrm{Kg/m}^3$).

1.2 Transparent Shielding Material-Metal Nanowire Networks

Several advanced materials are developed to resolve the issue of EMI. Considering the lightweight nature and minimal shield size, a flexible and transparent shield is chosen. Metal nanowires provide excellent conductivity and invariant shielding property under flexing.

Networks of silver nanowires (AgNWs) can be deposited to form transparent films with excellent shielding performance. To increase the conductivity of the composite film formed as a function of silver nanowire volume, the silver nanowires are doped with polymer composites [4].

2 Methodology

Transmission Line Method Based on Oblique Angle of Incidence. A planar four-layered head model is considered for the analysis of the work, considering air and brain layers to be infinite media as shown in Fig. 1. Only the vertical half of the user's head is taken. The incident angle is incident on the skin layer of the head surface for a four-layer head model. Figure 1 shows the parallel and perpendicular polarization of EM wave when incident angle strikes the head surface. The impedance of each layer is the sheet impedance and varied according to the polarization angle.

The adult and a child head models have the following head layers, skin, fat, bone, and brain. The thickness in mm of the head tissues in adults and children [6, 7] are shown in Tables 1 and 2. Based on the total body water content (TBW), the

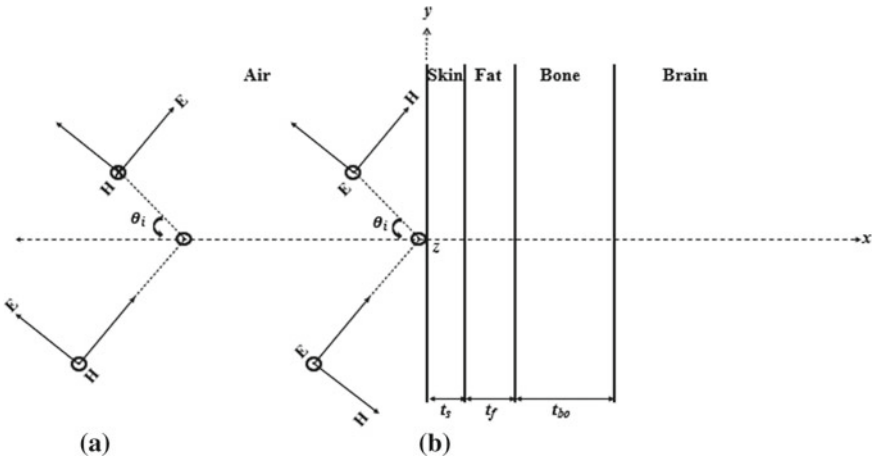

Fig. 1 **A** Parallel polarization, **B** perpendicular polarization of EM wave incident in air on to skin surface in a four-layered head model

Table 1 Thickness of head tissues in adult four-layer model

Head tissue	Thickness (mm)
Skin	1
Fat	2
Bone	7

Table 2 Thickness of head tissues in child four-layer model

Head tissue	Thickness (mm)
Skin	1
Fat	0.5
Bone	6.5

dependence on the dielectric properties of the head tissues such as complex relative permittivity and conductivity change accordingly. In the analysis, age-dependent dielectric properties of tissues are considered for both adult and child head models.

2.1 Analysis of Shielding Effectiveness Considering Head Model Alone

Using the transmission line analysis, the human head shielding effectiveness is calculated for a head region treating it as a plane shield of three layers. Assuming a small part of head to be laminated shield of first three layers for a four-layered adult or a child's head, the SE for the head is deduced from reflection and transmission coefficient, and impedance of head tissue using transmission line method [8]. The radiated EM wave's transmission coefficient entering into brain through skin, fat, and bone is

$$p = \frac{16 z_1 z_s z_f z_b}{(z_1 + z_s)(z_s + z_f)(z_f + z_b)(z_b + z_{br})} \tag{2}$$

where z_1, z_s, z_f, z_b, and z_{br} are the impedances of free space, skin, fat, bone, and brain with respect to the polarization angle. The impedances for TE and TM polarization, respectively, as shown below [8]

$$z_j = \frac{\eta_j}{\cos(\theta_j)} \tag{3}$$

$$z_j = \eta_j \cos(\theta_j) \tag{4}$$

$$K_j = \omega \sqrt{\mu_j \left(\varepsilon_j + \frac{\sigma_j}{j\omega} \right)} \tag{5}$$

K_1 is the wave-number of the air medium, as the incident angle is incident from the air medium first. The polarization angle for each medium is

$$\cos(\theta_j) = \sqrt{1 - \left(\frac{K_1}{K_j}\right)^2 \sin\theta_1^2} \tag{6}$$

With the new impedance equations formed from the polarization of EM wave, θ is varied from 0 to 90°. The reflection coefficients at air-skin, skin-fat, and fat-bone interfaces, respectively, are

$$q_{\text{as}} = \frac{(z_s - z_1)[z_s - z(l_1)]}{(z_s + z_1)[z_s + z(l_1)]} \tag{7}$$

$$q_{\text{sf}} = \frac{(z_f - z_s)[z_f - z(l_2)]}{(z_f + z_s)[z_f + z(l_2)]} \tag{8}$$

$$q_{\text{fb}} = \frac{(z_b - z_f)[z_b - z_{br}]}{(z_b + z_f)[z_b + z_{br}]} \tag{9}$$

where $z(l_1)$ and $z(l_2)$ are input impedances to the right of fat, bone, and brain.

$$z(l_1) = z_f \frac{z_b \cosh(\gamma_f l_2) + z_f \sinh(\gamma_f l_2)}{z_f \cosh(\gamma_f l_2) + z_b \sinh(\gamma_f l_2)} \tag{10}$$

$$z(l_2) = z_b \frac{z_{br} \cosh(\gamma_b l_3) + z_b \sinh(\gamma_b l_3)}{z_b \cosh(\gamma_b l_3) + z_{br} \sinh(\gamma_b l_3)} \tag{11}$$

where l_2 and, l_3 are the thickness of fat and bone tissues. γ_f and γ_b are the propagation constants of wave in fat and bone tissues of human head. The total transmission coefficient T of the EM wave radiated into skin, fat, and bone for a four-layered adult or a child's head is expressed as

$$T = p\left[\left\{\left(1 - q_{\text{as}} e^{-2\gamma_s l_1}\right)\left(1 - q_{\text{sf}} e^{-2\gamma_f l_2}\right)\left(1 - q_{\text{fb}} e^{-2\gamma_b l_3}\right)\right\}\right]^{-1} e^{\left(-\gamma_s l_1 - \gamma_f l_2 - \gamma_b l_3\right)} \tag{12}$$

For a four-layered head model (adult/child), the SE equation can be written from the total transmission coefficient T of the radiated wave as

$$\text{SE} = -20 \log_{10}|T| \tag{13}$$

Table 3 Material properties of shield and coating [9]

Material	DC conductivity (S/m)	Relative permittivity	Relative permeability
AgNW/PDDA	2.53e6	1	1
Ni	1.16e7	1	100

2.2 Analysis of Shielding Effectiveness Considering Head Model with AgNW/PDDA/Ni Laminated Shield

When an external AgNW/PDDA/Ni laminated shield is embodied in the mobile smartphone, the figure and equations for impedances, reflection coefficients, and transmission coefficient change for each layer as discussed. The reflection coefficients, transmission coefficient, and the input impedances of all the head layers along with the AgNW/PDDA/Ni laminated shield are expressed to find out the total transmission coefficient penetrating into the brain layer, T using the transmission line method. The dielectric properties of the shield material are given in Table 3. The shield with coating/lamination is assumed to be embedded on the mobile phone with the adult head (e.g.). The same figure can be drawn with the shield for the child head as well. A 1 mm distance is considered between the coating layer and the skin of the adult/child head.

With the help of characteristic impedances, wave numbers and polarization angles of the head tissues along with the laminated shield medium, the equation for T is expressed as

$$T = p\left(1 - q_{\mathrm{Sa}} e^{-2\gamma_S l_1}\right)\left(1 - q_{\mathrm{Sc}} e^{-2\gamma_c l_2}\right)\left(1 - q_{\mathrm{ca}} e^{-2\gamma_a l_3}\right)$$
$$\left(1 - q_{\mathrm{as}} e^{-2\gamma_s l_4}\right)\left(1 - q_{\mathrm{sf}} e^{-2\gamma_f l_5}\right)\left(1 - q_{\mathrm{fb}} e^{-2\gamma_b l_6}\right)^{-1} e^{\left(-\gamma_S l_1 - \gamma_c l_2 - \gamma_a l_3 - \gamma_s l_4 - \gamma_f l_5 - \gamma_b l_6\right)} \tag{14}$$

2.3 Determination of SAR from Head Shielding Effectiveness Using AgNW/PDDA/Ni Laminated Shield

In the proposed work, the SAR absorbed by the largest layer brain is numerically evaluated at four 5G frequencies. The shielding effectiveness for any barrier is defined in the electric field terms as

$$\mathrm{SE} = 20 \log_{10}\left(\frac{E_i}{E_t}\right) \tag{15}$$

E_i and E_t are incident and transmitted electric field strength. The incident electric field on the user's skin is calculated by substituting the value of incident power-density from ICNIRP guidelines for exposure limits from EMF [3], which is 40 W/m^2 when the frequency of the wave is above 2 GHz. E_t is obtained from SE values calculated from both with the AgNW/PDDA/Ni laminated film and without the film. The SAR entered into the brain (W/kg) is calculated with the transmitted electric field entering the brain layer from the laminated shield in both adult and child head, using Eq. (1).

3 Results and Discussion

Table 4 indicates the absorption SAR by brain of adult and child head models at four 5G lower and mid-band frequencies with incident angle variation (0°, 30°, 45°, 60°, and 89°), from the plots of shielding effectiveness of head and the incident angle of EM wave striking on the head surface. At lower frequency of 3.6 GHz in adult head model without shield, for TE polarization of EM wave, a minimum SAR absorption by the largest layer is 12.71 W/kg at normal incidence and 18.84 W/kg at maximum 89°. For TM polarization, at 89°, the SAR absorption by brain is 0.081 W/kg. However, with the AgNW/PDDA/Ni laminated transparent film, the SAR absorbed by the brain decreased from 3.78e-4 W/kg to 1.56e-6 W/kg; SAR increased to 4.6e-4 W/kg when the incident angle increased to 89°, in TE and TM polarization, respectively.

At 6 GHz, with laminated shield, the SAR has decreased from 1.85e-5 W/kg to 9.09e-6 W/Kg and has increased from 1.85e-5 W/kg to 2.94e-5 W/kg for TE and TM polarization, respectively. In child head model, from Table 5, the maximum SAR absorption by brain layer occurred with no shield used for all the incident angles. With the laminated silver nanowire shield, at 6 GHz, the SAR has decreased from 5.96e-4 to 7.79e-7 W/kg in TE polarization and SAR by brain has increased to 0.0017 from 5.96e-4 W/kg in TM polarization.

4 Conclusion

Theoretical analysis in a mathematical way is determined for determining SAR absorbed by the brain in four-layered aged head models using the concept of the transmission line method. A comparison of SAR estimation and reduction is performed in adult and child head models for fixed mobile frequencies of 6, 5, 4.5, and 3.6 GHz using the shielding effectiveness parameter by varying the angle of incidence of the electromagnetic wave. In general, a child's head absorbs more radiation than an

Table 4 SAR variation with five angles of incidence at lower and mid 5G frequencies without shield and with transparent AgNanowire and PDDA with nickel laminated shield (L.S) for both TE and TM polarization in a four-layered adult head

Frequency (GHz)	Incident angle (Degrees)	SAR absorbed by brain in four-layered adult head for TE polarization (W/kg)		SAR absorbed by brain in four-layered adult head for TM polarization (W/kg)	
		No shield	With L.S	No shield	With L.S
3.6	0	12.71	3.78e-4	12.71	3.78e-4
	30	13.36	3.56e-4	12.02	3.98e-4
	45	14.20	3.22e-4	10.96	4.22e-4
	60	15.41	2.59e-4	9.002	4.53e-4
	89	18.84	1.56e-6	0.081	4.60e-4
4.5	0	7.30	2.29e-4	7.30	2.29e-4
	30	7.61	2.10e-4	6.97	2.48e-4
	45	8.00	1.83e-4	6.45	2.71e-4
	60	8.56	1.36e-4	5.46	3.05e-4
	89	10.09	5.49e-7	0.06	3.87e-4
5.0	0	2.50	7.23e-5	2.50	7.23e-5
	30	2.59	6.53e-5	2.40	7.92e-5
	45	2.71	5.56e-5	2.25	8.86e-5
	60	2.87	4.00e-5	1.94	1.03e-4
	89	3.29	1.45e-7	0.03	1.53e-4
6.0	0	0.69	1.85e-5	0.69	1.85e-5
	30	0.71	1.63e-5	0.67	2.08e-5
	45	0.74	1.34e-5	0.63	2.40e-5
	60	0.77	9.09e-6	0.56	2.94e-5
	89	0.86	2.66e-8	0.008	5.07e-5

adult head owing to various factors such as water content and so on. With the use of transparent laminated AgNW/PDD/Ni film, the SAR is reduced considerably in the child model at 89° in TE polarization (7.79e-7 W/kg) and at normal incidence in TM polarization (0.0017 W/kg) for 6 GHz frequency. Hence, the SAR imbibed in by the brain layer of thickness 70.5 mm has decreased in TE polarization as the incident angle is progressed to 89° than in TM polarization in both adult/child's head models.

Table 5 SAR variation with five angles of incidence at lower and mid 5G frequencies without shield and with the transparent AgNanowire and PDDA with nickel laminated shield (L.S) for both TE and TM polarization in a four-layered child head

Frequency (GHz)	Incident Angle (Degrees)	SAR absorbed by brain in 4-layered adult head for TE polarization (W/kg)		SAR absorbed by brain in 4-layered adult head for TM polarization (W/kg)	
		No Shield	With L.S	No Shield	With L.S
3.6	0	12.71	3.78e-4	12.71	3.78e-4
	30	13.36	3.56e-4	12.02	3.98e-4
	45	14.20	3.22e-4	10.96	4.22e-4
	60	15.41	2.59e-4	9.002	4.53e-4
	89	18.84	1.56e-6	0.081	4.60e-4
4.5	0	7.30	2.29e-4	7.30	2.29e-4
	30	7.61	2.10e-4	6.97	2.48e-4
	45	8.00	1.83e-4	6.45	2.71e-4
	60	8.56	1.36e-4	5.46	3.05e-4
	89	10.09	5.49e-7	0.06	3.87e-4
5.0	0	2.50	7.23e-5	2.50	7.23e-5
	30	2.59	6.53e-5	2.40	7.92e-5
	45	2.71	5.56e-5	2.25	8.86e-5
	60	2.87	4.00e-5	1.94	1.03e-4
	89	3.29	1.45e-7	0.03	1.53e-4
6.0	0	0.69	1.85e-5	0.69	1.85e-5
	30	0.71	1.63e-5	0.67	2.08e-5
	45	0.74	1.34e-5	0.63	2.40e-5
	60	0.77	9.09e-6	0.56	2.94e-5
	89	0.86	2.66e-8	0.008	5.07e-5

References

1. Aniołczyk H (2018) Advanced materials for electromagnetic shielding: fundamentals, properties, and applications. John Wiley & Sons, New Jersey
2. Kumar G (2011) Mobile Tower/mobile phone radiation hazards
3. International Commission on Non-Ionizing Radiation Protection (2020) Guidelines for limiting exposure to electromagnetic fields (100 KHz to 300 GHz). Health physics 118(5), pp 483-524
4. He L, Sie CT (2016) Nanostructured transparent conductive films: fabrication, characterization and applications. Mater Sci Eng 109:1–101
5. Jayasree PVY et al (2010) Analysis of shielding effectiveness of single, double and laminated shields for oblique incidence of EM waves. Prog Electromagn. 22:187–202
6. Rajagopal B et al (2014) SAR assessment on three layered spherical human head model irradiated by mobile phone antenna. Hum-centric Comput Inf 4(1):1–11
7. Drossos A, Veli S, Niels K (2000) The dependence of electromagnetic energy absorption upon human head tissue composition in the frequency range of 300–3000 MHz. IEEE Trans Microw Theory Tech 48(11):1988–1995
8. Spandana PS, Jayasree PVY (2021) Numerical computation of SAR in human head with transparent shields using transmission line method. Prog Electromagn 105
9. Zhu X, Xu J, Qin F et al (2020) Highly efficient and stable transparent electromagnetic interference shielding films based on silver nanowires. Nanoscale 12(27):14589–14597

On the Security of RF-Based IoT Network with Randomly Located Eavesdropper

Vishal Narain Saxena, Juhi Gupta, and Vivek K. Dwivedi

Abstract Internet of Things (IoT) environments are comprised of a variety of electronic objects that transmit radio frequency (RF) signals. It further introduces the enticing possibility of using pre-existing signals for a variety of applications, including medical, industrial, and home automation. This work examines the secrecy performance of an RF-based IoT network in the presence of an eavesdropper (ED) located in a close communication range. It is considered that ED is attempting to wire-tap the secret information by having random waypoint (RWP) mobility in a communication range. Further, the novel analytical expressions for secrecy outage probability (SOP) and probability of strictly positive secrecy capacity (SPSC) in terms of Meijer's-G function are derived. Finally, to obtain a better understanding of the system's performance, the analytical results are expressed asymptotically in the high signal-to-noise ratio (SNR) regime and verified with analytical results.

Keywords Probability of SPSC · RWP mobility · SOP

1 Introduction

Nowadays, Internet of Things (IoT)-based applications are attracting a considerable amount of attention in both living and non-living areas among populations, as they have the potential to link large numbers of networks to the internet. The linked networks are used in a variety of IoT applications, including remote monitoring, medical applications, industry operations regulations, vehicle-to-everything communication,

V. N. Saxena (✉) · J. Gupta · V. K. Dwivedi
Department of Electronics and Communication, Jaypee Institute of Information Technology Noida, Noida, Uttar Pradesh, India
e-mail: vishal.saxena@jiit.ac.in

J. Gupta
e-mail: juhi@jiit.ac.in

V. K. Dwivedi
e-mail: vivek.dwivedi@jiit.ac.in

S. Rawat et al. (eds.), *Proceedings of Second International Conference on Computational Electronics for Wireless Communications*, Lecture Notes in Networks and Systems 554,
https://doi.org/10.1007/978-981-19-6661-3_9

waste disposal, and many more [1]. For the purpose of unhindered connectivity among IoT networks, radio frequency (RF) systems are evolved as a base model due to its omnipresent existence. This has resulted in extensive network coverage as well as flexible deployment [2]. In spite of the potential benefits, non-line-of-sight (nLoS) broadcasting effects make RF signals transmission more susceptible to eavesdropping. Consequently, an eavesdropper (ED) using an unauthorised network can try to acquire private information from a legitimate receiver. Therefore, information security in RF systems is a cause of great concern [3]. To deal with the aforementioned challenges, one of the solutions is to use visible light communication (VLC) as a transmission medium, which is more secure due to presence of LoS component, has a high data rate, and no electromagnetic intrusion [4]. However, VLC cannot operate in a medium that does not support LoS transmission, limiting its coverage capacity. Additionally, VLC operations in public areas where transmitted data can be read by multiple people, compromise its security. Therefore, in the present communication environment, physical layer security (PLS) is becoming popular in wireless transmission networks as a means of preventing private data from being wire-tapped [5]. The behaviour of the ED link was first described in [6], where the transmitter communicates with a legitimate receiver, while an unauthorised network attempts to overhear their private information. Further, secrecy analysis for various channel distributions is investigated in the literature, including weibull fading channel [7], generalised Gamma distribution [8] generalised-K distribution [9], and $\alpha - \mu$ distributions [10]. Moreover, a number of studies on the security of optical wireless communication (OWC) have been proposed. The authors of [11] investigated PLS of free space optics (FSO) with Málaga-$\mathcal{M}$ distribution, whereas [12] examined a detailed security analysis of a FSO link with Málaga-$\mathcal{M}$ distribution by considering three different realistic eavesdropping scenarios. Further, in [13], authors analysed the PLS of a VLC network with randomly positioned colluding EDs, while [14] examined PLS for non-clouding EDs. However, the majority of the work on PLS has focused on fixed location ED for RF and FSO networks, as well as randomly positioned ED within the LED coverage area for VLC networks. In a realistic scenario, an ED can be dynamically positioned anywhere in 3D-space and has the ability to affect the privacy of the systems, which is especially relevant in RF communication due to the nLoS nature of RF transmission. Therefore, the random waypoint (RWP) model can be used to represent the position of an ED terminal in the network in order to accommodate its mobility. In the RWP distribution, the user terminal proceeds with a random track in a convex domain. With the RWP distribution, an irregular iterative temporal node distribution has been created that is beneficial in performance monitoring [15, 16]. Therefore, motivated from the above-mentioned studies, the secrecy performance of an RF-based IoT network is examined in this work where the ED is considered to be RWP distributed in a 3D-space. The significant contributions of this paper are depicted below:

1. We have considered an RF-based IoT network where a source (S) transmits sensitive data to a legal IoT network (D) in an area where an unauthorised ED is present.

2. In a more realistic scenario, instead of a fixed-position ED [7–10], a RWP distributed ED is considered to be positioned in 3D-space and attempts to overhear the confidential information.
3. The new analytical formulation for the secrecy outage probability (SOP) and Probability of Strictly Positive Secrecy Capacity (SPSC) while taking into account various factors such as ED RWP distribution (1-D, 2-D, and 3-D distributions), path loss exponent (α), how far away the ED is from the S, and channel fading parameters are obtained.
4. Furthermore, at high signal-to-noise ratio (SNR), analytical expression is expressed asymptotically to obtain more insight into the system performance.

The remaining parts of the article are structured as follows: System and channel models for both main and ED links are depicted in Sect. 2. Section 3 explores the system's security performance; Sect. 4 discusses the results; and conclusion in Sect. 5.

2 System and Channel Model

It is considered that a source (S) is transmitting confidential information to an RF-based IoT network (D), which is being attempted to be overheard by a randomly distributed ED in a nearby space, as shown in Fig. 1. To be more specific, ED is considered to have a RWP distribution that is capable of attacking legitimate networks from any direction within a close communication range. In accordance with the dimensionality of the distribution, ED can be distributed in the form of a line, in the form of a circle, or even in the form of a sphere. Furthermore, the Nakagami-m distribution is to be considered for the legal as well as ED links. In addition, it is assumed that ED is an active eavesdropper, and therefore, the channel state information (CSI) of both ED and D is known to S.

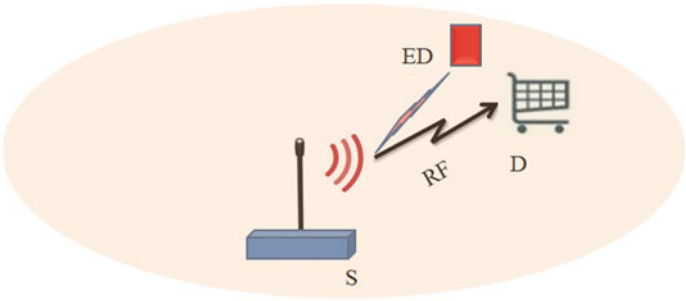

Fig. 1 RF-based IoT network with RWP distributed ED

2.1 Main Link Channel Model

It is considered that the S to D link is a Nakagami-m faded channel. The probability density function (PDF) and cumulative density function (CDF) of Nakagami-m are written as [17]

$$f_{\gamma_{SD}}(\gamma) = \left(\frac{m_d}{\bar{\gamma}_d}\right)^{m_d} \frac{\gamma^{m_d-1}}{\Gamma(m_d)} \exp\left(-\frac{m_d}{\bar{\gamma}_d}\gamma\right) \tag{1}$$

$$F_{\gamma_{SD}}(\gamma) = 1 - \frac{\Gamma\left(m_d, m_d\gamma/\bar{\gamma}_d\right)}{\Gamma(m_d)}, \tag{2}$$

where m_d ($m_d \geq 1/2$) is a fading parameter, $\bar{\gamma}_d$ is the average SNR, and $\bar{\gamma}_d = \Omega_t r_d^{-\alpha}$ where Ω_t is the transmitted power, r_d is the distance between S and D, and α is a path loss exponent, ($2 \leq \alpha \leq 5$) that is reliant upon the atmosphere [16].

2.2 ED Link Channel Model

It is considered that the S to ED link is a Nakagami-m faded channel. Therefore, the PDF of ED link (considering the average SNR at E, $\bar{\gamma_e} = \Omega_{t_e} r_e^{-\alpha}$) can be written as

$$f_{\gamma_{SE}}(\gamma/r_e) = \left(\frac{m_e r_e^{\alpha}}{\Omega_{t_e}}\right)^{m_e} \frac{\gamma^{m_e-1}}{\Gamma(m_e)} \exp\left(-\frac{m_e r_e^{\alpha}}{\Omega_{t_e}}\gamma\right) \tag{3}$$

Furthermore, it is assumed that ED is distributed randomly in a nearby space at D. Considering the range of r_e ($0 \leq r_e \leq R$), the end-to-end PDF of γ_{SE} in an ED mobility situation can be written as

$$f_{\gamma_{SE}}(\gamma) = \int_0^R f_{\gamma_{SE}}(\gamma/r_e)\, f_{r_e}(r_e)\, dr_e \tag{4}$$

where the distribution of r_e $\left(f_{r_e}(r_e)\right)$ can be define through RWP mobility.

A device that moves with the RWP mobility has an irregular distribution pattern that can be represented as algebraic expressions of the distance between S and ED. In RWP mobility, ED is assumed to be at a random location in the network operating locations. This location can change depending on the topologies of the network. In 1-D topology, ED's location is considered to be in a line with respect to S, where S is considered to be at the origin, where in 2-D and 3-D topologies, ED's location is considered in a circle and a sphere, respectively [18]. Following that, the PDF of r_e for RWP mobility can be expressed as [18]

$$f_{r_e}(r_e) = \sum_{i=1}^{n} B_i \frac{r_e^{\beta_i}}{R^{\beta_i+1}} \qquad 0 \le r_e \le R \tag{5}$$

in which the values of n, B_i, and β_i are correlated with topological dimensionality and are represented in [18].
Further substituting (3) and (5) into (4) and using $v = (r_e/R)^{\alpha}$, (4) can be rewritten as

$$f_{\gamma_{SE}}(\gamma) = \left(\frac{m_e}{\bar{\gamma}_{e_0}}\right)^{m_e} \frac{\gamma^{m_e-1}}{\alpha\Gamma(m_e)} \sum_{i=1}^{n} B_i \int_0^1 v^{m_e+\left(\frac{\beta_i+1}{\alpha}\right)-1} \exp\left(-\frac{m_e\gamma}{\bar{\gamma}_{e_0}} v\right) dv \tag{6}$$

where $\bar{\gamma}_{e_0} = \Omega_{t_e} R^{-\alpha}$ is the average SNR at the perimeter of the communication range. Further, representing $\exp\left(-\frac{m_e\gamma}{\bar{\gamma}_{e_0}} v\right)$ into Meijer's-G as $\exp\left(-\frac{m_e\gamma}{\bar{\gamma}_{e_0}} v\right) = G_{0,1}^{1,0}\left(\frac{-}{0} \middle| \frac{m_e\gamma}{\bar{\gamma}_{e_0}} v\right)$ ([19], Eq. (01.03.26.0004.01)) and, using ([19], Eq. (07.34.21.0084.01)), the PDF of the ED link with RWP mobility can be written as

$$f_{\gamma_{SE}}(\gamma) = \left(\frac{m_e}{\bar{\gamma}_{e_0}}\right)^{m_e} \frac{\gamma^{m_e-1}}{\alpha\Gamma(m_e)} \sum_{i=1}^{n} B_i G_{1,2}^{1,1}\left(\frac{m_e\gamma}{\bar{\gamma}_{e_0}} \middle|_{0,-(m_e+\varpi_i)}^{1-(m_e+\varpi_i)}\right), \tag{7}$$

where $\varpi_i = \frac{(\beta_i+1)}{\alpha}$. Thereafter, integrating (7) and using ([19], Eq. (07.34.21.0084.01)), CDF with RWP mobility can be obtained as

$$F_{\gamma_{SE}}(\gamma) = \left(\frac{m_e}{\bar{\gamma}_{e_0}}\right)^{m_e} \frac{\gamma^{m_e}}{\alpha\Gamma(m_e)} \sum_{i=1}^{n} B_i G_{2,3}^{1,2}\left(\frac{m_e\gamma}{\bar{\gamma}_{e_0}} \middle|_{0,-(m_e+\varpi_i),-m_e}^{1-m_e,1-(m_e+\varpi_i)}\right) \tag{8}$$

Furthermore, Fig. 2 represents the CDF of γ_{SE} with different ED's topologies at $\bar{\gamma}_{e_0} = 10$ dB. From the figure, it is observed that the possibility of obtaining the low power for the ED is larger in 3-D topology compared to 2-D topology, and similarly, the probability of getting low power in 2-D is more as compared to 1-D.

3 Security Analysis

For active ED, the S is aware of CSI for both D and ED links. As a result, the channel capacity at D and ED can be evaluated as $C_D = \log_2(1+\gamma_{SD})$ and $C_E = \log_2(1+\gamma_{SE})$. Afterwards, the positive secrecy capacity (C_t) can be written as [6]

$$C_t = \begin{cases} [C_D - C_E]^+, & \gamma_{SD} \ge \gamma_{SE} \\ 0, & \text{else} \end{cases} \tag{9}$$

where $[z]^+ \triangleq \max\{z, 0\}$.

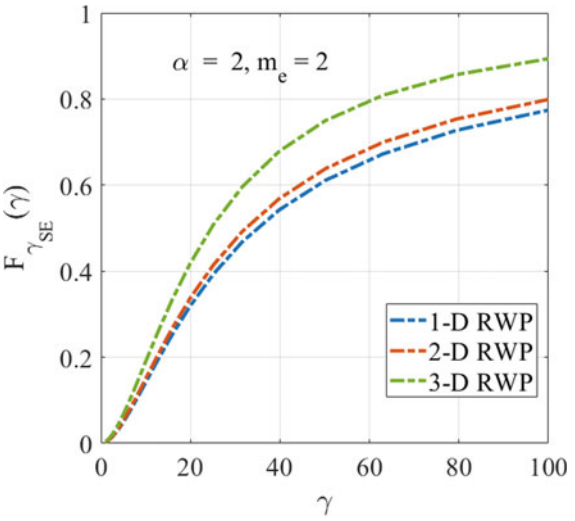

Fig. 2 CDF of ED at different topologies

3.1 Secrecy Outage Probability (SOP) Analysis

SOP evaluates the level of secure communication by estimating the probability of instantaneous secrecy capacity going below a certain secrecy rate R_t. As a result, the SOP for aforementioned system can be stated as [20]

$$P_{SOP} = Pr\left\{C_t \leq R_t\right\} = Pr\left\{\frac{1}{2}\left(\log_2\left(1+\gamma_{SD}\right) - \log_2\left(1+\gamma_{SE}\right)\right) < R_t\right\}$$
$$= Pr\left\{\gamma_{SD} < \theta\gamma_{SE} + \theta - 1\right\} = \int_0^\infty F_{_{SD}}\left(\theta\gamma_{SE} + \theta - 1\right) f_{SE}\left(\gamma_{SE}\right) d\gamma_{SE} \tag{10}$$

where $\theta = 2^{2R_t}$. For $\gamma_E \to \infty$, the lower bound of (10) can be rewritten as

$$P_{SOP} = \int_0^\infty F_{_{SD}}\left(\theta\gamma_{SE}\right) f_{SE}\left(\gamma_{SE}\right) d\gamma_{SE} \tag{11}$$

Thereafter, substituting (2) and (7) into (11) and using the identity $\Gamma\left(m_d, m_d\theta\gamma/\bar{\gamma}_d\right) = G_{1,2}^{2,0}\left(\frac{m_d\theta\gamma}{\bar{\gamma}_d}\Big|_{0,m_d}^{1}\right)$ ([19], Eq. (06.06.26.0005.01)), (11) can be modified as

$$P_{SOP} = P_{SOP_1} - P_{SOP_2}$$
$$= \left(\frac{m_e}{\bar{\gamma}_{e_0}}\right)^{m_e} \sum_{i=1}^{n} \frac{B_i}{\alpha \Gamma(m_e)} \int_0^{\infty} \gamma^{m_e-1} G_{1,2}^{1,1}\left(\frac{m_e\gamma}{\bar{\gamma}_{e_0}}\Big|_{0,-(m_e+\varpi_i)}^{1-(m_e+\varpi_i)}\right) d\gamma - \left(\frac{m_e}{\bar{\gamma}_{e_0}}\right)^{m_e}$$
$$\times \sum_{i=1}^{n} \frac{B_i}{\alpha \Gamma(m_e)\Gamma(m_d)} \int_0^{\infty} \gamma^{m_e-1} G_{1,2}^{1,1}\left(\frac{m_e\gamma}{\bar{\gamma}_{e_0}}\Big|_{0,-(m_e+\varpi_i)}^{1-(m_e+\varpi_i)}\right) G_{1,2}^{2,0}\left(\frac{m_d\theta\gamma}{\bar{\gamma}_d}\Big|_{0,m_d}^{1}\right) d\gamma \tag{12}$$

P_{SOP_1} can be calculated by using [19][Eq. 07.34.21.0009.01] and a few mathematical simplification as

$$P_{SOP_1} = \sum_{i=1}^{n} \frac{B_i}{\alpha} \frac{\Gamma\left(\frac{(\beta_i+1)}{\alpha}\right)}{\Gamma\left(1+\frac{(\beta_i+1)}{\alpha}\right)} \tag{13}$$

Further, utilising $\Gamma(m+1) = m\Gamma(m)$, P_{SOP_1} can be written as $P_{SOP_1} = \sum_{i=1}^{n} \frac{B_i}{(\beta_i+1)}$, which always returns a value equal to 1 for any combination of B_i and β_i in any topology. Following that, with the help of ([19], Eq. (07.34.21.0011.01)) and mathematical simplification, P_{SOP_2} is obtained, and SOP (P_{SOP}) can then be written as

$$P_{SOP} = 1 - \frac{1}{\Gamma(m_e)\Gamma(m_d)} \sum_{i=1}^{n} \frac{B_i}{\alpha} G_{3,3}^{3,1}\left(\frac{\bar{\gamma}_{e_0}}{\bar{\gamma}_d}\left(\frac{m_d\theta}{m_e}\right)\Big|_{0,m_d,\varpi_i}^{1-m_e,1+\varpi_i,1}\right) \tag{14}$$

Furthermore, at high SNR, analytical expression is expressed asymptotically in order to acquire a deeper understanding of system performance. As a consequence, the arguments of Meijer's-G of (14) may be inverted employing [19][Eq. 07.34.16.0002.01], and thereafter, using ([21], Eq. 41), the asymptotic formulation of (14) at high SNR is obtained as

$$P_{SOP} \underset{\bar{\gamma}_d \to \infty}{\approx} 1 - \frac{1}{\Gamma(m_e)\Gamma(m_d)} \sum_{i=1}^{n} \sum_{j=1}^{3} \frac{B_i}{\alpha} \left(\frac{\bar{\gamma}_d m_e}{\bar{\gamma}_{e_0}\theta m_d}\right)^{g(j)}$$
$$\times \frac{\prod_{p=1;p\neq j}^{3} \Gamma(c(j)-c(p))\,\Gamma(1+d(1)-c(j))}{\prod_{p=2}^{3} \Gamma(c(j)-d(p))} \tag{15}$$

where $c = [1, 1-m_d, 1-\varpi_i]$, $d = [m_e, -\varpi_i, 0]$, $c(j) - c(p) \neq 0, \pm 1, \pm 2, \ldots$, $c(j) - d(p) \neq 1, 2, \ldots$, and $g(j) = c(j) - 1$.

3.2 Probability of Strictly Positive Secrecy Capacity (SPSC)

SPSC is an essential criterion in secure transmission that is used to demonstrate the presence of secrecy capacity. As a result, the probability of SPSC is calculated as [20]

$$\begin{aligned} P_{SPSC} &= Pr\left\{C_t > 0\right\} = Pr\left\{\frac{1}{2}\left(\log_2\left(1+\gamma_{SD}\right) - \log_2\left(1+\gamma_{SE}\right)\right) > 0\right\} \\ &= Pr\left\{\gamma_{SD} > \gamma_{SE}\right\} = 1 - \int_0^\infty F_{_{SD}}\left(\gamma_{SE}\right) f_{SE}\left(\gamma_{SE}\right) d\gamma_{SE} \end{aligned} \tag{16}$$

Thereafter, substituting (2) and (7) into (16) and using ([19], Eq. 07.34.21.0009.01) as well as ([19], Eq. 07.34.21.0011.01), the probability of SPSC can be obtained as

$$P_{SPSC} = \frac{1}{\Gamma\left(m_e\right)\Gamma\left(m_d\right)} \sum_{i=1}^{n} \frac{B_i}{\alpha} G_{3,3}^{3,1}\left(\frac{\bar{\gamma}_{e_0}}{\bar{\gamma}_d}\left(\frac{m_d}{m_e}\right) \Big|_{0, m_d, \varpi_i}^{1-m_e, 1+\varpi_i, 1}\right) \tag{17}$$

In addition, to obtain an asymptotic expression, the Meijer's-G argument of (17) is inverted using ([19], Eq. (07.34.16.0002.01)), and then, utilising ([21], Eq. 41), the final expression at high SNR is derived as

$$\begin{aligned} P_{SPSC} \underset{\bar{\gamma}_d \to \infty}{\approx} & \frac{1}{\Gamma\left(m_e\right)\Gamma\left(m_d\right)} \sum_{i=1}^{n} \sum_{j=1}^{3} \frac{B_i}{\alpha}\left(\frac{\bar{\gamma}_d m_e}{\bar{\gamma}_{e_0} m_d}\right)^{g(j)} \\ & \times \frac{\prod_{p=1; p\neq j}^{3} \Gamma\left(c\left(j\right) - c\left(p\right)\right) \Gamma\left(1 + d\left(1\right) - c\left(j\right)\right)}{\prod_{p=2}^{3} \Gamma\left(c\left(j\right) - d\left(p\right)\right)} \end{aligned} \tag{18}$$

4 Numerical Results and Discussion

This section discusses analytically overall impact of various system parameters on system security performances, which is further supported by asymptotic results for $R_t = 0.1$.

Figure 3 depicts the SOP at various ED topologies. The figure shows that as the number of dimensions of the RWP distribution expands, the performance of the SOP gets better. This is because as the number of dimensions increases, the area in which the ED can move expands (1-D corresponds to movement in a line, 2-D corresponds to a circle, and 3-D corresponds to a sphere), putting more space between the ED and the legitimate device and making it less likely that information will be stolen.

Furthermore, Fig. 4 depicts the SOP for various values of the Nakagami-m fading parameters at two combinations of the path loss exponent. The graph demonstrates

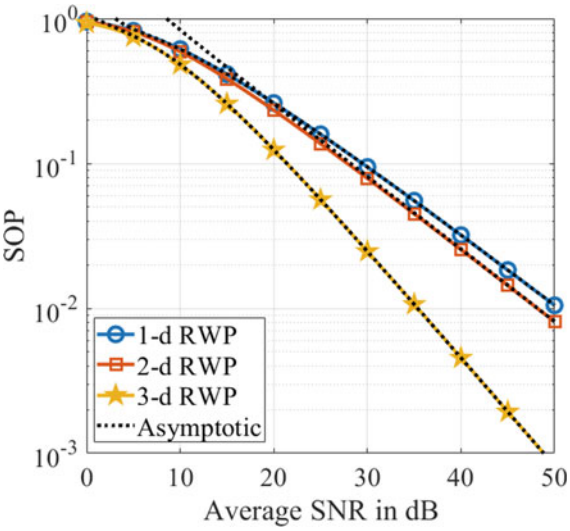

Fig. 3 SOP at different ED's topologies

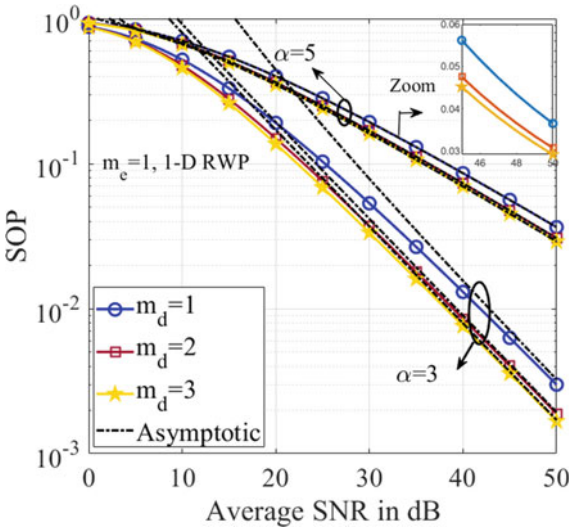

Fig. 4 SOP at different m_d and α

that SOP performance improves as m_d increases, and there is a significant enhancement in SOP performance with decreasing α.

The SOP performance for various positions of ED with respect to S is shown in Fig. 5 for $\Omega_t = 0{:}50$ dB and $\Omega_{t_e} = 0$ dB, and it can be seen that as ED moves away from S, the SOP performance improves. This is due to the fact, as ED moves away from S, the likelihood of being able to access information decreases.

Figure 6 demonstrates the impacts of different path loss exponents as well as S to ED distance on the probability of SPSC for $\Omega_t = 0 : 50$ dB and $\Omega_{t_e} = 0$ dB. From

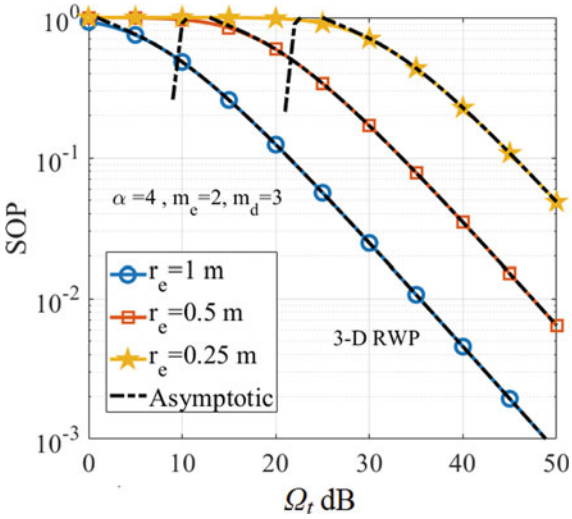

Fig. 5 SOP at different r_e

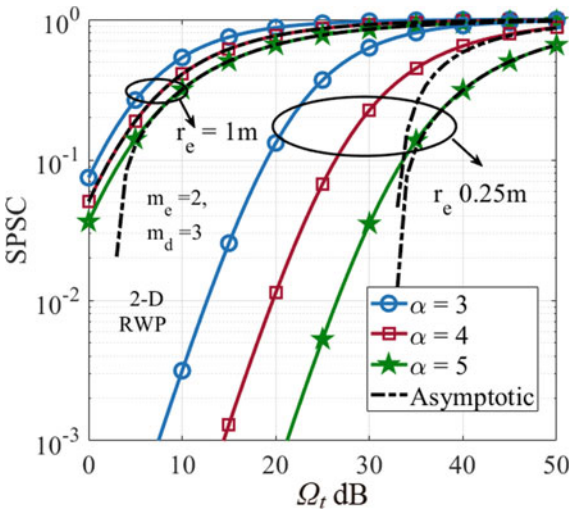

Fig. 6 SPSC at different α and r_e

the obtained results, it is seen that system condition improves as Ω_t increases, owing to the fact that the SD link is superior to the S-ED link. Aside from this, it has also been observed that decreasing α and increasing r_e results in improved performance.

Subsequently, in all the graphs, the asymptotic expressions at high SNR have excellent correlation with the obtained analytical expressions.

5 Conclusion

The security performance of RF-based IoT systems with randomly placed ED is examined in this work. The effectiveness of the system is evaluated using SOP and SPSC probability with RWP distributed ED in a closed communication space. In addition, the effects that the various system parameters have on the performance of the system's ability to maintain its security are analysed. These system parameters include the path loss exponent, the ED location dimensionality, the distance between S and ED, and the fading parameter. Moreover, all analytical formulas are written asymptotically in a high SNR regime.

References

1. Farooq MO, Kunz T (2017) IoT-RF: a routing framework for the internet of things. In: IEEE 28th annual international symposium on personal, indoor, and mobile radio communications (PIMRC), pp 1–7
2. Li W, Vishwakarma S, Tang C, Woodbridge K, Piechocki RJ, Chetty K (2022) Using RF transmissions from IoT devices for occupancy detection and activity recognition. IEEE Sensors J. 22(3):2484–2495
3. Pattanayak DR, Dwivedi VK, Karwal V, Ansari IS, Lei H, Alouini M (2020) On the physical layer security of a decode and forward based mixed FSO/RF co-operative system. IEEE Wirel Commun Lett 9(7):1031–1035
4. Saxena VN, Gupta J, Dwivedi VK (2021) Diversity combining techniques in indoor VLC communication. In: IEEE 4th international conference on computing, power and communication technologies (GUCON), pp 1–4
5. Yang Y, Wu L, Yin G, Li L, Zhao H (2017) A survey on security and privacy issues in internet-of-things. IEEE Internet Things J 4(5):1250–1258
6. Wyner AD (1975) The wire-tap channel. Bell Syst Tech J 54(8):1355–1387
7. Liu X (2013) Probability of strictly positive secrecy capacity of the Weibull fading channel. In: IEEE global communication conference (GLOBECOM), pp 659–664
8. Lei H, Gao C, Guo Y, Pan G (2015) On physical layer security over generalized gamma fading channels. IEEE Commun Lett 19(7):1257–1260
9. Lei H et al (2016) Performance analysis of physical layer security over generalized-K Fading channels using a mixture gamma distribution. IEEE Commun Lett 20(2):408–411
10. Lei H, Ansari IS, Pan G, Alomair B, Alouini M (2017) Secrecy capacity analysis over $\alpha - \mu$ fading channels. IEEE Commun Lett 21(6):1445–1448
11. Saber MJ, Sadough SMS (2017) On secure free-space optical communications over Málaga turbulence channels. IEEE Wirel Commun Lett 6(2):274–277
12. Ai Y, Mathur A, Verma GD, Kong L, Cheffena M (2020) Comprehensive physical layer security analysis of FSO communications over Málaga channels. IEEE Photon J 12(6):1–17
13. Cho S, Chen G, Coon JP (2018) Physical Layer Security in Visible Light Communication Systems With Randomly Located Colluding Eavesdroppers. IEEE Wireless Commun. Lett. 7(5):768–771
14. Pan G, Ye J, Ding Z (2017) On secure VLC systems with spatially random terminals. IEEE Commun Lett 21(3):492–495
15. Hyytia E, Virtamo J (2006) Spatial node distribution of the random waypoint mobility model with applications. IEEE Trans Mobile Comput 5(6):680–694
16. Aalo VA, Mukasa C, Efthymoglou GP (2016) Effect of mobility on the outage and BER performances of digital transmissions over Nakagami- *m* fading channels. IEEE Trans Veh Tech 65(4):2715–2721

17. Wang Y, Wang P, Liu X, Cao T (2017) On the performance of dual- hop mixed RF/FSO wireless communication system in urban area over aggregated exponentiated Weibull fading channels with pointing errors. Opt Commun 410(1):609–616
18. Govindan K, Zeng K, Mohapatra P (2011) Probability density of the received power in mobile networks. IEEE Trans Wirel Commun 10(11):3613–3619
19. Wolfram I (2010) Research, mathematica edition: version 8.0. Wolfram. Research, Inc., Champaign, IL
20. Pan X, Ran H, Pan G, Xie Y, Zhang J (2019) On secrecy analysis of DF based dual hop mixed RF-FSO systems. IEEE Access 7(1):66725–66730
21. Ansari S, Yilmaz F, Alouini M (2016) Performance analysis of free-space optical links over Málaga ($\mathcal{M}$) turbulence channels with pointing errors. IEEE Trans Wirel Commun 15(1):91–102

Design of Meandered Slot Antenna for Tire Pressure Monitoring System

MD. Ataur Safi Rahaman Laskar, Khan Masood Parvez, and SK. Moinul Haque

Abstract This communication presents the design procedure of a compact low-profile meandered slot antenna on FR-4 glass epoxy microwave substrate. The tire pressure monitoring system gives indication and assurance to the driver that the tires are operating at their expectations as a safety measure. A prototype with dimensions of 170 mm in length, 20 mm in width, and 1.58 mm in thickness has been developed and tested for the proposed meandered slot TPMS antenna operating at 412 MHz frequency band. The results of both simulations and experiments of the proposed TPMS antenna are presented and analyzed with parametric study.

Keywords TPMS · Meandered slot · Compact antenna · Slit line · Circular loop · Microstrip fed

1 Introduction

In view of vehicle tire safety, the modern automotive electronics manufacturing industry has made many standardization and improvements in the car. One of the major applications for tire safety is the tire pressure monitoring system (TPMS) keeping the views of vehicle safety and road accident. To describe the TPMS system, an electronic safety device is used to keep an eye on vehicle tires' internal air pressure, and it gives information to driver with a warning signal when air pressure becomes less in one or more tires. An instantaneous tire failure might result in a major traffic collision during the running condition on any highway. In addition to the increased risk of an accident from incorrect air pressure and loss of control, it can also be the cause of tire damage and that may lead to the frequent replacement of the vehicle tire. Moreover, the higher rolling resistance caused by underinflated tires reduces fuel efficiency when maintaining the same speed. The TPMS is thus regarded as the best driver assistance system. The transmitter and receiver of this system are located

MD. Ataur Safi Rahaman Laskar · K. M. Parvez (✉) · SK. Moinul Haque
Antenna Research Laboratory, Department of Electronics and Communication Engineering, Aliah University, Kolkata, India
e-mail: masoodrph@gmail.com

S. Rawat et al. (eds.), *Proceedings of Second International Conference on Computational Electronics for Wireless Communications*, Lecture Notes in Networks and Systems 554,
https://doi.org/10.1007/978-981-19-6661-3_10

3 to 100 m apart, making it a short-range wireless application. The frequencies use in between 300 to 960 MHz, specifically TPMS RF bands are 315 MHz ($\pm$ 10) in the USA/Japan and 413/434/868 MHz ($\pm$ 10) in Europe country.

The significance of tire pressure levels on vehicle safety has become more widely known in recent years. Using a tire pressure monitor system(TPMS) [1], a driver may be able to prevent a potentially hazardous driving situation by receiving early warning of such a safety-related notification. The utilization of wireless communication for TPMS applications has been documented by Shiming et al. [2]. Zeng and Hubing [3] found that the TPMS modules commonly used antennas, which are installed in each tire and significantly smaller than a wavelength at the operating frequency. The experimental results of the loop and whip antenna designs deployed in TPMS applications were examined in literature [3] with radiation efficiency and quality factor of these antennas on the various environmental factors. For TPMS and RFID purposes, Dinh et al. [4] designed compact normal-mode helical antenna (NMHA). For compact size and high gain operation, the authors in [5] presented an ultra-small helical antenna incorporating a parasitic element, which is ideal for TPMS. S. He [6] demonstrated a novel miniaturized lightweight antenna for TPMS and complex situations. The TPMS antenna has been the subject of numerous investigations, including printed antennas in [7]. In [8], the authors investigate the modeling of the TPMS signal strength range for use in vehicles. A simplified tire-wheel structure with a compact loop antenna installed inside of it nearly maintained the same radiation characteristics as an antenna in free space, as described in [9]. A polarization-diversity antenna for TPMS applications has been noted in [10]. Frequency reduction techniques by loop loading for wire and printed antennas have been discussed in [11]. The concept of using numerous loading arms to increase resistance is presented in [12]. The design of miniaturized slot antennas by applying slits, strips, and loops has been illustrated in [13]. Slot antennas with various types of meander slits have been described in [14]. However, in this modern era, vehicle standards and safety protocols have been increased constantly, but design of communicating antenna is still a very challenging task for TPMS in view of tire safety.

In this communication, a typical compact low profile meandered slot antenna has been designed using Ansoft HFSS electromagnetic solver tool [15] for tire pressure monitoring system. The size of proposed antenna is $170 \times 20 \times 1.58$ mm^3. A prototype for TPMS operation in the 412 MHz band (413 $\pm$ 10 MHz) has been constructed and the experimental results obtained. This antenna can be used to pass the tire pressure signals to the nearest automobile devices so that the problem can be solved quickly, and it can also be used to alert people of sudden accidents.

Table 1 Meandered slot antenna designing parameters

Parameter	Value (Unit: mm)	Parameter	Value (Unit: mm)
L_1	46	L_9	12.4
L_2	6	D_1	8
L_3	7	W_1	2
L_4	12	W_2	1
L_5	6	W_3	2
L_6	5	W_4	2
L_7	120	W_5	2
L_8	15	W_6	2.95

2 Antenna Design

The TPMS antenna required a low-profile and lightweight in general characteristics. In this communication, meandered slot antenna is designed with low profile, efficient impedance matching, and simple conversion to mass production characteristics utilizing lightweight, low-cost FR-4 printed circuit board.

As a radiating element, microstrip-fed slot antennas (MFSAs) are widely adopted. A conductive ground plane with a slot etched out at the top surface of the microwave substrate serves as the foundation of a slot antenna. A microstrip line printed at the bottom of the microwave substrate serves as the source of excitation. As a result of the current discontinuity in the ground plane, the electromagnetic radiation is emitted by the slot. For this meandered slot antenna construction, the microwave substrate employed is FR-4 glass epoxy, which has ε_r (permittivity) of 4.4 and tanδ (loss tangent) of 0.02. The value of length (L) and width (W) of proposed TPMS antenna is 170 mm and 20 mm, respectively. The standard thickness (H) of antenna is 1.58 mm. The dimensions of meandered slot antenna are listed in Table 1. Figure 1 (a) and (b) depicts the top and bottom surfaces of the symmetric antenna diagram, respectively.

3 Results and Discussions

It can be noted from Fig. 2 that simulated resonate frequency is 410 MHz with -31.75 dB depth in return loss characteristics, whereas the measured frequency is 412 MHz with −21.32 dB depth. Additionally, the −10 dB bandwidth is 8.14%. This resonance frequency is suitable for TPMS applications.

The normalized radiation characteristics are depicted in Fig. 3. The measured radiation characteristics are also included in Fig. 3 to verify the simulated response. The E-and H-plane characteristics are defined by the Phi value of zero and ninety

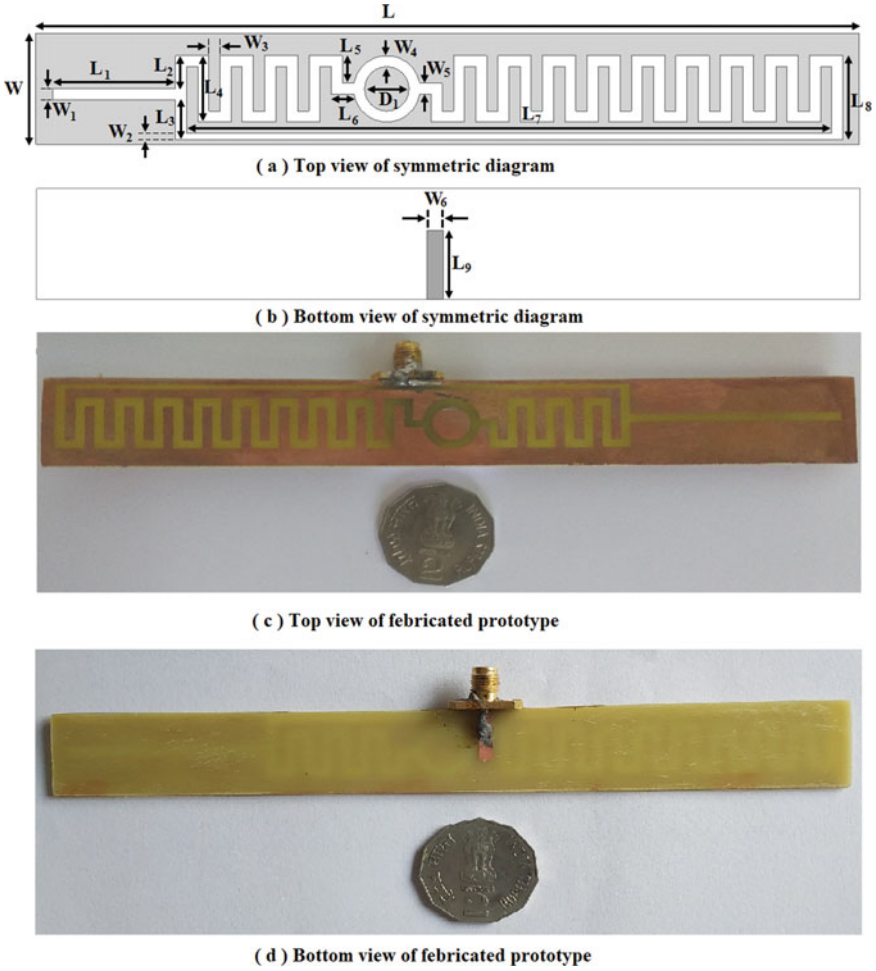

Fig. 1 Meandered slot TPMS antenna geometry **(a)** top view of symmetric diagram, **(b)** bottom view of symmetric diagram, **(c)** top surface of fabricated antenna topology, **(d)** bottom surface of fabricated antenna topology

degrees, respectively, in spherical coordinate system. Isotropic radiation characteristics are ideal condition for TPMS application. For the E-plane in Fig. 3, the isotropic characteristics are disturbed due to the smaller ground plane.

The simulated input impedance characteristics are presented in Fig. 4. The input resistance value is 50 Ω at resonate frequency 410 MHz, whereas imaginary part is 0 Ω.

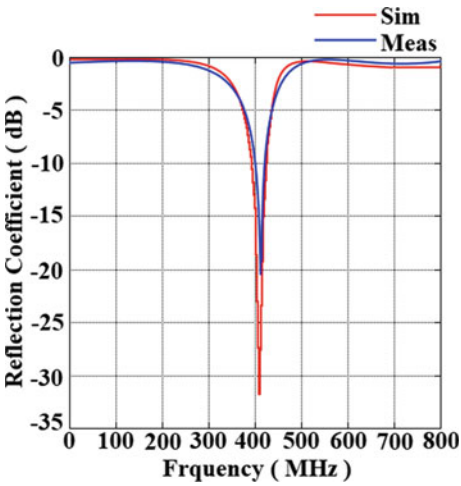

Fig. 2 Reflection coefficient of meandered slot antenna geometry

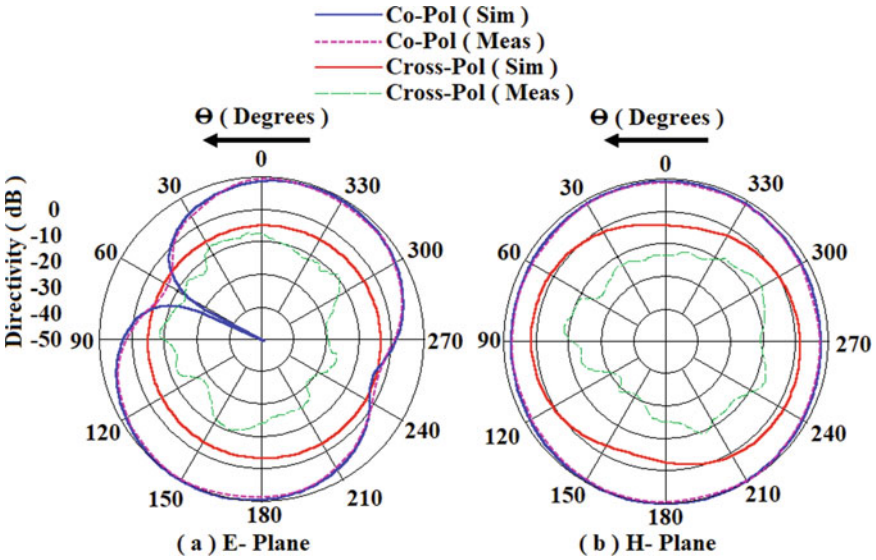

Fig. 3 Radiation pattern of proposed antenna at resonate frequency at 410 MHz

4 Impact of Geometric Variation of TPMS Antenna

The performance of the proposed antenna is affected differently by each geometrical parameter. In the following research paper, four sections of the TPMS antenna illustrated in Fig. 1 will be discussed and analyzed respectively, and the sections are: (i)

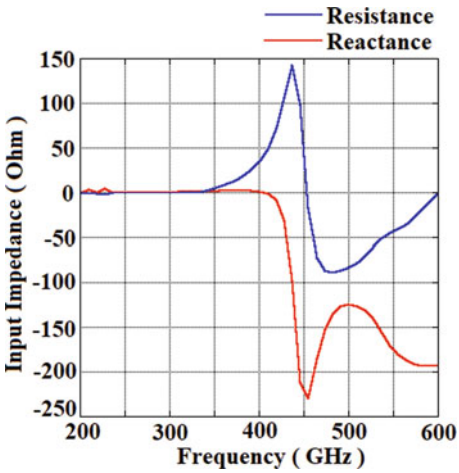

Fig. 4 Impedance characteristics of meandered slot antenna geometry

the thickness of the microwave substrate; (ii) the meandered loading sections; (iii) additional slit line; (iv) extended microstrip slit in left side and with circular loop in the middle. The impact of each sections is given below.

4.1 Impact of Thickness Variation of Microwave Substrate

The thickness of microwave substrate plays a pivotal role for designing a TPMS antenna. Moreover, the thickness of this TPMS antenna is restricted to 1.58 mm for lightweight and cost-effectiveness for TPMS applications.

In order to investigate the impact of the thickness on microwave substrate, we examined the different cases of microwave substrate thickness. The dimensions of the geometric shapes used in these parametric studies are the same as those presented in Fig. 1 with the exception of the thickness of the microwave substrate. The thickness variation with impact of reflection coefficient is displayed in Fig. 5. For thickness of microwave substrate 2 mm, resonate frequency is shifted from 410 to 690 MHz with poor reflection coefficient. The resonant frequency is 323 MHz for microwave thickness of 1 mm. It can be noted that the thickness of microwave substrate has an influence on resonant frequency.

4.2 Impact of Meandered Loading Section

In order to lower the resonance frequency, loading techniques are commonly used in antenna design. The loading section is chosen for this proposed meandered slot

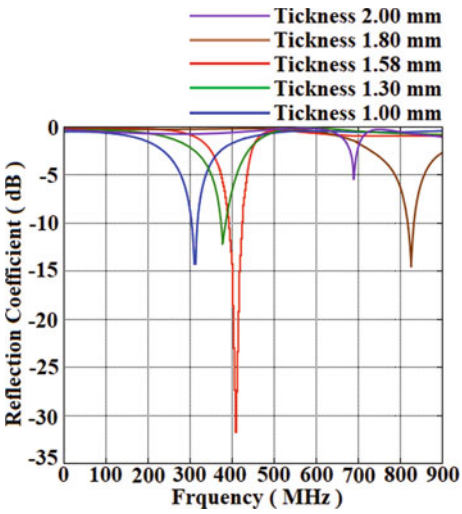

Fig. 5 Parametric variation for impact of the thickness on microwave substrate on reflection coefficient characteristics

antenna for two key reasons: (i) to decrease the size of antenna with compact ground plane and (ii) to reduction of resonance frequency.

Figure 6 represents the symmetric diagram of different meandered loading section are cutoff to examine the impacts of the meandered sections. Different meandered slit in which 1, 3, and 5 loading sections are cutoff, respectively, with unchanged geometrical shapes as demonstrated in Fig. 6. The impact of reflection coefficient is shown in Fig. 7. The resonance frequency will be affected as more meandered loading sections are eliminated. It can be observed that the loading meandered sections have significant impact on matching of reflection coefficient of proposed antenna.

4.3 Impact of Additional Slit Line (L_7)

The impact of additional slit line technique is applied in this proposed antenna to achieve required resonate frequency from 600 to 410 MHz with good reflection coefficient. The additional slit line (L_7) connects meander loading slit to the extended slit (L_1). The length of additional slit line is also a crucial factor to determine resonant frequency with good reflection coefficient.

4.4 The Impact of the Extended Microstrip Slit (L_1) in Left Side and with Circular Loop in the Middle

In this section, the impact of extended microstrip slit in left side with circular loop in the middle is reported. By optimizing the exact length of the extended microstrip

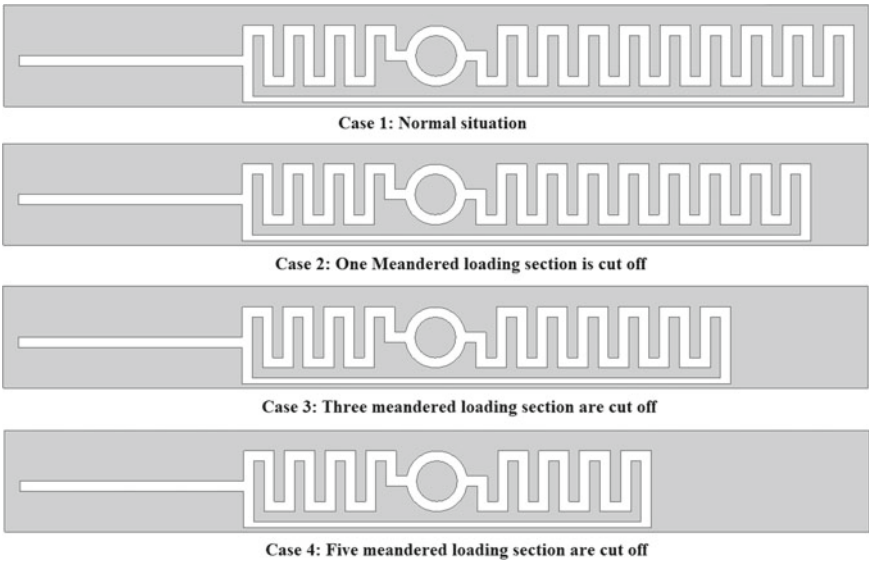

Fig. 6 Different cases of the meandered loading section cutoff

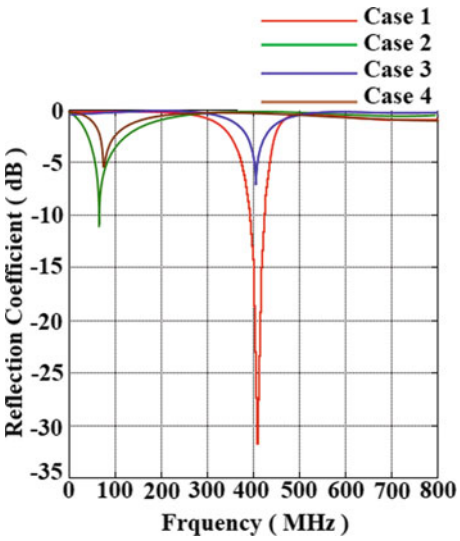

Fig. 7 Impact of the meandered loading section cut off on reflection coefficient

slit on left side with the position of circular loop in the middle of the antenna, it is shown that reflection coefficient of the antenna resonates at TPMS frequency band. The antenna design based on extended slit (L_1) and circular loop has been identified as case 2 and case 3 when compared to our proposed antenna, mentioned as case

1. The symmetric antenna topologies are depicted in Fig. 8 to better recognize the impact on antenna performances.

It is clearly seen from Fig. 9, that when we removed the circular loop from the center of proposed antenna, we got two different resonance frequencies. In addition, similar impact is also observed for removing the microstrip slit on one side (L_1) of the proposed antenna. It can be argued that the combined impact of each section makes this antenna suitable for TPMS applications.

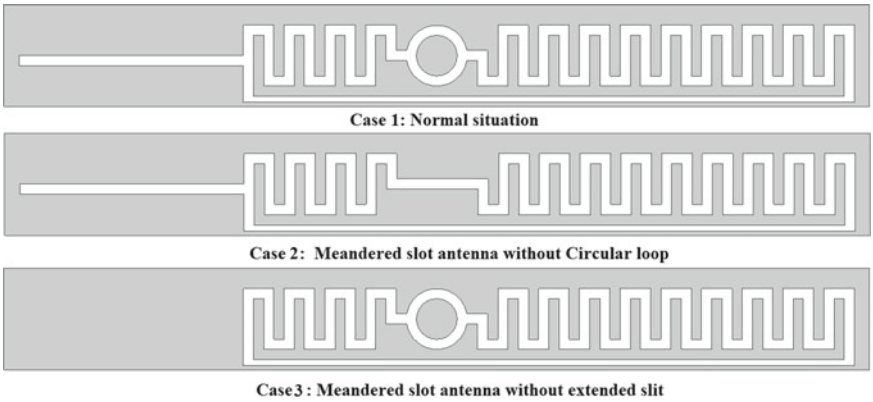

Fig. 8 Different cases of the meandered slot antenna without circular loop and extended slit

Fig. 9 Impact of the meandered slot antenna without circular loop and extended slit on reflection coefficient characteristics

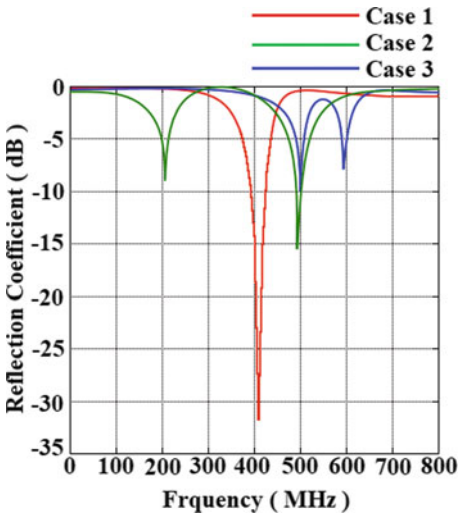

5 Conclusions

In this communication, a low-profile, lightweight antenna has been designed, optimized, fabricated, and measured. It is observed that the meandered slit with circular loop and an additional slit loading decreases the operating frequency of the slot, which is used for tire pressure monitoring systems. The simulated resonance frequency for meandered slot antenna is 410 MHz ($\pm$ 10) which is very close to 413 MHz ($\pm$ 10) applicable for tire pressure monitoring system. This TPMS antenna can be placed outside or inside of the vehicle, and the controller board can be placed anywhere in the vehicle. Two types of arrangements can be done while fitting these antennas. In TPMS communication network, this antenna is a good choice for its merits of low profile, low fabrication cost. The proposed antenna can be used in various vehicular communication systems as well.

References

1. Schrader Electronics, UK (2003) Smart valve RF tire pressure monitoring system Oct. 2003. http://www.schraderelectronics.com
2. Yu S, Tang J, Qiu H, Cao C (2007) Wireless communication based tire pressure monitoring system. In: 2007 international conference on wireless communications, networking and mobile computing 2007 Sep 21, pp 2511–2514. IEEE
3. Zeng H, Hubing T (2012) Investigation of loop and whip antennas in tire pressure monitoring systems. In: 2012 IEEE vehicular technology conference (VTC Fall) 2012 Sep 3 (pp. 1–5). IEEE
4. Dinh NQ, Teranishi T, Michishita N, Yamada Y, Nakatani K (2010) Simple design equations of tap feeds for a very small normal-mode helical antenna. In: 2010 IEEE antennas and propagation society international symposium 2010 Jul 11, pp 1–4. IEEE
5. Duc PT, Thuyen HD (2017) Proposal structure of very small helical antenna using parasitic element for TPMS. In: 2017 7th international conference on integrated circuits, design, and verification (ICDV) 2017 Oct 5, (pp 127–132). IEEE
6. He S, Xie J (2008) A novel compact printed antenna used in TPMS or other complex and variable environments. IEEE Trans Antennas Propag 56(1):24–30
7. Yegin K, Gleeson JP, Bally N, Snoeyink RJ, Heidtman RJ.: On-glass diversity tire pressure monitoring and FM antenna systems. In: 2005 IEEE antennas and propagation society international symposium 2005 Jul 3 (vol 1, pp 88–91). IEEE
8. Song HJ, Hsu HP, Wiese R, Talty T (2004) Modeling signal strength range of TPMS in automobiles. In: IEEE antennas and propagation society symposium. 2004 Jun 20 (vol 3, pp 3167–3170). IEEE
9. Tanoshita K, Nakatani K, Yamada Y (2007) Electric field simulations around a car of the tire pressure monitoring system. IEICE Trans Commun 90(9):2416–2422
10. Sun BH, Li JF, Liu QZ (2007) Polarisation-diversity antenna for TPMS application. Electron Lett 43(11):603–605
11. Ghosh B, Haque SM, Mitra D, Ghosh S (2010) A loop loading technique for the miniaturization of non-planar and planar antennas. IEEE Trans Antennas Propag 58(6):2116–2121
12. Sarabandi K, Azadegan R (2003) Design of an efficient miniaturized UHF planar antenna. IEEE Trans Antennas Propag 51(6):1270–1276
13. Haque SM, Parvez KM (2017) Slot antenna miniaturization using slit, strip, and loop loading techniques. IEEE Trans Antennas Propag 65(5):2215–2221

14. Parvez KM, Sinha S, Haque SM (2018) Miniaturization of slot antenna using meander slits. In: 2018 IEEE 88th vehicular technology conference (VTC-Fall) 2018 Aug 27, (pp 1–5). IEEE
15. Ansoft Corporation (2018) Pittsburgh, PA, HFSS ver. 19.2

Design and Analysis of Hybrid Plasmonic Waveguide-Based Symmetrical Directional Coupler Using Metal Bottom Layer

S. Radhakrishnan, G. Thavasi Raja, and D. Sriram Kumar

Abstract In this paper, the performance analysis on hybrid plasmonic waveguide (HPW)-based symmetrical directional coupler (DC) is proposed, which contains two parallel arms. In this analysis, one HPW arm performs as an input port and bar (parallel) output port; another HPW arm doings as a cross output port. The principle of DC is satisfied by the coupling of transverse magnetic field (TM) from the bar port to cross port. In the proposed DC, the mode characteristic parameters such as normalized mode area and propagation length are calculated by finite element method (FEM), and performance of the device is analyzed by certain parameters such as propagation loss, cross-talk, insertion loss, and coupling ratio. Hence, the proposed DC is designed with low cross-talk, low insertion loss, low propagation loss, and high propagation length, which could be appropriate for ultra-dense photonic integrated circuits (PICs).

Keywords Optical waveguides · Directional coupler · Finite element method

1 Introduction

Breaking the diffraction limit of light is the main advantage for surface plasmon polaritons (SPPs)-based optical devices compared with the conventional optical devices. SPP is defined as the coupling of combined electron plasma oscillations in the metal with the electromagnetic wave [1, 2]. Various theories and experimental analyses of SPPs-based waveguides have reported on the basics of gap and slot waveguide [3], metal film waveguides [4], and channel plasmonic waveguides [5]. In modern spans, hybrid plasmonic waveguide (HPW)-based photonic components are greatly attractive for their individual significance and uses. Generally, HPW is assembled by the high refractive index layer (e.g., Si) as a substrate, metal (i.e., Ag) as a cap, and low refractive index (e.g., SiO_2), which is interleaved in the middle of

S. Radhakrishnan (✉) · G. T. Raja · D. S. Kumar
Department of Electronics and Communication Engineering, National Institute of Technology, Tiruchirappalli 620 015, India
e-mail: srk3mail@gmail.com

S. Rawat et al. (eds.), *Proceedings of Second International Conference on Computational Electronics for Wireless Communications*, Lecture Notes in Networks and Systems 554,
https://doi.org/10.1007/978-981-19-6661-3_11

the dielectric (Si) and metal. As there is a dielectric and plasmonic arrangement in HPW, it deals a better compromise between the propagation loss and light confinement compared to pure plasmonic circuits. The HPW is compatible with silicon-on-insulator (SOI), planning that the facility to incorporate the silicon photonics and plasmonics on a single device configuration [6–13]. A detailed study on mode characteristic parameters such as normalized mode area and propagation length has reported using the HPW waveguide [14]. A theoretical analysis of the mode characteristic of HPW has been discussed with the help of the FEM method [15]. The optical DC is a principal component for making other optical devices such as modulators [16–18] power splitter [19, 20] and switches [21]. An experimental demonstration of HPW-based DC has reported with the propagation length of 53.6 μm and propagation loss of 0.081 dB/μm with the help of the FEM analysis [22]. An elliptic cylindrical nanowire HPW-based DC has reported a propagation loss of 0.076 dB/μm, propagation length of 60.99 μm for even mode and 56.18 μm for odd mode, transferring the energy about 80% from bar port to cross port [23]. In P substrate-based DC has proposed with 20 μm propagation length at 1550 nm working wavelength [24]. HPW-based DC has been conferred with cross-talk of − 22.3 dB and propagation length of 52.3 μm [25]. The maximum coupling efficiency about 80% was achieved using plasmonic cylindrical nanostructure [23]. However, numerous researchers have investigated the HPW-based DC with improved device performance. Hence, additional widespread analysis is required for enhancing the device performance with mode characteristics parameters and device evaluating parameters of the DC.

In this work, a new design of the DC is proposed (i.e.,) metal (Ag) as a bottom layer, dielectric (Si) as a top and the SiO_2 layer is inserted between metal and dielectric material. Numerical calculations evaluate the proposed DC with the help of 2-D full vectorial mode solver-based FEM. The mode characteristics parameters such as propagation length (194 μm for TM even mode and 91 μm for TM odd mode) and normalized mode area (0.13 μm^2 for TM even mode and 0.11 μm^2 for TM odd mode) are observed in the proposed DC. Similarly, the performance of the device is calculated by certain parameters such as propagation loss (0.044919 dB/μm), cross-talk (−24.1 dB), insertion loss (0.01673 dB/μm), and coupling ratio (99.6%).

2 Proposed Design and Basic Concept

The schematic structure, cross-sectional view, and electric field profiles of TM even mode and odd mode of the proposed symmetric DC are shown in Fig. 1a, b, c and d. The proposed DC contains two arms: One arm acts as an input arm as well as bar (parallel) output arm and the other arm acts as a cross output arm, as shown in Fig. 1a. In the proposed structure, the total width (W_1 and W_2) is 600 nm, and the gap (G) between the two arms is 100 nm, as shown in Fig. 1b. The silica layer (SiO_2) is sandwiched between silver (A_g) and silicon cap (Si). The heights of the Si (H_1), Ag (H_2), and SiO_2 (H_3) are chosen as 340, 100, and 50 nm, respectively. For the breaking of vertical symmetry, air is preferred as an upper cladding layer. The small ohmic loss

is the main benefit for choosing Ag in the proposed DC. The even modes are called symmetric modes, and its electric field profile propagates in the same directions, as shown in Fig. 1c. Similarly, the odd modes are called antisymmetric modes, and its electric field profile propagates in the opposite directions, as shown in Fig. 1d. Figure 1c and d shows that the TM polarized mode is strongly coupled at the SiO_2 layer in the arms. The performance of the device is examined by using a COMSOL Multiphysics designing tool version 5.4 [26]. At 1550 nm working wavelength, the refractive index of SiO_2, Si, and Ag is 1.445, 3.455, and 0.1453 + 11.3587i [27], respectively. Here, the light is transmitted at the direction of z-axis.

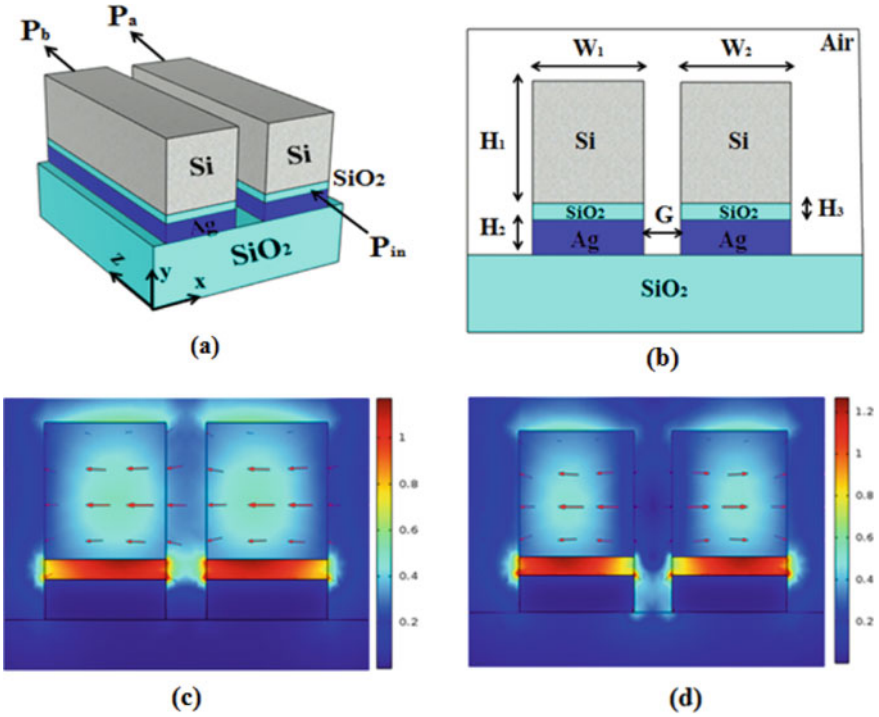

Fig. 1 Proposed directional coupler **a** formal diagram, **b** transection view and electric field distribution of, **c** TM even mode, **d** TM odd mode

3 Results and Discussion

3.1 Analysis of Mode Characteristics

Figure 2 depicts the effective index value (N_{eff}) of TM even and odd modes of the proposed DC concerning the gap between the waveguides. The even modes are having a larger effective index value than the odd modes. For TM even mode, the value of N_{eff} is increased while decreasing the gap between the waveguides. Similarly, for the TM odd mode, N_{eff}'s value is reduced while reducing the gap between the waveguides. The value of N_{eff} depends on the operating wavelength and the physical structure of the device. The N_{eff} value is the primary value for calculating the mode characteristics parameters and device performance parameters. At 1550 nm working wavelength, the obtained effective index values of odd and even modes are 2.20238 and 2.434375, respectively, at 100 nm gap between the two arms.

The propagation length (L_P) is defined as the length in which signal propagates at the e^{-1} power fall off from its actual input power. Therefore, the L_P is an essential mode characteristics parameter to determine the signal strength, and it depends on the physical parameters of the device as well as the operating wavelength. The variations in L_P corresponding with gap variation are displayed in Fig. 3a. For even modes of TM, the L_P is linearly decreased when the gap is increased between the two arms. For odd modes of TM, the L_P is not linearly varied corresponding with the gap variation. As mentioned above in L_P, the leading cause of variation is explained that the losses $[Im(n_{\text{eff}})]$ in TM even mode is lower than the TM odd mode. The propagation length (L_P) [19, 28] is calculated by

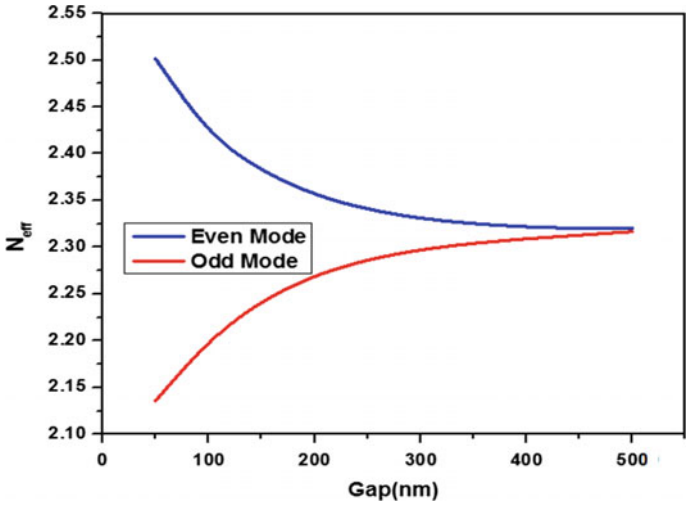

Fig. 2 Gap variation with N_{eff} variation in the proposed DC

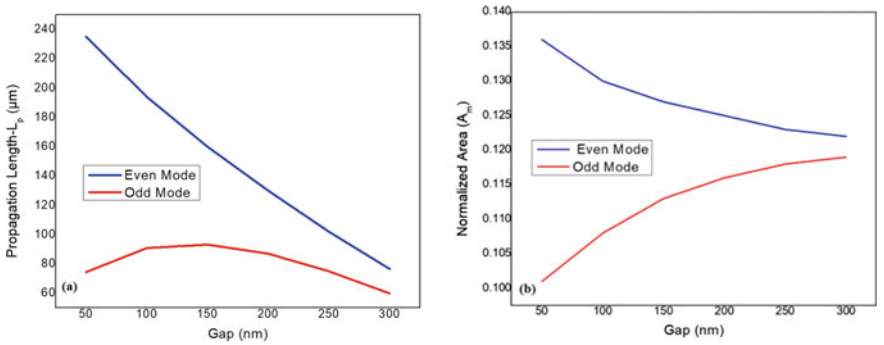

Fig. 3 Gap variation for **a** propagation length, **b** normalized mode area of the proposed DC

$$L_P = \frac{\lambda}{[4 \times \pi \times Im(n_{\text{eff}})]} \tag{1}$$

where λ indicates operating wavelength and $Im(n_{\text{eff}})$ represents the imaginary effective index value. In the proposed DC, the obtained L_P value of TM even and odd modes are 194 and 91 μm, respectively at a 100 nm gap between the two arms. Hence, the TM even modes are having higher L_P than TM odd modes.

The normalized mode area (A_m) is defined as the ratio of effective mode area to the diffraction limit mode area. Hence, the A_m is a vital mode characteristics parameter to determine the effective coverage area of the fundamental mode in the lateral cross-section of the proposed device. The variations of A_m corresponding with gap variation are displayed in Fig. 3b. For TM even modes, the A_m is decreased while increasing the gap between two waveguides, and for TM odd modes, the A_m is linearly increased while increasing the gap. The principal reason of aforesaid variations in A_m is described that the effective index mode values are influenced by electromagnetic flux density and operating wavelength. Hence, the A_m of TM even mode is higher than the TM odd modes. The normalized mode area (A_m) [19] is calculated by

$$A_m = \frac{A_{\text{eff}}}{A_0} \tag{2}$$

where effective mode area $A_{eff} = \left(\iint W(r)dA\right)^2 \Big/ \left(\iint W(r)^2 dA\right)$, $W(r)$ denotes the electromagnetic energy flux density and diffraction limited mode area $A_0 = \lambda^2/4$, λ represents the operating wavelength.

At 100 nm gap, the obtained values of the A_m for TM even and TM odd modes are 0.13 and 0.11 μm^2, respectively. Hence, the high propagation length (L_P) and low normalized mode area (A_m) are achieved in the proposed DC.

The proposed DC's mode characteristics are correlated with earlier works, as presented in Table 1. For the proposed DC design, the obtained L_p is higher than

Table 1 Comparison mode characteristics of the proposed structure with earlier works

References	Propagation Length (μm)	Normalized area (μm^2)
Bozhevolnyi et al. [2]	100	**
Oulton et al. [13]	40	**
Tian et al. [14]	2.6	6.727
Wang et al. [19]	63	0.35
Song et al. [20]	48	**
Zeng et al. [23]	43	**
Nikoufard et al. [24]	70	**
Okamoto [29]	53.6	**
Ahmed at al. [28]	60.99	**
Alam et al. [30]	20	**
Dai and He [6]	68.9	**
Dai et al. [31]	13.5	**
Kim [32]	90	**
Dai and He [33]	20	0.007
Kim et al. [7]	**	0.066
Huang et al. [9]	31	**
Proposed DC	194	0.13

the existing works, and the value of A_m is low compared with the cited references in Table 1. Hence, the high L_p, low A_m are achieved in the proposed DC

3.2 *Performance Analysis*

The coupling length (L_c) is defined as the required length for the coupling of maximum power from one arm to another arm, and it depends on the operating wavelength and effective index difference. The L_c is an important parameter of DC, used to estimate the device compactness. Figure 4a relates the coupling length (L_c) and propagation loss (α) of the DC with the gap variation. Here, the red line represents the L_c, and the blue line represents α. The L_c is gradually increased with the gap variation, as shown in Fig. 4a. The reason for the L_c variation is explained that the gap variation influences the effective index difference (Δn_{eff}) of the TM modes. As a result, the L_c is straight proportionate to the variation of gap. The propagation loss (α) describes how much power attenuates from its input power at a particular length. It depends on the interaction length (L), input (P_{in}), and output (P_{out}) power of the device. The propagation loss (α) is also a main parameter of the proposed device, and it is used to determine the signal propagation at a particular distance of

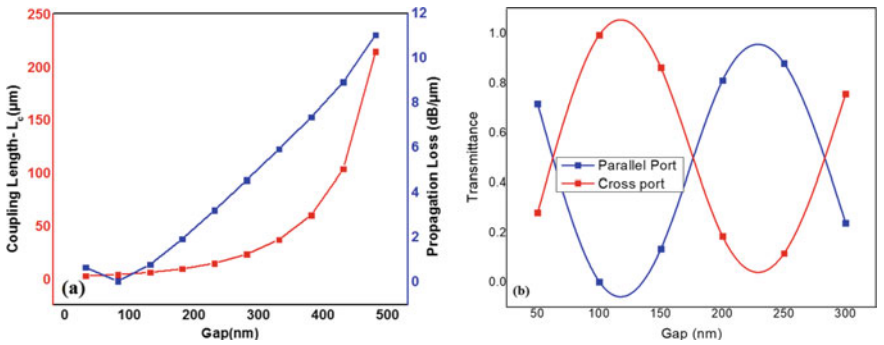

Fig. 4 Gap variation with **a** coupling lengths and propagation loss, **b** transmittance in the proposed DC

the coupler. At the equal value of interaction length (L) and coupling length (L_c), α value is gradually varied with the gap variation, as shown in Fig. 4a. The L_c is expressed as [27, 28, 31, 32].

$$L_c = \frac{\lambda}{2} \times \Delta n_{\text{eff}} \tag{3}$$

where Δn_{eff} represents the difference between even mode and odd mode of effective index, λ represents the operating wavelength. The propagation loss (α) is calculated [29] by

$$\alpha(dB) = \frac{10}{L} \times log\left(\frac{P_{\text{in}}}{P_b}\right) \tag{4}$$

where L represents the interaction length, P_{in} and P_b represent the input and cross port output power**.** At the 100 nm gap, the values of α and the L_c in the DC are 0.044919 dB/μm and 3.3761 μm, respectively. Transmittance curves are used to show the coupling of fundamental modes from one arm to another arm. The principle of DC is satisfied by coupling of bar (parallel) port power and cross port power, as shown in Fig. 4b. Here, the blue line represents the bar (parallel) port output power, and the red line indicates the cross port output power. The maximum power of 99.6% is transferred from bar port to cross port at the 100 nm gap. The optical power depends on the input power (P_{in}), coupling efficiency (F), interaction length (L), and coupling length (L_c) of the device. To enhance the performance of the device, the value of L is considered as 10 μm at the forthcoming calculations. The optical power is calculated from bar (parallel) port (P_a) and cross port (P_b), and it is expressed [6, 27, 29, 31–33] as

$$P_{\text{bar}}(P_a) = P_{\text{in}}\left[1 - Fsin^2\left(\frac{\pi L}{2L_c}\right)\right] \tag{5}$$

$$P_{\text{cross}}(P_b) = P_{\text{in}}\left[F sin^2\left(\frac{\pi L}{2L_c}\right)\right] \tag{6}$$

The value of F is unity for the symmetric structure of the proposed DC. The optical powers are useful components for determining the performance evaluating parameters of the device such as propagation loss, cross-talk, insertion loss, and coupling ratio.

The cross-talk (CT) is defined as the logarithmic function of undesired power (p_u) to the desired power (p_d) in cross port, and it is approximately equal to the logarithmic function of the square of the cosine value of normalized distance (qz). Figure 5a describes the relationship between the interaction length (L) and cross-talk (CT) of the proposed DC with different wavelengths. At 1550 nm operating wavelength, the CT is very low at 10 μm interaction length. The CT is varied according to the variation of λ and L. The leading cause of the variation in CT is explained that the even and odd modes of effective index value are changed due to the variation in wavelength and interaction length. CT is expressed [31] as

$$CT(\text{dB}) = 10 \times \log\left[p_u / p_d\right] \approx 10 \times \log\left[cos^2(qz)\right] \tag{7}$$

where $qz = \frac{\pi L}{2L_C}$. At 1550 nm working wavelength, the minimum cross-talk of − 24.1 dB is observed, at the interaction length of 10 μm, as shown in Fig. 5a.

The insertion loss (IL) is defined as the logarithmic function of input port power (P_{in}) to cross port output power (P_b). And, the coupling ratio (C) is defined as the ratio of the cross port power (P_b) to the sum of both output powers ($P_a + P_b$). Figure 5b relates the IL and percentage of coupling ratio (C) with the interaction length (L) variation. Here, the red line represents the IL and the blue represents the C. The IL and C are the important parameters to evaluate the device performance. At 10 μm of L, the observed value of IL is very low compared to the rest of the L values. Similarly, the observed value of C is very high at the 10 μm of L. The main cause of the variations in IL and C is clarified that the effective index value and the

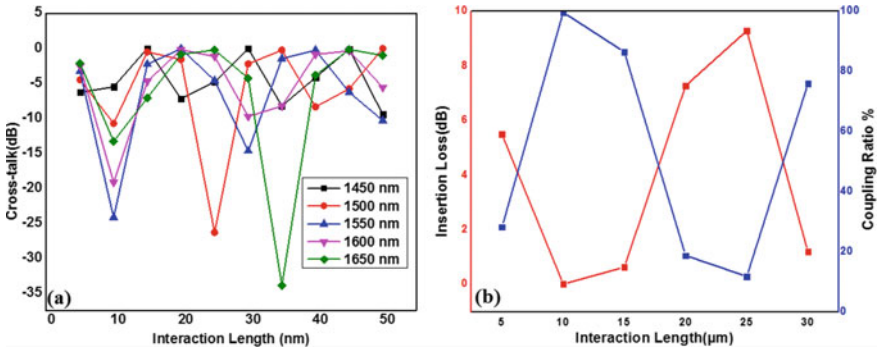

Fig. 5 Interaction length variation with **a** CT at various wavelengths, **b** IL and C in proposed DC

value of optical powers are varied with respect to the changes in interaction length. IL [6, 23] and C are expressed [6, 27, 28] as

$$IL(\text{dB}) = -10 \times \log\left(\frac{P_b}{P_{\text{in}}}\right) \tag{8}$$

$$C = \left(\frac{P_b}{P_a + P_b}\right) \times 100\% \tag{9}$$

At 1550 nm working wavelength, the low IL of 0.0167 dB/μm and high coupling ratio of 99.6% are achieved at 10 μm interaction length.

The proposed DC's performance analyses are correlated with existing works, as presented in Table 2. For the proposed DC designs, the obtained propagation loss is lower than the previous works. Similarly, the obtained value of coupling ratio in the proposed DC is significantly enhanced than the previous works. Hence, the low α and good C are achieved in the proposed symmetric DC.

From the aforementioned all plots, we come to know about the best value for the interaction length (L) and the gap (G) between the two arms are 10 μm and 100 nm, respectively, which is used for obtaining minimum CT, high C, and low IL at the working wavelength of 1550 nm in the planned DC. The TM mode is the dominant mode for the present structure of DC, and it is effectively coupled from bar port to cross port (i.e., coupling ratio is 99.6%). Hence, the principle of DC is fulfilled by coupling the TM mode from one arm to another arm. The performance of DC is analyzed with the help of mode characteristics parameters and device performance parameters.

Table 2 Comparison of device performance parameters of the proposed structure with existing works

References	Propagation loss (dB/μm)	Coupling ratio (%)
Chen et al. [5]	0.8	**
Kim et al. [7]	< 1	**
Wu et al. [8]	**	80
Sun et al. [16]	0.828	91
Sorger et al. [18]	− 0.1	**
Wang et al. [19]	**	90
Lou et al. [22]	0.07	**
Zeng et al. [23]	0.076	80
Dai and He [33]	**	85
Kim [32]	0.09	**
Proposed work	0.044919	99.6

4 Conclusion

A simple HPW-based DC is proposed, and its various parameters are analyzed with the support of finite element method-based simulation tool. The coupling mechanism is achieved via transferring of TM mode from bar port to cross port. The mode characteristic of proposed DC is realized with the help of propagation length (L_P) and normalized mode area (A_m). At 1550 nm working wavelength, high L_P (194 μm) is achieved for TM even mode, and low A_m (0.11 μm^2) is achieved for TM odd mode. Similarly, the performance of proposed DC is evaluated by specific parameters such as propagation loss (α), cross-talk (CT), insertion loss (IL), and coupling ratio (C). The result shows that low α (0.044919 dB/μm) and small L_c (3.3761 μm) are achieved at 100 nm gap between the two arms. Likewise, the little CT (-24 dB), low IL (0.0167 dB/μm), and high C (99.6%) are achieved at the interaction length of 10 μm. Hence, the proposed DC is used for forthcoming ultra-dense PICs with CMOS companionable fabrication.

References

1. Barnes WL, Dereux A, Ebbesen TW (2003) Surface plasmon subwavelength optics. Nat 424(6950):824–830
2. Bozhevolnyi SI, Volkov VS, Devaux E, Ebbesen TW (2005) Channel plasmon-polariton guiding by subwavelength metal grooves. Phys Rev Lett 95(4):046802
3. Bozhevolnyi SI, Volkov VS, Devaux E, Laluet JY, Ebbesen TW (2006) Channel plasmon subwavelength waveguide components including interferometers and ring resonators. Nature 440(7083):508–511
4. Gordon R, Brolo AG (2005) Increased cut-off wavelength for a subwavelength hole in a real metal. Opt Express 13(6):1933–1938
5. Chen L, Shakya J, Lipson M (2006) Subwavelength confinement in an integrated metal slot waveguide on silicon. Opt Lett 31(14):2133–2135
6. Dai D, He S (2009) A silicon-based hybrid plasmonic waveguide with a metal cap for a nano-scale light confinement. Opt Express 17(19):16646–16653
7. Kim JT, Ju JJ, Park S, Kim MS, Park SK, Shin SY (2010) Hybrid plasmonic waveguide for low-loss lightwave guiding. Opt Express 18(3):2808–2813
8. Wu M, Han Z, Van V (2010) Conductor-gap-silicon plasmonic waveguides and passive components at subwavelength scale. Opt Express 18(11):11728–11736
9. Huang Q, Bao F, He S (2013) Nonlocal effects in a hybrid plasmonic waveguide for nanoscale confinement. Opt Express 21(2):1430–1439
10. Guan X, Wu H, Dai D (2014) Silicon hybrid nanoplasmonics for ultra-dense photonic integration. Front Optoelectron 7(3):300–319
11. Alam MZ, Aitchison JS, Mojahedi M (2014) A marriage of convenience: hybridization of surface plasmon and dielectric waveguide modes. Laser Photonics Rev 8(3):394–408
12. Bian Y, Ren Q, Kang L, Yue T, Werner PL, Werner DH (2018) Deep-subwavelength light transmission in hybrid nanowire-loaded silicon nano-rib waveguides. Photonics Res 6(1):37–45
13. Oulton RF, Sorger VJ, Genov DA, Pile DF, Zhang X (2008) A hybrid plasmonic waveguide for subwavelength confinement and long-range propagation. Nat Photonics 2(8):496–500
14. Tian J, Zhang C, Liang X, Li H (2013) Mode analysis of a symmetric hybrid surface plasmonic waveguide for photonic integration. IEEE J Quantum Electron 49(3):331–334

15. Holmgaard T, Bozhevolnyi SI (2007) Theoretical analysis of dielectric-loaded surface plasmon-polariton waveguides. Phys Rev B 75(24):245405
16. Sun X, Zhou L, Li X, Hong Z, Chen J (2011) Design and analysis of a phase modulator based on a metal–polymer–silicon hybrid plasmonic waveguide. Appl Opt 50(20):3428–3434
17. Zhu S, Lo GQ, Kwong DL (2010) Theoretical investigation of silicon MOS-type plasmonic slot waveguide based MZI modulators. Opt Express 18(26):27802–27819
18. Sorger VJ, Lanzillotti-Kimura ND, Ma RM, Zhang X (2012) Ultra-compact silicon nanophotonic modulator with broadband response. Nanophotonics 1(1):17–22
19. Wang J, Guan X, He Y, Shi Y, Wang Z, He S, Holmström P, Wosinski L, Thylen L, Dai D (2011) Sub-μm^2 power splitters by using silicon hybrid plasmonic waveguides. Opt Express 19(2):838–847
20. Song Y, Wang J, Yan M, Qiu M (2011) Efficient coupling between dielectric and hybrid plasmonic waveguides by multimode interference power splitter. J Opt 13(7):075002
21. Perron D, Wu M, Horvath C, Bachman D, Van V (2011) All-plasmonic switching based on thermal nonlinearity in a polymer plasmonic microring resonator. Opt Lett 36(14):2731–2733
22. Lou F, Wang Z, Dai D, Thylen L, Wosinski L (2012) Experimental demonstration of ultra-compact directional couplers based on silicon hybrid plasmonic waveguides. Appl Phys Lett 100(24):241105
23. Zeng D, Zhang L, Xiong Q, Ma J (2018) Directional coupler based on an elliptic cylindrical nanowire hybrid plasmonic waveguide. Appl Opt 57(16):4701–4706
24. Nikoufard M, Heydari N, Pourgholi S, Khomami AR (2016) Novel hybrid plasmonic-based directional coupler on InP substrate. Photonics Nanostruct Fundam Appl 22:9–17
25. Holmgaard T, Chen Z, Bozhevolnyi SI, Markey L, Dereux A (2009) Design and characterization of dielectric-loaded plasmonic directional couplers. J Lightwave Technol 27(24):5521–5528
26. COMSOL Retrieved from https://doc.comsol.com/5.4/doc/com.comsol.help.rf/RFModuleUsersGuide.pdf
27. Radhakrishnan S, Raja GT, Kumar DS (2021) Numerical investigation on elliptic cylindrical nanowire hybrid plasmonic waveguide–based polarization beam splitter. Plasmonics 16(2):493–500
28. Ahmed R, Rifat AA, Sabouri A, Al-Qattan B, Essa K, Butt H (2016) Multimode waveguide based directional coupler. Opt Commun 370:183–191
29. Okamoto K (2010) Fundamentals of optical waveguides. Academic Press, United States
30. Alam MZ, Meier J, Aitchison JS, Mojahedi M (2007) Super mode propagation in low index medium. In: Quantum electronics and laser science conference, p JThD112. Optical Society of America
31. Dai D, Shi Y, He S, Wosinski L, Thylen L (2011) Gain enhancement in a hybrid plasmonic nano-waveguide with a low-index or high-index gain medium. Opt Express 19(14):12925–129236
32. Kim JT (2011) CMOS-compatible hybrid plasmonic slot waveguide for on-chip photonic circuits. IEEE Photonics Technol Lett 23(20):1481–1483
33. Dai D, He S (2010) Low-loss hybrid plasmonic waveguide with double low-index nano-slots. Opt Express 18(17):17958–17966
34. Gerd Keiser (2000) Optical fiber communications. International edition, McGraw Hill

Comparative Study of DOA Estimation and Smart Antenna Beam Forming for Next-Generation Core Networks

Nageswar Rao Thadikamalla and Prakasa Rao Amara

Abstract New challenges of current trending wireless communication technology to bring forth well-grounded and boundless services, which can provide the well-suited capacity for present communications. It is imperative to increase the channel capacity and bandwidth to minimize the noise or channel interference. An adaptive antenna array is one of the best one to enhance the channel capacity and improve the system performance by enhancing the gain of main beam pattern or lobe in desired user signal direction or angle of arrival and generate the nulls toward the interferer signal direction. In this, work or paper depicts the performance of antenna beamforming by changing the number of antenna elements and wave lengths of uniform linear antenna array.

Keywords Smart antenna · Beamforming · ULA · DOA · 5G Networks

1 Introduction

In modern days, there are several developments related to the wireless service applications like mobile communications, radar applications, 5G communications, and unmanned vehicular communication in the entire world. Hence, nowadays, number of users are increasing every day; this is the reason behind to improve the wider network area and improve the data rate is very higher to satisfy the costumers. Each user demanding more coverage and high data rates these can be achieved by adaptive smart antenna array system. An adaptive smart antenna consists of antenna array elements and the ability of signal processing to avoid the interferer signals. For the fact of nowadays, communication system using power full signal processor used in smart antenna. In smart antenna systems, the weights of the antenna array can

N. R. Thadikamalla (✉) · P. R. Amara
Department of Electronics and Communication Engineering, National Institute of Technology Warangal, Hanamkonda, Telangana 506004, India
e-mail: nr720052@student.nitw.ac.in

P. R. Amara
e-mail: aprao@nitw.ac.in

S. Rawat et al. (eds.), *Proceedings of Second International Conference on Computational Electronics for Wireless Communications*, Lecture Notes in Networks and Systems 554,
https://doi.org/10.1007/978-981-19-6661-3_12

be optimized by using the various beamforming algorithms [1]. According to that calculation of weights of antenna array produces the different types of beam pattern which indicates main beam is known as desired user position and generate the nulls in undesired user direction means that interfere user directions of linear array antenna [2].

Adaptive smart antenna systems or array antenna is one best one which utilize efficient spectrum of frequency thus satisfied the demand of next-generation wireless communication technology by enhance the system presentation. It also reduces the cochannel interference, and multipath effect also minimizes the noise [3].

To overcome drawbacks of previous technologies, this work has been proposed. The interpret scheme to improve the generalized exiting one based on the time-independent method. This interprets algorithm uses multiple signal classifications (MUSIC) which defined the true direction of the desired user signal direction [4–7].

By changing the inter-element spacing of the antenna elements to observe the desired user direction. Moreover, lets proposed an interpret algorithm based on the convention beamforming.

The work in this paper contribution of work clasified mainly three categories ‘conventional beamforming, null steering beamforming, and optimal beamforming [8–10].

2 Basic System Model

Figure 1 it represents elementary model of the uniform linear antenna array, the source of signals coming from the input or transmitter side.

Between the source and destination, there are number of buildings, tree, and weather environments effects on the sources of incoming signals. Those signals incidents on the surface of the antenna generate some angle; when is incident on the surface, at the same time, some noise can be generated; this can be minimized by applying some algorithms. The basic structure of linear antenna array revealed in Fig. 2; it shows how the incoming source signal incident on respective point by making an angle there. Functional block diagram of proposed system as shown in Fig. 3, it consists of number blocks antenna array, number of weights, DOA, and adaptive signal processor.

3 Signal Model and Theoretical Background of Smart Antenna

A smart antenna consists of number of antenna elements, let M denotes number of antenna elements. Let L being the number of incoming signals and N be the number of time steps, and the inter-element spacing is $\lambda/2$.

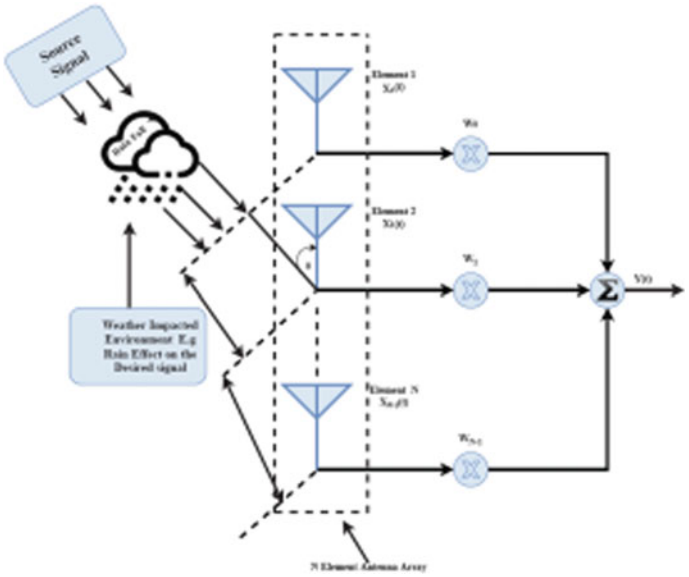

Fig. 1 System model of a smart antenna

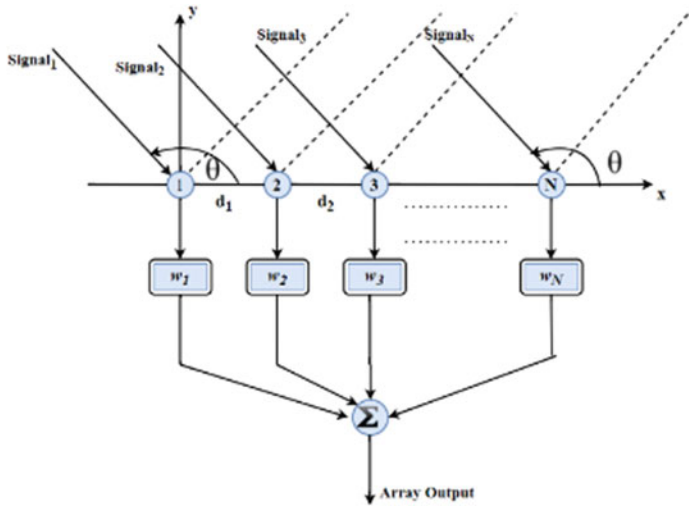

Fig. 2 Structure of a linear array

All the antenna elements are equally spaced; all incoming signals are incident at different antenna elements according to their incident angles [11, 12].

The incoming signal of the user one is defined as

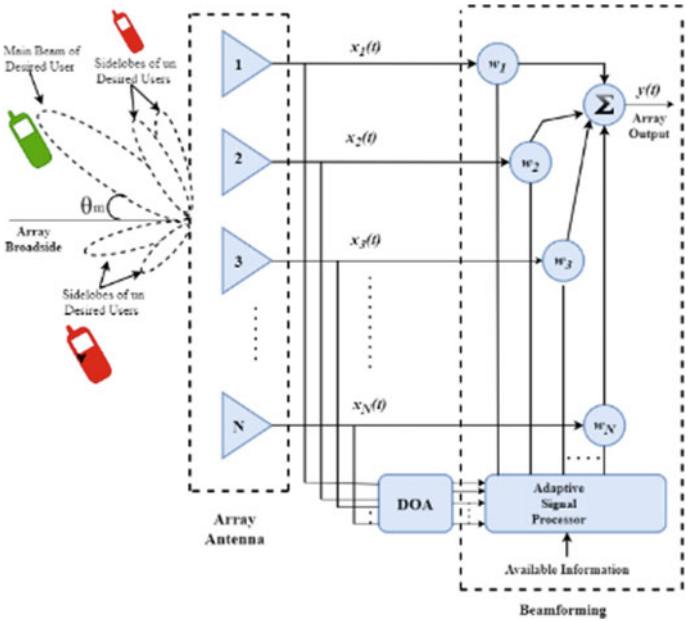

Fig. 3 Functional block diagram of a smart antenna system

$$s_1(t) = m_1 e^{j2\pi f t} \tag{1}$$

where m_1 is the modulating function of the signal one, total signal can be defined as

$$x_1(t) = s_1(t) + n(t) \tag{2}$$

where $n(t)$ is noise in the modulated signal.

$$x_m(t) = S_m(t) + n_m(t) \tag{3}$$

$$\boldsymbol{x_m(t)} = \sum_{i=}^{L} \boldsymbol{m_i e^{j(2\pi f t + \Delta_m)}} + \boldsymbol{n_m(t)} \tag{4}$$

where $m = 1, 2 \ldots\ldots M$

$$x_m(t) = n_m + \sum_{i=1}^{L} s_i(t) \tag{5}$$

Then, let define the array of signal on the form of vector notation

$$X(t) = (x_1(t) + x_2(t) + \ldots x_m(t))^T \tag{6}$$

Signal vector of incoming signals

$$s(t) = (s_1(t) + s_2(t) + \ldots x_m(t))^T \tag{7}$$

Noise vector is given as

$$n(t) = (n_1(t) + n_2(t) + \ldots n_{M(t)})^T \tag{8}$$

Let define the total output of array antenna is given by

$$y(t) = \sum_{m=1}^{M} w_m x_m \tag{9}$$

$$Y(t) = W^H X(t) \tag{10}$$

where T and H are the transpose and complex conjugate transpose.

The signal vector of antenna array is given by

$$R_{\mathrm{xx}} = \mathrm{ASA}^H + \sigma_{\mathrm{n}}^2 I \tag{11}$$

The MUSIC spectrum can be defined as following expression

$$P(\phi) = \frac{1}{a^H(\phi) \sum_N \sum_{\mathrm{N}}^H a(\phi)} \tag{12}$$

where $\sum_N$ is the noise eigenvector**.**

4 Beamforming of Smart Antenna and Array Factor

Antenna array beamforming and array factor of antenna array can be calculated by using given weights of the antenna element and is defined by the following equation [13]. Antenna array factor can be given by.

$$\mathrm{AF}(\phi) = \sum_{m=1}^{M} w_m e^{jkd(m-1)Cos(\phi)} \tag{13}$$

where 'M' is defined as number of array elements, 'ϕ' is the user direction, 'd' inter-element spacing of antenna array. w_m is the weights of the antenna element. The antenna array factor can be defined in the form of vector notation [14, 15].

$$\mathrm{AF}(\phi) = w^T a(\phi) \tag{14}$$

where w^T is known as weight vector. Normalized array factor can be defined as

$$\mathrm{NAF}(\phi) = \frac{\mathrm{AF}(\phi)}{\max(\mathrm{AF}(\phi))} \tag{15}$$

4.1 Conventional Beamformer

The conventional beamforming of smart antenna another name is defined as sum and delay beamformer all weights of the antenna array is all are equal magnitude [16]. The phase of the selected user angle can be steered in given angle of direction according to weights. The antenna array with this weight has unity response in the desired antenna direction. This beam former requires no information about the incoming signal expect the user position. This is why it is not influenced by the thermal noise of the antenna elements. The only error source is the eventual error on the desired look direction.

From the conventional beamforming, there are basically three types of plots mentioned defined as line-log or logarithmic plot of antenna array; it is best one to better clarification of side-lobe level of the antenna and its quality of it nulls. Coming to second one is line-lin or linear nature of beamforming plot of antenna, and last one is defined as polar form of the antenna radiation pattern as shown in figures.

4.2 Null Steering Beamforming of Smart Antenna

The strategy of null steering includes to control the composite weights and antenna element position [17, 18] to control the antenna phases and amplitudes strength only. It can be used to revoke an incoming plane wave direction and thus to generate a null in response of antenna pattern in angle of arrival of that incoming plane wave [19].

4.3 Optimal Beamforming

In the case of optimal beamforming, the beamforming was stable in the perception that the antenna weights that can be multiplied with the incoming signals at every antenna element were stable. Now, empower these antenna weights to modify or replace, depending on the acquired signal to attain certain issues. For this reason, try to modify these antenna weights to defeat the interference [20].

The weight of optimal beamformer, equation equals to $w = \mu_0 R_{\mathrm{xx}}^{-1} \mathrm{a}(\phi_0)$ from this equation R_{xx}, is correlation matrix of antenna array $a(\phi_0)$ is the steering vector in

the look direction, and μ_0 is a constant for an array constrained to have unit response in the look direction; this constant becomes μ_0 is constant.

These weights reduce the mean output power of the antenna array while maintain unity of the desired user direction [20–22]. Thus, to minimize the total noise of the system the output signal including the interferences and unwanted noise.

Position of the main user far from the interferer user, the error is low enough to detect if the moving user is crossing the interfere user the algorithm will either cancel out both the moving user and the interferer, or it will put a beam in their direction.

5 Simulation Results

From Fig. 4, it illustrates the comparision of different beamforms of the antenna; it observed for varying of number antenna elements antenna radiation pattern can be changes and its clear observe. The main user position at angle of 50 degrees and normalized antenna array factor can be changed at different values of M.

For the $M = 12$, 16, and 20, the different patterns of the antenna and desired user position and interferer user positions of ULA are as shown in Figs. 5 and 6.

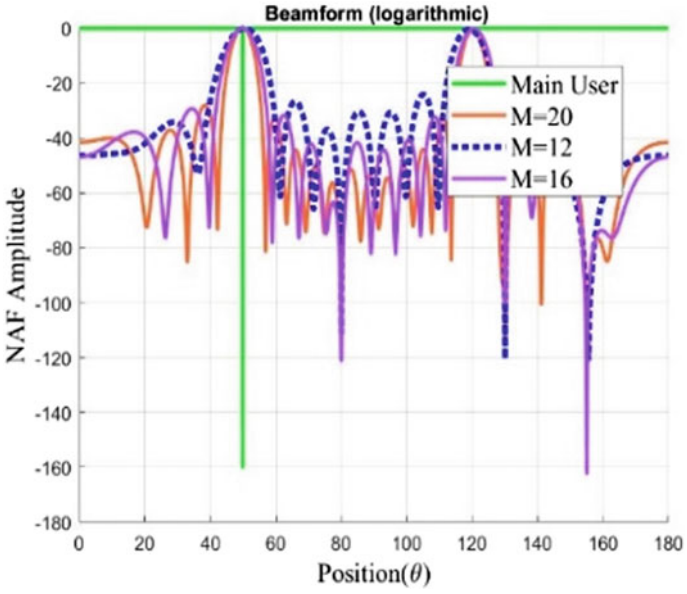

Fig. 4 Radiation pattern of uniform linear antenna array desired signal direction at 50^{θ}

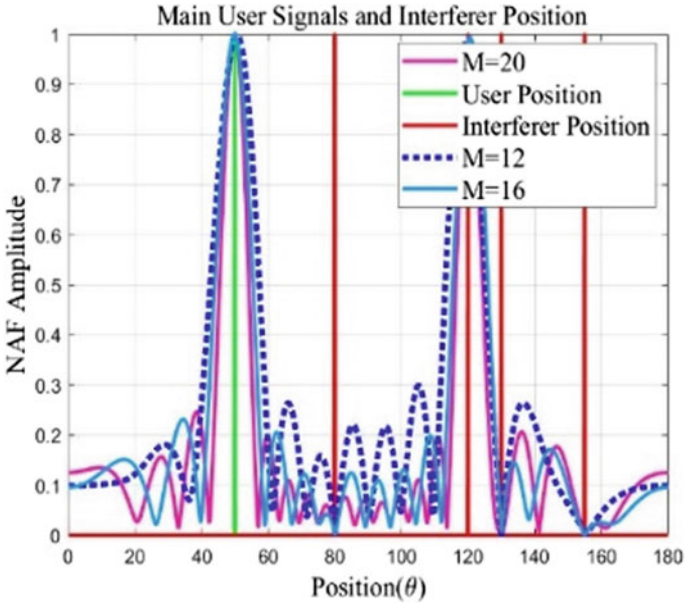

Fig. 5 Radiation pattern of uniform linear antenna array desired signal direction at 50^{θ} and undesired signal or interferer arrival direction at (80, 120, 130, 155^{θ})

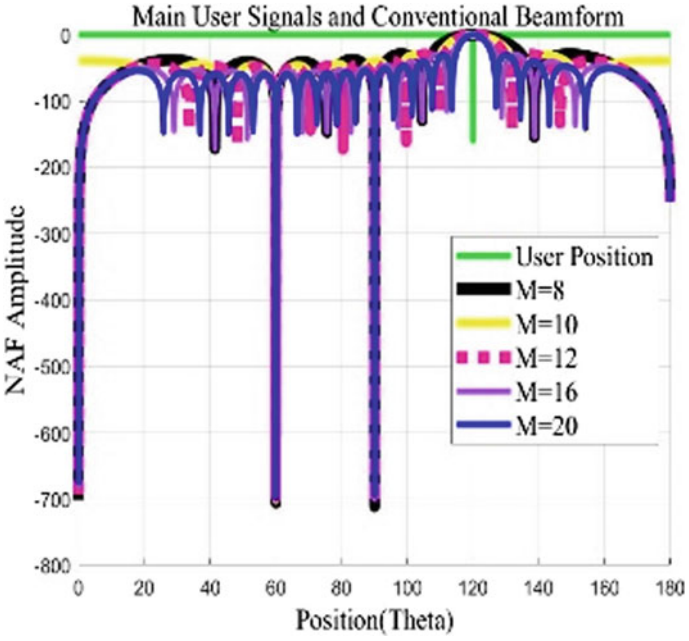

Fig. 6 Comparison of conventional beamformer radiation for $M = 8, 10, 12, 16, 20$ in logarithmic form at user direction 120^{θ} and undesired signal direction at 60 and 90^{θ}

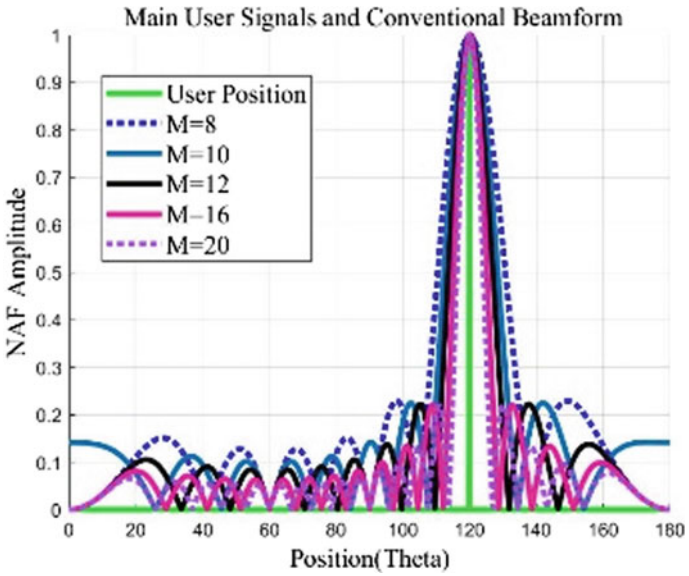

Fig. 7 Comparison of conventional beamformer radiation for $M = 8, 10, 12, 16, 20$ in line-in form at user direction 120^{θ}

5.1 Conventional Beamformer

From Fig. 6 and Fig. 7 are represents mainly two types of beamforming's mentioned as following logarithmic, linear form for different cases like different values of antenna elements ($M = 8, 10, 12, 16, 20$), it represents the how radiation pattern can be generated for different M vales and also find the user positions.

5.2 Null Steering Beamform

The comparisons of optimal beamforming and errors of uniform linear antenna array with different number of antenna elements like $M = 8, 16, 20$, represented in Fig. 8, Fig. 9, Fig. 11 and Fig. 13.

5.3 Optimal Beamforming Static Case and Dynamic Case

Figure 10 is indicating the response of array factor of antenna array with various antenna elements like ($M = 8$, 16 and 20). The main lobe at direction of desired

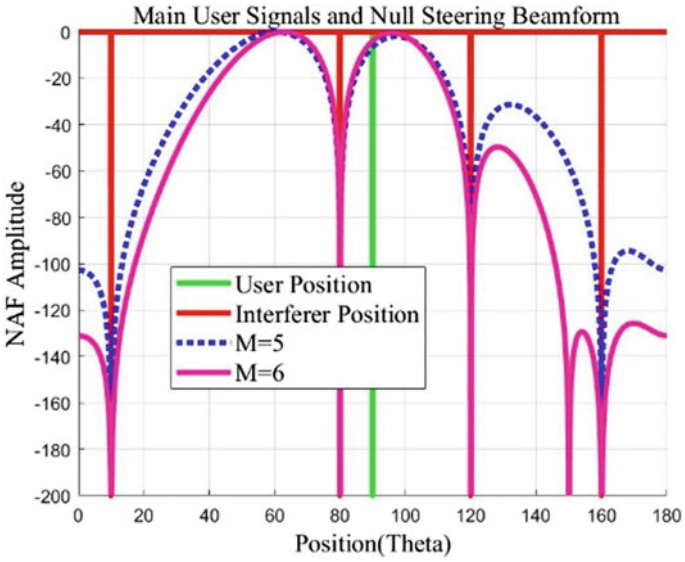

Fig. 8 Null steering beamformer radiation for $M = 6$ in logarithmic form at user direction 90^{θ} and null steering at 10, 80, 120, 150, and 160^{θ}

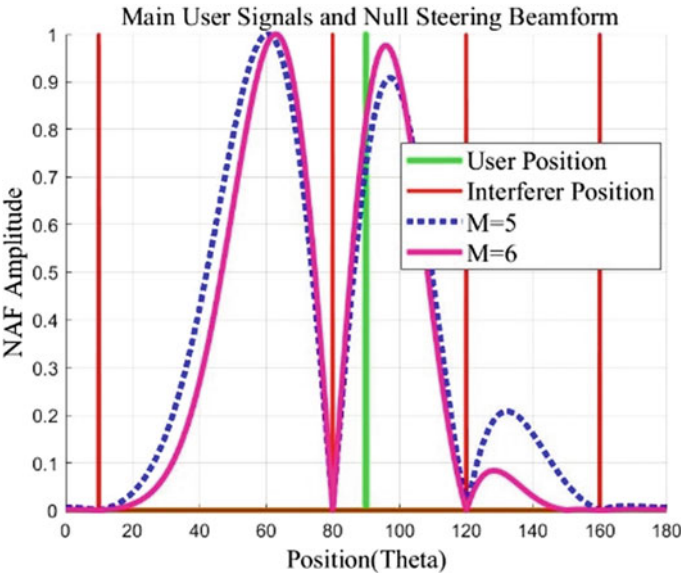

Fig. 9 Null steering beamformer radiation for $M = 6$ in linear form at user direction 90^{θ} and null steering at 10, 80, 120, and 160^{θ}

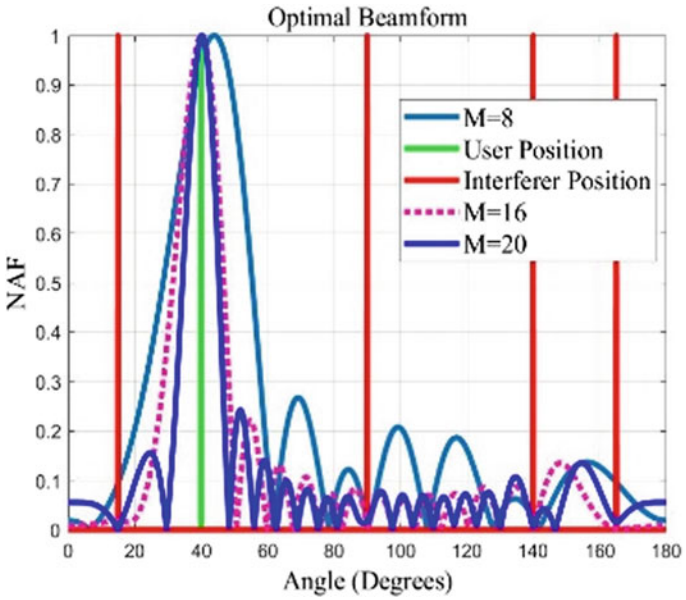

Fig. 10 Comparison of optimal beamformer radiation for ($M = 8$, 16, and 20) at user direction 40^{θ}

user signal at 40^{θ} and undesired user signal at directions at 10, 80, 120, and 160^{θ}. Figure 12 represents main lobe at desired user position at 90^{θ}.

5.4 DOA Estimation

Figures 14 and 15 illuminate user direction of arrival estimation of incoming user signal. It represents the real user power spectrum (P), log form of spectrum (P), and it's imitative of form.

Figure 16 depicts the real or desires user position and undesired or interferer user signal positions at an angle 35, 50, 80, 140, 165^{θ} and main user or desired user moving from 50 to 90^{θ}. Figure 17 depicts the wanted user and unwanted user directions at an angles 35, 50, 80, 140, 165^{θ}, increase the number of samples more distortion occurs in the signal observed in the Fig. 17.

Now, for example, where moving user range from 50 to 90^{θ} in the 1000 samples which is defined 100 windows with samples of 10. This represents the user speed is 0.04 degrees per samples. And 100 samples with 10 windows user speed is 0.4 degrees per sample. Of course, moment of user crossing the user at 80 degrees at that time only four users can be detected because crossing of two users will mask to each one.

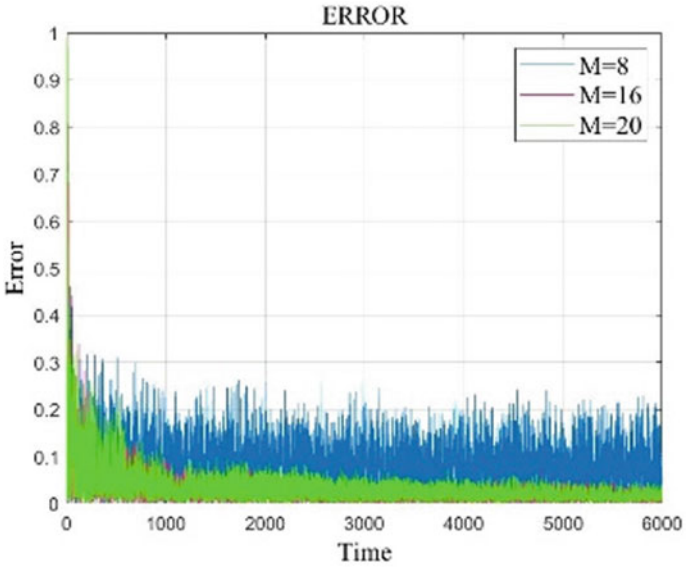

Fig. 11 Comparison of optimal errors in beamforming for (antenna elements $M = 8$, 16, and 20)

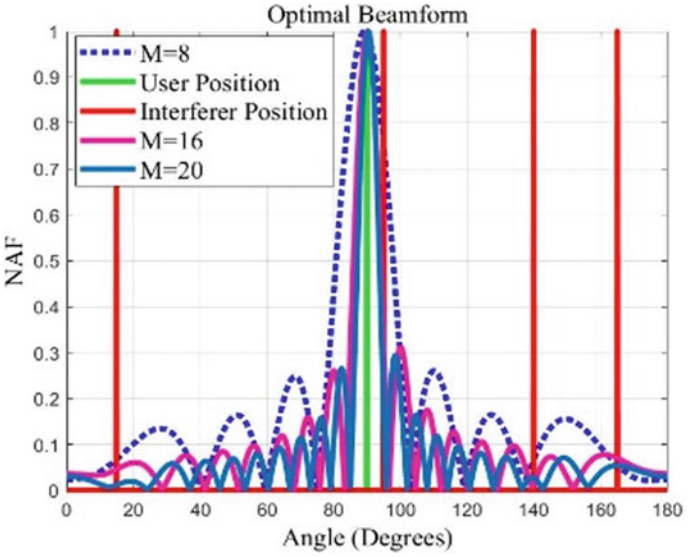

Fig. 12 Comparison of optimal beamformer radiation for ($M = 8$, 16, and 20) at user direction 95^{θ}

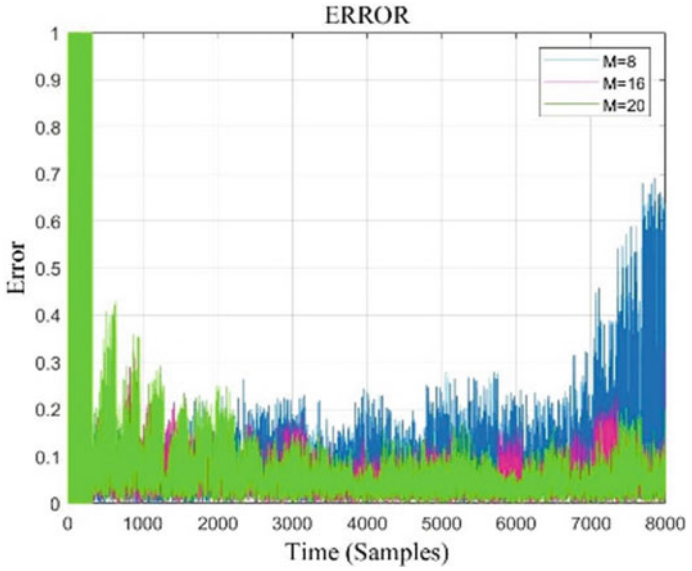

Fig. 13 Comparison of optimal beamformer error for ($M = 8$, 16, and 20)

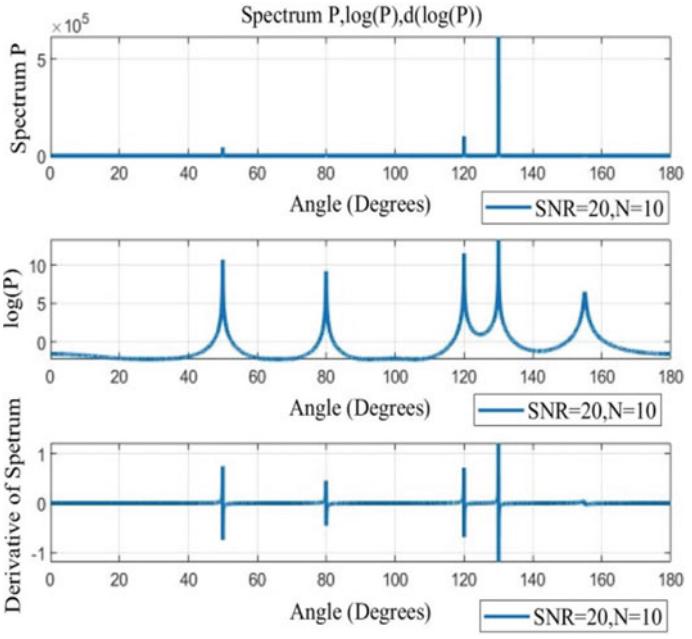

Fig. 14 Real user spectrum (P), log of power spectrum (P), and its imitative of user spectrum for value N = 10 and SNR = 20. In static case

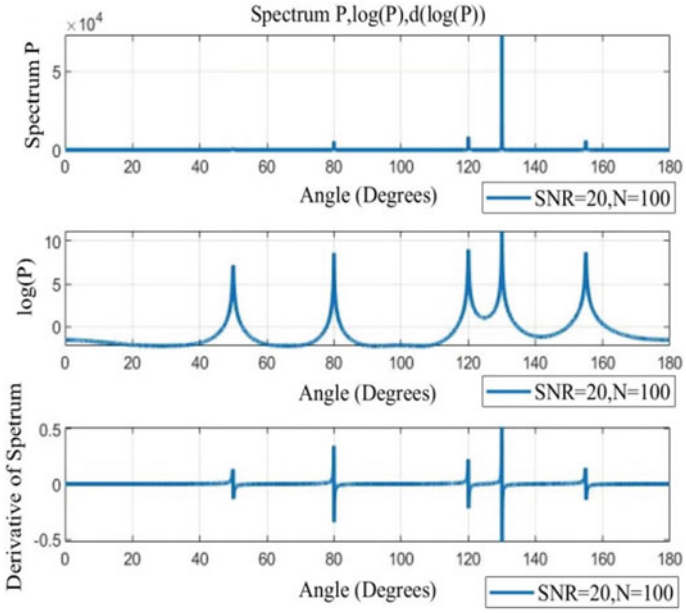

Fig. 15 Real user spectrum (P), log of spectrum (P), and its imitative of spectrum for value of N = 100 and SNR = 20. In static case

6 Conclusion

Here, there are three different beamforms of smart antenna systems; the weights of the system updated by using adaptive beamforming algorithms to obtain the desired user signal patterns. The conventional beamforming, null steering beamforming, optimal beamforming, and find the direction of arrival of estimation of the desired user achieved. The simulations in this work carried on intel(R) core (TM) i5-1035G1 CPU@1.00 GHz 1.19 GHz, 8 GB of RAM hardware, using MATLAB (R2021a) software.

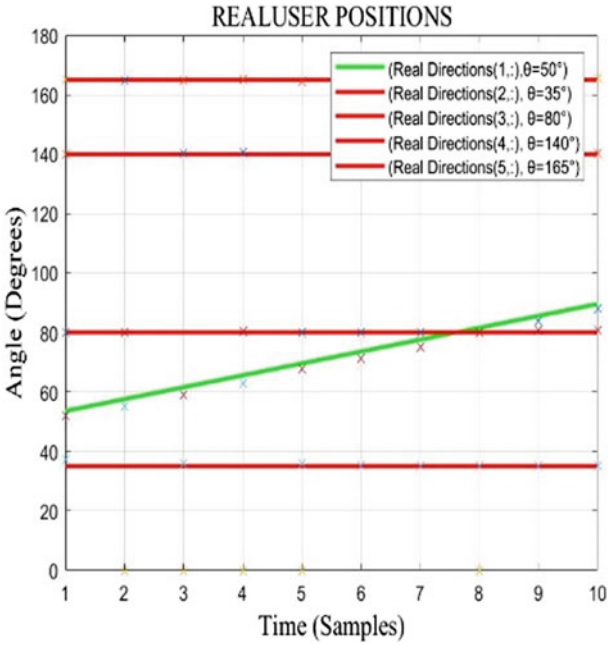

Fig. 16 Real user and calculated user position with the speed of user is 0.4 degrees per samples. In dynamic case

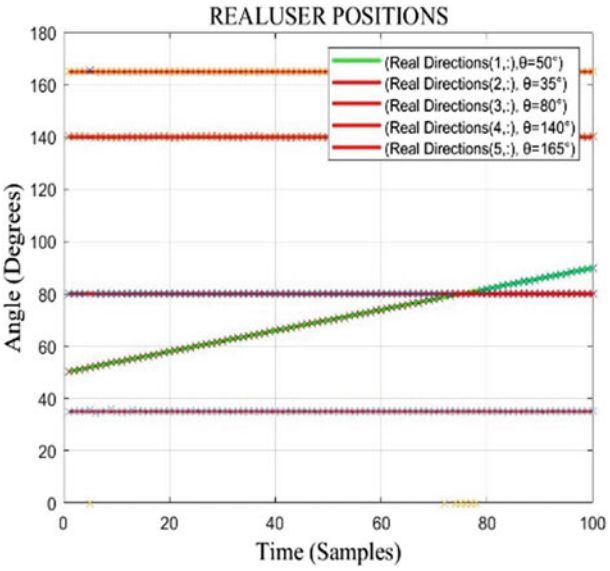

Fig. 17 Real user and calculated user position with the speed of user is 0.04 degrees per samples. In dynamic case

References

1. Belay H, Kornegay K, Ceesay E (2021) Energy efficiency analysis of RLS-MUSIC based smart antenna system for 5G network. In: 55th Annual conference on information sciences and systems (CISS), pp 1–5. https://doi.org/10.1109/CISS50987.2021.9400325
2. Yijie R, Xiaojun W (2021) Non-Blind DOA Estimation Method for 5G Mobile Terminal. In: IEEE International conference on signal processing, communications and computing (ICSPCC), pp 1–5. https://doi.org/10.1109/ICSPCC52875.2021.9564610
3. Obukhovets V (2021) Synthesis of multi-beam circular antenna array with DOA possibility. In: Radiation and scattering of electromagnetic waves (RSEMW), pp 8–11. https://doi.org/10.1109/RSEMW52378.2021.9494129
4. Rao TN, Rao VS (2012) Evaluation of MUSIC algorithm for a smart antenna system for mobile communications. In: International conference on devices, circuits and systems (ICDCS), pp 67–71. https://doi.org/10.1109/ICDCSyst.2012.6188676
5. Rares B et al (2018) Experimental evaluation of AoA algorithms using NI USRP software defined radios. In: 17th RoEduNet Conference: networking in education and research (RoEduNet), pp 1–6. https://doi.org/10.1109/ROEDUNET.2018.8514133
6. Balanis CA (2015) Antenna theory: analysis and design. Wiley
7. Ramakrishna Y, Kumari VR, Subbaiah PV (2017) Hybrid adaptive beamforming algorithms for smart antennas. In: 6th International conference on computer applications in electrical engineering-recent advances (CERA), pp 117–122. https://doi.org/10.1109/CERA.2017.8343312
8. Abohamra YA, Solymani MR, Shayan YR (2017) Optimum scheduling based on beamforming for the fifth generation of mobile communication systems. In: 8th IEEE Annual information technology, electronics and mobile communication conference (IEMCON), pp 332–339. https://doi.org/10.1109/IEMCON.2017.8117125
9. Biswas RN, Saha A, Mitra SK, Naskar MK (2018) Realization of adaptive beamforming in smart antennas on a reconfigurable architecture. In: Emerging trends in electronic devices and computational techniques (EDCT), pp 1–7. https://doi.org/10.1109/EDCT.2018.8405061
10. Shaikh S, Panda DK (2015) Linear, non-linear adaptive beamforming algorithm for smart antenna system. In: International conference on computer, communication and control (IC4), pp 1–4. https://doi.org/10.1109/IC4.2015.7375559
11. Tam K-C, Lau S-K, Tang S-K (2016) Estimation of source location and ground impedance using a hybrid multiple signal classification and Levenberg–Marquardt approach. J Sound Vib 374:279–296
12. Bellofiore S, Balanis CA, Foutz J, Spanias AS (2002) Smart-antenna systems for mobile communication networks. Part 1. Overview and antenna design. IEEE Antennas Propag Mag 44(3):145–154. https://doi.org/10.1109/MAP.2002.1039395
13. Oluwole AS, Srivastava VM (2018) Features and futures of smart antennas for wireless communications: a technical review. J Eng Sci Technol Rev 11(4)
14. Khalaf AA, El-Daly AR, Hamed HF (2016) Different adaptive beamforming algorithms for performance investigation of smart antenna system. In: 24th International conference on software, telecommunications and computer networks (SoftCOM), pp 1–6. https://doi.org/10.1109/SOFTCOM.2016.7772134
15. Rao AP, Sarma NV (2014) Adaptive beamforming algorithms for smart antenna systems. Methods 4(8):10–11
16. Saxena P, Kothari AG (2014) Performance analysis of adaptive beamforming algorithms for smart antennas. IERI Procedia 10:131–137
17. Boustani B, Baghdad A, Sahel A, Badri A, Ballouk A (2018) Adaptive algorithm for smart antenna system. In: 6th International conference on multimedia computing and systems (ICMCS), pp 1–5. https://doi.org/10.1109/ICMCS.2018.8525905
18. Hidayat R, Agustina E (2017) Digital beamforming of smart antenna in millimeterwave communication. In: International conference on broadband communication, wireless sensors and powering (BCWSP), pp 1–5. https://doi.org/10.1109/BCWSP.2017.8272564

19. Bouchoucha Y, Hasnaoui S (2018) Beamforming using linear antenna arrays for photonic applications. In: International conference on internet of things, embedded systems and communications (IINTEC), pp 59–63. https://doi.org/10.1109/IINTEC.2018.8695273
20. Sasi A, Jaya J (2020) Multilevel optimized beam forming technique for 5G. In: 6th International conference on advanced computing and communication systems (ICACCS), pp 957–960. https://doi.org/10.1109/ICACCS48705.2020.9074419
21. Hoshino K, Sudo S, Ohta Y (2019) A study on antenna beamforming method considering movement of solar plane in HAPS system. In: IEEE 90th vehicular technology conference (VTC2019-Fall), pp 1–5. https://doi.org/10.1109/VTCFall.2019.8891546
22. Patra S, Mandal SK, Mahanti GK, Pathak NN (2021) Linear and non-linear synthesis of unequally spaced time-modulated linear arrays using evolutionary algorithms. Radioeng 30(3)

Circular Substrate-Integrated Waveguide Cavity-Backed Slot Antenna for Ka-Band

E. Aparna, Gopi Ram, and G. Arun Kumar

Abstract A planar circular substrate-integrated waveguide (SIW) cavity-backed annular ring slot antenna is analyzed. A coaxial probe is connected to propagate the TM_{210} mode in the circular SIW cavity. An annular ring slot can be used as radiator in the cavity to agitate the fields inside cavity. The proposed design (13×13 mm^2) is simulated using computer simulation tool (CST). At 28 GHz, it characterized with a return loss of 14.9 dB and a gain of 5.28 dBi. The designed antenna is appropriate for usage in the millimeter wave (MMW) band.

Keywords Circular SIW cavity · Annular ring slot · TM_{210} mode · Ka-band · CST · Eigen mode solver

1 Introduction

Present generation, the millimeter wave (MMW) wireless communication systems have grabbed industrial and academic exposure. Experimental results show that 28 GHz band is one of the suitable band for 5G MMW systems [1]. To operate at MMW band, a cavity-backed slot antenna (CBSA) characterized with a good amount of gain, and front-to-back ratio could be a good candidate for such a high-frequency application. However, the conventional CBSA integration with planar circuits requires additional components which makes system become large. As an another possibility, patch antennas and slot antennas have been described [2]. But, microstrip antennas have low-radiation efficiency at MMW frequencies. In order to succeed this, substrate-integrated waveguide (SIW) technique is proposed [3]. This

E. Aparna · G. Ram (✉) · G. A. Kumar
National Institute of Technology Warangal, Hanamkonda, Telangana, India
e-mail: gopiram@nitw.ac.in

E. Aparna
e-mail: ea721058@student.nitw.ac.in

G. A. Kumar
e-mail: g.arun@nitw.ac.in

S. Rawat et al. (eds.), *Proceedings of Second International Conference on Computational Electronics for Wireless Communications*, Lecture Notes in Networks and Systems 554,
https://doi.org/10.1007/978-981-19-6661-3_13

economical SIW CBSA structures have features with a low profile and highly integrable compared to conventional cavity-backed slot antennas. Several rectangular and circular SIW cavity-backed slot antennas have been analyzed at the X band [4–6]. In [5, 6], an SIW cavity-backed square ring slot antenna with an SIW feeding network was proposed. In [4], split slot ring (SSR) is loaded in SIW cavity to perform at X band. These designs are utilized dominant mode to operate at X band. In [7], a proximity-coupled fed excites the higher-order modes (TM_{020} and TM_{120}) into the top layer of the circular SIW cavity. By utilizing these higher-order modes, the proposed antenna in [7] has been operated at Ka-band, but it is a multilayer structure which occupies more volume. A compact cavity-backed low-profile single-layer cavity-backed circular SIW antenna is studied in this paper. On the cavity's top plane, an annular ring slot acts as a radiator.

A coaxial probe is connected to excite the higher-order mode (TM_{210}) in the circular cavity. The simulated results show that proposed antenna operates at 28 GHz with return loss 15 dB for MMW applications.

The paper is structured as follows; in Sect. 2, we discuss about theory and design of a circular SIW cavity resonator and antenna configuration, in Sect. 3 describes about the obtained simulated results, and in Sect. 4 describes about the conclusion and future scope.

2 Theory and Design

2.1 Circular SIW Cavity Resonator Overview

To construct the circular SIW cavity, annular array of metallic vias embedded through the dielectric substrate; the detailed structure is shown in Fig. 1. This array of metallic vias replaces the vertical metal walls which are connecting the top and bottom conducting layers of the cavity.

Conventionally, the circular cavity radius is calculated with the following Eq. (1) [9].

$$r_{\text{eff}} = \frac{c}{2\pi\sqrt{\varepsilon_r}} \frac{P_{\text{nm}}}{f_{\text{nmp}}} \tag{1}$$

where f_{nmp} is the corresponding mode resonance frequency, c depicts the velocity of light in vacuum, ε_r depicts the dielectric constant value, r_{eff} depicts the conventional circular cavity radius, P_{nm} is m^{th} root of the n^{th} order of the first kind Bessel function value. Table 1 provides the standard Bessel function root values.

The performance of an SIW circular cavity resonator is equivalent to that of a standard circular cavity resonator with a circular SIW cavity's effective radius (r_{eff}). r_{eff} is indicated in Fig. 1. The constructed circular SIW cavity radius (r_{siw}) is calculated from following equation [10].

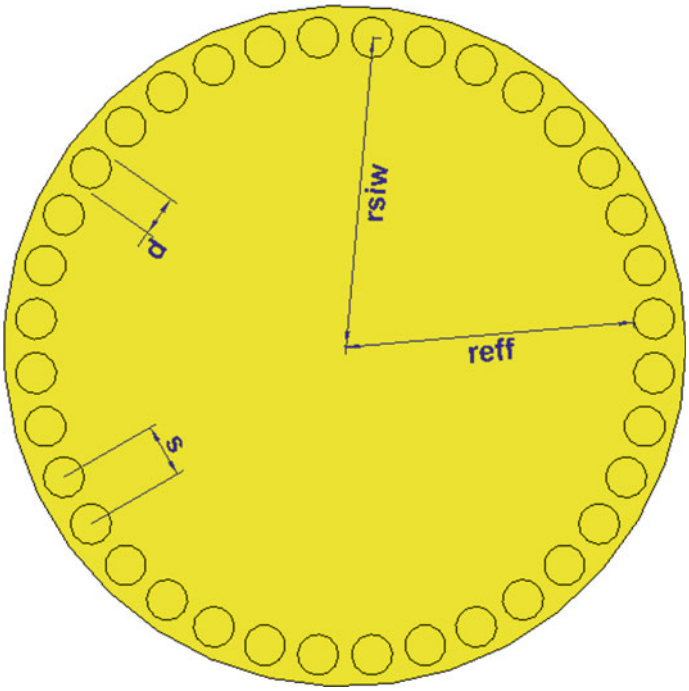

Fig. 1 Configuration of circular SIW cavity

Table 1 List of P_{nm} values

m / n	1	2	3
0	2.405	5.520	8.654
1	3.832	7.016	10.174
2	5.135	8.417	11.620
3	6.380	9.761	13.01

$$r_{\text{siw}} = r_{\text{eff}} + \frac{d^2}{2 \times 0.95 \times s} \tag{2}$$

In Eq. (2), d denotes the diameter of the metallic vias; s denotes the adjacent pitch distance between the metallic vias. In order to prevent energy leakage between adjacent vias, the array of vias configuration should be satisfying the following equations [11]

$$d < \frac{\lambda_g}{5} \tag{3}$$

$$s \leq 2d \tag{4}$$

where λ_g is guided wavelength

$$\lambda_g = \frac{\lambda_0}{\sqrt{\varepsilon_r - \left(\frac{\lambda_0}{\lambda_c}\right)^2}} \tag{5}$$

where λ_0 denotes the operating wavelength, λ_c denotes the cutoff wavelength, ε_r denotes the substrate dielectric constant value.

2.2 The Proposed Antenna Structure

The designed antenna structure is composed of two metallic layers with thickness 0.035 mm and RT-Duroid 5880 substrate with ε_r value of 2.2 and a $\tan\delta$ of 0.0009 as given in Fig. 2. The metal vias are embedded into the substrate in an annular array manner to form a circular SIW cavity. The two circular-shaped metal layers are attached through the metal posts. An annular ring slot is embedded on the top metal layer of the cavity with radius r_{slot} to perform as a radiator. When the circular SIW cavity design parameters are resonant with slot design parameters, the energy radiates utmost outside the cavity [12]. The annular ring slot radius is determined by considering the circumference of the slot, about $1.5\lambda_g$ [13].

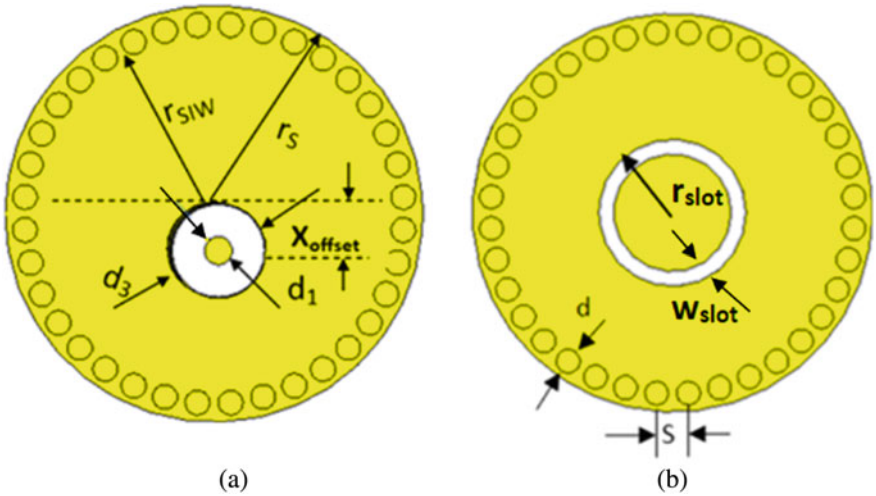

Fig. 2 **a** Bottom-layer construction **b** Top-layer construction

Table 2 List of proposed antenna specifications

Parameters	Dimensions (mm)	Parameters	Dimensions (mm)
SIW cavity radius (r_{siw})	6.06	Via diameter (d)	0.8
Effective radius (r_{eff})	5.90	Via spacing (s)	1.0572
Patch radius (r_s)	6.12	Slot ring radius (r_{slot})	2.45
Substrate height	1.57	Slot ring width (w_{slot})	0.5
Substrate length	13	Coaxial cable inner conductor diameter	0.817
Substrate width	13	Coaxial feed outer conductor diameter	2.92

A coaxial probe feeds the proposed design at a distance of x_{offset} from the origin of the SIW cavity. The optimized design parameters from the above equations are listed in Table 2.

3 Results and Discussions

As shown in Fig. 3a, when no annular ring slot is loaded in the circular cavity, dominant mode (TM_{010}) is propagated at 12 GHz frequency, while the TM_{210} mode is propagated at 28 GHz frequency approximately. The propagating frequencies are calculated in CST Eigen mode solver; those values are matching with the theoretical calculation of Eq. (1) with little difference due to the synthesized side walls in the cavity. As shown in Fig. 3b, when an annular ring-shaped slot is loaded on the top layer of circular SIW cavity, the fields inside the cavity are agitated and radiate out, and we can observe that at the resonant frequency the annular slot ring terminal has the maximum electric current.

Form Fig. 4a, we can observe that by varying the radius of SIW cavity, a large amount of shift is observed in resonance frequency. Whereas, a slot radius variation shows that shift in a small amount of frequency as shown in Fig. 4b. These two parameters are optimized in such a way to operate the 28 GHz.

The simulation is conducted in CST studio suite 2017 version. The simulated return loss characteristics of the designed antenna are shown in Fig. 5. From Fig. 4b results, the annular slot optimized radius is considered to radiate the antenna at 28 GHz frequency. As shown in Fig. 6, the maximum gain obtained by the antenna is 5.28 dBi. Depending on the annular ring slot position and surface currents distribution along the slot, makes the main lobe direction is shifted. This squinted beam radiation as shown in Fig. 6 can be utilized for point-to-point communication.

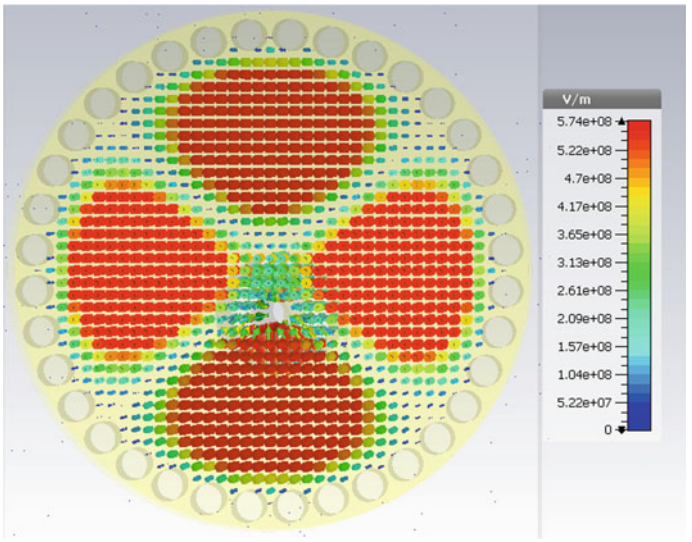

(a)

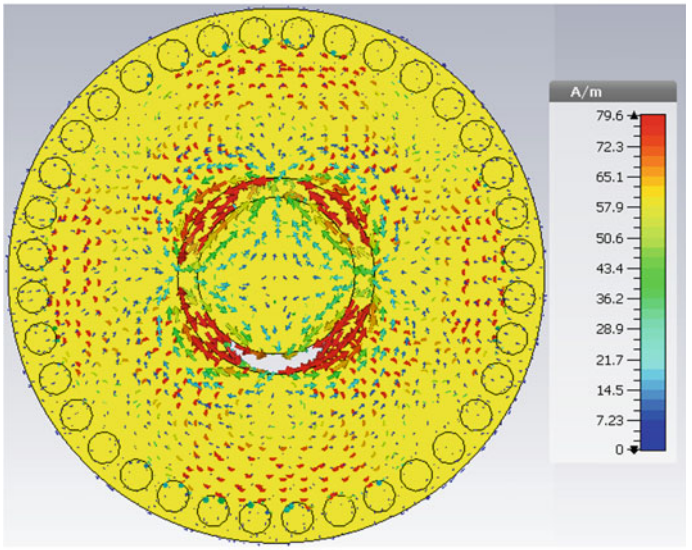

(b)

Fig. 3 **a** TM_{210} mode distribution in cavity simulated in CST (Eigen mode solver), **b** Surface current distributions on the circular SIW cavity-backed annular ring slot antenna at 28 GHz resonant frequency

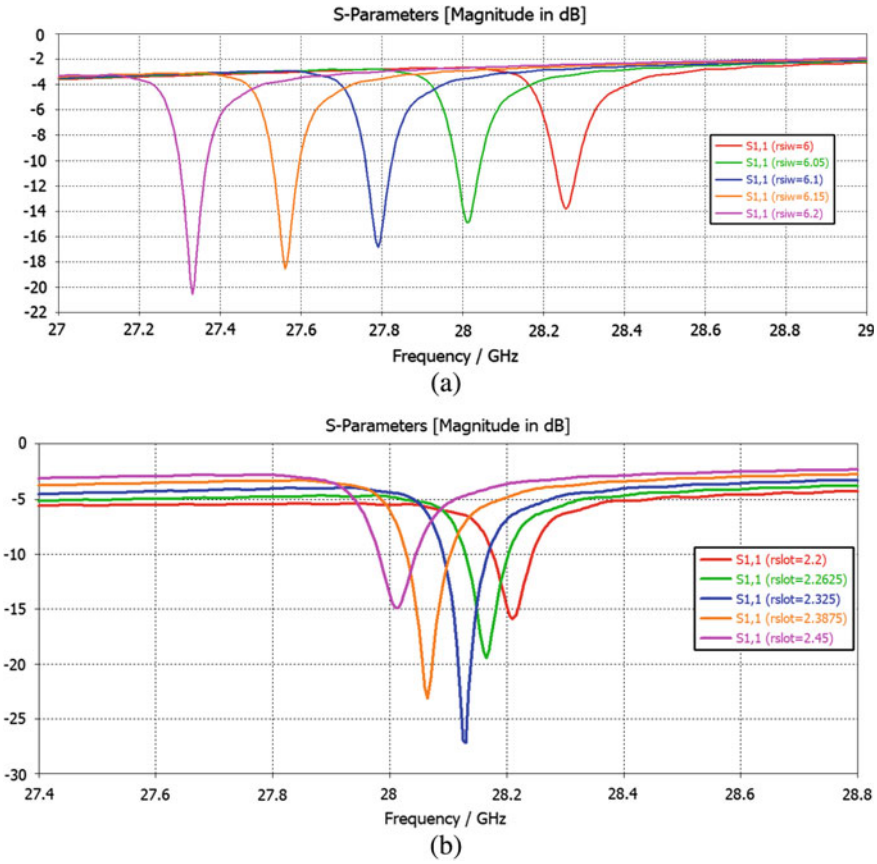

Fig. 4 Variation in return loss as a function of antenna parameter: **a** Radius of circular SIW cavity **b** Radius of annular ring slot

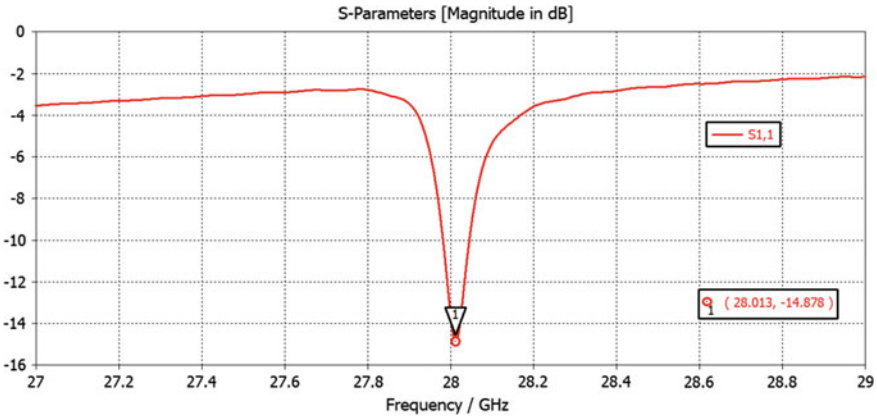

Fig. 5 Simulated return loss of the proposed circular SIW cavity-backed annular ring slot antenna

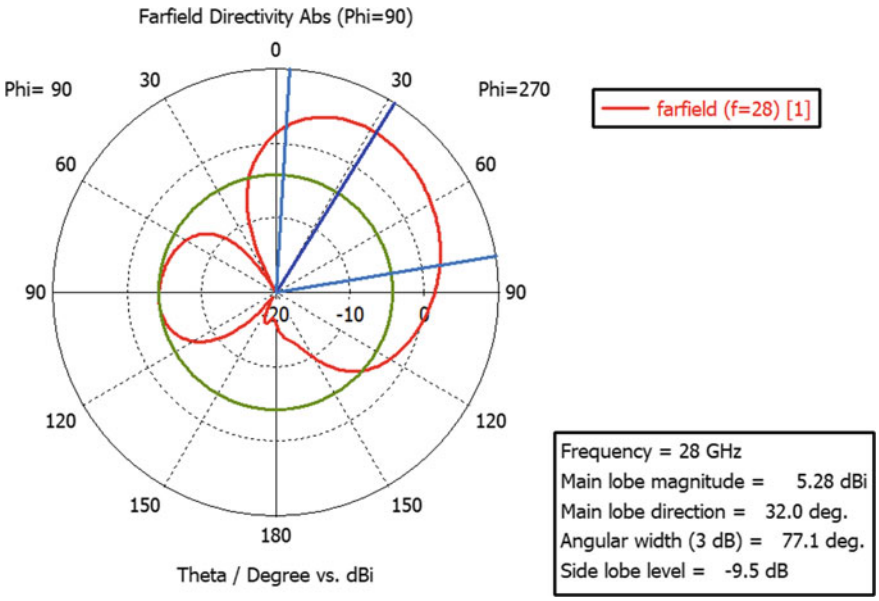

Fig. 6 Radiation pattern of antenna at 28 GHz

4 Conclusion

A planar Ka-band circular SIW cavity-backed slot antenna (CBSA) has been presented in this paper. The simulation results show that TM_{210} mode is propagated in the proposed cavity at 28 GHz. An annular ring slot is used to radiate the proposed antenna at 28 GHz with a gain of 5.28 dBi. This cavity-backed slot antenna minimizes backside radiation thereby improving the front-to-back ratio (FBR). Moreover, the cavity-backed SIW antenna structures have a higher power handling capability than microstrip antennas. As a result, the proposed antenna could be suitable for being used in MMW band. This proposed single-element design can be extended to MIMO SIW CBSA design, and the MIMO SIW CBSA can be employed as aperture sharing antennas for sub-6 GHz and MMW band applications.

References

1. Rappaport TS et al (2013) Millimeter wave mobile communications for 5G cellular: it will work! IEEE Access 1:335–349. https://doi.org/10.1109/ACCESS.2013.2260813
2. Yang W, Ma K, Yeo KS, Lim WM (2016) A compact high-performance patch antenna array for 60-GHz applications. IEEE Antennas Wirel Propag Lett 15:313–316. https://doi.org/10.1109/LAWP.2015.2443054
3. Deslandes D, Wu K (2001) Integrated microstrip and rectangular waveguide in planar form. IEEE Microw Wirel Components Lett 11(2):68–70

4. Huang JQ et al (2016) Compact coaxial probe-fed CP substrate integrated waveguide cavity-backed antenna utilizing slot split ring. Prog Electromagn Res Lett 60(April):107–112. https://doi.org/10.2528/PIERL16041105
5. Kim D, Lee JW, Cho CS, Lee TK (2009) X-band circular ring-slot antenna embedded in single-layered SIW for circular polarisation. Electron Lett 45(13):668–669. https://doi.org/10.1049/el.2009.0901
6. Lacik J (2013) Circularly polarized SIW square ring-slot antenna for X-band applications. Microw Opt Technol Lett 55(11):2562–2568. https://doi.org/10.1002/mop
7. Hong T, Zhao Z, Jiang W, Xia S, Liu Y, Gong S (2019) Dual-band SIW cavity-backed slot array using TM020 and TM120 modes for 5G applications. IEEE Trans Antennas Propag 67(5):3490–3495. https://doi.org/10.1109/TAP.2019.2900394
8. Cassivi Y, Perregrini L, Arcioni P, Bressan M, Wu K, Conciauro G (2002) Dispersion characteristics of substrate integrated rectangular waveguide. IEEE Microw Wirel Components Lett 12(9):333–335. https://doi.org/10.1109/LMWC.2002.803188
9. Pozar DM (2012) Microwave engineering. Wiley, Hoboken, NJ
10. Wu K, Xu F (2005) Guided-wave and leakage characteristics of substrate integrated waveguide. IEEE Trans Microw Theory Tech 53(1):66–73
11. Bozzi M, Georgiadis A, Wu K (2011) Review of substrate-integrated waveguide circuits and antennas. IET Microwaves Antennas Propag 5(8):909–920. https://doi.org/10.1049/iet-map.2010.0463
12. Kumar A, Kumar M, Singh AK (2021) Substrate integrated waveguide cavity backed wideband slot antenna for 5g applications. Radioeng 30(3):480–487. https://doi.org/10.13164/re.2021.0480
13. Morishita H (1991) Analysis of a cavity-backed annular slot antenna with one point shorted. IEEE Trans Antennas Propag 39

Design and Analysis of a Slotted MIMO-Based Antenna for WLAN Applications

Bharani Bandi and Srikalyani Nageti

Abstract This research presents a slotted MIMO antenna for improved isolation. The proposed antenna is designed on an FR-4 substrate with a dielectric constant of 4.4 and a height of 1.6 mm. The operating frequency is 5.4 GHz, which is useful for WLAN applications. Initially, a two-element MIMO is constructed without any isolation technique, but the desired antenna shows self-isolation with required values. After that an analysis was performed to enhance isolation. For further improvement, a parasitic element like a series of diamond-shaped structures is proposed. A further 2 × 2 meander line structures is proposed. The distance between the two radiating elements is 5 mm and is maintained for both the designs. For impedance matching, a quarter-wave feeding technique is proposed. As a result of the investigation, the meander line structure enhanced isolation by 7 dB while simultaneously achieving a low return loss. S-parameters, antenna radiation characteristics, envelope correlation coefficients (ECCs), and diversity gains are explored to evaluate the performance of the suggested MIMO antenna systems. The proposed antenna has a diversity gain (DG) of > 9 dB and ECC (envelope correlation coefficient) of 0.01. For the simulation, CSTMW 2018 was used. The proposed antenna has an overall dimension of 46 × 20 × 1.6 mm. There is a lot of evidence that MIMO with a meander line structure is a good choice for wide LAN applications.

Keywords Slotted · MIMO antenna · ECC · DG · Parasitic element

1 Introduction

There are a variety of standards that must be followed for wireless communication technology to be widely employed in today's electronic gadgets, such as Bluetooth and Wi-Fi. Researchers all over the world are become more interested in MIMO antennas. Multipath fading can be avoided by utilizing several antennas at both the

B. Bandi (✉) · S. Nageti
Department of Electronics and Communication Engineering, Vignan's Institute of Information Technology (A), Visakhapatnam, India
e-mail: bavanabharani@gmail.com

S. Rawat et al. (eds.), *Proceedings of Second International Conference on Computational Electronics for Wireless Communications*, Lecture Notes in Networks and Systems 554,
https://doi.org/10.1007/978-981-19-6661-3_14

transmitter and receiver end with MIMO technology. As a result, excessive mutual coupling between antenna elements might reduce variety. In order to construct MIMO antennas, it is vital to have such low mutual coupling. With the rapid expansion of wireless communication systems, the demand for channel gain, channel capacity, channel bandwidth, and data transfer rate has increased. On the transmitter and receiver, MIMO technology plays a significant role, with several antennas on each ends. Data speed and transmission range can be boosted and multipath fading can be reduced by employing MIMO antennas. However, mutual coupling may occur if antennas are too close to one another in space. In order to obtain a significant separation between the two radiating components, MIMO antennas use at least two radiating components. When it comes to portable gadgets, the useful area is woefully inadequate. Various methods have been employed to minimize the coupling between MIMO elements. Defective ground structure (DGS) structure is used in the present research work to improve the isolation between two antenna elements [1]. As a result, an unique metamaterial MIMO antenna with a short inter-antenna element distance of 7.5 mm is employed. Meta-inspired decoupling networks are used to reduce isolation between WLAN frequencies in [2]. The meta-inspired decoupling network is set up and structured in such a way that it increases the separation of different bands. It can be found in [3]. UWB-MIMO antennas in the UWB frequency band have more than 16 dB of isolation between them, as shown in [4, 5], which presents a lightweight multiple-input multiple-output (MIMO) antenna for ultra-wideband (UWB) applications. The antenna modules are constructed of perpendicular to each other in order to maintain high separation, and the small slot is used to minimize antenna reciprocal coupling [6]. A lightweight dual-band WLAN MIMO antenna with improved isolation is suggested. Meandering inverted F-antennas were used to build the antenna system. WLAN bandwidth is obtained by combining two meandering monopoles. By etching an inverted T-slot on the ground and a meandering resonant extension, a high level of separation between two antenna components is achieved [7]. A compact antenna with dual-band multiple-input multiple-output (MIMO) antennas was designed to operating at fifth generation (5G) band (3.3–3.6 and 4.8–5.0 GHz). Moumita et al. [8] reported regarding MIMO antenna functioning. AP reddy et al. discussed about the mutual coupling with the help of metamaterial-based split ring resonator [9]. A two-element MIMO antenna design focused on negative metamaterial (MNG) was proposed for WiMAX (2.5–2.8 GHz), WLAN (3.2–5.9 GHz), and ITU band (8.15–8.25 GHz) applications to improve isolation. In [10], the author has demonstrated that incorporating a neutralization line between the two-planer inverted F-antennas allows for high isolation. The isolation is provided a T-junction is used to provide good isolation [9]. Another study reports An FSS-based multiband MIMO is reported in [10-12, 13]. İn the present research work, we got good isolation due to incorporating a series of metamaterial unit cells between the two antennas, with this incorporation we achieved low mutual coupling.

The motivation of this study is to improve isolation in wireless application frequencies by using various parasitic element structures. A parasitic element like a series of diamond-shaped structure is proposed, and then, a meander line structure is proposed. Compared to that the meander line structure is optimized in such a way that it

can enhance the isolation by 7 dB. The design and analysis were carried out using CSTMW software.

2 Analysis of MIMO Antenna

2.1 MIMO Antenna without Isolation Technique

In this section, a two-element MIMO antenna with 5 mm spacing is demonstrated. The proposed antenna is placed on an FR-4 dielectric substrate with a 1.6 mm height. To bring out the new antenna design, the basic rectangular antenna is modified. The basic rectangular patch is etched with a radius of 2 mm, and then, a diamond shape is added at the center, and at the sides, half a circle and half a diamond-shaped half structure with equal distances are used. Finally, the proposed structure operates at a resonant frequency of 5.4 GHz. The proposed design dimensions are as follows: W_g width of the ground 46 mm, ground length L_g 20 mm, feed width W_f 0.2 mm, feed length L_f 7 mm, width of the quarter-wave feed W_q and length of the quarter-wave feed L_q 3 mm, and radius R is 2 mm. Proposed MIMO is shown in Fig. 1 with dimensions. After simulation, the S_{11} is $-$ 25 dB and the reflection coefficient S_{21} is $-$ 21 dB. The S-parameters of the MIMO are depicted in Fig. 2. Figure 3 depicts the gain of the MIMO is 2.21 dB.

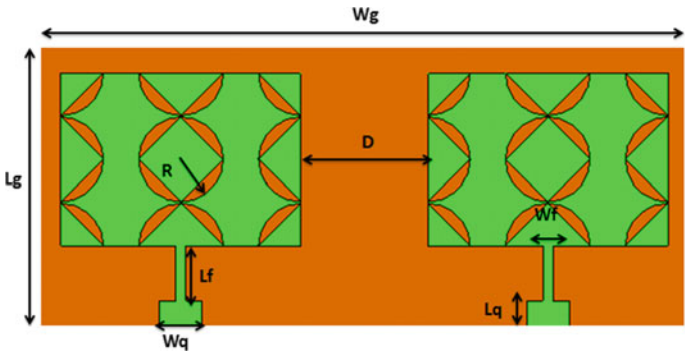

Fig. 1 Proposed MIMO

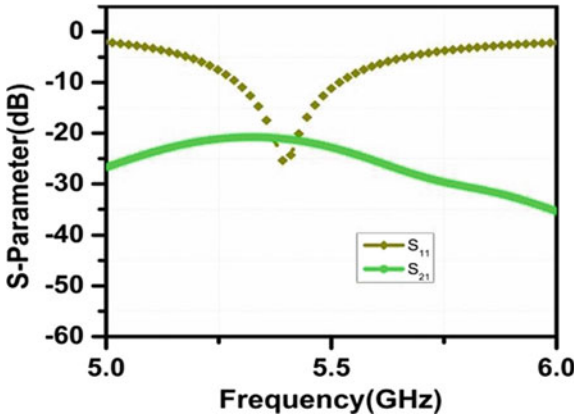

Fig. 2 MIMO S-parameter

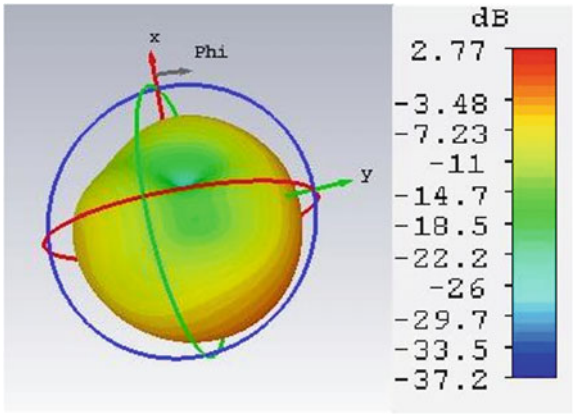

Fig. 3 Gain of the MIMO

2.2 MIMO Antenna with Isolation Structure-1

In this section, there is discourse on improving the isolation between the two elements by using parasitic elements like a series of diamond-shaped structures. Figure 4 shows the proposed MIMO with an isolation structure. The radius of R_1 and R_2 has dimensions of 2 and 1 mm, respectively. With a propped isolation structure, S_{21} is improved by 4 dB. Compared to the structure without isolation, the corresponding S-parameter simulated result is shown in Fig. 5.

2.3 MIMO Antenna with Isolation Structure-2

In this section, for further improvement of isolation between the radiating elements a 2 × 2 meander line structure is proposed. The dimensions of the MIMO structure

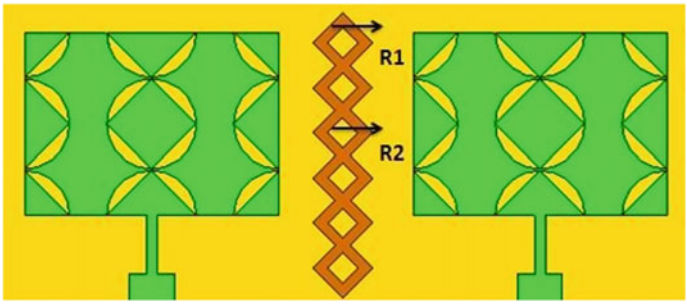

Fig. 4 MIMO with isolation structure-1

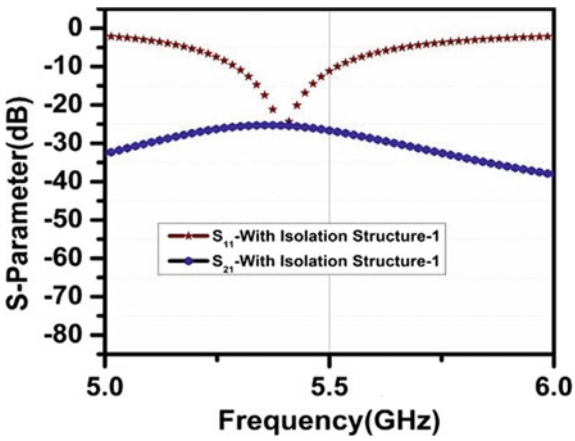

Fig. 5 MIMO with isolation structure-1 S-parameters results

show Fig. 6, and the dimensions of the meander line with $X = 3$, $Y = 3.5$, and $Z = 3.2$ mm are shown in Fig. 7. The corresponding simulated S-parameter results are shown in Fig. 8. The S_{11} is $-$ 51 dB and $S_{21}$is $-$ 32DB, respectively. Figure 9 represents the 2D radiation pattern; Fig. 10 shows the MIMO characteristics of the present structure which looks like envelope correlation coefficient and diversity gain. The two parameters satisfy the required values of the proposed MIMO with ECC < 0.1 and DG > 9.

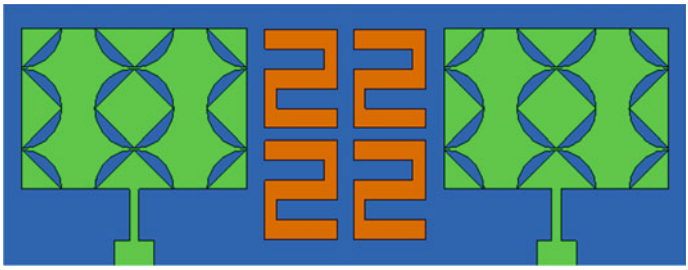

Fig. 6 MIMO with isolation structure-2

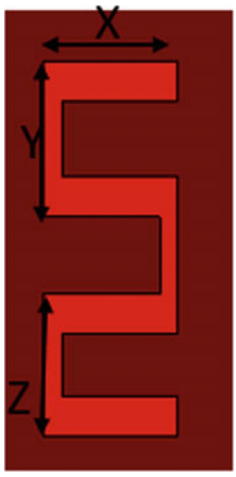

Fig. 7 Dimensions of meander line

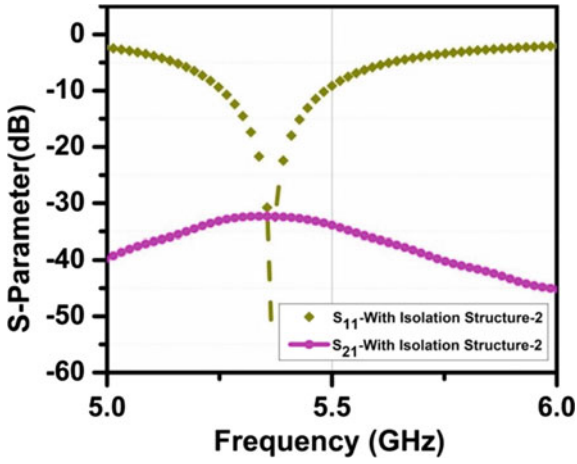

Fig. 8 MIMO with isolation structure-2 S-parameters results

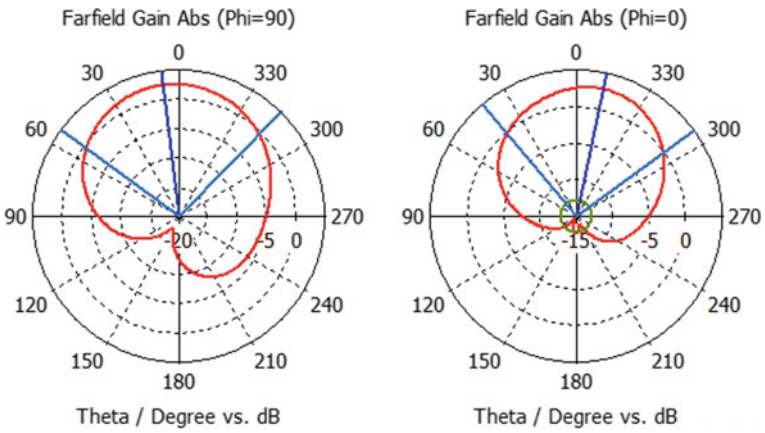

Fig. 9 MIMO with isolation structure-2D results

3 Results and Discursion

In this work, the analysis of the desired system without isolation and with two isolation structures is proposed. The proposed two-element antenna without an isolation structure is described in Sect. 2, from the structure, self-isolation is achieved. For good isolation, a series of diamond structures are proposed in Sect. 3. Finally, further improvement of meander line isolation structure − 2 is proposed. The results of the $S_{11}$and S_{21} parameter so for the proposed design is shown in Fig. 11. When compared to the isolation achieved without and with isolation structure-1, isolation structure-2 improves isolation by 7 dB. Table 1 shows the comparison table for the present research with existing works.

4 Conclusion

In the present research paper, two elements MIMO with two different isolation structures are proposed for isolation improvement. WLAN applications for improved isolation, two-element structures have been proposed. Isolation structures 1 and 2 analyzing the 2 × 2 meander line, it is clear that the isolation has improved. The antenna, which is 46 × 20 mm in size, has a simple design. The proposed MIMO system performs well in terms of envelope correlation coefficient (ECC 0.1) and diversity gain (DG > 9 dB). The present system found meander lines, which can help to improve the isolation of a MIMO antenna without lowering its accuracy.

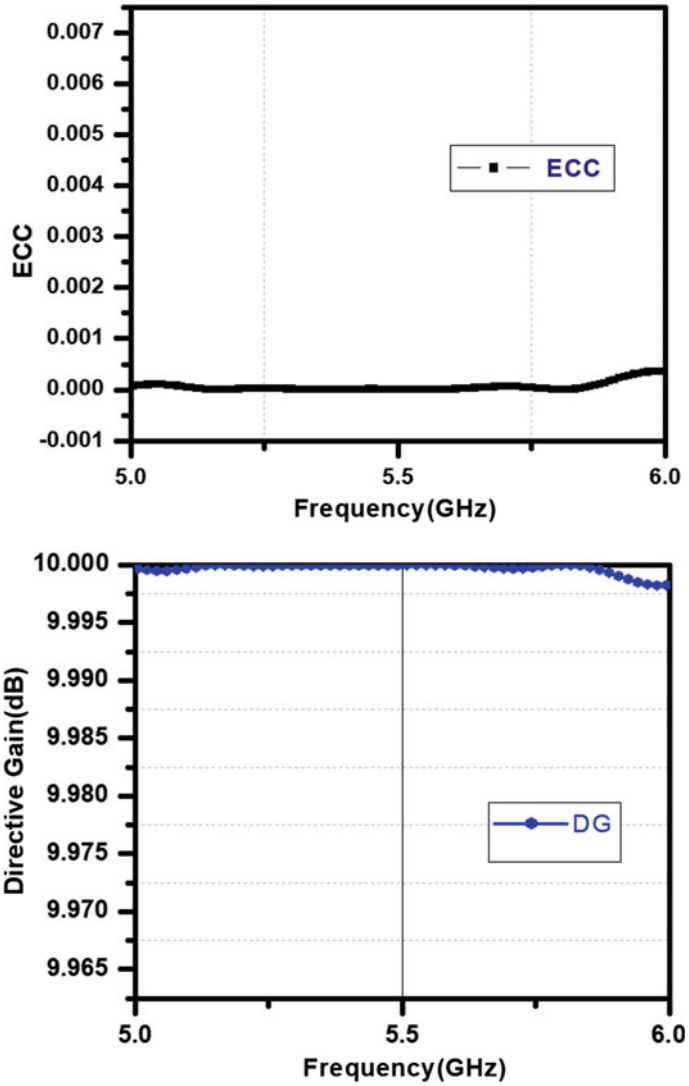

Fig. 10 MIMO **a** ECC **b** DG

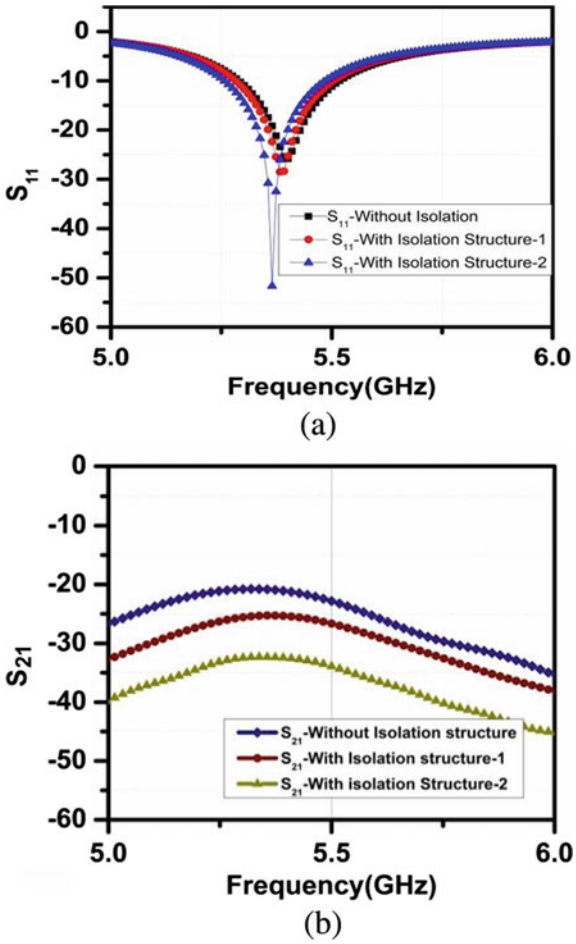

Fig. 11 S-parameters versus Frequency as **a** S_{11} and **b** S_{21}

Table 1 Comparison of proposed work with published works

References antenna	Dimensions (mm^2)	Number of elements	Isolation (dB)	ECC	DG(dB)
Suneetha et al. [9]	40 × 44	2	> 24	< 0.0002	> 9.999
Saleem et al. [11]	70 × 50	2	< 30	< 0.25	–
Iqbal et al. [12]	37 × 44	2	< 24.5	< 0.007	> 9
Proposed work	46 × 20	2	> 30	0.00012	9.98

References

1. Kiem NK, Phuong HN, Hieu QN, Chien DN (2015) A novel metamaterial MIMO antenna with high isolation for WLAN applications, vol 2015, Article ID 851904. https://doi.org/10.1155/2015/851904
2. Roy S, Chakraborty U (2020) Mutual coupling reduction in a multi-band MIMO antenna using meta-inspired decoupling network. Wirel Pers Commun 114:3231–3246. https://doi.org/10.1007/s11277-020-07526-5
3. Zhu X, Yang X, Song Q, Lui B (2017) Compact UWB-MIMO antenna with metamaterial FSS decoupling structure. EURASIP J Wirel Commun Networking
4. Lima AM, Cunha NH, Silva JP (2020) Effect of metamaterial cells array on a microstrip patch antenna design. J Microwaves Optoelectron Electromagnet Appl 19(3). https://doi.org/10.1590/2179-10742020v19i3886
5. Ren J, Hu W, Yin Y, Fan R (2014) Compact printed MIMO antenna for UWB applications. IEEE Antennas Wirel Propag Lett 13
6. Deng J, Li J, Zhao L, Guo L (2017) A dual-band inverted-F MIMO antenna with enhanced isolation for WLAN applications. 1536-1225(c)2016IEEE,AWPL-04-17-0595
7. Yan K, Yang P, Yang F, Zeng LY, Huang S (2018) Eight-antenna array in the 5G smartphone for the dual-band MIMO system. 978-1-5386-7102-3/18/$31.00 ©2018IEEE
8. Chanda M, Sarmah K, Goswami S, Sarma KK (2019) 2×1 MIMO antenna at 2.4 GHz with improved isolation. 978-1-7281-1380-7/19$31.002019IEEE
9. Suneetha P, Naik, KS, Muthusamy P (2022) Isolation enhancement of metamaterial structure MIMO antenna for WiMAX/WLAN/ITU band applications Int J Microwave Wirel Technol 1–11 https://doi.org/10.1017/S1759078721001719
10. Wu X, Han G, Feng C (2019) Dual frequency MIMO antenna with neutralization line. In: IEEE Transaction, pp 1–2. https://doi.org/10.1109/CSQRWC.2019.8799229
11. Saleem R, Bilal M, Chattha HT (2019) An FSS based multiband MIMO system incorporating 3D antennas for WLAN/WiMAX/5G cellular and 5G Wi-Fi applications. IEEE Access. https://doi.org/10.1109/ACCESS.2019.2945810
12. Iqbal A, Saraereh AO, Bouazizi A, Basir A (2018) Metamaterial-based highly isolated MIMO antenna for portable wireless applications. Electron 7(10):267. https://doi.org/10.3390/electronics7100267

A Wideband High-Gain Circularly Polarized Meta-Material-Loaded MIMO Antenna of C/S/X Band for Drone Communications

SD. Sairam and D. Sriram Kumar

Abstract A novel tri-wideband diamond-shaped split ring resonator loaded in the circular radiator with circularly polarized antenna for Wi-Fi, sub-5G communication, and X-band CubeSat communication has been proposed. The circular radiator is designed exactly for 8 GHz. For the requirement of multiple wideband frequencies, a diamond-shaped slot is etched, so the radiator produces the second higher resonance at 5 and 8 GHz by adding the reactive loading (parasitic strip). The third higher resonance frequency was obtained by etching the diamond-shaped slot inside the radiator with exact loading. The metallic patch radiated for wideband resonance by changing the ground patch size with optimized dimension. The proposed antenna radiates at (2.6–4.6), (5.2–6.8) and (8.6–11.55) GHz of return loss above 10 dB with the bandwidth of 2000, 1600, 2950 MHz. The proposed structure with a size of 85 $\times$ 85 $\times$ 1.6 mm^3 has been designed using CST, and the equivalent circuit is realized by ADS software. The designed MIMO antenna is suitable for CubeSat X-band and high-altitude pseudo-satellite applications.

Keywords Circular polarization · High gain · Diamond-shaped metamaterial · MIMO antenna · 5G and CubeSat · High-altitude pseudo-satellite communication

1 Introduction

Monopole circular patch antennas have the significant characteristics of omnidirectional pattern with a finite ground panes [1, 2]. The patch generally consists of a ground plane and the substrate placed above the ground structure. The metallic patch is connected with a perfect transmission line, and two shorting pins are placed at the top patch to the ground patch. Multiple input and multiple output techniques are unique methods to allow a high data rate and increase the spectrum efficiency and the channel capacity. Different approach has been proposed so far to increase the

SD. Sairam (✉) · D. S. Kumar
Department of Electronics and Communication Engineering, National Institute of Technology, Tiruchirappalli, India
e-mail: sairambe.dvk88@gmail.com

S. Rawat et al. (eds.), *Proceedings of Second International Conference on Computational Electronics for Wireless Communications*, Lecture Notes in Networks and Systems 554,
https://doi.org/10.1007/978-981-19-6661-3_15

Fig. 1 Drone communication

performance of the antenna. The space and the position of the multiple antennae are the major role for considering the bandwidth, gain of MIMO design [3, 4]. For conventional passive radar has two channels, the surveillance medium for target echoes and the receptor for the direct patch signal [5–8]. The surveillance medium gathers the reflections from the static scatters and a direct path signal. The direct path signal is an effective channel, and it is important in the surveillance channel [9, 10]. For surveillance and identifying the object by using the single antenna digital passive radar (SDPR). Single receiver channel is only one channel that can be used at the receiving end. At the receiving channel, it can desirable of high line of sight signal-to-noise ratio (SINR) (Fig. 1).

Surveillance mode, it is preferable to cancel the line of sight path interference (multipath), and the echoes of targeted object signal should receive exactly. The direct signal masks the objective target echoes and occupies the entire wide-angle receiver frequency that attenuates the performance of the detection. Using the optimized receiver configuration for the direct signal, by using that, the capability of detection is maximized [11, 12]. The designed antenna is a compact and lightweight structure for the use of drone applications. In MIMO, the essential characteristics such as envelop correlation coefficient (ECC), total active reflection (TARC), directive gain (DG), active reflection coefficient (ARC) are deliberate. The proposed design concept and feeding techniques, their optimized dimensions are analyzed in Sect. 2. The numerical results and calculations of the designed structure are depicted in Sect. 3. In Sect. 4, draws the conclusions.

2 Tri-Band Antenna Design

2.1 Antenna Configuration

The physical parameter of the present tri-wideband MIMO structure is appeared in Fig. 2. The numerical dimension of the designed structure is 85 × 85 mm^2. It is designed with a RT Duroid material has 2.20 dielectric constant, and thickness

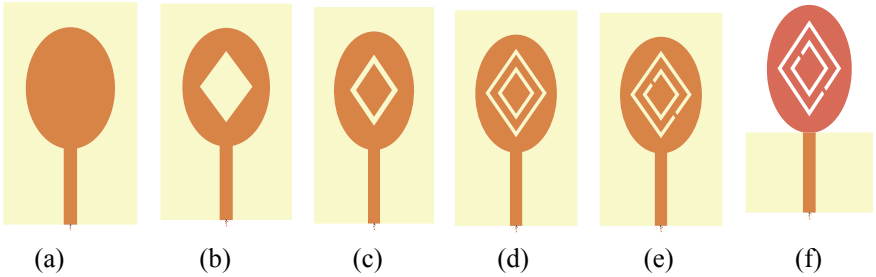

Fig. 2 **a, b, c, d, e, f** Design evolution of tri-wideband antenna elements

is 1.6 mm between the ground and patch. The proposed structure consists of three radiators by the diamond shape slot which follows a metamaterial characteristic with an optimized split gap. The two diamond shape radiator provides the two different resonant frequency points, and the outermost circular patch radiates for a single resonant frequency. The three radiators and the full ground sections operate with the three resonant frequencies with narrow bandwidth. For the wideband considerations, the ground plane etched with the small rectangular position with the transmission feed length gives the wider bandwidth and high gain.

In Fig. 3, shows the return loss value for the design evolution of the proposed structure. The basic tri-wideband antenna with 90-degree parasitic strip feeding method achieves port isolation greater than − 10 dB. To further improve, the wideband isolation should be less than − 10 dB by adding the parasitic strip in many elements. The feeding point of inner radiator reacts as a freeloading resonator that creates high combine path to electron flows through first antenna radiator to another radiator.

2.2 Optimized Tri-Wideband Antenna Element

Figure 4 proposed tri-wideband structure with optimized dimension. The radiator consists of three-section circular patch, diamond shape radiator with 1 mm spacing slot of second diamond shape radiator. Both the inner and outer diamond shape radiator connects parasitic strip plays an important role in tri-band frequency.

The MSF lines at an offset distance from the middle of the circular patch with 50 Ω impedance match and connect with the parasitic strip between the diamond shape radiators. The geometry refinement and the parametric analysis of the designed antenna design were simulated out by advanced design system. The optimal design parameter values shown in Table 1. The proposed modeling of the first element can be calculated by using the below equations and to match the antenna impedance to the transmission line impedance at 50 Ω,

For $\frac{W_a}{h} \leq 1$,

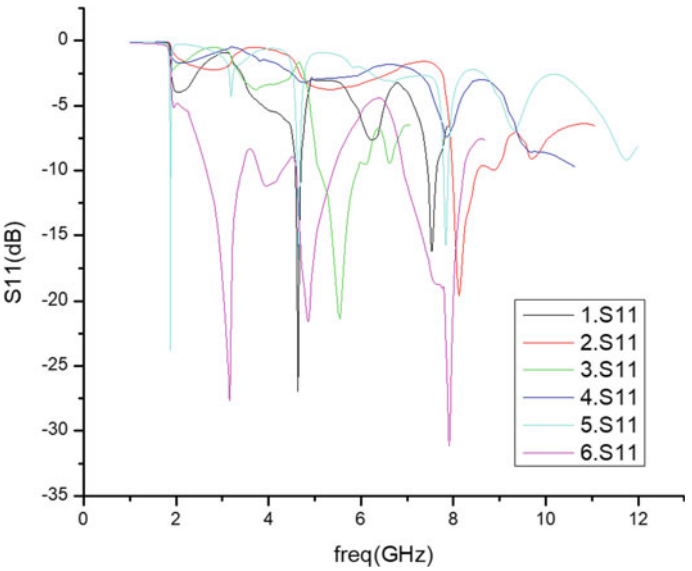

Fig. 3 Return loss of the 6 stage of proposed structure

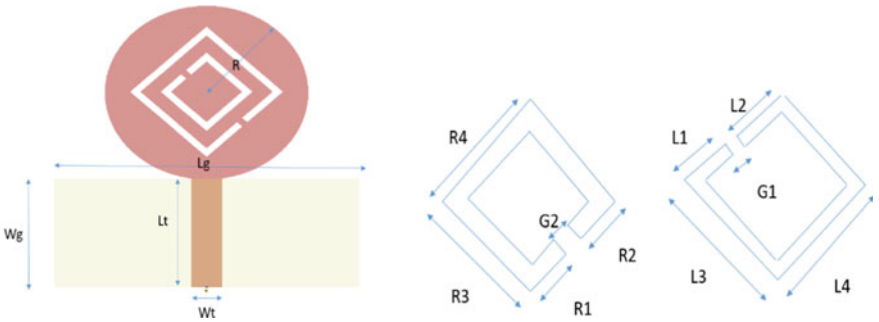

Fig. 4 Proposed tri-wideband structure

Table 1 Optimized dimensions of proposed design (mm)

Parameter	Values	Parameter	Values
W_g	12.5	L_2	2
L_g	30	L_3	4.5
L_t	12.5	L_4	4.5
W_t	3	G_2	0.5
R	10	R_1	3.5
G_1	0.5	R_2	3.5
L_1	2	R_3,R_4	7.5, 7.5

$$Z_0 = \frac{60}{\varepsilon_{\text{reff}}} \ln\left(\frac{8h}{W_a} + \frac{W_a}{4h}\right) \tag{1}$$

where

$$\varepsilon_{\text{reff}} = \frac{\varepsilon_{\text{r}} + 1}{2} + \frac{\varepsilon_{\text{r}} - 1}{2}\left(\frac{1}{\sqrt{1 + 12\frac{h}{W_a}}} + 0.004\left(\left(1 - \frac{W_a}{h}\right)^2\right)\right) \tag{2}$$

For $\frac{W_a}{h} \geq 1$

where,

$$Z_0 = \frac{120\pi\sqrt{\varepsilon_{\text{reff}}}}{\frac{W_a}{h} + 1.393 + 0.667\ln\left(\frac{W_a}{h} + 1.444\right)} \tag{3}$$

$$\varepsilon_{\text{reff}} = \frac{\varepsilon_{\text{r}} + 1}{2} + \frac{\varepsilon_{\text{r}} - 1}{2}\left(\frac{1}{\sqrt{1 + 12\frac{h}{W_a}}} + 0.004\left(\left(1 - \frac{12h}{W_a}\right)^{\frac{-1}{2}}\right)\right) \tag{4}$$

where Z_0, W_t is the width of the transmission line. $\varepsilon_{\text{reff}}$ is the effective permittivity; ε_r is the relative permittivity. The dimension of the transmission line feed network calculated by using the below equations.

Width of the transmission line,

$$W_t = \frac{2h}{\pi}\left(B - 1 + \frac{\varepsilon_r - 1}{2\varepsilon_r}\left[\ln(B - 1) + 0.39 - \frac{0.61}{\varepsilon_r}\right]\right) \tag{5}$$

$$B = \frac{60\pi^2}{Z_0\sqrt{\varepsilon_{\text{r}}}} \tag{6}$$

Length of the transmission line,

$$L_a = \frac{\lambda}{4\sqrt{\varepsilon_{\text{reff}}}} \tag{7}$$

2.3 MIMO Design

Four-port four-antenna multiple input and multiple output (MIMO) antenna is shown in Fig. 5 with a ground defected structure with dimensions of $L_g \times W_g$ ($85 \times 85 \times 1.6$) mm^3. RT Duroid 5880 material is used as dielectric substrate with 2.2 relative permittivity with the thickness of h = 1.6 mm. Four antennas are placed orthogonal to

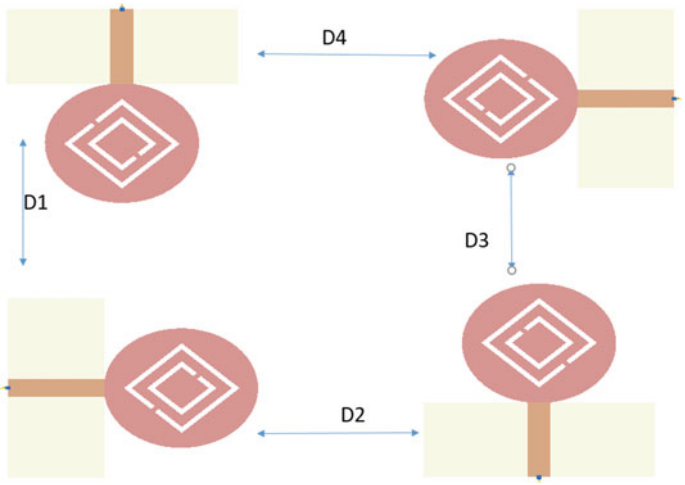

Fig. 5 Proposed MIMO antenna

each other with a 30db isolation that bring down the mutual coupling of the adjacent antennas.

3 Results and Discussion

3.1 S-Parameter

The proposed radiator design shown in Fig. 6 was simulated S-parameter against frequency using advanced design system. The output shows the proposed antenna provides accurate impedance matching and impedance bandwidth (S_{11} *and* $S_{22} \leq -$ 10 dB) from 2.642 to 4.2, 5.2 to 6.8, and 8.753 to 11.55 GHz. Thus, the required bandwidth for UWB and RADAR application is satisfied. The resulting plot shows the port isolation (S_{21} and S_{12}) is below $-$ 20 dB for the entire resonating frequency. Mutual coupling is finer than $-$15 dB for identified to be admissible for real-time approach.

3.2 VSWR, Gain, and Directivity

Figure 7 shows the simulated peak gain, voltage standing wave ratio, directivity, and the radiation efficiencies of one port excitation of the proposed MIMO antenna. The designed antenna gains ranges from 2.1 to 8.1 dBi of the entire resonant frequency, and the directivity is also equal to the gain value. The VSWR has been maintained

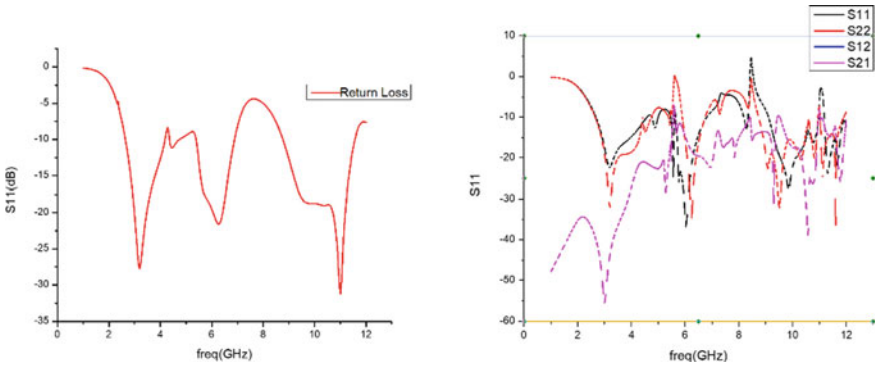

Fig. 6 **a, b** S-parameter values of proposed single and MIMO antenna design

less than 2 for the operating frequency regions which show in Fig. 9. The efficiency of radiations is above 60% in the wideband frequencies, and it drops to about 30% at the non-resonant frequency ranges.

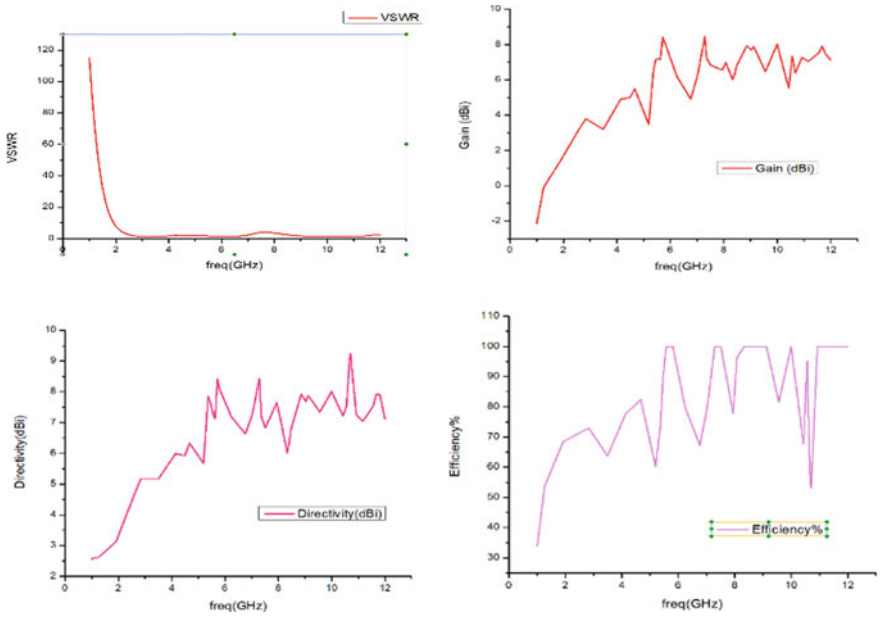

Fig. 7 **a, b, c, d** VSWR, gain, directivity, and efficiency values of proposed single and MIMO antenna design

3.3 Radiation Pattern and Axial Ratio

The 3-dimensional radiation of the designed structure has been studied with all 4 ports. Simulated radiation pattern (xoz, xoy, and yoz) planes at 3.6, 5.8, 9.1, 10.05 GHz are represented in Fig. 8. The tri-wideband MIMO proposed structure consisting of 4 patches; each element was located perpendicular to each patch; the patterns of port 2 and port 1 are almost similar with a, 90° rotation. The radiation pattern of the H-plane is quasi omnidirectional (xoz—second port and xoy—first port). The MIMO proposed design has been achieved 90-degree patterns to reduce the effect of coupling toward the near patches.

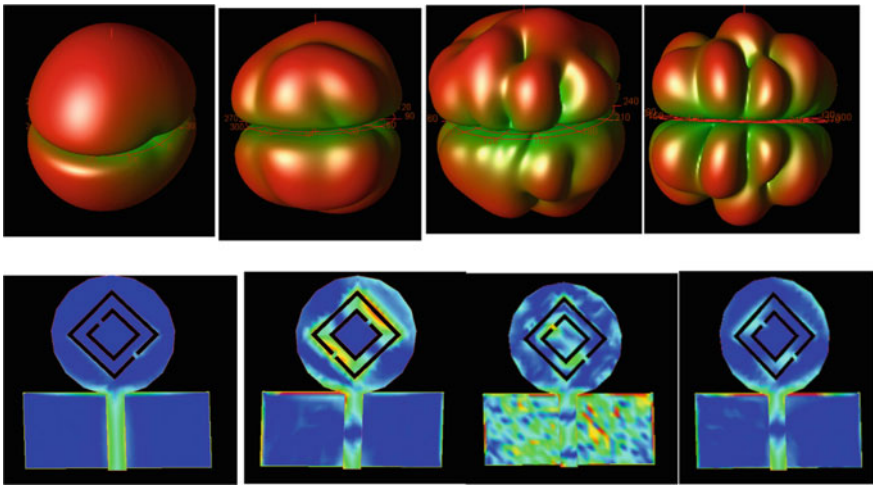

Fig. 8 3D radiation pattern and its current distribution

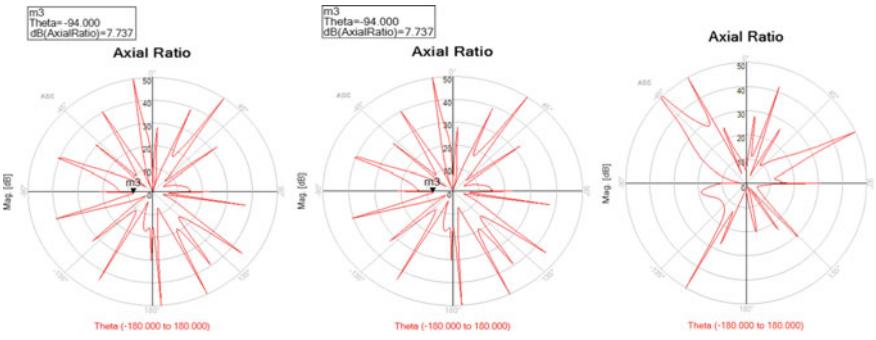

Fig. 9 Axial ratio of Tri-band frequency (AR = 1)

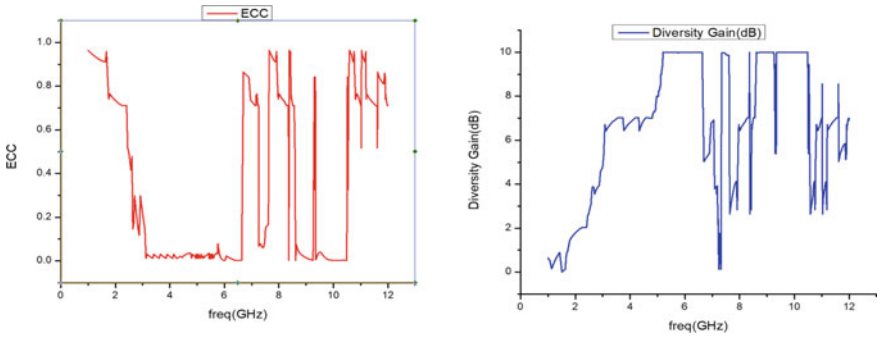

Fig. 10 ECC and diversity gain

3.4 Diversity Performance

The envelope correlation coefficient (ECC) and diversity gain (DG) is an important characteristics performance of the MIMO antenna. Based on the return loss parameter (S_{11}), the ECC value can be calculated as,

$$\rho_e = \frac{\left|S_{11}^* S_{12} + S_{21}^* S_{22}\right|^2}{\left(1 - |S_{11}|^2 - |S_{21}|^2\right)\left(1 - |S_{22}|^2 - |S_{12}|^2\right)} \tag{8}$$

Diversity gain,

$$\mathrm{DG} = 10\sqrt{1 - |\rho_e|^2} \tag{9}$$

Figure 10 shows the results of ECC and diversity gain of the entire operating frequency by the proposed structure. ECC should be lesser than 0.5 value of the tri-wideband resonance range. The diversity gain should be greater than 5dBi for the entire bandwidth frequencies, which shows the designed metallic structure is perfect of the diversity systems.

4 Conclusion

A circularly polarized multiple-port and multiple-patch radiator has wideband characteristics is focused in this work. The offset multiple input ports are deployed to input the inner layer of the radiator patch with perfect impedance matching. The antenna isolation has highly enhance by the position of the adjacent patches to reduce the decoupling. The designed antenna achieves a larger impedance bandwidth 2.642–4.2, 5.2–6.8, and 8.7–11.55 GHz. The proposed structure states that the acceptance value of mutual coupling of − 15 dB and the ECC has lower than 0.04 of the resonance

frequency, with a compact structure; the designed metallic patch can be achieving the desired conditions for the MIMO/diversity systems.

References

1. Delaveaud C, Leveque P, Jecko B (1994) New kind of microstrip antenna: the monopole wire-patch antenna. Electron Lett 30:1–2
2. Wu JY, Row JS, Wong KL (2001) A compact dual-band microstrip patch antenna suitable for DCS/GPS operations. Microw Opt Technol Lett 29:410–412
3. Zhao A, Ren Z (2019) Size reduction of self-isolated MIMO antenna system for 5G mobile phone applications. IEEE Antennas Wirel Propag Lett 18(1):152–156
4. Wang H, Zhang R, Luo Y, Yang G (2020) Compact eight-element antenna array for triple-band MIMO operation in 5G mobile terminals. IEEE Access 8:19433–19449
5. Griffiths HD (2003) From a different perspective: principles, practice and potential of bistatic radar. In: Proceedings of the international conference on radar pp 1–7. IEEE, Adelaide, SA, Australia
6. Kuschel H, O'hagan D (2010) Passive radar from history to future. In: Proceedings of the 11th International IRS, pp 1–4. IEEE, Vilnius, Lithuania
7. Palmer J, Palumbo S, Summers A, Merrett D, Searle S, Howard S (2011) An overview of an illuminator of opportunity passive radar research project and its signal processing research directions. Digit Signal Process 21(5):593–599
8. Liu J, Li H, Himed B (2015) On the performance of the cross-correlation detector for passive radar applications. Signal Process 113:32–37
9. Wan X, Yi J, Zhao Z, Ke H (2014) Experimental research for CMMBbased passive radar under a multipath environment. IEEE Trans Aerosp Electron Syst 50(1):70–85
10. Colone F, O'Hagan DW, Lombardo P, Baker CJ (2009) A multistage processing algorithm for disturbance removal and target detection in passive bistatic radar. IEEE Trans Aerosp Electron Syst 45(2):698–722
11. Barott WC, Engle J (2014) Single-antenna ATSC passive radar observations with remodulation and keystone formatting. In: Proceedings of the IEEE Radar Conference, pp 159–163. IEEE, Cincinnati, OH, USA
12. Bączyk MK, Kulpa K, Samczyński P, Malanowski M (2015) The impact of reference channel SNR on targets detection by passive radars using DVB-T signals. In: Proceedings of the IEEE radar conference, pp 708–712. IEEE, Arlington, UA, USA
13. Kang L, Li H, Wang X, Shi X (2015) Compact offset microstrip-fed MIMO antenna for band-notched UWB applications. IEEE Antennas Wirel Propag Lett 14
14. Tariq S, Naqvi SI, Hussain N, Amin Y (2021) A metasurface-based MIMO antenna for 5G millimeter-wave applications. IEEE Access
15. Kim KS, Yoo JS, Kim JW, Kim S, Yu JW, Lee HL (2019) All-around beam switched antenna with dual polarization for drone communications. IEEE Trans Antennas Propag 68(6)

Black Widow Optimization and Long Short-Term Memory-Based Channel Estimation in MIMO–NOMA for mmWave Systems

Belcy D. Mathews and M. Tamilarasi

Abstract Non-orthogonal multiple access (NOMA) methods are being actively explored to overcome some of the major difficulties in 5th generation (5G). When NOMA methods are used with millimeter wave (mmWave) multiple-input multiple-output (MIMO), channel estimation (CE) becomes extremely difficult task. To bring out the benefits of NOMA and mmWave, a proper CE process is required. This paper proposes a black widow optimization–long short-term memory-based estimator network (BOLSTMEN) to estimate the channel for mmWave-MIMO systems. The proposed BOLSTMEN adopts a hybrid beamforming (HBF) technique for reducing the system complexity and hardware cost of the MIMO network. A coarse estimation of the channel is first made from the received pilot symbols, and this estimate is given as the input to BOLSTMEN to fine estimate the channel coefficients. Simulation results prove that the designed BOLSTMEN provides improved classification performance and spectral efficiency when compared with the conventional CE models.

Keywords Black widow optimization · Channel estimation · Hybrid beamforming · Long short-term memory · MIMO

1 Introduction

Because of its large bandwidth and improved spectral efficiency, the mmWave technology has gained a lot of interest as the need for radio spectrum resources increases [1]. The mmWave paired with massive antenna array has become a superior technology for 5G communication systems as the conventional transceiver could adjust for relatively significant propagation loss utilizing the beam gain offered by the

B. D. Mathews (✉) · M. Tamilarasi
Puducherry Technological University, Puducherry, India
e-mail: mathews.d.belcy@pec.edu

M. Tamilarasi
e-mail: tamilarasim@pec.edu

S. Rawat et al. (eds.), *Proceedings of Second International Conference on Computational Electronics for Wireless Communications*, Lecture Notes in Networks and Systems 554,
https://doi.org/10.1007/978-981-19-6661-3_16

massive antenna array [2]. The mmWave-MIMO system helps to decrease the hardware complexity and energy usage. In general, a radio frequency (RF) chain can support only one user at a time interval to avoid interference with other users and the number of users is constrained by the number of radio frequency chains [3]. For a dense network, a linear operation cannot separate the signals from different users [4]. However, by using the superposition coding at the sender and successive interference cancellation (SIC) at the user, NOMA technology can overcome this fundamental limitation [5]. NOMA system can accommodate multiple users at the same time–frequency resource and transform individual channel gains into multiplexed gain via superposition coding, which is different from the conventional beamspace MIMO [6]. Hence, the quantity of supported users in a MIMO–NOMA technology can be higher than the number of RF chains, and a considerable increase in the downlink sum rate is also observed [7].

Rather than the traditional SIC technique, we make use of the effect of deep learning (DL) as well as the multilayer neural networks (MNNs) to reach accurate signal detection in MIMO–NOMA [8]. Deep learning, a part of machine learning, has made a significant development in recent years, and it is being utilized in various industries.

Wireless multipath fading channels lead to inter-symbol interference (ISI). A receiver with the information of channel impulse response (CIR) which is normally estimated by a separate channel estimator is required to take out the channel effects from the received data [9]. The two kinds of CE techniques are blind CE and pilot-based CE. Pilot-based CE can be of block type and comb type. To achieve CE in block type, orthogonal frequency division multiplexing (OFDM) symbols are transmitted periodically with pilots on every subcarriers. The block-type pilot-based CE scheme is suitable for frequency-selective and slow fading channels [10]. All symbols in comb-type OFDM have pilot tones on the frequently distributed subcarriers. In pilot-based CE, the least square (LS) and minimum mean squared error (MMSE) techniques can also be applied. MMSE methods surpasses LS algorithms in most cases, but they are more complicated [11]. To carry out the pilot-based CE using DL method, we designed a BOLSTMEN model in which the pilot signals in the channel are optimized using BWO algorithm which is different from other optimization algorithms with fixed learning rate.

This paper is organized as follows. The literature for optimization-based and neural network-based CE techniques and its limitations is given in Sect. 1. Section 2 explains the proposed BOLSTMEN model for efficient CE. Section 3 provides the experimental analysis with graphs. The paper is concluded, and the future work is given in Sect. 4.

2 System Model

The system model of the proposed BOLSTMEN model is shown in Fig. 1. Firstly, the input is given to a converter block, which converts the serial stream of data to

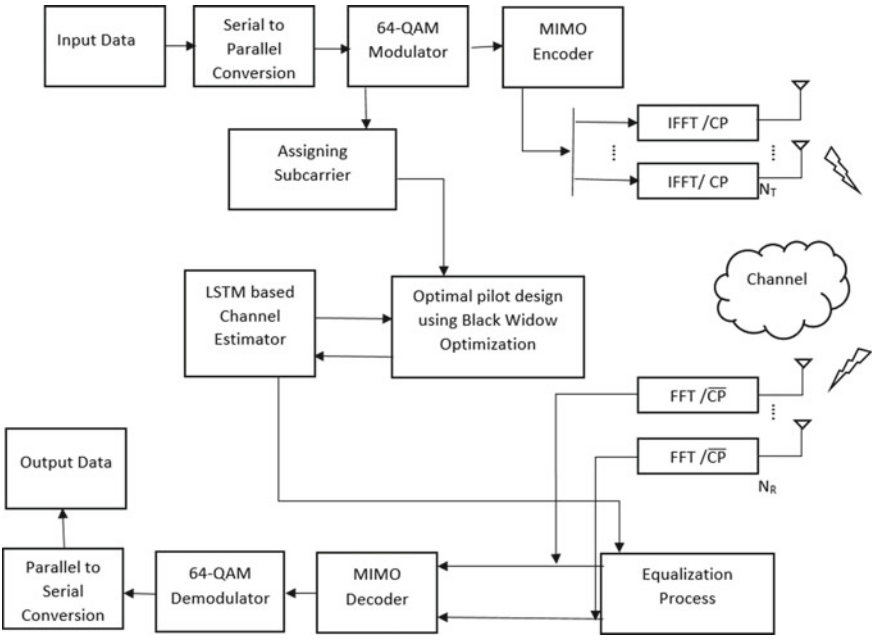

Fig. 1 Block diagram of the proposed black widow optimized LSTM channel estimator network (BOLSTMEN)

a parallel data. The data are then passed to a 64-QAM block, which uses a single radio wave to represent six bits of parallel data, where K symbols form a modulated data block. The modulator has a connection to the sub-carrier block, where the pilot blocks are generated. Then, a MIMO encoder block is connected. Inverse fast Fourier transform (IFFT) is used to convert the signals to time domain. A cyclic prefix (CP) is also added to combat multipath fading. BWO is employed to optimize and identify the best pilot symbols. The optimal pilot symbols are then given to the LSTM network for efficient CE.

2.1 Hybrid Beam Forming in MIMO-NOMA

We take a downlink MIMO–NOMA in a macro-cell with radius 500 m which is depicted in Fig. 2. The BS provides p_{bs} transmit power, and equally distributes it among the N antennas. As a result, BS broadcasts a superimposed signal based on NOMA's properties. All M UEs are randomly distributed in a cell to create a MIMO–NOMA scenario. Here, $p_n = \frac{p_{\text{bs}}}{N}$ represents the transmitted power by a single antenna. In MIMO–NOMA, the UE closer to the BS can use SIC to cancel the interference signal. The SIC is supposed to operate with a few or no faults in this case. In addition, the BS is responsible for clustering the UEs and also determines

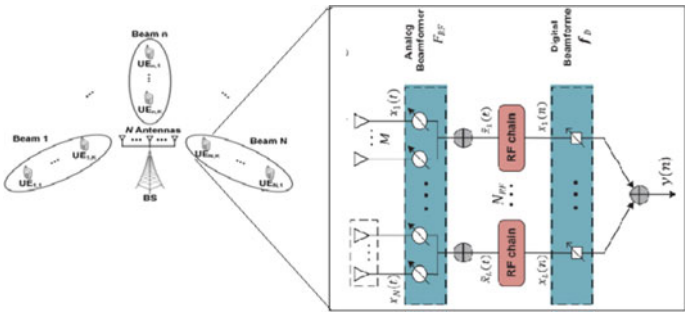

Fig. 2 System model for hybrid beamforming in MIMO–NOMA model showing the data transmission flow among users

each UE's transmit power. Rayleigh fading as well as an additive white Gaussian noise (AWGN) affect signal received at each UE.

The BS transmits the superimposed signal

$$x_n = \sum_{k=1}^{K} \sqrt{\propto_{n,k}} p_n s_{n,k} \tag{1}$$

where $s_{n,k}$, $\propto_{n,k}$, $and p_n$ denote the transmitted signal, power allocation coefficient, and the transmit power of each beam with K number of users, respectively. The signal received by the $UE_{n,k}$:

$$y_{n,k} = h_{n,k} \sum_{n=1}^{N} w_n x_n + n_{n,k} \tag{2}$$

where $h_{n,k}$ represents the Rayleigh fading channel vector that is calculated from the BS to the $UE_{n,k}$. Precoding vector is denoted $w_{n..}$ And precoding matrix, $\boldsymbol{W} = [w_1, w_2, \ldots..w_n], where\ \ w_n \in \boldsymbol{C}^{1\times N}$ and $n_{n,k}$, is the AWGN, and $h_{n,k}$ can be expressed as,

$$h_{n,k} = s_{n,k}\sqrt{d_{n,k}^{-\delta}} \tag{3}$$

where $d_{n,k}$ is the separation between BS and $UE_{n,k}$. Path loss exponent is represented as δ. Following the principle of NOMA, the power allocation coefficient, $\alpha_{n,k}$ at each UE is expressed as,

$$0 \le \alpha_{n,k} \le 1, \sum_{k=1}^{K} \alpha_{n,k} = 1, \alpha_{n,k} \in \forall \tag{4}$$

where ∀ denotes the set of feasible power allocation coefficients. The receiver has N isotropic antenna elements which is sub-divided into L subsets of antenna arrays containing M antenna elements in every subset. The number of RF chains, N_{rf} is taken less than the number of antenna in HBF. Instead of all antenna elements, each antenna array subset is connected to a single RF chain. The HBF scheme depicted in Fig. 2 gets a single desired signal $s_d(t)e^{j2\pi fct}$ with an angle of arrival (AOA) θ_d and k interference signals $i_k(t)e^{j2\pi fct}$ with different angles of arrival $\theta_k, k = 1, 2, 3, \ldots K$. The received signal $x_m(t)$ of l^{th} sub-array at each m^{th} antenna element $(m = 1, 2, 3, \ldots M)$ includes desired narrow band signal, interference signal, and an AWGN signal $v(t)$. Therefore, the output at the l-th sub-array $x_l(t)$ is expressed as,

$$x_l(t) = \sum_{m=0}^{M-1} s_d(t)e^{j2\pi fct(t-(\frac{sin\theta_d}{2\pi fc}.\tau_d)} + \sum_{m=0}^{M-1} i_k(t)e^{j2\pi fct(t-(\frac{sin\theta_k}{2\pi fc}.\tau_k)} + v(t) \quad (5)$$

where d, the distance between neighboring antenna array elements considered to be 0.5τ throughout this study. The symbols τ_d, τ_k represent the propagation delays of desired signal as well as the k-th interference signal to a reference point, the array's initial element. And c is the speed of light. The signal $x_l(t)$ with $(l = 1, 2, 3 \ldots L)$ runs through L, RF chains with L ADCs and down converters, based on measured baseband signal in a matrix–vector notation for all L subsets.

$$x(n) = F_{\mathrm{RF}}^{H} As(n) + F_{\mathrm{RF}}^{H} v(n) \quad (6)$$

where F_{RF}^{H} is the diagonal of the matrix with a phase shift, $As(n)$ is the input to the analog beamforming part, and $v(n)$ is the nose vector. After the application of digital beamforming vector $f_D \in C^{N_{RF\times 1}}$, in the digital beamforming part, Eq. (6) becomes,

$$y(n) = f_{\mathrm{D}}^{H} F_{\mathrm{RF}}^{H} As(n) + f_{\mathrm{D}}^{H} F_{\mathrm{RF}}^{H} v(n) \quad (7)$$

The signal amplitude and phase can be varied by varying the digital beamforming vector $\boldsymbol{f}_D$.

2.2 Optimal Pilot Design Using Black Widow Optimization Method

Along with the information bits, training symbols are also transmitted to ensure the pilot-aided channel estimation (PACE). The transmit vector $x[k]$ can be expressed as $X \in C^{N_{t\times N_r}}$ when it is stacked in a matrix. To ensure a full rank PACE, a minimum of N_t training symbols must be transmitted. The training symbols matrix is made up of orthogonal sequences that have been subjected to $XX^t = \mu I_{\mathrm{NT}}$ where μ is the signal power associated with training symbols. BWO is utilized to ensure the optimal pilot

symbol selection. It is a novel meta-heuristic population-based optimization scheme, proposed based on the characteristics of black widow spiders.

- Initialization—An array of possible variables of the problem has to be initialized to resolve an optimization problem. For the solution of an optimization issue, a dimensional value M_{var} and an array of widow $1 \times M_{\text{var}}$ are initialized. The array is described as:

$$\text{widow} = [x_1, x_2, \ldots . x_{\text{Mvar}}] \tag{8}$$

The fitness of a widow is determined using the fitness function f,

$$\text{Fitness} = f(\text{widow}) \tag{9}$$

The widow represents the portion of the data received across the channel, while M_{var} denotes the total number of pilots symbols assigned to the channel, $x_1, x_2, \ldots . x_{\text{Mvar}}$ are used to represent the channels. The fitness is evaluated based on the received signal strength in terms of their BER and MSE.

- Procreate—an array called alpha $\propto$, same as the widow array but with random number of elements, is created, and then, an offspring array is produced by using α by the following equations where $\times$ 1 and $\times$ 2 are parents, $y1$ and $y2$ are offspring.

$$y_1 = \propto x_1 + (1 - \propto) x_2 \tag{10}$$

$$y_2 = \propto x_2 + (1 - \propto) x_1 \tag{11}$$

This process is repeated for $\frac{M_{\text{var}}}{2}$ times, in random manner and the offspring, and parents are added to an array and sorted by their fitness values.

- Cannibalism—the first type of cannibalism in the BWO algorithm is sexual cannibalism, in which a black widow spider eats her spouse during mating. The second type of cannibalism is sibling cannibalism, in which stronger spiders eat their weaker siblings. This method establishes a cannibalism rating depending on the number of survivors and uses the fitness value to determine the stronger and weaker individuals.
- Mutation—here, an M_{pop} number of elements are selected randomly, and a new array is formed by exchanging their positions.
- Convergence—the three stopping conditions of this algorithm are (i) predefined epoch (ii) no change in the fitness value of the best widow and (iii) attaining a certain level of accuracy.

2.3 LSTM Network-Based Channel Estimation

Formation of pilot pattern is the most important part in the pilot-aided CE process for OFDM systems. Block-type pilot pattern-aided CE effectively eliminates the frequency-selective fading by adding pilot symbols into all the subcarriers in an OFDM signal.

Structure of LSTM Network

A MIMO wireless communication system is taken, and the received signal is,

$$y = \boldsymbol{H}x + n \tag{12}$$

where n is the AWGN, $\boldsymbol{H}$ is represented as the channel impulse response, and x represents the networks input signal. The LSTM network has input unit, hidden unit, and output unit. The role of input unit is to get the input data. The hidden unit has LSTM cells, and the output unit provides the predicted results. Each LSTM cell has an input gate, forgot gate, and output gate. The term i_t indicates the input gate, which checks the possibility of storing a data in the cell, and it also stops the unwanted data from entering to memory unit. Forgot gate, f_t, decides whether to accept or reject a data from the cell state $\boldsymbol{C}_{t-1}$. The output gate $\boldsymbol{o}_t$ determines the output data. In an LSTM network, the data flow of these gates follows the equations given below.

$$\boldsymbol{f}_t = \sigma\left(\boldsymbol{W}_f[\boldsymbol{x}_t, \boldsymbol{h}_{t-1}\right] + \boldsymbol{b}_f) \tag{13}$$

$$\boldsymbol{i}_t = \sigma(\boldsymbol{W}_i[\boldsymbol{x}_t, \boldsymbol{h}_{t-1}\right] + \boldsymbol{b}_i) \tag{14}$$

$$\boldsymbol{o}_t = \sigma(\boldsymbol{W}_o[\boldsymbol{x}_t, \boldsymbol{h}_{t-1}\right] + \boldsymbol{b}_o) \tag{15}$$

where $\boldsymbol{W}_f$, $\boldsymbol{W}_i$, $and\, \boldsymbol{W}_o$ are the weight matrices in the current input state $\boldsymbol{x}_t$ and $\boldsymbol{b}_f$, $\boldsymbol{b}_i$, and $\boldsymbol{b}_o$ are the bias terms. The previous short-term output is denoted as $\boldsymbol{h}_{t-1}$.The current long-term state of the network $\boldsymbol{C}_t$ can be calculated as

$$\boldsymbol{C}_t = \boldsymbol{f}_t * \boldsymbol{C}_{t-1} + \boldsymbol{i}_t * \boldsymbol{g}_t \tag{16}$$

where

$$\boldsymbol{g}_t = \tanh\left(\boldsymbol{W}_c\left[\boldsymbol{x}_t, \boldsymbol{h}_{t-1}\right] + \boldsymbol{b}_g\right) \tag{17}$$

The output y of the LSTM network is

$$\boldsymbol{y} = \boldsymbol{h}_t = \boldsymbol{o}_t * \tanh(\boldsymbol{C}_t) \tag{18}$$

Construction of BOLSTMEN

The LSTM network can process only 1D data at its input. Hence, the complex channel state information (CSI) is separated into real and imaginary components and processed to form a time-sequence input. The time-sequence number is same as the number of OFDM symbols. Then, the 1D CNN network gets this processed data, and the channel feature vectors are retrieved. Unlike frequency domain channel estimation (FDCE), the feature variables to be estimated are compressed using a 1D maxpooling layer in time domain channel estimation (TDCE). After the feature extraction and compression, the data are forwarded to the LSTM network. For the CE in this work, the learning network, i.e., the LSTM network, accepts the CSI matrix as the input. For FDCE, the CSI matrix is expressed as $\boldsymbol{H} \in \boldsymbol{C}^{T\times N}$, and for TDCE, the CSI matrix is expressed as $\boldsymbol{G} \in \boldsymbol{C}^{T\times NL}$. The conventional LS algorithm is used for the estimation of CSI at the pilot symbols, and the CSI at the data symbols is taken as 0 in the beginning. So, the LSTM input is $\boldsymbol{H} \in \boldsymbol{C}^{T\times N} + \text{LS}$ for FDCE and $\boldsymbol{G} \in \boldsymbol{C}^{T\times NL} + 0$ for TDCE. The LSTM network needs a sequence data at its input, and the CSI in a sequence form is given by,

$$\boldsymbol{G} = \{g_1, g_2, \ldots . g_t\} \tag{19}$$

where $g_t \in \boldsymbol{C}^{1\times NL}$ denotes the CSI at the T^{th} OFDM symbol. After extracting the real an imaginary parts, the CSI data become $\boldsymbol{G'} \in \boldsymbol{R}^{T\times 2NL}$ and $g'_t \in \boldsymbol{R}^{1\times 2NL}$. The preprocessed CSI is then forwarded to CNN, and its primary goal is to extract and pick a frequency feature vector. A convolution operation on $\boldsymbol{G'}$ is done by the CNN network, and the frequency feature vector is extracted using its filters. Once the data are preprocessed, its output parameters do not change, and it is represented as $\boldsymbol{G''} \in \boldsymbol{R}^{T\times 2NL}$. The output data dimensions of the CNN are compressed by the maxplooing network for TDCE. Once we set the maxpooling window size as $1 \times L$, the output data dimension becomes $\boldsymbol{G''} \in \boldsymbol{R}^{T\times 2N(1\times L)}$. Based on the previous inputs, current inputs, and the future data, the proposed BOLSTMEN predicts the current CSI. Each time LSTM network predicts a channel response that gives an output for channel estimation. We use BWO algorithm to update the set of pilot symbols used in BOLSTMEN which intern enhances the performance of CE.

3 Experimental Analysis

The experimental analysis is done in Matlab software, and the simulation settings is given in Table 1. In specific, the carrier frequency is selected as 28 GHz which is used for mmWave applications in general. The standard value of bandwidth 1 GHz is considered for the simulation.

Table 1 Simulation setting

Parameters	Values
Channel bandwidth	1 GHz
Carrier frequency	28 GHz
Small cell coverage	500 m
The number of BS antenna, Nt	64
The number of RF chains	4
Time period of symbol	171 ms
CP length	10 ms
Total number of pilot	200

3.1 Simulation Results

Figure 3a gives the analysis of bit error rate (BER) vs the SNR value of the proposed BOLSTMEN for different modulation schemes like 64-QAM, 16-QAM, QPSK, as well as 8-PSK. From this result, it is clear that 64-QAM modulation used in BOLSTMEN is more effectively helping in the reduction of the BER. The average estimated BER is observed less than 0.1, which is significantly an acceptable range for data transmission in the network.

Figure 3b gives the analysis of sum rate vs SNR for the reference tone of the proposed BOLSTMEN for various modulation schemes like 64-QAM, 16-QAM, QPSK, and 8-PSK. From this analysis, it is observed that the modulation scheme 64-QAM gives the highest sum rate in comparison with any other modulation schemes, and it is used in the BOLSTMEN for a better performance. Figure 4 graphically represents the analysis of mean square error (MSE) versus SNR values of the reference signal for different batch size of BOLSTMEN. The MSE values are calculated by taking the difference between the proposed DL model's predictions and the actual values, squared it and then averaged.

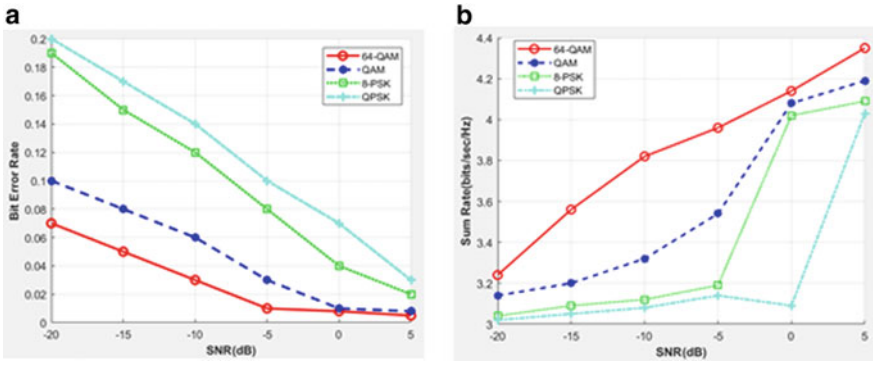

Fig. 3 **a** Analysis of bit error rate (BER), **b** Analysis of sum rate versus SNR

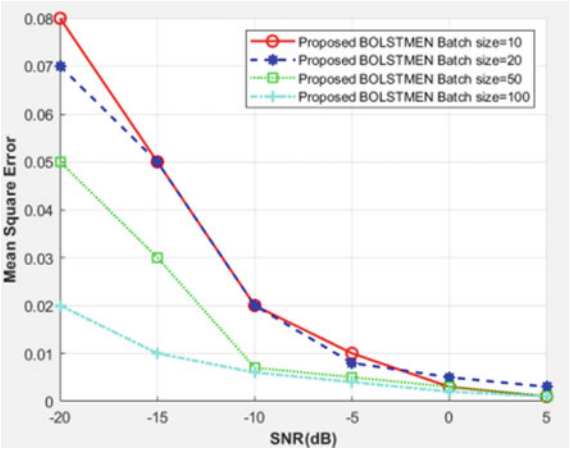

Fig. 4 Mean square error (MSE) of BOLSTMEN for different batch size values

4 Conclusion

In this research work, a novel optimization-aided pilot design with a deep learning-based BOLSTMEN model is proposed for MIMO–NOMA system for mmWave applications. The proposed model is mainly focusing on the CE process. This BOLSTMEN model has an accuracy of 99.7% and a specification rate of 99.8%. In this work, a statistical analysis to verify the superiority of this proposed model is also performed. The performance evaluation and statistical analysis results show that the proposed model has higher spectral efficiency than the conventional DL-based CE approaches. This model is more scalable to a large amount of data as its computational complexity is less than the conventional CE algorithms. This LSTM model can work effectively on any online deployment whose channel conditions do not match with those employed in the training stage. In the future, we will apply more effective optimization methods and deep learning techniques to carry out more effective channel estimation.

References

1. Xiao M, Mumtaz S, Huang Y, Dai L, Li Y, Matthaiou M, Karagiannidis GK, Björnson E, Yang K, Chih-Lin I, Ghosh A (2017) Millimeter wave communications for future mobile networks. IEEE J Sel Areas Commun 35:1909–1935
2. Wu Q, Li GY, Chen W, Ng DWK, Schober R (2017) An overview of sustainable green 5G networks. IEEE J Wireless Commun 24:72–80
3. Wei L, Hu RQ, Qian Y, Wu G (2014) Key elements to enable millimeter wave communications for 5G wireless systems. IEEE J Wireless Commun 21:136–143
4. Han S, Chih-Lin I, Xu Z, Rowell C (2015) Large-scale antenna systems with hybrid analog and digital beamforming for millimeter wave 5G. IEEE Commun Mag 53:186–194

5. Jin S, Liang X, Wong KK, Gao X, Zhu Q (2014) Ergodic rate analysis for multipair massive MIMO two-way relay networks. IEEE Trans Wireless Commun 14:1480–1491
6. Fan L, Jin S, Wen CK, Zhang H (2015) Uplink achievable rate for massive MIMO systems with low-resolution ADC. IEEE Commun Lett 19:2186–2189
7. Jin S, Wang X, Li Z, Wong KK, Huang Y, Tang X (2015) On massive MIMO zero-forcing transceiver using time-shifted pilots. IEEE Trans Veh Technol 65:59–74
8. Rao X, Lau VK (2014) Distributed compressive CSIT estimation and feedback for FDD multi-user massive MIMO systems. IEEE Trans Signal Process 62:3261–3271
9. Orosi G (2016) The arithmetico-geometric sequence: an application of linear algebra. Int J Math Educ Sci Tech 47:766–772
10. Sobhi-Givi S, Shayesteh MG, Kalbkhani H (2020) Energy-efficient power allocation and user selection for mmWave-NOMA transmission in M2M communications underlaying cellular heterogeneous networks. IEEE Trans Veh Technol 69:9866–9881
11. Belmekki BEY, Hamza A, Escrig B (2020) Outage analysis of cooperative NOMA for millimeter wave vehicular networks at intersections. In: IEEE 91st vehicular technology conference (VTC2020-Spring), pp 1–6. IEEE, Antwerp, Belgium
12. Elbir AM, Papazafeiropoulos AK (2019) Hybrid precoding for multiuser millimeter wave massive MIMO systems: a deep learning approach. IEEE Trans Veh Technol 69(1):552–563
13. Balevi E, Andrews JG (2021) Unfolded hybrid beamforming with GAN compressed ultra-low feedback overhead. IEEE Trans Wireless Commun
14. Chen S, Ng SX, Khalaf E, Morfeq A, Alotaibi N (2021) Particle swarm optimization assisted b-spline neural network based predistorter design to enable transmit precoding for nonlinear MIMO downlink. Neurocomput 458:336–348
15. Hernandes AG, Abrão T (2021) Spectrum sensing optimization in uncalibrated massive antennas systems. Phys Commun 49:101484
16. Darzikolaei MA, Mollaei MRK, Najimi M (2022) An effective PSO-based power allocation for target tracking in MIMO radar with widely separated antennas. Phys Commun 51:101544
17. Shah MH, Dang X (2020) Low-complexity deep learning and RBFN architectures for modulation classification of space-time block-code (STBC)-MIMO systems. Digital Signal Proc 99:102656
18. Hoffmann M, Kryszkiewicz P, Kliks A (2021) Increasing energy efficiency of massive-MIMO network via base stations switching using reinforcement learning and radio environment maps. Comput Commun 169:232–242
19. Gizzini AK, Chafii M, Ehsanfar S, Shubair RM (2021) Temporal averaging LSTM-based channel estimation scheme for IEEE 802.11 p standard. arXiv preprint arXiv:2106.04829

Design and Analysis of Compact Dual-Band Antenna for Body Area Network Applications

Mamta Devi Sharma, Ajay Yadav, Sarthak Singhal, and Ritu Sharma

Abstract A compact Ultrawide Band (UWB) antenna with an additional "Industrial Scientific and Medical" (ISM) band is explored in this article for "Wireless Body Area Network" (WBAN). The antenna employed a hybrid-shaped radiator with the perforated ground to obtain the entire UWB spectrum (3.1–10.6 GHz). An additional ISM band (2.4–2.484 GHz) is realized by adding an L-shaped parasitic strip with the patch. The proposed dual-band antenna has a considerable gain, omnidirectional radiation pattern for the entire operational band. Furthermore, time-domain analysis has been done for the designed structure in side-by-side and front-to-front alignments. The biological performance of the antenna has been optimized with the CST simulator by employing the structure of a three-layered phantom of the human body. The obtained specific absorption rate values are within the specified limit as advised by the international originations, and demonstrated results have confirmed that the designed antenna good candidate for wearable application.

Keywords Human body · Industrial scientific and medical · Specific absorption rate (SAR) · UWB · WBAN

1 Introduction

Body-worn antennas have attracted significant interest from the researchers, investigators, and industry persons in the present era because they have diverse applications such as sports activity monitoring, security, health monitoring, and military applications. Widely used frequency bands for WBAN are ISM band from 2.4 to 2.448 GHz

M. D. Sharma (✉)
Global Institute of Technology, Jaipur, Rajasthan, India
e-mail: 2019rec9017@mnit.ac.in

A. Yadav
Jaipur Engineering College and Research Center, Jaipur, Rajasthan, India

M. D. Sharma · S. Singhal · R. Sharma
Malaviya National Institute of Technology, Jaipur, Rajasthan, India

S. Rawat et al. (eds.), *Proceedings of Second International Conference on Computational Electronics for Wireless Communications*, Lecture Notes in Networks and Systems 554,
https://doi.org/10.1007/978-981-19-6661-3_17

[1], WLAN from 5.15 to 5.725 [2], upper ISM from 5.75 to 5.82 GHz [3], and UWB. However, with the emerging technologies, existing wireless communication systems require multi-band and wideband antennas, which reduce the overall system size and weight [4]. The UWB systems are highly reliable for WBAN systems because of their significant features such as wide bandwidth, high data rate, and robustness to interference. Another frequency band, i.e., the ISM band highly utilized for wearable applications. Various methods have been presented in the literature to design the UWB antenna that integrated lower narrow bands like Bluetooth and GSM [5–11]. However, these methods are classified into two categories like (i) inserting the slots/slits of $\lambda/4$ or $\lambda/2$ length in conductive parts and (ii) employing the extra resonant elements for generating another frequency band with desired higher frequency band. In [5], a Bluetooth integrated with UWB band antenna was intended by adding a slot on the edge of the patch. In [6], a rectangular slot has been inserted in the middle of the U-shaped radiating part of the antenna to achieve dual bands, i.e., Bluetooth and UWB. Snake-shaped slot etched in the staircase-shaped patch for designing Bluetooth-integrated antenna with UWB band [7]. In [8], a pair of Γ-shaped inverted metallic strips with the hexagonal patch, to produce a dual-band antenna that covers the "Bluetooth" and spectrum of UWB bands, has been presented by the authors. In [9], a quasi U-shape patch antenna was designed with four stubs to cover Bluetooth and UWB bands for automotive communications. A metamaterial-based dual-band antenna structure with "L-band and UWB" bands with reconfigurable features has been designed in [10]. In [11], a miniaturized resonator with the addition of a capacitor was implemented to create a Bluetooth-integrated UWB antenna. The ISM and UWB bands are widely used in bio-medical imaging, monitoring in sports, cognitive for ambient energy, or military applications. An antenna can be deployed near, on, and inside the human body for the abovementioned applications. Therefore, another characteristic to study in this work is the effect of biological tissue on antenna performances. For this, the designed antenna must be evaluated in "free space" and in local closeness to the biological tissue. In [12–16], authors investigated SAR analysis methods, time-domain analysis, and effects on antenna performance in the human body.

In this work, a dual-band antenna compacted in size for wearable applications that incorporated the ISM band with the UWB band is designed and analyzed. This antenna has a hybrid shape radiator with an additional parasitic strip to achieve dual-band characteristics, i.e., the ISM band with the UWB spectrum. The S_{11}, radiation patterns, antenna gain, and efficiency are analyzed in free space. Moreover, the proposed antenna performance for wearable applications has been verified by calculating SAR. Section 2 provides the design methodology of the suggested antenna. All simulated results are described in Sect. 3 with the parametric study. In Sect. 4, the outcomes due to human proximity on antenna performance are analyzed with the time-domain characteristics of the antenna. Section 5 shows the conclusion of the presented investigation.

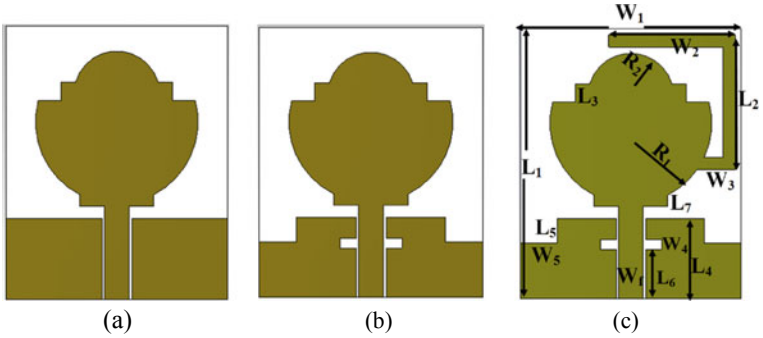

Fig. 1 Step by step design approach for ISM-integrated UWB antenna **a** primary antenna, **b** UWB antenna, **c** proposed antenna

2 Design Approach for Dual-Band Antenna

2.1 UWB Hybrid-Shaped Monopole Antenna

The proposed UWB antenna is designed on FR-4 dielectric, with 4.4 permittivities, loss factor of 0.02, 1.6 mm thickness, and overall size of 22 × 18 mm^2. The hybrid radiator is excited by a 50 Ω coplanar feed line with width $W_f = 2$ mm. A hybrid radiator is chosen here, which primarily has a semicircular patch with rectangular and small semicircular shape elements at the top side of the substrate. The ground plane is chamfered at the upper sides, and two slits have etched on the ground plane to extend the bandwidth as presented in Fig. 1a and b.

2.2 Design Approach for ISM-Integrated UWB Antenna

A strip of approximately a quarter wavelength is widely used to create extra resonance. Therefore, by assigning an additional parasitic strip of slightly greater than quarter wavelength to the primary radiator, dual-band behavior is obtained in this work. The following equation is used to calculated strip length for desired resonance frequency:

$$f_{r(2.45\ \text{GHz})} = \frac{C}{4L_T\sqrt{\frac{\varepsilon_r+1}{2}}} \tag{1}$$

where C = Speed of light(m/sec)
L_T = Total length for quarter wavelength (mm)$(W_2 + L_2 + W_3)$
f_r = Resonant frequency (GHz), and
ε_r = Dielectric constant

The final optimized structure geometry is presented in Fig. 1c.

3 Antenna Design and Analysis

Figure 1 displays the stages of the compact dual-band antenna. The primary antenna has a hybrid-shaped radiator with a rectangular strip and rectangular ground plane, covering the frequency band from 3.4 to 9.8 GHz. To achieve a compact UWB band (from 3.1 to 10.6 GHz), rectangular ground plane is chamfered at the upper sides, and two slots are etched, as seen in Fig. 1b. An extra resonance strip is added to the proposed antenna to produce resonance at 2.45 GHz for the ISM band. This design works for the UWB band with ISM for wearable applications (presented in Fig. 2). The augmented sizes of the designed structure are mentioned in Table 1.

Figure 3a shows the effect on S_{11} with slots location in the ground plane. The location of slots has a significant impact on impedance matching and bandwidth. As exhibited in Fig. 3b, the length L_T of the extra radiating strip also tunes the resonant frequency of the both bands (ISM and UWB bands). It is clear that by optimizing the value of L_T at 24.4 mm, an extra desired resonant frequency for the ISM band is achieved.

Figure 4a and b displays the radiation characteristics at various frequency options, i.e., 2.45, 4.5, 7.5, and 9.8 GHz, in the "*E*-plane and *H*-plane". It is observed from

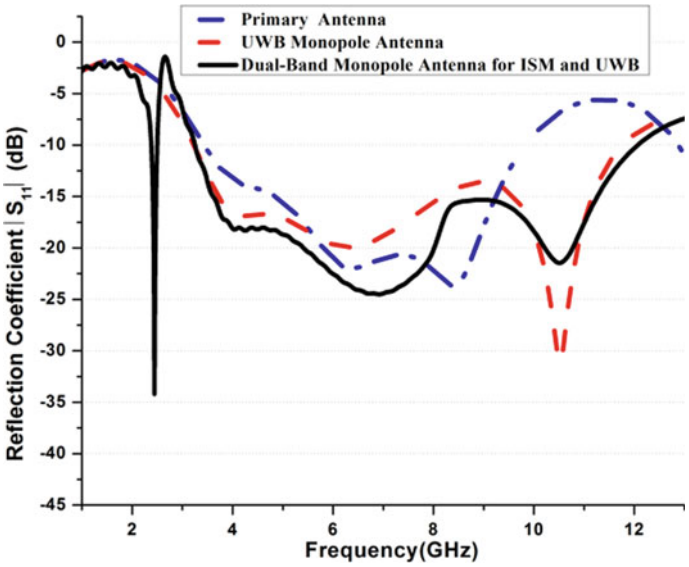

Fig. 2 Reflection coefficient (S_{11}) versus frequency plot

Table 1 Dimensions of the designed antenna

Parameters	Value (mm)	Parameters	Value (mm)	Parameters	Value (mm)
L_1	22	W_1	18	L_6	4.5
L_2	11	W_2	10.3	L_7	0.92
L_3	1.5	W_3	3.1		
L_4	6.6	W_4	0.8		
L_5	2.1	W_5	3		
R_1	6.5	R_2	3.5		

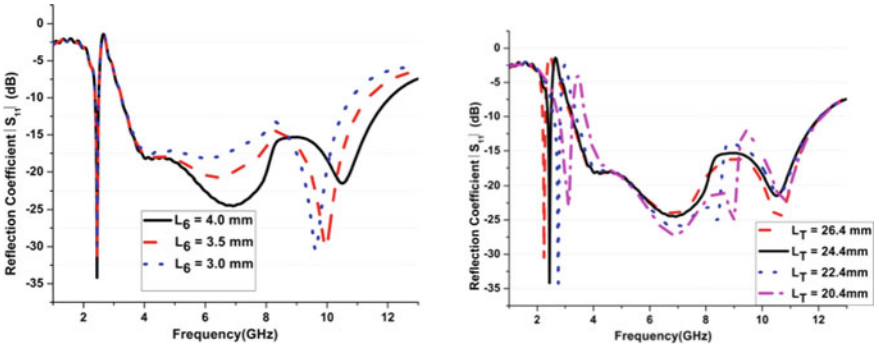

Fig. 3 Parametric effects on S_{11} for **a** L_6 and **b** L_T

Fig. 4 that the antenna has almost bidirectional characteristics in the "*E*-plane and Omni-directional in *H*-plane".

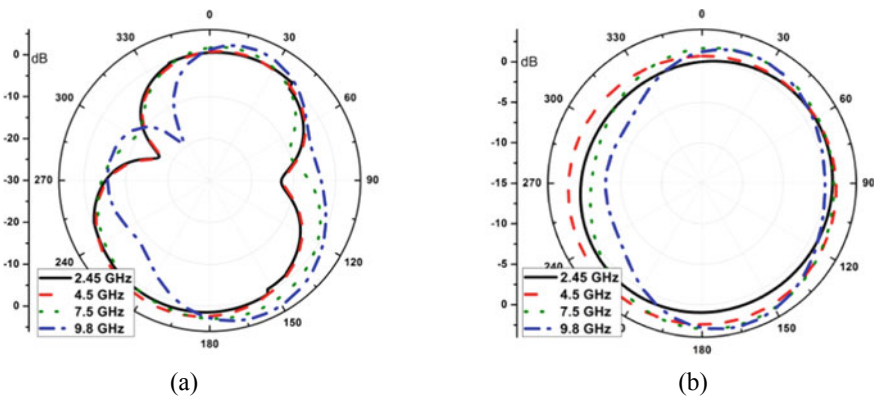

Fig. 4 Radiation patterns: **a** *E*-plane and **b** *H*-plane

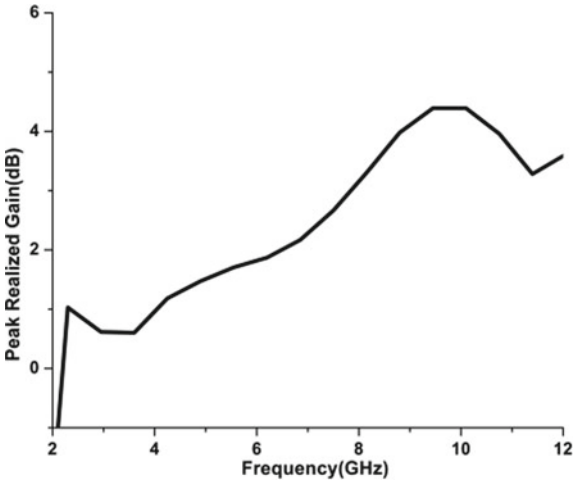

Fig. 5 Gain (dB) versus frequency plot

The realized peak gain of the designed antenna fluctuates from 1.02 to 4.38 dBi in the entire UWB spectrum and is presented in Fig. 5.

4 Performance Study of the Antenna in Presence of Human Proximity

The primary issue in front of the designer is the consequence of human body tissues on antenna operations in wearable applications. Mainly, due to body tissues, various antenna performance parameters are changed like radiation pattern of the antenna, signals to be blocked by the body, a detuning in resonant frequency, reduction in gain, and radiation efficiency. Human tissue safety is also essential in the same trends and is ensured by calculated Specific Absorption Rate (SAR). The "SAR" is the amount of EM power absorption by the body tissues. It is safe for the human body, with a recommended limit of "1.6 W/kg for 1 g of tissue and 2 W/kg for 10 g of tissue" by the Federal Communications Commission (FCC). The time-domain investigation and the SAR analysis are carried out to study the EM interaction effect on the performance of the proposed antenna.

4.1 Time-Domain Analysis

The antenna has modeled on a rectangular "three-layered phantom model" and calculates S_{21}, group delay in two arrangements, i.e., front to front and side by side with the phantom model. The two identical antennas are placed 30 cm apart at 5 mm above the phantom model. Figure 6 shows the reflection coefficient variation with

frequency in the "free space" and on the phantom. It can be seen from Fig. 6, that at the higher frequencies, the band gets shifted toward the lower side, and impedance gets changed in the presence of human tissues. The obtained group delay is less than 1.8 ns for both configurations in free space and with a three-layered phantom as shown in Fig. 7a and b.

The electrical and dielectric properties of the three-layer model are given in Table 2 [16]. The overall dimension of the modeled phantom is $34 \times 10 \times 1.6$ cm^3.

Furthermore, the isolation magnitude (S_{21}) is calculated, with and without the phantom model for both configurations to study the system characteristics in the wearable scenario. The outcomes are exhibited in Fig. 8. It is seen that the structure maintains good isolation which is less than − 35 dB in "free space" and also in near

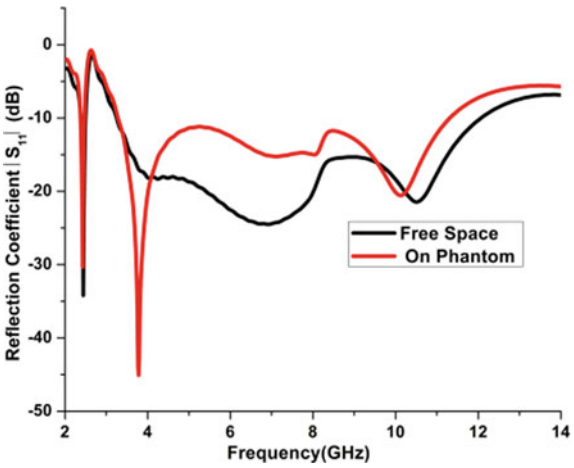

Fig. 6 Reflection coefficient (S_{11}) versus frequency plot without and with human phantom

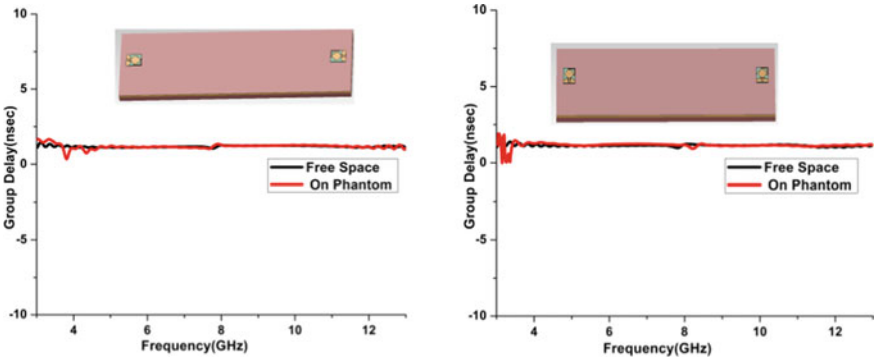

(a) Front to Front (b) Side by Side

Fig. 7 Group delay with and without phantom

Table 2 Electrical and dielectric properties of three layers (from 1 to 12 GHz)

Tissue	Thickness (mm)	Density (kg/m^3)	Relative permittivity (ε_r)
SKIN	2	1100	40–27.6
FAT	4	910	5.42–4.33
MUSCLES	10	1041	54.3–37.15

closeness to the human body. Figure 9 illustrates the fidelity factor which is defined as the normalized amplitude of the transmitted and accepted signals for the front-to-front and side-by-side configurations. The obtained fidelity factors of the proposed system are 93 and 91% for front to front and side by side, respectively.

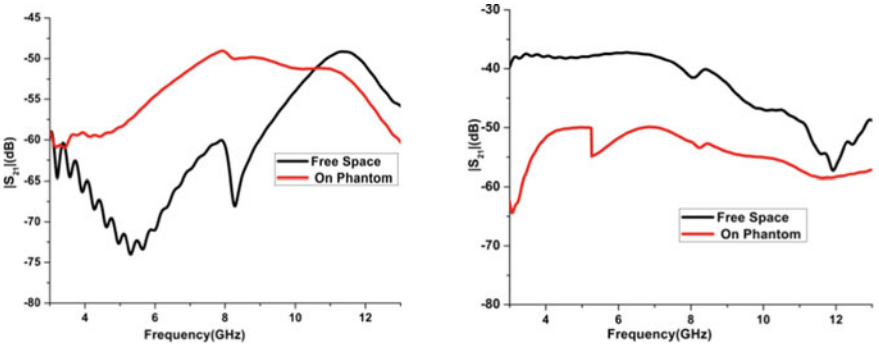

(a) Front to Front (b) Side by Side

Fig. 8 S_{21} (dB) with and without phantom

Fig. 9 Normalized incident and received pulses

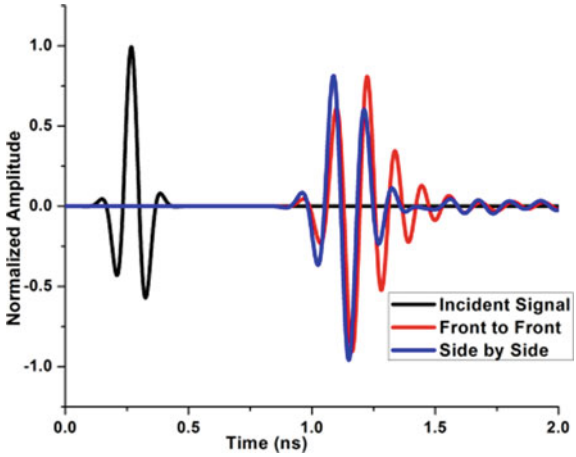

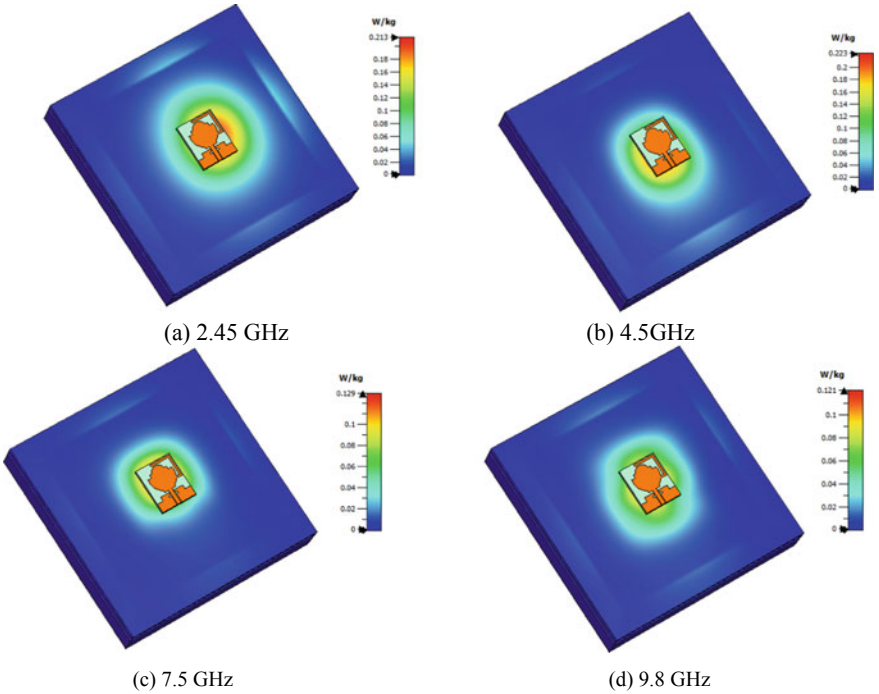

(a) 2.45 GHz (b) 4.5GHz

(c) 7.5 GHz (d) 9.8 GHz

Fig. 10 Specific absorption rate (SAR) at **a** 2.45 GHz, **b** 4.5 GHz, **c** 7.5 GHz, and **d** 9.8 GHz

4.2 Specific Absorption Rate:

"SAR" is a quantity of electrical energy that absorbed by the human body when exposed to an EM field. The SAR is determined at different frequencies for the proposed dual-band antenna at 2.45, 4.5, 7.5, and 9.8 GHz with 10 mW input power for 10-g tissues. Figure 10a, b, c, d shows the SAR at different frequencies, i.e., 0.213, 0.221, 0.129, and 0.121 W/kg at 2.45, 4.5, 7.5, and 9.8 GHz, respectively.

5 Conclusion

A dual-band UWB antenna with a cohesive ISM band is modeled for wearable applications. The antenna operates in the ISM band (2.4–2.484 GHz) with the UWB band (3.1–10.6 GHz). The modified circular-shaped radiator with slots and the chamfered ground plane covers the UWB band. An extra L-shaped strip is added to produce dual-band characteristics at ISM and UWB bands. The proposed antenna performances are investigated with and without the human body concerning frequency and time-domain characteristics. Further, SAR analysis has also been carried out

at different frequencies at 2.45, 4.5, 7.5, and 9.8 GHz for 10-g tissues. All obtained values are below the maximum permissible limit, i.e., 2 W/Kg for 10-g tissues defined by FCC & IEEE C95.1.2005. The obtained results are compared to the recently investigated works as itemized in Table 3, and it can be seen that the presented antenna is a suitable candidate for wearable application.

Table 3 Comparison with previously reported designs in the literature

References	Substrate (ε_r)	Overall Size (mm^3)	Working Freq Range (GHz)	Peak Gain	SAR (W/kg) (Input power) at 5 mm distance
Rahman et al. [11]	Rogers RO4003(3.3)	30 × 31 × 1.5	2.45, 3.1–10.6	NR	NR
Martínez-Lozano et al. [12]	FR-4(4.4)	40 × 36 × 1.52	2.7–11.4	6.6 dBi	NR
Mohandoss et al. [13]	FR-4(4.4)	32 × 32 × 1.6	2.9–15	NR	3.1, 6.8, 10.6 GHz 0.03, 0.07, 0.06 in Skin (1 mw) for 1 g Tissues
Varshini and Rao[14]	Rogers RT/Duroid 5880(2.2)	35 × 32 × 1.52	1.8, 2.4 and 5 and 8.9	NR	Ranges 0.09–0.25 in Skin (1 mw) for 1-g Tissues
Nadh et al. [15]	Rogers RT/Duroid 5880(2.2)	30 × 25 × 0.8	3.1–11.5	5.25 dB	3.6, 7.2, 8, 10.5 GHz 0.873, 1.14, 1.2, 1.55 (100 mW) for 10-g Tissues
Proposed Work	FR-4(4.4)	22 × 18x1.6	2.45 and 3.1–12.0	4.38 dBi	2.4, 4.4, 7.5, 9.8 GHz 0.213, 0.221, 0.129, 0.121 (10 mW) for 10-g Tissues

NR-Not Reported

References

1. Sharma MD, Yadav A, Singhal S, Sharma R (2020) Design and simulation of flexible substrate based wearable antenna for WBAN applications. In: IEEE International conference on recent advances and innovations in engineering (ICRAIE), pp 1–6. https://doi.org/10.1109/ICRAIE51050.2020.9358347
2. Al-Sehemi A, Al-Ghamdi A, Dishovsky N et al (2018) Design and performance analysis of dual-band wearable compact low-profile antenna for body-centric wireless communications. Int J Microw Wireless Technol 10(10):1175-1185. https://doi.org/10.1017/S1759078718001058
3. Ehteshami N, Sathi V, Ehtechami M (2012) Experimental investigation of a circular polarized flexible polymer/composite microstrip antenna for wearable applications. IET Microw Antennas Propag 6(15):1681–1686. https://doi.org/10.1049/iet-map.2012.0395
4. Al-Sehemi A, Al-Ghamdi A, Dishovsky N, Atanasova G, Atanasov N (2020) Flexible polymer/fabric fractal monopole antenna for wideband applications. IET Microw Antennas Propag 1–13. https://doi.org/10.1049/mia2.12016
5. Xiong L, Gao P (2012) Dual-band planar monopole antenna for Bluetooth and UWB applications with WIMAX and WLAN band notched. Prog Electromagnet Res Lett 28:183–194. https://doi.org/10.2528/PIERL11111702
6. Mishra KS, Gupta KR, Vaidya A, Mukhejee J (2011) A compact dual-band fork-shaped monopole antenna for Bluetooth and UWB applications. IEEE Anten Wirles Propag Lett 10. https://doi.org/10.1109/LAWP.2011.2159572
7. Liu Y-F, Wang P, Qin H (2014) Compact ACS-fed UWB monopole antenna with extra Bluetooth band. Electron Lett 50(18):1263–1264. https://doi.org/10.1049/el.2014.1038
8. Elhabchi M, Srifi MN, Touahni R (2018) A novel dual band hexagonal antenna for Bluetooth and UWB applications with single band notched. Adv Electromagnet 7. https://doi.org/10.7716/aem.v7i5.755
9. Yang B, Qu S (2017) A compact integrated Bluetooth UWB dual-band notch antenna for automotive communications. Int J Electron Commun (AEÜ) 80:104–113. https://doi.org/10.1016/j.aeue.2017.06.031
10. Heydari S, Pedram K, Ahmed Z, Zarrabi FB (2017) Dual band monopole antenna based on metamaterial structure with narrowband and UWB resonances with reconfigurable quality. Int J Electron Commun (AEÜ) 81:92–98. https://doi.org/10.1016/j.aeue.2017.07.015
11. Rahman MU, Jahromi MN, Mirjavadi SS, Hamouda AM (2019) Compact UWB band-notched antenna with integrated Bluetooth for personal wireless communication and UWB applications. Electronics 8:158. https://doi.org/10.3390/electronics8020158
12. Martínez-Lozano A, Blanco-Angulo C, García-Martínez H, Gutiérrez-Mazón R, Torregrosa-Penalva G, Ávila-Navarro E, Sabater-Navarro JM (2021) UWB-printed rectangular-based monopole antenna for biological tissue analysis. Electron 10:304. https://doi.org/10.3390/electronics10030304
13. Mohandoss S, Thipparaju RR, Karthik V, Palaniswamy SK, Marudappa P (2019) Investigations of specific absorption rate and temperature variations for an UWB antenna for wireless applications. Prog Electromagnet Res M 78:83–92. https://doi.org/10.2528/PIERM18111603
14. Varshini K, Rao TR (2016) Thermal Distribution based Investigations on electromagnetic interactions with the human body for wearable wireless devices. Prog Electromagnet Res M 50:141–150. https://doi.org/10.2528/PIERM16071703
15. Nadh PB, Madhav BTP, Kumar SM, Rao MV, Anilkumar T (2019) Circular ring structured ultra-wideband antenna for wearable applications. Int J RF Microw Comput Aided Eng 29(4):e21580. https://doi.org/10.1002/mmce.21580
16. IEEE standard for safety levels with respect to human exposure to the radio frequency electromagnetic fields, 3 kHz to 300 GHz. IEEE Standard C95.1–2005 (2006)

Design and Analysis of X-Band Conformal Antenna Array for Spaceborne Synthetic Aperture Radar Applications

Bala Ankaiah Nunna and Venkata Kishore Kothapudi

Abstract When compared to traditional SAR, the synthetic aperture radar (SAR) technology on the spaceborne platform offers numerous benefits. The radar design, however, is confronting significant new obstacles due to the spaceborne platform's unique aerodynamic shape and flying characteristics. The design and development of conformal antenna is aerodynamically efficient. By considering the new features of the platform and conformal design requirements, it is designed for spaceborne synthetic aperture radar. The antenna specifications are derived from the radar's required performance as well as realistic antenna placement factors aboard a satellite. Conformal antennas are one of these new types of antennas. A conformal antenna is one which conforms to a specific shape. The goal is to create a conformal antenna that can be fitted into structures. Because of the antenna integration, the structures are less obtrusive and less visible to the naked eye. The design of X-band (9.65 GHz) single conformal antenna, 1×2, 1×4, 1×8, and 1×10 series-fed conformal antenna arrays is presented in this paper for spaceborne synthetic aperture radar applications.

Keywords Conformal antenna · Spaceborne · Synthetic aperture radar · Microstrip patch antenna · Series-fed

1 Introduction

SAR technology enables all weather conditions in imaging, and they have been deployed in a number of missions aimed at observing Earth from spacecraft. Although the majority of currently spaceborne SAR systems work in the frequency bands (L, C, and X-bands), there is an increasing demand to analyze in other frequencies [1].

B. A. Nunna (✉) · V. K. Kothapudi
Center of Excellence Advanced RF Microwave and Wireless Communications, Department of Electronics and Communication Engineering, Vignan's Foundation for Science, Technology, and Research (VFSTR), Vadlamudi, Guntur District, Andhra Pradesh 522213, India
e-mail: balaankaiah@ieee.org

V. K. Kothapudi
e-mail: v.k.kothapudi@ieee.org

S. Rawat et al. (eds.), *Proceedings of Second International Conference on Computational Electronics for Wireless Communications*, Lecture Notes in Networks and Systems 554,
https://doi.org/10.1007/978-981-19-6661-3_18

An imaging radar mounted on a moving platform is referred to as a spaceborne SAR [2]. The traditional SAR antenna is often mounted in the vehicle's nose cone region, and it needs a matching radome to adjust to diverse flight situations [3]. In light of the spacecraft's aerodynamic shape, the conformal SAR antenna offers significant benefits in terms of enhancing electromagnetic interference resistance and decreasing payload [4]. A number of demonstrator experiments have been created for the use of conformal SAR, in which the method of employing repetitive calibration is used to reduce side-lobe levels of the antenna radiation pattern [5].

The major goal is to create an antenna system that can provide higher performance while also being readily integrated with other systems [6]. It is because of payload space limitations, aerodynamic drag reasons where antennas shapes have to adapt the surface for non-planar structure in order to minimize its radar cross-section [7]. Thus, applying a microstrip antenna to a curved surface suits for a variety of applications such as civil or military aircrafts, cars, media van satellite communication, and wearable applications [8]. In [9], conformal antenna is configured with enhanced bandwidth for aircraft applications is presented. A 1×4 antenna array is conformed on cylinder surface with a diameter of 90 mm [10]. In this paper [11], design of 4-element and 8-element conformal antennas on cylinder surface with different curvatures has been presented. In [12], conformal antennas are placed on cylinder surfaces with different inter-element spacing, and different radius of curvatures has been studied. In this paper [13], 3×3 series-fed planar array for X-band, 1×3 series-fed linear array for X-band in [14], and 10 element linear array for K–band is presented in [15]. In this paper [16], performance analysis of microstrip conformal antenna array is presented with different curvature at 2.4 GHz with the gain of 6 dB.

2 Conformal Antenna Array Design

This section describes the design process for conformal antenna arrays, with distinct configurations. In this paper, a single conformal antenna, 1×2 series-fed, 1×4 series-fed, 1×8 series-fed, and 1×10 series-fed conformal arrays, has been designed and analyzed for spaceborne SAR applications. These arrays are designed at X-band (9.65 GHz). The simulations were carried out in CST MWS software. These 9.65 GHz single conformal antenna used microstrip line feeding technique. It is used to match the impedance of the antenna. Series-fed conformal antenna arrays have been used series feeding for the array. The antenna spacing is taken as 0.7λ in arrays. In this work, the loss tangent $\tan\delta = 0.0009$ is considered; material substrate with relative permittivity $\in r = 2.2$ is chosen for all designs, with RT/Duroid-5880 substrate [17].

2.1 A Single Conformal Antenna

A single conformal antenna is designed at the frequency of 9.65 GHz. Microstrip line feeding is used in the design for matching the antenna impedance. The patch antenna is designed as planar antenna and then bent on a cylinder surface with the radius of 10 mm to make conformal antenna. The top view of the single conformal antenna is presented in Fig. 1a. The optimized dimension of the single conformal antenna is given in Table 1. The |S11| for the single conformal antenna is presented in Fig. 1b. The input reflection coefficient is − 25.76 dB. The surface current distribution is shown in Fig. 1c. Figure 1d, e, and f demonstrates the simulated radiation pattern of XY-plane, YZ-plane and XZ-plane, respectively. Figure 1g presents simulated 3D far-field gain. The simulated gain is 5.47 dBi, and SLL is − 13.8 dB for the single conformal antenna design.

By varying radius of cylinder surface, the obtained input reflection coefficient is shown in Fig. 2a. The cylinder radiuses are considered as 5, 10, 15 mm. The effect of cylinder radius on radiation pattern is analyzed in YZ-plane Fig. 2b. The inter-element spacing between the elements is considered by using the below equation.

$$d = \frac{\lambda}{1 + \sin\theta} \tag{1}$$

d = Inter-element spacing between the elements
θ = Maximum scan angle.
λ = Free space wavelength at 9.65 GHz.

1 × 2 Series-fed Conformal Antenna Array Series feeding technique is used with microstrip line edge feed for 1 × 2, 1 × 4, 1 × 8, and 1 × 10 arrays. The phase difference between the elements is zero-degree phase. The top view of 1 × 2 series-fed conformal antenna array is presented in Fig. 3a. The series-fed conformal antenna arrays (1 × 2, 1 × 4, 1 × 8, and 1 × 10) optimized dimension are given in Table 2. The simulated input reflection coefficient |S11| for the 1 × 2 series-fed conformal array is presented in Fig. 3b. The obtained S11 is − 24.66 dB. The surface current distribution is shown in Fig. 3c. Figure 3d, e, and f demonstrates the simulated radiation pattern of XY-plane, YZ-plane, and XZ-plane, respectively. Figure 3g shows simulated 3D far-field gain. The simulated gain is 9.77 dBi, and SLL is − 30.8 dB for the 1 × 2 series-fed conformal antenna array.

1 × 4 Series-fed Conformal Antenna Array The top view of the 1 × 4 series-fed conformal antenna array is shown in Fig. 4a. The cylinder radius is considered as 10 mm for the 1 × 4 conformal antenna array. The simulated input reflection coefficient for the 1 × 4 series-fed conformal antenna array is presented in Fig. 4b. The obtained |S11| is − 19.73 dB. The surface current distribution is shown in Fig. 4c. Figure 4d, e, and f demonstrates the simulated radiation pattern of XY-plane, YZ-plane, and XZ-plane, respectively. Figure 4g shows simulated 3D far-field gain. The simulated gain is 12.7 dBi, and SLL is − 22.5 dB for the 1 × 4 series-fed conformal antenna array.

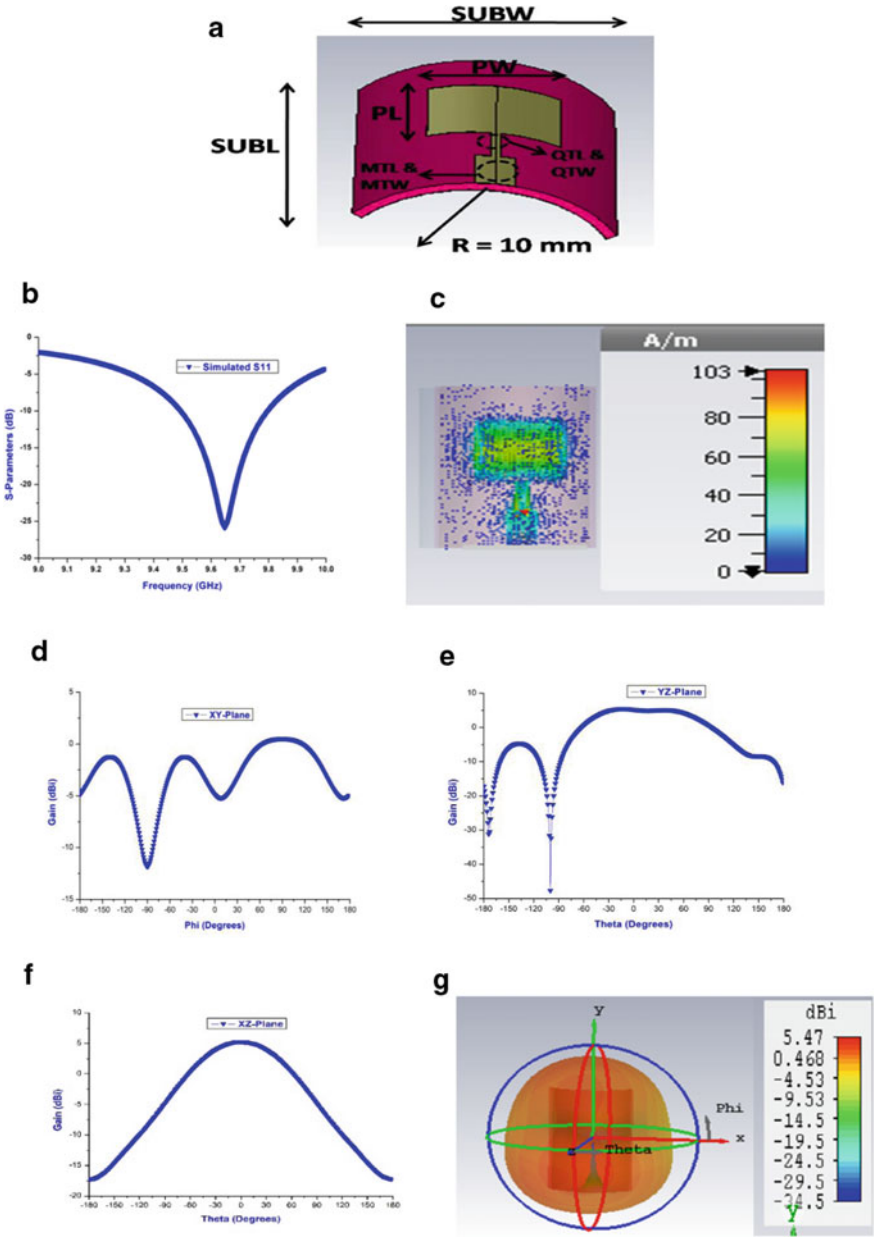

Fig. 1 **a** Top view of single conformal antenna **b** Input reflection coefficient **c** Simulated surface current distribution **d** Radiation pattern (XY-Plane) **e** Radiation pattern (YZ-Plane) **f** Radiation pattern (XZ-Plane) **g** Simulated far-field gain

Table 1 Single conformal antenna

Parameter	Value (mm)
PL	10
PW	10
QTL	5
QTW	0.716
MTL	5.5
MTW	2.46
SUBL	25
SUBW	20

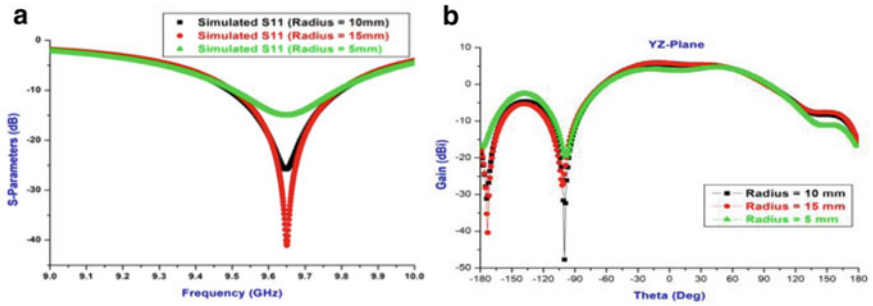

Fig. 2 **a** Input reflection coefficient **b** Radiation pattern (YZ-Plane)

1 × 8 Series-fed Conformal Antenna Array The top view of the 1 × 8 series-fed conformal antenna array is shown in Fig. 5a. The cylinder radius is considered as 10 mm for the 1 × 8 conformal antenna array. The surface current distribution is shown in Fig. 5b. The simulated input reflection coefficient for the 1 × 8 series-fed conformal antenna array is presented in Fig. 5c. The obtained |S11| is − 20.21 dB. Figure 5d shows simulated 3D far-field gain. Figure 5e, f, and g demonstrates the simulated radiation pattern of XY-plane, YZ-plane, and XZ-plane, respectively. The simulated gain is 15.1 dBi, and SLL is − 16.2 dB for the 1 × 8 series-fed conformal antenna array.

1 × 10 Series-fed Conformal Antenna Array The top view of the 1 × 10 series-fed conformal antenna array is shown in Fig. 6a. The cylinder radius is considered as 10 mm for the 1 × 10 conformal antenna array. The surface current distribution is shown in Fig. 6b. The simulated input reflection coefficient for the 1 × 10 series-fed conformal antenna array is presented in Fig. 6c. The obtained |S11| is − 23.19 dB. Figure 6d shows simulated 3D far-field gain. Figure 6e, f, and g demonstrates the simulated radiation pattern of XY-plane, YZ-plane, and XZ-plane, respectively. The simulated gain is 16.1 dBi, and SLL is − 15.2 dB for the 1 × 10 series-fed conformal antenna array.

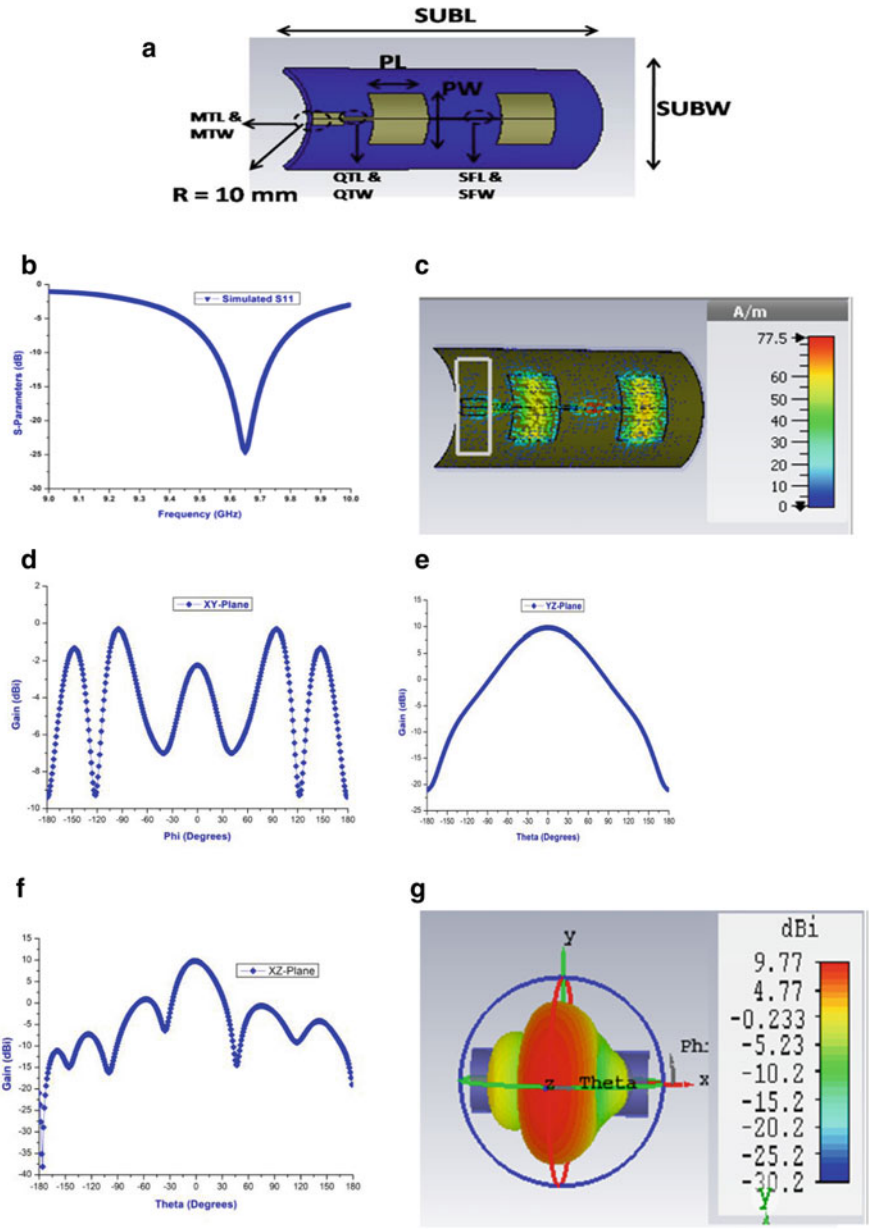

Fig. 3 **a** Top view of 1 × 2 series-fed conformal array antenna **b** Input reflection coefficient **c** Simulated surface current distribution **d** Radiation pattern (XY-Plane) **e** Radiation pattern (YZ-Plane) **f** Radiation pattern (XZ-Plane) **g** Simulated far-field gain

Table 2 Optimized dimensions of the 1 × 2, 1 × 4, 1 × 8, and 1 × 10 conformal array antenna

Parameter	Value (mm)
PL	10
PW	10
QTL	5
QTW	0.716
MTL	5.5
MTW	2.46
SFL	22
SFW	1
SUBL for 1 × 2 array	50
SUBW for 1 × 2 array	20
SUBL for 1 × 4 array	90
SUBW for 1 × 4 array	20
SUBL for 1 × 8 array	185
SUBW for 1 × 8 array	20
SUBL for 1 × 10 array	225
SUBW for 1 × 10 array	20

3 Conclusion

Because of its wide use, the cylinder is most popular in the field of conformal antennas. Conformity refers to the ability to bend with a specific radius within a confined space. This research paper presents the X-band (9.65 GHz) conformal antenna arrays for spaceborne synthetic aperture radar applications. The antenna structure features a great gain performance and a low side-lobe level due to its conformal dimensions. The performance analysis of single conformal antenna, 1 × 2, 1 × 4, 1 × 8, 1 × 10 series-fed conformal antenna array is shown in Table 3 and also compared with other designs given in Table 4. Modern aircraft systems require conformal antennas since they include a variety of antennas projecting from the primary structure, as well as a variety of communication systems, including satellite communication. Large apertures necessitate the use of conformal antennas and arrays, which are required for satellite communication and military aerial surveillance radars such as active electronically scanned arrays or multi-mode radars.

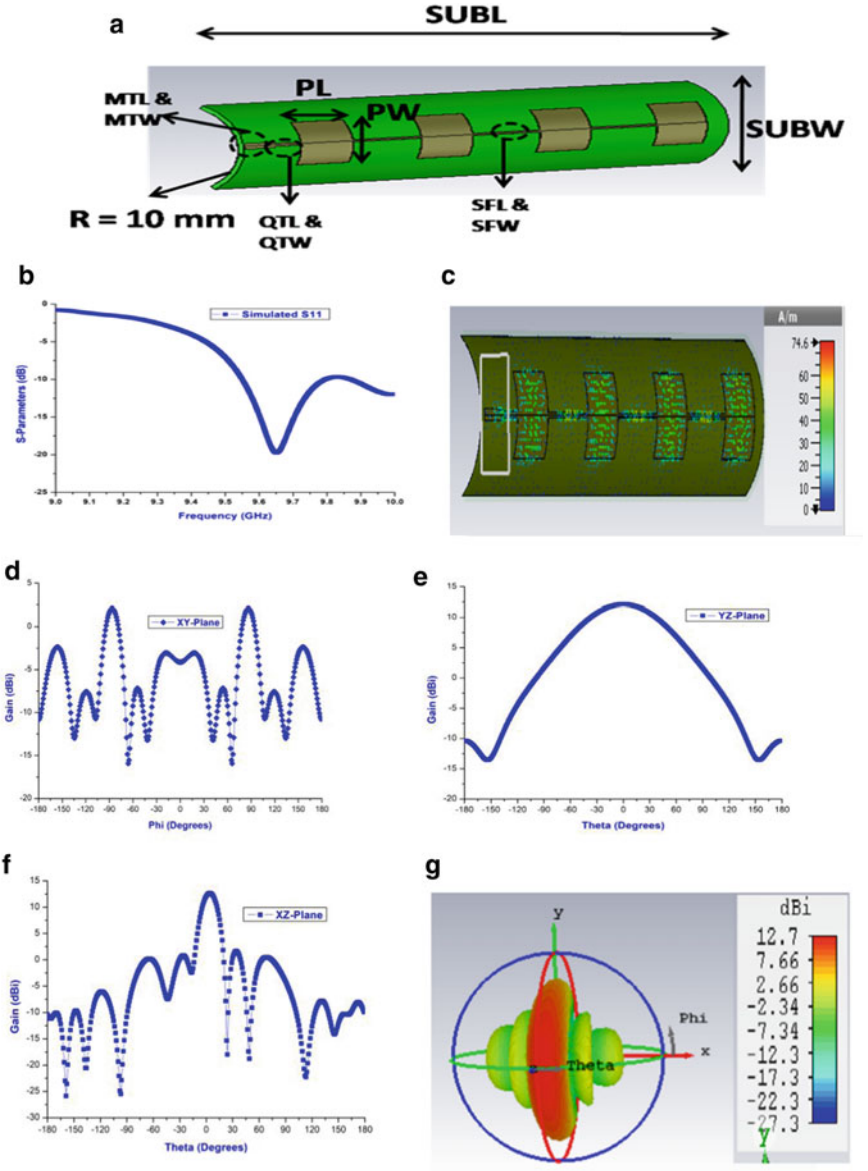

Fig. 4 **a** Top view of 1 × 4 series-fed conformal array antenna **b** Input reflection coefficient **c** Simulated surface current distribution **d** Radiation pattern (XY-Plane) **e** Radiation pattern (YZ-Plane) **f** Radiation pattern (XZ-Plane) **g** Simulated far-field gain

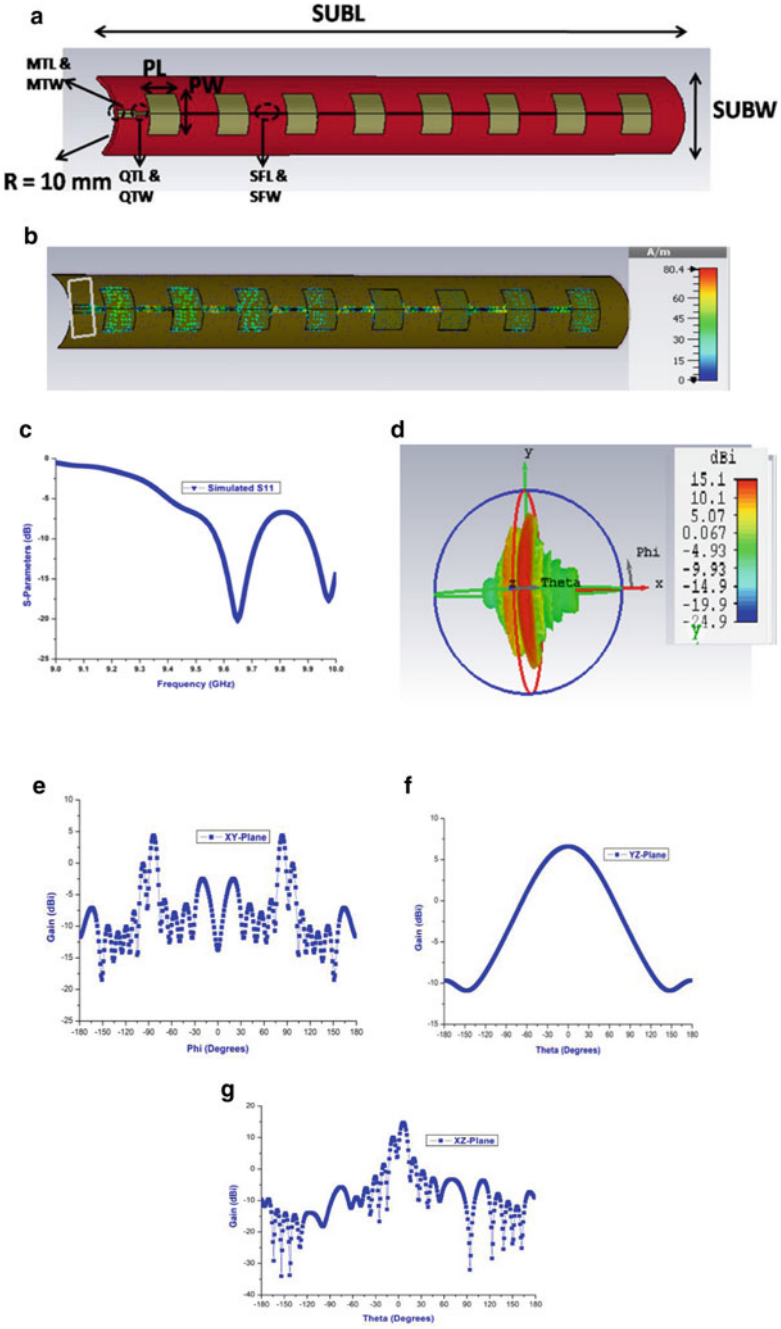

Fig. 5 **a** Top view of 1 × 8 series-fed conformal array antenna **b** Simulated surface current distribution **c** Input reflection coefficient **d** Simulated far-field gain **e** Radiation pattern (XY-Plane) **f** Radiation pattern (YZ-Plane) **g** Radiation pattern (XZ-Plane)

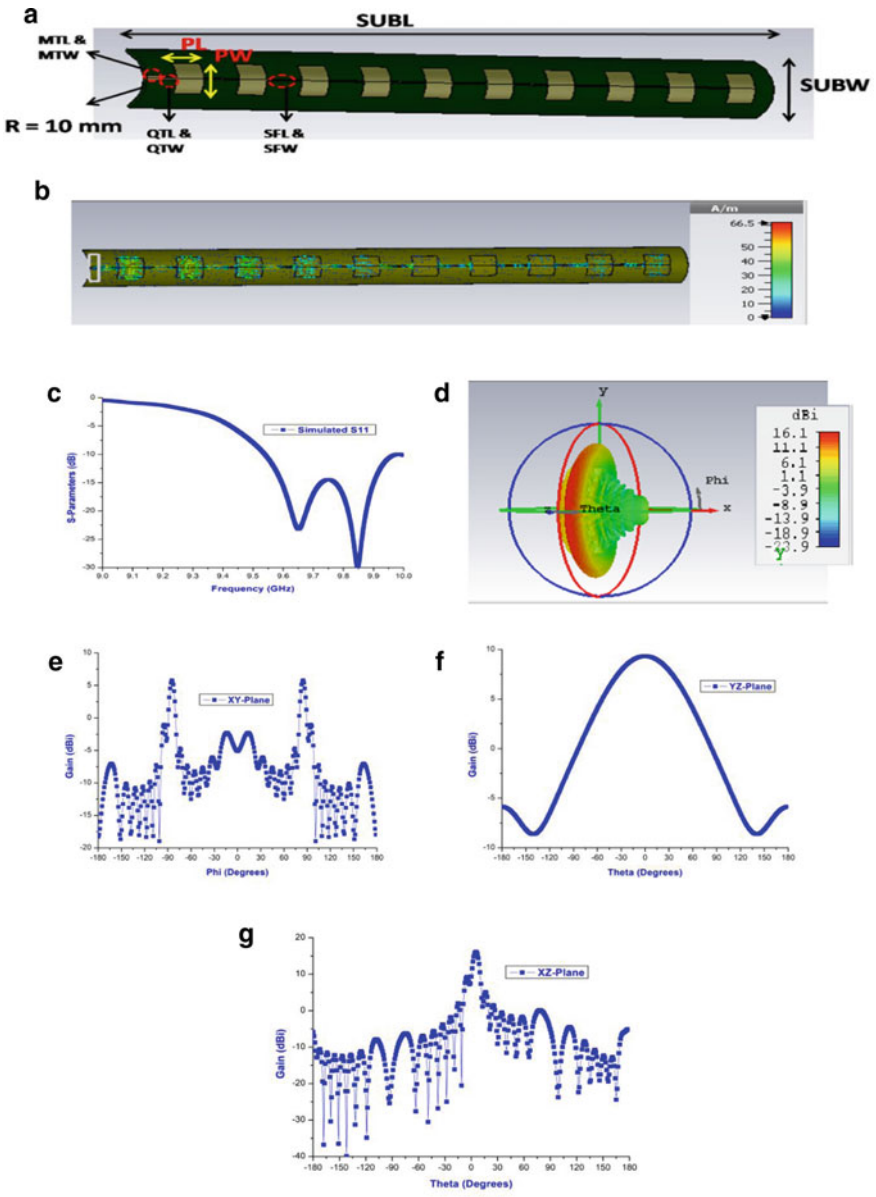

Fig. 6 **a** Top view of 1 × 10 series-fed conformal array antenna **b** Simulated surface current distribution **c** Input reflection coefficient **d** Simulated far-field gain **e** Radiation pattern (XY-Plane) **f** Radiation pattern (YZ-Plane) **g** Radiation pattern (XZ-Plane)

Table 3 Performance analysis of conformal antenna arrays

Parameter	Single	1 × 2 array	1 × 4 array	1 × 8 array	1 × 10 array
S11 (dB)	− 25.76	− 24.66	− 19.73	− 20.21	− 23.19
Bandwidth (GHz)	9.5–9.8	9.54–9.75	9.55–9.78	9.57–9.72	9.54–9.75
VSWR	1.10	1.12	1.22	1.21	1.14
Gain (dBi)	5.47	9.77	12.7	15.10	16.10
SLL (dB)	− 13.8	− 30.8	− 22.5	− 16.2	− 15.2

Table 4 Comparison with other designs

Article	Frequency (GHz)	Antenna array	Gain (dB)	SLL (dB)
Monica and Jothilakshmi [9]	5.2	1 × 2	9	Na
Patil et al. [10]	2.34	1 × 4	12.02	Na
Shankar and Beenamole [11]	10	4, 8 element	5.8	Na
Kumari et al. [16]	2.4	4 element	6	Na
This work	9.65	1 × 10	16.10	− 15.2

References

1. Bekers DJ et al (2019) A Ka-band spaceborne synthetic aperture radar instrument: a modular sparse array antenna design. IEEE Antennas Propag Mag 61:97–104
2. Cumming IG, Wong FH (2005) Digital processing of synthetic aperture radar data: algorithms and implementation. Artech House
3. Anderson Jr. JD (2006) Hypersonic and high-temperature gas dynamics, second edition. American Institute of Aeronautics and Astronautics. https://doi.org/10.2514/4.861956
4. Zhou R, Sun J, Wei S, Wang J (2017) Synthesis of conformal array antenna for hypersonic platform SAR using modified particle swarm optimisation. IET Radar Sonar Navig 11:1235–1242
5. Knott P et al (2012) SAR experiments using a conformal antenna array radar demonstrator. Int J Antennas Propag 2012:1–7
6. Josefsson L, Persson P (2006) Conformal array antenna theory and design: josefsson/conformal array antenna theory and design. Wiley. https://doi.org/10.1002/047178012X
7. Brookner E (1997) 1996 International symposium on phased array systems and technology-highlights. IEEE Aerosp Electron Syst Mag 12:12–17
8. Yuan N, Nie X-C, Gan Y-B, Yeo T-S, Li L-W (2007) Accurate analysis of conformal antenna arrays with finite and curved frequency selective surfaces. J Electromagn Waves Appl 21:1745–1760
9. Monica J, Jothilakshmi P (2020). A design of bandwidth-enhanced conformal antenna for aircraft applications. IETE J Res 1–13. https://doi.org/10.1080/03772063.2020.1829507
10. Patil S, Madhu AR, Sudhendra C, Rukmini, TS, Biswas D (2015) Design and implementation of a conformal omnidirectional microstrip antenna array on cylindrical surface, vol 2, p 5
11. Shankar SG, Beenamole KSA (2015) Comparative study on arc conformal arrays for different curvatures, p 4
12. Beenamole KS, Sreejith CA, Shankar G (2016) Studies on conformal antenna arrays placed on cylindrical curved surfaces, p 3
13. Kothapudi VK, Kumar V (2018) A 6-port two-dimensional 3×3 series-fed planar array antenna for dual-polarized X-band airborne synthetic aperture radar applications. IEEE Access 6:12001–12007

14. Kothapudi VK, Kumar V (2019) VERTICAL polarized 1×3 series-fed linear array with gain and front-to-back ratio enhancement for airborne sar-x applications. Prog Electromagn Res M 80:169–179
15. Kothapudi VK, Kumar V (2019) SFCFOS uniform and Chebyshev amplitude distribution linear array antenna for k-band applications. J Electromagn Eng Sci 19:64–70
16. Kumari P, Chauhan B, Vijay S (2016) Performance analysis of microstrip conformal antenna array and effect of mutual coupling for different curvature. Int J Comput Appl 135:30–35
17. Kothapudi VK, Kumar V (2018) Compact 1×2 and 2×2 dual polarized series-fed antenna array for X-band airborne synthetic aperture radar applications. J Electromagn Eng Sci 18:117–128

A Compact Ultra-Wideband Antenna with Artificial Materials for Ground-Penetrating Radar Applications

Nitesh Kashyap, Ankit Kumar Maurya, Aditya Aman, and R. K. Sarin

Abstract For short-pulse ground-penetrating radar (GPR) application, a compact ultra-wideband (UWB) antenna is proposed. We have designed artificial material (AM) on both the ground and patch portions of the antenna in order to increase the radiation ability of the antenna. Two designs (one with and another without artificial material) are simulated, measured, and compared in order to validate the proposed antenna design. The results show that the suggested antenna operates across the whole UWB spectrum from 3 to 15 GHz and has a − 8 dB impedance bandwidth of 200% (3.0–15.0 Hz). It is useful for GPR application as well as in many other wireless systems due to its wide bandwidth, high gain, and directivity.

Keywords Ground-penetrating radar · Ultra-wideband · Radiation gain

1 Introduction

Broad-band antennas nowadays are becoming more popular and have lots of applications in microwave imaging, satellite communication [1, 2], GPR. GPR is a geophysical process that uses a nondestructive method of finding buried objects inside the earth surface; this method creates a revolution in this modern era as the conventional method is destructive in nature and very costly and requires more man power in it. The main advantage of GPR over other methods is that it works in a prevaricating

N. Kashyap (✉) · A. K. Maurya · A. Aman · R. K. Sarin
Department of Electronics and Communication Engineering, Dr. B R Ambedkar National Institute of Technology, Jalandhar, India
e-mail: kashyapn@nitj.ac.in

A. K. Maurya
e-mail: ankitkm.ec.19@nitj.ac.in

R. K. Sarin
e-mail: sarinrk@nitj.ac.in

S. Rawat et al. (eds.), *Proceedings of Second International Conference on Computational Electronics for Wireless Communications*, Lecture Notes in Networks and Systems 554,
https://doi.org/10.1007/978-981-19-6661-3_19

way. It means that to find the buried substances and materials, for example, pipes and cables no holes or trenches have to be dug. The ultra-wide bandwidth (UWB) of the GPR's receiving and transmitting antennas must range from a few megahertz to several gigahertzes. [3, 4]. Therefore, it is a bit challenging to design such an antenna which is planar in structure and have UWB. Because of their low profile, planar shape, and simplicity of fabrication, printed circuit broadband antennas, like tapered slot antennas and bow-tie antennas [4, 5], are generally used in GPR equipments. The exponential tapered antennas have higher gain, larger bandwidth, and more directional radiation than bow-tie antennas. Various tapered antenna designs have recently been researched and described in literature, including the antipodal tapered slot antenna and the linear tapered slot antenna [6–10] and many more. Conventionally, we use flared horn antenna for GPR application. The advantage over this antenna is that they have compact and planner structure. Desirable features for GPR antenna are wideband, high gain, good impedance matching, unidirectional radiation pattern, small and compact in size and high directivity. So, in order to fulfill all this requirements, we have to design an antenna which is planar and having all this characteristics. If we reduce size of antenna, then gain and bandwidth are also reduced; these are the main tradeoff for small size antenna, so we tried to retain these things [11]. By using an array of antennas, it can effectively increase the gain but along with that power distribution and coupling need to be considered, which makes it complicated design [12–15]. Slotting can be done for compactness and gain improvements; however, this will reduce the antenna's directivity. High dielectric constant lenses can be used to increase gain, but its improvement is restricted. The loading of artificial materials (AMs) on antennas has also been widely exploited by researchers in addition to the numerous approaches previously stated. Numerous common AM techniques, including as frequency selective surfaces, zero-index materials, gradient meta-surfaces, and photonic crystals, have been applied to the antenna [16–18].

So, we have designed a patch antenna which is exponential tapered, and we have created some artificial material such as reflectors and lens for fulfill the requirements. The most beneficial thing about these materials is that they do not create any additional size and cost in fabrication. They are created on the empty surface of the substrate on both the side (i.e., on patch and ground side).

In this letter, we have compared both the results with and without the artificial materials and also compare the dimensions of the designed antenna. The antenna is simulated with CST software and then fabricated to perform s-parameter measurements for validation.

2 Antenna Configuration

Figure 1a describes the geometry of an antenna without artificial material. The FR4 epoxy is chosen as the dielectric substrate because of its loss tangent ($\tan \delta = 0.021$),

relative permittivity ($\in_r = 4.2$), and thickness (h = 1.6 mm). The original antenna also has four metal components: a top patch, bottom patch, ground, and a feed line.

In the xoy plane, the feed line and ground are each symmetrical. Both areas are flaring in opposite directions. The metal is composed of copper, which has a conductivity of 5.9×10^7 Sm^{-1} and a thickness of 50 μm. The parameters for the curvature in the following equations mentioned in Table 1 illustrate the exponential curves of the radiation patches and ground. Other parameters are given in Table 2.

3 Result of Designed Antenna with and Without AM

The various characteristic plots of the proposed antenna with and without AM have been described in this section. Simulated and experimental results have been discussed.

Simulation Results

Inside this section, the simulation results of the designed antenna array structures are discussed. All simulations have been carried out using CST simulation software. The chapter carries a comparative analysis of simulated results and experimented results to prove the validity of the proposed work.

S Parameters

Figure 2 shows the simulated result showing frequency versus return loss graph with and without AM. The test frequency range spans from 0.5 to 15 GHz. We have compared the result by showing the S11 parameters of both the CUWBA with and without AM. The result shows that the antenna with AM has a impedance bandwidth of nearly 200% and resonates for almost 12 GHz of frequency range which proves the compact ultra-wideband antenna (CUBWA) have an ultra-wideband.

Comparative Analysis of Radiation Pattern

The simulated CUWBA radiation pattern from 3 to 15.0 GHz is shown in Fig. 3. The gain of CUWBA with artificial material is somewhat higher at lower frequencies and considerably higher above 3 GHz when compared to the original CUWBA. In

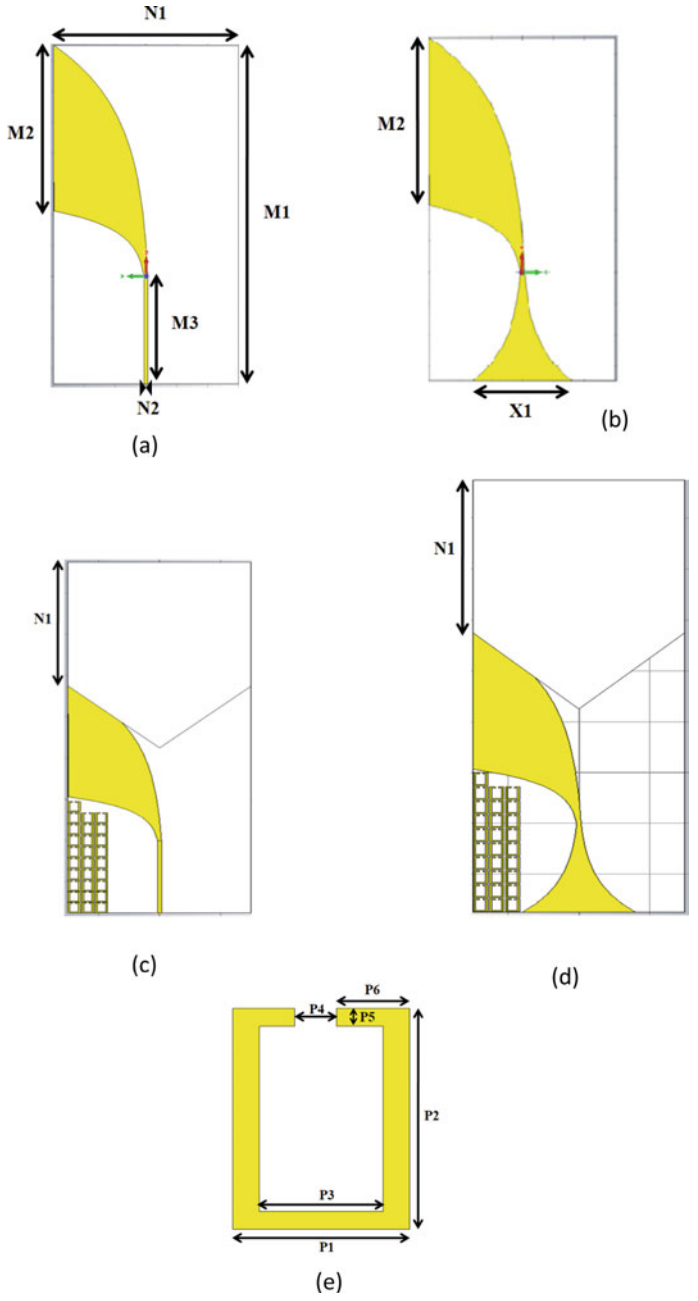

Fig. 1 **a** Front look of designed antenna structure without AM, **b** Back View of designed antenna structure without AM, **c** Front view of designed antenna structure with AM, **d** Back view of designed antenna structure with AM

Table 1 Equation and curvature parameters of designed antenna shown below

Curve	Equation	A	a
Outer curve	$y = A+e^{ax}$	−1.6	0.046
Inner curve	$y = A+e^{ax}$	−0.4	0.16
Curve of ground	$y = -(A+e^{-ax})$	−0.4	0.16

Table 2 Dimension of the CUWBA and AM

M1	M2	M3	N1	N2	X1	P1	P2	P3	P4	P5	P6	H
110	53.69	35.03	60	1.2	32	04	05	2.8	0.95	0.4	1.65	1.6

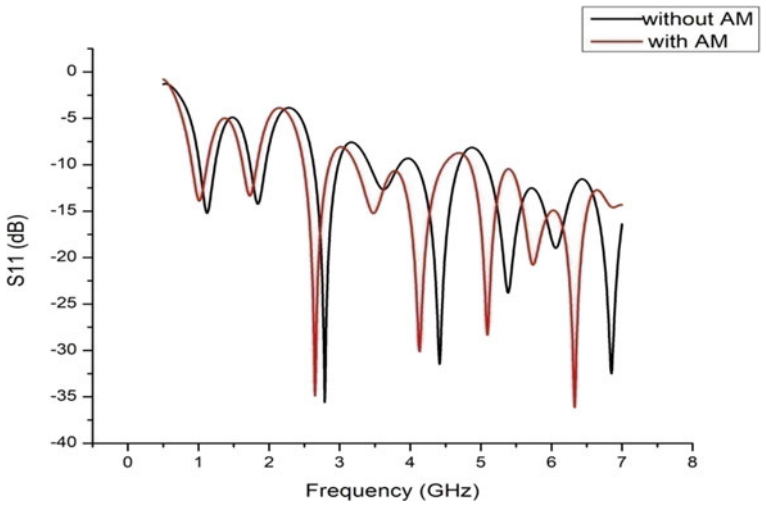

Fig. 2 Frequency versus return loss with and without AM

comparison to most planar antennas, the maximum gain can be reach up to 11.2 dBi higher. Consequently, the enhanced ATSA with artificial material is a wideband antenna having a 200%, − 8 dB impedance bandwidth (3–15 GHz). In comparison to the CUWBA without AMs, the CUWBA with AMs has a larger gain. Figure 3 shows the proposed antenna's radiation pattern, and this will undoubtedly contribute in this antenna's suitability for GPR applications. The azimuth component in this image is represented by Phi, the elevation component by Theta, and the magnitude in dB for both polarizations is represented by E Absolute. Additionally, Table 3 compares the operating frequency spectrum, gain enhancement techniques, and other features in order to separate our findings from those of other previous studies. The 2D and 3D radiation patterns of the proposed antenna are given in the Figs. 4 and 5 respectively.

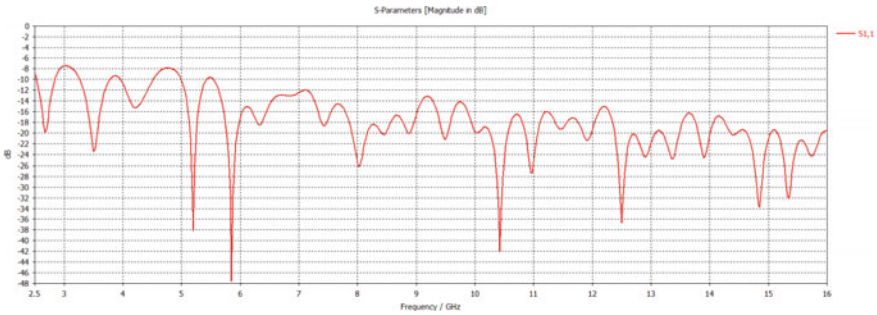

Fig. 3 Frequency versus return loss with AM (2.5–16 GHz)

Table 3 Comparison of the designed antenna with published works

References	Bandwidth (%)	Maximum gain (dBi)	Gain enhancement mechanism
Designed Antenna	200	12.4	Resonant reflector and non-resonant lens
Guo et al. [2]	177	14.1	Resonant reflector and non-resonant lens
[19]	137.5	14	Anisotropic zero-index metamaterials
[20]	168.8	17.7	High permittivity cover
[21]	104	12	Non-resonant lens

4 Conclusion

We have adopted broadband non-resonant artificial material such as lens and resonant reflector in CUWBA. By creating AMs on both the empty side of the substrate, i.e., on the patch side and ground side, the overall performance of the antenna increases. The most advantageous thing is that the compactness and the cost of the antenna remain constant. In this letter, we have compared the CUWBA with and without artificial material and fabricated it and further measured to compare their performance and reveal the gain enhancement technique. We have seen from the simulation and experimental results that the proposed CUWBA design with AMs has the advantage over CUWB without AMs, and this makes it suitable to use in GPR and in many broadband applications.

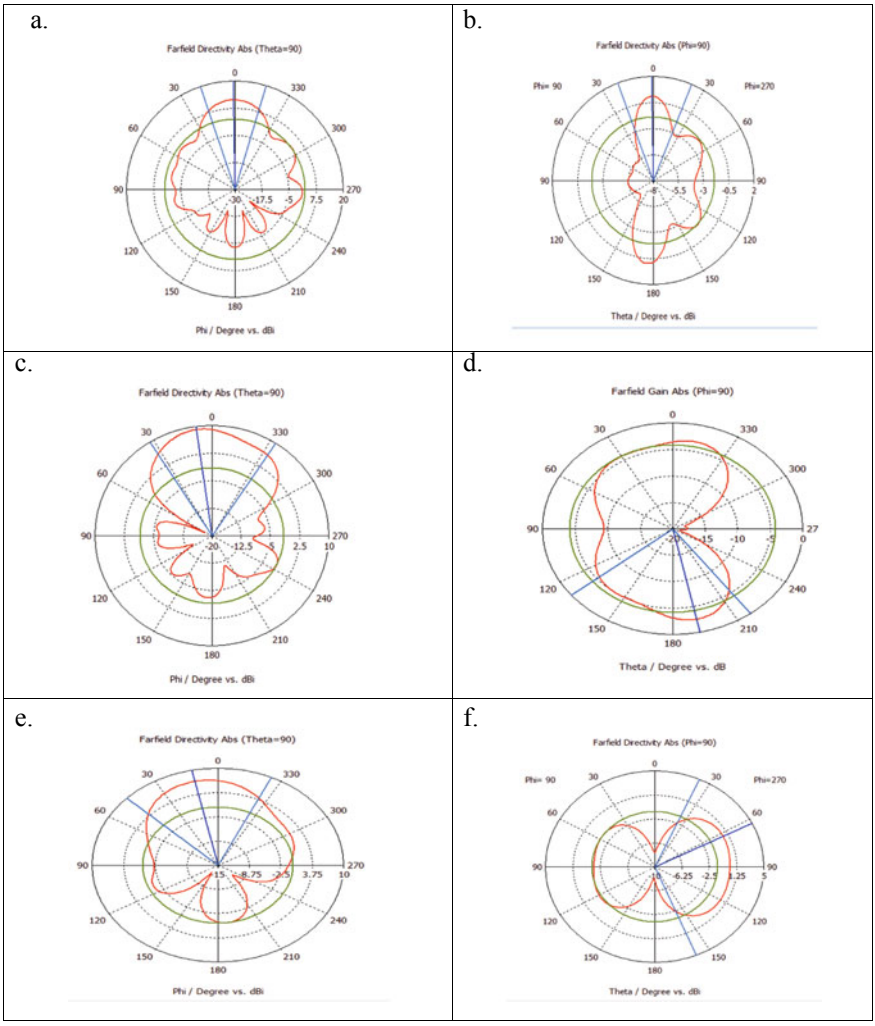

Fig. 4 **a** The proposed antenna's far-field pattern at 6 GHz with AM, **b** Far-field pattern of the designed antenna at 6 GHz without AM, **c** Far-field pattern of the designed antenna at 4.5 GHz with AM. **d** Far-field pattern of the designed antenna at 4.5 GHz without AM. **e** Far-field pattern of the designed antenna at 3 GHz with AM, **f** The proposed antenna's far-field pattern at 3GHz without AM

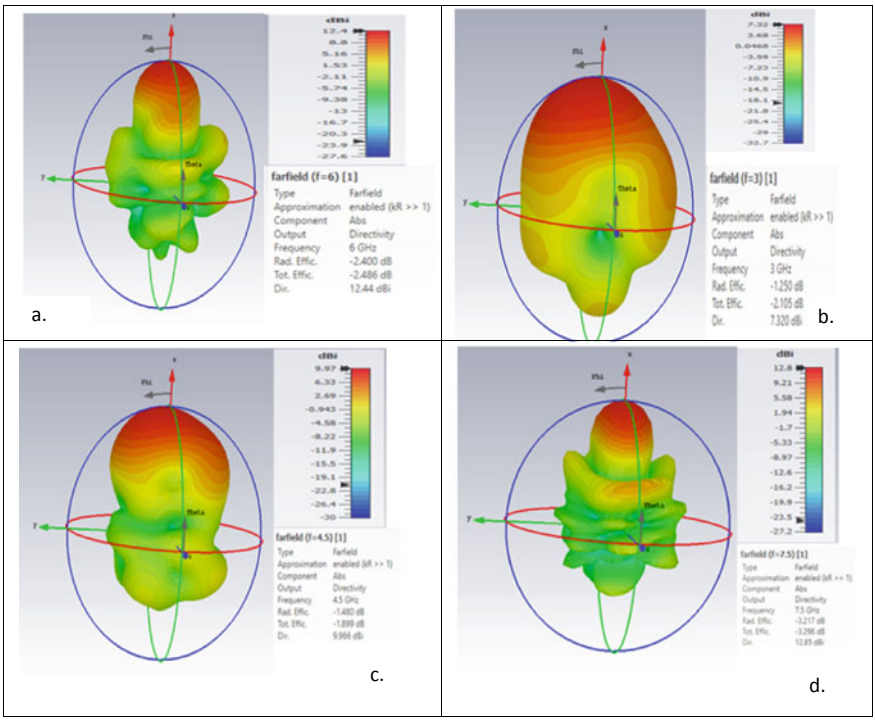

Fig. 5 **a** The designed antenna's radiation pattern at 6 GHz with AM, **b** The designed antenna's radiation pattern at 3 GHz without AM, **c** The designed antenna's radiation pattern at 4.5 GHz with AM, **d** Radiation pattern of the designed antenna at 7.5 GHz without AM

References

1. Balanis CA (2016) Antenna theory: analysis and design, 4th edn. Wiley, Hoboken, NJ
2. Guo L, Yang H, Zhang Q, Deng M (2018) A compact antipodal tapered slot antenna with artificial material lens and reflector for GPR applications. IEEE access 6:44244–44251
3. Shao J, Fang G, Ji Y, Tan K, Yin H (2013) A novel compact tapered-slot antenna for GPR applications. IEEE Antennas Wirel Propag Lett 12:972–975
4. Wu B, Ji Y, Fang G (2010) Analysis of GPR UWB half-ellipse antennas with different heights of backed cavity above ground. IEEE Antennas Wirel Propag Lett 9:130–133
5. Chen NW, Chuang CT, Shi JW (2007) A W-band linear tapered slot antenna on rectangular-grooved silicon substrate. IEEE Antennas Wirel Propag Lett 6:90–92
6. Soliman M, Wu Z (2007) Design, simulation and implementation of UWB antenna array and it's application in GPR systems. In: The second European conference on antennas and propagation, (EuCAP) pp 1–5. IET
7. Cristofani E, Becquaert M, Lambot S, Vandewal M, Stiens JH, Deligiannis N (2018) Random subsampling and data preconditioning for ground penetrating radars. IEEE Access 6:26866–26880
8. Ahmed A, Zhang Y, Burns D, Huston D, Xia T (2015) Design of UWB antenna for air-coupled impulse ground-penetrating radar. IEEE Geosci Remote Sens Lett 13(1):92–96
9. Hood AZ, Karacolak T, Topsakal E (2008) A small antipodal Vivaldi antenna for ultrawide-band applications. IEEE Antennas Wirel Propag Lett 7:656–660

10. Ahadi M, Nourinia J, Ghobadi C, Ellis MS, Mohammadi B (2019) Compact planar UWB elliptical Vivaldi antenna. In: 2019 5th conference on knowledge based engineering and innovation (KBEI), pp 128–131. IEEE
11. Umar SM, Ullah S, Ahmad F (2019) Gain enhancement technique in Vivaldi antenna for 5G communication. In: 2019 2nd International conference on computing, mathematics and engineering technologies (iCoMET), pp 1–4. IEEE
12. Bruder J, Carlo J, Gurney J, Gorman J (2003) IEEE standard for letter designations for radar-frequency bands. IEEE Aerospace & Electronic Systems Society, pp 1–3
13. Garg R, Bahl IJ, Bhartia P, Ittipiboon A (2000) Microstrip antenna design handbook. Artech House, Dedham, MA
14. Win MZ, Dardari D, Molisch AF, Wiesbeck W, Jinyun Zhang W (2009) History and applications of UWB. Institute of Electrical and Electronics Engineers
15. Daniels DJ, Gunton DJ, Scott HF (1988) Introduction to subsurface radar. In: IEE Proc F Commun Radar Signal Proc 135(4):278–320. IET
16. Spagnolini U (1997) Permittivity measurements of multilayered media with monostatic pulse radar. IEEE Trans Geosci Remote Sens 35(2):454–463
17. Agrawall NP, Kumar G, Ray KP (1998) Wide-band planar monopole antennas. IEEE Trans Antennas Propag 46(2):294–295
18. Zhou B, Cui TJ (2011) Directivity enhancement to Vivaldi antennas using compactly anisotropic zero-index metamaterials. IEEE Antennas Wirel Propag Lett 10:326–329
19 Sun M, Chen ZN, Qing X (2012) Gain enhancement of 60-GHz antipodal tapered slot antenna using zero-index metamaterial. IEEE Trans Antennas Propag 61(4):1741–1746
20 Cao W, Zhang B, Liu A, Yu T, Guo D, Wei Y (2012) Gain enhancement for broadband periodic end-fire antenna by using split-ring resonator structures. IEEE Trans Antennas Propag 60(7):3513–3516
21 Chen L, Lei Z, Yang R, Fan J, Shi X (2014) A broadband artificial material for gain enhancement of antipodal tapered slot antenna. IEEE Trans Antennas Propag 63(1):395–400

A Study on Tunable SIW-Based Self-Diplexing Antenna

Vaibhav Aggarwal, Sudhansh Kesharwani, Aditya Khosla, Prashant Upadhyay, and Arvind Kumar

Abstract In this paper, an approach to understanding tunable self-diplexing antenna using substrate-integrated waveguide technology is presented. The put-forth antenna uses two quarter-mode SIW cavity resonators for radiation, which are acquired by splitting a half-mode SIW cavity with the help of two open-ended slots. Microstrip feedlines are used to excite both quarter-mode cavity resonators. The two slits of different lengths, which radiate at two distinct resonant frequencies, are etched on the top surface of the cavity. The dimensions of the antenna are calibrated, and very high isolation of better than −30 dB is obtained between the input ports that helps to realize a self-diplexing phenomenon. To realize the frequency tuning characteristic, a narrow slit has been introduced on each resonator. By changing the slit location, the operating frequency can be tuned over 1 GHz frequency span, while all other parameters remained unchanged. Moreover, the design shows unidirectional and stable radiation pattern at both operating frequencies while maintaining planar and simple configuration.

Keywords Self-diplexing antenna · Tunability · Substrate-integrated waveguide (SIW)

V. Aggarwal · S. Kesharwani · A. Khosla · A. Kumar
School of Electronics and Communication Engineering, Vellore Institute of Technology, Vellore, India

P. Upadhyay
Department of ECE, Madanapalle Institute of Technology and Science, Madanapalle, Andhra Pradesh, India

A. Kumar (✉)
Department of Electronics and Communication Engineering, Visvesvaraya National Institute of Technology, Nagpur, India
e-mail: arvindkumar@ece.vnit.ac.in

S. Rawat et al. (eds.), *Proceedings of Second International Conference on Computational Electronics for Wireless Communications*, Lecture Notes in Networks and Systems 554,
https://doi.org/10.1007/978-981-19-6661-3_20

1 Introduction

Currently, modern wireless communication systems are getting more and more advanced; the demand for compacted, light-weight, and high-performance multi-functional antennas has seen a rise [1–4]. Integrated media-rich equipments and transceiver used in satellites with different sending and receiving frequencies need dual frequency antenna with high isolation between its input ports [5–7]. Therefore, new dual-band antennas need to be designed with requirement of low profiling and low-cost fabrication process. The size of the device depends on the size of the antenna incorporated. In the process, the dual frequency self-diplexing antennas capable of minimizing and simplifying of high-order diplexing circuital network at RF front-end systems have gained considerable attention. These help in reducing the costs and complexity [7, 8]. Several self-diplexing antennas using microstrip antennas have been shown in the literature given. Self-diplexing antenna using SIW technology guarantees high isolation between its ports [9–13]. Self-diplexing antenna takes substantial space because of full cavity SIW cavity resonator in case of [9, 10]. In the current day scenarios, SIW antennas need to be extremely small with low weight and condensed combination with wireless systems. Therefore, the concept of a half-mode SIW (HMSIW) and quarter-mode SIW (QMSIW) in self-duplexing antenna was introduced [11–14]. These schemes can reduce the size to a great extent by applying a half-mode SIW (HMSIW) (50% miniaturization) and quarter-mode SIW (QMSIW), (75% miniaturization) while preserving equivalent performance [15, 16]. HMSIW-and QMSIW-based design furthermore requires less amount of drilled vias (forming lateral walls of SIW) improving the mechanical stability of the structure and is easy and cost-effective during fabrication. We need to make the antennas small but should not come in the cost of performance which is very common in case of antennas. Functionality should be given greatest priority.

In the proposed work, a QM/HM SIW-based cavity-backed tunable self-diplexing antenna topology is presented. By positioning a slated one open-ended rectangular slot in HMSIW resonator, two QMSIWs are realized. HMSIW is divided into two unequal halves by the slot. Two slits are also added to make the antenna tunable. Each QM resonator is excited with the help of microstrip feedlines. The antenna exhibits high isolation between the input ports.

2 Half-Mode/Quarter-Mode Substrate-Integrated Waveguide

The design of the cavity is based on the use of classical equations of waveguides and rectangular cavities. The design begins with the determination of the resonant frequency (f_r) of rectangular cavity that resonates at its fundamental TE101 mode [6]. The SIW cavity resonator can be constructed in a dielectric substrate by four rows of the metallic vias implementing the side walls. The resonant frequency (f_r)

of an SIW cavity resonator for its dominant (TE110) mode can be determined by using (1), considering it as a dielectric-filled (ε_r dielectric constant) conventional rectangular waveguide.

$$f_r = \frac{c}{2\sqrt{\varepsilon_r}}\sqrt{\left(\frac{1}{W_{\text{eff}}}\right)^2 + \left(\frac{1}{L_{\text{eff}}}\right)^2} \tag{1}$$

$$\text{where,} \quad W_{\text{eff}} \quad \text{or} \quad L_{\text{eff}} = W \quad \text{or} \quad L - 1.08\frac{d^2}{p} \tag{2}$$

where f_r, ε_r, and c denote the resonant frequency of cavity resonator, relative permittivity, and the speed of light in vacuum, respectively. The design guidelines suggested in [20–22] restrict via diameter d and pitch distance p to d $\leqslant \lambda/10$ and $s \leq 2d$, where λ is wavelength at the frequency of interest. This condition prevents the leakage of energy from the side walls.

$$E_z = E_o sin\frac{\pi y}{a} sin\frac{\pi x}{a} \tag{3}$$

$$H_z = \frac{j\pi E_o}{k\eta a} cos\frac{\pi x}{a} sin\frac{\pi x}{a} \tag{4}$$

$$H_z = \frac{-j\beta E_o}{k\eta a} sin\frac{\pi y}{a} cos\frac{\pi x}{a} \tag{5}$$

$$H_z = H_z = H_z = 0 \tag{6}$$

$$\beta = \beta_z = \beta_{110} = \sqrt{k^2 - 2\left(\frac{\pi}{a}\right)^2} \tag{7}$$

$$k = \omega\sqrt{\mu\varepsilon} \tag{8}$$

where β_z is phase constant in z-direction, η is intrinsic impedance of a dielectric inside the cavity, and k is wave number, and ω, ε, and μ represent angular frequency, permittivity, and permeability in the cavity resonator, respectively.

The electric field distribution of the SIW cavity resonator is plotted in Fig. 1a using a commercial CST electromagnetic simulation tool. The electric field for the dominant mode of the SIW is perpendicular to the top and bottom metallic plates, while the direction of the magnetic field is perpendicular to the side walls and parallel to top and bottom surfaces [7]. Therefore, perfect magnetic walls are available for the *A-A'*, *B-B'*, *C-C'*, and *D-D'* planes in Fig. 1a. When the SIW is cut on *A-A'*/*D-D'* along the perfect magnetic wall, the HMSIWs are realized as shown in Fig. 1b. Similarly, when HMSIW resonators are cut along $O - C \,/\, O - B$, QMSIWs are realized as shown in Fig. 1c. The HMSIW and QMSIW cavities haven't only miniaturized the size, but also preserve half and quarter of the field distribution of original cavity,

respectively. The resonant frequency of HMSIW (f_{HM}) and QMSIW $\left(f_{\mathrm{QM}}\right)$ can be estimated using Eqs. (9) and (10), respectively.

$$f_{\mathrm{HM}}=\frac{c}{\sqrt{2\varepsilon_{r,\mathrm{eff}}}}\sqrt{\left(\frac{1}{W_{\mathrm{eff,HM}}}\right)^2+\left(\frac{1}{2L_{\mathrm{eff,HM}}}\right)^2} \tag{9}$$

$$f_{\mathrm{QM}}=\frac{c}{\sqrt{2\varepsilon_{r,\mathrm{eff}}}}\sqrt{\left(\frac{1}{2W_{\mathrm{eff,QM}}}\right)^2+\left(\frac{1}{2L_{\mathrm{eff,QM}}}\right)^2} \tag{10}$$

It is noted that cavity resonators are excited by using 50 Ω microstrip line (MSL), and the transition from MSL to SIW is realized by adjusting the via wall at feeding point.

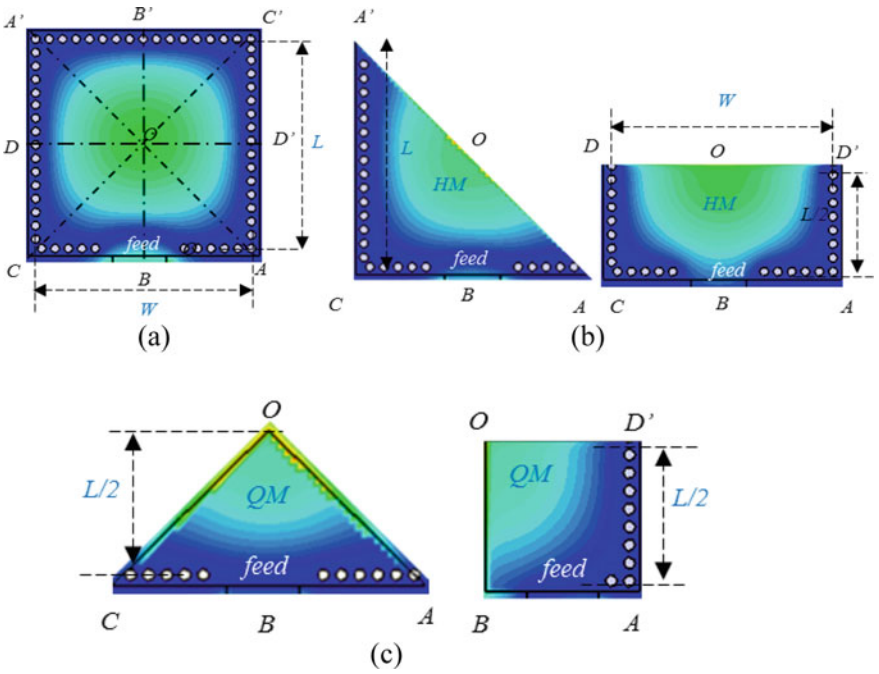

Fig. 1 Simulated E-field distributions within **a** full-mode SIW, **b** HMSIW, and **c** QMSIW at resonant frequencies

3 Proposed Design

The prevailing design of a self-diplexing antenna with its response [11] with substrate-integrated waveguide technology with resonant frequencies 6.46 and 7.11 GHz is shown in Fig. 2.

In order to make the existing antenna tunable, we have added two perpendicular slits of width 0.3 mm in both the quarter-mode SIW resonator-based antennas. To tune the antenna resonate frequency, one needs to change the position of these slits as deprived in Fig. 3. It was observed that the position of these slits is not affecting the impedance matching characteristics of respective frequency. Moreover, this tunability can be realized by using suitable switching frequency. The proposed design concept of the tunable antenna is shown in Fig. 3, Table 1.

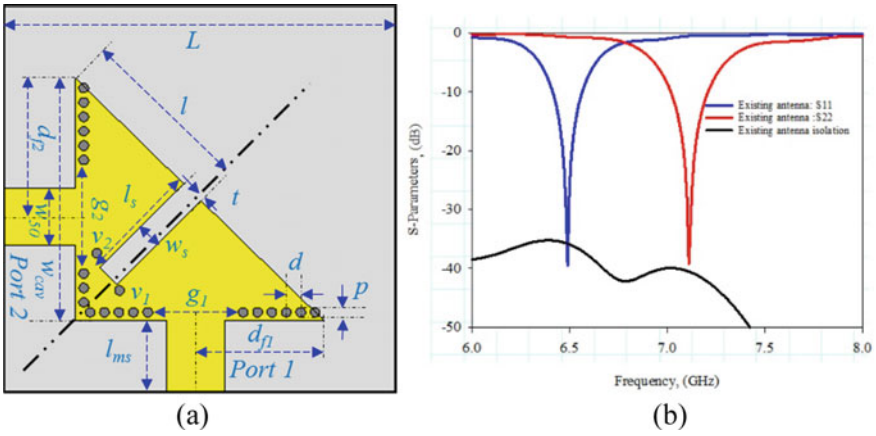

Fig. 2 **a** Schematic of existing design and **b** results of existing design

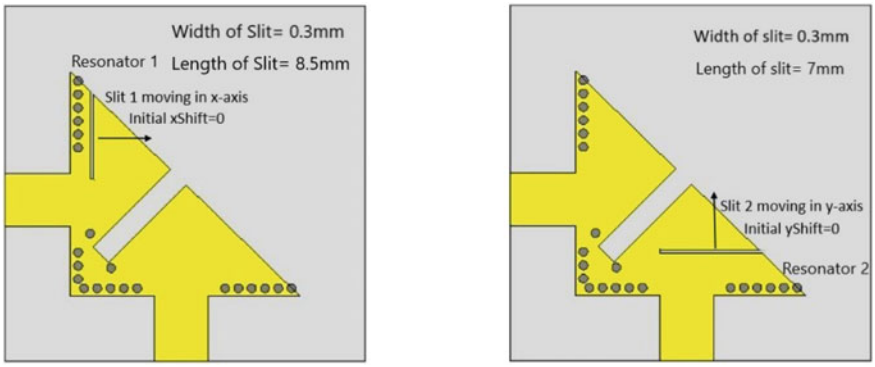

Fig. 3 Schematic of the proposed antenna

Table 1 Dimensions of the proposed design

Parameters	Values (mm)	Parameters	Values (mm)
L	32.5	l_{ms}	6.0
w_{cav}	20.2	l	14.5
l_s	9.9	h	*1.57*
g_1	7.1	w_s	2.0
d_{f1}	10.7	d_{f2}	11.58
g_2	8.2	p	1.2

4 Design Configuration and Analysis

To represent the required antenna in detail, the geometrical configuration with the design is shown in Fig. 3. In the proposed design, the HMSIW cavity resonator operating in the dominant mode is split into two unequal parts by etching one open-end slanted rectangular slot. Fundamentally, this slot transforms the HMSIW cavity resonator into two unequal quarter-mode-like cavity resonators/radiators. We have inserted one slit in each of the quarter-mode cavity resonators to make the antenna tunable. Further, to excite these resonators individually, we have used a 50-Ω microstrip line for each of them. It is seen that each of the quarter-mode resonators radiates independently. The slits are placed in such a way that the impedance can be matched to the corresponding frequency.

The electric field distribution of the proposed design at resonant frequencies of 6.46 and 7.11 GHz is shown in Fig. 4. It can be clearly observed that the nature field distribution is similar to the fundamental mode.

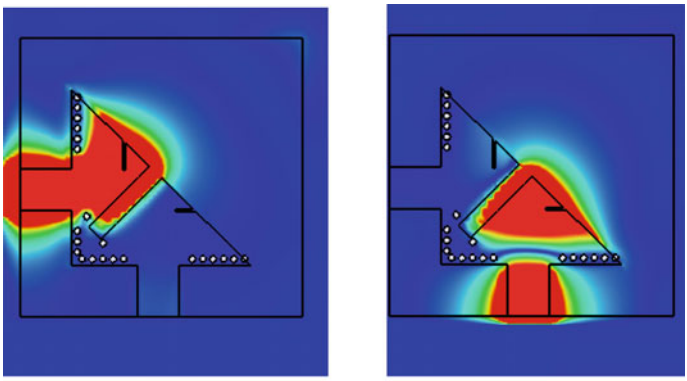

Fig. 4 Electric field distribution **a** Port1 on at a frequency of 7.11 GHz **b** Port2 on at a frequency of 6.46 GHz

5 Parametric Analysis

To show the tuning characteristics of the proposed design, we will add slits one by one in both the QM resonators. In the initial phase of our research, we experimented by adding either two vertical or two horizontal slits but eventually we realized that the slits have to be perpendicular to each other, just like the resonators for optimal results. The analysis is performed with help of time domain-based CST 2019 software.

In case of the parametric study of tunability of resonator 1, the slit in the resonator 2 is positioned at parameter Y_{shift} equals 7 for best result, while we move slit in the resonator 1 horizontally in positive x direction using the parameter X_{shift} ranging from 1 to 6, with a spacing of 1 mm.

The effect of slit's position in the resonator 1 on the S-parameters of the proposed diplexer is presented in Fig. 5.

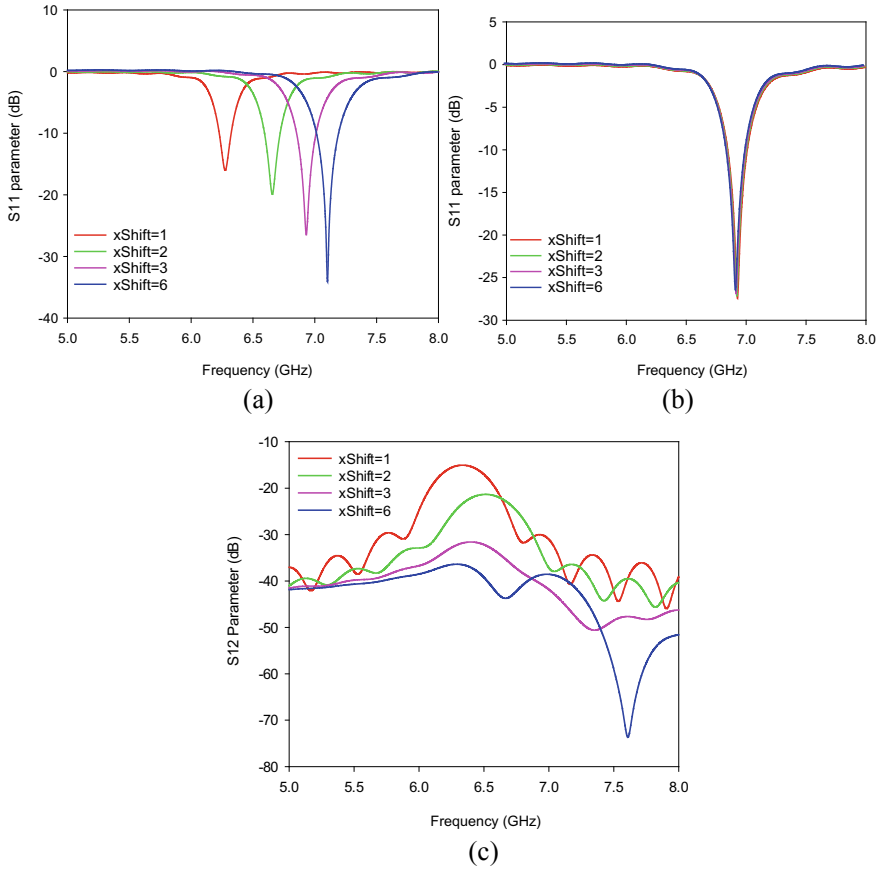

Fig. 5 When resonator 1 is tuned, keeping slit 2 constant at $Y_{\text{shift}}= 7$. **a** S11 parameter, **b** S22 parameter, and **c** S21 and S12 parameter

From the above results, we can observe that the maximum output of − 34.6 dB is received when the value of parameter X_{shift} equals 6. We can also observe that any change in the position of slit in resonator 1 doesn't affect our output of resonator 2.

Similarly, in case of the parametric study of tunability of resonator 2, the slit in the resonator 1 is positioned at parameter X_{shift} equals 7 for best results as just observed from the above analysis, while we move slit in the resonator 2 in positive y direction using the parameter Y_{shift} ranging from 1 to 7, with a spacing of 1 mm.

In Fig. 6, we have shown the best results while excluding the overlapping frequency ranges Tables 2 and 3.

From the above results, we can observe that the maximum output of − 36.2 dB is obtained when the parameter Y_{shift} equals 7. Also, any change in position of slit in resonator 2 doesn't affect our output of resonator 1. So, we can conclude that

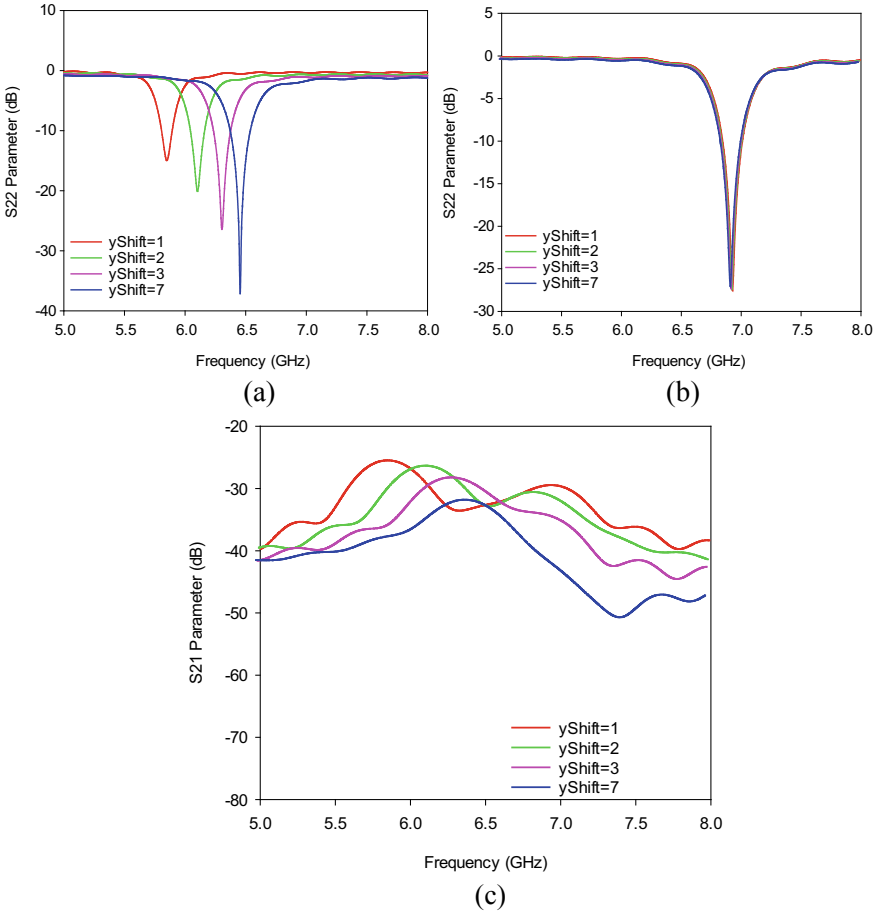

Fig. 6 When resonator 2 is tuned, keeping slit 1 constant at $X_{\text{shift}} = 6$. **a** S22 parameter, **b** S11 parameter, and **c** S21 and S12 parameter

Table 2 Optimized results when resonator 1 is tuned

S. No.	X_{shift}	Bandwidth (MHz)	Resonant frequency (GHz)
1.	1	90	6.27
2.	2	130	6.65
3.	3	160	6.93
4.	6	200	7.11

Table 3 Optimized results when resonator 2 is tuned

S. No.	Y_{shift}	Bandwidth (MHz)	Resonant frequency (GHz)
1.	1	100	5.85
2.	2	120	6.10
3.	3	140	6.31
4.	7	160	6.46

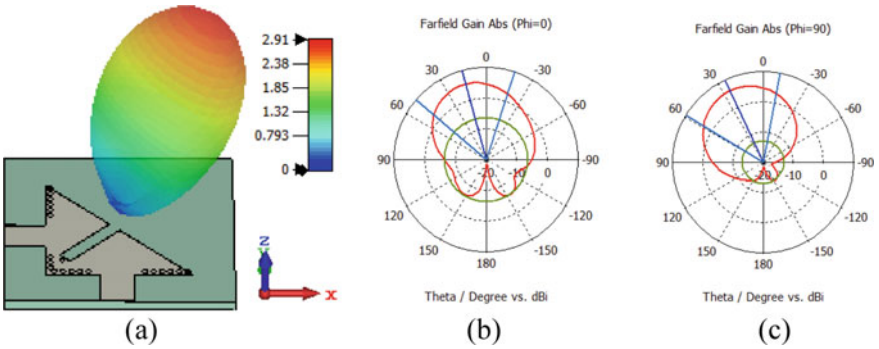

Fig. 7 Radiation pattern at frequency 7.11 GHz. **a** 3D, **b** polar at $\Phi = 0°$, and **c** polar at $\Phi = 90°$

our resonators are mutually isolated. To have a better understanding, the radiation pattern for the antenna at resonant frequencies of 6.46 and 7.11 GHz when either of the ports is shown in Figs. 7 and 8.

6 Conclusion

A compact tunable self-diplexing antenna based on SIW technique is presented in this paper. Two quarter-mode cavity resonators, placed orthogonally to each other, are used for radiation. The quarter-mode resonators are acquired from half-mode SIW resonator by inserting a slanted one open-ended rectangular slot. Each quarter-mode resonator radiates independently, at the corresponding resonance without affecting

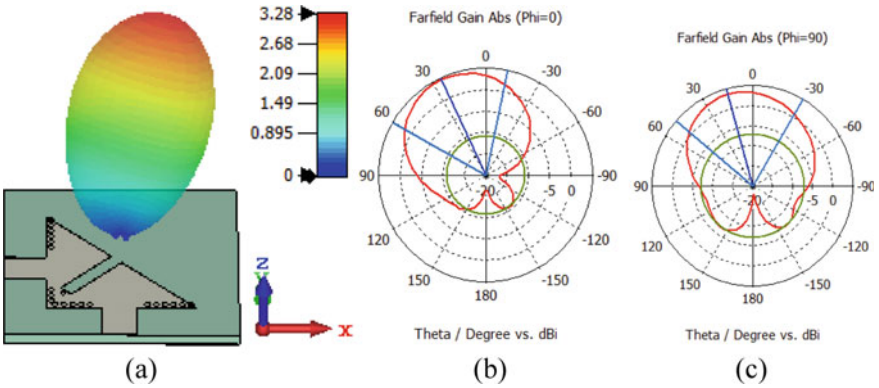

Fig. 8 Radiation pattern at frequency 6.46 GHz. **a** 3D, **b** polar at $\Phi = 0°$, and **c** polar at $\Phi = 90°$

other. We have inserted two perpendicular slits placed one in each of the quarter-mode cavities to make the antenna tunable. The resonant frequencies for resonator 1 and 2 are 7.11 and 6.46 GHz, respectively. The resonator 1 operates in frequency range 6.2–7.2 GHz, while the resonator 2 operates in 5.8–6.5 GHz. Also, both the resonators of the antenna are mutually isolated. The proposed antenna exhibits an isolation of better than − 30 dB between the input ports, which makes it suitable for a self-diplexing applications.

References

1. Chaturvedi D (2020) SIW cavity-backed 24° inclined-slots antenna for ISM band application. Int J RF Microw Comput Aid Eng 30(5)
2. Kumar A, Al-Hasan MJ (2020) A coplanar-waveguide-fed planar integrated cavity backed slotted antenna array using TE33 mode. Int J RF MicrowComput Aid Eng 30(10)
3. Kumar A, Raghavan S (2016) A design of miniaturized half-mode SIW cavity backed antenna. In: 2016 IEEE Indian antenna week (IAW 2016)
4. Chaturvedi D et al (2019) Wideband HMSIW-based slotted antenna for wireless fidelity application. IET Microw Antennas Propag 13(2):258–262
5. Kumar A, Saravanakumar M, Raghavan S (2018) Dual-frequency SIW-based cavity-backed antenna. Int J Electron Commun 97:195–201
6. Althuwayb A et al (2021) Design of half-mode substrate integrated cavity inspired dual-band antenna. Int J RF Microw Comp Aid Eng 31(2)
7. Kumar A, Raghavan S (2017) Broadband dual-circularly polarised SIW cavity antenna using a stacked structure. Electron Lett 53(17):1171–1172
8. Pramodini B et al (2022) Design and investigation of dual-band 2 × 2 elements MIMO antenna-diplexer based on half-mode SIW. IEEE Access 10:79272–79280
9. Kumar A, Althuwayb AA (2021) SIW resonator-based duplex filtenna. IEEE Antennas Wirel Propag Lett 20(12):2544–2548
10. Althuwayb AA et al (2022) Substrate integrated waveguide (SIW) cavity-backed slot antenna with monopole-like radiation for vehicular communications. Appl Phys A 128(3):1–7
11. Kumar A, Chaturvedi D, Raghavan S (2018) Design of a self-diplexing antenna using SIW technique with high isolation. Int J Electron Commun 94:386–391

12. Chaturvedi D, Raghavan S (2019) Design and experimental verification of dual-Fed, self-diplexed cavity-backed slot antenna using HMSIW technique. IET Microw Antennas Propag 13(3):380–385
13. Kumar A, Imaculate Rosaline S (2021) Hybrid half-mode SIW cavity-backed diplex antenna for on-body transceiver applications. Appl Phys A Mater Sci Process 127(11)
14. Chaturvedi D, Raghavan S (2019) Dual-band, dual-fed self-diplexing antenna. In: 2019 13th european conference on antennas and propagation (EuCAP), pp 1–5. IEEE
15. Chaturvedi D et al (2018) A substrate integrated waveguide based antenna-triplexer. In: 2018 Asia-pacific microwave conference (APMC)
16. Saravanakumar M et al (2018) SIW cavity-backed self-triplexing antenna with T-shaped slot. In: 2018 Asia-pacific microwave conference (APMC)
17. Kumar A (2019) Design of self-quadruplexing antenna using substrate-integrated waveguide technique. Microw Opt Technol Lett 61(12):2687–2689
18. Kumar A, Raghavan S (2017) Broadband dual-circularly polarised SIW cavity antenna using a stacked structure. Electron Lett 53(17):1171–1172
19. Kumar A, Raghavan S (2018) Bandwidth enhancement of substrate integrated waveguide cavity-backed bow-tie-complementary-ring-slot antenna using a shorted-via. Def Sci J 68(2):197
20. Luo GQ, Hu ZF, Dong LX, Sun LL (2008) Planar slot antenna backed by substrate integrated waveguide cavity. IEEE Antennas Wirel Propag Lett 7:236–239
21. Kumar A (2020) Wideband circular cavity-backed slot antenna with conical radiation patterns. Microw Opt Technol Lett 62(6):2390–2397
22. Iqbal A, Selmi MA, Abdulrazak LF, Saraereh OA, Mallat NK, Smida A (2020) A compact substrate integrated waveguide cavity-backed self-triplexing antenna. IEEE Trans Circuits Syst II Express Briefs 67(11):2362–2366

Experimental Implementation of COVID-19 Safety Measures in Ride-Sharing Cabs Using Deep Learning and Internet of Things

Tanisha Rakshit, Aayush Shrestha, Sakshi Chhabra, and Sumit Kumar Jindal

Abstract Increased urbanization and on-demand mobility have resulted in the boon of many ride-sharing companies. Besides providing faster, economical, and comfortable rides, these rideshares are also environment-friendly as they save a lot of energy. This research work presents a model which would be beneficial for the passengers riding these carpools as it would not only help to curb the spread of infection in current pandemic but also detect whether the driver is drowsy or not to prevent possible road accidents. The proposed web application includes three detections based on novel deep learning algorithms implementing face recognition, facemask, and drowsiness detection of the driver with an alert mechanism to send immediate email alerts to the company and driver. The novelty of the proposed application is that the current and live status of the driver is continuously recorded using latest technologies like convolutional neural networks (CNNs), histogram of oriented gradients (HOG), support vector machine (SVM) classifier, and computer vision. In addition to this, a real-time vehicle tracking device is also implemented using Node MCU, Global Positioning System (GPS) module, and Blynk app to keep the company updated about the real-time location of the rideshare. The name of the recognized driver is displayed as output. Face mask and drowsiness detection is done with an accuracy of 99%, and the real-time location of the cab is indicated in Google Maps on the Blynk app. The proposed web application would be very beneficial for ride-sharing companies in the current COVID situation.

Keywords Convolutional neural networks · Deep learning · IoT · Artificial intelligence · GPS tracker

T. Rakshit · A. Shrestha · S. Chhabra · S. K. Jindal (✉)
Vellore Institute of Technology, Vellore, Tamil Nadu, India
e-mail: sumitjindal08@gmail.com

S. Rawat et al. (eds.), *Proceedings of Second International Conference on Computational Electronics for Wireless Communications*, Lecture Notes in Networks and Systems 554,
https://doi.org/10.1007/978-981-19-6661-3_21

1 Introduction

Rideshares are becoming widely popular as they are more convenient, easily available, and provide better customer service. Implementing recent, new technologies like artificial intelligence, deep learning, and IoT have become the prime aspect for the growth of ride-sharing companies. In the proposed model, the authors have used these fundamental technologies to build a web application with the features of face recognition, face mask detection, and drowsiness detection of the driver with real-time location tracking of the vehicle. Face recognition is one of the latest technologies. It involves artificial intelligence techniques enhancing deep learning with lots of processing of data with higher accuracy and faster processing time [1]. It has been deployed for security and various other applications for retail, hospitality, banking, and ride-sharing industries. A facial recognition system is a biometric tool which identifies or recognizes a person based on certain physiological aspects and then matching the facial features extracted with that of a known face present in the database. It is typically employed in the proposed model by the ride-sharing companies to detect the face of the drivers based on a dataset of recognized faces. The input image is first captured through webcam, and the algorithm then measures various facial features known as nodal points or landmarks on the face. These could include depth of eye sockets, distance between the nose and chin, and distance between the two eyes or nose. Each program measures the facial features or nodal points extracted, and the data obtained is then converted into a mathematical formula that corresponds a unique facial signature [2]. The signature obtained is then compared to a database of known faces, and all these take place in a matter of seconds. Hence, this technology is a highly efficient and reliable biometric tool. The present pandemic situation has made everyone aware about the significance of wearing masks and maintaining social distance [3]. The virus can spread through respiratory droplets generated from an infected person while coughing, speaking, or sneezing, and the virus remains viable turning the immediate environment of an infected person into a source of transmission. However, in rideshares, it becomes impossible to maintain proper social distance, hence comes the necessity to wear masks to prevent any infection caused due to the virus. The proposed web application consists of a mask detector model trained using convolutional neural networks with a very high accuracy. In case the driver does not wear any mask, an email alert is sent immediately to the company and driver so that appropriate action could be taken [4]. The National Highway Traffic Safety Administration reported that per annum about 100,000 car crashes that happen involves drowsy or fatigue driving [5]. It becomes necessary for ride-sharing companies to take appropriate measures to prevent such accidents from happening and ensure the best customer service. Hence, in the proposed web application, a facial landmark detection algorithm is implemented by using a pre-trained model trained on iBUG dataset which calculates eye aspect ratio to detect whether the driver is drowsy or not. In case found drowsy, again an email alert is sent to the company and driver. In case of any accidents or emergency, it becomes necessary for the ride-sharing companies to stay updated about the vehicle so that immediate

actions can be taken if required. Real-time tracking is also important in terms of security as companies can easily track the vehicle in case of any vehicle thefts [6]. Global Positioning System helps to keep a real-time track of the exact position of the vehicle and helps the company to monitor the route of the rideshare [7].

2 Literature Survey

Face recognition has been around for decades. However, recent years have seen more widespread adoption of this technique as it has a faster processing time and higher accuracy. Most of the face recognition designs depend on two major modules; namely, feature extraction and the classification can be done by several techniques like using HOG for extraction and SVM for classification. For higher accuracy, CNN is used for the training [8]. Face recognition is also useful in curriculum learning. It is a type of learning in which the difficulty of solving a task keeps on increasing and is inspired by the fact that humans can solve easy problems first and then followed by more sophisticated ones. The CL algorithm proposed in [9] divides the images of the faces that need to be trained into smaller subsets based on the head pose angle obtained from the absolute sum of the raw, pitch, and yaw angles. These subsets obtained are fed to deep CNN in order of increasing difficulty. This algorithm improves the accuracy of face recognition to a large extent. Iris and face recognitions are the most advanced and accurate biometric recognitions that are being adopted all over the world to prevent crimes, enhance security, and create better service for customers as these technologies can identify a person accurately without the need for any physical ID. In [10], some approaches are stated which give a lesser processing time for iris and face recognitions by implementing the deep CNN algorithms. The approaches include transfer learning using VGG16 and VGG19. In [11], the outputs of two different artificial neural networks, namely principal component analysis and artificial neural network (PCA–ANN) and linear discriminant analysis (LDA–ANN), are combined to generate a hybrid output which enhances the accuracy. Feature extraction is done using edge detectors, and the final result has been combined using the logical OR operation. Due to the current pandemic situation, safety precautions have become the first priority for any ride-sharing company. COVID-19 causes acute respiratory disease and can be spread easily via droplets while sneezing, coughing, or speaking. Hence, wearing masks has been made mandatory by World Health Organization (WHO) in all public places. In [12], a deep learning technique has been used to distinguish people wearing a mask from those without wearing one. A Raspberry Pi-based face mask detection model is developed with an alarm system for people detected without wearing a mask. The open-source neural network library, namely Keras running on top of TensorFlow, can be used for implementing and training the datasets with a faster processing speed and accuracy [13]. The majority of accidents caused each year is due to drink and drive. Ride-sharing companies require a constant monitoring system to check whether the driver is drowsy or not. A similar model has been proposed in [14] where the facial landmarks of the person's image are detected, mainly the eye

coordinates using the Dlib library, and the eye aspect ratio along with the eye closure ratio is calculated to detect whether the person is drowsy or not based on a certain threshold value. Driver's facial expressions can also be used to detect whether he is drowsy or not [15]. The driver's face, eyes, and mouth regions are tracked, and the threshold values obtained from the extracted features of the eye region are combined with that of mouth region and head pose angle. The iterated function system (IFS) algorithm has been used for selecting the best extracted features that could be utilized for classification, and SVM classifier has been used to classify the various stages of drowsiness. The result obtained shows that the efficiency is increased from 84 to 88% as compared to the existing systems. Using convolutional neural networks, a non-intrusive algorithm is developed for driver drowsiness detection based on his yawning behavior [16]. The VGG16 architecture is modified to include other features like using ReLU as an activation function for intermediate layers, sigmoid as the activation function for final dense layers, and normalization of the batch. The yawning detection dataset (YAWDD) has been used, and the method is more accurate than many of the existing algorithms. GPS is widely used all over the world to track the position of the objects in real time. It is necessary for ride-sharing companies to monitor the route of the vehicles. In [17], a similar model is proposed using various technologies like General Packet Radio Service (GPRS), Global System for Mobile Communications (GSM), GPS, and Internet where the real-time location and ground speed of the vehicle are acquired. Also, limits are set for speed, and SMS alerts are sent in case the pre-defined limits are exceeded. The vehicle is monitored for all its stops and movements. The intelligent vehicle monitoring system is also proposed using GPS/GSM technologies [18]. The key technologies that have been used are communication, Geographic Information System (GIS), and wireless positioning. This model can effectively curb thefts of vehicle or vehicle hijacking. A similar model has been proposed in [19] using GSM/GPS technologies; however, Internet of things has been utilized here. Internet of things (IoT) has become a widely popular technology nowadays, and many prospects are arising based on IoT.

3 System Model

3.1 Flowcharts

3.2 Datasets Used

For face recognition of the driver, a dataset of all known recognized faces is taken for the training process. For face mask detection of the driver, a Kaggle dataset of 1900 images is taken for each of the two categories "with mask" with images of faces wearing masks and "without mask" for images of faces without wearing any masks is taken for the training process. For the drowsiness detection of the driver, shape predictor 68 face landmarks.dat is used which is a pre-trained dataset created by

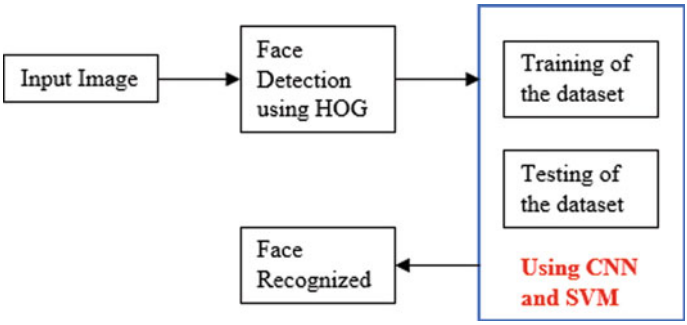

Fig. 1 Face recognition of driver

iBUG. Then, it has been used by Dlib to recognize facial landmarks for drowsiness detection.

3.3 Face Recognition

In Fig. 1, the face is first being detected from the webcam using the histogram of oriented gradients method. Post-face detection, it is sent for the training process using deep convolutional neural networks. The encoding of the image takes place, and the network automatically trains itself to generate 128 measurements of the face. For the classification of the image, a linear SVM classifier has been used to find the closest match of the image from the database of known faces provided. The training of the model happens in a few seconds, and the result obtained is the name of the person which has the closest match with the one present in the database.

3.4 Face Mask Detection

Figure 2 shows the face mask detection flowchart, and Fig. 3 shows the driver drowsiness detection flowchart. In Fig. 2, data preprocessing is done first in which all the images of the dataset are converted into arrays which would be used for training. The images are loaded using the Keras preprocessing methods. Then, they are appended to lists. Along with the list, corresponding labels "with mask" and "without mask" are fed. Then, the data is tested and trained. About 20% of data is given for testing and the remaining 80% for the training. The modeling part is done by the convolutional neural network but instead of that MobileNet is used as it is faster and more accurate. Two models, the base model and head model, are used where the base model is ImageNet which contains some pre-trained models specifically for images. The layers are then flattened and added with an activation layer called rectified linear

units (ReLU). The graph is plotted between epochs and loss/accuracy, and they are the x and y axes, respectively, as shown in Fig. 4.

After the mask detector model is obtained, a face detector model is required for which a couple of pre-trained face detector files are loaded into the code. The function "detect_predict_mask" takes the input arguments—FaceNet which has the two face detector files, MaskNet which has the trained mask detector model, and frame for capturing the real-time video input. Based on region of interest, the facial features are extracted, the face is detected, and accuracy of wearing a mask is also labeled along with the rectangular frame.

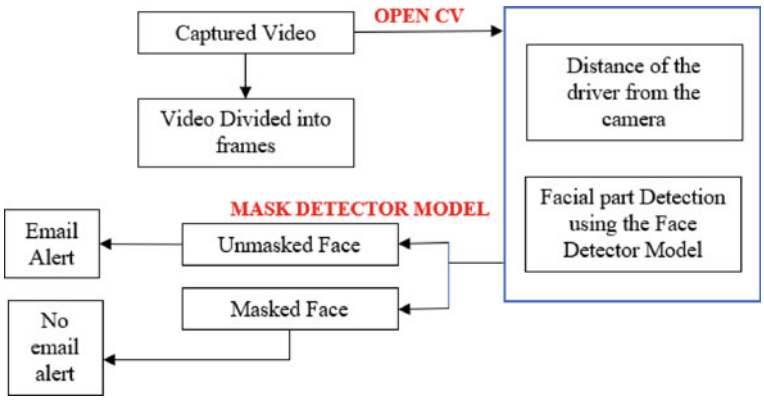

Fig. 2 Face mask detection of the driver

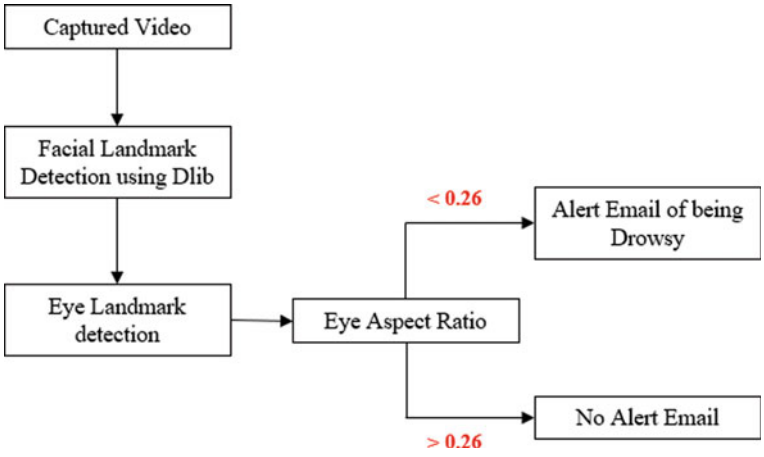

Fig. 3 Driver drowsiness detection

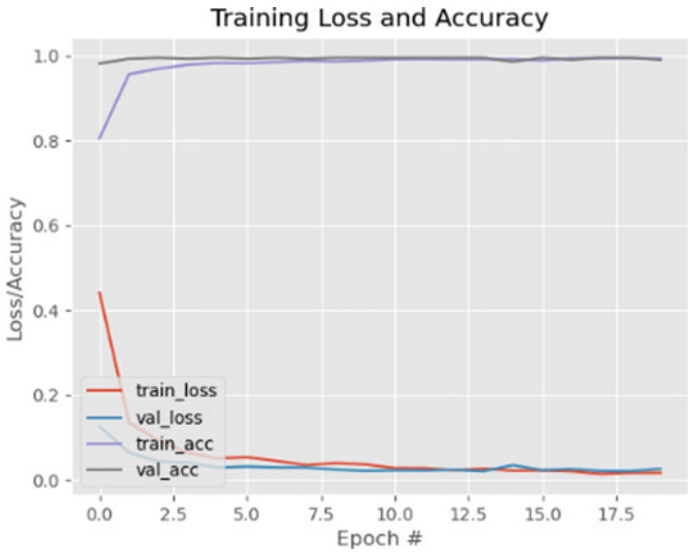

Fig. 4 Training versus test loss and accuracy

3.5 Drowsiness Detection

In Fig. 3, the pre-trained library of Python called Dlib is used for facial landmark detection. Sixty-eight facial landmark coordinates were estimated using this library, and it was trained on the iBUG dataset which is an open-source dataset containing 600 images of different facial annotations. The indexes of the 68 coordinates are denoted in Fig. 5. The coordinates help to detect locations of different facial features as every facial feature, e.g., nose, eyes, ears, etc., will have unique index values.

The detected face from the webcam is passed into the shape predictor model which extracts all the 68 facial coordinates of the input image. After the 68 facial

Fig. 5 Sixty-eight facial landmark coordinates from iBUG dataset

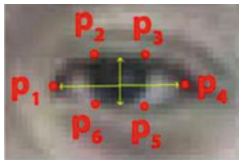

Fig. 6 Landmarks of the eye for calculating EAR

landmarks are initialized, the landmark coordinates depicting the left eye from 37 to 42 and right eye from 43 to 48 are obtained to calculate the Euclidean distances. The eye aspect ratio (EAR) is then calculated for each of the eyes. EAR is the ratio of the height to the width of the eye and is calculated by the formula given by Eq. 1.

$$\text{EAR} = \frac{(|p2 - p6| + |p3 - p5|)}{2 * |p1 - p4|} \tag{1}$$

The details of the eye landmarks are depicted in Fig. 6.

The numerator of the EAR ratio depicts the vertical distance or the height of the eye, while the denominator depicts the horizontal distance or the width of the eye. When the eye is open, the vertical distance is maximum so the EAR increases, and when the eye is closed, the vertical distance decreases thus decreasing the EAR value. The threshold value of the EAR is found out to be 0.26 [14] upon closing the eyes while 0.30 with the eyes completely open. If the EAR goes below 0.26, the driver is depicted to be sleepy or drowsy.

3.6 Web Application

The web application developed acts as the display device for the proposed model. Python has been for the server-side programming by importing flask for the back end. The client-side programming has been coded using JavaScript, HTML, and CSS for developing the front end of the application. The api.py created connects the back-end server to the front-end server for the application to run smoothly. The front end of the web application is depicted in Fig. 7.

3.7 Hardware Implementation

The flowchart of the hardware implementation for the real-time location tracking of the vehicle is shown in Fig. 8.

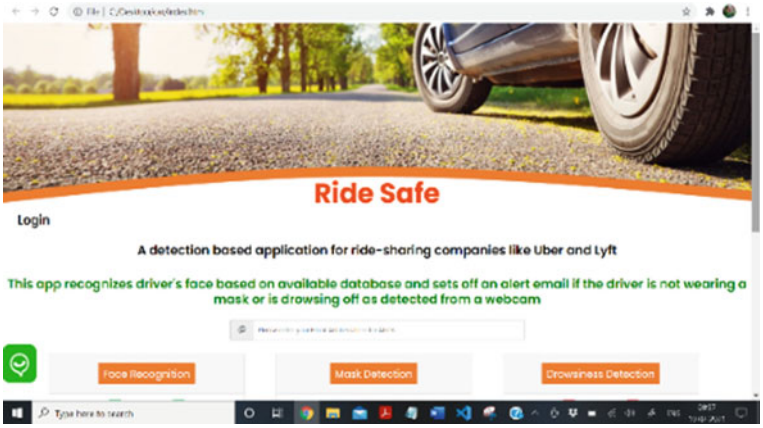

Fig. 7 Front end of the web application

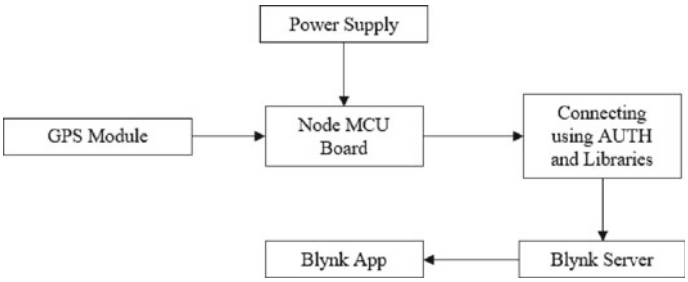

Fig. 8 Hardware implementation

4 Results and Discussions

In Fig. 9, the face of the person is detected from a live webcam. The rectangular frame around the detected face is drawn based on the (x, y) coordinates of the detected face or the face location. The name of the person with the closest match from the database of known faces is displayed below the frame. In case the face is not recognized, "Unknown" is displayed below the frame. The frame is displayed in green for the known face while red for the unknown.

The face mask is being detected from the live webcam with an accuracy of 99% in Fig. 10. The face mask detector model was obtained after training the Kaggle datasets for two hours. Again, the rectangular frame was drawn based on the coordinates of the face location.

The eye landmark detection takes place which detects whether the driver is drowsy or not. In Fig. 11, the eye aspect ratio is around 0.30 which is above the threshold; hence, the driver is not drowsy.

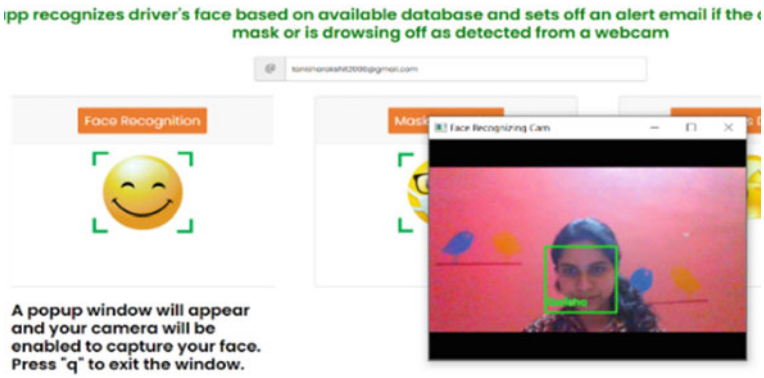

Fig. 9 Face is detected from live webcam

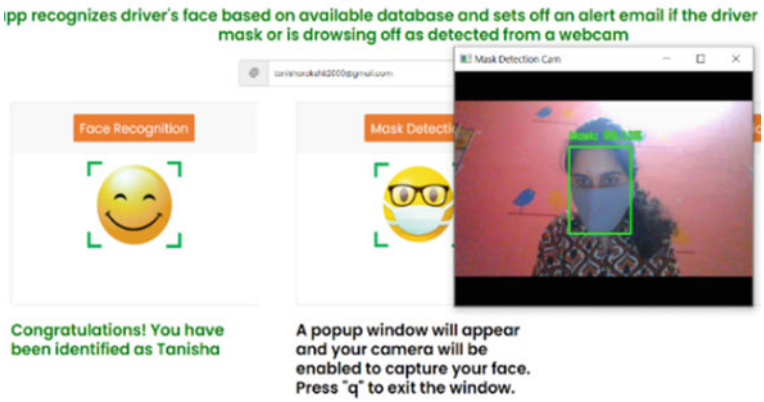

Fig. 10 Face mask is detected

In Fig. 12, the message is displayed that the driver has been following the medical guidelines of wearing a mask and that the driver is careful and is responsible. No email alert is sent to the mail ID.

In Fig. 13, face mask is not detected with an accuracy of 99.54%.

The driver is drowsy with an eye aspect ratio lesser than the threshold of 0.26 as depicted in Fig. 14. The message of being drowsy is also displayed along with the eye landmark detection via the webcam.

An email alert is sent immediately to the mail id of the driver and company as shown in Fig. 15 for both the cases, where the face mask of the driver is not detected and the driver is drowsy. It can be sent simply by mentioning the email id wherein the alert needs to be sent by mentioning it in the web application.

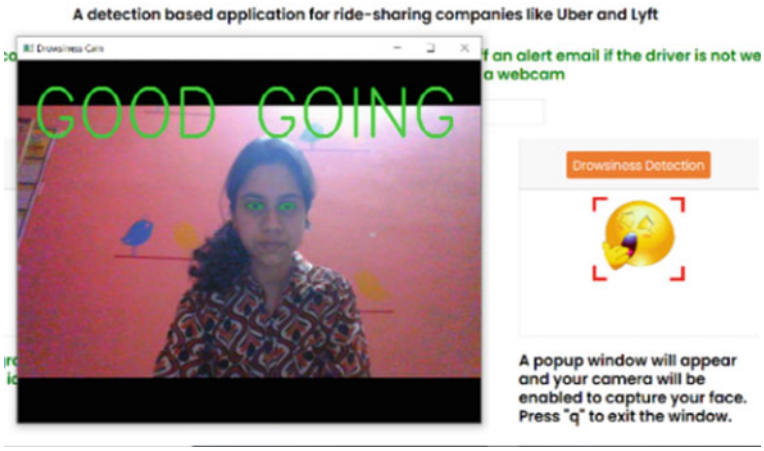

Fig. 11 Eye landmark detection

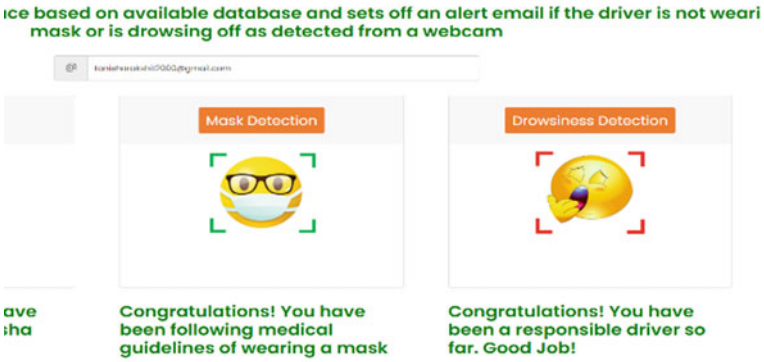

Fig. 12 Message is displayed on web app

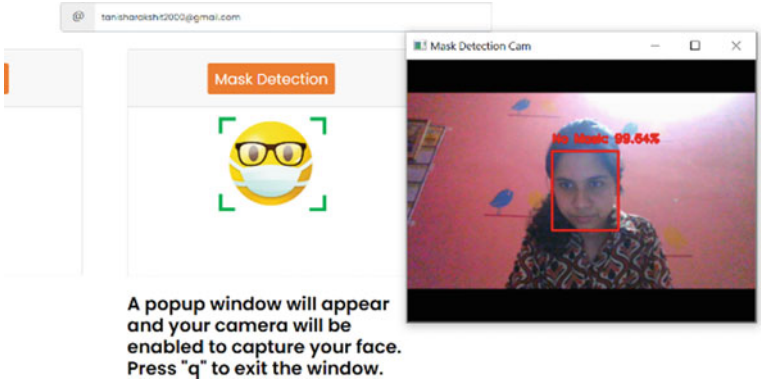

Fig. 13 Face mask is not detected

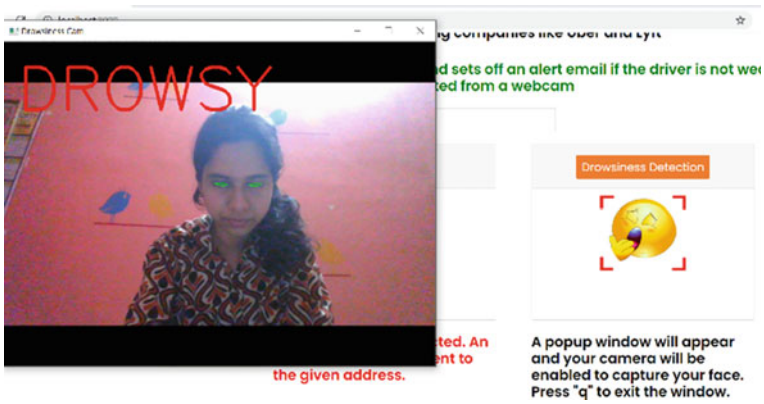

Fig. 14 The user is drowsy

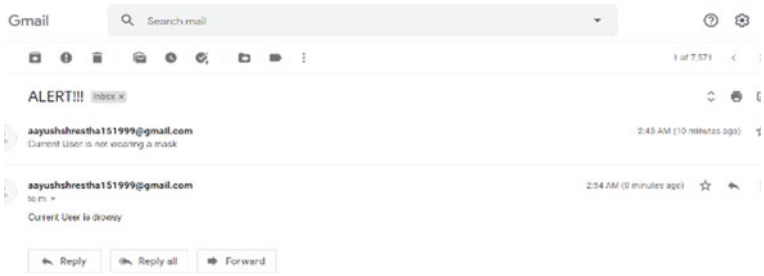

Fig. 15 Alert email is sent

Figure 16 shows the hardware setup. The imported Blynk libraries and the authentication token help to connect the Node MCU with the server. The coordinates of latitude and longitude of the cab are displayed on the serial monitor at a baud rate of 115,200 once the client connection is established with Blynk's IP address.

Figure 17 depicts that the real-time location is being tracked on Google Maps using the Blynk app so that the company can easily monitor the rideshare. Along with latitude and longitude, other parameters like direction, speed, and number of satellites are also being displayed in the widgets or buttons that have been created on the dashboard. The comparative study of the proposed model with the existing literature is depicted in Table 1.

5 Conclusion

The novelty of the proposed application is that it tracks the current, live status of the driver; that is, it makes certain that the driver wears his mask and is alert all the time.

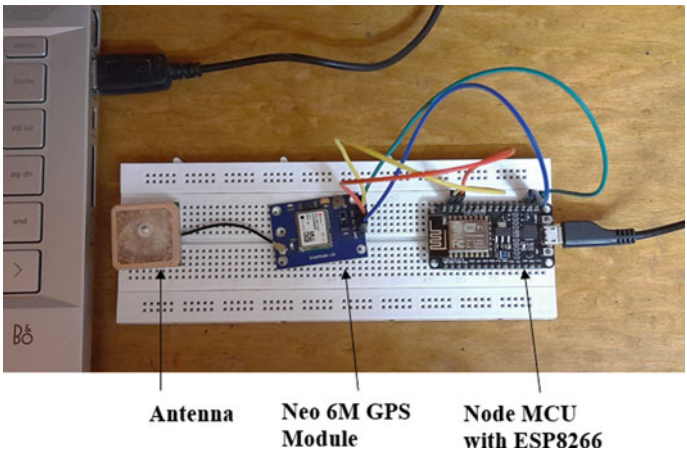

Fig. 16 Hardware setup of the proposed model

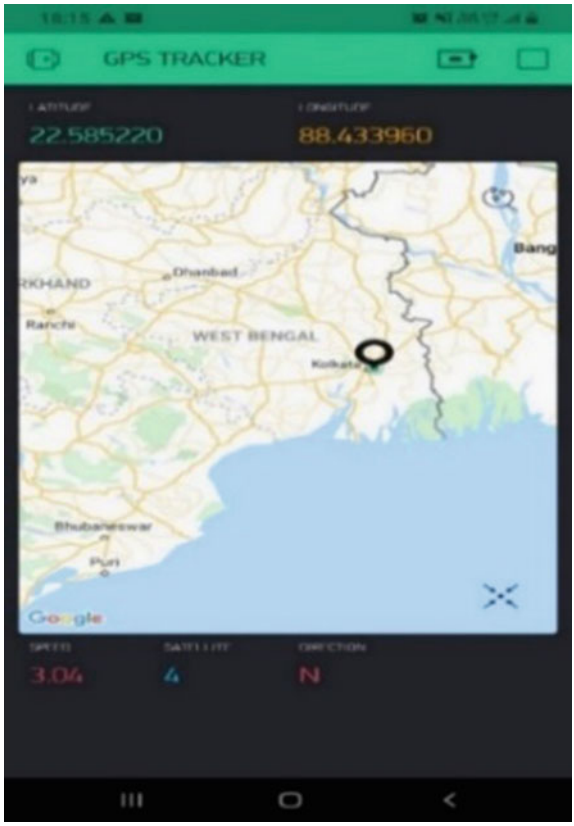

Fig. 17 Location being tracked on Google Maps

Table 1 Comparative study of the proposed model with the existing literature

S. No.	Title	Proposed model	Comparison
1	Design and evaluation of a real-time face recognition system using convolutional neural networks [8]	Trained on a dataset of recognized faces using convolutional neural networks and SVM classifier, and the model is integrated on a web app	Trained on AT&T datasets using convolutional neural networks. Maximum recognition accuracies obtained were 98.75 and 98%
2	Real-time face mask recognition with alarm system using deep learning [12]	The dataset is taken from Kaggle with 1900 images of persons with mask and without mask and trained for over two hours to get an accuracy of 99%. An email alert is sent in case mask is not detected	The dataset was trained on 26,000 images and achieved an accuracy of 96%. The system develops a Raspberry-Pi based real-time face mask recognition that alarms and captures the facial image if the person detected is wearing a mask or not
3	A novel approach for detection of driver drowsiness using behavioral measures [15]	Detected driver drowsiness from the eye aspect ratio with an accuracy of 100%, wearing glasses and without wearing glasses. An email alert is sent in case driver is drowsy	Detects drowsiness from facial features extracted from mouth, eyes, and head and then passing it through the IFS algorithm and SVM classifier

In the other available applications in the market, the mask and drowsiness detection takes place only at the commencement of the ride. The model has been trained using novel deep learning algorithms like CNN, SVM, and HOG to give a higher accuracy in the output. Integrating the model with IoT has also made the real-time application of the model quite easy for the present COVID-19 pandemic situation. The application will be extremely useful to the ride-sharing companies as it will help them to imbibe trust in the passengers and maintain a standard customer service. The web application has been successfully implemented using specific modules, libraries of Python, and growing technologies like IoT, AI, and deep learning.

Conflict of Interest On behalf of all authors, the corresponding author states that there is no conflict of interest.

References

1. Diaz YM (2021) Benchmarking lightweight face architectures on specific face recognition scenarios. Springer. https://doi.org/10.1007/s10462-021-09974-2
2. Fredj HB (2020) Face recognition in unconstrained environment with CNN. Springer. https://doi.org/10.1007/s00371-020-01794-9

3. Loey M (2020) A hybrid deep transfer learning model with machine learning methods for face mask detection in the era of the COVID-19 pandemic. ScienceDirect. https://doi.org/10.1016/j.measurement.2020.108288
4. Nieto-Rodriguez A (2015) System for medical mask detection in the operating room through facial attributes. Springer. https://doi.org/10.1007/978-3-319-19390-8_16
5. Aulia S (2021) Comparison of different classifiers for drowsiness detection based on facial expression recognition. Springer. http://jonuns.com/index.php/journal/article/view/494
6. Galarza EE (2018) Real time driver drowsiness detection based on driver's face image behaviour using a system of human computer interaction implemented in a smartphone. In: International conference on information technology and systems. Springer. https://doi.org/10.1007/978-3-319-73450-7_53
7. Adardour HE (2020) Outdoor Alzheimer's patients tracking using an IoT system and Kalman filter estimator. Springer. https://doi.org/10.1007/s11277-020-07713-4
8. Pranav KB, Manikandan J (2020) Design and evaluation of a real time face recognition system using convolutional neural networks. In: Third international conference on computing and network communications. ScienceDirect
9. Büyüktaş B (2020) Curriculum learning for face recognition. In: 2020 28th European signal processing conference (EUSIPCO). IEEE Explore. https://doi.org/10.23919/Eusipco47968.2020.9287639
10. Muthazhagan B. Ameliorated face and iris recognition using deep convolutional networks. Springer. https://doi.org/10.1007/978-3-030-57024-8
11. Sarkar SD (2020) Face recognition using artificial neural network and feature extraction. In: 2020 7th international conference on signal processing and integrated networks (SPIN). https://doi.org/10.1109/SPIN48934.2020.9071378
12. Militante SV (2020) Real-time facemask recognition with alarm system using deep learning. In: 2020 11th IEEE control and system graduate research colloquium. https://doi.org/10.1109/ICSGRC49013.2020.9232610
13. Pooja S (2021) Face mask detection using AI. Springer. https://doi.org/10.1007/978-981-33-4236-1_16
14. Mehta S (2019) Real-time driver drowsiness detection system using eye aspect ratio and eye closure ratio. In: International conference on sustainable computing in science, technology and management
15. Venkata Subbaiah D (2021) A novel approach for detection of driver drowsiness using behavioural measures. Springer. https://doi.org/10.1007/978-981-15-5397-4_41
16. Sreelakshmi KK (2020) A non-invasive approach for driver drowsiness detection using convolutional neural networks. Springer. https://doi.org/10.1007/978-981-15-5788-0_13
17. Almomani IM (2011) Ubiquitous GPS vehicle tracking and management system. IEEE. https://doi.org/10.1109/AEECT.2011.6132526
18. Liu Q (2006) Research and design of intelligent vehicle monitoring system based on GPS/GSM. In: 2006 6th international conference on ITS telecommunications. https://doi.org/10.1109/ITST.2006.288858
19. Mangla N (2017) A GPS-GSM predicated vehicle tracking system, monitored in a mobile app based on Google Maps. In: 2017 international conference on energy, communication, data analytics and soft computing (ICECDS). IEEE. https://doi.org/10.1109/ICECDS.2017.8389989

Kabaddi: A Quantitative Approach to Machine Learning Model in Pro Kabaddi

Pratima Singh, Binayak Parashar, Samarth Agrawal, Krishnay Mudgal, and Pranjali Singh

Abstract The purpose of this study was to analyse the performance of competing teams in the Pro Kabaddi League and predict their chances of winning in the upcoming seasons. Pro Kabaddi League is a professional league played in India every year (except in 2020) since 2014. Kabaddi is a contact sport originated in India which is quite rigorous and tactical. Thus, there is a lot of scope for analytical research in this sport. This paper delivers a profound analysis of every team participating in the Pro Kabaddi League over the past seven seasons. To conduct this research all data and related statistics were gathered from the official website of the Pro Kabaddi League. The dataset is curated manually and contains more than 25 variables. This study develops a quantitative approach towards predefined tactics of attack and defence to expand our understanding of the strengths and weaknesses of each team. The analysis is expected to help alleviate the burden of the investors while also assisting them in choosing reasonable strategies for winning their matches. This paper leverages an ensemble of machine learning algorithms for forecasting the tournament result. The paper delivers multiple models to predict tournament winners. Logistic regression (LR), decision tree (DT), k-nearest neighbour (KNN), support vector machine kernel linear (svmKerLin) and kernel radial (svmKerRad) and neural network algorithms are included in this research. This will help in better prediction and more investments in the Pro Kabaddi tournament. Another purpose of this paper is to develop a model which helps in better prediction techniques, thereby serving as a stepping stone for deeper analysis in the future for similar problems. This research aims to find

P. Singh (✉) · B. Parashar · S. Agrawal · K. Mudgal
Department of CSE, Ajay Kumar Garg Engineering College, Ghaziabad, Uttar Pradesh, India
e-mail: singhpratima.15@gmail.com

B. Parashar
e-mail: parasharbinayak@akgec.ac.in

S. Agrawal
e-mail: Samarth2012037@akgec.ac.in

P. Singh
Department of CSE, Banasthali University, Rajasthan, India

S. Rawat et al. (eds.), *Proceedings of Second International Conference on Computational Electronics for Wireless Communications*, Lecture Notes in Networks and Systems 554,
https://doi.org/10.1007/978-981-19-6661-3_22

a correlation between pre-established hypotheses and the results achieved through decision-making algorithms to plot real-time winning predictions of the game.

Keywords Kabaddi · Pro kabaddi · Machine learning · Algorithms · Sport · Raids and tackles · Correlation · Tournament · Analytics

Abbreviations

BB	Bengaluru Bulls
BW	Bengal Warriors
DD	Dabangg Delhi
defPtsPerMat	Defence points per match
DT	Decision Tree
GG	Gujrat Giants
HS	Haryana Steelers
JPP	Jaipur Pink Panthers
KNN	K-nearest neighbour algorithm
LR	Logistic Regression
NN	Neural network algorithm
PPR	Patna Pirates
PPL	Puneri Paltan
svmKerRad	Support vector machine kernel radial algorithm
svmKerLin	Support vector machine kernel linear algorithm
TTL	Tamil Thalaivas
TTI	Telugu Titans
UM	U Mumba
UPY	UP Yodha

1 Introduction

Kabaddi is a very intensive and tactical contact team sport that has great passion in India. Lots of kabaddi tournaments are played both domestic and international but there has not been significant analysis of the latest data. To give a little insight into Kabaddi rules, this game is played between two teams of seven players; the objective of the game is to go into the opposing team's half-court, touch as many of defending team members as possible, and return to own half-court without getting tackled by the defenders. Points are given for each player tagged by the raider, while the defending team gets a point for stopping the raider. Players have to discontinue the game once they get tackled or tagged by the opposing team but can be brought back if a team scores a point by tackle or raid. This research focuses primarily on

the Pro Kabaddi League [1–9] which is a professional Kabaddi tournament which is been held annually in India since 2014. This paper provides a deep insight into the performance of the teams that participate in this professional tournament.

The dataset that is used to analyse is curated by collecting all the previous season's statistics from season 1 to season 7 available at the official Pro Kabaddi League website [10–13] to ensure the validity and credibility of the data taken. Overall, the dataset used spans more than 600 matches played by 12 different teams. The foremost goal of this paper is to forecast the tournament winner. The upcoming content in the paper consist of following sections: Similar to any data analysis based experiment Sect. 2 handles the pre-processing Kabaddi Matches data of all the past season's statistics from season 1 to season 7 available at the official Pro Kabaddi League website. Section 2 consists of the basic cleaning/ Treatment of the Data for analysis purpose, Sect. 3 consist of steps taken for further exploratory data analysis of the Same.). Section 4 consists of applying several machine learning algorithm such as KNN, logistic regression, decision tree, and SVM to predict the different winning and losing chances in the game. Section 5 consists of model building step of prediction followed by result analysis/discussion in Sect. 6 and Conclusion in Sect. 7 of the paper.

2 Data Set Preparation

A collection of data, usually denoted in tabular format, with columns depicting dissimilar variables and rows denoting different instances of the set is called a dataset. Preparing the dataset is an essential process as it determines the outcome of the model developed utilizing it and it is the core of any analytics. The dataset should always be prepared by keeping in mind the target variable and choosing correct features according to it. Our main objective in curating this dataset is to discover all such attributes that could act as a deciding factor in forecasting the result of the upcoming seasons. The dataset is constructed by collecting all the past season's statistics from season 1 to season 7 available at the official Pro Kabaddi League website to ensure the validity and credibility of the data taken. Thus, the data prepared eventually is mostly quantitative with more than six hundred matches played till now. The data set includes separate features showing the attack and defence performances of each team over the past seasons. It includes the data of the total number of raids, number of successful raids, number of unsuccessful raids, number of empty raids, total number of tackles and number of successful and unsuccessful tackles. The dataset also includes match-winning factors like the total number of super raids and the points earned by it to individual teams, similarly, the dataset also includes the total number of super tackles and the total all-out points of each team. It includes the data of total number of raids, number of successful raids, number of unsuccessful raids, number of empty raids, total number of tackles and number of successful and unsuccessful tackles. The dataset also includes match winning factors like the total number of super raids

and the points earn by it to individual teams, similarly, dataset also includes the total number of super tackles and the total all-out points of each team.

The result of a season depends solely on the outcome of each match. Therefore, those attributes have been added that determine the performance of each team in every match played by them. Accordingly, 11 more attributes have been added in the post-processing phase to increase the accuracy of the model. Target variable (tournament wins) is added that takes input as 1's and 0's. 1 represents at least one win in all the past seasons and 0 is denoted for those teams which have not been able to win any past tournaments.

3 Descriptive Analysis

Descriptive analytics is a statistical method that is applied to search and recapitulate pre-recorded data to recognize patterns or meanings. Data virtualization and illustrative statistics are the two major tools that help to visualize and resonate with the data more efficiently. We have used different attributes and features relative to each team to deduce preferable correlations like:

Matches.
Wins.
Draws.
Losses.
Total Raids.
Successful Raids.
Unsuccessful Raids.
Empty Raids.
Number of Super Raids.
Total raid points.
Total Tackles.
Successful Tackles.
Unsuccessful Tackles.
Super Tackles.
Total All Out Tackles.
Total Defence Points.
Tournament Wins.

These attributes make our dataset consistent and hence improving the accuracy of the model. To achieve better accuracy some more attributes have been inculcated in the data set like raids attempted per match, raid points earn per match, Unsuccessful raids per match, defence points per match, super raids per match, match win probability, match draw probability, losing probability, raid success probability, tackles success probability and super tackles probability (Figs. 1 and 2; Table 1).

From the above figures and graphs, it's evident that team Patna Pirates are performing consistently well in the Pro Kabaddi League since past seasons as they

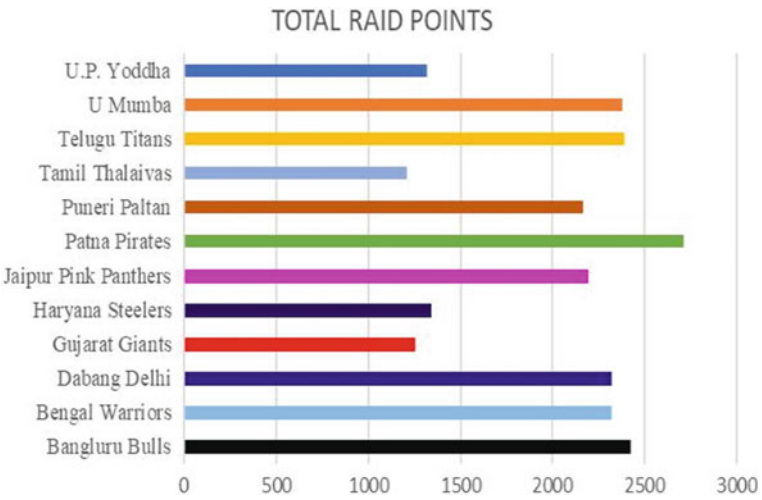

Fig. 1 Total raid points by each team

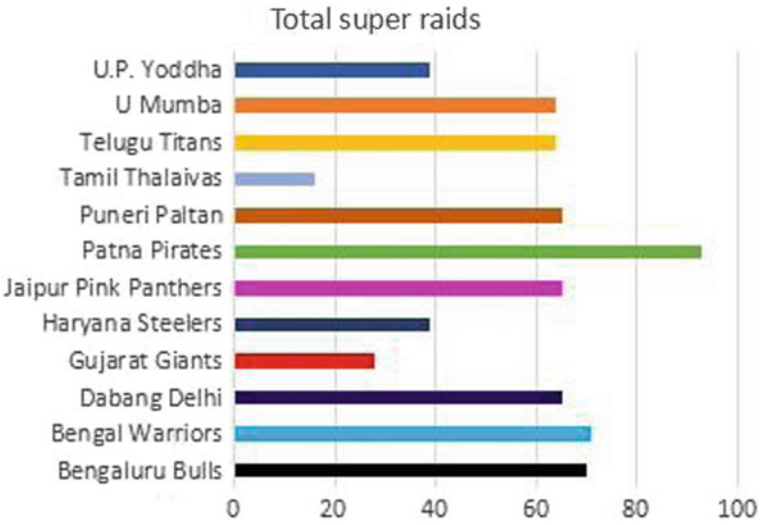

Fig. 2 Total Super raids by each team

have scored higher raid points than other competing teams which proves why they are three-time champions in the tournament. Teams like U. P. Yodha, Tamil Thalaivas, Haryana Steelers and Gujarat Giants [14–18] have participated in the Pro Kabaddi League [19–21] much late in 2017 thus their raid points and the total number of raids are comparatively less. Descriptive analytics provides obligatory understandings into the performance of the sport at the cumulative level and the team level.

Table 1 Descriptive statistics of essential variables

Variables	Mean	Std.	Min.	Max.
Wins	49.25	17.970304	15	81
Total all out points	260.166667	88.109	108	398
No. of super raids	56.583	21.572	16	93
Total raid points	2002.75	550.75	1207	2712
Successful raids	1596.41	428.36	1003	2129
Matches	108.83	29.53	66	134
Total raids	4643.5	1240.96	2866	5774
Successful tackles	962.5	260.306	535	1264
Empty raids	1999.83	553.2	1193	2466

It similarly supports constructing analytical models by providing dependent variable attributes.

4 Methodology

The methodology is the explicit technique used to recognize, choose, process, and examine information about a topic. This model predicts the winning outcome of each team in a season by implementing supervised learning. At the start of the model building process, the data is segregated into two parts. The first 50% of data is utilized in training and building the model and the remaining 50% is employed in testing the model to check the ultimate accuracy (Table 2).

Understanding the variables and their implied meaning is a necessary first step in building models. This process is known as feature engineering. To execute this process deeper understanding and profound knowledge is required about the domain under research.

The dataset is curated by manual scripting of overall team performances over the past seasons from the official website of Pro Kabaddi League. The tournament win attribute is created manually portraying the past winners as 1 and others as 0. The dataset used has over 25 features which appreciably impacts the result of the tournament. As the data was manually scripted there were negligible outliers. To determine the independent and dependent variables in the data set, a correlation matrix is intended.

Observing the correlation of the tournament wins with other attributes, it was found that the maximum value of correlation is found to be 0.764 with wins attribute and the minimum value of the correlation of the target variable was found to be -0.489. Subsequently, whichever feature has a larger correlation with the target variable, i.e. tournament wins are as follows:

- Unsuccessful Raids

Table 2 Correlation of important variables

Features	Tournament wins	Wins	Total all out points	No. of super raids	Total raid points	Successful raids	Matches	Total raids	Successful tackles	Empty raids
Tournament wins	1	0.76	0.68	0.66	0.65	0.63	0.63	0.63	0.62	0.62
Wins	0.76	1	0.94	0.84	0.85	0.84	0.84	0.84	0.91	0.83
Total all out points	0.68	0.94	1	0.93	0.95	0.95	0.92	0.92	0.9	0.9
No. of super raids	0.66	0.84	0.93	1	0.95	0.94	0.92	0.92	0.9	0.9
Total raid points	0.65	0.85	0.95	0.95	1	1	0.98	0.98	0.95	0.96
Successful raids	0.63	0.84	0.95	0.94	1	1	0.98	0.98	0.95	0.96
Matches	0.63	0.84	0.92	0.92	0.98	0.98	1	1	0.97	1
Total raids	0.63	0.84	0.92	0.92	0.98	0.98	1	1	0.97	0.99
Successful tackles	0.62	0.91	0.95	0.9	0.95	0.95	0.97	0.97	1	0.97
Empty raids	0.62	0.83	0.9	0.9	0.96	0.96	1	0.99	0.97	1

- Total defence points
- Empty raids
- Successful tackles
- Total Raids
- Matches
- Successful Raids
- total raid points
- No. of super raids
- Total all-out points
- Wins (Figs. 3 and 4; Table 3).

As various attributes have wide-ranging values, feature scaling has been applied such that the range of all attributes should be normalized so that each feature contributes approximately respectively to the model. Feature Scaling is a method to normalize the independent features available in the data in a fixed range. It is accomplished during the data pre-processing [22–26] to handle extremely varying magnitudes or standards or units. Ignoring feature scaling can force the machine learning algorithm to consider greater values high and smaller values as the low, irrespective of the unit of the values.

As shown in Table 4, the attributes of the dataset have a wide range of values like feature total defence points has the maximum and minimum value of 582 and 1367, respectively, with a range of 785 which has been reduced from − 0.59 to 0.40. On

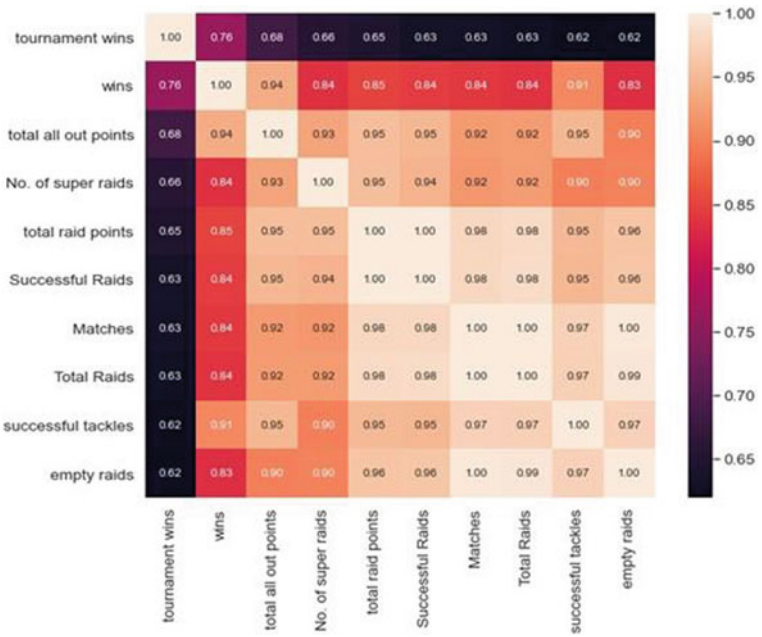

Fig. 3 Heatmap of correlation between important variables

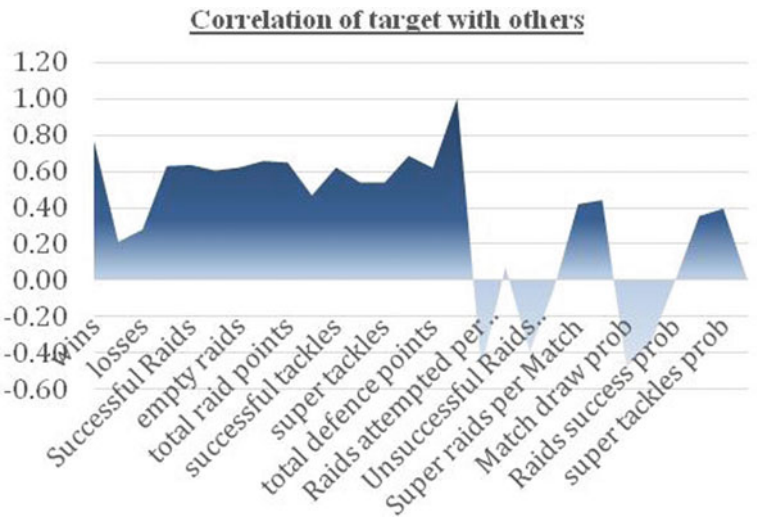

Fig. 4 Area graph of the correlation between important variables and tournament wins

Table 3 Correlation of each attribute

Attributes	Correlation
Unsuccessful raids	0.603
total defence points	0.618
Empty raids	0.619
Successful tackles	0.620
Total raids	0.627
Matches	0.633
Successful raids	0.633
Total raid points	0.647
No. of super raids	0.655
Total all out points	0.684
Wins	0.764

the other hand, the Number of super raids attribute has a lower range of values of 77 with a maximum of 93 and a minimum of 16. To represent data graphically feature scaling is implied on all the attributes of the data set leaving the target variable, i.e. tournament wins as it has discrete values 1 and 0 to represent the unbiased results of the previous seasons.

After feature scaling Table 5 is denoting a relationship between the defence points per match (defPtsPerMat), the teams and the match win probability of each team. Graph (Fig. 5) is plotted in contour mapping to represent and validate the table. It's observed from the table that the team having a match with higher defence points have a higher chance of winning.

Table 4 .

Features	Before		After		
	Min	Max	Min	Max	
Matches	66	134	− 0.63	0.37	
Wins	15	81	− 0.52	0.48	
Total raids	2866	5774	− 0.61	0.38	
Successful raids	1003	2129	− 0.53	0.47	
Unsuccessful raids	650	1301	− 0.63	0.39	
Empty raids	1193	2466	− 0.63	0.36	
No. of super raids	16	93	− 0.53	0.47	
Total raid points	1207	2712	− 0.53	0.47	
Unsuccessful tackles	847	1999	− 0.62	0.38	
Total all out points	108	398	− 0.52	0.48	
Total defence points	582	1367	− 0.59	0.40	

Table 5 Defence points and win probability of each team

Teams	defPtsPerMat	Match win prob.
BB	− 0.20	0.04
BW	− 0.41	0.03
DD	− 0.44	− 0.19
GG	0.52	0.33
HS	− 0.11	0.06
JPP	− 0.09	− 0.05
PPR	0.17	0.19
PPL	0.31	− 0.15
TTL	− 0.48	− 0.56
TTI	− 0.01	− 0.11
UM	0.43	0.44

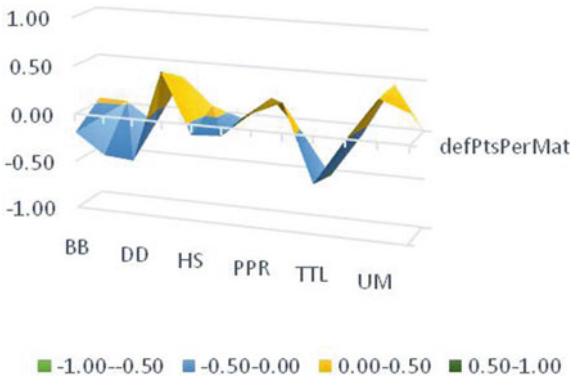

Fig. 5 Contour graph of defence points and match win probability of each team

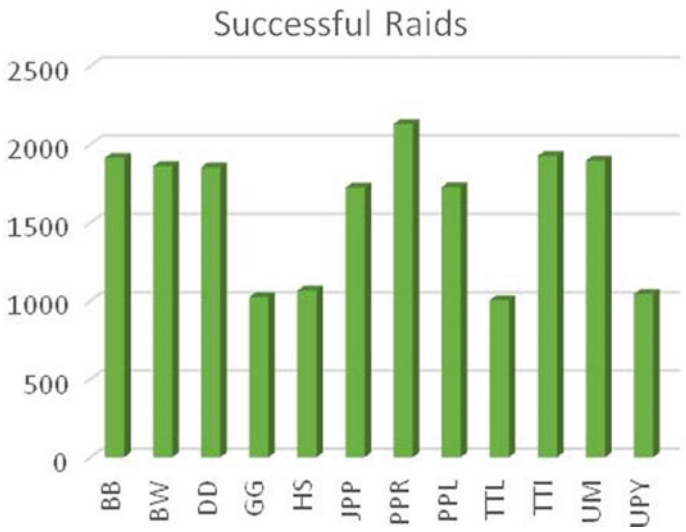

Fig. 6 Total successful raids of each team

Each team's attacks and defence has to be compared to get an improved overview of which team is playing better than others and in which department. To build a strong team in Kabaddi, it should excel in defence as well as in attack as lacking in any one of them can lead to its disadvantage. Therefore, graphs of attack and defence have been plotted to get a better aspect of each team's performance.

Graph (Fig. 6) shows the number of successful raids attempted by each team and graph (Fig. 7) demonstrate the unsuccessful raids. It is quite evident from the graph that Patna Pirates (PPR) have higher successful raids than others which proves their wins in the past seasons. Conversely, team Puneri Paltan (PPL) has the lowest successful raids and high unsuccessful raids which validates why they haven't won any seasons before.

Graph (Figs. 8 and 9) illustrates the number of successful tackles and unsuccessful tackles, respectively. Observation shows that UMumba (UM) has the maximum number of successful tackles, but Patna Pirates (PPR) [27] have maximum unsuccessful tackles. From all the above graphical representations it's quite comprehensible that Patna Pirates (PPR) [28] has the best attack and UMumba (UM) [29, 30] has the best defence. This observation also validates the hypothesis that the team that has a better attack than the opponent team has a better hand at winning.

Altogether seven models are built using a regression-based algorithm, tree-based algorithm, support vector-based algorithm, K-nearest neighbour based-algorithm, neural network-based algorithm. Tree-based algorithms like decision tree (DT) and random forest (RF) have been included. K-nearest neighbour (KNN) [30] algorithm has been used. In support vector-based algorithm Support vector machine kernel linear (svmKerLin) and support vector machine kernel radial (svmKerRad) [31, 32] have been included. Logistic regression (LR) [33–35] is also employed.

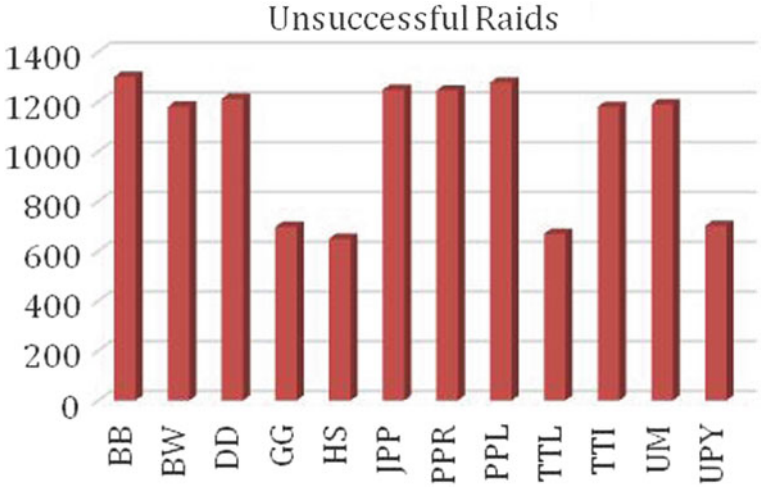

Fig. 7 Total unsuccessful raids by each team

Fig. 8 Total successful tackles by each team

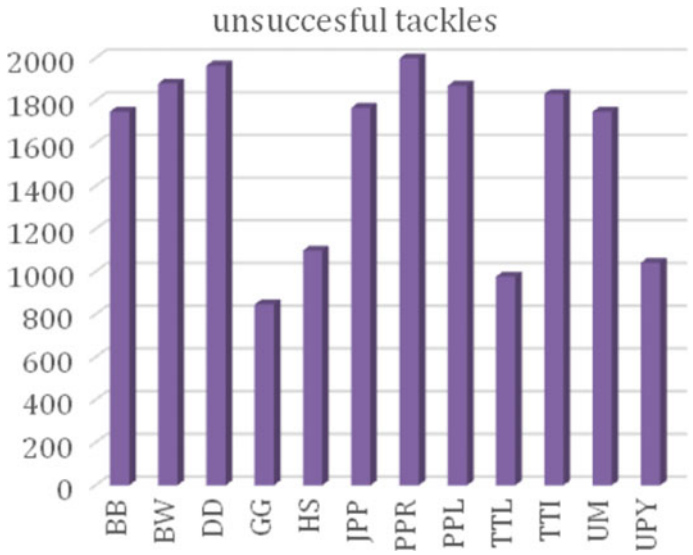

Fig. 9 Total unsuccessful tackles by each team

5 Model Building

Model building is an indispensable objective in machine learning for performing any predictions. The models are designed from the processed data such that they can provide the appropriate and precise results for future implementation. The refined and processed data set acts as a mentor for proper training of the model. The model is trained several times with different inputs to enhance its experience on the data provided for learning. Post-training, a crucial step comes which is testing. Testing determines the deviation of the outputs produced by the model from the actual outputs. To test the accuracy, the model is passed to a testing phase.

During the testing phase, the model is tested with different values as inputs that produce their results. These results are compared with the actual results to calculate the accuracy of the model. Different algorithms work with different approaches, therefore, producing different results. Therefore, various algorithms are included in the model to determine which model works best for the model under research.

The dataset provided consists of a combination of more than a hundred discrete and continuous values. The target attribute has two discrete values while the other attributes have continuous values for inputs therefore hypothetically, algorithms that work for both regression and classification problems should produce better results.

Practically, the data set in use has a combination of both regression and classification therefore to find the best fit model, the accuracies of different models are compared in this paper. The algorithms used to predict the target attributes includes random forest (RF) [30, 31] decision tree (DT), SVM kernel Linear and SVM kernel radial [32–34]. The models produced were trained on the algorithms with 50% data

to achieve better accuracy. After the training phase, all the models were tested with the remaining 50% of the data.

This paper uses two methods of spitting of data for testing, one is automatic algorithmic-based splitting and the other is manual splitting. The algorithmic-based splitting has divided the total data into two halves with a random selection of the input values on the other hand manual splitting includes the splitting of data manually. For achieving a better model, during the manual splitting process, the content is picked to make sure that the model prepared is trained and tested well.

Manual splitting has produced better results in many algorithms. It can be best explained that the data used for training was significantly good to produce a better model which is giving better results.

6 Results and Discussion

The paper consists of the different supervised learning algorithms on regression and classification. These algorithms include decision tree(DT), random forest, logistic regression, support vector machines (SVM), K-nearest neighbour linear and K-nearest neighbour radial. The comparison of the accuracies of the models is depicted in Table 6 (Fig. 10).

From Table 6 it is evident that the accuracies of the models built with manual splitting are better than automatic algorithmic splitting based models. It can be observed that tree-based models are producing better results than others. The accuracy achieved by the K-nearest neighbour algorithm is at $n = 2$, where n represents neighbour. Support vector machine (svmRadLin) generates the above accuracy at gamma (γ) = auto, where gamma is a constant value. The above two parameters are necessary to obtain maximum accuracy values (Fig. 11).

From the comparison graph (Fig. 12), it's easy to interpret that manual splitting increased the mode's accuracy. But, it doesn't affect the regression-based algorithm's outcome in this case.

Table 6 Accuracy comparison of different models in manual and algorithmic splitting

Algorithms	Accuracy	
	Manual splitting (%)	Algorithmic splitting (%)
dt	100	83.34
knn	50	66.67
svmKerRad	83.34	50.00
svmKerLin	50.00	83.34
nn	83.34	33.34
lr	50.00	50.00

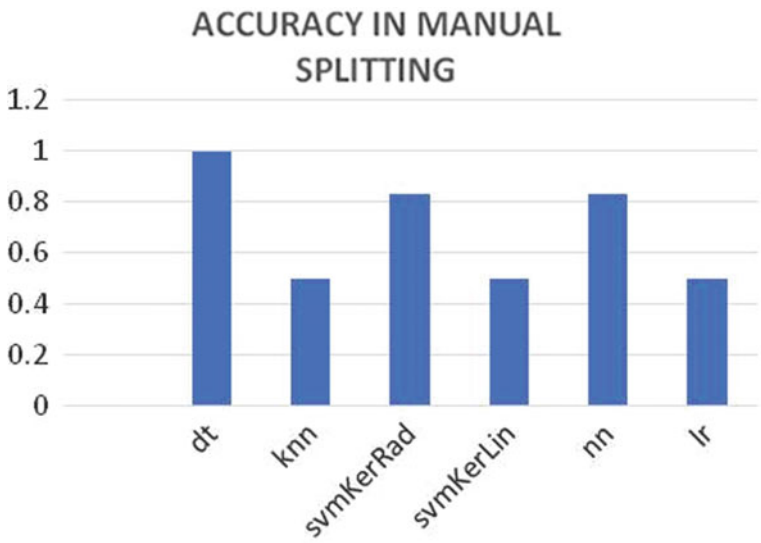

Fig. 10 Accuracy in manual splitting in all algorithms

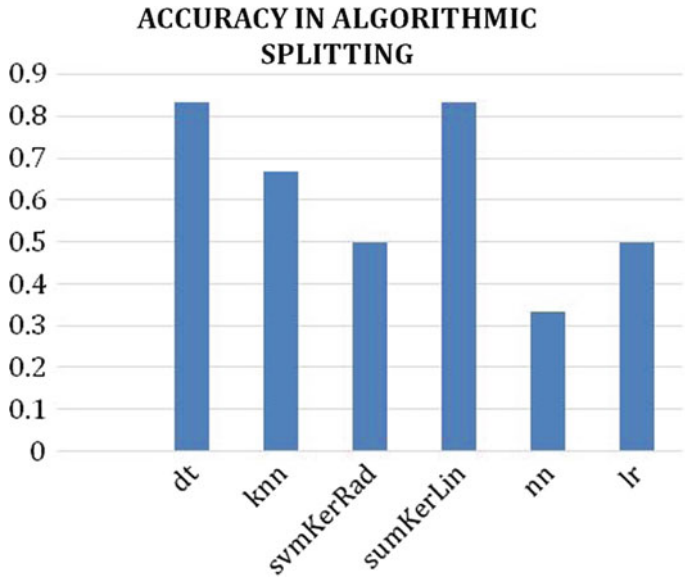

Fig. 11 Accuracy in algorithm splitting in all algorithms

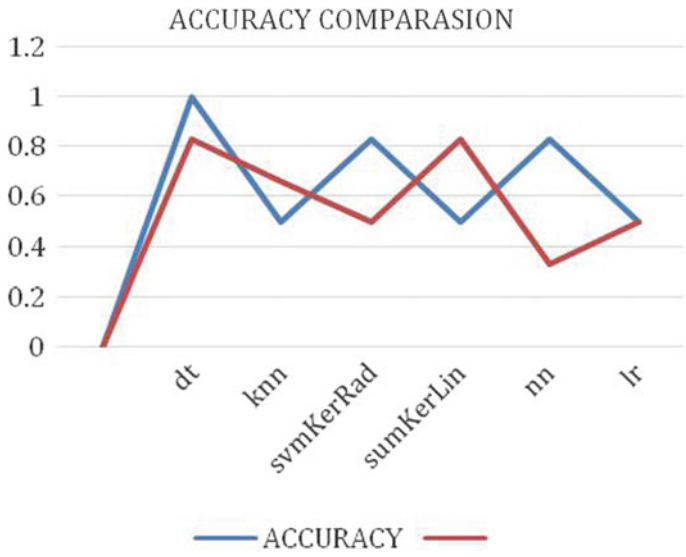

Fig. 12 Line graph of accuracy comparison in manual and algorithm splitting

It is quite understandable from the correlation Table 3 that attributes like successful raids, unsuccessful and empty raids have values of correlation 0.633, 0.619 and 0.603, respectively, which are quite analogous. From these values, it can be concluded that there is a similar degree of correlation between these attributes which contradicts the orthodox hypothesis that tournament win generally depends on the number of successful raids attempted by a team.

Another interesting result observed is that the number of super raids feature has shown the highest correlation with tournament wins which is the target variable.

As mentioned in Graph (Fig. 6) team Patna Pirates have the best attack and team U Mumba has the best defence. However, U Mumba has won only one season, conversely Patna Pirates have scored three wins which bring to our statement that a team with the better attack has a higher chance of winning than the tournament than the team with better defence.

The results and findings of this research have across-the-board insinuation in the game of kabaddi. The research provides a deeper insight into the sport of kabaddi from a quantitative outlook. This paper will serve as a stepping stone in sports analytics and will be an example for similar deep problems.

7 Conclusion

This research has covered the tournament of Pro Kabaddi League with an analytic approach. Being an inherited game of India, Kabaddi being less popular than other

sports like cricket, lacks any scientific augmentation so far. This research paper focuses on breaking all such predetermined beliefs and show that Kabaddi as a sport can improve a lot by applying analysis. The research includes proper analysis of supervised machine learning algorithms based on regression and classification models to get a crystal clear conclusion for this research. Research technique and its results are pioneering and have the prospect to bring a revolution in the future of the game. The research conducted on the Pro Kabaddi suggested that the teams should give more focus on their attacks. The research denies the myth that successful raids are more important than unsuccessful raids or empty raids as they are all found to be equally important to win a tournament. The research suggests that a strategic approach is extremely important and the old myths might not be always true.

To completely utilize the benefits of this research thorough and devoted understanding is necessary. Graphical virtualization and model prediction together with justifiable results and hypotheses are crucial takeaways that one can receive through this research paper.

Declaration

- The data has changed post-analysis.
- The data was downloaded on 27th November which consists of statistics of a total of seven seasons.
- There is no conflict of interest among the authors.
- The project is not sponsored by any entity or individual.
- No funding has been provided for this project.

References

1. [Online]. Available https://en.wikipedia.org/wiki/Tamil_Thalaivas
2. [Online]. Available https://en.wikipedia.org/wiki/Haryana_Steelers
3. [Online]. Available https://en.wikipedia.org/wiki/Jaipur_Pink_Panthers
4. [Online]. Available https://en.wikipedia.org/wiki/U_Mumba
5. [Online]. Available https://en.wikipedia.org/wiki/Bengal_Warriors
6. [Online]. Available https://en.wikipedia.org/wiki/Bengaluru_Bulls
7. [Online]. Available https://en.wikipedia.org/wiki/Dabang_Delhi
8. [Online]. Available https://en.wikipedia.org/wiki/Puneri_Paltan
9. [Online]. Available https://en.wikipedia.org/wiki/Gujarat_Giants
10. Parmar M (2017) KABADDI: from an intuitive to a quantitative approach for analysis, predictions and strategy. In: Proceedings of 5th international conference on business analytics & intelligence (BAIConf2017), Chicago
11. Biswas MM, Bauri MR (2016) Relative performance analysis of Indian and foreign players in pro-kabaddi. Int J Recent Sci Res 4(7):10282–10284
12. Sardar DS, Pandey AK (2016) An estimation of kabaddi performance based on selected physical fitness components. Ind J Phys Educ Sports Appl Sci 6(4)
13. [Online]. Available https://www.sportskeeda.com/kabaddi?page=1
14. [Online]. Available https://en.wikipedia.org/wiki/Patna_Pirates
15. [Online]. Available https://www.prokabaddi.com/stats
16. [Online]. Available https://en.wikipedia.org/wiki/Pro_Kabaddi_League
17. [Online]. Available https://en.wikipedia.org/wiki/Telugu_Titans

18. [Online]. Available https://en.wikipedia.org/wiki/UP_Yoddha
19. [Online]. Available https://www.kabaddiadda.com
20. [Online]. Available https://www.startv.com/our-stories/game-on-india/
21. Times of India (Daily News Paper)
22. [Online]. Available https://matplotlib.org/stable/tutorials/colors/colormaps.html#sphx-glr-tutorials-colors-colormaps-py
23. [Online]. Available https://www.tutorialspoint.com/scikit_learn/scikit_learn_support_vector_machines.htm
24. [Online]. Available https://scikit-learn.org/stable/modules/generated/sklearn.ensemble.RandomForestClassifier.html
25. [Online]. Available https://scikitlearn.org/stable/modules/generated/sklearn.modelselection.train_test_split.html?highlight=train#sklearn.model_selection.train_test_split
26. [Online]. Available https://towardsdatascience.com/first-neural-network-for-beginners-explained-with-code-4cfd37e06eaf
27. Goud PSHV, Roopa MY, Padmaja B. Player performance analysis in sports: with fusion of machine learning and wearable technology
28. Patel MM, Datta NK. A review on selected physical and physiological components of inter-collegiate kabaddi and Kho-Kho players. Pacific Academy of Higher Education and Research University, Udaipur
29. Pantzalis VC, Tjortjis C. Sports analytics for football league table and player performance prediction
30. Hughes MD, Bartlett RM (2002) The use of performance indicators in performance analysis. J Sports Sci 3(20):739–754
31. Gudmundsson J, Horton M (2017) Spatio-temporal analysis of team sports. ACM Comput Surv 4(50):123–129
32. Kumar G (2013) Machine learning for soccer analytics. University College Dublin, Dublin
33. Lago-Peñas C, Lago-Ballesteros J, Rey E (2011) Differences in performance indicators between winning and losing teams in the UEFA champions league. J Hum Kinet 27:135–146
34. McCabe A, Trevathan J (2008) Artificial intelligence in sports prediction information technology. In: New generations, pp 1194–1197
35. Goddard J (2005) Regression models for forecasting goals and match results in association football. Int J Forecasting 21:331–334

Prediction of Positive and Negative Sentiments for Twitter Data Using Machine Learning

Meenu Gupta, Rakesh Kumar, and Tarun Gautam

Abstract Analysis of sentiment is one of the important field in Natural Language Processing (NLP) used to find the emotions using the text. It is an approach to identify the mentality, perspective or feelings of the individual towards anything, administration, film and so on by dissecting the feelings and surveys shared via online media. Different online media networks such as Facebook, Twitter, etc., permit individuals to share their perspectives with others. Twitter become the most well-known online media network that permits clients to share data via the short messages called tweets on a continuous premise. A huge number of individuals associate with one another simultaneously, and a tremendous measure of information is created in seconds. To utilize this information, we build up a Twitter visualization and sentiment analysis system. The dataset used for sentiment analysis is collected from the Twitter website. The pre-processing steps are applied for cleaning the collected dataset by removing hashtags like watchwords. Application Programming Interfaces (APIs) are used to perform sentiment analysis after cleaning the data. This will dissect the estimations as positive and negative for a specific item and administration that helps associations, ideological groups and average folks to comprehend the viability of their endeavours and better dynamic. Our results show that it can handle information progressively, and get envision data consistently.

Keywords Sentiment analysis · Visualization · Real-time · Twitter · Lexicon-based approach

M. Gupta (✉) · R. Kumar · T. Gautam
Chandigarh University, Gharuan, Punjab, India
e-mail: meenu.e9406@cumail.in

R. Kumar
e-mail: rakesh.e8623@cumail.in

T. Gautam
e-mail: tarun1gautam@gmail.com

S. Rawat et al. (eds.), *Proceedings of Second International Conference on Computational Electronics for Wireless Communications*, Lecture Notes in Networks and Systems 554,
https://doi.org/10.1007/978-981-19-6661-3_23

1 Introduction

Sentiment analysis [1] is a moving exploration field inside natural language processing (NLP) that forms frameworks that attempt to recognize and separate sentiments inside the text. Sentiment analysis permits associations, political gatherings and average folks to follow sentiments towards a particular item or administrations for better dynamic to improve their item or administration. The objective of sentiments analysis is to distinguish sentiments, disposition and perspective of individuals towards an item or support and characterize them as positive, negative and unbiased from the gigantic sum of information as surveys, tweets, remarks and input. Twitter is one of the mainstream Social Media Networks (SMN) among all the other SMNs such as Facebook, YouTube, Instagram, etc., for publically sharing musings, sentiments, perspectives, and conclusions with the world. Sentiment analysis helps in naturally changing a huge chaotic measure of information into a coordinated structure in a few moments [2]. In the research paper, we proposed that we used an open online source to proceed towards sentiment analysis by using a set of inbuild libraries present in Python programming to get the information from Twitter and perform the sentiment analysis on topics of any famous hashtags and retweets which are in trend furthermore, breaking down the thoughts of people regarding that trending topic or hashtag.

In present era, Twitter [3] is widely used as a huge data source to collect continuous data for a system on trending hashtags and topics all throughout the world. With the help of Twitter APIs (Application Programming Interface) [4], we can collect hashtags easily. We store the separated data from the Twitter into the CSV file. Once we get the data in the csv file, then we can start the sentiment analysis of people. We start our process with the data cleaning, then we calculate the subjectivity score of each record present. In this proposal, we used web-based interface (Twitter), where we can find the hashtags or catchphrases on the recent and popular topics easily for performing sentiment analysis. In our website, we can see the data as table which compares sentiments, sentiment score, and subjectivity score, and then we visualize them as pie chart and pattern chart. Tweets are consistently removed in ongoing and its yield is constantly refreshed.

2 Literature

In 2020, the novel coronavirus (COVID-19) pandemic was the most talked-about issue on social media. People were utilizing social media sites like Twitter to voice their opinions and exchange information on a variety of issues surrounding the COVID-19 stay-at-home directive. The authors of [5] worked into people's feelings and sentiments towards reopening in the United States. The social media network

Twitter was chosen for research and investigation of Tweets in order to identify sentimental, emotive, and triggering terms in relation to the reopening. Researchers analysed several social media datasets regarding lockdown and remain at home during the COVID-19 epidemic.

In [6], the authors proposed to make a noble philosophy to differentiate the feelings on the web rating posts in the security exchange. They chose Sina account (Sina is a Chinese website), a standard financial site, as the test stage for gathering financial survey data. The process is a consolidated sentiment analysis methodology that employs a machine learning approach based on the support vector machine and a summing autoregressive model. In a small amount of time, an online media client can receive and share a large number of messages. As a result, information may be created fast and disseminated throughout the world. In [7], authors constructed a stage, namely real-time information visualization and analysis (RIVA), for investigating known points via web-browser perceptual interface. As information sources, two online services are used: Twitter and news websites. Apache Spark and Apache Zeppelin were combined in the framework. As a result, the larger live information stream gains adaptability. If two types of refutation are encountered, the outcome may be poor. In [8], the authors used Twitter data for sentiment analysis and visualization, R programming is being used. In their research, they classified sentiment extreme as certain bad and unbiased. They used a dictionary technique, which was carried out with the help of Word cloud, a R package that provides a large amount of data. To discover feelings, a corpus of word reference information is used. Bar and pie graphs were used to present the findings. Using an individual sentiment score to introduce leads to a better outcome.

In [9], the authors performed opinion investigation. In their examination work, they used sentiment analysis at the sentence level to research and summarize various survey points. They got the details from Internet movie database. There were a variety of elements that contributed to the blunder rate. Because of the multiple ramifications, some previous terms were given incorrect ratings. Other problems, such as grammatical errors, disjointed sentences and deceptive wording in provisos, can contribute to incorrect outcomes. The formula was unable to deal with some perplexing expressions of sentiment in the content, resulting in substantial misclassifications. In [10], the authors noticed that the display of emotion order is influenced by text pre-handling strategies. They offered six different preprocessing strategies, each of which demonstrates how sentiment extremity order affects Twitter. Number of experiments were conducted on five different datasets using four classifiers in order to confirm efficacy of a few pre-planning tactics. The deletion of unwanted URLs, deleting the stop words, and deleting the numbers have no effect on the exhibition of classifiers, according to the findings of the trials. Order precision is also increased by eliminating refutation and increasing abbreviations. That is how, removing stop words, digits and URLs helps to reduce noise while leaving execution unaltered.

In [11], the authors introduced a system which incorporates temporal arrangement estimating models anda multivariate relapse strategy which forecast absolute vehicle sales month to month. They used deseasonalizing technologies to manage

different types of data. The mathematical results reveal that by combining combination multivariate relapse information with deseasonalizing procedures, predicting vehicle deals foresees more precise anticipating results. Using cross-breeding data comprising sentiment of digital media and financial exchange esteems, most common estimating execution might boost gauging precision. As a result, the deseasonalizing methodology aids in the expansion of expectation execution for both condition and choice components. In [12], S3D, a semisupervised spam detection structure, was proposed. In S3D, four lightweight indicators were used to consistently spot spam tweets, and models were refreshed intermittently in group mode. In which spam tweets are recognized on a regular basis. Spammers are difficult to discriminate in framework due to the lack of client data in their dataset. When a spam client is identified, it might have an adverse effect on other customers. As a result, spam detection at the tweet level complements spam detection at the client level.

In [4], the grammatical form labels were used to get rid of designs that described the intensity of ridicule in tweets. They used Apache Open NLP to complete a variety of NLP tasks. Their tests demonstrate excellent results when using the method they picked, but if the preparation set was larger, the results could be even better. Due to the limited preparation set, all of the possible wry examples were not covered.

3 Methodology

The digital world encouraged lot of people towards social media, which created a high level of communication between user and the provider, still some organizations are there that do not indulge them into the social media. Methodology of working in this project is given with complete description. The proposed Twitter-based sentiment analysis methodology is shown in Fig. 1.

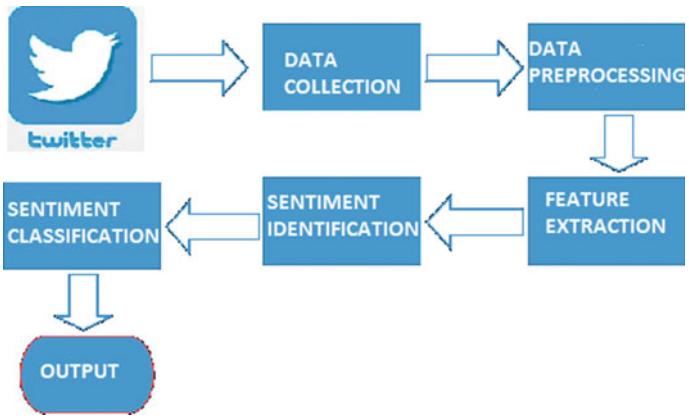

Fig. 1 Architecture of work proposed

3.1 Data Collection

We picked social media platform (Twitter) as the information assortment because it's well known these days. To extract the tweets, a Twitter API is required that could deliver a set of posts at a time which is enforced by the social media platform. The API can be accessed using Tweepy library of python. We can download twitter messages continuously with the help of Twitter streaming API. It is valuable to get a high volume of tweets, or for making a live feed utilizing a website stream or client stream. We can use this platform's streaming API to recover tweets are getting posted for any hashtag or keyword (Figs. 2 and 3).

Twitter Authentication: In this, we collect the four parts of information from our social media platform (Twitter) API key, API mysterious, Access token also and Access token mystery.

Accessing Twitter Data: post confirmation, we have to interface with Twitter Streaming API. Python programming library tweepy empowers us so that we can interface with Twitter and store the information. When the Twitter Validation administration confirms the API, it generates a token makes it accessible to the API for every worker exchange. Utilizing this token, data is gathered utilizing hashtags/catchphrases. To get to the information, we utilize the below commads, and this downloads the information and put away in a csv (csv is a file extension) documents as dataset.

```
auth = OAuthHandler(ckey, csecret).
auth.set_access_token(atoken, asecret).
twitterStream = Stream(auth, listener()).
```

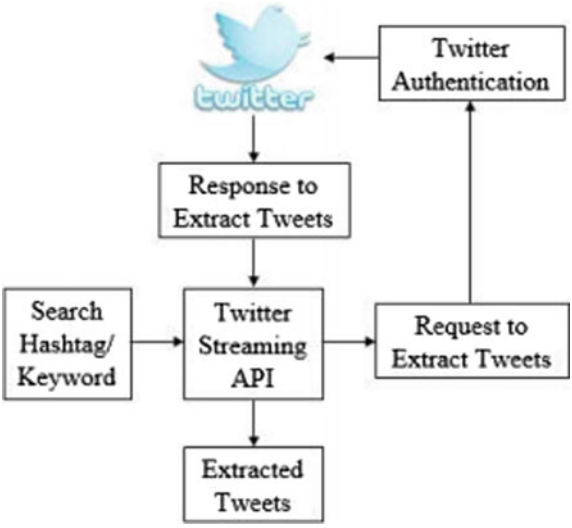

Fig. 2 Data collection process

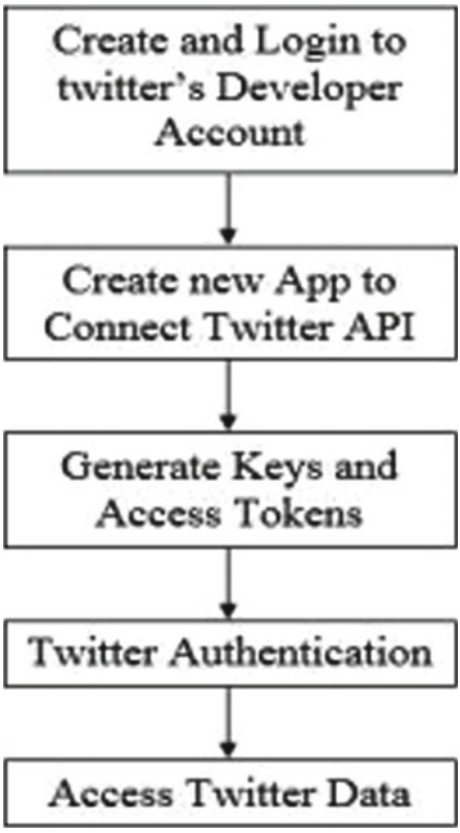

Fig. 3 Twitter Authentication

twitterStream.filter(track = [inp]).

3.2 Data Pre-processing

Information gathered from Twitter is not in proper structure and chaotic, communicated in different angles by utilizing different accents, slangs, the setting of composing and so forth. Subsequently, information pre-processing comprises of information cleaning and removing the stop word.

Data Cleaning. It incorporates deletion of pointless information like HTML tags, blank areas and special characters/symbols happens from the social media website (Twitter) dataset. This commotion doesn't bode well, in this manner, they should be eliminated. Information cleaning is accomplished by bringing in normal articulation (RE) library of Python programming. Cycle of cleansing information for our framework is as per the following:

a. In 1st step, eliminates the unwanted URL's. URL isn't taken as a fundamental component in posts of social media platform (tweets) and for straightforwardness, URLs are eliminated.
b. Controllers on twitter, for example, '@zyx' are additionally eliminated as these do not give any kind of loads in slant arrangement.
c. following stage is for eliminating accentuation. From this point onward, the expulsion of unique character happens.
d. Non-text based substance and substance which are insignificant for investigation are recognized and disposed of.
e. Additional spaces are likewise supplanted with single space.
f. Void areas (Spaces) all along are too taken out.

Removing Stop Words. Stopword expulsion is finished by disposing of the superfluous words from the social media platform (Twitter) informational index. The cycle of stopword expulsion is as per the following:

1. Above all else, tokenization happens. "Tokens" are normally singular words and "tokenization" is by picking a sample of data and separating this to single words.
2. After that, every one of the superfluous words are taken out after tokenization, for example 'a', 'an', 'the', etc. These superfluous words are stopwords which do not have any meaning. After expulsion of stopwords, just significant words that leads to estimation location are left. By deleting stopword and tokenization is accomplished with the help of Python library which is known as NLTK.

Lemmatization: Lemmatization is one of the most popular text pre-processing methods which is responsible for combining several inflected words with the same meaning into the root forms, for example, machine, machines, machine's, machines'. TextBlob is one of the approach used for lemmatization in handling complex words in textual data. TextBlob is simpler, like numerous highlights of NLTK [13].

3.3 Feature Extraction

Highlight extraction is a significant advance in assessment gathering which produces a rundown of item, angle, highlights and feelings. The reason for highlight extraction is to extricate assessment sentences which contain at least one highlights, angles and conclusions. In the greater part of occurrences, angle words are things and thing remarks, their assessment words are modifiers and verb modifiers. Here, in exploration task, highlights are extricated utilizing the Python library TextBlob. Following pre-processing stage, as it were fundamental words left in tweets that are utilized for examination. In the following stage, these removed highlights are characterized into notions.

3.4 Sentiment Identification

After include mining, we recognize the positive and negative direction of words. These highlights looked into assessment list of word from tremendous arrangement of corpora in Python library TextBlob to discover the assessments. Highlights are looked into the positive and the negative word rundown of the word reference. On the off chance that the keyword is available in positive assessment list of words, at that point the positive estimation is appointed to the relating highlight. On off chance that the keyword is available in the negative list of words, at that point the negative feeling is relegated to the relating highlight. In the event that the word is absent in these two list of words, at that point feeling is taken as unbiased. In this way, the last we determine the polarity score of the tweet by taking away the negative value from the positive value. The extremity value is a buoy goes from [− 1 to 1]. This extremity value permits us so that we can order tweets as per extremity which is examined in the following stage [14, 15].

3.5 Sentiment Classification

In this stage, we are categorizing the tweets by calculating the extremity score. We have grouped the assumption of two datasets. In the first dataset, we have grouped the feelings into 3 classes. A value less than 0 is considered negative and above 0 is considered positive and the rest of the other having value of 0 is considered neutral. Now in the second dataset, we have grouped the data of 3 classes that we have created recently/in the last step. In this, we determine the extremity score of the tweets which is a little higher than 0 is taken as positive and the tweets having a value close to 0 are taken as neutral, and last the tweets having an extremity score of a little less than 0 are considered as negative [16–18].

3.6 Subjectivity Identification

We can found subjectivity in illustrative sentences. Abstract sentences are assessments which characterize feelings the people regarding a specific point or topic. There are numerous types of emotional articulations, like perspectives, claims, wishes, feelings, questions and hypotheses. The abstract state is "I like gold tone," albeit the target expression incorporates realities and has no view or assessment. For example, "the shade of this telephone is gold" is a goal sentence. An abstract sentence may not communicate any assumption. In this framework, we check the subjectivity score for the posts on social media platform (tweets) utilizing the library TextBlob work. Library TextBlob as of now has a word reference which consists of subjectivity score

of the words. Due to modifiers, we see increment in subjectivity. For model, "Excellent" is highly emotional as compared to "Great" subjectivity is scope of qualities inside [0.0, 1.0]. Here, value 0.0 is level headed and value 1.0 is extremely emotional.

3.7 Output Presentation

The last period of our supposition examination is the representation of the outcomes. We have used pie diagrams, dotted graph and tables to see outcomes. We utilize a Matplotlib library to make pie diagrams and pattern diagram to make the graphs and outlines. This is mathematical expansion to math is NumPy. What's more, we utilized Pandas library of Python for table representation. Pandas is Python's product library to control and examination the information composed for the Python language. It gives information structures furthermore, tasks to control mathematical tables and time successions.

4 Results

Twitter data is collected for performing analysis on tweets on any popular topic using hashtag or keyword. In our experiment, we store tweets into dataset. We choose the former CEO and founder of Microsoft Corporation, Bill Gates tweets to perform analysis. These are the 100 recent tweets which are collected. Our dataset shows the detailed analysis of tweets into three categories such as positive, negative and neutral. Below Pie Chart Fig. 4 represents the results of 100 recent tweets by Bill Gates.

According to pie chart, we observed that 69% tweets are positive, 17% tweets are neutral and 14% tweets are negative. These results show that the majority of people has a positive sentiment towards Bill Gates. We visualize our results with a dot graph which is shown in Fig. 5. This graph is generated according to the polarity score

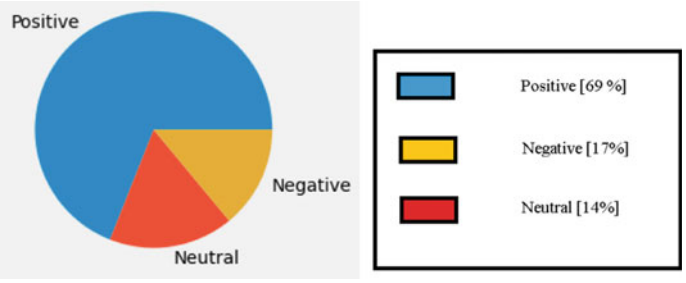

Fig. 4 Results for Tweets in dataset

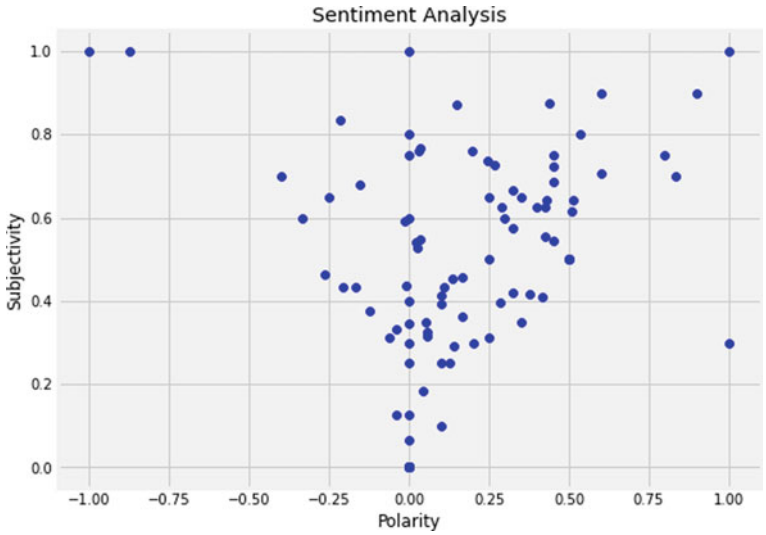

Fig. 5 Polarity and subjective sentiment analysis dot graph

where values vary from − 1 to 1 and the subjectivity where values lie between 0 and 1.

5 Conclusion

Twitter is a popular microblogging website that keeps people stay up to date on what's happening across the globe at any given time. In this work, the machine learning methods have been applied to outperform three models: unigram, feature-based model and tree kernel model. As a result, the emotions of tweets retrieved from Twitter are concluded by our proposed approach. The nuance and difficulty of the expressed opinions add to the complexity. Product reviews, for example are quite simple. More challenging are books, movies, art and music. As emoticons, neutralisation, negation handling and capitalization/internationalization is a large part of the Internet, we can use them as well.

References

1. Mamta EK (2019) A real-time twitter sentiment analysis and visualization system: TwiSent. Academic Press
2. Nemes L, Kiss A (2021) Social media sentiment analysis based on COVID-19. J Inf Telecommun 5(1):1–15
3. Arun K, Srinagesh A, Ramesh M (2017) Twitter sentiment analysis on demonetization tweets in India using R language. Int J Comput Eng Res Trends 4(6):252–258
4. Bouazizi M, Ohtsuki TO (2016) A pattern-based approach for sarcasm detection on twitter. IEEE Access 4:5477–5488
5. Emtiaz Ahmed M, Rafiqul Islam Rabin M, Naz Chowdhury F (2020) COVID-19: social media sentiment analysis on reopening. arXiv e-prints, arXiv-2006
6. Wu DD, Zheng L, Olson DL (2014) A decision support approach for online stock forum sentiment analysis. IEEE Trans Syst Man Cybern Syst 44(8):1077–1087
7. Wu YT, Hsieh HY, Sigalingging XK, Su KW, Leu JS (2017, November) RIVA: a real-time information visualization and analysis platform for social media sentiment trend. In: 2017 9th international congress on ultra modern telecommunications and control systems and workshops (ICUMT). IEEE, pp 256–260
8. Sivananda D, Asmai SA, Abidin ZZ, Abas ZA, Ahmad S (2021) Sentiment analysis dashboard using twitter data in power BI. Manuscr Editor 2021:61
9. Thet TT, Na JC, Khoo CS (2010) Aspect-based sentiment analysis of movie reviews on discussion boards. J Inf Sci 36(6):823–848
10. Jianqiang Z, Xiaolin G (2017) Comparison research on text pre-processing methods on twitter sentiment analysis. IEEE Access 5:2870–2879
11. Pai PF, Liu CH (2018) Predicting vehicle sales by sentiment analysis of Twitter data and stock market values. IEEE Access 6:57655–57662
12. Sedhai S, Sun A (2017) Semi-supervised spam detection in Twitter stream. IEEE Trans Comput Soc Syst 5(1):169–175
13. Taboada M, Brooke J, Tofiloski M, Voll K, Stede M (2011) Lexicon-based methods for sentiment analysis. Comput Linguist 37(2):267–307
14. Zagibalov T, Carroll JA (2008) Unsupervised classification of sentiment and objectivity in Chinese text
15. Tripathy A, Rath SK (2017) Classification of sentiment of reviews using supervised machine learning techniques. Int J Rough Sets Data Anal (IJRSDA) 4(1):56–74
16. Wu C, Shen L, Wang X (2009, November) A new method of using contextual information to infer the semantic orientations of context dependent opinions. In: 2009 international conference on artificial intelligence and computational intelligence, vol 4. IEEE, pp 274–278
17. Khairnar J, Kinikar M (2013) Machine learning algorithms for opinion mining and sentiment classification. Int J Sci Res Publ 3(6):1–6
18. Pang B, Lee L, Vaithyanathan S (2002) Thumbs up? Sentiment classification using machine learning techniques. https://arxiv.org/pdf/cs/0205070

Virtual Machine Allocation Using Genetic-Based Algorithm in Cloud Infrastructure

Ankita Srivastava and Narander Kumar

Abstract Virtualization is the essence of cloud computing. It facilitates the providers by virtualizing the storage, servers and other resources which aids in providing the computing services on shared and demand basis via internet. Virtual machine allocation is critical to achieving this goal, which accounts for effective resource usage with minimum expenditure. An efficient allocation results in effective resource utilization thus reducing wastage. This article proposes a genetic-based method exploiting the dual chromosome representation technique. The primary objective is to lessen the imbalance in resource utilization by reducing resource wastage. Another aim is to limit the power usage of the data center by diminishing the active servers' volume. Lastly, the algorithm is evaluated against other existing work corresponding to several metrics which is further supported by the simulation procedure. The analysis from the result obtained displays a better performance of the algorithm by improving resource wastage, active server's volume, CPU, and memory utilization.

Keywords Resource allocation · Virtual machine allocation · Cloud computing · Genetic algorithm · Optimization · Nature-inspired algorithm

1 Introduction

An internet-based paradigm, cloud computing, where the task is executed using the resources with the shared mode. Thousands of systems are networked together to execute the task provided by the users. It's a hybrid of parallel and distributed computing. In this, computing resources are furnished as the storage, physical servers, network, bandwidth, etc. Data centers are where these resources are stored and structured. Service providers are in charge of these data centers. Majority of the corporate

A. Srivastava · N. Kumar (✉)
Department of Computer Science, Babasaheb Bhimrao Ambedkar University (A Central University), Lucknow, India
e-mail: nk_iet@yahoo.co.in

S. Rawat et al. (eds.), *Proceedings of Second International Conference on Computational Electronics for Wireless Communications*, Lecture Notes in Networks and Systems 554,
https://doi.org/10.1007/978-981-19-6661-3_24

companies rely on the cloud to get a multitude of benefits such as pricing model, on-demand scalability, reliability, robustness, and elimination of maintenance responsibility. Virtualization is the crux of cloud computing. It facilitates in providing the resources of a server through the various secluded executing environment through virtual machines (VMs). These VMs are hosted on physical machines (PMs). The mapping of VMs to PMs is termed virtual machine allocation (VMA). An efficient VMA aids in making the most usage of the resources and lowers the cloud infrastructure's energy consumption. Several VMA techniques have been studied by several researchers but they lack the balance between resource waste and energy consummation. This imbalance usage of resources may expedite excessive resource wastage. Additionally, energy consumption varies directly with the volume of active servers. This imbalance in the multi-dimensional resources has captivated a lot of researchers to bestow an effective solution to the given issue. The VMA issue is addressed in this research by proposing an effective algorithm which meet following objectives:

- Reduce the imbalance in the usage of the resources in the cloud.
- Allocate VMs to the server using the genetic algorithm-based approach.
- Minimize the resource wastage of the server and hence exploit the resources to its full capacity.
- Sacle down the servers serving the user demands and hence bring down the number of active servers.
- The reduction in active servers ultimately depletes the energy usage of the data center, and hence the cost incurred by the data center is also reduced to a large extent.

Later part of the article is divided in the given sections: Sect. 2 represents the recent study in the concerning area. Section 3 provides the problem formulation along with the algorithm proposed. Section 4 performs the validation of the study and interpretation of the result obtained. Finally, the suggested work is concluded in conjunction with the future scope in Sect. 5.

2 Literature Survey

Cloud computing works on the pay-as-you-go principle. There is a continuous fight between operational expenditure and capital expenditure concerning resources of the cloud. It's important to strike a stability between resource use and energy usage. A resource can be exploited efficiently only when there is no wastage. The reduced volume of PMs deploying VMs on them tends toward low energy consumption. A well-organized allocation of VMs mitigates the energy usage up to a large extent. The researchers have given a lot of effort to this issue. The following are certain works that are being discussed:

Several bin packing algorithms have been applied for VM allocation. Some algorithms like first fit (FF) algorithm, best fit decrease (BFD) algorithm, and their variations are the heuristic algorithms that work on as classic NP-hard bin packing problems. In comparison to other optimization problems, these techniques are simple and have low complexity. They don't consider the various objectives which need optimization. In [1], the technique has been discussed to allocate VMs on PMs by narrowing down the energy usage and optimizing the resource wastage. This work did not account for reducing the active servers' number. The author has implemented stochastic integer programming to perform VMA. It optimized the provisioning cost in cloud infrastructure under various pricing and payment plan [2]. A clustering technique had been introduced, K-means for VMA, and performs load balancing resulting in reduced idle time [3]. A fuzzy-based heuristic VM consolidation had been proposed to obtain higher QoS and energy balance [4]. A novel bin-packing heuristic algorithm medium fit was presented in [5]. FF and best-fit algorithm were applied on the PMs then if a suitable host was not obtained, the search was performed on the inactive PMs, and further medium-fit algorithm was applied on the servers with active status, and the host having the best power efficiency was selected. It provided an equilibrium between energy use and resource waste, and even a decrease in SLA violations.

Furthermore, several metaheuristic algorithms were implemented to settle the VMA issue. A genetic method with a hybrid version for VM allocation had been provided that uses less energy [6]. The algorithm worked with small-scale PMs but how much it is effective with a large scale of PMs was not given. A PSO-based approach was discussed with reduced energy consumption [7]. An Ant Colony based technique had been presented which performs a selection of PMs in nearby proximity for hosting VMs and data on them [8]. Its main objective was to narrow down the network traffic and bandwidth usage. A multi objective virtual machine placement (MOVMP) [9] technique established a resource consumption factor in order to fully exploit resource utilization and cut down the number of underutilized. It minimized power usage and SLA violations by limiting the number of migrations. A discrete version of PSO has been introduced [10]. In this, firstly the VMs searching for host were sorted in reverse order by CPU utilization, then suitable PM with the resources demanded was searched and allotted to VM. For overcoming the VMA problem, two optimization techniques were proposed [11]. It gave two optimization methods for resolving the VMA problem. The first one was done with the lexicographical ordering method where VMA was solved for each objective with the preference order O1, O2, and O3. Another method employed was the weighted sum approach providing the non-dominated solution. It gave an optimized solution for downsizing the VMs quantity, power consummation and resource waste. A new methodology was introduced for balancing resource usage for maximizing its utilization [12]. First, PMs were classified per the resource accessibility, then VMs were classed according to resource demands, and finally, the VMs were deployed on the PMs relying on their cosine similarity.

3 Dynamic Resource Allocation

The primary goal of the technique put forward is to efficiently assign VMs to PMs in order to diminish resource waste and parallelly minimize the active servers' volume.

3.1 Problem Formulation

Suppose a system having *'w'* PMs and *'v'* VMs which is represented as;

$$V_m = \{1, 2, 3 \ldots v\} \tag{1}$$

$$P_m = \{1, 2, 3 \ldots w\} \tag{2}$$

Each VM is denoted by v_a and PM is denoted by p_b. A binary decision variable denoted as χ_{ab} represents an allocation of VM a to PM b. If a VM a is deployed on PM b then it has value 1 otherwise 0. A variable h_b binary in nature decides whether the PM b is hosting any VM or not. If any VM is deployed to PM b then h_b has value 1 otherwise 0. It is represented as:

$$\chi_{ab} = \begin{cases} 1 \text{ if VM } a \forall a \in V_m \text{ is allocated to PM } b \forall b \in P_m \\ 0 \text{ otherwise} \end{cases} \tag{3}$$

$$h_b = \begin{cases} 1 \text{ if the PM } b \forall b \in P_m \text{ is in use} \\ 0 \text{ otherwise} \end{cases} \tag{4}$$

Let βm_a and βc_a represent the memory and CPU constraint of VM a and Tc_b and Tm_b symbolizes the CPU and memory of a PM b. The main motive of this work is:

$$\text{Minimize } f(X) = \sum_{b=1}^{m} \text{RW}_p \tag{5}$$

Subject to following constraints:

$$\sum_{b=1}^{w} \chi_{ab} = 1 \forall i \in V \tag{6}$$

$$\sum_{a=1}^{n} \chi_{ab}.\beta c_a \leq Tc_b.h_b \forall b \in P \tag{7}$$

$$\sum_{a=1}^{n} \chi_{ab}.\beta m_a \leq Tm_b.h_b \forall \in P \tag{8}$$

These constraints assure that every VM is allotted to one single PM although a PM can host more than one server. A PM can host only those numbers of VM whose summative CPU and memory load is lower than its capacity.

3.2 Fitness Model

The study aims to lessen resource waste along with the preference given to the volume down the active servers. Resource wastage of a PM p can be given as:

$$\mathrm{RW}_p = \frac{\left|N_p^{\mathrm{cpu}} - N_p^{\mathrm{mem}}\right| + \lambda}{T_p^{\mathrm{cpu}} + T_p^{\mathrm{mem}}} \tag{9}$$

where RW_p stands for resource wastage of PM p, N_p^{cpu} represents the unutilized CPU and N_p^{mem} denotes the memory of PM p and T_p^{cpu} and T_p^{mem} denotes CPU and memory usage of PM p and λ has a small positive real value. The summation of resource wastage for the whole system can be identified as:

$$\sum_{b=1}^{w} RW_b = \frac{\sum_{b=1}^{w} h_b.\left|\left(Tc_b - \sum_{a=1}^{n}(\chi_{ab}.\beta c_a)\right) - \left(Tm_b - \sum_{a=1}^{n}(\chi_{ab}.\beta m_a)\right)\right| + \lambda}{\sum_{a=1}^{n}(\chi_{ab}.\beta c_a) + \sum_{a=1}^{n}(\chi_{ab}.\beta m_a)} \tag{10}$$

3.3 Modified Genetic Algorithm

Genetic algorithm is practiced in various optimization problems to enhance the efficiency of the algorithm.

Chromosome Encoding: Each individual is depicted by two sets of chromosomes. One set represents the mapping of VMs to PMs. The span of the chromosome is equivalent to the quantity of VMs. This chromosome is the vector of integer values containing values from 1 to w. Each value corresponds to the indices of PM allotted to the VM. The other set represents the binary status of PMs. Here, the size of the chromosome is equivalent to the size of the PMs. This chromosome contains binary information. Each index represents whether the PM is hosting any VM or not. Figure 1 depicts the same.

Initialization: Each individual is generated through the random allocation of VM to PM. Each VM is allocated randomly to PM with the probability $1/m$.

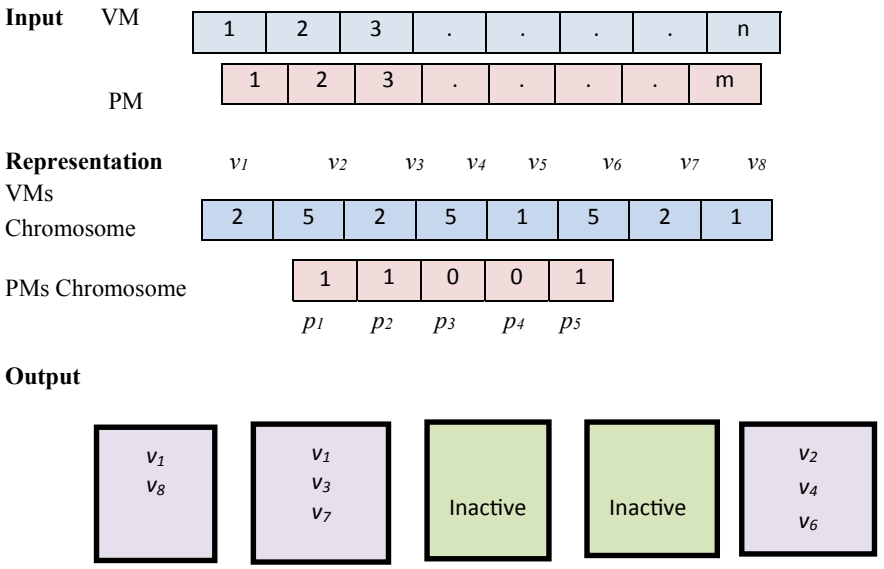

Fig. 1 Representation of genetic chromosome for cloud

Selection: The two best-fit individuals are drawn from the population based on their fitness as determined by the fitness function.

Crossover: The best crossover proves to be an efficient allocation and reduce wastage of resources. An order 1 crossover [13] is implemented on the VMs allocation chromosome. Order1 crossover chooses a series of successive items from one parent at random, with the remaining entries coming from the other parent. Figure 2 represents the encoding.

Single point crossover [14] is implemented on the PMs status chromosome. The chromosome is divided into two segments at random. The first part of a child's inheritance comes from the first parent, whereas the second part comes from the second parent.

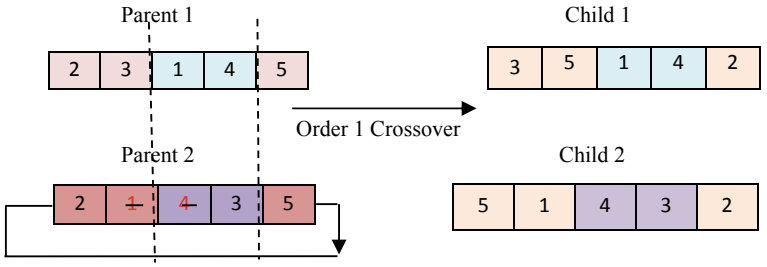

Fig. 2 Crossover representation

Mutation: The mutation operation deals with the exploration of the neighbors of the current individuals facilitating the local search mechanism. A separate mutation operator is designed for both chromosomes. Switch mutation randomly selects the two best fitted individuals from the PMs chromosome and switches a least fitted entry from them. This mutation modifies the status of PMs.

VM allocation mutation traverse along the allocation chromosome of VM and checks for the corresponding PMs status in PMs chromosome and if the status is 0 then it put the VM into the redeploy list. All the PMs with a status value of 1 are ranked corresponding to the best fit decrease algorithm and the VM list to be redeployed is deployed onto the sorted PMs. If these PMs are unable to fulfill the requirement, then a PM with the status value 0 and strong enough to hold the resources required by VM is allotted and its status is changed to 1.

4 Simulation

4.1 Performance Metrics

The performance metrics considered in this algorithm are resource wastage, active servers' volume, CPU utilization and memory utilization. The memory utilization U_{mem} and CPU utilization U_{CPU} for active machines z are equated as follows:

$$U_{\text{mem}} = \frac{1}{z} \sum_{b=1}^{z} \left[\frac{\sum_{a=1}^{v} \chi_{ab} * \beta m_a}{T m_b} \right] \tag{11}$$

$$U_{\text{CPU}} = \frac{1}{z} \sum_{b=1}^{z} \left[\frac{\sum_{a=1}^{v} \chi_{ab} * \beta c_a}{T c_b} \right] \tag{12}$$

4.2 Experimental Setup

The suggested algorithm's performance is assessed by simulating it and comparing it to previous work. The simulation is accomplished on PC Intel Core CPU i3-7020U and 4.0 GB Ram and Windows 10 Home as the operating system and Cloudsim platform is utilized. Initially, generations of the population produced are started with 30 and the individual data is set as 50. The method is assessed against FF algorithm, BFD algorithm and MOVMP [9]. FF algorithm deploys VM to the first PM having enough resources to hold VM. The BFD algorithm arranges the list of VMs with downscale order and allots the best fitted server which can fulfill the demand of VM. The result of the analysis obtained is summarized as:

It is observed from Fig. 3 that the total resource wastage of the system has been minimized up to large extent using the intended algorithm compared to other existing algorithms. The resource wastage has decreased to more than 50% as compared to FF and around 24% decrement can be observed with respect to BFD and 10% as against MOVMP. The volume of active PMs is also measured using the algorithm. It is found out that the suggested algorithm has deployed VMs efficiently such that PMs are utilized in a balanced way and a large number of VMs can be contained in lesser number of PMs which can be inferred from Fig. 4. The suggested work utilizes 14% less PMs against FF and 4% less PMs as oppose the BFD while 2% reduction in case of MOVMP. The proposed study has utilized the resources in an efficient way resulting in reduced wastage and enhancing the utilization of CPU resources and memory resources and it can be visualized in Figs. 5 and 6.

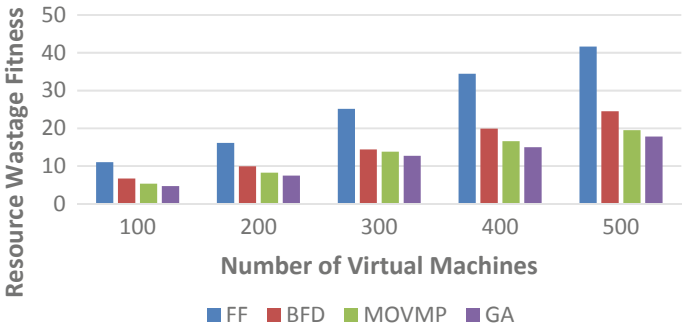

Fig. 3 Resource wastage fitness

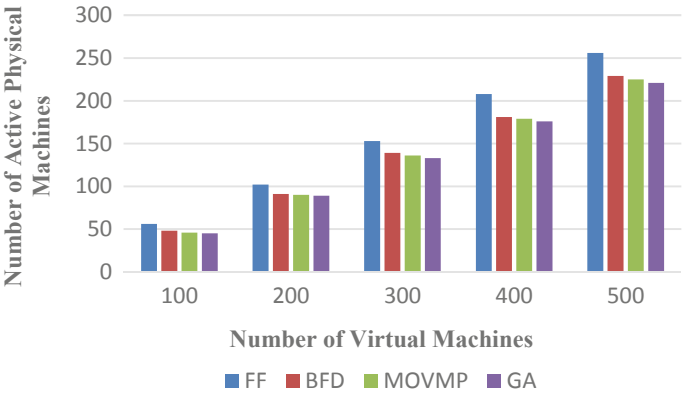

Fig. 4 Number of active physical machines

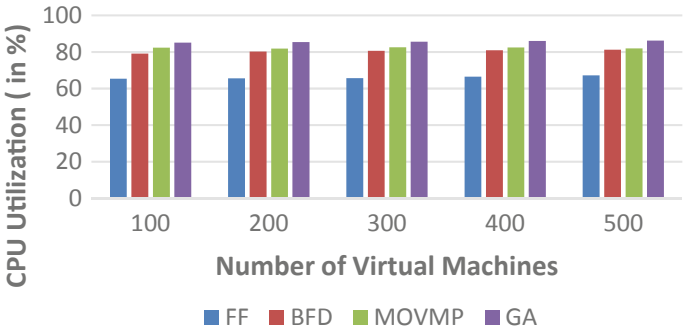

Fig. 5 CPU utilization

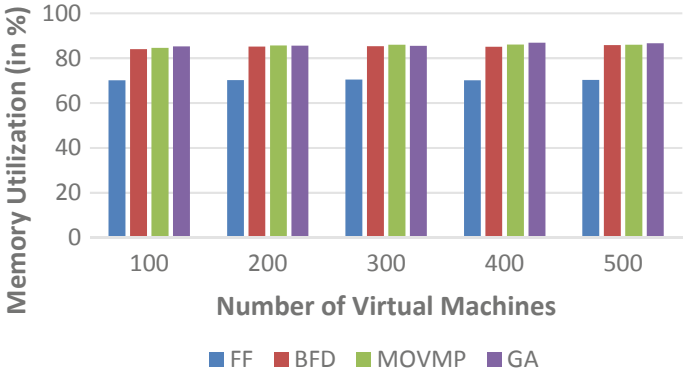

Fig. 6 Memory utilization

5 Conclusion

This paper has contributed a novel procedure for VM allocation for the cloud. The main aspiration of the work is to bring down resource wastage which enhances the usance of the resources and lessen down the volume of PMs in active mode to narrow down the energy consumed through data centers. A dual chromosome genetic algorithm based VM allocation technique is being used here. One chromosome represented a coding for VM and the other chromosome represented coding for the state of PMs. The work is being simulated on the real-world dataset and inspected against the FF and BFD algorithms on the ground of several performance metrics. The simulated result obtained displays the greater efficacy of the proposed work. The work has shown more than 50% reduction in resource wastage and utilizes 14% lesser PMs compared to FF. While wastage is minimized up to 24% and 4% less PMs are required to fulfill the users' request as against BFD. 10% curtailment in wastage

and 2% drop in active machines is observed as oppose to MOVMP. In the future, the work can incorporate more strategies to reduce SLA violations.

References

1. Beloglazov A, Buyya R (2010) Adaptive threshold-based approach for energy-efficient consolidation of virtual machines in cloud data centers. MGC@ Middleware 4(10.1145):1890799-803
2. Chaisiri S, Lee BS, Niyato D (2009) Optimal virtual machine placement across multiple cloud providers. In: Proceedings of IEEE Asia-Pacific services computing conference (APSCC). IEEE, pp 103–110
3. Adrian B, Heryawan L (2015) Analysis of K-means algorithm for VM allocation in cloud computing. In: International conference on data and software engineering (ICoDSE). IEEE, pp 48–53
4. Monil MA, Rahman RM (2016) VM consolidation approach based on heuristics, fuzzy logic, and migration control. J Cloud Comput 5(1):1–8
5. Moges FF, Abebe SL (2019) Energy-aware VM placement algorithms for the OpenStack neat consolidation framework. J Cloud Comput 8(1):1–4
6. Tang M, Pan S (2015) A hybrid genetic algorithm for the energy-efficient virtual machine placement problem in data centers. Neural Process Lett 41(2):211–221
7. Abdessamia F, Tai Y, Zhang WZ, Shafiq M (2017) An improved particle swarm optimization for energy-efficiency virtual machine placement. In: 2017 international conference on cloud computing research and innovation (ICCCRI). IEEE, pp 7–13
8. Shabeera TP, Kumar SM, Salam SM, Krishnan KM (2017) Optimizing VM allocation and data placement for data-intensive applications in cloud using ACO metaheuristic algorithm. Eng Sci Technol Int J 20(2):616–628
9. Gupta MK, Jain A, Amgoth T (2018) Power and resource-aware virtual machine placement for IaaS cloud. Sustain Comput Inform Syst 1(19):52–60
10. Ibrahim A, Noshy M, Ali HA, Badawy M (2020) PAPSO: a power-aware VM placement technique based on particle swarm optimization. IEEE Access 8:81747–81764
11. Regaieg R, Koubaa M, Ales Z, Aguili T (2021) Multi-objective optimization for VM placement in homogeneous and heterogeneous cloud service provider data centers. Computing 103:1255–1279
12. Gohil BN, Gamit S, Patel DR (2021) Fair fit—a load balance aware VM placement algorithm in cloud data centers. In: Advances in communication and computational technology. Springer, Singapore, pp 437–451
13. Poon P, Carter J (1995) Genetic algorithm crossover operators for ordering applications. Comput Oper Res 22(1):135–147
14. Agrawal RB, Deb K, Agrawal R (1995) Simulated binary crossover for continuous search space. Complex Syst 9(2):115–148

Deep Learning-Based Specific Emitter Identification

N. B. Srinivasulu, Yaswanth Chalamalasetti, and Barathram Ramkumar

Abstract For various autonomous wireless network deployments, knowledge and analysis of the radio frequency (RF) environment have become essential. One such scenario is, presence of adversaries who are attempting to interrupt the RF communication by hostile behaviors such as jamming or spoofing. Specific emitter identification (SEI) is the associated with signal received from transmitter. In order to learn the specific high-dimensional properties that can be utilized as "fingerprints" for identifying and classifying the transmitters, the SEI takes advantage of the in-phase (I) and quadrature-phase imbalance (i.e., IQ imbalance) found in all transmitters. Machine learning approaches have gained popularity because they can analyze, learn and even anticipate the RF signals and associated properties that define an RF environment. In this paper, a deep learning (DL)-based system was proposed to identify and classify the RF transmitters. The real-time signals (IQ data) are collected from six transmitters: USRP-2900 (universal software radio peripheral), BladeRF, HackRF, FS-i6 transmitter, 3DR 433 MHz Radio Telemetry module, and TS835 5.8 GHz video transmitter. RF signals are received using USRP-2900. Finally, the RF transmitters are classified using convolutional neural network (CNN). The proposed system achieved 98.58% accuracy for three class transmitters and 93.75% accuracy for six class transmitters.

Keywords RF fingerprinting · IQ imbalance · USRP · Machine learning · Convolutional neural network · Confusion matrix

N. B. Srinivasulu (✉) · Y. Chalamalasetti · B. Ramkumar
Wireless Communication Lab, School of Electrical Sciences, Indian Institute of Technology Bhubaneswar, Jatani, Khordha, Odisha 752050, India
e-mail: 20ec06012@iitbbs.ac.in

Y. Chalamalasetti
e-mail: cy10@iitbbs.ac.in

B. Ramkumar
e-mail: barathram@iitbbs.ac.in

S. Rawat et al. (eds.), *Proceedings of Second International Conference on Computational Electronics for Wireless Communications*, Lecture Notes in Networks and Systems 554,
https://doi.org/10.1007/978-981-19-6661-3_25

1 Introduction

The ability to locate, identify and characterize radio frequency (RF) signal sources (also known as RF emitters) is critical for applications such as tracking objects, finding cell phone, recognizing jammer, and detecting the occurrence of a signal. Identification of transmitters has become increasingly crucial as wire- less networks become more autonomous. A wireless sensor network (WSN), for example, relies on authentic signals; nevertheless, rogue transmitters can taint the RF signals, jeopardizing the sensor network's utility. The presence of such risks highlights the necessity for approaches that detect and validate identity of transmitter regardless of communication technologies or network protocols.

However, precisely recognizing a transmitter and characterizing it in real-time remains a difficult task.

Machine learning (ML) approaches to be effective; a transmitter must have a unique feature or attribute, regardless of the signals transmitted by emitter. The rise time signature, which is formed by tiny fluctuations in component values during the process of manufacturing, is commonly used property. When malevolent entities are present, it performs poorly. Furthermore, the rise time feature is not available commercially, so it cannot be utilized as a standard signature. Due to the usage of oscillators, unbalanced low pass filters and noisy mixers, *'IQ imbalance'* is another compromised feature during manufacture [1]. In this work, we used IQ data for the feature extraction. Despite the fact that there are strategies to adjust for this imbalance [2], all transceivers have this unique IQ imbalance. A brief literature overview of classification and identification of RF signals explained below. In [3], Y. Xiao had demonstrated the identification of non-cooperative micro-UAVs based on RF signals and classified the RF signals using k-nearest neighbor (KNN) by considering the cyclostationarity and spectrum-based features. In [4], M. Ezuma designed a system to identify the UAVs from Bluetooth and Wi-Fi emitters. A Markov model-based naive Bayes judgment method is used to detect RF signals from any source. Bluetooth and Wi-Fi signals are detected based on modulation and bandwidth features. In [5], Y. J. J. Teoh proposed a novel ML method to detect the RF signals based on the features; the number of packets, Received Signal Strength (RSS) over time transmission and packet size. Logistic regression (LR) is used for the classification, but it has less accuracy. In [6] Mohammad F. AlSa'd designed the deep learning (DL)-based method to detect the RF signals. A deep neural network (DNN) is used to classify and identify the RF signals based on the DFT features. But, this method has less classification accuracy for more than two transmitters. In [7], D. Roy proposed and implemented RF adversarial learning (RFAL) framework and generative adversarial nets [8] to detect rogue transmitters. They classified the data using CNN (accuracy 89%). In [9], U. Satija had developed an SEI system based on spectral features and variational mode decomposition (VMD).

In the above literature review, it was observed that (a) only ML-based algorithms have been analyzed in SEI but DL methods were not examined. (b) In some methods, synthetic signals are used for making the RF database. In this paper, the proposed

system is developed using a DL-based algorithm (CNN), and real-time signals are used to make the database. This paper is organized as follows. In Sect. 2, the proposed system and its subsystems are described. The results are summarized in Sect. 3, followed by the conclusion.

2 Proposed System

This section presents the system model used to create the RF database and test the viability of an RF emitter identification system. First, the subsystems, the system model and then, how to generate the RF database. Each component in the experimental setup will be discussed. Finally, the CNN is used to create an RF emitter detection and identification system to see if the produced RF database can be used in real-world applications. The system model shown in Fig. 1.

2.1 RF Database Development

In this section, the development of RF database system is shown in Fig. 3. This system contains two subsystems which are transmission and reception. These are explained below.

Transmission (Tx) In this system, the audio signal is transmitted using a software—defined radio (SDR) setup as shown in Fig 3; it contains SDR (RF transmitter) with antenna and PC is connected to SDR through the PCI cable. The signal processing will be done using GNU Radio software installed on PC. To learn about the features of RF transmitters, the following list of transmitters are used to build our database:

- USRP-2900 (frequency 70 MHz–6 GHz), shown in Fig. 2a.
- BladeRF (frequency 47 MHz–6 GHz), shown in Fig. 2b.
- HackRF (frequency 1 MHz–6 GHz), illustrated in Fig. 2c.
- Fs-i6 transmitter (frequency 2.4 GHz), shown in Fig. 2d.
- 3DR Telemetry module (frequency 433 MHz), shown in Fig. 2e.
- TS835 video transmitter (frequency 5.8 GHz), shown in Fig. 2f.

In this work, the data is collected from software-defined radios (SDR) to develop the suggested model. Then conducted indoor experiments to discriminate between three RF transmitters to validate the proposed technique. Three SDRs are used,

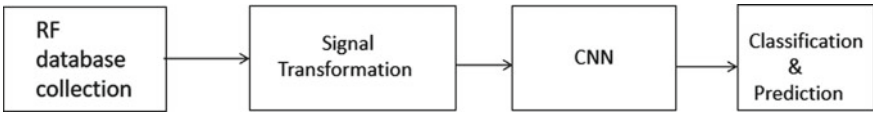

Fig. 1 Proposed system model

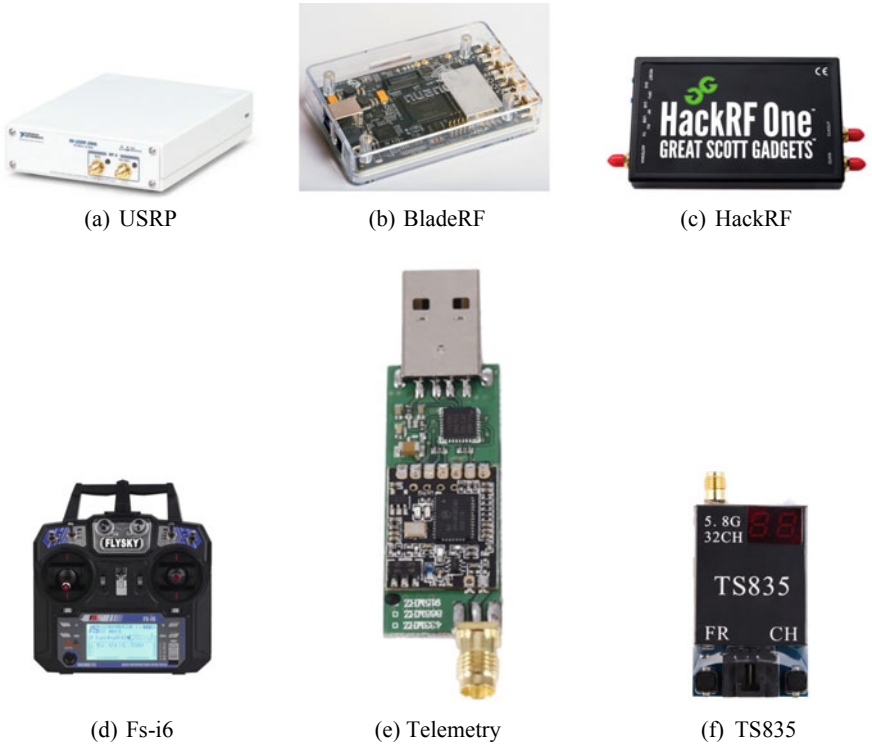

(a) USRP (b) BladeRF (c) HackRF

(d) Fs-i6 (e) Telemetry (f) TS835

Fig. 2 RF transmitters

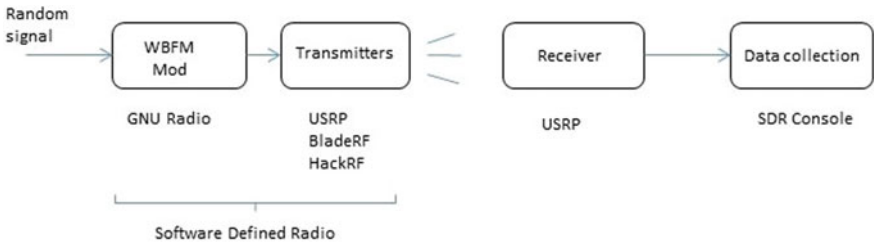

Fig. 3 Transmission and reception of signals

namely, USRP-2900, BladeRF, and HacRF. Figure 3 illustrates the transmission and reception of signals. The SDRs were configured to transmit audio signal and this signal was sampled at a sample rate of 48 kHz. Then the signal is modulated using wide band frequency modulation (WBFM) and transmitted through the USRP sink block on 900 MHz at a sampling rate of 768 kHz. Similarly, for BladeRF and HackRF osmocom sink block is used. The signal processing and data transfer were done by using GNU Radio. Figure 4 shows the flow graph.

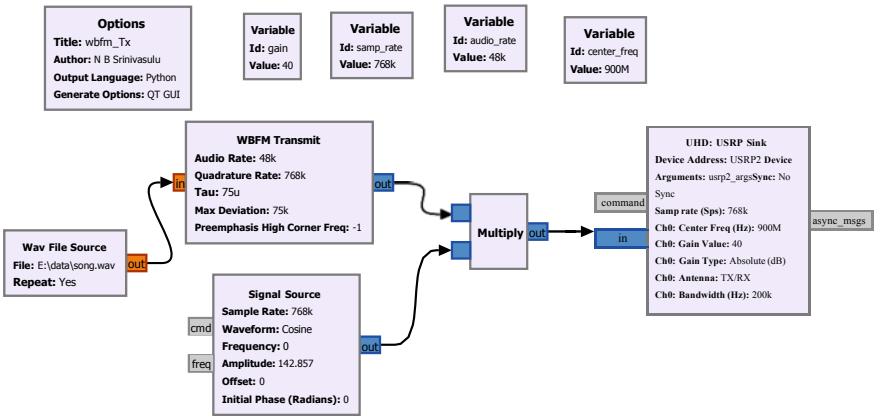

Fig. 4 Flow diagram for data collection in GNU radio

Table 1 Configuration parameters for transmission

Parameters	Values
Transmitter frequency	900 MHz
Bandwidth	200 kHz
Transmitter gain	40 dB
Samples/transmitter	900 K
Transmitters	3 and 6

Reception (Rx) in this section, USRP-2900 is used to receive the IQ data and the data is recorded and stored them on file using the SDR console. The data is also collected from other transmitters such as Fs-i6, 3DR Telemetry module and TS835 module. In this work, the RF data is collected in the format of a .csv file, which contains I and Q values in columns. To eliminate data unevenness difficulties seen in machine learning, 900K training instances are collected from each transmitter. Table 1 lists the parameters used to configure each transmitter. The data collection consisted of two sets: (i) using 3 transmitters with 1.8 GB size, 2700 K rows and two columns, and (ii) using 6 transmitters with 3.2 GB size, 5400 K rows and two columns. The experimental setup for development of RF database shown in Fig. 5.

2.2 Signal Transformation

In this method, the complex RF data is transformed into latent information that can be used for efficient detection. Due to IQ imbalance in transmitters in this work, the amplitude and phase parameters are calculated from IQ values.

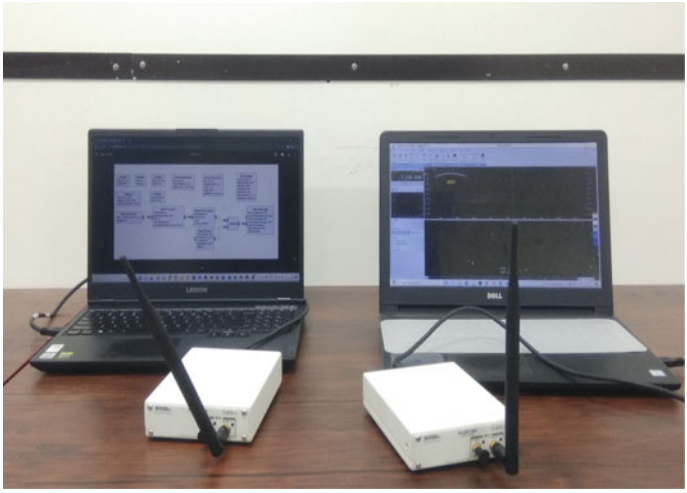

Fig. 5 Experimental setup for development of RF database

2.3 Machine Learning Libraries and Performance Metrics

Several libraries and tools make deep learning frameworks feasible using vastly parallel GPU architectures to eliminate the need to program traditional neural network training routines. In this work, *Keras*, *Sklearn, Numpy, Pandas*, and *Matplotlib* libraries in Python have been used, whereas *Keras* is for developing and evaluating deep learning model. *Adam* optimizer has been used for better learning rate, "accuracy" performance metric to describe the effectiveness of the CNN model, "categorical cross-entropy" as a loss function for multiclass classification. However, accuracy can sometimes be a deceiving parameter when the data is non-uniformly distributed.

2.4 Implementation of CNN

An essential reason for using convolutional neural networks was to identify the correlation between samples of IQ scores. As illustrated in Fig. 6, the CNN has four Conv2D layers with 256 and 128 filters, an long short-term memory (LSTM) layer, and two dense layers with 128 and three nodes. Dropout of 0.4 is used after each convolution layer. Kernels sizes of (1, 3) and (2, 2) are used for convolution and dense layers, except for the softmax layer of the output nodes. Using CNN, 98.58 and 93.75% accuracy have been achieved for three and six transmitters. Figures 7 and 8 show the accuracy plots and confusion matrices.

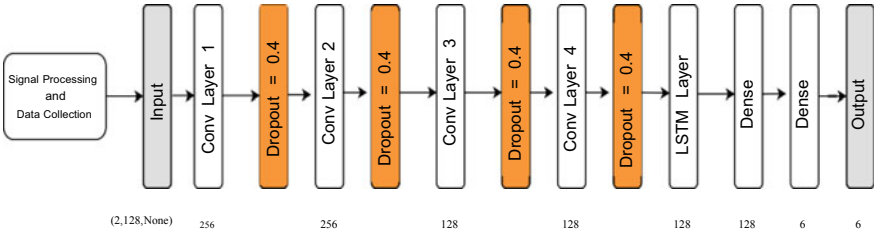

Fig. 6 Implementation of CNN for classification of RF transmitters

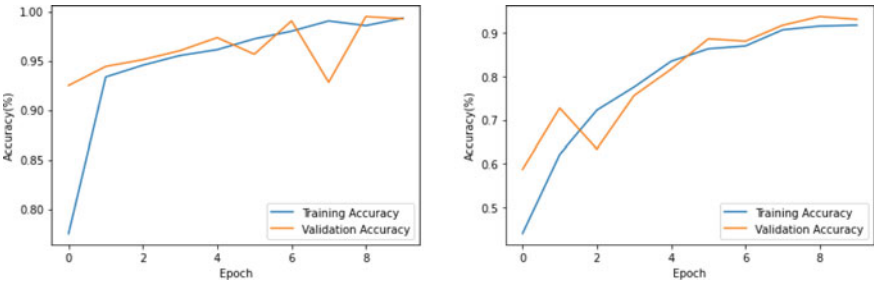

(a) 3 RF Transmitters (b) 6 RF Transmitters

Fig. 7 Transmitter classification accuracy plot using CNN

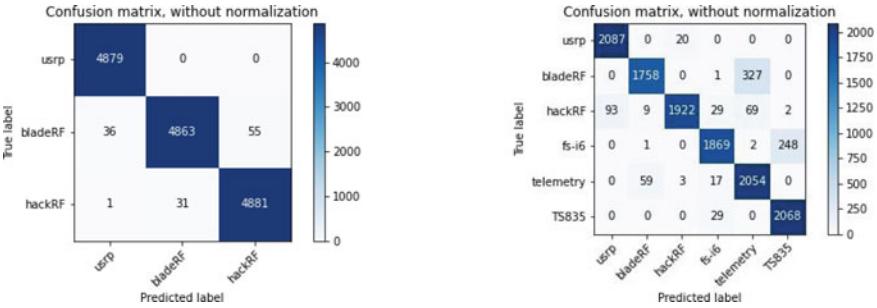

(a) 3 RF Transmitters (b) 6 RF Transmitters

Fig. 8 Transmitter classification using confusion matrix

3 Conclusion

In this paper, the authors look at the problem of recognizing RF transmitters of similar types in the presence of hostile signals and suggest that most machine learning techniques would be ineffective in adversarial scenarios. A deep learning-based model is proposed and implemented to identify the transmitters. Using USRP-2900, the raw

IQ data is collected and used it to train the model. The convolution neural network is implemented and this model is able to discriminate three and six transmitters with 98.58% and 93.75%, respectively.

Acknowledgements This research work was carried out with support of Impacting Research, Innovation and Technology (IMPRINT)-2 Programme of DST/SERB with MHRD, Govt. of India.

References

1. Valkama M, Renfors M, Koivunen V (2001) Advanced methods for I/Q imbalance compensation in communication receivers. IEEE Trans Signal Process 49(10):2335–2344
2. Tubbax J et al (2003) Compensation of IQ imbalance in OFDM systems. In: IEEE international conference on communications, pp 3403– 3407, May 2003
3. Xiao Y, Zhang X (2019) Micro-UAV detection and identification based on radio frequency signature. In: 2019 6th international conference on systems and informatics (ICSAI), pp 1056–1062, Nov 2019
4. Ezuma M, Erden F, Kumar Anjinappa C, Ozdemir O, Guvenc I (2020) Detection and classification of UAVs using RF fingerprints in the presence of Wi-Fi and Bluetooth interference. IEEE Open J Commun Soc 1:60–76
5. Teoh YJJ, Seow CK (2019) RF and network signature-based machine learning on detection of wireless controlled drone. In: 2019 photonics and electromagnetics research symposium—spring (PIERS-Spring), pp 408–417, June 2019
6. Al-Sa'd MF, Al-Ali A, Mohamed A, Khattab T, Erbad A (2019) RF-based drone detection and identification using deep learning approaches: an initiative towards a large open source drone database. Future Gener Comput Syst 100:86–97
7. Roy D, Mukherjee T, Chatterjee M, Blasch E, Pasiliao E (2020) RFAL: adversarial learning for RF transmitter identification and classification. IEEE Trans Cogn Commun Netw 6(2):783–801
8. Roy D, Mukherjee T, Chatterjee M, Pasiliao E (2019) Detection of rogue RF transmitters using generative adversarial nets. In: 2019 IEEE wireless communications and networking conference (WCNC), pp 1–7, Apr 2019
9. Satija U, Trivedi N, Biswal G, Ramkumar B (2019) Specific emitter identification based on variational mode decomposition and spectral features in single hop and relaying scenarios. IEEE Trans Inf Forensics Secur 14(3):581–591
10. Rani S et al (2021) Amalgamation of advanced technologies for sustainable development of smart city environment. IEEE Access 9:150060–150087
11. Rani S, Kataria A, Sharma V, Ghosh S, Karar V, Lee K, Choi C (2021) Threats and corrective measures for IoT security with observance of cybercrime. In: Wireless communications and mobile computing 2021

A Comprehensive Security Review on Cloud Computing

Sameer Farooq and Priyanka Chawla

Abstract Both in academics and industry, cloud computing technology is gaining traction. Despite its significance and promise for increased IT effectiveness and cost savings, legal ambiguities around information processing, particularly across major economies, remain on both the client and supplier sides. In the perspective of this, this article attempts to provide a review of contemporary published research on privacy challenges and legal frameworks for data security in cloud platforms. We choose to concentrate on data flow between both the U. S. and the European Union due to a general intricacy of international law. Our findings indicated considerable disparities in jurisdiction and security requirements awareness between these two countries. As a result, we've identified a significant multitude of challenges that have to be explored in future Cloud Technology development.

Keywords Virtualization · On-demand self-service · CIA · Authentication access control · Broken authentication session · Cloud models: cloud deployment models · Public cloud · Private cloud · Hybrid cloud · Cloud delivery models · IaaS · PaaS · SaaS

1 Introduction

Today, cloud computing is considered to be an area that is progressive supplies dynamically flexible services as well as on interest, equipment, and pc software virtualization over the internet. Nowadays, the area that is growing is cloud computing, in distributed computing in which adaptable solutions are delivered dynamically on-demand through hardware and software virtualization over the Internet. Leasing and resources that are released may be the biggest advantages in cloud computing as per an

S. Farooq (✉) · P. Chawla
Lovely Professional University, Phagwara Jalandhar, Punjab 144401, India
e-mail: sameerfarooq.lpu@gmail.com

P. Chawla
e-mail: priyanka.22046@lpu.co.in

S. Rawat et al. (eds.), *Proceedings of Second International Conference on Computational Electronics for Wireless Communications*, Lecture Notes in Networks and Systems 554,
https://doi.org/10.1007/978-981-19-6661-3_26

individual requirement. Also, the two sorts of plans which can be offered by the cloud provider, particularly the demand plan that is a short term long-term plan also makes it attractive. The intelligent infrastructure transparency, scalability, monitoring, and security it provides also attracts user's choice. Cloud technology is among the most swiftly technological innovations in computers. There are several benefits, but along with privacy concerns, that is one of the major drawbacks of cloud-based solutions. This research will look into several privacy issues that occur while using cloud-based services in a multi-tenant scenario, as well as alternative solutions. The study also highlights cloud models that include computation as both an implementation model and a framework for the ongoing delivery of services. Data are quite important in almost any continuing organization or cloud hosting. Data leaks or mismanagement can break investor trust and lead to the company's downfall. Cloud technology is often used explicitly or implicitly in many organizations. Any security breach in cloud applications will have an impact on cloud services including the continued business of the enterprise. This is one of the primary factors why global leading tech firms are paying a greater emphasis on privacy and security. Cloud-based defense spending is predicted to expand about 42%, according to a Forbes forecast of 2015. Another comprehensive survey found that IT security spending grew by 79.1% through 2015, representing overall annual growth of further over 10%. In 2011, the International Data Corporation (IDC) found 74.6% of business customers regarded security as just a serious problem. Our publication compiles a broad range of peer-reviewed literature on cloud computing security issues as well as countermeasures. This study usually attempts to examine cloud computing, security challenges, and threats, as well as innovative solutions which may help alleviate possible cloud threats. Cloud technology has already been viable since 2008. However, the overall view of cloud computing security has been that it needs considerable changes to achieve higher levels of flexibility on a broad basis. According to another survey, the majority of issues affecting the clouds require an instant solution. Business organizations have advanced dramatically in combating risks associated with cloud technology adaptations. However, there is always progress to be made to meet the maturity level of traditional hosting.

2 Cloud Architecture

Cloud computing is on-demand, Internet computing where administrator shares information, processing, and storage resources with cloud users via the Internet network. This model is enabled global on-appetite shared pool access of arranged computing resources. Businesses and consumers who have access to cloud computing and storage space options can collect and manage their data in third-party network infrastructure. Cloud technology is simply a pool of resources that can be scaled up and down in response to customer demand and pay. This is provided like a self-service model on the web, with very little interaction with the enterprise needed. Alternative techniques of offering items with innovative, technological, and monetary potential

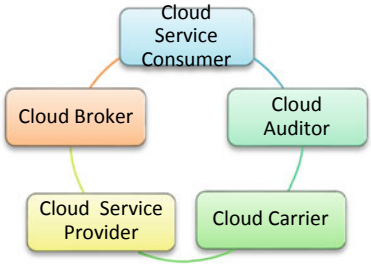

Fig. 1 Cloud-based actors

are now possible, thanks to cloud technology. According to cloud architecture, as referenced by NIST, you can find five players being major impact and are relying on cloud computing, alongside its safety implications [1]. The survey paper is targeting security perceptions and risks related to the service user and service provider. The five major players in cloud computing on basis of their roles are Fig. 1.

The survey paper is targeting security perceptions and risks related to the service user and service provider. The five major players in cloud computing on basis of their roles are Fig. 1.

i. ***Cloud Service Consumer (CSC)***: Also known as a cloud user, a CSC is a person who receives continuing services from a cloud platform and bills for them based on their utilization.
ii. ***Cloud Auditor*****:** Cloud auditor could be the person or third party who evaluates services, security, performance, information system operations, etc., of the cloud independently.
iii. ***Cloud Broker*****:** A cloud broker would be someone who serves as an interface between a hosting company and a cloud client to keep the business flowing efficiently.
iv. ***Cloud Service Provider (CSP)***: is a person or a company that owns cloud solutions and provides them to consumers for a monthly or annual fee based on consumption.
v. ***Cloud Carrier***: A mediator that conveys and delivers cloud solutions from a service provider to a cloud platform consumer.

2.1 Cloud Security Implications Concerning Deployment and Delivery

The cloud deployment model and delivery model are the two most aspects that are important in a cloud platform to determine the level of vulnerability and security issues. As per NIST, standards there are three delivery and deployment models [1, 2]. Relying on their distribution and execution, these models have their security concerns. The next sections go into each of these approaches and their associated security concerns.

2.1.1 Cloud Deployment Models

Cloud infrastructure deployment is based upon three models also known as cloud deployment models [3]. These include private cloud, public cloud, and hybrid cloud. These models define the usage and implementation of cloud architecture. Table 1 defines each deployment model along with its security challenges and implication.

2.1.2 Cloud Delivery Models

According to NIST, industrially adapted delivery models include IaaS, PaaS, and SaaS. Table 2 details these models, as well as the security challenges and implications they include.

3 Data Security Challenges and Issues

Enterprise computing stores data within the organization's data servers thus holds its full administration and control [4]. The data is stored beyond consumers' place in remote cloud data centers in the case of cloud computing. Therefore, cloud computing requires implementing more security policies in addition to the general security audits to make sure that data is safe from any vulnerability or security breach. Generate, storage, utilize, distribute, archive, and delete are the six stages of the data life cycle [5].

Data may be in any of these stages and must be secured in every stage to avoid the dangerous implications of a data breach in case of a cyberattack. Data at rest refers to the archiving and storage phases, whereas data in use refers to the usage phase, data in transit refers to the sharing phase, and data after delete refers to the trash phase. To protect data in transit or rest stage encryption is used but the issue remains in data after the deleted stage (data remanence) though that may be prone to data scavenging attack [6]. The remanence data is often the most neglected issue [6]. The data that remains after delete is known as remanence data. The remanence data has some physical attributes with which data can be regenerated after-delete [7]. Even after the deletion of storage media, it can still be reconstructed as it leaves some physical characteristics after deleting [7, 8]. Cloud computing uses path tracing also known as data lineage for auditing, particularly in public clouds [6].

Confidentiality, integrity, and availability (CIA triad) are the three most important aspects of data. Authentication, authorization, and non-repudiation are the other three properties that are required for individuals who access data [9]. Confidentiality refers to data not being revealed to unauthorized individuals [10]. The term "integrity" refers to the fact that data kept in data centers is not altered by unauthorized individuals. When a cloud client requests information, availability relates to the ability to access it without interruption at any time. Authentication verifies that an individual has the authority to access their particular information. The process of deciding whether or

Table 1 Cloud deployment model—security implication and challenges

Deployment model	Definition	Challenges	Implications
Private cloud	The cloud architecture is not accessible to the public and is merely designed for some individual or organization, only those can get access to it, and then such a kind of architecture is known as private cloud. Since the resources and data are controlled by the lone organization, this architecture offers higher-end security to its consumers	Higher deployment and management expenses, as well as increased expenditures for skillsets and mitigating risk, are all difficulties in the private cloud. Return on the investment and payback period are the most important aspects of this implementation approach. Because security deployments are based primarily on vulnerability assessment, security coverage is often inadequate	The security implications are positive and moderately strong, and the enterprise maintains a significant impact over the deployment architecture, methods, and technologies
Public cloud	The cloud architecture where everyone has access that is free the IT resources whether it is an individual or organization, resources are built free open to the basic public by the cloud supplier. The IT resources may include applications, processing, or storage resources available completely without charge. Nobody has full control over these cloud resources. The architecture may include specific risks for the organizations like not enough control that may lead toward serious data security problems and low network performance	The security risks are too high since the resources are distributed among several users rather than being dedicated. This not only increases the security complexity of assuring that all services and information access are secure, but it also entails mitigating outer vulnerabilities and hazards	Security implications are positive because it has a huge consumer and transaction ratio. The cloud service provider uses implement once and uses multiple times model that has layered comprehensive security. This approach also reduces security implementation costs

Table 2 Cloud delivery model—security implication and challenges

Delivery model	Definition	Security roles, risks and threats
Infrastructure as a Service [IaaS]	The base of the cloud architecture is Infrastructure-as-a-Service (IaaS). It serves as the framework for the other two tiers' implementation. IaaS is a cloud infrastructure service that encompasses routers, servers, storage, and other network equipment. The consumer utilizes these services on an ongoing basis depending on their needs and only pays for what they utilize. Operating systems and applications are deployed and executed as part of IaaS services. The cloud infrastructure is managed and controlled by the IaaS provider, but the user has authority over the applications and operating systems installed. If the customer understands resource management, he will get the most out of IaaS. In actuality, IaaS seems to be a little storage facility in which the customer needs to set up their server, storage, and other tools. Examples: Amazon Elastic Compute Cloud (EC2), EMC Atmos. Google Storage service	This is a fantastic model the cloud customer develops the application and needs not to bother regarding infrastructure. The security roles are shared equally by the service provider and the customer. Threats and risks are separately layered in the IaaS model. IaaS is a provider-consumer shared risky model
Platform as a Service [PaaS]	Platform as a Service (PaaS) provides consumers with cloud infrastructure capabilities for executing and deploying acquired or custom-built applications. PaaS, in its broadest sense, refers to cloud service providers' provisioning of app development platforms as a service. For creating and delivering applications on cloud provider infrastructures, the PaaS platform typically involves an Integrated Development Environment (IDE), which comprises an editor, compiler, and developing and deploying features. The client has no command or management over the physical infrastructure while using PaaS, such as the networks, workstations, OS, or memory, but he does have control over the applications and the environments in which they are deployed. Customers who use PaaS simply pay for the underlying software applications they need, such as database, operating system installations, and interfaces, as well as the accompanying maintenance costs. Examples: Google App Engine, Microsoft Azure Platform	It is a fantastic approach wherein the cloud client provides the framework shell with application form information, along with licensing, resources, and information. The customers who do not want to spend higher capital expenditure on infrastructure or lacks infrastructure management expertise prefer PaaS Infrastructure for their organizations. In PaaS, the cloud provider is more responsible for security roles than consumers the reason is its more central control than the customer, unlike IaaS. It is a provider-consumer risk-sharing approach, similar to IaaS, but the ongoing organization takes a huge responsibility because it supports more tiers

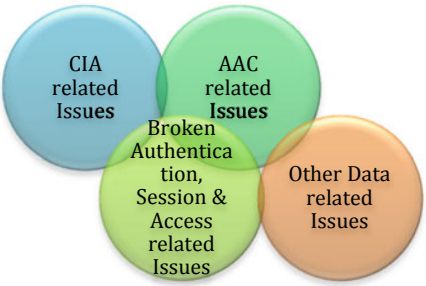

Fig. 2 Data security related issues

not an individual is permitted to view or write information is known as authorization. Before doing the task for which they are permitted, users should be authenticated. Non-repudiation can be defined as a promise not to deny once a user has completed any activity. The four primary concerns in cloud data security are shown in Fig. 2 (Table 3).

4 Cloud Threats Vulnerabilities and Countermeasures

All cloud technology, like all the other fields of information technology, has a plethora of security challenges to be addressed. Those threats encompass policy, management, technology, and the legislation [22–26].

4.1 Attack Vectors

Hardware systems, virtualization technologies, and network connections are the three key pathways of intrusion, according to recent research. Outside, internal, and cloud insider or carrier attacks are attributed to these dimensions, accordingly [22].

4.2 Open İssues and System Vulnerability

Kindly cloud is indeed a commercialized collection of technologies, processes, people, and infrastructure. Clouds, like every core technology system, personnel, or organization, have weaknesses. A few of the cloud's concerns are mentioned below. The aforementioned are some of the relevant challenges and risks that require immediate action:

Table 3 Cloud computing—data security issues, challenges and precautions

	Data security issues and challenges	Methods, actions, procedures for mitigation
Confidentiality, integrity and availability related security issues	The data is the topmost critical component of every organization. Any compromise in the CIA of data may lead to big losses to the business organization using cloud computing. Maintaining confidentiality, integrity, accuracy, steadiness, availability, and reliability of data over its life cycle is one of the security flaws in the CIA triad [11]. Cloud infrastructure distribution and multi-tenancy make it more complex and difficult than enterprise computing for the CIA triad According to Aldossary and Allen [12], integrity must be evaluated not just at the database level, as well as at the level of competition. According to computational integrity, only authorized programs are permitted to retrieve the content and use it for computations. The abnormalities should be avoided in any case of normal computing. To maintain integrity and confidentiality there should be proper effectual Identity Access Management. Another challenge is the data loss and data unattainability that causes loss of availability in cloud computing	The few significant methods for mitigation of CIA triad related security risks and challenges are as follows: • When the data are generated, classify it, segregate sensitive ones, outline policies and methods for accessing various kinds of data. Additionally, define archiving and destroying policies for data too • Encryption of both transit and rest data with an algorithm like AES and RSA. Various encryption algorithms and types are explained in [12, 13]. The AES-256-bit encryption algorithm is used by Amazon S3 [14] • The issue of confidentiality can be solved by the encryption technique but it cannot defend data software package bugs and erroneous patterns [12]. Hashing can be used for integrity check but it comes with the cost of heavy bandwidth band time consumption • Must have proper recovery and backup procedures in addition to appropriate logical and physical protection • Service level agreements should define exactly the kind of data to be shared, when to be shared and how to be • Identity access management (IAM) practices for user identification must be implemented efficiently for data accessing • For availability implement data replication, redundancy, backups, and systems that are resilient [15] • In case the ongoing cloud service fails implement a retrieval plan • The data dispersion practice may be employed to deal with the availability problem if other methods do not work [5] • The retrieval strategy must be in action plans, in case of device or network hack or data deletion, or corruption • Third-party auditing (TPA) can be used to check the integrity of data. Numerous authors [12, 16, 17] insist on data integrity auditing with third parties because of their being specialization in auditing • Do perhaps not keep the encryption keys combined with encrypted data [15]

(continued)

Table 3 (continued)

	Data security issues and challenges	Methods, actions, procedures for mitigation
Authentication and access control (AAC) related security issues	The complete process for verifying and approving the identity of the user to connect, access, and use cloud resources is known as authentication and access control (AAC). The credentials are stored in the access control list (ACL) of the enterprise server in case of enterprise computing that is used later for authentication and authorization. In a cloud, this is done through a virtual network. The similar resource pooling of applications executed by different cloud consumers of the same cloud service provider makes public clouds more vulnerable while authentication than private clouds [5]. Also, the authentication based on passwords is not quite effective as the passwords are subjective to the different kinds of social engineering attacks or physical thefts. Cloud computing uses token-designed APIs to authenticate customers, who connect with the cloud via tokens allocated by API instead of passwords [5] The authentication of the cloud is not only for users but machines too need to authenticate for authorizing various automated tasks like system updating, cloud backup, remote monitoring, and patching in case of faults or failure [18]. The remote access and device independence of cloud applications add certain types of risks and vulnerabilities, thus tokens, smart cards, biometrics, and OTP over the phone like strong authentication methods should be used. The ACC-related security issues can be mitigated with the numerous available standards and methods	The few significant methods for mitigation of ACC related security risks and challenges are as follows: • Use a single sign-on policy whenever applicable • The biometric is a more authentic form of single sign-on authentication [19] • Multi-factor authentication like AWS can be used for access management and identification [14] • The authentication like two-factor, adaptive, and knowledge-based are very effective in cloud computing for data protection. We can adopt cryptosystems to such types of authentications [20] • The IDS, IDPS, and firewalls can be implemented at different layers of cloud infrastructure for effective data security [20] • The identity management solutions from third parties like McAfee Cloud Identity Manager, Azure Active Directory from Microsoft, or Okta Identity Management are available and can be used for cloud identity solutions. The new popular service that incorporates infrastructure is Identity Management-as-Service (IDaaS) can also be employed cloud identity solutions [21] • The open standards like security assertion markup language (SAML) or XML-based organization for the advancement of structured Information standards (OASIS), Open Authorization (OAuth) must be used by cloud applications in between security domains for authentication and authorization data exchange, sharing of private resources in between users via tokens instead of credentials [5]

i. ***Malicious Insider***: Inside a cloud's environment, a tenacious insider would come up with new ways to attack and defend the track.
ii. ***Account hijacking***: Accessibility to the cloud over the Internet is among the most appealing features, but it also poses the risk of identity breach. Losing access to a privileged profile potentially results in a large loss.
iii. ***Data breach***: While moving data, from cloud user to service provider, there is the possibility of harmful, accidental, or intentional loophole.
iv. ***Browser and Interface vulnerability***: Vulnerability in the interface of cloud provider's API poses a risk that is significant whenever along with social engineering and browser attacks, the harm is too far.
v. ***Security flaws in shared technology***: Leveraging the use of more resources allows hackers a one-of-a-kind target, leading to the disruption that is out of scale to its value. Clouds or virtualization orchestration is a good example of sharing technology.
vi. ***Denial of Service (DoS)***: Since all people share the same hardware and system assets, a denial-of-service attack on all users may be inflicted with just an attack on the cloud provider.
vii. ***Abusive use***: Several cloud services features, such as the use of trail durations to start a DDoS or swarm assault, can be used for unethical reasons.
viii. ***Injection attack vulnerability***: Administrative layer injection flaws such as Operating system injections, SQL injection, and LDAP injection can pose a significant risk for various cloud users.
ix. ***Availability***: The likelihood that an operational system works when required and as required.
x. ***Internet Protocol***: ARP spoofing, IP address spoofing, and DNS poisoning are all intrinsic issues in IP.
xi. ***Changes to Business Model***: Cloud adoption entails a fundamental shift in the customer's business strategy. As a result, IT administration in organizations and businesses must adapt or face peril.

4.3 Countermeasures

The risks of threats and loopholes within the cloud are documented properly in form of cloud security policies. Mitigation strategies and regulations must be developed by both the service provider and the service consumer to minimize the effect of risks identified in their evaluation. The following are a few of the finest control strategies and tactics to take into account:

i. ***Scanning for harmful activities***: The data encryption while strongly suggested adds new risks because encrypted information is not readable to the Firewall or IDS. In a conclusion, having the right controls and risk mitigation procedures in place for vulnerable computer software moving through encryption is crucial.
ii. ***Encryption***: Since data in a cloud deployment approach may transit across several geographical zones, it is critical that it should be encrypted end-to-end.

iii. ***Business Continuity plans***: A business continuity process is a plan of documenting the company's response in the case of an incident that results in the loss of all or part of enterprise activity.
iv. ***Interfaces and APIs***: To automate administration, secure browser interfaces and APIs are essential. The service provider must ensure that all risks are minimized.
v. ***Insider attacks***: When it comes to hiring and replacing staff and contractors, cloud providers must be cautious. It must also make sure to strengthen internal security policies and hardware of the organization to stop attacks.
vi. ***Securing leveraged resources***: The cloud service provider has to protect resources like orchestration, monitoring tools, and hypervisors. Because they are being shared due to the multi-tenancy model of the cloud.
vii. ***Cloud user's validation***: The service provider in the cloud must maintain proper policies and precautions that are adequate to screen the cloud user's validation and to avoid essential features of the cloud used for malicious intent.

5 Conclusion

Since vulnerabilities are typically found much too late to stop catastrophes, cloud computing security is evolving in real time. Because of its challenging nature, sophisticated infrastructure, and leveraged resources, cloud technology poses a unique and significant threat to all players. It is critical for all parties and operators to be aware of the threat and to take appropriate measures to mitigate it. To mitigate the risk, security should be built into every tier of a cloud platform, employing the most cutting-edge techniques and technology. Customers, suppliers, agents, carriers, regulators, and everybody else in the network need merely follow certain guidelines to effectively safeguard the entire cloud framework ecosystem, otherwise, they face severe massive and sometimes business-critical danger.

Security engineering offers the finest approaches, procedures, and policies for designing infrastructure and applications that are intended toward security, sustainability, and resilience, according to a recent survey. One might continue expanding on this comprehensive study to provide such guidance for a wider range of applications and circumstances. More exploration into the systems development life cycle for cloud services is also necessary to include new upgrades such as technical modeling and container solutions, such as Docker, to enhance security at a fundamental level. Furthermore, research on the link between instruction and a user's influence on security has an ideal weight. To completely grasp the forthcoming issues, demands, and implications of security awareness training for cloud users and cloud suppliers, further investigation is recommended.

References

1. National Institute of Standards and Technology (2011) NIST cloud computing reference architecture. https://www.nist.gov/publications/nist-cloud-computing-reference-architecture
2. Modi C, Patel D, Borisaniya B, Patel A, Rajarajan M (2012) A survey on security issues and solutions at different layers of cloud computing. J Supercomput 63(2):561–592
3. Kuyoro SO, Ibikunle F, Awodele O (2011) Cloud computing security issues and challenges. Int J Comput Netw (IJCN) 3(5):247–255
4. Subashini A, Kavitha V (2011) A survey on security issues in service delivery models of cloud computing. J Netw Comput Appl 34(1):1–11
5. Reed A, Rezek C, Simmonds P (2011) Security guidance for critical area of focus in cloud computing V3.0, cloud security alliance (CSA), pp 1–177
6. Bhadauria R, Sanyal S (2012) Survey on security issues in cloud computing and associated mitigation techniques. Int J Comput Appl 47(18):47–66
7. Sabahi F (2012) Secure Virtualization for cloud environment using hypervisor-based technology. Int J Mach Learn Comput 2(1):39–45
8. Gallagher PR (1991) A guide to understanding data remanence in automated information systems. The Rainbow Books, Chaps. 3 and 4
9. Pesante L (2017) Introduction to information security. https://www.us-cert.gov/sites/default/files/publications/infosecuritybasics.pdf. Accessed on 20 Aug 2017
10. Worlanyo E (2017) A survey of cloud computing security: issues, challenges and solutions. http://www.cse.wustl.edu/~jain//cse570-15/ftp/cld_sec/index.html. Accessed on 20 Aug 2017
11. Rouse M (2017) Data integrity. http://searchdatacenter.techtarget.com/definition/integrity. Accessed on 21st Aug 2017
12. Aldossary S, Allen W (2016) Data security, privacy, availability and integrity in cloud computing: issues and current solutions. Int J Adv Comput Sci Appl 7(4)
13. Sun Y, Zhang J, Xiong Y, Zhu G (2014) Data security and privacy in cloud computing. Int J Distrib Sensor Netw 10(7):1–9
14. Amazon Web Services: Overview of Security Processes (2016). https://d0.awsstatic.com/whitepapers/aws-security-whitepaper.pdf. Accessed on 20 Aug 2017
15. CSCC security for cloud computing ten steps to ensure success. cloud standards customer council, 2015, pp 1–35
16. Wang C, Chow S, Wang Q, Ren K, Lou W (2013) Privacy-preserving public auditing for secure cloud storage. IEEE Trans Comput 62(2):362–375
17. Balusamy B, Venkatakrishna P, Vaidhyanathan A, Ravikumar M, Devi Munisamy N (2015) Enhanced security framework for data integrity using third-party auditing in the cloud system. In: Proceedings of the artificial intelligence and evolutionary algorithms in engineering systems. advances in intelligent systems and computing, vol 325. Springer, pp 25–31
18. Rouse M (2017) Authentication. http://searchsecurity.techtarget.com/definition/authentication. Accessed on 21 Aug 2017
19. Shinder DL (2014) Authentication in the cloud. http://resources.infosecinstitute.com/authentication-cloud/#gref. Accessed on 21 Aug 2017
20. Jakimoski K (2016) Security techniques for data protection in cloud computing. Int J Grid Distrib Comput 9(1):49–56
21. Ferrill T (2017) The best identity management solutions of 2017. https://www.pcmag.com/article2/0,2817,2491437,00.asp. Accessed on 21 Aug 2017
22. Coppolino L, D'Antonio S, Mazzeo G, Romano L (2016) Cloud security: emerging threats and current solutions. Comput Electr Eng. https://doi.org/10.1016/j.compeleceng.2016.03.004
23. European Network and Information Security Agency (2009) Cloud computing: benefits, risks and recommendations for information security. https://resilience.enisa.europa.eu/cloud-security-and-resilience/publications/cloud-computing-benefits-risks-and-recommendations-for-information-security/
24. Ramachandran M (2015) Software security requirements management as an emerging cloud computing service. Int J Inf Manage 36(4):580–590

25. Roundup of Cloud Computing Forecasts and Market Estimates (2015). http://www.forbes.com/sites/louiscolumbus/2015/01/24/roundup-of-cloud-computing-forecasts-and-market-estimates-2015/#56c0b0f0740c. Retrieved 2 May 2016
26. Wang C (2009) Cloud computing checklist: how secure is your cloud? For Res. https://www.forrester.com/report/Cloud+Computing+Checklist+How+Secure+Is+Your+Cloud/-/E-RES55453

Discrimination of Normal and Abnormal Knee Joint VAG Signals Using EMD

Abhishek Singh, Kapil Gupta, and Varun Bajaj

Abstract Knee is the most intricate joints in the body. This joint faces immense reaction forces during daily routine work that may vary around three to seven times of the body weight. These high reaction forces may convert small malfunctioning into severe conditions and can be avoided by early detection of knee health conditions. Vibroarthrography (VAG) is the most emerging tool to detect knee joint abnormalities. In this paper, an application of the empirical mode decomposition (EMD) is presented to discriminate between normal and abnormal knee joint VAG signals. EMD is employed to decompose VAG signals into several intrinsic mode functions (IMFs). Twelve different nonlinear, entropy, and shape-based features are elicited from each IMF provided by EMD. Kruskal–Wallis (K–W) test is employed to identify the best suitable features to discriminate between normal and knee joint affected VAG signals. The simulation results with the publicly available VAG database are included to show the effectiveness of the presented work.

Keywords Knee abnormalities · Vibroarthrography · Empirical mode decomposition · Kruskal–Wallis test

1 Introduction

Knee joint is one of the most commonly injured and complex joints in the human body. It joins the thigh bone (known as femur) and lower leg bone (known as tibia). The knee joint is a sort of hinge joint that allows bending and straightening movements. This

A. Singh · K. Gupta (✉) · V. Bajaj
PDPM-Indian Institute of Information Technology Design and Manufacturing, Jabalpur, Madhya Pradesh 482005, India
e-mail: 20peco06@iiitdmj.ac.in

A. Singh
e-mail: 20mecp01@iiitdmj.ac.in

V. Bajaj
e-mail: varunb@iiitdmj.ac.in

S. Rawat et al. (eds.), *Proceedings of Second International Conference on Computational Electronics for Wireless Communications*, Lecture Notes in Networks and Systems 554,
https://doi.org/10.1007/978-981-19-6661-3_27

joint has to face an enormous reaction force that is nearly equal to the weight of the human body [1]. The degradation of these joints is being common in elderly people [2]. Osteoarthritis is the most common knee joint complication caused by articular cartilage degeneration. According to the WHO statics, symptomatic osteoarthritis affects 9.6% of males and 18.0% of women in the world [2]. In case of severe knee complications, the patient needs to go for a knee replacement, which is an invasive technique that includes the removal of dented and worn out surface of knee joint [2]. In the knee replacement technique, a surgeon has to remove and replace the damaged and worn out part with components made up of plastic and metals. This procedure sounds expensive and complex too. Therefore, an easier and more economical approach is required for the timely detection of knee joint abnormalities. Various traditional techniques like computer tomography (CT), X-ray imaging, and magnetic resonance imaging (MRI) are available for the screening of knee-related abnormalities, but these traditional techniques are unable to identify the minute changes that come in the early stage [3]. Computer-aided diagnosis is the need of the hours [4, 5]. Vibroarthrography (VAG) is the most emerging tool to diagnose various knee-related disorders [3]. VAG signals are generated from the movements of the femur and tibia and can capture the knee joint abnormalities in a better way [6]. VAG signals are generated around the mid-patella region and measured using an accelerometer when the leg is moving. The nature of VAG signal is nonlinear and non-stationary, and cannot be examined with the help of a naive signal processing technique. Some of the salient features of the VAG signal are listed below: [7].

1. VAG signals are non-stationary in nature because the quality of joint surfaces in contact may vary from one angular position (point in time) to a next during joint articulation.
2. Normal and aberrant VAG signals have varied amplitude and frequency-based properties.
3. The friction between the femoral condyle and the layer above the patella causes an aggregation of many vibrations as the leg moves, the potential of the VAG signal becoming a multi-component signal is also high.
4. The noise may be introduced to the signal during data recording, a priori assessment of the signal-to-noise ratio (SNR) of VAG signals is difficult.

In the literature, various researchers proposed different computer-aided discrimination systems to distinguish between normal and knee-joint affected VAG signals. For example, authors in [8] utilized the wavelet decomposition method to decompose VAG signals into several wavelet coefficients. For the categorization of normal and pathological VAG signals, Ranggayyan and Wu [9] derived several entropy-based characteristics. In another study, the same group [10] extracted fractal dimension-based features from the VAG signals. Time–frequency distribution (TFD) of input VAG signal has been scrutinized using double-density dual-tree complex wavelet transform (DTCWT) by Sharma et al. [2]. The short-time fourier transform (STFT) approach has been employed to fetch statistical characteristic features from VAG signals by Mrunal et al. [11]. For reliable identification of knee joint pathologies

with minimal time, a new approach is introduced in [12]. TQWT has been introduced to deconstruct the VAG signals into sub-band signals, and entropy information is retrieved from each sub-band by Mascarenhas et al. in [13]. Various other machine learning-based approaches are described in the literature. The selection of more appropriate features for a machine learning classifier is difficult and time-consuming. Therefore, this study presents automated discrimination of normal and knee joint affected VAG signals by utilizing empirical mode decomposition (EMD) and Kruskal–Wallis (KW) test. EMD is applied to disintegrate VAG signals into several intrinsic mode functions (IMFs). Twelve different nonlinear, entropy, and shape-based features are elicited from the IMFs. Kruskal–Wallis (K–W) test is used to discriminate the best suitable features to identify normal and knee joint affected VAG signals. This remainder of this article is assemble as follows: Sect. 2 presents the information about the dataset, decomposition technique, and features extraction. Sect. 3 contains the findings of this study along with a brief discussion. Sect. 4 depicts the conclusion of the work.

2 Material and Method

The layered diagram of the presented system is shown in Fig. 1.

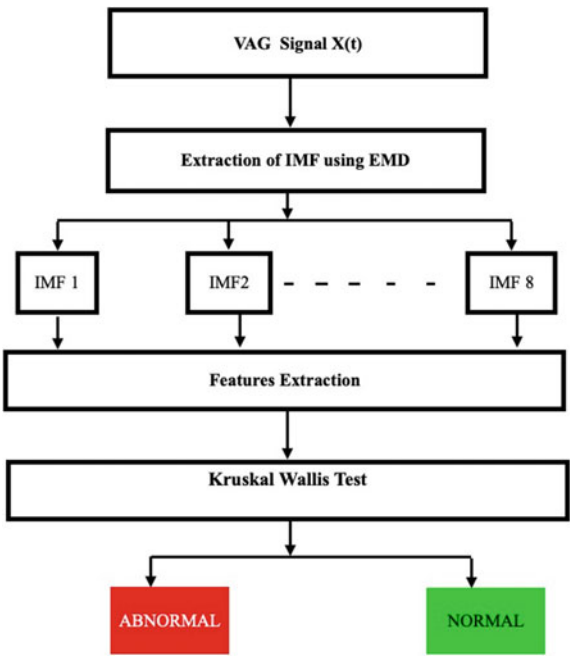

Fig. 1 Layered diagram of the presented system

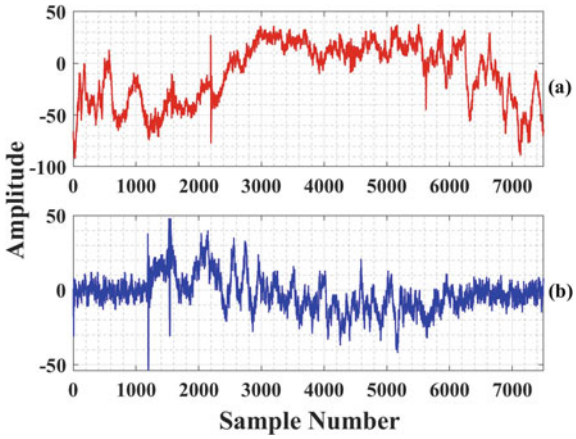

Fig. 2 Typical VAG signals of **a** abnormal **b** Normal subject

2.1 Dataset

A publicly available VAG data set is used to validate this study. The data set is obtained from 51 normal and 38 abnormal volunteers [14]. To record the VAG signal each volunteer was said to sit on a bench, and an accelerometer setup was utilized to acquire VAG signals. The volunteers were told to swing their leg from extension to flexion and back to an extension, which means from zero degrees to one hundred forty degrees and back to zero degrees again, such that the movement process completes in 4 sec [15]. The dataset is recorded with a sampling frequency of 2 kHz. Before digitizing the signal, it was filtered and amplified. This process had been done in the laboratory of the University of Calgary, Canada. The details of the data can be found in [14]. VAG signals of normal and unhealthy subjects are represented in Fig. 2.

2.2 Emperical Mode Decomposition (EMD)

EMD is a data-dependable and adaptable approach. The EMD method does not involve any prerequisites about the signal's stationarity or linearity. The essence of the EMD is to decompose nonlinear and non-stationary VAG signals $z(t)$ into various intrinsic mode functions (IMFs) [16, 17]. Each IMFs must have to satisfy the following criteria: (1) the total of maxima (max) or minima (min) and the number of zero crossings should be the same or differ by no more than one. (2) the average scores of the envelope formed by the local maxima and the envelope provided by the local minima is zero at any moment in time.

The EMD procedure for an input VAG signal $z(t)$ can be summed up as follows [16]:

1. Identify max and min of the input VAG signal $z(t)$.

2. With the help of cubic line interpolation connect the local max and localmin to obtain upper and lower envelope $V_u(t)$ and $V_l(t)$, respectively.
3. Estimate the local mean as $m_e(t)$

$$m(t) = [V_u(t) + V_l(t)]/2 \tag{1}$$

4. Extracts the details.

$$h_1(t) = z(t) - m_e(t) \tag{2}$$

5. Decide whether $h_1(t)$ belongs to IMF, with the help of previously discussed two conditions.
6. Repeat the process from 1 to 4 until the first IMF is obtained.

As first IMF is extracted, interpret $p_1(t) = h_1(t)$, is the lower temporal scale in $z(t)$. To obtain the remaining IMFs, produce residue $r_1(t) = z(t) - p_1(t)$, which is processed as a new signal. Repeat all the steps over the new signal until the final residue is obtained in the form of nearly constant or from which no more IMFs can be evoked. The input VAG signal $z(t)$ can be symbolize as at the end of the decomposition.

$$Z(t) = \sum_{n=1}^{N} p_n(t) + res_N(t) \tag{3}$$

where N represents the total generated IMFs, $p_n(t)$ represents the nth IMF, and $res_N(t)$ denotes the residue term. Each IMF obtained from Eq. (3) is posses of consequential local frequency, different IMFs never possess the same frequency at the same time. The IMFs obtained from decomposition of normal and problematic VAG signals are shown in Fig. 3.

2.3 Features Extraction

To analyze the graphical variation of each IMF, and to discriminate between normal and abnormal VAG signals. We have extracted twelve different features, defined as follows [18, 19]:

– **Mean (M)**: The mean is the average value of dataset. Computed as

$$\text{Mean} = \frac{1}{n} \sum x_i \tag{4}$$

– **Root Mean Square (RMS)**: It is also known as quadratic mean and is termed as the square root of the mean square. It is expressed as,

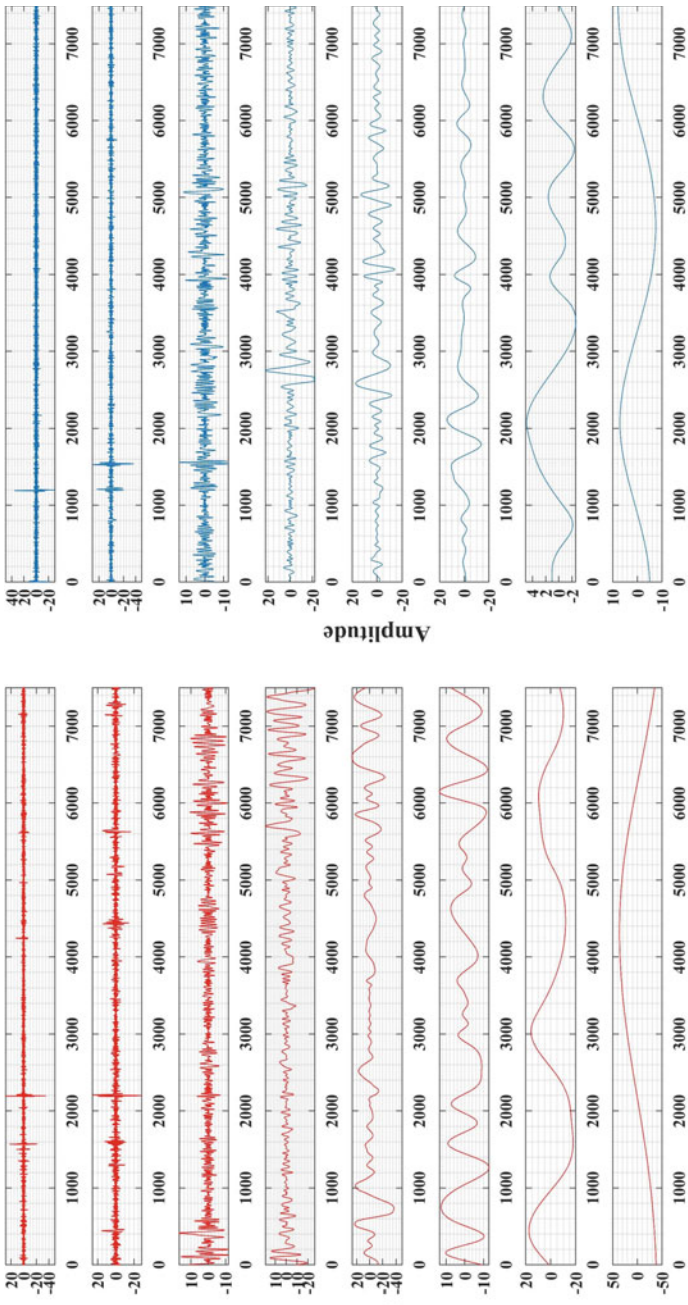

Fig. 3 Imfs of **a** Abnormal **b** Normal knee joint VAG signal

$$\text{RMS} = \sqrt{\frac{1}{n}\sum_{i=1}^{n} x_i^2} \tag{5}$$

– **Standard Deviation** (σ): It is the estimation of variations of a set values. Higher the value of σ indicates values spread over a wider range and value close to mean for lower value of σ. This is expressed as,

$$\sigma = \sqrt{\frac{n}{n-1} \times \sum_{i=1}^{n} (x_i - x_m)^2} \tag{6}$$

– **Shanon Entropy (ShanEn)**: It is the average amount of information in x. It is given as

$$HShanEn(x) = -\sum_{i=1}^{N-1} X(pi(x))2(\log 2(pi(x)))^2 \tag{7}$$

– **Log Energy Entropy (LogEn)**: The expression of LogEn is given as,

$$HLogEn(x) = -\sum_{i=1}^{N-1} X(\log 2(pi(x)))^2 \tag{8}$$

The more regularity in the VAG signal will result in a lesser value of entropy.

– **Threshold Entropy (TE)**: Entropy thresholding is a method of selecting an optimal threshold value for a signal by selecting the data intensity from a signal histogram that has the highest entropy of the total signal.
– **Sure Entropy (SE)**: SE is depends on the Stein's unbiased risk estimator. It's a technique for measuring aspects of information in order to accurately describe a signal.
– **Norm Entropy (NE)**: It is evaluated as

$$\frac{\sum_{i,j=1}^{N} |t(i,j)|^p}{N} \tag{9}$$

where p indicates the power and it must reside in the range of 1 to 2.

– **Permutation Entropy (PE)**: Permutation entropy is an adaptable time series technique that gives a quantifiable quantification of the complexity of a dynamic system.
– **Skewness (Sk)**: The skewness deals with the symmetry of distribution heaviness of the distribution of the tail. Expression for the evaluation of *Sk* is given by

$$S_k = (\text{Mean} - \text{Mode})/\text{Standard Deviation} \tag{10}$$

– **Kurtosis (K)**: Kurtosis gives facts about the flatness of the curve. The expression of kurtosis is given as

$$\beta_2 = \frac{\mu_4}{\mu_2^2} \tag{11}$$

where β_2 belongs to Kurtosis, μ_4 belongs to the fourth central moment, and μ_2 belongs to the second central moment of distribution.

– **Simple squared integral (SSI)**: It expresses the energy contain of VAG signals. It is given as,

$$\text{SSI} = \sum_{i=1}^{i=N-1} x_i^2 \tag{12}$$

2.4 Kruskal–Walis (K–W) Test

The K-W test is a more generalized form of the two-class Wilcoxon rank test and one-way analysis of variance (ANOVA) test. ANOVA is a parametric test that can be applied to a normally distributed continuous variable. Whereas, KW is a non-parametric statistical test, that compares the contretemps between two or more distinguishable sampled classes on a single, infrequently dispersed continuous variable. K-W test is a generalized form of a two-class Wilcoxon rank test and a one-way analysis of variance (ANOVA) test [19, 20].

3 Results and Discussion

The selection of most suitable feature to discriminate between normal and abnormal VAG signals is a time-consuming task. Therefore, in this work input VAG signal is disintegrated into several IMFs by applying EMD algorithm. Twelve different entropy-based and statistical features are evaluated from each IMF. KW test is used to discriminate the most suitable feature. The probabilistic values for entropy-based features are depicted in Table 1. It is obvious from the Table 1, all entropy-based features are suitable for IMF-1. NE, TE, and SrE are suitable for IMF-2. Only TE is suitable for IMF-3. Only PE is suitable for IMF-4. PE and TE are suitable for IMF-5. No any entropy-based features are appropriate for the rest of the IMFs.

The probabilistic values for statistical-based features are mentioned in Table 2. It can be noted from Table 2, RMS, STD, SSI, and IVAG are suitable for IMF-1.

RMS, STD, and IVAG are suitable for IMF-2. Mean is suitable for IMF-8. No any statistical-based features are suitable for the rest of the IMFs. This work has been

Table 1 Probabilistic values for entropy-based features

Imf No	ShanEn	LogEn	NE	TE	PE	SrE
Imf-1	0.0065	2×10^{-5}	0.0002	0.0002	0.0449	1.28×10^{-5}
Imf-2	0.0573	0.0472	0.0377	0.0001	0.7553	0.0407
Imf-3	0.868	0.2531	0.7084	0.0039	0.4001	0.2531
Imf-4	0.4298	0.5061	0.3136	0.4703	0.0018	0.3943
Imf-5	0.4671	0.2707	0.3237	0.0428	0.0016	0.1735
Imf-6	0.9255	0.8926	0.9503	0.3448	0.2619	0.9255
Imf-7	0.7711	0.868	0.9669	0.8762	0.7474	0.9388
Imf-8	0.9751	0.5962	0.8031	0.589	0.7632	0.8926

Table 2 Probabilistic values for statistical-based features

Imf No	M	RMS	STD	Sk	K	SSI
Imf-1	0.28	0.0034	0.0034	0.4735	0.1941	0.004
Imf-2	0.5962	0.0496	0.0496	0.6327	0.3829	0.0521
Imf-3	0.1096	0.0981	0.0891	0.693	0.2619	0.9917
Imf-4	0.4059	0.4059	0.4059	0.5061	0.1836	0.3885
Imf-5	0.1941	0.4545	0.4482	0.0097	0.0865	0.442
Imf-6	0.6551	0.9586	0.9669	0.4735	0.6035	0.9751
Imf-7	0.3186	0.8598	0.8762	0.7791	0.6254	0.8031
Imf-8	0.0276	0.8597	0.8598	0.884	0.1487	0.868

simulated on the system having Intel processor, 16 GB RAM, and 1 TB hard drive, with the help of MATLAB software.

4 Conclusion

In this study, an application of EMD is explored to disintegrate between knee joint affected and healthy control VAG signals. EMD is a non-stationary signal processing technique that has been used for decomposing VAG signals into multiple IMFs. Twelve different features are elicited from each IMF. In order to find the most relevant features, a non-parametric K-W test is applied. It is concluded from this work entropy-based features are most suitable to distinguish between normal and knee joint affected VAG signals. The results suggested EMD and KW test-based algorithm can be utilized to design an automated screening system for identifying knee joint diseases in a clinic. In the future, a suitable machine learning algorithm will be employed for automated classification of VAG signals.

References

1. Jac Fredo AR, Josena TR, Palaniappan R, Mythili A (2017) Classification of normal and knee joint disorder vibroarthrographic signals using multifractals and support vector machines. Biomed Eng: Appl, Basis Commun 29(03):1750016
2. Sharma M, Sharma P, Pachori RB, Gadre MV (2019) Double density dual-tree complex wavelet transform-based features for automated screening of knee-joint vibroarthrographic signals. In: Machine intelligence and signal analysis. Springer, Singapore, pp 279–290
3. Krishnan S, Rangayyan RM, Bell GD, Frank CB (2000) Adaptive time-frequency analysis of knee joint vibroarthrographic signals for noninvasive screening of articular cartilage pathology. IEEE Trans Biomed Eng 47(6):773–783
4. Gupta K, Bajaj V, Ansari IA (2021) OSACN-Net: automated classification of sleep apnea using deep learning model and smoothed gabor spectrograms of ECG signal. IEEE Trans Instrum Meas 71(19):4002109
5. Gupta K, Bajaj V, Ansari IA (2022) An improved deep learning model for automated detection of BBB using ST spectrograms of smoothed VCG signal. IEEE Sens J. https://doi.org/10.1109/JSEN.2022.3162022
6. Rangayyan RM, Wu Y (2010) Screening of knee-joint vibroarthrographic signals using probability density functions estimated with Parzen windows. Biomed Signal Process Control 5(1):53–58
7. Krishnan S (1999) Adaptive signal processing techniques for analysis of knee joint vibroarthrographic signals. University of Calgary, pp 1–263. https://doi.org/10.11575/PRISM/23830
8. Umapathy K, Krishnan S (2006) Modified local discriminant bases algorithm andits application in analysis of human knee joint vibration signals. IEEE Trans Biomed Eng 53(3):517–523
9. Rangayyan RM, Wu YF (2008) Screening of knee-joint vibroarthrographicsignals using statistical parameters and radial basis functions. Med Biol Eng Compu 46(3):223–232
10. Rangayyan RM, Oloumi F, Wu Y, Cai S (2013) Fractal analysis of knee-joint vibroarthrographic signals via power spectral analysis. Biomed Signal Process Control 8(1):23–29
11. Shidore MM, Athreya SS, Deshpande S, Jalnekar R (2021) Screening of knee-joint vibroarthrographic signals using time and spectral domain features. Biomed Signal Process Control 68:102808
12. Balajee A, Venkatesan R (2021) Machine learning based identification and classification of disorders in human knee joint–computational approach. Soft Comput 25(20):13001–13013
13. Mascarenhas E, Nalband S, Fredo AJ, Prince AA (Feb 2020) Analysis and classification of vibroarthrographic signals using tuneable 'Q' wavelet transform. In: 2020 7th international conference on signal processing and integrated networks (SPIN). IEEE, pp 65–70
14. Rangayyan RM, Krishnan S, Bell GD, Frank CB, Ladly KO (1997) Parametric representation and screening of knee joint vibroarthrographic signals. IEEE Trans Biomed Eng 44(11):1068–1074
15. Rangayyan RM, Wu Y (2009) Analysis of vibroarthrographic signals with features related to signal variability and radial-basis functions. Ann Biomed Eng 37(1):156–163
16. Bajaj V, Pachori RB (2011) Classification of seizure and nonseizure EEGsignals using empirical mode decomposition. IEEE Trans Inf Technol Biomed 16(6):1135–1142
17. Pachori RB, Bajaj V (2011) Analysis of normal and epileptic seizure EEGsignals using empirical mode decomposition. Comput Methods Programs Biomed 104(3):373–381
18. Bajaj V, Pachori RB (2012) EEG signal classification using empirical mode decomposition and support vector machine. In: Proceedings of the international conference on soft computing for problem solving (SocProS 2011) December 2022, 2011. Springer, New Delhi, pp 623–635
19. Gupta K, Khare SK, Bajaj V, Ansari IA (2021) Automatic detection of hypertension by flexible analytic wavelet transform using electrocardiogram signals. High performance computing for intelligent medical systems, pp 1–1 to 1–18
20. Machado M, Flores P, Claro JC, Ambrósio J, Silva M, Completo A, Lankarani HM (2010) Development of a planar multibody model of the human knee joint. Nonlinear Dyn 60(3):459–478

Anomaly-Based DNN Model for Intrusion Detection in IoT and Model Explanation: Explainable Artificial Intelligence

Bhawana Sharma, Lokesh Sharma, and Chhagan Lal

Abstract IoT has gained immense popularity recently with advancements in technologies and big data. IoT network is dynamically increasing with the addition of devices, and the big data is generated within the network, making the network vulnerable to attacks. Thus, network security is essential, and an intrusion detection system is needed. In this paper, we proposed a deep learning-based model for detecting intrusions or attacks in IoT networks. We constructed a DNN model, applied a filter method for feature reduction, and tuned the model with different parameters. We also compared the performance of DNN with other machine learning techniques in terms of accuracy, and the proposed DNN model with weight decay of 0.0001 and dropout rate of 0.01 achieved an accuracy of 0.993, and the reduced loss on the NSL-KDD dataset having five classes. DL models are a black box and hard to understand, so we explained the model predictions using LIME.

Keywords Intrusion detection system (IDS) · ML · DL · DNN · KNN · SVM · DT · LIME

1 Introduction

In recent years, IoT has been widely used in many fields such as smart cities, healthcare, and automobiles [1]. With the advancement in network technologies, there is growth in connected devices and big data in IoT systems [2], and the network is more prone to attacks. Thus, network security is essential, and there is a need to detect

B. Sharma (✉) · L. Sharma
Department of Information Technology, Manipal University Jaipur, Dehmi Kalan, Jaipur, Rajasthan 303007, India
e-mail: bhawana2104@gmail.com

L. Sharma
e-mail: lokesh.sharma@jaipur.manipal.edu

C. Lal
Department of Intelligent Systems, Cybersecurity Group, TU Delft, Mekelweg 5, Delft 2628, South Holland, The Netherlands

S. Rawat et al. (eds.), *Proceedings of Second International Conference on Computational Electronics for Wireless Communications*, Lecture Notes in Networks and Systems 554,
https://doi.org/10.1007/978-981-19-6661-3_28

the attacks, and measures should be taken to prevent the devices from such attacks [3]. Different types of new attacks are rapidly increasing with the enlargement in network size. Therefore, efficient intrusion detection systems (IDS) are needed to detect intrusions or attacks in the IoT networks.

IDS are classified into two types. One is signature-based IDS in which pre-stored signatures are matched to detect attacks, and another is anomaly-based IDS in which any deviation from normal behavior is identified as attacks [4]. In signature-based IDS, it is difficult to identify new or unknown attacks because it works on matching with predefined attacks, and thus anomaly-based IDS are used for today's network, which detects the attacks based on behavior and can detect new attacks or unknown attacks. In an anomaly-based IDS, there can be false positives as any deviation from normal is classified as an attack, so an efficient technique is needed to reduce the number of false positives. Efficient ML and DL techniques can remove this weakness.

Nowadays, machine learning (ML)/deep learning (DL) techniques are widely used for the computation of large datasets and are providing good results [5]. Thus, researchers are also using ML and DL techniques in the field of cyber security and proposed various models based on ML/DL methods for NIDS in IoT networks such as KNN/SVM and DNN/CNN [6, 7].

ML and DL models are a black box and are hard to understand as they provide only predictions and not the explanation, so the explainable AI concept is introduced, and researchers are working in this field [8, 9]. Models are visualized and explained using LIME. LIME is the most popular method for the explanation of models as it explains the predictions made by the model [10]. In this paper, we proposed DNN-based NIDS, where we reduced the number of features using the filter method and then applied the DNN model for classification and explained the prediction using LIME.

2 Literature Review

In recent years, the field of anomaly-based intrusion detection systems has been drawing the attention of many researchers. In IoT networks, different models based on ML/DL are proposed for IDS, such as SVM/KNN and DNN/CNN. Deep learning techniques have achieved good results in NIDS.

Shone et al. have proposed deep learning and evaluated the model on a publicly available NSL-KDD dataset [11]. Al-Zewairi et al. have proposed the DL model and evaluated it on a publicly available UNSW-NB 15 dataset, and achieved an accuracy of 99% [12]. Alrashdi et al. proposed anomaly-based detection for IoT system: A DIoT using random forest classifier and evaluated the model on the UNSW-NB15 dataset and achieved an accuracy of 99.34% [13]. Xiao et al. proposed a CNN-IDS model and used the KDDCup99 dataset for evaluating the model and achieved an accuracy of 94.0% [14]. Verma et al. proposed a 1D-CNN model and utilized the NSL-KDD dataset for evaluation, and showed an accuracy of 79% and a high detection rate [15]. Ge et al. proposed an FNN model for intrusion detection and

utilized BoT-IoT dataset to train and then evaluate the proposed model for different attack classes, and the multi-class classification model achieved an accuracy above 99% [16].

Fenanir et al. applied different Machine learning-based models on publicly available NSL-KDD and UNSW-NB15 datasets and showed the highest accuracy using a Decision tree (DT) [17].

In [10], Zhou et al. proposed stabilized Lime for model explanation and applied random forest classifier on breast cancer dataset, where the classifier achieved the accuracy of 95% and explained the model using a specific instance of the dataset.

The literature study showed that the different ML and DL techniques are applied to detect the attacks; however, there are certain issues that need to be resolved. The class imbalance issue needs to be solved. The number of features needs to be reduced, which reduces the computation cost. ML and DL models are hard to understand and need explanation methods that explain the predictions of the model.

3 Proposed Framework

We proposed DNN-based NIDS to detect attacks in IoT networks in this paper. We have mainly four phases: data preprocessing (normalization and encoding), feature reduction (selecting the most promising features), feature preprocessing (splitting the dataset), then the last phase is training, and testing model, as shown in Fig. 1.

Dataset description: Researchers are using different publicly available datasets to evaluate the model. NSL-KDD dataset is the standard dataset used for evaluation and is widely used by researchers for NIDS [18]. It contains a total of 41 features, out of which three are symbolic values, the rest are numeric values, and one label shows normal and attacks classes. The label has a total of 23 attack classes, which are then grouped into four main attack classes, namely, Probe, DoS, U2R, and R2L. The total number of records in the dataset is 125972, containing five classes Normal (67,342), DoS (45,927), Probe (11,656), R2L (995), and U2R (52).

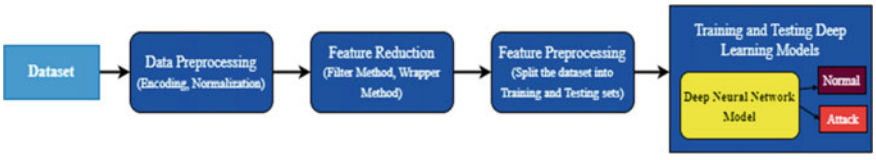

Fig. 1 Workflow of proposed methodology

3.1 Data Pre-Processing

In this phase, features are encoded and normalized. We convert the symbolic features into numeric values for calculation using the label or one-hot encoding. In our experiment, we used label encoding and converted the 3 symbolic features, namely 'protocol type,' 'flag,' and 'service,' into numeric values [19]. Five classes in 'attack label', namely, DoS, Normal, Probe, R2L, and U2R are converted into numeric values 0, 1, 2, 3, and 4 using label encoding. In label encoding, the labels are assigned depending on the alphabetic order.

We normalized the dataset using the Min–Max technique to fit the dataset in the model. The values are normalized within the range of [0, 1] so that the model is not biased to higher values of the dataset. The mathematical Eq. (1) shows the Min–Max normalization, where C is the column values, Cmin is the minimum, Cmax is the maximum values of column, and Cnew is the new value.

$$\text{Cnew} = (\text{C} - \text{Cmin})/(\text{Cmax} - \text{Cmin}) \tag{1}$$

3.2 Feature Reduction

In this phase, we reduce the number of features by selecting the most important features and achieve higher accuracy with minimum numbers of features. By the reduction of features, we can reduce the training time of the model and computational cost. Redundant features are also removed from the dataset to reduce feature size.

In our experiment, we have used the filter method for feature reduction, and we found the correlation between the features and highly correlated features are identified. In our dataset, we applied the Pearson correlation coefficient method, and the correlation value is calculated. The features with a value greater than the threshold value of 0.95 are considered highly correlated, and out of the two features, one is dropped. We dropped six features out of highly correlated features, and the dataset is reduced, containing 36 features.

3.3 Feature Preprocessing

In this phase, after encoding, normalization, and feature reduction, the processed data is transformed into a form that can be fed into the model for training. We divided the dataset into two sets: training and testing. We split the dataset into 75% training set to train the model and 25% testing set for testing the model. The training set is further split into 60% training and 15% validation set.

3.4 Training and Testing

Finally, the processed data is then fed into the model for training and testing. Model is trained using 60% training dataset, and 15% validation dataset is used to validate the model on an unseen dataset. The model detects the normal/attack types during the training phase and calculates the training accuracy. The model is verified using testing data in the testing phase, and then we calculate the testing accuracy. The model consists of dense hidden layers with different numbers of neurons in each layer and the activation function.

Experimental set up

We build our model using the deep learning Keras library and Google Colab, and TensorFlow. We constructed a DNN model using three dense hidden layers of 64 neurons in each layer. Since there are five classes in the dataset, the last layer is fully connected, containing five neurons. We used the ReLU activation function in each dense layer, and in the last layer, we applied a soft-max function, and then the model is compiled, and loss is calculated using sparse categorical cross-entropy and depending upon the loss, we update the weights using Adam optimizer as shown in Fig. 2. We used the NSL-KDD dataset as described above for the experiment and trained the DNN model, and also tuned the model with different hyperparameters. We applied different weight decay values and epochs and compared the accuracy and loss. The model trained on 0.001, 0.0001, 0.00001 weight decay, and 0.01 dropout rate for 50 epochs.

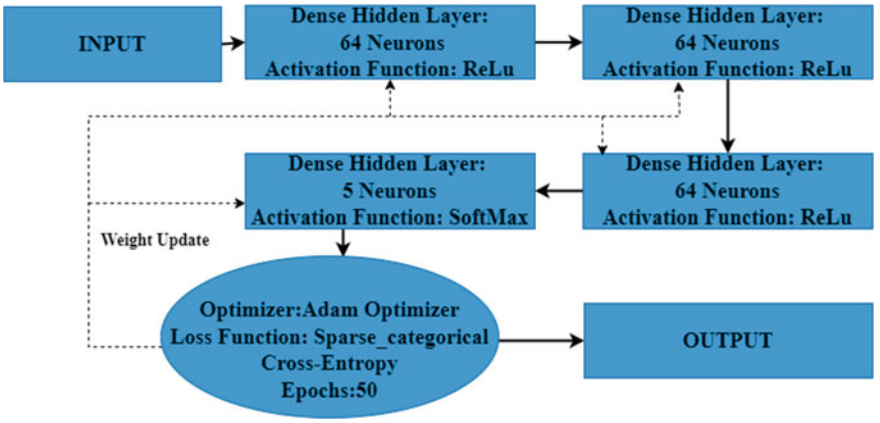

Fig. 2 Architecture of DNN model

4 Evaluation and Analysis

In this paper, we implemented the DNN model for NIDS on Google Colaboratory, evaluated the performance in terms of different evaluation metrics, and compared the model with other ML techniques for classification. We have used the publicly available NSL-KDD dataset for evaluation having numeric and symbolic features. We encoded the dataset using label encoding, and the symbolic features were converted into numeric values using label encoding. The filter-based method is applied for feature reduction, where correlation is calculated between features, and highly correlated features are identified. Then the dataset with reduced features is then applied to our DNN model.

We trained the DNN model with three different weight decay values 0.001, 0.0001, and 0.00001 and the dropout rate of 0.01. The model achieved an accuracy of 99.3% with a weight decay of 0.0001 and a dropout rate of 0.01, and a reduced loss of 0.3.

4.1 Result and Analysis

There are different parameters for model performance. We evaluated the model in terms of the following metrics:

1. **Confusion Matrix**: It is the table where the rows show the true labels and the column shows the predicted labels of the testing dataset. True Positive (TP) is the record count of the attack class correctly classified as the attack class. The record count of the normal class correctly classified as normal is True Negative (TN). False Positives (FP) is the record count of the normal class but is classified as an attack class. The record count of the attack class but classified as normal class is False Negative (FN). The confusion matrix of DNN model is shown in Fig. 3, where the diagonal values show the number of records and the percentage of TP. The model correctly predicted 16,718 records as Normal class, which is 53.08% of total records in the testing dataset.
2. **Accuracy and Loss**: The fraction of records that are correctly predicted/classified as attack and normal class to the total number of predictions is termed accuracy. Figure 4a shows the accuracy of the DNN model trained with three different weight decay values of 0.001, 0.0001, and 0.00001 are 0.985, 0.993, and 0.995, respectively. The error in the predicted and the actual value is termed as loss, and according to the loss, the weights are updated. Loss is less for the DNN model having 0.00001 weight decay, as shown in Fig. 4b. The accuracy of the DNN model is higher for weight decay value 0.00001, but the training time is 382 ms, whereas the model with 0.0001 weight decay has a training time of 315 ms.

Our DNN model with a 0.0001 weight decay and dropout rate of 0.01 achieved the accuracy of 0.993 and reduced loss and 315 ms training time of the model.

We applied different machine learning techniques and compared the accuracy with the proposed DNN model. KNN, decision tree (DT), and support vector machine

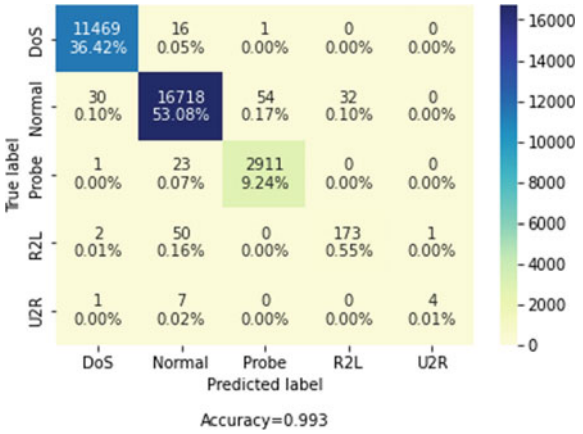

Fig. 3 Confusion matrix of DNN model

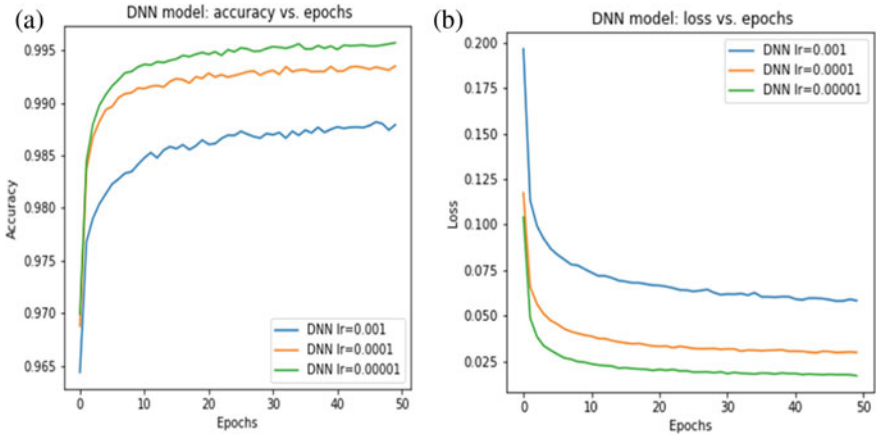

Fig. 4 **a** Accuracy versus epochs **b** Loss versus epochs of DNN having weight decay values $lr = 0.001, 0.0001, 0.00001$

(SVM) techniques are applied to the dataset, and we achieved the accuracy of 0.992, 0.988, and 0.984, respectively. Our proposed DNN model achieved an accuracy of 0.993, having a weight decay of 0.0001, and the training time taken is 315.78 ms, whereas with the weight decay of 0.00001, the accuracy achieved is 0.995, but the training time is 382.72 ms.

5 Model Explanation Using LIME

Machine learning and deep learning models are 'Black boxes' and are hard to understand, so we focus on the explanation of a specific instance. We used LIME for the explanation of the prediction done by the model on the dataset. This verifies that the predictions are the same as actual values.

Instance predicted as normal

We selected the specific instance whose actual value is normal and is predicted as normal, as shown in Fig. 5. On the left of the fig, we see that the model predicted the instance as normal with 99% prediction, and in the center, it shows the features of interest, which helps in the prediction, and in the right, it shows the feature value of the instance. Top ten features are selected for prediction.

Instance predicted as Probe

Similarly, we selected another instance, the actual probe which is correctly predicted as the probe. The model predicted probe with 100% accuracy, as shown in Fig. 6.

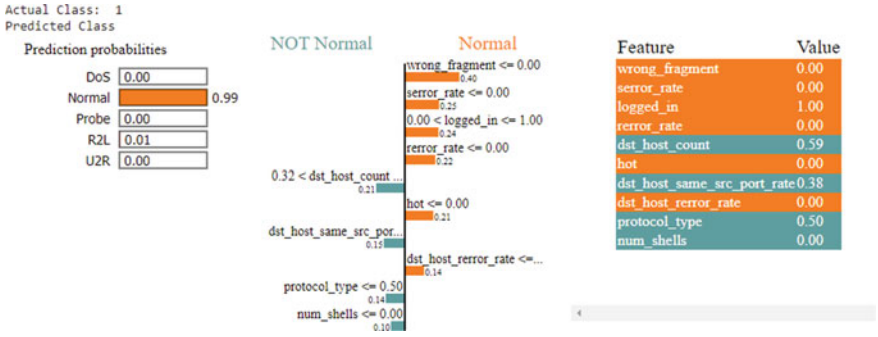

Fig. 5 Normal class predicted as normal

Fig. 6 Probe class predicted as probe

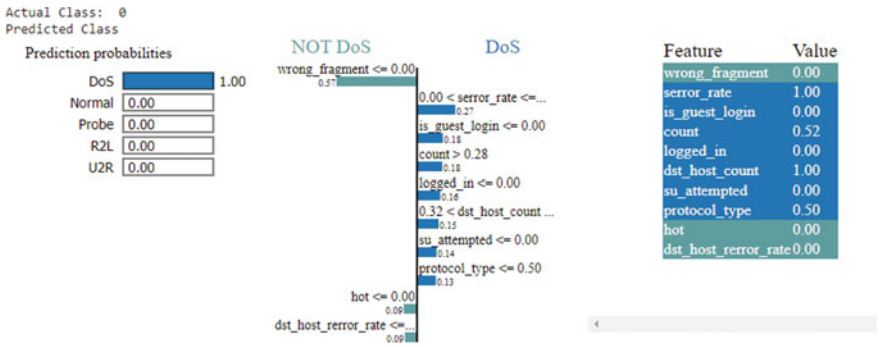

Fig. 7 DoS class predicted as DoS

Instance predicted as DoS

We selected the third instance, which is actual DoS and is predicted as DoS with 100% accuracy as shown in Fig. 7.

6 Conclusion

Nowadays, researchers are seeking interest in intrusion detection systems using machine learning (ML)/deep learning (DL) techniques. In this paper, we proposed a DNN model for intrusion detection, where we reduced the features using the filter method and then tuned the model with the weight decay regularization technique. We compared the model with other machine learning techniques and found that the DNN model achieved the highest accuracy. The model explanation is done using LIME as it is hard to understand the predictions, and for that, we selected three different instances for model verification. Our future work is to remove the class imbalance issue using GANs, reduce the DNN model's training time, and implement the model on real-time IoT systems.

References

1. Da Xu L, He W, Li S (2014) Internet of things in industries: a survey. IEEE Trans Ind Inf 10(4):2233–2243
2. Al-Fuqaha A, Guizani M, Mohammadi M, Aledhari M, Ayyash M (2015) Internet of things: A survey on enabling technologies, protocols, and applications. IEEE Commun Surv Tutorials 17(4):2347–2376
3. Lin J, Yu W, Zhang N, Yang X, Zhang H, Zhao W (2017) A survey on internet of things: architecture, enabling technologies, security and privacy, and applications. IEEE Internet Things J 4(5):1125–1142

4. Sharma B, Sharma L, Lal C (2019) Anomaly detection techniques using deep learning in iot: a survey. In: 2019 international conference on computational intelligence and knowledge economy (ICCIKE), pp 146–149. https://doi.org/10.1109/ICCIKE47802.2019.9004362
5. Chaabouni N, Mosbah M, Zemmari A, Sauvignac C, Faruki P (2019) Network intrusion detection for iot security based on learning techniques. IEEE Commun Surv Tutorials 21(3):2671–2701
6. Ahmad Z, Shahid Khan A, Wai Shiang C, Abdullah J, Ahmad F (2021) Network intrusion detection system: a systematic study of machine learning and deep learning approaches. Trans Emerg Telecommun Technol 32(1):4150
7. Al-Garadi MA, Mohamed A, Al-Ali AK, Du X, Ali I, Guizani M (2020) A survey of machine and deep learning methods for internet of things (iot) security. IEEE Commun Surv Tutorials 22(3):1646–1685
8. Ribeiro MT, Singh S, Guestrin C (2016) "Why should i trust you?" Explaining the predictions of any classifier. In: Proceedings of the 22nd ACM SIGKDD international conference on knowledge discovery and data mining, pp 1135–1144
9. Samek W, Wiegand T, Muuller K-R (2017) Explainable artificial intelligence: understanding, visualizing and interpreting deep learning models. arXiv: preprint arXiv:1708.08296
10. Zhou Z, Hooker G, Wang F (2021) S-lime: stabilized-lime for model explanation. In: Proceedings of the 27th ACM SIGKDD conference on knowledge discovery & data mining, pp 2429–2438
11. Shone N, Ngoc TN, Phai VD, Shi Q (2018) A deep learning approach to network intrusion detection. IEEE Trans Emerg Top Comput Intell 2(1):41–50. https://doi.org/10.1109/TETCI.2017.2772792
12. Al-Zewairi M, Almajali S, Awajan A (2017) Experimental evaluation of a multi-layer feed-forward artificial neural network classifier for network intrusion detection system. In: 2017 international conference on new trends in computing sciences (ICTCS). IEEE, pp 167–172
13. Alrashdi I, Alqazzaz A, Aloufi E, Alharthi R, Zohdy M, Ming H (2019) Ad-iot: Anomaly detection of iot cyberattacks in smart city using machine learning. In: 2019 IEEE 9th annual computing and communication workshop and conference (CCWC). IEEE, pp 0305–0310
14. Xiao Y, Xing C, Zhang T, Zhao Z (2019) An intrusion detection model based on feature reduction and convolutional neural networks. IEEE Access 7, pp 42210–42219
15. Verma AK, Kaushik P, Shrivastava G (2019) A network intrusion detection approach using variant of convolution neural network. In: 2019 international conference on communication and electronics systems (ICCES). IEEE, pp 409–416
16. Ge M, Syed NF, Fu X, Baig Z, Robles-Kelly A (2021) Towards a deep learning-driven intrusion detection approach for internet of things. Comput Netw 186:107784
17. Fenanir S, Semchedine F, Baadache A (2019) A machine learning-based lightweight intrusion detection system for the internet of things. Rev d'Intelligence Artif 33(3):203–211
18. NSL-KDD|dataset (2009) https://www.unb.ca/cic/datasets/nsl.html. [Online; Accessed 19 Oct 2021]
19. Sharma B, Sharma L, Lal C (2022) Feature selection and deep learning technique for intrusion detection system in iot. In: Proceedings of international conference on computational intelligence. Springer, pp 253–261

Design and Analysis of Electrocardiogram Heart Rate Variability Monitoring Systems

Yashas Bharadwaj, Shubham Yadav, Apeksha Murdeshwar, K. Harshitha, Pramod Kumar, Dolly Sharma, Mukesh Kumar Sinha, and K. Vaishali

Abstract In recent years, the treatment of cardiovascular disorders has increased dramatically, and there is a need to develop low-cost yet effective sensors' system to detect the same. This can be done with standard heart-rate variability (HRV) values obtained by analyzing the ECG signal through the transducer. Due to most electrocardiogram system device measurements suffering from poor validity, large amounts of missing data and reliability only at rest or during low-intensity exercise, which makes the existing devices less authentic. This study promotes a genuine estimation of HRV parameters to provide personal feedback about a person's lifestyle. The proposed low-cost electrocardiogram device measures the ECG signal and calculates parameters like HRV and heart rate to understand a healthy heart better. The signal from the transducer is filtered out to reduce noise, and then sent to an amplifier for amplifying the signal, and finally sent to a microcontroller to calculate the beats per minute or the heart rate. The MCU also computes the R-R interval value which is used to calculate the HRV. This is further communicated to the server using a wireless device such as a LoRa which supports wireless communication protocols like the LoRa, ZigBee, or the Bluetooth 5.0 technology. It promises to deliver a low-cost composite, non-invasive electrocardiogram tool for evaluating autonomic function.

Keywords Electrocardiogram · Heart rate variability · Monitoring systems · Microcontroller · Health systems

Y. Bharadwaj (✉) · S. Yadav · A. Murdeshwar · K. Harshitha · P. Kumar
Electronics and Communication Engineering, Manipal Institute of Technology, Manipal Academy of Higher Education, Manipal 576104, India
e-mail: yashasbharadwaj58@gmail.com

P. Kumar
e-mail: p.kumar@Manipal.edu

D. Sharma
Department of Mechatronics, Manipal Institute of Technology Manipal Academy of Higher Education, Manipal 576104, India

M. K. Sinha · K. Vaishali
Department of Physiotherapy, Manipal College of Health Professions, Manipal Academy of Higher Education, Manipal 576104, India

S. Rawat et al. (eds.), *Proceedings of Second International Conference on Computational Electronics for Wireless Communications*, Lecture Notes in Networks and Systems 554,
https://doi.org/10.1007/978-981-19-6661-3_29

1 Introduction

Over the past many decades, deaths from cardiovascular disease have risen steadily across the globe [1]. Furthermore, the COVID-19 pandemic has been recorded as a severe threat to our health and economy, causing numerous fatalities [2]. As a result, cardiovascular patients stand on the edge of adverse complications. The inspiration for the same was drawn after evaluating the pre-existing methods used and talking to various age groups. Most of them were against the opinion of going to the hospital for check-ups.

As a consequence, heart ailments continue to worsen unnoticed. Apart from this, the doctors also presented their point of view. They required a light cost sensor since the current sensor they were using was an imported and a costly one, and a portable one that could be worn and carried anywhere without any hassle. The electrocardiogram is one of the several sensors in the wearable sensor network. Since various mental and physical factors such as stress, hypertension, and chronic illnessestend to affect the heart in a nastier way [3]. Thus, the early prediction and monitoring of heart rate are essential. The ideal heart rate of a normal healthy human being varies between 60 and 100 beats per minute. Usually, a lower heart rate can mean that the person has a more efficient heart functioning and better cardiovascular fitness, close to 40 beats per minute when considering an athlete. But, a higher heart rate of more than 100 beats per minute can mean hypertension and lead to heart attacks, and if it falls lower than 50 can lead to less oxygen being pumped to the brain, causing dizziness, tired, or weak. A person's age also affects the average heart rate [4, 5]. Thus, a wearable electrocardiogram system works in real time to check the heart rate and HRV and alert the user whenever necessary. The method comprises a computing module-based central processing unit, a transducer electrode for sensing the heartbeats directly, and an oscilloscope or any device to display the ECG signal obtained. An alert system also monitors the HRV constantly and alerts the user whenever it crosses a particular critical value. The module can analyze the piezoelectric transducer sensor data, and the data is then passed through a second-order RC filter and then amplified using an instrumentation amplifier. The output from the instrumentation amplifier is then fed to the displaying device to view the obtained ECG signal in real-time. It has a wireless communication-enabled computing module used for calculating the heart rate and helps in relaying the data to the server for more processing and detailed visualization. The microcontroller also computes the HRV value using the output obtained from the comparator that can be used to calculate the R-R interval [6] for the more detailed working of a person's heart. It has an intelligence of its own, powered by on-device computing. This allows it to make decisions independently and alert the user whenever necessary instead of consulting the server for processing and actuation. Hence, the wearable electrocardiogram system redefines the MedTech industry in the twenty-first century by attenuating the hardships both doctors and patients face.

2 Literature Review

The low-cost wearable electrocardiogram system offers many advantages over conventional, stationary ECG monitoring systems. It requires intelligence at every node apart from the central processing unit. Substantial research is going on in the field of robotics and self-driving cars lately. But, despite extensive research is done in the MedTech industry, an integrated smart wearable system that is both economical and inexpensive at the same time has not been designed yet that can be used by doctors and the public alike. The oscillating behavior of the consecutive beat intervals of the heart makes it extremely difficult to analyze various underlying illnesses [7], efforts have been put into developing systems that measure heart rate variability. Most of the techniques involve a few electrodes and a bulky signal-processing system. S. Pehr et al. have developed an ECG application embedded into a bed to make the monitoring process comfortable for the patient. Flexible capacitive electrodes have been used to reduce the discomfort caused by traditional stiff electrodes [8]. However, this arrangement is expensive. In [9], a dedicated ultrasound system directly connected to the heart is made for continual monitoring during and post-cardiac surgery. However, it requires an open heart and is thus invasive.

The current clinical grade systems being used in hospitals are bulky and too expensive. Di Xue et al. have proposed an Analog Front End design tested on LTspice that makes ECG detecting systems wearable and tries to solve the aforementioned problem of bulkiness [10]. The growing interest in wearable medical devices has paved the way for complex ECG systems to fit into compact systems. Studies have compared wearable alternatives based on Photoplethysmography (PPG) to the conventional ECG measuring systems [11]. Their performance in non-stationary conditions is still doubtful and needs to be studied. Dobbs, W. C. et al. have quantified the accuracy of portable ECG devices for measuring various HRV metrics [12]. The data has been deemed acceptable owing to the benefit of reduced cost.

Early attempts at ECG data acquisition using a portable microprocessor-based system were suitable for short-term monitoring [13]. The ECG signal is recorded based on Laplacian Potential Mapping of the body in [14]. This arrangement is compact and eliminates the need for wire leads. Low-cost systems with clinical-grade data acquisition capabilities are crucial for countries like India, where access to healthcare is limited. Sayed Tanvir Alam et al. have developed a low-cost system that depends on MATLAB for processing [15]. The partially filtered signal is fed to a clamper circuit to clip off the negative voltages to zero. The signal is later fed into an Arduino Board for real-time monitoring and analyzed offline using MATLAB. Similarly, a system that adds the functionality of sending the remotely recorded data for further diagnosis to medical professionals has been built [16]. The monitoring and recording of data can also be performed using LabVIEW [17]. A simple wireless ECG system for education practice has been designed using Arduino Nano [18]. The filters are implemented on MATLAB. This low-cost system is geared for use in universities for educational purposes only and not in a hospital setting. Thus, the precision and power-consumption aspects haven't been addressed. Feature extraction and detection

techniques can be used to detect peaks and identify various HRV metrics like R-R intervals and QRS complex [19].

In this paper, the modern solutions require optimized and creative data points along with the various parameter triggers. But what sets this solution is its extremely user-friendly experience and completely automated module from collecting the transducer data to alerting the user about the health of his heart. Above all, it comes with a sustainable and ergonomic module that can be used by a layman who is very new to IoT.

The paper is organized as follows: Sect. 1 consists of brief description of the device, Sect. 2 explain the background of the research and its advantages over the existing technology, Sect. 3 described the methodology which is used in this research, Sect. 4 depicts the comparison of simulated results with ideal parameter, and Sect. 5 concludes the paper.

3 Methodology

The minor ECG fluctuations can be picked up with the help of a transducer electrode attached to the skin. These signals have much noise; hence, noise filtering and amplification will give us an accurate ECG waveform, which can be displayed on any screen or oscilloscope, as shown in Fig. 1. The amplified output can also be used to extract various vital parameters of ECG waves with the help of a microcontroller.

3.1 Electrode

A piezoelectric transducer picks up vibrations from the heartbeats and converts them into electrical output signals. To record the ECG, we need this transducer that

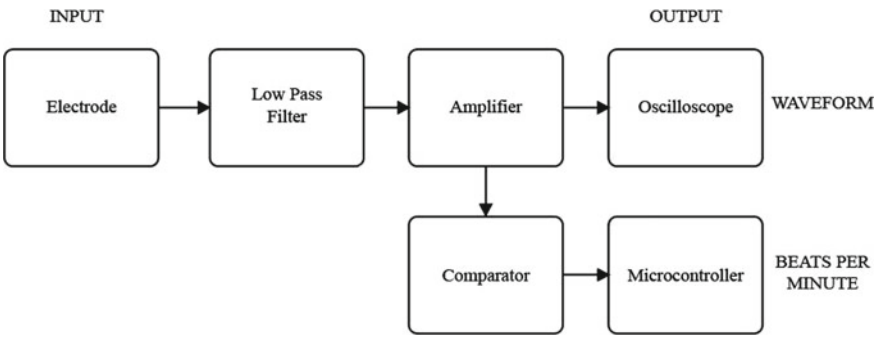

Fig. 1 Basic block diagram of HRV system

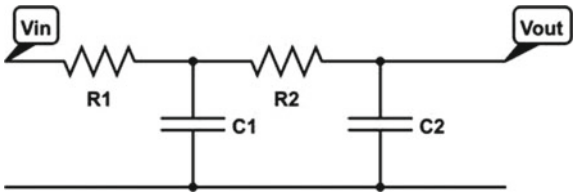

Fig. 2 Second order low pass filter

converts the ionic potentials generated into electronic signals, which electronic instruments can measure. A transducer consists of multiple electrodes, which measure the potential difference between their applied points on the human body.

3.2 Low Pass Filter

Low pass filter lowers high-frequency components of a signal with the help of a series of resistors and capacitors, as shown in Fig. 2. At low frequencies, the capacitor has a higher impedance than the resistor and hence most of the input is passed to the output. With increase in frequency, the capacitor impedance reduces and hence output decreases. The ECG signal levels are low in magnitude (1–5 mV), so a filter is required to reduce the induced noise. This noise maybe due to various sources like poor contact between body and electrode, noise due to body movements, mains hum (50 Hz), and noise from electrical equipment's in the environment. The cut-off frequency for a second-order low pass filter can be calculated with Eq. (1).

$$f_c = \frac{1}{2\pi\sqrt{R_1 R_2 C_1 C_2}}\text{Hz} \tag{1}$$

3.3 Instrumentation Amplifier

Instrumentation amplifier provides a large amount of gain for very low-level signals [20], as in the case of ECG signals. The significant properties of instrumentation amplifiers are very high input impedance, large common-mode rejection ratio (CMRR), and high gain. A very high CMRR is essential for Instrumentation Amplifier as the ECG signal voltage (less than 5 mV) detected by the piezoelectric electrodes will be accompanied by a sizeable common-mode component (up to 1.5 V). The minimum common-mode rejection for standard ECG as specified by the Association for the Advancement of Medical Instrumentation (AAMI) is 89 db. CMRR of a differential amplifier can be expressed as in Eq. (2)

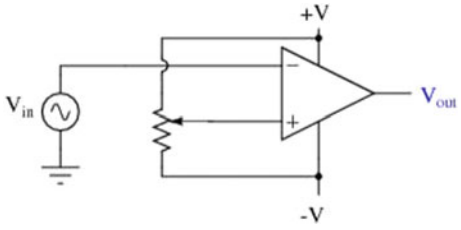

Fig. 3 Comparator circuit with variable reference voltage

$$\text{CMRR} = \frac{\text{Differential gain}}{\text{Common mode gain}} = \frac{A_{\text{dm}}}{A_{\text{cm}}} \tag{2}$$

Output of the instrumentation amplifier can be connected to an oscilloscope to analyze the obtained amplified ECG waveform.

3.4 Comparator and Microcontroller

Amplified ECG waveform is passed through an Operational Amplifier working as a comparator with appropriate reference voltage to filter out the ECG peaks like P, R, and T peaks, as shown in Fig. 3. These peaks can be passed to a microcontroller wo calculate various parameters of an ECG wave such as, PR interval, QRS complex, QT interval, RR interval. These peaks can be used to investigate possible heart problem symptoms, like chest pain, palpitations, dizziness, and heavy breathing.

4 Result and Description

The schematic diagram for the ECG circuit is shown in Fig. 4. Each component is placed in the sequence mentioned in the block diagram of the HRV system in Fig. 1. The analysis of ECG signals was simulated on LT Spice to categorize sample ECG dataset, sourced from standard clinical ECG devices and determine P, Q, R, S, and T wave timing. The electrocardiogram circuit uses signals generated from Ag/AgCl electrodes for real-life simulation. The heart signals are collected using Ag/AgCl disposable electrodes. The signals collected by the electrodes are very low amplitude and contain unwanted electrical signals, usually due to impulsive noise caused by muscle contraction, continuous respiration, and motion artefacts [21]. Mains hum (50 Hz/60 Hz) is filtered out using a second-order RC filter having a cut-off frequency 40 Hz, by Eq. (1). Output of 2nd order low pass filter is shown in Fig. 5.

Substituting the values R1 = 4000, R2 = 4000, C1 = 1μF, C2 = 1μF in Eq. (1), we get fc = 40 Hz.

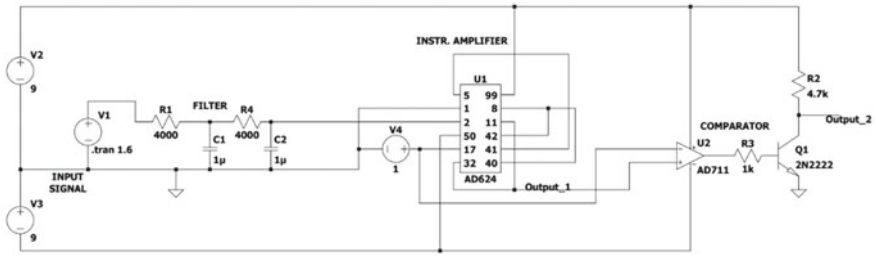

Fig. 4 Circuit diagram of HRV system

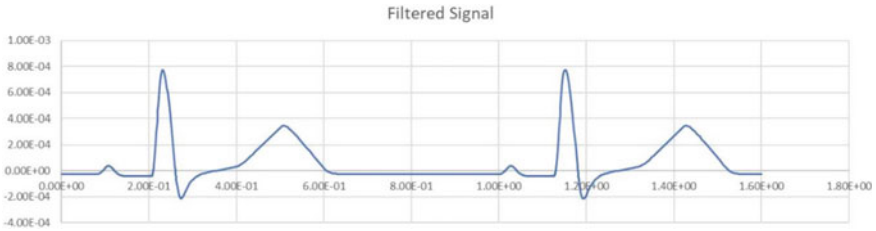

Fig. 5 Filtered signal of input ECG wave

After the noise filtering, low amplitude filtered input signals of the amplitude of −0.4 mV to 1.2 mV are passed through an instrumentation amplifier AD624, with a high common-mode rejection ratio, low power consumption, and offset current, which amplifies the filtered signal where the amplifier has been set a gain of 1000, the voltage generated by the amplifier contains positive and negative cycles, so a reference voltage of 1 V is added to convert the bipolar output (ranges −0.4 mV to 1.2 mV) to unipolar (ranges 0.6 mV to 2.2 mV) [22]. Output of instrumentation amplifier is shown in Fig. 6.

The output from the amplifier of amplitude 0.8 V to 1.8 V is fed to comparator AD711 to compare the output analog voltage values with respect to reference voltage

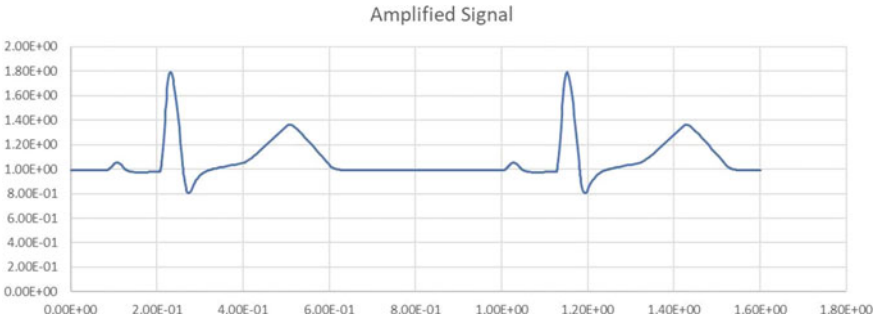

Fig. 6 Amplified and filtered ECG waveform

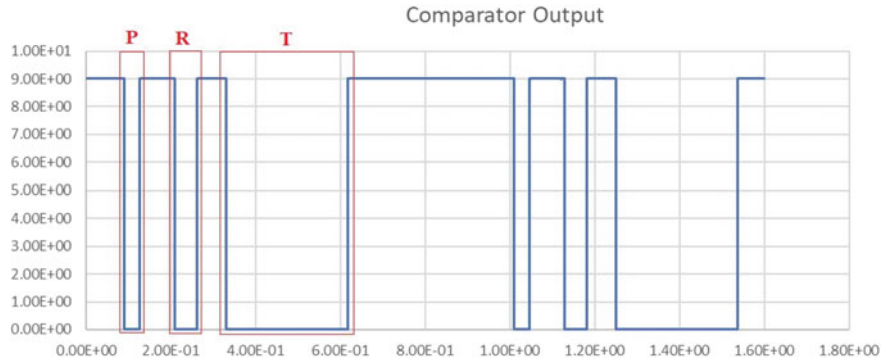

Fig. 7 Output of comparator

1 V. It converts the analog voltage signal into a digital signal if the difference of the input voltage changes and negative and positive signs remain constant, keeping output unchanged. Reference [23] The output square wave from the comparator is sent into the transistor to eliminate the square wave's negative half, keeping the new pulse range between 0 and 9 V, as shown in Fig. 7. The output ECG signal is fed to the microcontroller with the help of a timer; it analyses the ECG signal and displays RR interval with some other vital intervals. [24] ECG signals can also be displayed on a digital storage oscilloscope and is compared with standard ECG waveform. The microcontroller reads the data per millisecond and analyzes the input ECG signal for 1 min before displaying the parameter intervals in milliseconds.

A standard ECG signal consists of five types of waves P-, Q-, R-, S-, and T-wave. Reference [25] The information from these components is used to predict cardinal respiratory disorders for reliable cardiovascular evaluation, including diagnosing upcoming arrhythmia events of a patient understanding cardiovascular and autonomic nervous system under high blood pressure.

PR interval, RR interval (RR), QT interval (QT), and QRS interval are attained from the ECG signal, R is the peak value with the highest amplitude used to measure the heartbeat rate. Reference [25] RR interval is double of QT interval on an immaculate heart, which should have a value less than 0.44 s.

The P, QRS, and T waves reproduce the rhythmic electrical depolarization and repolarization of the myocardium, leading to ventricles' contractions. The most projecting feature is the QRS complex, and R denotes the peak of the QRS complex. [26] A normal QRS should have the duration of less than 3 mm or 0.06 to 0.12 s. If the time period exceeds 3 mm, it is suspected to be an abnormal intraventricular conduction velocity linked with increased adverse cardiac events and heart failures.

Table 1 Comparison of ideal and simulated ECG parameters

	Parameters	Ideal values (ms)	Simulated values (ms)
1	PR interval	120–200	119.959451
2	QRS complex	60–110	52.1385507
3	QT interval	<440	407.749206
4	RR interval	600–1500	920.005202

The body's blood flow must be sufficient, and any changes lead the person can lose consciousness or suffer discomfort in the front of the chest. Sometimes, sudden cardiac death can exist [26]. Therefore, a continuous observation of heart activity and online analysis system are important. Comparison of ideal PR interval, RR interval, QT interval and QRS complex; with the obtained simulation values is displayed in Table 1.

5 Conclusion and Future Scope

The proposed idea of a low-cost wearable electrocardiogram system can monitor the heart rate as well as the HRV value without any human intervention. Apart from the heart rate calculation and the R-R value for HRV, by the microcontroller it has to offer, it also has an in-built alert mechanism that alarms the user when the deal goes above or below a setpoint. Above all, the user can also have a detailed look at his heart functioning on a display monitor. This idea will enable the users to monitor their heart remotely and frequently to avoid the unavoidable with the least effort, and due to its sustainable and ergonomic approach, it can have a bright future ahead. The novelty of the system is its simplicity and cost-effectiveness. The use of a comparator makes the ECG parameters readily available without the need for heavy processing. The prospect includes converting it to a compact wearable product that can be worn comfortably, not interfere with day-to-day activities, and can be used as fitness equipment. It should also transmit essential data to a mobile application or ground station to record the actions. This wireless transmission can be achieved by designing a suitable medical antenna. Microstrip antennas are widely used in medical application like imaging, diagnosis, and treatment. Flexible microstrip antennas can be kept in contact with the human skin as well. The developed antenna can be as small as 0.25 mm in thickness and work at 2.45 GHz.

References

1. Roth GA, Mensah GA, Johnson CO, Addolorato G, Ammirati E, Baddour LM, Barengo NC, Beaton AZ, Benjamin EJ, Benziger CP, Bonny A (2020) Global burden of cardiovascular diseases and risk factors, 1990–2019: update from the GBD 2019 study. J Am Coll Cardiol 76(25):2982–3021
2. Kulkarni P, Mahadevappa M, Alluri S (2020) COVID-19 pandemic and the impact on the cardiovascular disease patient care. Curr Cardiol Rev 16(3):173–177
3. Vrijkotte TG, Van Doornen LJ, De Geus EJ (2000) Effects of work stress on ambulatory blood pressure, heart rate, and heart rate variability. Hypertension 35(4):880–886
4. Jose AD, Collison D (1970) The normal range and determinants of the intrinsic heart rate in man. Cardiovasc Res 4(2):160–167
5. Reardon M, Malik M (1996) Changes in heart rate variability with age. Pacing Clin Electrophysiol 19(11):1863–1866
6. Reed MJ, Robertson CE, Addison PS (2005) Heart rate variability measurements and the prediction of ventricular arrhythmias. QJM 98(2):87–95
7. Buccelletti E, Gilardi EMAN, Scaini E, Galiuto LEON, Persiani ROBE, Biondi ALBE, Basile FLOR, Silveri NG (2009) Heart rate variability and myocardial infarction: systematic literature review and metanalysis. Eur Rev Med Pharmacol Sci 13(4):299–307
8. Pehr S, Zollitsch D, Güttler J, Bock T (March 2019) Development of a non-contact ECG application unobtrusively embedded into a bed. In: 2019 IEEE sensors applications symposium (SAS). IEEE, pp 1–6
9. Hoff L, Espinoza A, Ihlen H (Nov 2008) Cardiac monitoring using transducers attached directly to the heart. In: 2008 IEEE ultrasonics symposium. IEEE, pp 749–752
10. Xue D, Cai R, Liu Y (May 2021) Design of amplifier for wearable human ECG sensor with low power and low noise. J Phys: Conf Ser 1907(1):012058. IOP Publishing
11. Georgiou K, Larentzakis AV, Khamis NN, Alsuhaibani GI, Alaska YA, Giallafos EJ (2018) Can wearable devices accurately measure heart rate variability? A systematic review. Folia Med 60(1):7–20
12. Dobbs WC, Fedewa MV, MacDonald HV, Holmes CJ, Cicone ZS, Plews DJ, Esco MR (2019) The accuracy of acquiring heart rate variability from portable devices: a systematic review and meta-analysis. Sports Med 49(3):417–435
13. Le-Huy P, L-Huillier JP, Omerzouk Y, Yvroud E (Oct 1983) Microprocessor-based ambulatory ecg monitoring system. In: The seventh annual symposium on computer applications in medical care, 1983. Proceedings. IEEE, pp 917–918
14. Shin K, Hwang HT, Kim YH, Kim JP, Yeo HS, Han W, Hwang J, Lee JW, Park JC (Jan 2006) WHAM: a novel, wearable heart activity monitor based on Laplacian potential mapping. In: 2005 IEEE engineering in medicine and biology 27th annual conference. IEEE, pp 7361–7364
15. Alam ST, Hossain MM, Islam MK, Rahman MD (2018) Towards development of a low cost and portable ECG monitoring system for rural/remote areas of Bangladesh. Int J Image, Graph Signal Process 10(5)
16. Ertola JP, Figueira S, Carlsen M, Palaniappan U, Rondini K (Oct 2016) Low-cost electrocardiogram device for preventive health care in rural populations of developing countries. In: 2016 IEEE global humanitarian technology conference (GHTC). IEEE, pp 646–655
17. Murugappan M, Thirumani R, Omar MI, Murugappan S (March 2014) Development of cost effective ECG data acquisition system for clinical applications using LabVIEW. In: 2014 IEEE 10th international colloquium on signal processing and its applications. IEEE, pp 100–105
18. Bednar T, Orenicova D, Borik S, Babusiak B (Sept 2019) A simple wireless ECG system for education practice. In: 2019 IEEE 20th international conference on computational problems of electrical engineering (CPEE). IEEE, pp 1–4
19. Deb S, Islam SMR, RobaiatMou J, Islam MT (Feb 2017) Design and implementation of low cost ECG monitoring system for the patient using smart device. In: 2017 international conference on electrical, computer and communication engineering (ECCE). IEEE, pp 774–778

20. Goel A, Singh G (2013) Novel high gain low noise CMOS instrumentation amplifier for biomedical applications. In: 2013 international conference on machine intelligence and research advancement, pp 392–396. https://doi.org/10.1109/ICMIRA.2013.83
21. Alam ST, Hossain MM, Islam MK, Rahman MD (2018) Towards development of a low cost and portable ECG monitoring system for rural/remote areas of Bangladesh (5):24–32
22. Alfarhan KA, Mashor MY, Saad ARM (2016) A review of wireless ECG monitoring system design. Int Acad Eng Med Res 1(2)
23. Yang G, Cai X, Wang F, Cui S, Zhao L (2012) Research of portable ECG monitoring device. Adv Comput, Commun, Control Autom, LNEE 121:213–220
24. Sayyed RH, Farooqui M, Khan AR, Rabbani G (2017) A simple portable ECG monitor with IoT. Int J Innovative Res Sci, Eng, Technol 6(7):13573–13578
25. Mandala S, Di TC (2017) ECG parameters for malignant ventricular arrhythmias: a comprehensive review. J Med Biol Eng 37(4):441–453
26. Muthuchudar A, Baboo SS (2013) A study of the processes involved in ECG signal analysis. Int J Sci Res Publ 3(3)

Third Eye for Blind Person

Saumyata Bhargava, Ranjana Sharma, Lakshay Lohumi, Lakshay Chauhan, and Rachit Patel

Abstract Eyes are the most essential part of the human body. They help us to see the world in a beautiful and colorful manner. Eyes allow a human being to observe and sense the things around and lacking that may lead to many problems and difficulties. The traditional methods for blind people are walking with a dog, walking with the help of guardians, using a fordable stick and so on. According to WHO, about 39 million people are estimated as blind in the whole world. They suffer with a lot of hardships and difficulties. Hence, the 'third eye for blind' is an innovation which helps the blind person to move with speed and comfort. This can be done using ultrasonic wave sensors, moisture sensor, buzzer, light sensors, GPS and GSM modules that will help in navigation. Third eye for blind will be a holding device that will help the visually impaired people to move by themselves in any environment. It reduces the work of caretakers of the blind person. It provides the opportunity to navigate the blind person if lost, as the position will be notified with the help of GSM. Hence, blind people can perceive the world by using sensors and can gain advantage using the latest technologies.

Keywords Proximity sensors · Moisture sensors · Global positioning system (GPS) · Buzzer · Arduino nano · Arduino IDE · Light dependent resistor (LDR) sensors · Global system for mobile communication (GSM)

1 Introduction

Sensors basically help to sense the environmental conditions and react according to the desired needs. A sensor is a device which is used to transform a physical variable system into signals that are readable by the user [1]. In the modern technology era, smart devices have become the most usable consumer devices. Smart devices and sensor technology play a very important and impressive role in human life. Smart devices make life easier with various functions embedded in it. Similarly, sensors

S. Bhargava · R. Sharma · L. Lohumi · L. Chauhan · R. Patel (✉)
ABES Institute of Technology, Ghaziabad, India
e-mail: rachit05081gece@gmail.com

S. Rawat et al. (eds.), *Proceedings of Second International Conference on Computational Electronics for Wireless Communications*, Lecture Notes in Networks and Systems 554,
https://doi.org/10.1007/978-981-19-6661-3_30

have great importance at home and at various places with high performances [2]. These functions can be communication, email, searching, taking pictures, messaging, sending photos, locating devices, and many more. With the help of smartphones, all of this has become a piece of cake. But this pleasure is only not available for blind people.

Blind people can live a comfortable life and do things according to their wills but to do this, they face a lot of difficulties compared to normal people. One of the biggest problems that blind people face is that due to their lack of visibility they cannot use smart devices, especially smartphones. Although there are many gadgets available for blind people [3], there is no such advanced gadget available in the market that can provide the visually impaired people with a whole environment analyzer that will help them to walk with ease and with minimal efforts.

So, this project will provide the blind people an opportunity to blind people to walk with comfort and analyze the environment using various sensors.

With the utilization of this smart and advanced gadget on a huge scale, and with advancements in this gadget, it can definitely become a game changer that will profit the blind people to walk with ease individually. This gadget will allow the blind people on their own with a single stick holding in their hands. The third eye will help the blind to move with greater speed in any conditions by certainly analyzing the environment using buzzers and sensors, and in case, the blind person is lost their guardians will be able to detect and find them using GPS modules embedded in the system [4, 5]. This gadget will also help the blind people to analyze the day and night with light sensors.

1.1 Existing Models

Till now, many technologies have been developed and made available to the market for visually impaired people, but they are hard to operate and not very accurate. They are more expensive and do not solve the problem. Here are some examples of prototypes and gadgets that have been proposed to solve the problem.

Here was one example where there was a device that detected the angle of the person for sensing the obstacles, but it was to be worn on the head only [5]. This makes it heavy to be worn for longer distances and makes the walk uncomfortable. Also, there were some applications available that gave only real-time object detection using mobile phones [6]. But for that blind person will have to engage their guardians continuously with them. Also, there were systems that only detected the object and the directions of the object and beeps accordingly but if the beep fails by any case the blind person will not be able to detect the sound. There were devices that only detect objects and water [7]. But they were wearable only, hence making it uncomfortable to be worn for a long time and the water on the ground cannot be detected. There were devices that detect objects for Arabic language only [8]. They were more language specific and not subject specific. There were devices that only detect the objects and

not anything else. This limited the gadgets to detect only distance which increased the cost of the product.

1.2 Proposed Model and Working

So, after analyzing all the above problems, we have tried to eradicate these problems with our gadget. So, our model is a hands-on model that has covered many aspects to fulfill the needs of a blind person using technology. It covers various aspects that will help the blind person to see and will solve many of the problems that have been discussed. Third eye for blind will help the blind people with a master combination of many proximity sensors and GPS systems. Here are some of the points that have been proposed in our gadget. Our gadget will detect any kind of obstacle that will come in its range and will act accordingly [9]. In this gadget, there are different proximity sensors to sense the environment and act accordingly. In this, there is a distance sensor to sense the object if the object or person comes within the defined range [10]. And if the object is found, then the buzzer will beep and will inform the blind person to stop or change the direction. Also, there is a vibrator available on the hands of the stick that will vibrate, and hence if the buzzer fails then also, we will have an indicator to inform the blind person. Therefore, it will provide double protection to the blind person. Similarly, it has a moisture sensor that will sense the water and will make a beep sound and will vibrate as soon as the water is touched by the gadget and will let the blind person know about the water near it so that person will move in another direction. It also has a GPS tracking system embedded in it that will track the blind person and if the person is lost [11]. It will also notify their guardian through a GSM module with a messaging system [12]. Also, our gadget will have a light dependent resistor (LDR) that will guide the other people about the user at night. And hence, our gadget covers various aspects that will help the blind person (Fig. 1).

The blind stick is integrated with an ultrasonic distance sensor, water sensor, light dependent sensors, buzzer, vibrator, GPS and GSM module, and external power supply. Our proposed gadget first uses ultrasonic sensors to detect the objects [9]. On sensing obstacles, the sensor passes this data to the microcontroller. The microcontroller then processes this data and calculates if the obstacle is close enough.

The microcontroller will be embedded with programs to handle the gadgets [10]. If the object is close enough, then the buzzer starts beeping. Also, along with that the vibrator will also vibrate. If the gadget touches the surface of water, then also it will process the data through the microcontroller and will make a beep sound and vibrate. The gadget also detects if there is light or darkness in the room through LDR sensors, and if there is darkness in the room, then LEDs will glow to let the other person know that there is someone in front of them. It also has a global positioning system (GPS) tracking system which tracks the user [11], and if the person is lost, then the microcontroller will process the data, and the global system for mobile communication (GSM) module will send the information of the lost person to the

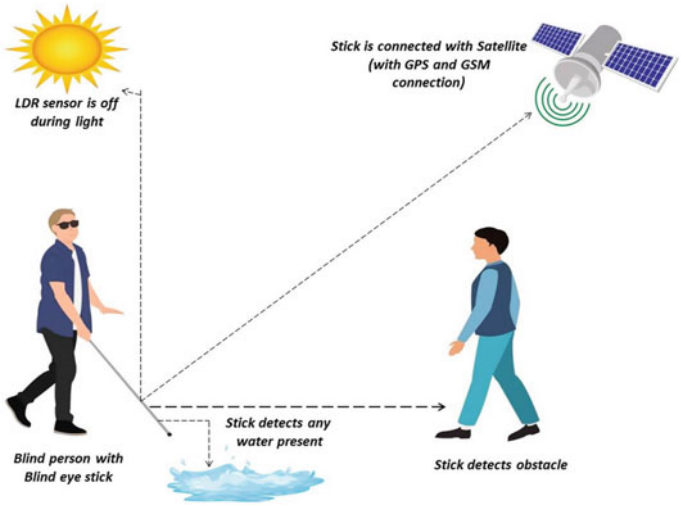

Fig. 1 Block diagram of third eye for Bbind

guardians of the blind person so that the guardians of the blind person could know where the blind person is [12]. All the components assembled in the stick (device) have a supply voltage.

Now, to calculate the distance, we should know the speed and time. The formula used will be

$$\text{Distance} = \text{Speed} \times \text{Time} \tag{1}$$

The ultrasonic sensor detects the ultrasonic wave which is transmitted by the ultrasonic transmitter. When any object is detected, the wave is reflected back to the sensor which is detected by the ultrasonic receiver. Now, using the Arduino Nano, distance can be calculated simply. The ultrasonic sensors will be connected to pin A4 and A5 of Arduino Nano. After the sensor detects the object, it will pass the data to the microcontroller which will beep using a buzzer on D2 and will also vibrate. Similarly, this device can detect the liquid in its path using a moisture sensor that helps to detect the water [13], and this system is implemented by attaching the sensors with Arduino Nano on pin D12. The flow of current depends on the quality of water, so we use an operational amplifier as it can amplify weak electric signals as well [14]. The sensor works faster with dusty effluent water. If any liquid is present at the bottom of the device, then the wires become shorted, and current starts flowing through the device. This will send a signal to the Arduino Nano, and after processing the signal, a beep is heard from the buzzer along with vibrator as an output of the water detection system. Darkness detection system is also present in this device. Light dependent resistors (LDR) are used as the device which can detect darkness [15]. LDR works on the principle of photoconductivity. The resistance of and LDR

may have the following resistances:

$$\text{Daylight} = 5000\Omega \tag{2}$$

$$\text{Dark} = 20000000\Omega \tag{3}$$

When light falls on the LDR of our gadget, then the resistance of the LDR will decrease, and hence, it will stop glowing, and if there is no darkness, then the LDR will glow. LDR will be connected to pin A0 of Arduino Nano, and the light will be connected to A1. LDR will have 2 pins, such as one on ground and other on supply. The GPS will be connected to the Arduino Uno to track the user. An emergency switch or button is provided which can be used when the user is in danger. Just by clicking on that switch, the GSM 900 will send the signal to their guardians. Here, pin A0 will be connected to the button, and A1 will be connected to the buzzer, this buzzer beeps to ensure the user that the message signal is getting delivered to their guardians. A sim module needs to be implemented in the gadget to send the signals.

2 Flowchart for Our Gadget

Here, the power will be provided to the module through batteries attached. The sensor will scan the obstacles like for objects, moisture or water, light. If any obstacles are found, then the buzzer and vibrator will work else not. Also, for GPS and GSM, the circuit will be formed with another Arduino (Fig. 2).

3 Results and Simulation

Third eye for a blind person is an innovative gadget that will help the blind person using the latest technologies and will reduce their dependence on other people.

The combination of distance sensor, moisture sensor, light sensors, and GPS and GSM module will give a wholesome approach to the solution of navigation problems faced by blind people. This stick will help them to walk with ease and comfort. Third eye for blind is more affordable in comparison with other features available. Also, it is easy to implement more features by doing simple programming to the Arduino. Hence, it will immensely help the visually impaired people to move with greater care and efficiency (Fig. 3).

Here for simulation, we shall assume ultrasonic sensor and moisture sensors and LDR sensors as alternative resistance. Also, we shall add an LDR bulb to perform our simulation. Here, we shall take the voltage of 5 V. The ultrasonic sensor will be on pin A4 and A5, the moisture sensor will be on pin A2, the LDR sensor will be on pin A0, and the LED bulb will be on A1. The positive end of the buzzer would be

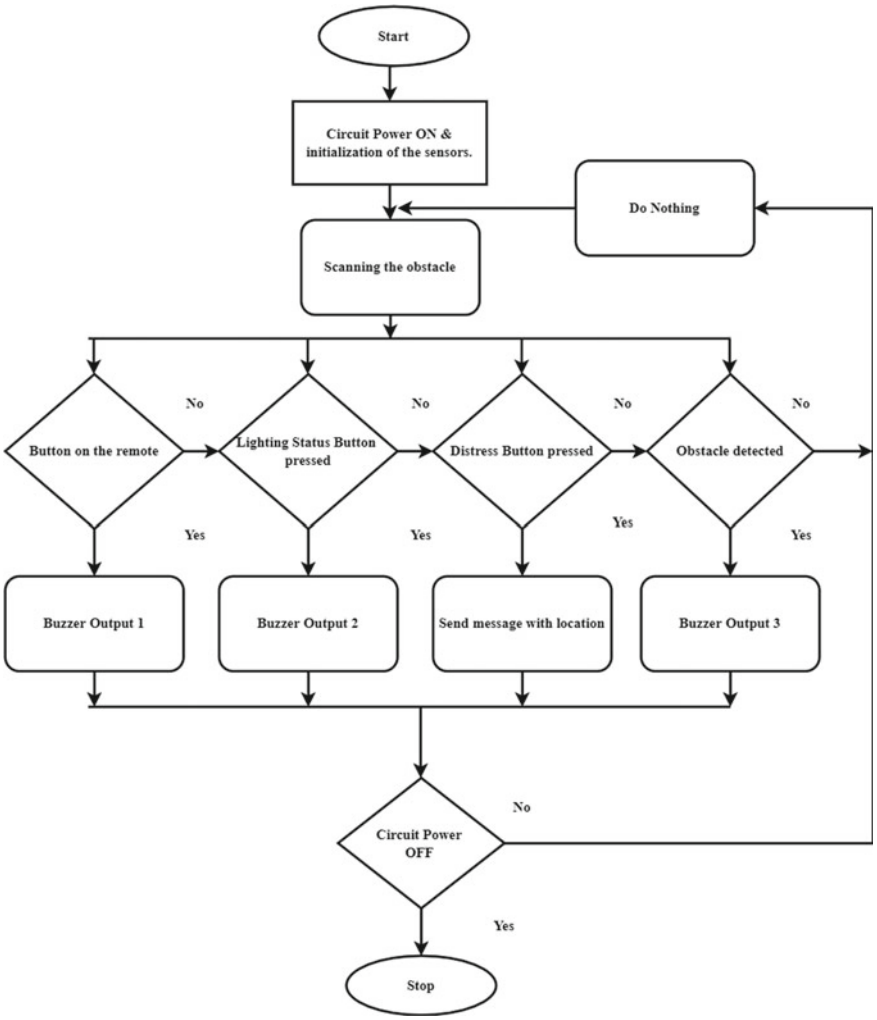

Fig. 2 Flowchart of third eye for blind

connected on D2 of the Arduino and the negative end on ground. After connecting the pin, we shall vary the alternative resistance to get the results. Here, we shall take the intensity of light to be less than 200 Lumens to light the bulb. The moisture sensor will beep if the value of water content in soil is more than 100% else the buzzer will not beep, and the vibrator will not vibrate. The ultrasonic sensor will buzz if the person is in the range of 2–60 cm else the buzzer will not buzz, and the vibrator will not vibrate (Fig. 4 and Tables 1 and 2).

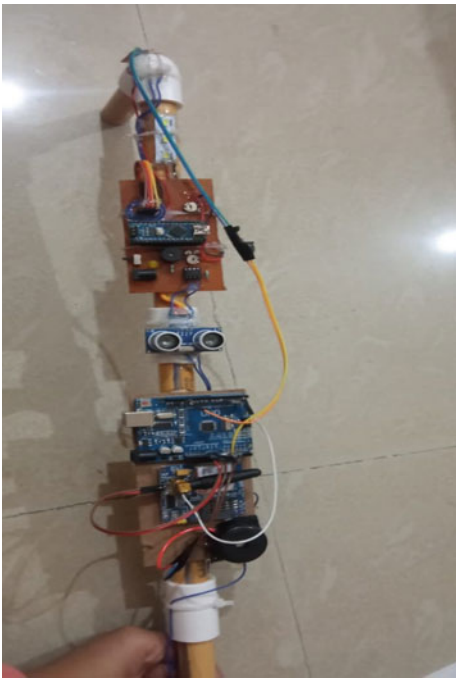

Fig. 3 Hardware implementation of our model

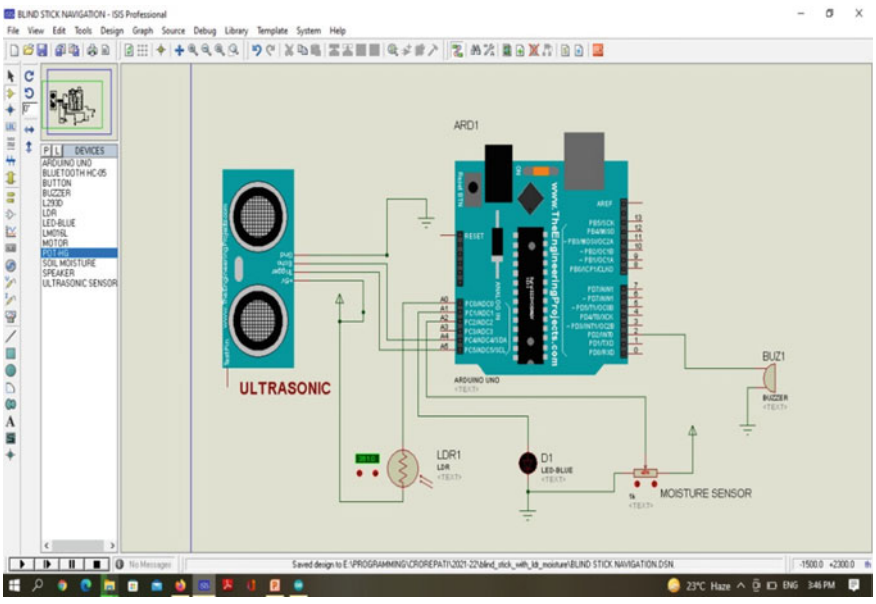

Fig. 4 Simulation of our model

Table 1 Expenses of all components used in our project

Components	Quality	Price (USD)
Arduino Nano	1	$7.90
Arduino Uno	1	$10.16
GPS	1	$6.33
GSM 900	1	$15
Vibrator	1	$0.36
Buzzer	2	$0.29
LDR sensor	1	$2.49
Moisture sensor	1	$1.29
Ultrasonic sensor	1	$1.39
Light and wires,	1	$0.66
Switch	1	$0.01
Total cost	13	$45.88

Table 2 Comparison table

Parameters	Traditional gadgets	Third eye for blind	How it helps
Cost	$50 [15]	$45.88	More affordable
Distance sensor range	4 cm [16]	2 cm-60 cm	More accuracy
Weight	200gm [5]	100gm	Convenient to use
SMS facility	Has bluetooth connectivity for SMS	Has GPS connectivity for SMS	Track the user

4 Conclusion

With the improvements in the living standards of the general people, we have become so materialistic that we have forgotten how physically disabled people live their lives with so much difficulty. Eyes are responsible for observing and listening to the entire world. Disability of such an important organ of the human body may cause serious problems that a normal human being cannot even imagine and hence going around and enjoying the basic facilities becomes so difficult for blind people. Hence, we have tried to contribute a little bit to such people with our engineering knowledge that will help the blind people. This gadget is more affordable, reliable and has flexibility in it that will help the visually impaired people to walk with confidence and faith. Third eye for blind will help the blind people with a master combination of many proximity sensors like distance sensor, moisture sensor, LDR sensor, and GPS and GSM module. It will reduce the work of people who walk with blind people as their directors. Hence, blind people can perceive the world by using sensors and can take the advantage of technologies with full confidence and happiness.

References

1. Binder MD, Hirokawa N, Windhorst U (eds) (2009) Sensor. In: Encyclopedia of neuroscience. Springer, Berlin, Heidelberg. https://doi.org/10.1007/978-3-540-29678-2_5318
2. Kang B, Kim S, Choi M, Cho K, Jang S, Park S (2016) Analysis of types and importance of sensors in smart home services. In: 2016 IEEE 18th international conference on high performance computing and communications; IEEE 14th international conference on smart city; IEEE 2nd international conference on data science and systems (HPCC/SmartCity/DSS), pp 1388–1389. https://doi.org/10.1109/HPCC-SmartCity-DSS.2016.0196
3. Whitney GJ (1998) New technology assistive devices to assist blind and partially sighted people to travel within and use the built environment. In: 9th international conference on road transport information and control, 1998. (Conference publication no. 454), pp 55–58. https://doi.org/10.1049/cp:19980154
4. Rose C, Britt J, Allen J, Bevly D (2014) An integrated vehicle navigation system utilizing lane-detection and lateral position estimation systems in difficult environments for GPS. IEEE Trans Intell Transp Syst 15(6):2615–2629. https://doi.org/10.1109/TITS.2014.2321108
5. Lin CH, Cheng PH, Shen ST (2014) Real-time dangling objects sensing: a preliminary design of mobile headset ancillary device for visual impaired. In: 2014 36th annual international conference of the IEEE engineering in medicine and biology society, pp 5723–5726. https://doi.org/10.1109/EMBC.2014.6944927
6. Tosun S, Karaarslan E (2018) Real-time object detection application for visually impaired people: third eye. In: 2018 international conference on artificial intelligence and data processing (IDAP), pp 1–6. https://doi.org/10.1109/IDAP.2018.8620773
7. Arvitha MVS, Biradar AG, Chandana M (2021) Third eye for visually challenged using echolocation technology. In: 2021 international conference on emerging smart computing and informatics (ESCI), pp 391–395. https://doi.org/10.1109/ESCI50559.2021.9397015
8. Albraheem L et al (2015) Third eye: an eye for the blind to identify objects using human-powered technology. In: 2015 international conference on cloud computing (ICCC), pp 1–6. https://doi.org/10.1109/CLOUDCOMP.2015.7149661
9. Ushimi N et al (2002) On-line navigation of mobile robot among moving obstacles using ultrasonic sensors. In: Birk A, Coradeschi S, Tadokoro S (eds) RoboCup 2001: Robot Soccer World Cup V. RoboCup 2001. Lecture notes in computer science, vol 2377. Springer, Berlin, Heidelberg. https://doi.org/10.1007/3-540-45603-1_63
10. Cuartielles D, Iriepa N, Rodriguez C, Lopez E, Garcia J (2020) Educational Robots with Arduino: annotated prototypes. In: Moro M, Alimisis D, Iocchi L (eds) Educational Robotics in the context of the maker movement. Edurobotics 2018. Advances in intelligent systems and computing, vol 946. Springer, Cham
11. Wei-Tai L, Jun W, Jin-Pei Y (2013) Software designing and simulation of GPS receiver. In: Yang G (eds) Proceedings of the 2012 international conference on communication, electronics and automation engineering. Advances in intelligent systems and computing, vol 181. Springer, Berlin, Heidelberg. https://doi.org/10.1007/978-3-642-31698-2_75
12. Xie J, Xiao J (2015) Research of mobile vehicle information acquisition system based on GPS satellite positioning. In: Deng Z, Li H (eds) Proceedings of the 2015 Chinese intelligent automation conference. Lecture notes in electrical engineering, vol 336. Springer, Berlin, Heidelberg
13. Sunil Kumar S, Aithal G, Venkatramana Bhat P (2021) Design, calibration, and experimental study of low-cost resistivity-based soil moisture sensor for detecting moisture at different depths of a soil. In: Chiplunkar N, Fukao T (eds) Advances in artificial intelligence and data engineering. Advances in intelligent systems and computing, vol 1133. Springer, Singapore
14. Eberharter T, Brasseur G (1997) Improvements of the charge amplifier used in a capacitive angular-position sensor. In: IEEE instrumentation and measurement technology conference sensing, processing, networking, vol 2. IMTC proceedings, pp 1273–1277. https://doi.org/10.1109/IMTC.1997.612403

15. Ram Kumar RP, Sumanth AVNS, Sai Sumanth R, Thakur A, Chintala AS, Geethanjali B (2021) Smart street lighting system: an approach towards effective power utilization. In: Marriwala N, Tripathi CC, Jain S, Mathapathi S (eds) Soft computing for intelligent systems. Algorithms for intelligent systems. Springer, Singapore
16. Tahmidul Kabir AZM, Deb Nath N, Pramanik M, Alam TI (2019) Intelligent path-finder for the blind. In: 2019 1st international conference on advances in science, engineering and robotics technology (ICASERT), pp 1–5. https://doi.org/10.1109/ICASERT.2019.8934811

IoT-Enabled Fire Detection System for a Smart Home Environment

Jinugu Harsha Vardhan Reddy, Kasu Pravachana Evangelin, Suganthi Evangeline, and Balapanur Julian Deva Sundar

Abstract The main reason for fire accidents is carelessness, short circuit, and environmental conditions. They cause threat to people's lives and their property. Eventually, the alerts about such incidents should given early to prevent damages. The real-time notification is the most critical issue in fire detection systems. In this paper, an IoT-enabled fire detection system is designed and tested using Cisco packet tracer and Tinkercad. The simulation results showed that this system is capable to detect smoke, and immediate actions are taken by altering the people.

Keywords IoT · Smart home · Alert · Cisco · Tinkercad

1 Introduction

So, what if? We had a device to protect people from fire accidents within a fraction of seconds without the help of a police force. This thought stuck in the minds of Stanley Bennett Peterson and Duane D. Pearsall in 1965, which made them invent a smoke detector. There are types of smoke detectors in this. They are ionization, photoelectric, and a combination of the two which is commonly called a "dual detector". The Cisco packet tracer is used for this project "smoke detection with fire prevention". It is mostly used in malls, movie theaters, hospitals, hotels, and also in smart homes. Just a thought, what if? This whole device is controlled with mobile. Here comes the Internet of things (IoT), what is IOT? It tells about network of things. It is fixed firmly and deeply with the sensors, software which it will send signals or data to connected devices with Internet in wireless mode. In this, the alarm is connected for it. According to the survey of United State (U.S) Fire Administration, the alarms will work for only in the range of 8–10 years. After this expiry time, alarm as to replace

J. H. V. Reddy · K. P. Evangelin · S. Evangeline (✉) · B. J. D. Sundar
Karunya Institute of Technology and Sciences, Coimbatore, India
e-mail: evangelineme4@gmail.com

K. P. Evangelin
e-mail: pravachanaevangelin@karunya.edu.in

S. Rawat et al. (eds.), *Proceedings of Second International Conference on Computational Electronics for Wireless Communications*, Lecture Notes in Networks and Systems 554,
https://doi.org/10.1007/978-981-19-6661-3_31

with the new one. The National Fire Protection Association (NFPA) confirms every smoke alarm as to be changed after its expiry time, and also the batteries of the alarm have to be changed for every six months. The sales and business of the smoke detector in 2020 are valued at 1.80 billion USD and also. It is expected in 2026, the market will reach approximately 2.90 billion USD at the CAGR of 8.3% in the forecast period 2021–2026. The actual market was increased by smartphones to the smoke detector business market with in the forecast period. The smoke detector is connected to alarm when the fire threat comes in your home or property the alarm rings immediately you can call fire department [1]. This smoke detector will reduce the deaths in fire accidents. Approximately, 50% and 890 lives will be saved annually if all homes use this smoke detector [2]. 74% of the fire accident homes in 2014–18. Almost four out of six homes did not install smoke detector were caused by death. When the fire starts, the smoke detector will detect some particles in the air, and it will send the signals to alarm through IoT sensor which it is inbuilt in the detector after receiving the signals, the alarm starts ringing then you and your family can exit safely from the fire accidents and you can save your family's life.

In future due to damage of ozone layer, the UV rays of sun may directly fall on earth mainly it causes fire accidents at agriculture fields and forest areas so, there is a lot of scope in future to the smoke detectors. Well, here, we will go to in-depth learning about making of smoke detector and fire prevention with smartphones with the help of IoT in Cisco packet tracer.

2 Related Works

See Table 1.

3 Methodology

In this paper, we explained how IoT-enabled fire detection system for smart home environment implementing and simulating using Cisco packet tracer (version 8.1.0) and the Tinkercad software. In the Cisco packet tracer software, the designing of smart home environment with various smart devices is used such as windows, doors, smoke detector sensors, fire sprinkles, garage door, old car, siren, switches (2960-24TT). Smartphone-PT and home gateway (DLC100) are used to control the smart devices.

In Tinkercad software, to design the fire detection system, the components are used such as piezo buzzer, breadboard, resistors, red and green LED, LCD (16×2) display, gas sensor. Arduino Uno R3 is the microcontroller, and it is the main component which can able to control the things like reading the smoke details using smoke sensor, sending messages to LCD display used to displays the present conditions and activating piezo buzzer. Arduino Uno boards can read inputs from sensors and turn

Table 1 Comparative Study of various other approaches with proposed work

S. No.	Paper	Hardware	Merits	Limitations
1	[3]	MQ-135, MQ-2, MQ-7, and MQ-9 Raspberry Pi, ESP8266 ESP-01 Wi-Fi module	The proposed system successfully gathers sensor readings from the gas sensors, sends data via a wireless connection, and stores it in the Webserver	Not applicable for other smoke
2	[4]	PIC microcontroller, smoke sensor	The design will increase safety and reliability by reducing the risks to life and property	Complexity in design
3	[5]	8051 microcontrollers	The system can effectively and efficiently help control possible consequences with in the sort of loss of lives and properties	No remote alert option
4	[6]	MQ-2, STM32	The paper discusses the sensitivity characteristics and the temperature and humidity effect of the smoke sensor	No result was provided
5	[7]	Arduino, flame sensor	An Arduino-based prototype of the proposed device is made and tested by creating artificial smoke and flame. Test results prove that the proposed fire protection system responds quickly and effectively	GSM and LCD interfacing can be included for updating the alert messages
6	Proposed work	Arduino, smoke sensor, Cisco packet tracer, Wi-Fi	The proposed work is executed in hardware and software. It includes Wi-Fi module for further analysis	NIL

them into outputs like displaying, turning on LEDs, activating motors, publishing something online. The block diagram is presented in Fig. 1.

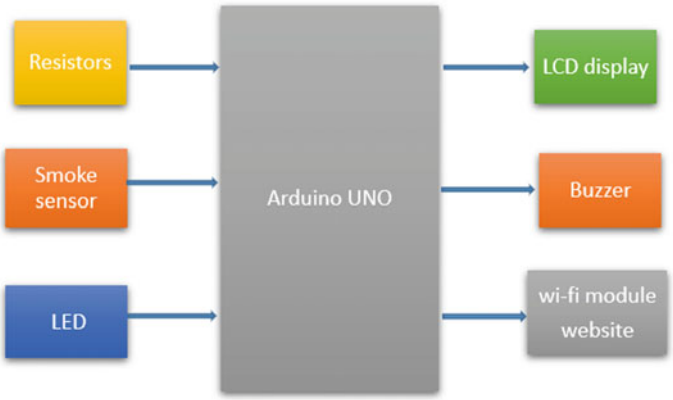

Fig. 1 Block diagram of proposed method

4 Software

4.1 Cisco Packet Tracer

The newly released Cisco packet tracer version 8.1.0 is making it easier for a student for designing and simulating complex and large networks without using the physical components. This latest version of Cisco packet tracer (8.1.0) added so many new devices, smart objects, and fixed some bugs in the old version. The key features of the Cisco packet tracer are unlimited devices, E-learning supports the majority of networking protocols, visualizing networks, interactive environment, self-placed, real-time mode, and simulation mode. Cisco packet tracer 8.1 makes improvements on accessibility, usability, and security.

4.1.1 Home Gateway

Gateway is the bridge of network that can able to connect directly to a wide-area network (WAN), while the routing process happening and can operated by an Internet service provider. A gateway is a single device that can do both jobs of a router and a modem. The home gateways have four Ethernet ports and sometimes Ethernet act as the router in home gateway, and it has a wireless access point is SSID. Home gateway can configure some protocols such as WEP/WPA-PSK/WPA2-PSK/WPA/WPA2 to secure wireless connections. The coverage range of the home gateway is 250 m. The default IP address present in the home gateway (LAN) is 192.168.25.10, and it is also acts as a DHCP server. Dynamic host configuration protocol (DHCP) is used to connect automatically assigned IP addresses to the network using a client–server architecture. The settings of all IoT devices change to DCHP serves to make to connect the default address of the home gateway system.

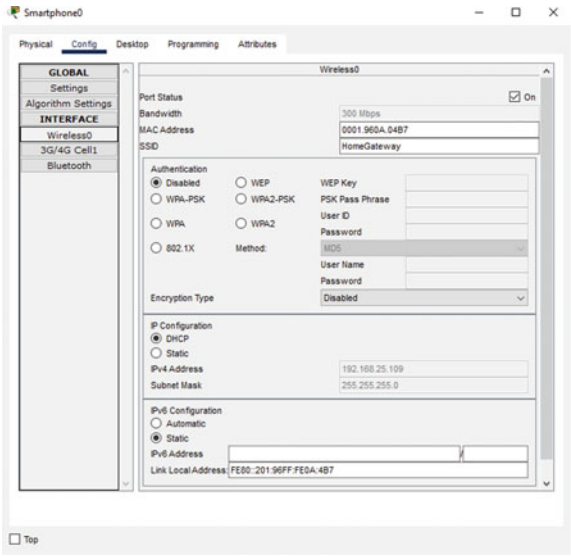

Fig. 2 IoT server wireless settings

4.1.2 Smartphone

Smartphones are used to communicate with smart devices. Figure 2 indicates the IoT server wireless settings interface in monitoring and controlling the devices.

In the Web browser of the smartphone, give the IP address of the home gateway is to connect all IoT devices. Login ID for Web browser in smartphone: admin and password for Web browser in smartphone: admin.

Figure 3 defines the connection status of all smart devices in the smart home list to the IoT server in the smartphone via a Web browser.

Figure 4 defines the condition settings of smart sensors and devices that are connected to the smartphone for IoT-enabled fire detection system for a smart home environment.

4.1.3 Implementation of Software Design

For the implementation of the smart home environment in the Cisco packet tracer, we have used a smoke detector, windows, doors, garage door, fire sprinklers, IoT server, siren, home gateway (DLC100), smartphone, switches (2960-24TT) (Table 2).

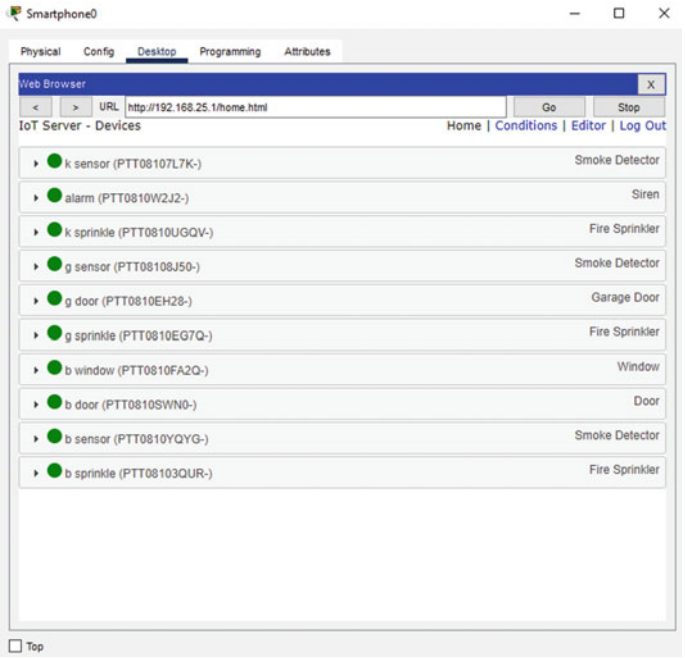

Fig. 3 List of devices that are connected to the smartphone

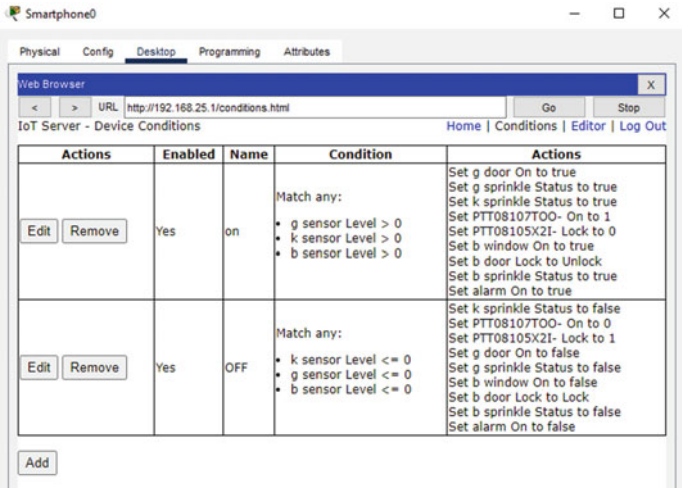

Fig. 4 Pre-set conditions for the smart home environment

Table 2 Components and their specifications for design

S. No.	Components	Specifications
1	Door	Connect to the home gateway and provide an event based on function
2	Window	It reads CO_2, CO variable sets in the environment objects and changes these variables when the user activates window opening/closing
3	Smoke detector	Detects smoke. Used an old car to change the smoke level
4	Fire sprinkler	It opens when there is a fire effected in the surrounding and used to puts out fire
5	Garage door	Door opens/closes accordingly when there a car moving/staying
6	Old car	Used to change CO_2, CO, and smoke levels
7	Siren	Provides sound when the fire or smoke detects
8	Smartphone-PT	Connects to the home gateway to access smart objects
9	Home gateway (DLC100)	It is the main body that can connects the smart sensors, objects using its default IP address
10	Switch (2960-24TT)	It is the key building block for any network to control the devices connected

4.2 Tinkercad

Tinkercad is a free online source platform, which can provide the sources for designing and simulating the electronic circuits and programming on Arduino Uno microcontroller without using physical objects or components. It is easy to design circuits and simulate the outputs. The main features of Tinkercad are file exportation, file editing, 3D designs, circuits, code blocks, presets. It also provides a schematic view of the designed circuit.

5 Hardware

Arduino Uno is based on an 8-bit ATmega328P microcontroller. Arduino Uno has 14 digital I/O pins and 6 analog pins, 16 MHz quartz crystal, an ICSP header, reset button, USB interface to connect the board and computer. It has 32 KB flash memory and 2 KB SRAM. Arduino Uno board has different pins. Some of the pins and specifications are explained below. Because of its simplicity and compact, we have selected Arduino (ATMEGA328p) for our experiment. Since it is capable of interfacing both analog and digital signals, the prototype designed can be upgraded in future also (Figs. 5 and 6).

Gas sensor is a device that detects harmful gases in the air. The gas is sensed and creates a potential difference in the element. The greater the concentration greater

Fig. 5 Arduino Uno

Fig. 6 Gas sensor

Fig. 7 LCD 16 × 2

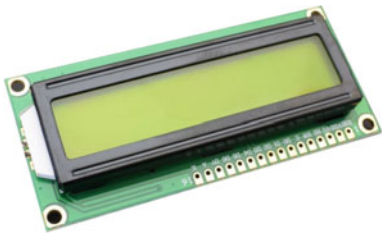

the output voltage. If there is a gas or smoke leak, it will automatically activate and send a signal to the buzzer, informing you. This way we can sense the danger and be careful (Fig. 7).

LCD means liquid crystal display.16 × 2 displays 16 characteristics per line, and there are 2 lines. 16 × 2 LCD interface has 8 data bits (DB0-DB7) and 3 control pins (RS, R/W*, E). The data bits are connected to the 8 pins of the microcontroller. The operating voltage of this LCD is 4.7–5.3 V. LCD screens are widely used in battery-powered devices because they consume very little power.

6 Results and Discussion

The components that are used to design the IoT-enabled fire detection-based system are Arduino Uno, resistors, red and green LED, smoke detection sensor, piezo buzzer, LCD, breadboard, jumper wires. Arduino Uno is the main body to connect and

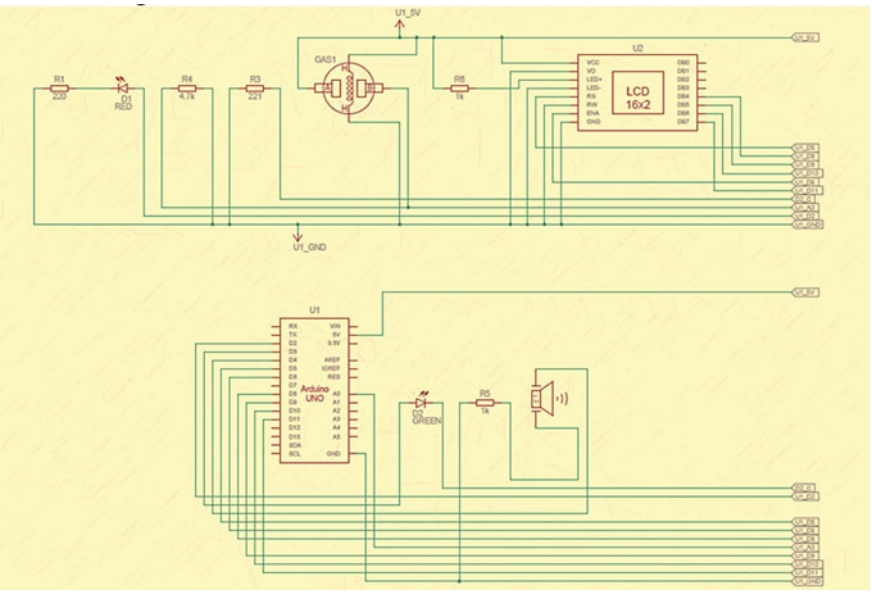

Fig. 8 Schematic view of hardware devices connections

function the components, and it acts as microcontroller board, which can take the analog inputs and their changes to digital outputs. The LCD is used to display the digital outputs of the circuits. Resistors are used to manage the power supply, and it reduces the damages of the LED when the power supply is flowing in the circuit. A Piezo buzzer is used to make sounds when the fire is detected from the environment. The smoke sensor detects the smoke from the environment. Jumper wires are used to connect the components. Figure 8 indicates the schematic view of smoke detection.

The LCD has 16 pins, 14 digital pins, and 2 pins are control the backlight if it has a backlight. In that 16 pins, D0-D7 are data pins, VSS and VDD are the power supply pins, and one pin is for contrast control, three control pins (register select, read/write, enable). VSS is connected to the ground, and VDD is connected to the power supply of the Arduino board.

Figure 9 indicates the circuit view of smoke detection with the Arduino code for programming the devices according to the conditions. The Arduino code is written based on the connections of devices to the Arduino board.

Figure 10 indicates the detection of smoke. When the smoke is detected, the buzzer produces the sound to alert the people in that particular environment. The LCD shows “ALERT”, “SMOKE”, and the red LED glows brightly when there is smoke detected, then after the smoke level comes to the normal condition it displays “SAFE”, “ALL CLEAR”, and green LED glows brightly. It helps the people who are nearer to the fire affecting the area, and it makes awareness to the people to be alert. The implemented design is given in Fig. 11. The sensitivity characteristics of MQ-2 sensor are presented in Fig. 12.

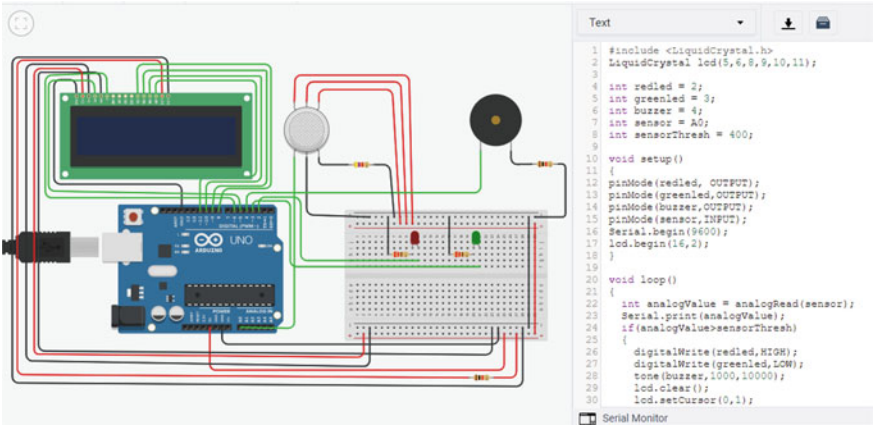

Fig. 9 Circuit view with Arduino code

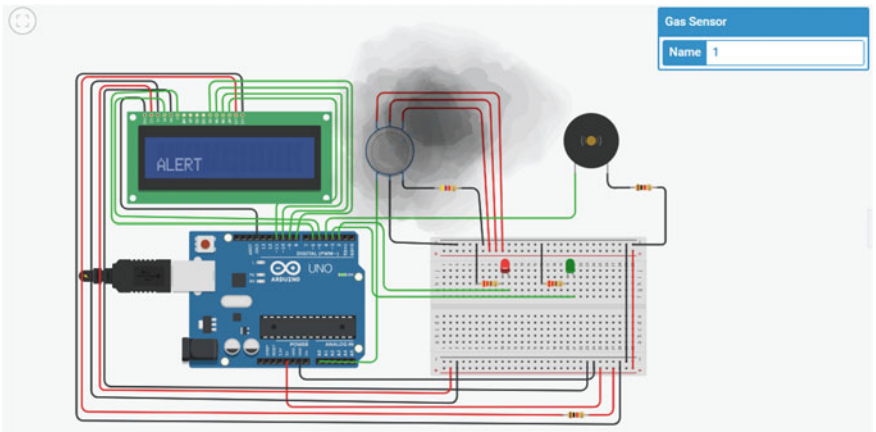

Fig. 10 Detection of smoke

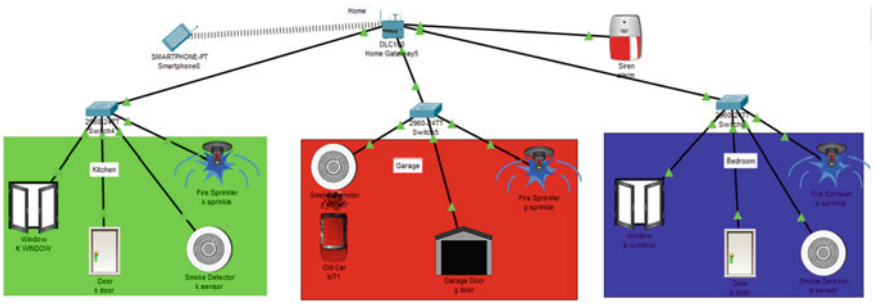

Fig. 11 Detection of smoke in the garage

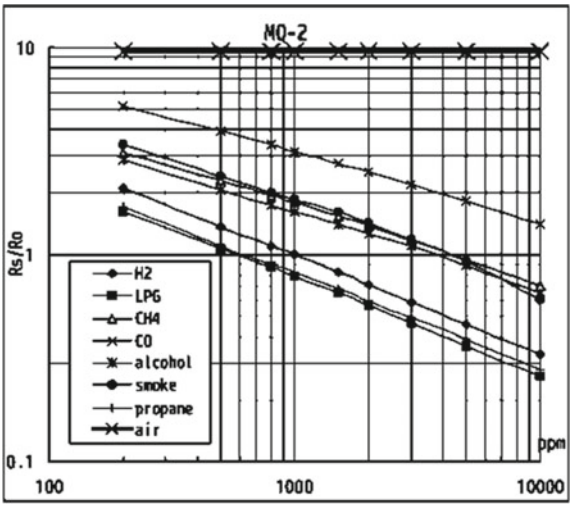

Fig. 12 Sensitivity characteristics of MQ-2 (*Source* MQ-2 datasheet)

References

1. Ahrens M (2009) Smoke alarms in US home fires. National Fire Protection Association, Fire Analysis and Research Division, Quincy, MA
2. Rohde D, Corcoran J, Sydes M, Higginson A (2016) The association between smoke alarm presence and injury and death rates: a systematic review and meta-analysis. Fire Saf J 81:58–63
3. Sanger JB et al (Nov 2019) Detection system for cigarette smoke. In: 2019 4th international conference on information technology, information systems and electrical engineering (ICITISEE). IEEE, pp 145–149
4. Islam T, Abdullah SA, Sarowar G (2013) Enhanced wireless control system for smoke and fire detection. Int J Comput Electr Eng 5(2):233–236
5. Ahmed B, Olaniyi A (2016) An ionization-based smoke detection and control system
6. Yin H (Aug 2016) Smart home smoke detection and relay contract based on STM32. In: Proceedings of the 2016 5th international conference on environment, materials, chemistry and power electronics, p 475
7. Habib MR et al (2019) Quick fire sensing model and extinguishing by using an arduino based fire protection device. In: 2019 5th international conference on advances in electrical engineering (ICAEE), pp 435–439. https://doi.org/10.1109/ICAEE48663.2019.8975538

Digital Backend Optimization Techniques for Post-Route and Sign-Off Challenges in ASIC Design

Nikhil Danthamala, Vijitaa Das, and Vishwnatha Hanchinal

Abstract Complexity in IC design has increased with technological innovation, which has produced a variety of routing issues. As a result, despite adopting a variety of patterning methodologies and procedures, timing closure issues and the electro-migration problem at the sign-off stage remained a problem. ASIC's real objective is to tape out at the appropriate moment without any design limitations. To solve these issues, time optimization and IR drop reduction in VLSI are crucial. This work suggests enhanced implementation strategies that can be used at each stage of the place and route flow in ASIC design to address the timing and IR drop issues. To reach the goal, the suggested approaches can be applied to any current physical design flow.

Keywords Timing optimization · Critical nodes · IR drop analysis · PG pattern · ECO optimization

1 Introduction

There are some places in the physical design where we need to pay closer attention if we want to prevent chip breakdown given how quickly technology is scaling. The move toward smaller process nodes makes it difficult to obtain design closure [1]. Finding, analyzing, and fixing problems are a crucial task, especially early in the design process.

N. Danthamala (✉)
Department of Electronics and Communications Engineering, National Institute of Technology, Goa, India
e-mail: nikhildanthamala@gmail.com

V. Das
Department of Electronics Design Technology, National Institute of Electronics and Information Technology, Calicut, India

V. Hanchinal
Design Engineer, NXP Semiconductors, Austin, USA

S. Rawat et al. (eds.), *Proceedings of Second International Conference on Computational Electronics for Wireless Communications*, Lecture Notes in Networks and Systems 554,
https://doi.org/10.1007/978-981-19-6661-3_32

According to recent studies, the performance of the chip suffers when low-power IC design is prioritized. Targeting critical nodes is one such issue that causes timing critical violations and voltages (IR) dips to arise in the design. These problems happen when crucial sections are neglected [2]. Each level of the physical design has its own obstacles, and each stage depends on the yield produced at the physical verification closure of the stage before it. The methods now in use are insufficiently useful to pass these tests.

Section 1 of this paper will address timing closure restrictions, and Sect. 2 will discuss how traditional approaches to reducing IR drop hotspots are failing. In Sect. 1, a better timing optimization technique is put forth with the aim of concentrating more on critical nodes after the post-route stage and optimizing them with the least amount of routing disruption while providing the worst negative slack (WNS), area, power, and maximum transition violation improvements. routing.

In Sect. 2, a better IR drop optimization technique is suggested to lessen the difficulties associated with dynamic IR drop and IR drop hotspots. Its goal is to increase the number of stripes in order to decrease the resistances in the current power grid that are leading to larger IR dips. This study demonstrates how functional blocks are properly analyzed and optimized following each stage of the physical design flow. The goal of this job is to meet the final sign-off checks by overcoming all obstacles that arise during tape out of the design.

2 Literature Survey

Numerous characteristics, including time, power, area, signal integrity, reliability, etc., can be improved through physical design. Additionally, as these criteria are improved, time is negatively impacted [1]. Timing violations are difficult to spot in the early stages of design, but they become obvious during tape out and result in actual violations. This may eventually result in an IC's performance becoming subpar [2].

In accordance with Moore's Law, as new IC designs are released, the number of transistors grows exponentially, and the computational difficulty of timing closure also rises. Understanding the general structure of the functional unit, block is the first step before beginning the optimization experiment.

We must determine the timing sensitive path and the power-hungry section in the design. The timing critical path can occasionally result in an increase in power [3]. After the circuit has been evaluated, we must comprehend how to maximize timing and power and how to employ different techniques to converge timing and power gain. The numerous optimization strategies utilized to achieve timing convergence, and gain power must not have a negative effect on the system's overall efficiency in order to obtain high-quality performance from the design [4].

The time of signal transmission decreases with an increase in clock frequency, making it impossible to match the timing requirements of the design. Clock gating, multi-threshold voltage, power domains, and other significant approaches are also

applied at advanced technological nodes to achieve reduced power consumption. Therefore, it causes conflict between the temporal restrictions' trade-offs [5].

Dynamic IR drop, robustness brought on by the power distribution to the semiconductor, and the ability to use switching patterns to affect timing closures are all factors [6]. Timing violations result from an increase in IR drop on the clock and/or on the data channels. During at-speed scan testing, excessive switching causes a high current flow on the power/ground network and a rise in IR drop, which causes the device to time out [7].

3 Methodology

3.1 Targeted Critical Nodes Optimization

This optimization technique's goal is to focus only on the key nodes that the user has listed in a text file that will be submitted to the tool for reference and optimized only for those nodes that have been provided. The user should write down all the selected nodes that are causing timing critical design violations in a text file (Fig. 1).

A critical node is essentially one via which a gate's output is shared concurrently by two additional gates, causing those routes to setup and hold critical. Nodes are chosen by referring to instances, networks, and paths including crucial nodes, which are then sent directly to the software through a text file for optimization (the tool that has been used to illustrate critical nodes circuit is Cadence Virtuoso). The flows

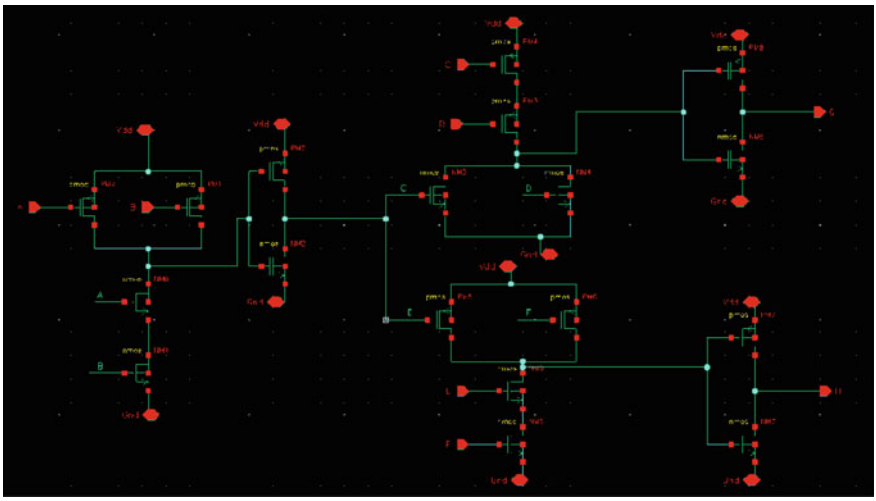

Fig. 1 Image illustrating critical nodes

shown below will assist in understanding how essential nodes are chosen and how they might be made more effective.

We cannot manually optimize or apply patches to remove these essential nodes and improve timing for each node individually because the design is too complex. Instead, we choose the top critical nodes and provide them in a file so that the tool knows which nodes to optimize.

In the flow diagram below, the blocks outside of the red dotted line should be completed by the user and then invoked to the tool once more because they correspond to actions taken internally by the EDA tool. The two activities of checking placement and checking DRC are the basis for choosing critical nodes. These two processes will help us understand which nodes are violated and require rapid repair. The following information, which is the result of the two actions, will be contained in the target-based text file (Fig. 2).

The GigaOpt constraints generator is now fed with the targeted text file (Fig. 3), which provides priority to the nodes in the file and refines the nodes with regard to congestion as well. Then delivered to the GigaOpt Eco routing, which modifies the setup and hold durations of the nets and nano-route to perform global and detailed routing, causing nodes to clear out of criticality.

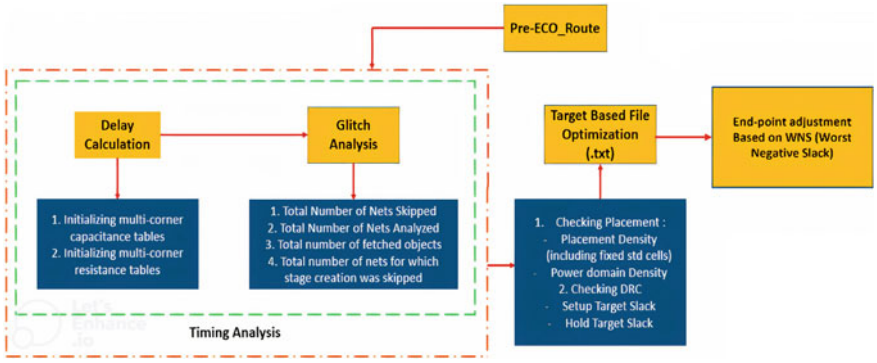

Fig. 2 Selection of critical nodes

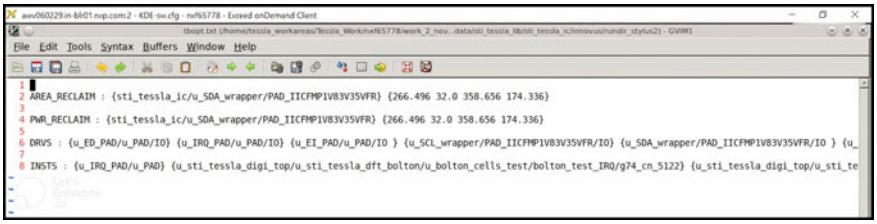

Fig. 3 Targeted optimization text file (.txt)

3.2 IR Drop Spotting and Its Optimization

After voltage (IR) drop on the power rails gets large on deep sub-micron CMOS technology, the issue becomes problematic. When continuous current travels via an unreliable network with changing resistance, a static IR drop happens. In other words, the circuit is not in steady state when the static IR drop happens. Dynamic IR drop is dependent on the rate at which instances switch, as opposed to static IR drop.

Traditional IR drop analyzes were used to produce more dynamic IR drop at the sign-off stage and as a result, were unable to satisfy the demands of advanced process nodes for accuracy and dependability. The major goal is to reduce IR loss by quickly identifying hotspots where significant voltage drops occur that are greater than an IC's threshold and prohibit it from reaching the desired performance.

When an IR drop is discovered during tape out, the flow has historically been sent back to the implementation phases where iterations are repeated to address the problems. The detection of IR drop ECO flow can be introduced to achieve sign-off clean. Most design violations are addressed and repaired by using the cell spreading and cell padding techniques, but certain violations are still missed, leading to IR drop hotspots.

The user must first locate the hotspots. Then, those blocks are subjected to PG patterns. The user specifies and manages these patterns. The different metal layers, from M0 to M15, nets, and other elementary groups should be indicated by pattern name and file in PG patterns. We employed M0 through M5 for our design's power planning.

The above flow illustrates how the power calculations will be carried out after the post-CTS and post-route stages, once the design has been fully implemented. Analysis of the static IR is performed using leakage power. When doing static IR drop analysis, it will look for violations and try to fix them by inserting power grids from the patterns that have been defined by users in accordance with the design.

The user must determine whether there are any critical violations during the dynamic IR drop analysis. If so, they must first pinpoint all the grids that are contributing to the greatest IR loss. At this level, violations typically happen as a result of layers being added on top of each other to correct some of these violations. An appropriate metal layer can be selected to obtain the least IR drop by creating a report on the resistance of least resistive path (RLRP). This will facilitate effective power distribution across the network. Once violations have been corrected, users can continue with ECO routing. ECOs steer clear of the laborious processes involved in entirely reimplementing the design. ECOs improve chip efficiency and make sure that changes made after optimization have not unintentionally changed the chip's behavior.

After the post-route stage, it is still difficult to achieve the IR drop margin by removing all actual infractions. During sign-off checks, some unresolved violations will eventually impact time routes. STA will assist in locating the critical paths that are brought on by cells or instances that are susceptible to changes in power, voltage, resistance, time, and user-defined paths. Cells will be used for the conventional VDD

margin analysis. The software in this flow is aware of both the current and nearby delays on the path. There are created switching circumstances that depend on critical timing routes and timing slack. Based on PG resistance and timing analysis, it finds proximity aggressors around voltage and crucial sensitive moments. As a result, this analysis will proceed as follows:

- The input design database must be loaded by the user.
- The next step is to find the important pathways whose time was violated.
- It is vital to notify the worst violated victim and aggressor nets, as well as the IR drop hotspots, during the analysis of IR drops.
- Then, ECO optimization will be carried out here.
- In the ECO fixing stage, resizing of cells and their aggressors, buffer addition or deletion, and cell swapping are done to remedy setup and hold violations.
- The final step is a second check for key pathways.
- A database will then be created by the software to store the corrected IR-aware time.

4 Results

4.1 Targeted Critical Nodes Optimization

In order for the design to pass timing closure, it plainly has a number of timing critical nets and routes that have to be enhanced. Table 1 lists crucial timing analysis parameters such WNS, TNS for setup and hold modes.

The magnitude of WNS for setup mode is 289 ps, and the magnitude of TNS is 3879 ps, as can be seen in the table below. Likewise, in hold mode, WNS and TNS have magnitudes of 317 ps and 4247 ps, respectively.

Therefore, Table 2's outcomes after applying targeted optimization, where timing is satisfied to an extreme where design can pass timing closure, are significantly more sophisticated than Table 1's.

Table 1 Table illustrating timing in the design before targeted optimization

Before targeted opt	Setup mode				Hold mode			
	All	Reg2Reg	Reg2Cgate	default	All	Reg2Reg	Reg2Cgate	Default
WNS (ns)	−0.289	−0.061	0.005	−0.289	−0.317	−0.054	0.140	−0.317
TNS (ns)	−3.879	−0.956	−0.478	−3.879	−4.247	−0.259	−0.667	−4.247
All paths	8894	8357	532	4565	8894	8357	532	4588

Table 2 Table illustrating timing in the design after using targeted optimization

After targeted opt	Setup mode				Hold mode			
	All	Reg2Reg	Reg2Cgate	default	All	Reg2Reg	Reg2Cgate	Default
WNS (ns)	0.115	0.096	0.000	0.115	4.863	0.527	0.675	4.863
TNS (ns)	7.855	0.000	0.000	7.855	7.954	0.777	2.475	7.954
All paths	8846	8349	8349	475	8846	8349	22	475

4.2 Detection and Optimization of IR Drop

Figure 4 clearly demonstrates that a sizable IR drop represents red hotspots over a conventional cell area. The standard cells start to establish output slowly because of the lower voltage supply as IR drop increases, i.e., the voltage provided to the standard cells is not 100% due to drop. The time of the IR drop pathways is also impacted as a result of the delayed output establishment, resulting in timing errors in the WNS design and path errors that cause chip failure. We increase the parallel metal 5 (M5) layers to address the static IR decrease. In order to decrease the cell instance's resistivity, which limits the flow of current toward the voltage supply, more metal 5 layers are being added. We included decoupling capacitors (DECAP) cells to prevent dynamic IR decrease. To lessen IR drop, these are inserted alongside the conventional cells. The capacitor serves as a power bank. These are transient capacitors that were inserted between the power and ground rails of the design to prevent functional failure brought on by dynamic IR drop (Fig. 5 and Table 3).

Following the application of PG metal stripes, the number of violations decreased from 2686 to 814 in the aforementioned table, and further violations decreased to 242 following STA ECO optimization. The addition of metal layers to power grids has been found to improve WNS with minimal impact on TNS, while timing is unaffected by ECO optimization.

The graph in Fig. 6 below shows the relationship between the quantity of currently existing critical instances and the design's IR decrease. As we can see, the IR loss is very little when essential instances are reduced by using user-defined patterns and ECO optimization. The important instances near 100 are also showing a voltage drop of 0.115 mV prior to utilizing PG pattern. After PG pattern implementation, that value dropped to 0.055 mV, and after ECO optimization over PG pattern implementation, those values dropped to 0.035 mV with 100 important instances.

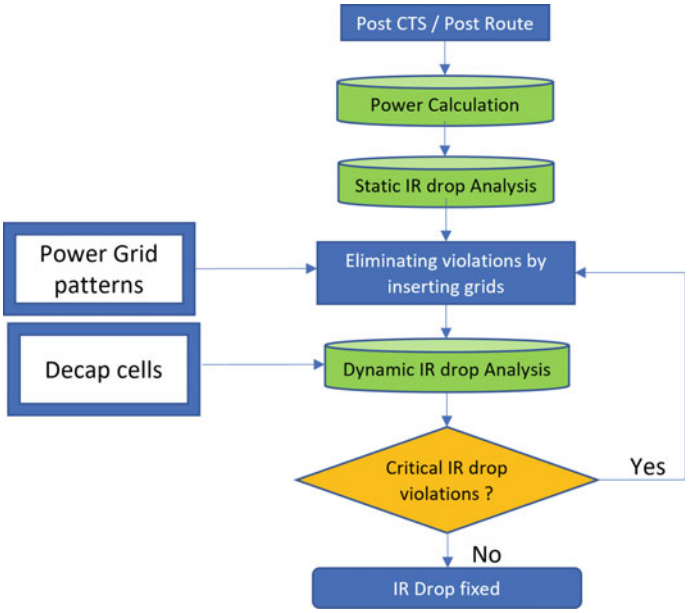

Fig. 4 Flow illustrating insertion of power grid

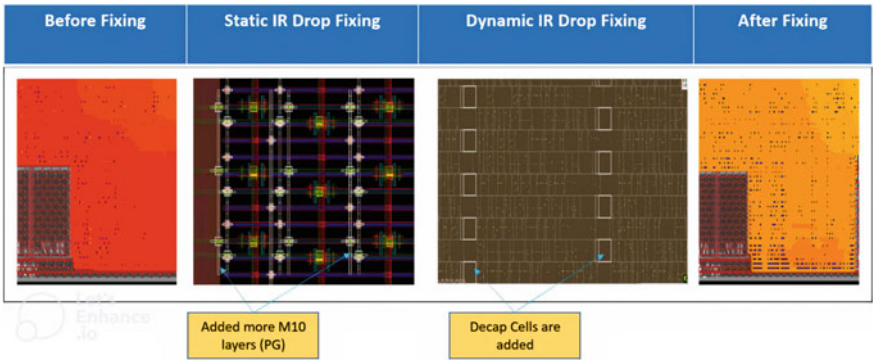

Fig. 5 PG grid application to reduce static and dynamic drop

Table 3 Improvement in IR drop following application of PG pattern and ECO optimization

	Before using PG pattern	After using PG pattern	After ECO optimization
IR drop > 30 mV	2686	814	242
WNS (ns) for all	−0.675	−0.612	−0.612
TNS (ns) for all	−21.855	−21.828	−21.828

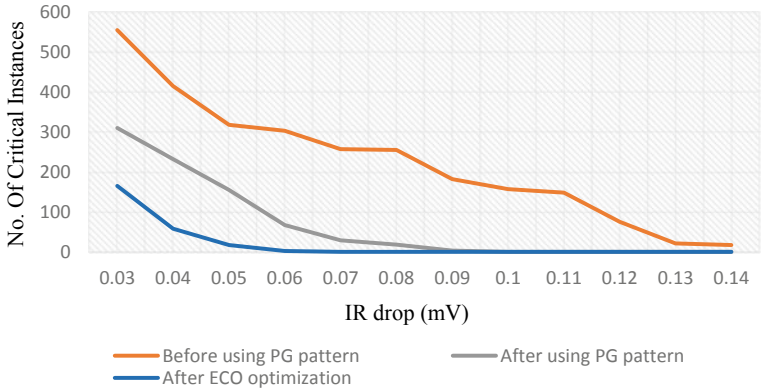

Fig. 6 Graph comparing IR drop for different techniques used

Table 4 Table comparing runtime in the design

Circuit design	Without targeted opt	With targeted opt
Parsing data	1.22 min	50 secs
Post-route optimization	9 min	4 min
Design runtime	1.05 h	52 ins

4.3 Runtime Comparison

The design's runtime with and without targeted optimization is shown in Table 4.

Cadence Innovus Stylus is used to conduct the trials. It takes 50 s to parse the data using targeted optimization using text file. By presuming that all nodes are essential and attempting to improve the setup and hold period, the post-route optimization step without targeted opt is a direct optimization of the design. In order to locate essential nodes, it scans every node in the design, which requires more time, i.e., nine minutes and resources. However, with targeted opt, we will supply the crucial nodes via a text file, eliminating the need for the tool to perform a second round of node-searching. As a result, the time required is reduced, coming in at only 4 min.

The table below also includes information about the total runtime of the designs.

5 Conclusion

In this work, sign-off concerns caused by critical nodes and IR drop were discussed, and a potential and effective solution were offered. The robustness of the power grid benefits from methods that use a collection of techniques for analyzing and resolving

breaches as embraced in our design. Additionally, we have talked about how timing path violations might lead to increased IR drop that ultimately fails sign-off checks.

Building a power grid with existing voltage-dropping power lines will make it difficult for the circuit to function properly, resulting in an increasing number of violations, which in turn cause the chip to completely fail and more importantly, the entire design to fail. The flow is advantageous for decreasing runtime while increasing accuracy and speed at the same time. We must ensure that speed and complexity of the design meet at a tradeoff point where we can achieve less noticeable drag while expecting output, even though we are dealing with chips with declining technology nodes.

References

1. Gandhi U, Bustany I, Swartz W, Behjat L (2019) A reinforcement learning-based framework for solving physical design routing problem in the absence of large test sets. In: 2019 ACM/IEEE 1st workshop on machine learning for CAD (MLCAD), Canmore, AB, Canada, pp 1–6. https://doi.org/10.1109/MLCAD48534.2019.9142109
2. Washak J, Alexandru C, Zhu D (2019) Development of an automatic bidirectional wireless charging system for mobile devices. In: 2019 IEEE wireless power transfer conference (WPTC). London, United Kingdom, pp 380–384. https://doi.org/10.1109/WPTC45513.2019.9055552
3. Hey LA (2008) Power aware smart routing in wireless sensor networks. In: 2008 next generation internet networks, Krakow, pp 195–202. https://doi.org/10.1109/NGI.2008.33
4. Kidav JU, Sivamangai DNM, Pillai DMP, Sreejeesh SG (2019) Design and physical implementation of array signal processor ASIC for sector imaging systems. In: 2019 32nd international conference on VLSI design and 2019 18th international conference on embedded systems (VLSID), Delhi, NCR, India, pp 448–453. https://doi.org/10.1109/VLSID.2019.00095
5. Vishweshwara R, Venkatraman R, Udayakumar H, Arvind VN (2009) An approach to measure the performance impact of dynamic voltage fluctuations using static timing analysis. In: 2009 22nd international conference on VLSI design. https://doi.org/10.1109/vlsi.design.2009.45
6. Arvind HNV (2009) An approach to measure the performance impact of dynamic voltage fluctuations using static timing analysis. In: VLSI design, 2009 22nd international conference on publication date: 5–9 Jan
7. Wang L-T, Wu C-W, Wen X (eds) (2006) VLSI Test principles and architectures: design for testability. Morgan Kaufmann, San Francisco
8. Saini S, Kumar AM, Veeramachaneni S, Srinivas MB (2010) An alternative approach to buffer insertion for delay and power reduction in VLSI interconnects. In: 2010 23rd international conference on VLSI design
9. Zhang K (n.d.) Challenges and opportunities in nano-scale VLSI design. In: 2005 IEEE VLSI-TSA international symposium on VLSI design, automation and test, 2005
10. Mao C-C (2015) Low-power IC design challenge. VLSI design, automation and test (VLSI-DAT). https://doi.org/10.1109/vlsi-dat.2015.7114563
11. Lee H-HS (2015) IC design challenges and opportunities for advanced process technology. VLSI design, automation and test (VLSI-DAT). https://doi.org/10.1109/vlsi-dat.2015.7114549
12. Zhou Y, Yan Y, Yan W (2017) A method to speed up VLSI hierarchical physical design in floorplanning. In: 2017 IEEE 12th international conference on ASIC (ASICON). https://doi.org/10.1109/asicon.2017.8252484

Impact of High-Performance Transistor on Performance of Static Random Access Memory for Low-Voltage Applications

Bhawna Rawat and Poornima Mittal

Abstract In this paper, four SRAM bit cells, two each of 6T and 7T (using typical and high-performance transistors), are described. Their performance is compared in terms of static noise margins, leakage current, write time, and global variation. The cell with most stable static noise margin values is the 7T1 cell with value of 91 mV for both read and hold operation, while its write margin is 120 mV. The weakest performance is recorded for the 6T cell with 0 mV read static noise margin. It also registers the highest leakage current values of 441 and 116 pA for Q = '0' and '1', respectively. The cell with best write time requirement of 30 ns is the 7T1 cell. Whereas, in terms of global variation analysis, the cell that outperforms against others is 6T1 with least variation in its hold, read, and write margin values for maximum variation caused by fabrication inconsistencies.

Keywords High-performance transistor · Write time · Global variation · Leakage current

1 Introduction

Static random access memory is an indispensable component of most microprocessors. It is a common component for most processing-based circuits. With the growing market appetite for low power, portable devices, the designing for circuit components has shifted to the nanometer vicinity. This decline in technology node facilitates power reduction, high-density integration, and economic feasibility for the device. But, it also subjects the cell to noise susceptibility and process variations [1]. Additionally, at lower technology node, the leakage power caused by sub-threshold

B. Rawat (✉) · P. Mittal
Delhi Technological University, Delhi, India
e-mail: bhawnarawat12@gmail.com

P. Mittal
e-mail: Poornimamittal@dtu.ac.in

S. Rawat et al. (eds.), *Proceedings of Second International Conference on Computational Electronics for Wireless Communications*, Lecture Notes in Networks and Systems 554,
https://doi.org/10.1007/978-981-19-6661-3_33

current dominates the total power dissipation for the design. Conventionally, reduction in leakage is achieved by supply voltage (V_{DD}) scaling; but this results in speed and noise margin degradation for the bit cells [2, 3]. The near-threshold operation due to nominal V_{DD} has low leakage power consumption and has lesser degradation in speed, compared to sub-threshold region [4]. It is also observed that technology node scaling may also degrade read and write margin for the cell. Therefore, to improve cell performance using high-performance transistors in the cell design is an alternative approach.

Standard MOSFET can be designed with varying threshold voltages (V_{TH}), the cell with nominal threshold voltage is referred to as standard threshold voltage cell. The V_{TH} for the cell can be altered by varying the channel doping; as the channel doping increases, the gate V_{TH} increases, because the gate voltage needed to deplete more majority carries before a minority carrier channel can be formed [5]. A high-performance transistor is a device that has lower V_{TH} in comparison with a typical transistor. The advantage of using high-performance transistors for designing SRAM bit cell is that they provide a convenient mechanism to improve the delay for the circuit [6]. Therefore, in this paper, two different topologies for 6T and 7T SRAM bit cells are discussed. For each bit cell topology, a typical cell and a high-performance-based cell are taken into consideration. This is done to analyze the impact of a high-performance transistor on the functioning of a bit cell. The 6T cell has been the industry benchmark for a long duration, due to its high packaging density and fast differential sensing [7]. But its performance has suffered significantly due to the drastic scaling in technology node and the reduction in V_{DD} [8]. Therefore, researchers have proposed different 7T bit cell topologies. The 7T cell is able to achieve commendable results at lower technology node and scaled V_{DD}, without adding much area penalty to the cell. Therefore, 7T cells are also gaining popularity. Consequently, to study the impact of high-performance transistor on the bit cell performance, two cells of 6T and 7T topology each are considered in this paper. The cells described in the paper are evaluated for static noise margin, leakage current, write time, and global variation analysis. The rest of the paper is categorized into four sections—Sect. 2 details the topology of the different 6T and 7T cells, while the simulation results for all the cells are analyzed in Sect. 3. Section 3 is further divided into four subsections each dedicated to static noise margin, leakage current, write time, and global variation analysis, respectively. The findings of the paper are comprehensively summarized in Sect. 4.

2 Different SRAM Bit Cell Topology

Various bit cell topologies are reported in literature. All cells in this paper are designed at 32 nm technology node, and the width dimensions for all the bit cells are shown in Table 1. The 6T cell has been the most prevalent SRAM cell, due to its fast sensing, symmetrical topology, and high packaging density. The schematic for the conventional 6T cell is illustrated in Fig. 1a. The data storage core for the 6T cell

Table 1 Transistor width dimension for different SRAM bit cells (in nm)

	M1	M2	M3	M4	M5	M6	M7
6T	64	64	96	96	128	128	–
6T1	64	64	166	96	128	128	–
7T	64	64	96	96	128	128	64
7T1	64	64	96	96	128	128	64

is composed of a back-to-back connected inverter pair (M1-M3 and M2-M4). This internal core for 6T is accessed via transistors—M5 and M6; the access transistors works in conjugation with the bitline pair—BL and BLB, signals to perform the read and write operation. For a very long duration, the 6T SRAM bit cell was the industry standard for cache memory implementation. But with technology node reduction and scaling of V_{DD}, the performance for the 6T SRAM bit cell has experienced a tremendous decline. Therefore, researchers have modified the 6T SRAM bit cell topology to improve its performance. One such 6T cell (6T1) was described by Suvarna and Mikie in 2019 [9]. The schematic design for 6T1 is depicted in Fig. 1b, and it is a modified version of the 6T design, which uses both access transistors to perform both the read and write operation. While, the 6T1 SRAM cell resolves the conflict by isolating the access transistors for the two operations; the M5 transistor works in conjugation with WBL during the write operation, whereas the M6 transistor along with RLB is responsible for the read operation. Another modification that is made in the 6T1 cell in comparison with the 6T is cell that the M3 transistor in the inverter core is always biased in the cut-off region; as the gate and drain for the transistor are shorted.

An SRAM bit cell topology consisting of seven transistors (7T) was reported by Aly and Bayoumi [10] in 2007. The 7T cell has differential ended topology and is reliant on BL and BLB for both its access operations—read and write operation. In the 7T cell, the information is retained by the inverter couple (M1-M3 and M2-M4). The mutual connection between the inverter couple is reliant on transistor M7, controlled by signal; W. The M7 transistor has the ability to connect/disconnect the back-to-back connection between the inverter couple as per need of the circuit. The main function for the M7 transistor is to reduce the mutually connected inverter pair to a cascaded inverter topology when the cell is operational in write mode. Else, the mutual feedback between the inverters is maintained. Therefore, the 7T cell is operational differentially for read mode and single-ended for write mode. The schematic of the 7T cell is illustrated in Fig. 1c.

A different 7T cell (7T1) design was described in 2021 by Rawat and Mittal [11]. The 7T1 cell is a modification of the 7T design and uses a high-performance NMOS transistor in its topology. In the 7T1 cell, the information is retained by an inverter pair formed by transistors M1-M3 and M2-M4. The mutual connection between the inverter couple is facilitated by the M5 transistor. The access operations - write and read, for the cell are single ended in nature performed via M6 and M7 transistors, respectively. The diagrammatical representation for the 7T1 cell is presented in the

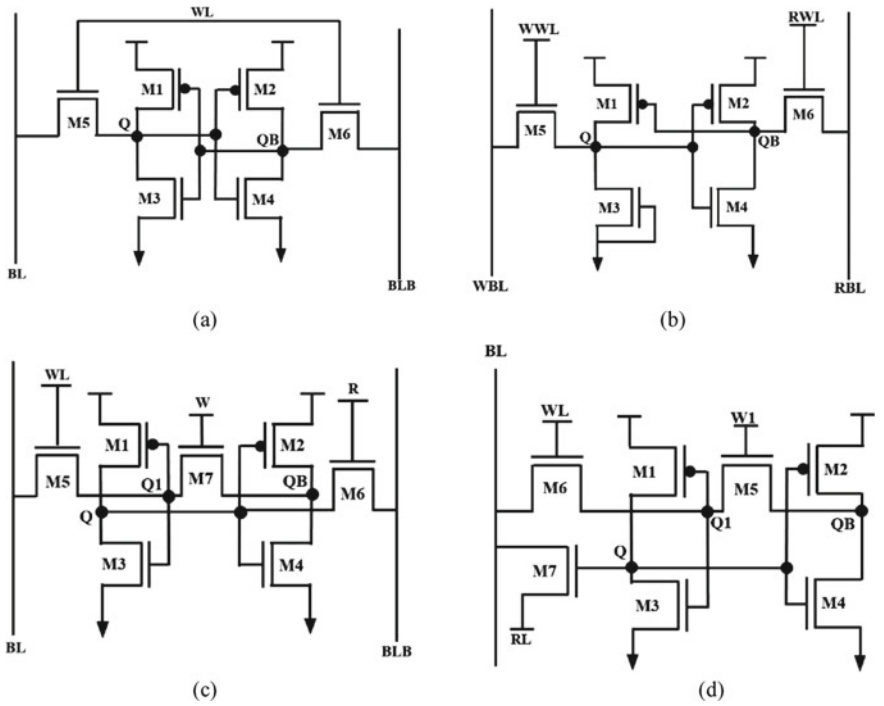

Fig. 1 Circuit representation for the **a** 6T, **b** 6T1, **c** 7T, and **d** 7T1 SRAM bit cell

Fig. 1d. A high-performance NMOS transistor (M3) helps in facilitating a faster writing for the cell. As the write delay for the circuit is inversely reliant on the $V_{DD} - V_{TH}$ factor; as the V_{TH} for the bit cell decreases, the $V_{DD} - V_{TH}$ factor increases, and thereby the write delay decreases.

3 Experimental Results and Analysis

3.1 Noise Margin Analysis

With the reduction in technology, node a cells vulnerability to noise increases. Also, as the V_{DD} for the bit cell is scaled, the impact of noise on the cell becomes prominent. A cell is required to be operational for three different operations—read, write, and hold. Consequently, for each cell, the noise margin resilience to each operation is to be calculated. The resilience of an SRAM bit cell to noise margin is measured using the static noise margin (SNM) metric for the read and hold operation. Whereas, for the write operation, the write margin (WM) is calculated. The SNM is determined as the side of the largest square that fits inside the smaller lobe of the butterfly curve

[12]. While, the WM for the bit cell is defined as the difference between the WL voltage and the BL voltage during the trip point [13]. The static noise margins for the three operations—read, write, and hold for the 6T, 6T1, 7T, and 7T1 cells are compared in Fig. 2, and the values are shown in Table 2.

As can be observed, the SNM value for 6T1 and 7T1 is same for the hold and read operation. The same is attributed to the single-ended topology of the read operation for the cell. But the employment of M3 in the cut-off region throughout the operation of the 6T1 cell has negatively impacted its SNM value. Whereas, the SNM values for 7T1 cell are fairly high. The SNM values for hold and read operation are different for the 6T and 7T cell owing to their differential read operation. A differential read operation causes the read current to pass through the storage node of the cell, thereby increasing its susceptibility to noise. This results in decrement in SNM value for the cell during the read operation. While, on the basis of WM all the cell register, a similar values as can also be inferred for Fig. 2, except 7T cell, which registers a very high WM value of 164 mV.

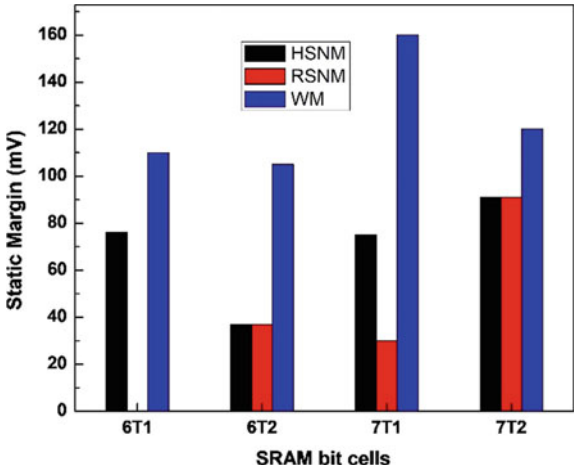

Fig. 2 Graphical comparison of static noise margin values for various SRAM bit cells

Table 2 Performance of all the SRAM bit cells for static noise margin, leakage current, global variation, and write delay

	Static noise margin (mV)			Leakage current (nA)		Global variation (mV)			Write delay
	HSNM	RSNM	WM	Q = 0	Q = 1	HSNM	RSNM	WM	
6T	76	0	110	441	116	53	0	98	50
6T1	37	37	105	229	50	21	18	50	100
7T	75	30	160	31	4	56	0	100	130
7T1	91	91	120	28	3.5	68	68	90	30

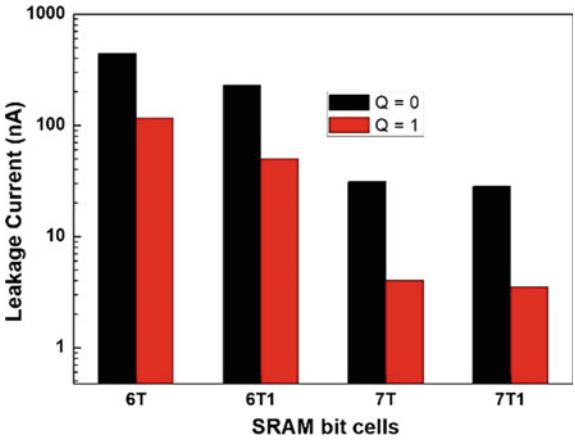

Fig. 3 Comparison of the leakage current values obtained for Q = '0' and Q = '1' for the different SRAM cells

3.2 Leakage Current

One of the major concerns of the circuits designed in the nanometer vicinity is the increased propensity of leakage current. The decreased channel length for the device facilities easy conduction of electrons in the OFF state, thereby resulting in high leakage current. As a consequence, evaluation of leakage current for circuits designed at lower technology node is essential. For an SRAM circuit, the leakage current is caused by three major components—gate leakage, sub-threshold leakage, and reverse junction leakage [14]. The different SRAM cells described in the paper are all evaluated for leakage current. As expected, the 6T cells register higher leakage in comparison with the 7T cells. This is because both the 6T cells were designed with higher aspect ratios for higher performance. But, the 6T1 cell was reported in 2019 and is an improvement over the 6T cell; consequentially, its leakage current is lower than the 6T1 cell. Both 7T designs have better leakage current performance when compared with the 6T designs. But of the two 7T cells, the 7T1 cell had slightly better performance; the single-ended circuitry for the 7T1 cell reduces the leakage current outlets for the 7T1 cell. The 7T SRAM bit cell being of the differential ended nature has a slightly higher leakage current. The leakage current values for the different cells are graphically compared in Fig. 3 and listed in Table 2.

3.3 Write Delay Analysis

During the write operation, the SRAM bit cell has to deliberately cause a discharge event through the bitline (s) to result in a data change at the storage node. Consequently, write operation for an cell is the most time-consuming process. Therefore, it usually is the process that determines the minimum timing requirement for the cell. As a result, it is a parameters that defines the timing analysis for the bit cell.

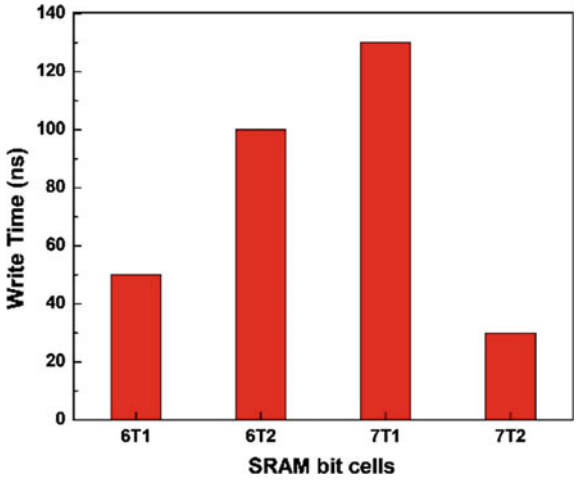

Fig. 4 Graphical comparison for the write time values for the different SRAM bit cells

The different cells are compared for the write timing requirement in Fig. 4, and the values are listed in Table 2.

The highest write time is required by the 7T cell of 100 ns to perform a successful write operation. This is because the 7T cell reduces the back-to-back inverter pair topology to a cascaded inverter configuration during the write operation (this improves cells stability to noise) but does not take any additional remedy to improve the write time for the cell. A similar topology is used by 7T1 cell as well, but it relies on a high-performance NMOS (M5) to enhance the write time requirement for the cell. Also, the 7T cell was reported for 180 nm technology node and 1.1 V supply voltage, whereas the analysis is being performed at a fairly low technology node. Thereby, impacting the performance for the 7T cell. The 6T cell on the other hand has fairly fast write operation; this is in keeping with the differential nature of the cell. Whereas, the 6T1 SRAM bit cell is single-ended and therefore witness a rise in write time requirement.

3.4 Global Variation Analysis

A variation in performance of a circuit designed at nanometer vicinity can be observed due to fabrication imperfections such as oxide thickness, line edge roughness, and discrete random dopant [15]. These fabrication imperfections are accounted for and analyzed using the global variation analysis. This analysis is used to determine the maximum range of variation in the SNM of a bit cell when it is subjected to maximum variation due to fabrication imperfections.

A cell is deemed resilient to global variations if the variation in its static noise margins is minimal for worst case global variation. In this sections, the cells are compared for the range of variation that a cell may observed because of global

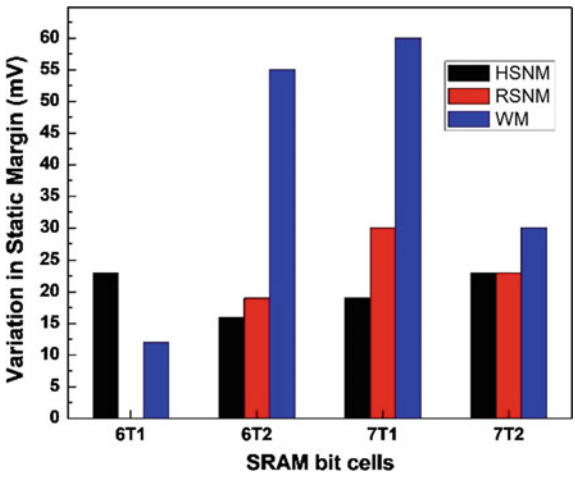

Fig. 5 Graphical comparison for the maximum variation in the static noise margin values for different SRAM bit cell under global variation

variation. The highest variation in performance for the hold operation is for the 7T1 cell, while the least variation in performance is observed for 6T1 cell. While, for the read operation, the cell with the highest variation in performance is for 7T cell, while the least is for 7T1 cell. The write margins for the 7T cell are highly vulnerable to global variations. While, the WM is least vulnerable for the 6T cell. The variation in the static noise margin values for all the operation of a cell is graphically compared in Fig. 5 and shown in Table 2.

4 Conclusion

SRAM bit cells form the core for designing cache memory, which are a prevalent form of memory used in most microprocessors. With the declining technology node to increase cell packaging density and scaling supply voltage to minimize the power requirement, the performance of the bit cell has plummeted. The conventional SRAM bit cell has experienced decline in its performance, so SRAM bit cells designed using high-performance transistors are being reported in the literature. In this paper, a comparison of typical SRAM cell with high-performance transistor-based SRAM cell is performed. Four SRAM bit cell topologies, 2 each (1 typical and other high-performance transistor-based) of 6T and 7T, are described. Their performance in terms of static noise margins, leakage current, write time, and global variation analysis is presented in the paper. The 7T1 cell with the most stable static noise margin value of 91 mV for both read and hold operation, while its write margin is 120 mV. The cell with the weakest static noise margin performance is the 6T cell as it registers a failure in read operation as its read static noise margin value is 0 mV. It is also the cell that registers the highest leakage current values of 441 pA and 116 pA for Q = '0' and '1', respectively. But this cell has a superior performance in terms of write

time, with a timing requirement of 50 ns; a cell with an even better write time is the 7T1 cell, with a write time requirement of 30 ns. Whereas, in terms of global variation analysis, the cell that outperforms against other cells is the 6T1 cell with the least variation in its hold, read, and write margin values for maximum variation caused by fabrication inconsistencies.

References

1. Divya Mittal P (Dec 2021) Parametric extraction and comparison of different voltage-mode based sense amplifier topologies. In: 2021 3rd international conference on advance in computing, communication control and networking. https://doi.org/10.1109/ICAC3N53548.2021.9725671
2. Chen G, Sylvester D, Blaauw D, Mudge T (2010) Yield driven near threshold SRAM design. IEEE Trans Large Scale Integr (VLSI) Syst 18(11):1590–1598
3. Kim TH, Liu J, Kim CH (2007) An 8T sub-threshold SRAM cell utilizing reverse short channel effect for write margin and read performance improvement. Processing IEEE custom integrated circuits conference (CICC), pp 241–244
4. Mittal P, Rawat B, Kumar N (2022) Tetra-variate scrutiny of diverse multiplexer techniques for designing a Barrel shifter for low power digital circuits. Microprocess Microsyst 90:104491
5. Mohammed MU, Nizam A, Chowdhury MH (2018) Performance stability analysis of SRAM cells based on different FinFET devices in 7 nm technology. In: 2018 IEEE SOI-3D-subthreshold microelectronics technology unified conference (S3S). https://doi.org/10.1109/S3S.2018.8640161
6. Weste NH, Harris D (2015) CMOS VLSI design: a circuits and systems. Person Education. Perspective, Noida, India
7. Patil S, Bhaaskaran VSK (2017) Optimization of power and energy in FinFET based SRAM cell using adiabatic logic. 2017 International conference on nextgen electronic technologies silicon to software (ICNETS2). https://doi.org/10.1109/ICNETS2.2017.8067966
8. Mittal P (2016) Static random access memory cell design based on all-p organic, hybrid, and complementary organic thin-film transistors. Organic Thin-Film Transistor Applications, CRC Press, pp 261–286
9. Surana N, Mekie J (2019) Energy efficient single-ended 6-T SRAM for multimedia applications. IEEE Trans Circuits Syst II Express Briefs 66:1023
10. Aly RE, Bayoumi MA (2007) Low-power cache design using 7T SRAM cell. IEEE Trans Circuits Syst II Express Briefs 54(4):318–322
11. Rawat B, Mittal P (2021) A 32 nm single ended single port 7T SRAM for low power utilization. Semicond Sci Technol 36(9):095006
12. Singh P, Vishvakarma SK (2017) Ultra-low power high stability 8T SRAM for application in object tracking system. IEEE Access 6:2279–2290
13. Rawat B, Mittal P (2022) A comprehensive analysis of different 7T SRAM topologies to design a 1R1W bit interleaving enabled and half select free cell for 32 nm technology node. Proc Royal Soc A: Math, Phys, Eng Sci 478(2259)
14. Rawat B, Mittal P (2022) A reliable and temperature variation tolerant 7T SRAM cell with single bitline configuration for low voltage application. Circuits, Syst Signal Proc. https://doi.org/10.1007/s00034-021-01912-5
15. Singh J, Mohanty SP, Pradhan DK (2013) Robust SRAM designs, and analysis. Springer, New York

A Full-Swing, High-Speed, and High-Impedance Hybrid 1-Bit Full Adder

Chinmay Malkhandi and Rathnamala Rao

Abstract In this paper, an attempt has been made to design a high-speed architecture for a 1-bit full adder. The proposed circuit uses a hybrid structure that combines CMOS logic and Transmission gate logic for design and implementation. Using both CMOS and Transmission gate logic in a design can provide the advantages of both the logic design. The SPICE simulations for the proposed full adder circuit have been performed with TSMC 180 nm CMOS Technology. The proposed full adder circuit has 23.63% less carry delay than the sum delay, which can be exploited for use in more complex systems like multi-bit adders where the carry path becomes the critical path. The speed of the proposed full adder is found to improve by 32.6% and 8.03% for sum and carry, respectively, with respect to CMOS implementation and by 1.62% and 21.02% with respect to some of the best-reported architectures in the literature. The proposed circuit has been found to have high input impedance and a low output impedance along with a full swing of voltages at the output.

Keywords Full adder · Hybrid design · CMOS logic · Transmission gate · Critical path

1 Introduction

With the increased usage of high-speed electronic devices like mobile phones, supercomputers, and high-speed servers, high-speed circuit design is increasingly in demand. An adder [1] is one of the elementary components required for any digital design, which can be used not only for addition but also for complex arithmetic operations like subtraction, multiplication, and division. It can be used in the ALU unit of microprocessors, micro-controllers, and various signal processing blocks for doing

C. Malkhandi · R. Rao (✉)
National Institute of Technology, Surathkal, Karnataka, India
e-mail: malarathna@nitk.edu.in

S. Rawat et al. (eds.), *Proceedings of Second International Conference on Computational Electronics for Wireless Communications*, Lecture Notes in Networks and Systems 554,
https://doi.org/10.1007/978-981-19-6661-3_34

arithmetic, and logical operations. As a result, designing an adder having high performance, and low-power consumption has become one of the important research areas. Commonly, many design considerations like high-speed, low-power, low-transistor count, area-efficient design, etc. have been considered in the past research.

With the need for a high performance circuit design, the emphasis should also be toward having a reliable circuit producing little or no glitches, drawing minimum power from the input ports along with the capability to drive a big load. As a result, there is a need to develop a 1-bit full adder that not only provides a high-speed operation but also draws less current from the previous stage and can drive the output load, providing full swing of voltages [2].

There are two ways to optimize a design, the first one is the 'architectural optimization', where the design can be optimized for the longest critical path and the other being the 'circuit optimization', where the design can be optimized by making changes in the PMOS and NMOS sizes and connections in the circuit.

In this paper, we propose a high-speed full adder having high input impedance and low output impedance providing a full swing of voltage. The proposed full adder consists of a hybrid combination of CMOS logic and transmission gate logic. With the use of hybrid design approach, the advantages of both CMOS logic and transmission gate logic are captured, resulting in a design having high-speed, high input impedance and low output impedance with full voltage swing at the output. Based on LT-SPICE simulation with TSMC CMOS 0.18μm process technology, the proposed full adder is proven to have the minimum delay as compared to some of the results found in the literature. The SPICE simulations also show that the proposed full adder has less carry delay than the sum delay. This is advantageous as in the complex designs using several units of 1-bit full adder, the carry path often becomes the critical path for the entire design.

This paper is organized as follows. Section 2 reviews some of the full adder designs proposed in the literature. Section 3 describes the design of our proposed hybrid full adder. Section 4 shows the results of the SPICE simulation. Finally, a brief conclusion is presented in Sect. 5.

2 Previous Works

Various low-power full adders have been presented in literature—[3–5] are reviewed. The conventional CMOS full adder [2] is realized in Fig. 1. This design is an optimized version of the actual CMOS implementation with certain PMOS and NMOS circuits reused for optimization of power and area and is different from the conventional Pull-Up-Network (PUN) and Pull-Down-Network (PDN) design [1]. The main disadvantage of the CMOS full adder is its low speed, which is because of many series-connected NMOS and PMOS, increasing the logical effort [2].

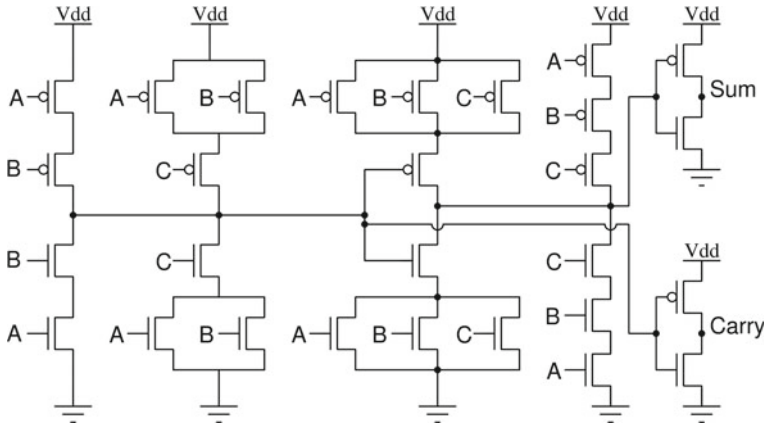

Fig. 1 CMOS implementation of full adder

To overcome the issue of slow response, transmission gates are used as it offers less capacitance compared to other gate-connected logic styles like CMOS. The main disadvantage of TFA is high power consumption than its CMOS counterpart.

Later, researchers focused on the hybrid logic approach for improving the overall performance. In 2006, Chiou-Kou Tung et al. [3] proposed two High Performance Low-Power Full Swing Full Adders (HPLPFSFA), having two different blocks for generating sum and carry. For generating the sum, a hybrid combination of CMOS logic, pass transistor logic, and transmission gate logic [1] are used and for generating the carry only CMOS logic is used.

A Low-Power High-Speed Hybrid Full Adder (LPHSHFA) using 3-XOR designs were proposed by Chiou-Kou Tung et al. [4] in 2007. The circuit uses CMOS and pass transistor logic for generating the sum, while for generating carry, only CMOS logic is used. In 2014, Partha Bhattacharyya et al. [5] proposed a Low-Power High-Speed Hybrid 1-bit Full Adder Circuit (LPHSHFA) using CMOS and pass transistor logic, providing one of the best results presented in the literature.

3 Proposed 1-Bit Full Adder

In some of the previous work, more focus is on optimizing the power drawn from the supply source while the power drawn from the previous stage also becomes an important factor to consider. The proposed circuit having a high input impedance draws less current from the previous stage thereby reducing the power drawn.

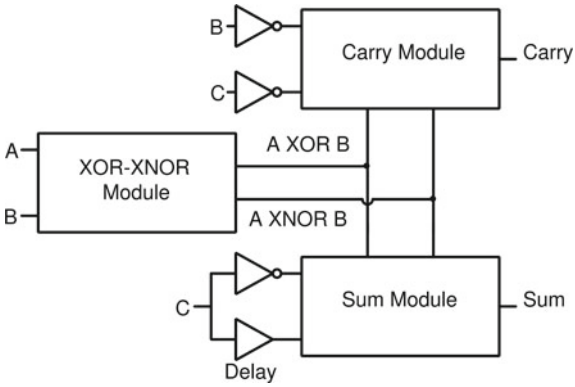

Fig. 2 Block diagram of proposed circuit

3.1 Design Approach for the Proposed Circuit

Implementing the input and output stages of the proposed circuit using CMOS logic style provides high input impedance and low output impedance along with providing a full swing of voltage from 0 to Vdd at the output. While implementing the intermediate stages with the transmission gate logic style enables high-speed.

From the equations for Sum and Carry of a 1-bit full adder given in Eqs. 1 and 2, it can be observed that the XOR and XNOR operations are essential for the generation of sum and carry.

$$\text{Sum} = A \oplus B \oplus C = ((A \odot B).C' + (A \oplus B).C)' \tag{1}$$

$$\text{Carry} = A.B + C.(A \oplus B) = ((A \oplus B).C' + (A \odot B).B')' \tag{2}$$

3.2 Different Blocks of the Proposed Circuit

The block diagram of the proposed circuit, in Fig. 2 shows that there are three modules, the XOR-XNOR module, the Sum module, and the Carry module.

3.2.1 XOR-XNOR Module

The proposed circuit generates XOR and XNOR separately in the XOR-XNOR module as shown in Fig. 3. Generating XOR and XNOR separately avoids any delay due to the inverter in case XNOR is generated by inverting XOR or vice-versa.

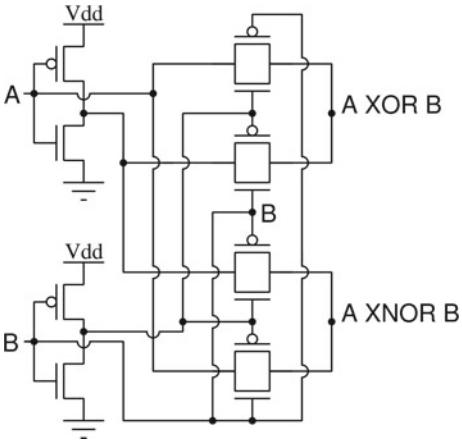

Fig. 3 XOR-XNOR module

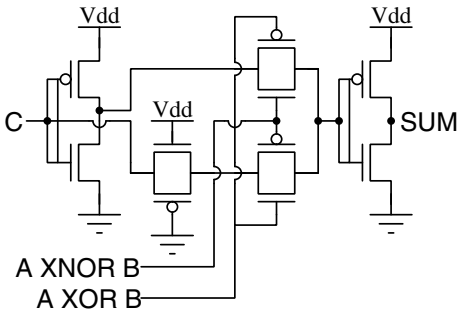

Fig. 4 Sum module

3.2.2 Sum Module

The Sum module takes 3 inputs: $A \oplus B$, $A \odot B$, and C. It can be seen from Fig. 4 that the input C is fed into an inverter and a delay element,[1] to match the path delays of C and C' before reaching the transmission gate, controlled by $A \oplus B$ and $A \odot B$. Finally, the inverter stage provides low impedance and a full swing of voltages at the sum output.

3.2.3 Carry Module

The carry module shown in Fig. 5 is almost similar to the sum module, where the transmission gates are controlled by $A \oplus B$ and $A \odot B$. The inputs B' and C' are directly taken from their earlier generation in XOR-XNOR module and the Sum

[1] Delay element is a simple transmission gate with PMOS permanently connected to GND and NMOS permanently connected to Vdd.

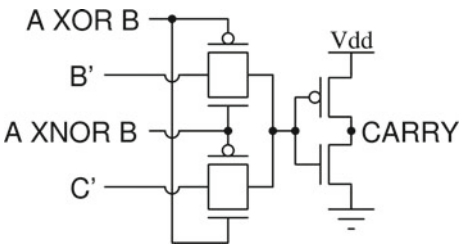

Fig. 5 Carry module

module, respectively. Similar to the sum module, the final stage is a CMOS inverter providing advantages discussed in previous section.

3.3 Proposed Circuit

Combining all the modules in Sect. 3.2, the proposed circuit is shown in Fig. 6. The sizes of PMOS and NMOS used in Fig. 6 are tabulated in Table 1.

For sizing, the reference NMOS width and the reference gate length are taken to be the minimum widths and lengths allowed by the TSMC 180 nm pdk, i.e., 240 nm and 180 nm respectively. The reference PMOS width is taken to be 2.5 times the NMOS width. Generally the PMOS width is taken to be 2–3 times that of NMOS width [1, 2]. An inverter designed with the ratio of PMOS width to NMOS width equal to a nominal value of 2.5, gives a symmetric Voltage Transfer Characteriztics [1, 2]. The PMOS Mp1 and the NMOS Mn1 have W and L equal to the reference widths and lengths as the output is fed to only two transmission gates.[2] For the MOSFETs Mp2 and Mn2, the L equals the reference gate length and W has been taken 4 times the reference width as the output is fed to four gate terminals, hence it requires more strength. To match the delays of the signal C and C' the PMOS Mp3 and the NMOS Mn3 have L equal to the reference gate length while W has been taken 2 times the reference width while the MOSFETs Mp8 and Mn8 have W equal to the reference widths and the L has been taken to be 2 times the reference gate length. The PMOS Mp4, Mp5, Mp6, Mp7, Mp9, Mp10, Mp11, and Mp12 and the NMOS Mn4, Mn5, Mn6, Mn7, Mn9, Mn10, Mn11, and Mn12 which are used in the transmission gates have W and L equal to the reference widths and lengths. The PMOS Mp13, and Mp14 and the NMOS Mn13, and Mp14 which serve as an output stage has also been sized as per the reference widths and lengths.

[2] Transmission gates have relatively less capacitance as compared to some gate-connected logic like CMOS [1, 2].

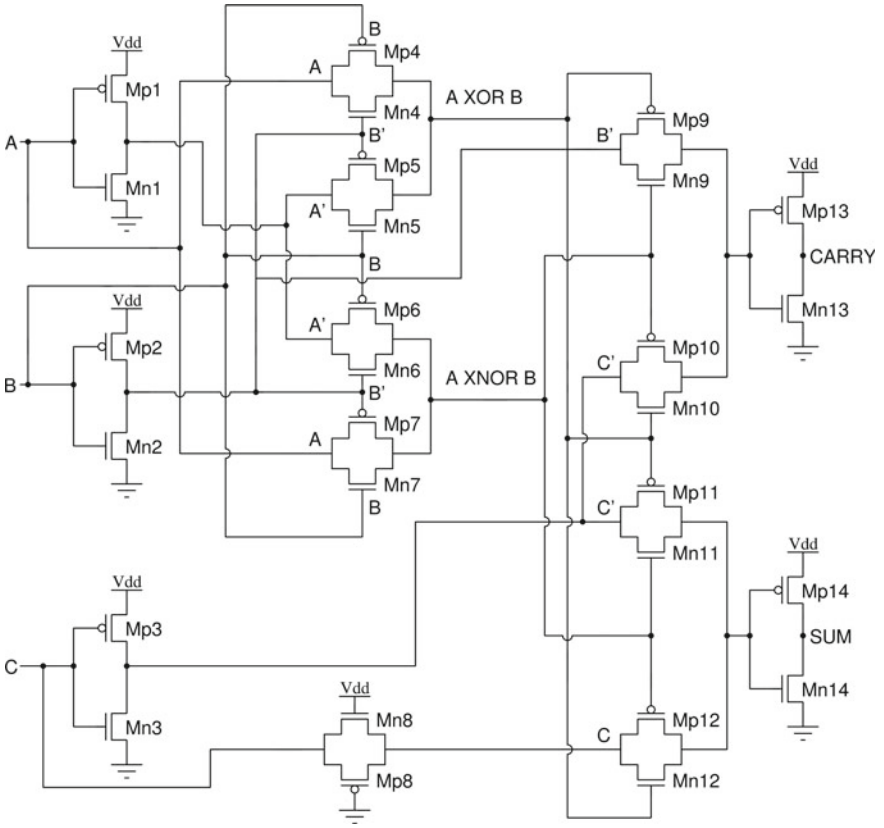

Fig. 6 Proposed 1-bit full adder circuit

Table 1 Transistor sizes of the proposed circuit

Transistor name	Width (W) (μm)	Length (L) (μm)
Mp1, Mp4, Mp5, Mp6, Mp7	0.6	0.18
Mn1, Mn4, Mn5, Mn6, Mn7	0.24	0.18
Mp2	2.4	0.18
Mn2	0.96	0.18
Mp3	1.2	0.18
Mn3	0.48	0.18
Mp8	0.6	0.36
Mn8	0.24	0.36
Mp9, Mp10, Mp11, Mp12, Mp13, Mp14	0.6	0.18
Mn9, Mn10, Mn11, Mn12, Mn13, Mp14	0.24	0.18

4 Simulation and Results

For Simulations, an open source tool LT-SPICE has been used with TSMC-180nm technology. The circuits presented in the literature [3–5] have been re-simulated. The input waveforms shown in Fig. 7 are given in such a way that when one of the input makes a transition from $0 \rightarrow 1 \rightarrow 0$, other two inputs are constant. This process is carried out for all the combinations of non-transitioning input. As shown in

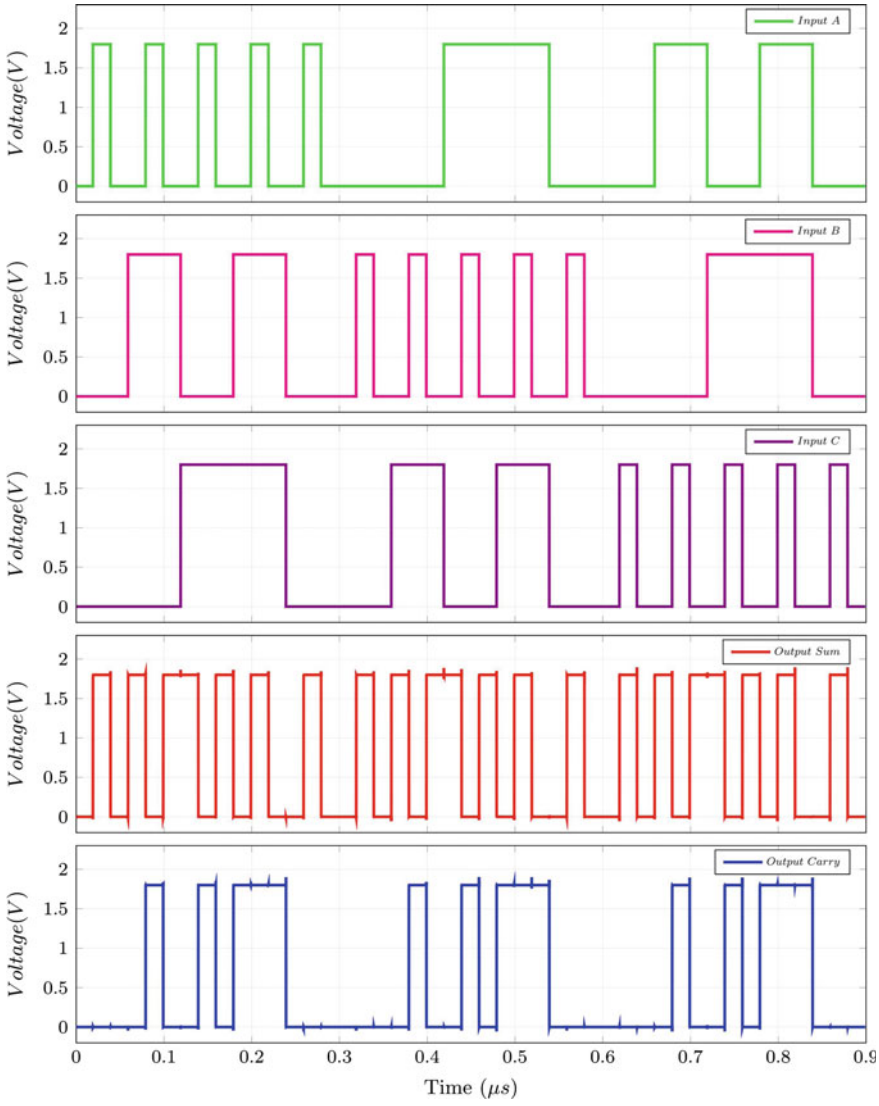

Fig. 7 Simulation results

Table 2 Delay comparison of different high-speed full adders

Design	Sum delay (ps)	Carry delay (ps)	Power consumption (μW)	No. of transistors
CMOS	179.5	100.47	0.74	28
TFA [3]	124.32	95.27	0.64	26
HPLPFSFA [3]	123.21	79.38	0.49	26
LPHSHFA [4]	1047.61	79.10	3.61	24
LPHSHFA [5]	123.05	116.89	0.423	16
Proposed	120.92	92.39	0.94	28

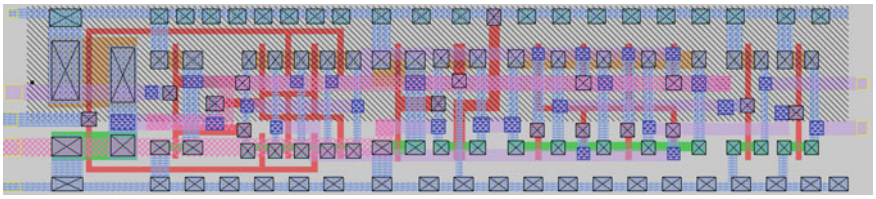

Fig. 8 Layout of the proposed circuit

Fig. 7, from 0–300 ns *A* is the transitioning input while *B* and *C* are non-transitioning inputs. Here *A* is transitioning for every combination of *B* and *C* then from 300–600 ns, *B* becomes the transitioning input and transitions for all combinations of *A* and *C* and from 600–900 ns *C* is the transitioning input. The path delays of different paths originating from each primary input and terminating at each primary output have been measured and the maximum delay values among them are obtained and tabulated in Table 2.

The results tabulated in Table 2 shows that the proposed full adder has 23.63% less carry delay than the sum delay, which can be exploited for use in more complex systems like multi-bit adders where the carry path becomes the critical path. The speed of the proposed full adder is found to be improved by 32.6% and 8.03% for sum and carry, respectively, with respect to the CMOS implementation and by 1.62% and 21.02% with respect to some of the best-reported designs [5] in the literature. The power consumption of the proposed circuit is 27.19% more with respect to the CMOS implementation and more by 122.2% with respect to best-reported design [5].

The layout of the proposed circuit has been drawn using MAGIC Tool with TSMC 180nm technology and the post-layout simulation has been carried out using the NG-SPICE tool. Table 3 shows the comparison between the pre-layout and the post-layout simulations. The post-layout delays are found to be more than the schematic simulation results by 59.5% for Sum delay, 67.74% for Carry delay, and 119.148% for power consumption. The delay and power consumption values deteriorate in post-layout simulations due to the wire delays and various other parasitics, which are taken into consideration while doing post-layout simulations (Fig. 8).

Table 3 Schematic and post-layout comparison

	Sum delay (ps)	Carry delay (ps)	Power consumption (μW)
Schematic	120.92	92.39	0.94
Post-layout	192.69	155.15	2.06

5 Conclusion

The proposed full adder circuit as shown in Fig. 6 has a structure where the inputs *A*, *B* and *C* are not directly passed to the output. Instead, they are fed to the gate terminal of the MOSFET which makes it a design with high input impedance. The output stage of the proposed circuit is an inverter for both outputs. Connecting an inverter at the output not only improves the fanout, but also provides low impedance as seen from the output side and also allow a full-swing of voltage. The simulation waveforms in Fig. 7 show that the proposed circuit is a glitch-free and reliable circuit. The simulation results show that the proposed full adder is free from glitches and can be used in designs requiring fast full adders.

References

1. Chandrakasan AP, Rabaey JM (2016) Digital Integrated Circuits—A Design Perspective, 2nd edn. Pearson Education India
2. Weste N, Harris D (2015) CMOS VLSI Design—A Circuits and Systems Perspective, 4th edn. Pearson Education India
3. Tung C-K, Shieh S-H, Hung Y-H, Tsai M-C (2006) High-performance low-power full-swing full adder cores with output driving capability. In: IEEE Asia Pacific conference on circuits and systems, pp 614–617. IEEE. https://doi.org/10.1109/APCCAS.2006.342063
4. Tung C-K, Hung Y-C, Shieh S-H, Huang G-S (2007) A low-power high-speed hybrid cmos full adder for embedded system. In: IEEE design and diagnostics of electronic circuits and systems, pp 1–4. IEEE. https://doi.org/10.1109/DDECS.2007.4295280
5. Bhattacharyya P, Kundu B, Ghosh S, Kumar V, Dandapat A (2015) Performance analysis of a low-power high-speed hybrid 1-bit full adder circuit. IEEE Trans Very Large Scale Integr (VLSI) Syst 23(10):2001–2008. https://doi.org/10.1109/TVLSI.2014.2357057

High-Speed Multiplexed Feedback D Flip-Flop

Vinay Kushwaha and Rathnamala Rao

Abstract This work proposes a new high-speed architecture of a positive edge-triggered D flip-flop. A multiplexed feedback push-pull network is used to decrease the clock to q delay and setup time of the flip-flop. This multiplexed network acts as feedback as well as a charging network. It was observed that this architecture reduces the propagation delay by 21 and 23% compared to push-pull isolation and conventional D flip-flop. The proposed D flip-flop design can be utilized in critical paths of a pipelined system to improve the speed. The circuit is designed on 180 nm technology and tested for 1× load at various process corners using the Cadence Virtuoso tool.

Keywords D flip-flop · Multiplexed feedback push-pull network · Setup time

1 Introduction

D flip-flops (DFF) are among the most frequently used elements in any digital system [3]. D flip-flops are mainly used for data storage and synchronization. Most of the modern processors are pipelined, and DFFs form an integral part of this pipeline. The control path of processors is usually implemented as finite state machines (FSM), and DFF's are an integral part of any FSM [5]. Hence, the performance of DFF can influence the performance of the overall system.

Area, speed and power are the three basic performance metrics that are frequently used to compare the performance of any digital system [6]. The speed of a DFF plays an important role in the overall speed of the system, which uses several DFF in it. In this paper, a new high-speed DFF architecture, namely multiplexed feedback push-pull D flip-flop is proposed.

V. Kushwaha (✉) · R. Rao
National Institute of Technology, Surathkal, Karnataka, India
e-mail: vinaykmw@gmail.com

R. Rao
e-mail: malarathna@nitk.edu.in

S. Rawat et al. (eds.), *Proceedings of Second International Conference on Computational Electronics for Wireless Communications*, Lecture Notes in Networks and Systems 554,
https://doi.org/10.1007/978-981-19-6661-3_35

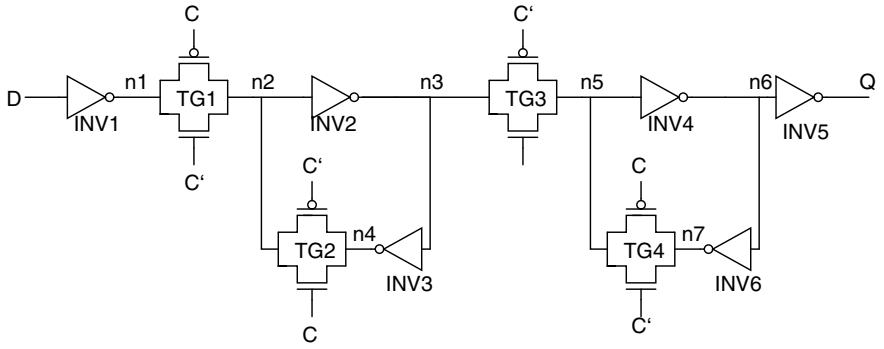

Fig. 1 Conventional DFF

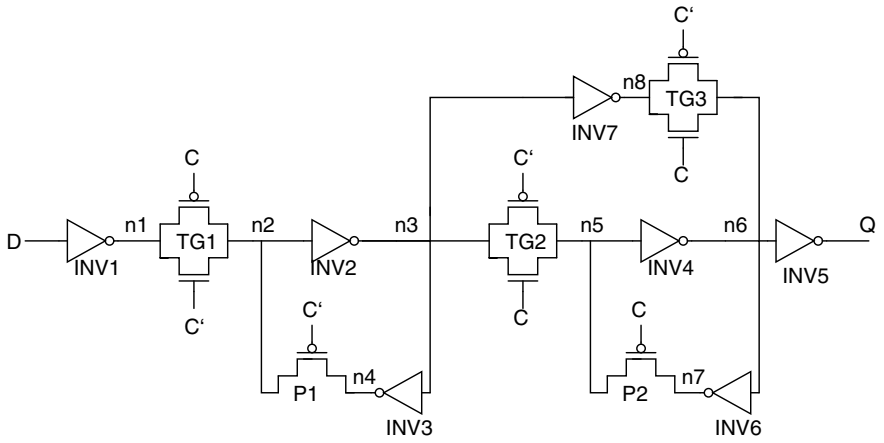

Fig. 2 Push-pull isolation DFF

Several DFF architectures, namely conventional DFF [5, 6], low area DFF [4, 5], push-pull DFF [5], push-pull isolation DFF [5], are proposed in various literature. The conventional [5, 6] low-risk DFF architecture shown in Fig. 1 [5, 6] is frequently used in most designs. It has two level-sensitive latches connected in a master-slave configuration. DFF based on dynamic logic is discussed by Shaikh [7]. Dynamic logic is very fast as compared to static logic, but due to leakage issues, it is not suitable for standard cell library-based application.

A push-pull isolation DFF architecture was proposed by Uming Ko and Pores T.Balsare [5], which has a smaller clock to q delay as compared to the conventional low-risk DFF. Figure 2 shows the architecture of push-pull isolation DFF. This circuit has additional charging and discharging paths which reduce the clock to q (C to Q) delay as compared to the conventional DFF. However, this adds four transistors contributing to 6% higher power compared to conventional DFF. In addition to this, the effective capacitance at node n3 has also increased which may affect the setup

time of the circuit. Further improvement in speed can be achieved by reducing the setup time of push-pull isolation DFF.

In this paper, a novel multiplexed feedback (MUXFB) push-pull DFF is proposed which improves the clock speed by reducing the setup time. The proposed circuit is discussed in Sect. 2. Section 3 discusses the results of the simulation and compares the performance of the proposed circuit with conventional and push-pull isolation DFF. Section 4 concludes the work.

2 Proposed Circuit Design

The schematic of multiplexed feedback (MUXFB) push-pull DFF is shown in Fig. 3. In this design, the feedback inverter is used as a push-pull network when clock is high. When clock is low, it is used as a feedback network.

In the push-pull isolation DFF proposed by Uming Ko and Pores T.Balsare, inverter INV2 (ref Fig. 2) has to drive two inverters (INV3, INV7) and one transmission gate(TG2). This results in increased setup time. Hence, in the proposed circuit, modifications are done such that inverter INV2 drives only one transmission gate and one inverter, thereby reducing the capacitance at node n3, as a result of this, setup time decreases. Additional load is removed from node n3. In this design, when the clock is 0, only the master stage is active. Master latch stores the data given at input. When the clock becomes one, the slave stage turns on, and data propagates to Q.

The charging path to node n6 in MUXFB push-pull DFF is through the inverter 'INV2' transmission gate 'TG2' and inverter 'INV4' represented as path 1 in Fig. 3. The current fed by this path is represented by 'i1'(ref Fig. 3). The push-pull path for charging the node n6 is through 'TG3', 'INV6', 'TG4' and the current fed is represented as 'ip' (ref Fig. 3). Summation of 'ip' and 'i1' is total current ('it'). Note that the currents 'i1' and 'ip' are supplied by inverters INV4 and INV6, respectively. The current must rise or fall simultaneously in both charging paths to quickly charge and discharge the node. This makes the transition of output node Q faster. The proposed circuit is simulated using Cadence Virtuoso [2] with SCL180 nm technology [1]. The supply voltage is 1.8 V. The results are discussed in Sect. 3.

3 Results

Simulations are carried out to monitor the current and voltage variation in the circuit. Figures 4 and 5 show the variation of voltage at the output node (V(Q)) as well as the currents 'i1' and 'ip'. As seen from Fig. 4, when the output node (Q) makes a transition from one to zero, the current in the push-pull network (ip) rises first and then current of path 1 (i1) rises, this results in faster charging of node n6 and hence output (Q) dischange from one to zero quickly. Two currents i1 and ip help in faster charging of node n6. Same can be observed in Fig. 5 when node (Q) makes transition

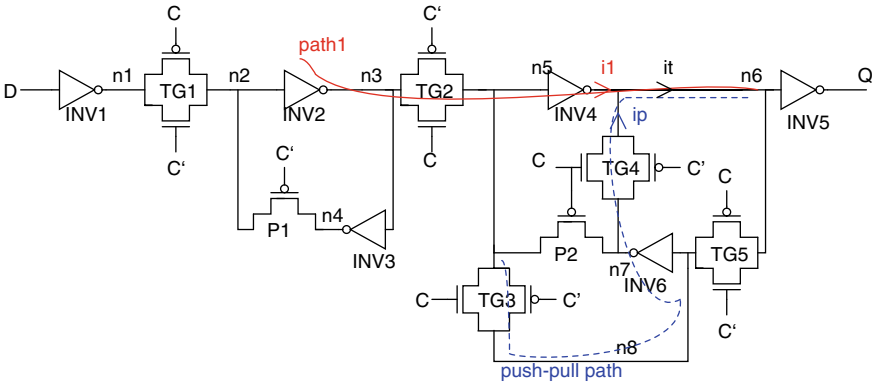

Fig. 3 Multiplexed feedback push-pull DFF

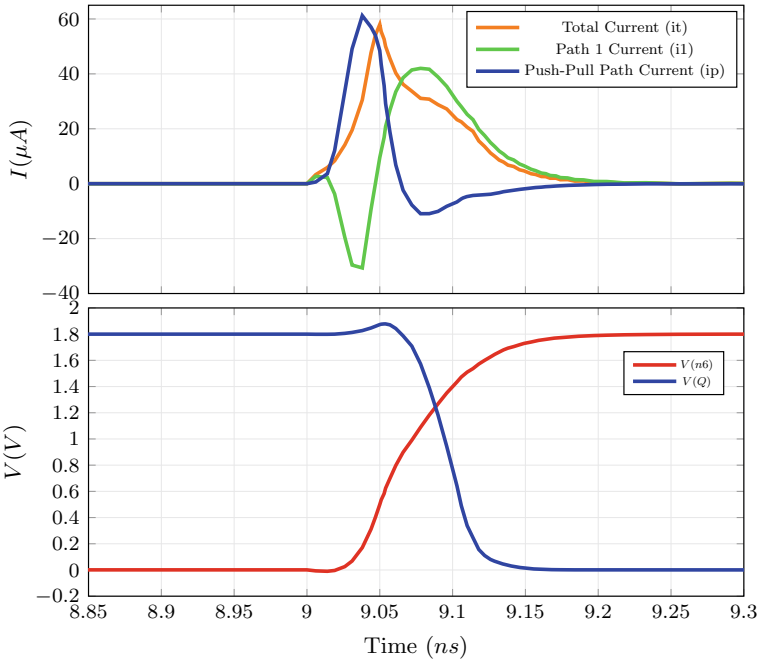

Fig. 4 Voltage and current while V(Q) discharges

form zero to one. Current in push-pull path falls faster than path 1 current, leading to a quick discharge of node (n6), resulting in faster transition of output node (Q).

The performance of MUXFB PP DFF is compared with conventional and push-pull isolation DFF in terms of setup time, propagation delay, clock to q delay and energy consumption. Results are given in Table 1. In order to have a fair comparison, all the three DFF architecture are simulated using SCL180nm technology and

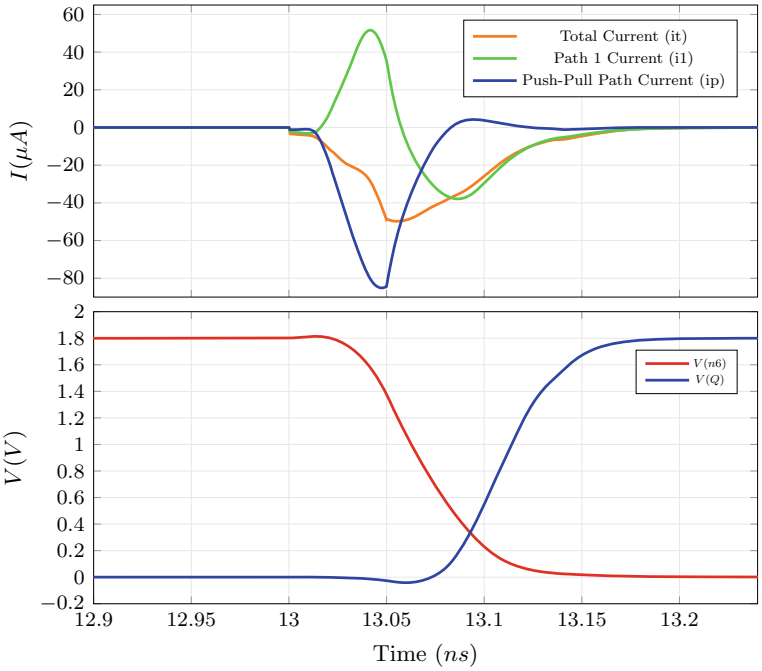

Fig. 5 Voltage and current while V(Q) charges

Table 1 DFF comparison

Table	D flip-flop architecture		
	Conventional [5, 6]	Push-pull isolation [5]	MUXFB DFF
Setup rise (ps)	134	163	107
Setup fall (ps)	156	180	136
C to Q fall (ps)	113	86	75
C to Q rise (ps)	127	87	90
PD (rise) (ps)	261	250	197
PD (fall) (ps)	269	266	210
Energy f Jouls	42.6	53.7	57.9

optimized for 1× load. Input and output inverters are added to isolate the data stored in the latch and provide buffered input and outputs. Setup time is calculated as the skew between clock edge and D input edge where clock to q delay increases by 5% of the minimum clock to q delay [3]. Minimum clock period of DFF is sum of clock to q delay and setup time, this is called propagation delay(PD) of DFF [3]. Results are shown in Table 1.

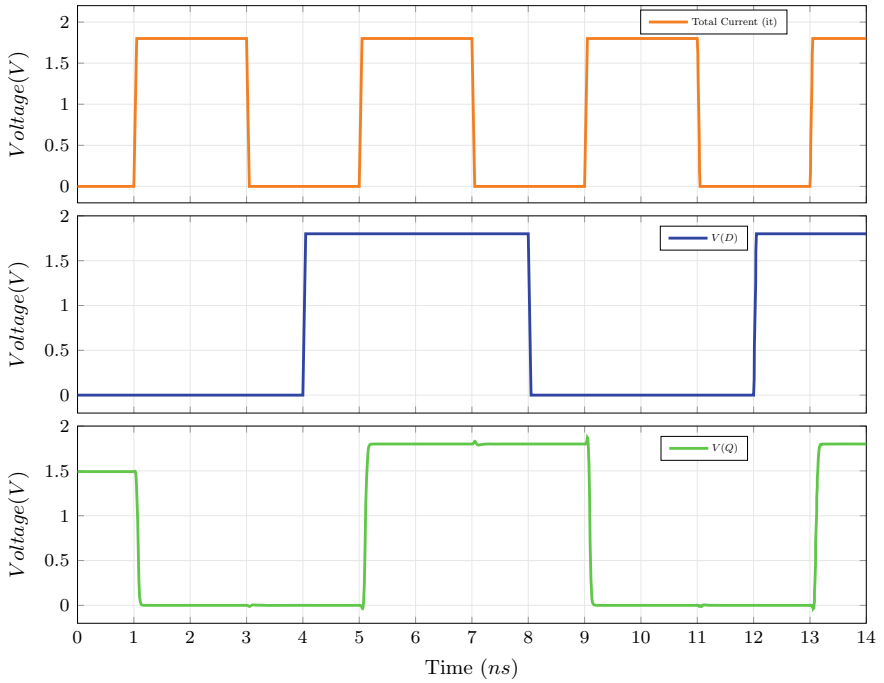

Fig. 6 Input (D), output (Q) wave-forms for MUXFB push-pull DFF

As seen from Table 1 the proposed architecture MUXFB DFF improves the setup time by 16% on average as compared to conventional DFF. Push-pull isolation DFF has degraded setup time as compared to conventional and proposed DFF. Even though the average C to Q delay of the proposed circuit has improved greatly from conventional DFF by 31%, the improvement is marginal compared to push-pull isolation DFF. Hence, the total propagation delay of DFF, which is the sum of C to Q and setup time, has improved by 23% in the proposed circuit compared to conventional DFF and 21% compared to push-pull isolation DFF.

Energy consumption of all designs is evaluated for one rise and one fall transition of output Q, at clock period of 4ns with clock rise and fall time of 50 ps. Energy consumption of the proposed design is 7.8% as compared to push-pull isolation DFF and 36% compared to conventional DFF. Output (Q), input (D) and clock of proposed DFF are shown in Fig. 6. MUXFB push-pull DFF performs well without spikes and voltage drops at the output node.

Monte Carlo analysis for 500 samples was done for the clock to q delay of MUXFB push-pull DFF. A mean of 85ps and 71ps was obtained for rise delay (ref Fig. 8) and fall delay (ref Fig. 7, respectively. The standard deviation of 1.09 ps and 1.02 ps is observed for rise and fall delay, respectively. Corner analysis for SS, FF, FS, SF, TT corners is given in Table 2. MUXFB push-pull DFF has 61 ps and 69 ps clock to q fall and rise delay in the fastest corner and 97 ps and 121 ps in the slowest

Table 2 Corner analysis MUXFB DFF

Table	Process corners				
	TT	FF	SS	SF	FS
Setup rise (ps)	107	85	146	105	106
Setup fall (ps)	136	106	189	120	148
Propagation delay (rise) (ps)	198	154	267	190	197
Propagation delay (fall) (ps)	211	167	286	191	255
C to Q fall (ps)	75.2	61	97	71	77.5
C to Q rise (ps)	90.3	69	121	85.3	91.4
Energy f Jouls	57.00	61.00	53.40	65.70	56.60

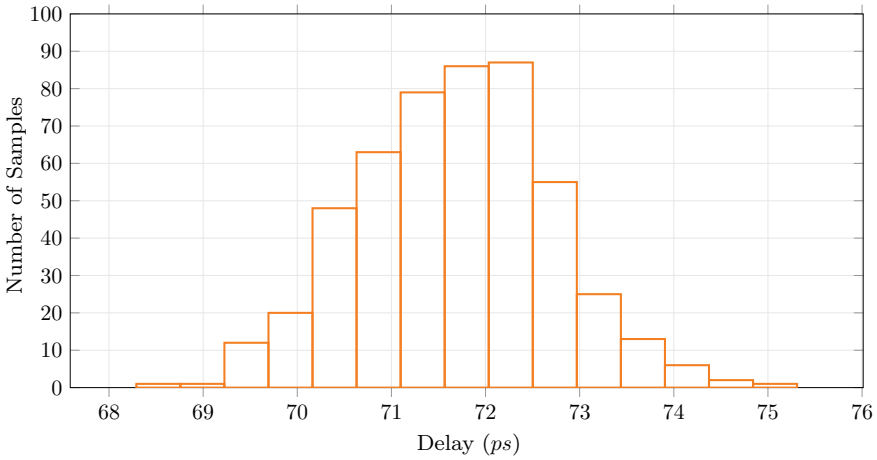

Fig. 7 Monte Carlo clock to q fall delay

corner, respectively. The worst-case propagation delay of MUXFB push-pull DFF is 286 ps in the SS corner, which is comparable to the typical propagation delay of conventional DFF.

4 Conclusion

Proposed MUXFB push-pull DFF performs better in terms of propagation delay than the push-pull isolation DFF proposed in [5] and convention DFF [6]. Push-pull isolation DFF has the drawback of higher setup time, which the proposed architecture reduces without increasing C to Q delay. The worst case performance of the proposed design in a slow corner is comparable to the performance of conventional DFF and push-pull isolation DFF in the typical corner. The proposed DFF structure can be

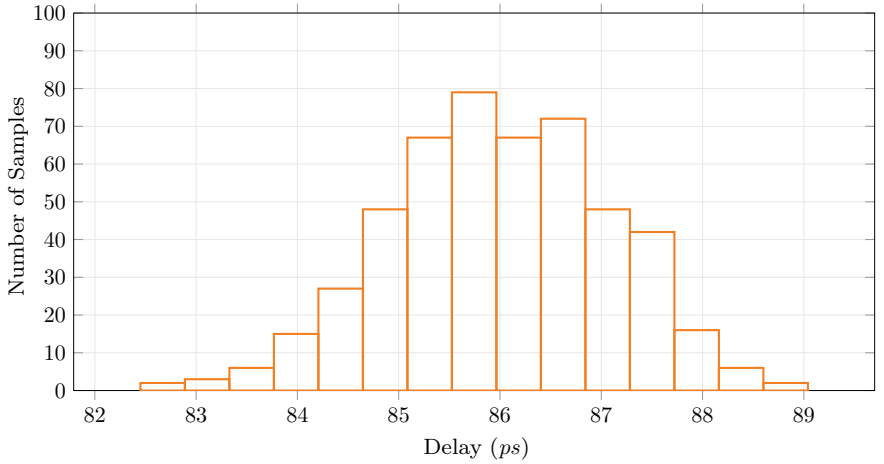

Fig. 8 Monte Carlo clock to q rise delay

used in critical paths of digital systems where high speed is required. Because of higher energy consumption and area, the proposed design should be used in paths where speed is critical factor. For further improvements, power reduction techniques can be applied to improve the design in terms of power.

References

1. Basu J (2019) From design to tape-out in scl 180 nm cmos integrated circuit fabrication technology. IETE J Educ 60(2):51–64
2. Brunvand E (2010) Digital VLSI Chip Design with Cadence and Synopsys CAD Tools. Addison-Wesley. https://books.google.co.in/books?id=YippPgAACAAJ
3. Consoli E, Palumbo G, Pennisi M (2011) Reconsidering high-speed design criteria for transmission-gate-based master–slave flip-flops. IEEE Trans Very Large Scale Integr (VLSI) Syst 20(2):284–295
4. Ko U, Balsara P (1995) High performance, energy efficient master-slave flip-flop circuits. In: 1995 IEEE symposium on low power electronics. digest of technical papers, pp 16–17. https://doi.org/10.1109/LPE.1995.482413
5. Ko U, Balsara P (2000) High-performance energy-efficient d-flip-flop circuits. IEEE Trans Very Large Scale Integr (VLSI) Syst 8(1):94–98. https://doi.org/10.1109/92.820765
6. Rabaey J (1996) Digital integrated circuits: a design perspective. Prentice Hall electronics and VLSI series, Prentice Hall. https://books.google.co.in/books?id=MJt4QgAACAAJ
7. Shaikh J, Rahaman H (2018) High speed and low power preset-able modified tspc d flip-flop design and performance comparison with tspc d flip-flop. In: 2018 international symposium on devices, circuits and systems (ISDCS), pp 1–4. https://doi.org/10.1109/ISDCS.2018.8379677

Efficient Noise Immune Robust Ternary Subtractor Designs*

Yogesh Shrivastava and Tarun Kumar Gupta

Abstract Binary Logic-based circuits are restricted due to larger area occupied by interconnects, higher power consumption and large delay. To overcome all these limitations ternary logic circuits are used. In this paper ternary logic based subtractors are proposed, and compared with the existing designs. The subtractors proposed are based on Carbon Nanotube Field Effect Transistor (CNFET). The proposed subtractors display improvements in power, delay and other performance parameters. To observe the effect of noise, noise immunity curve of existing and proposed designs is drawn, with calculation of average noise threshold energy. To observe the robustness of the proposed and existing designs the diameter of Carbon Nano Tube (CNT) is varied and impact over performance is observed.

Keywords CNFET · PDP · EDP · Power consumption · Subtractor

1 Introduction

The conventional electronic circuits utilized the traditional Metal oxide Semiconductor Field Effect (MOSFET) devices to implement binary logic circuits. The binary logic-based devices has the limitations; higher power consumption, delay and area of interconnects. The interconnects capture the largest area among all the components of the die. To use the interconnects area effectively, use of multi valued logic in place of two valued logic can be used. Due to closeness with natural base the ternary logic is the best suitable option to implement logic circuit designs [1–3]. The ternary logic has three digits: 0, 1, and 2. In the early years of development the ternary logic circuits were designed utilizing the conventional MOSFET devices. In the recent years the non-conventional devices such as Carbon Nanotube Field Effect Transistors (CNFET) are emerged and found most suitable to implement the ternary logic circuits.

Y. Shrivastava (✉) · T. K. Gupta
Maulana Azad National Institute of Technology, Bhopal, Madhya Pradesh 462003, India
e-mail: yogesh.21june@gmail.com

S. Rawat et al. (eds.), *Proceedings of Second International Conference on Computational Electronics for Wireless Communications*, Lecture Notes in Networks and Systems 554,
https://doi.org/10.1007/978-981-19-6661-3_36

1.1 CNFET

The CNFETs are constructed using Single Wall CNTs (SWCNTs). The CNT is grown under the gate and over the substrate connecting the source and drain. The CNT placed between source and drain provide the medium for drain current. Therefore, the drain current depends upon the structure (Such as diameter) and number of CNT. The armchair, zigzag and chiral are the types of CNFET derived from the chirality vector(n, m). The armchair has the chirality (the tube's atom arrangement's angle) of n, n, the zigzag has the chirality $n, 0$ and chiral type has the chirality n, m. Among the three types, zigzag type is found most suitable to implement the digital circuit, since it shows the semiconducting properties. The threshold voltage V_{th} of the CNFET depends upon the diameter of the CNT (D_{CNT}), and the D_{CNT} is depends on the chirality of the tube. The existing and proposed work on exploited this property of CNFET. In this work CNFETs of chiralities (19, 0), (13, 0) and (10, 0) are use to design the ternary subtractor circuits. The threshold voltage of (19, 0) CNFET is 0.559 V, the threshold voltage of (13, 0) CNFET is 0.428 V, and the threshold voltage of (10, 0) CNFET is 0.289 V. The CNFETs with the similar properties were utilized in [4–14]. The HSPICE simulator with Stanford CNFET 32 nm model is used to simulate the existing and proposed ternary subtractor circuits [15, 16].

The brief details of the subsequent sections are as follows. The literature survey is discussed in the following section. The proposed circuits the described in Sect. 3. Section 4 discusses the results of the analysis and the conclusion is drawn in Sect. 5.

2 Review of Ternary Logic-Based Circuits

As discussed in the previous sections, the earlier designs were implemented using CMOS-FETs, given in [17, 18]. In [17], multiplexer-based ternary adders, subtractors, and ALUs were designed. In [18], the ternary logic circuits were designed using MOSFETs of different V_{th}. The circuits of [17, 18] consume higher power, lags in speed and their Power Delay Product (PDP) is higher due to the use of MOSFETs. In [4], the ternary half adder is proposed with ternary multiplier circuits. The circuit of [4] displays less power consumption, lesser delay, and less PDP compared to [17, 18], due to the use of CNFET-based circuits. In [6] ternary logic circuits were proposed using negation of literals technique and uses ternary logic gates to realizes the ternary half adder, ternary full adder, ternary half subtractor and ternary full subtractor, similar techniques were followed and ALU was designed in [9]. In [5], the circuits were designed using NAND and NOR gates in place of AND and OR gates, since the circuits realized using NAND and NOR gates realized less transistors, the performance proposed designes were improved over past proposed designs. In [19], the ternary half adder was realized using transistor-based designs in place of gate level, the similar topology was followed in [11, 14]. In [14], the teranry decoder is modified to convert the ternary signal into binary and the subsequent stages were

designed accordingly, due to this the delay, power consumption and PDP of the circuit is reduced. The noise analysis performed in [14] over existing and proposed designs, by obtaining the butterfly curve of the subtractor designs. The strategy similar to [14] is followed in this paper to design proposed subtracator circuits. The transistor logic-based circuits utilized less transistors due to that the power consumption, delay and PDP of such circuits was improved.

The circuits discussed above followed the similar pattern, in which the decoder decodes the three level logic into two level form and then it applied on intermediate stage followed by encoder stage, which recovers the logic again in three level ternary logic circuit.

3 Proposed Designs

3.1 Decoder Design

Figure 1 displays the circuit of proposed ternary decoder, the truth table of this decoder is same as the decoder proposed in [18]. As shown in Fig. 1, the proposed decoder uses a Positive Ternary Inverter (PTI), an Negative Ternary Inverter (NTI) and two binary inverters. The PTI's output for logic 0 is 2, for logic 2 is 0, however, it gives logic 2 for input 1 [4–6, 17, 18]. The NTI inverts the higher and lower levels but gives 0 output at input 1. As shown in Fig. 1, the supply voltage of inverter is connected with the output of PTI, and input of inverter1 is output of NTI(A_0). Therfore, when A is 1, PTI gives ternary level 2 as output and NTI gives ternary level 0 as output making A_1 high. For rest of the inputs the circuits works in the similar fashion.

3.2 Intermediate Stage

The intermediate stage shown in Fig. 2 realized by connecting PCNFET and NCNFET with chirality(13, 0) in pull-up and pull-down network, respectively. As shown in Fig. 2 the outputs of intermediate stages are $SUB0$, $\overline{SUB2}$, and $\overline{Borrow}$. The outputs of intermediate stages are fed into encoder stage. The chirality of the CNFET used in Fig. 2 is (13, 0).

3.3 Encoder Designs

Encoder design 1 The Standard Ternary Inverter (STI) of [4] and ternary carry encoder of [19] shown in Fig. 3, are used in this paper as Encoder design 1.

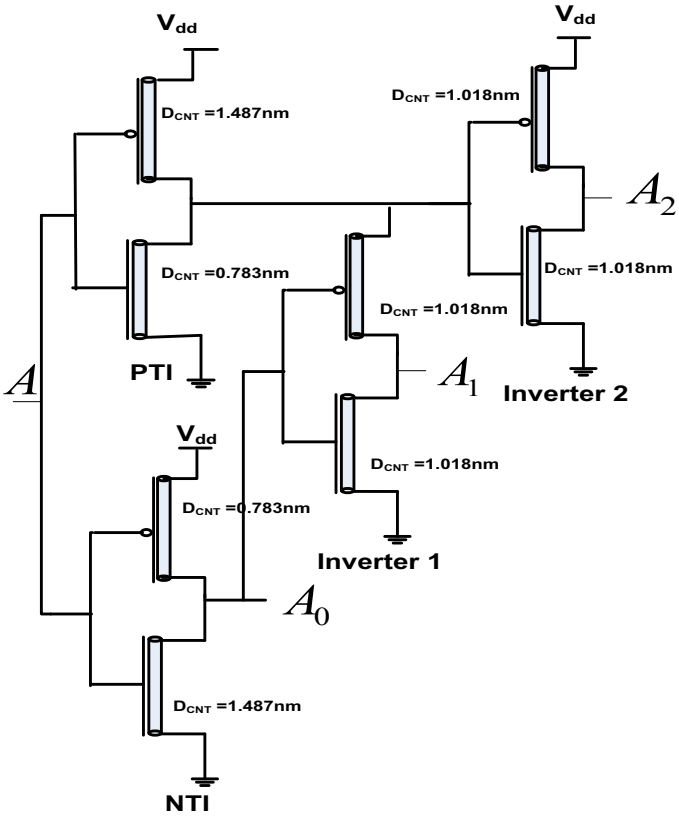

Fig. 1 Proposed ternary decoder

Encoder design 2 The low power encoder of [20] and the proposed Borrow encoder 2, shown in Fig. 4, is used here in combination and referred as Encoder design 2. The difference between Encoder design 1 and Encoder design 2 is extra diode pair M2 and M6 connected between supply voltage and ground. This arrangement increase the resistance for current flowing between supply voltage and ground.
Encoder design 3 The low delay encoder of [20] and the proposed Borrow encoder 3, shown in Fig. 5, are used here in combination as Encoder design 3. The serially connected diode pair of Fig. 4 are connected parallelly, to reduce the resistance between supply voltage and ground for current.

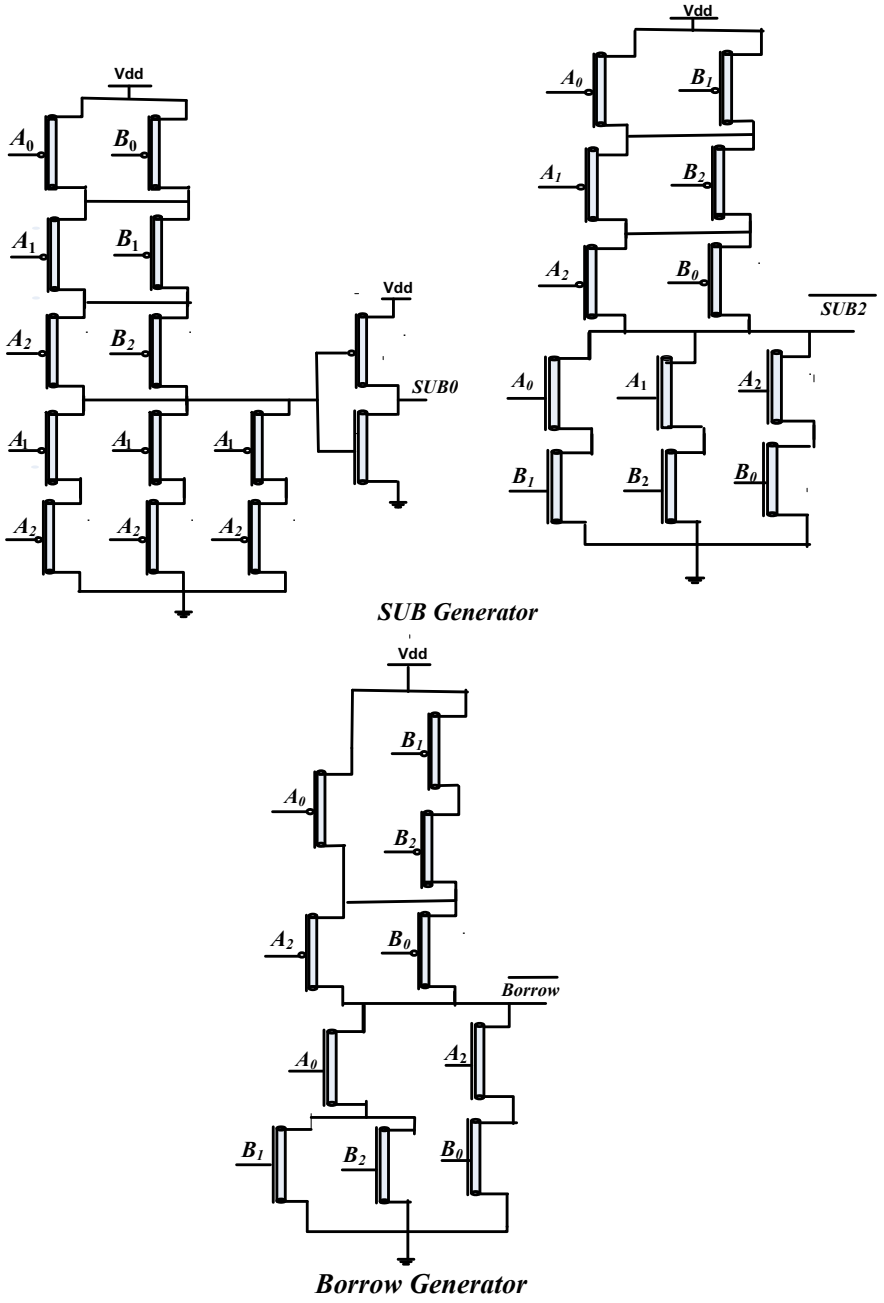

Fig. 2 Subtractor intermediate stage

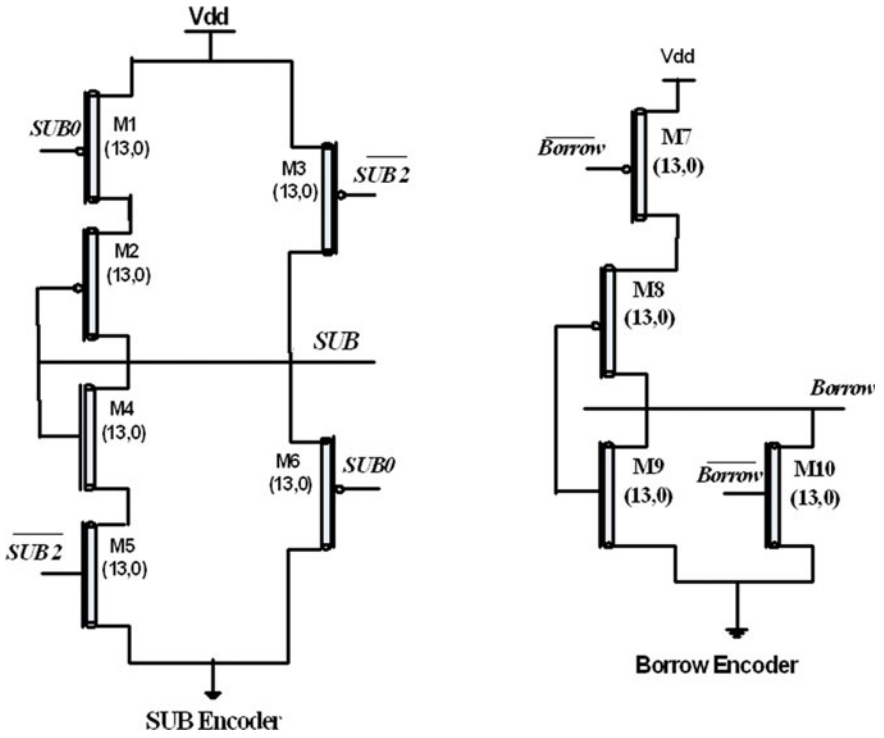

Fig. 3 Encoder design 1

3.4 Proposed Subtractor Designs

The proposed ternary subtractor design1 is realized by connecting proposed decoder, intermediate stage and Encoder design 1. Similarly the proposed teranry subtractor design 2 is realized by feeding output of proposed decoder to intermediate stage and the output of intermediate stage to Encoder design 2. The proposed ternary subtractor design 3 is obtained by connecting proposed decoder, intermediate stage and Encoder design 3.

4 Results and Discussion

The existing and proposed ternary subtractor designs are computed for 400 ns, on HSPICE simulator with CNFET Stanford model dedicated to 32 nm channel length to obtain the power consumption. The delay is calculated by overlaying input and output transient waveform and calculating the average delay between 50% rise to 50% fall. The Power Delay Product (PDP) is the multiplication of consumed power

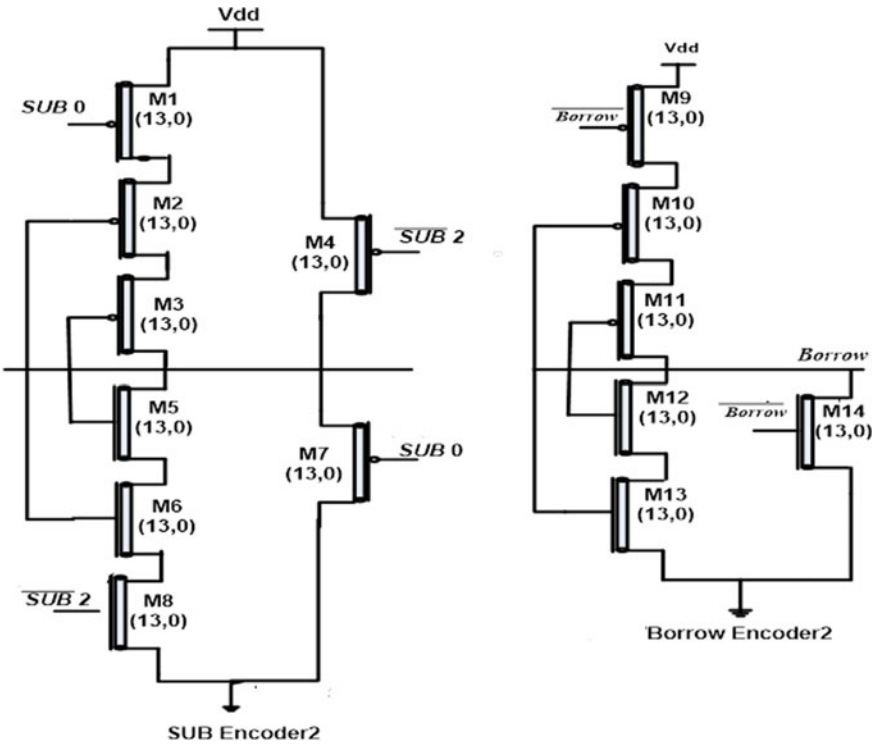

Fig. 4 Encoder design 2

and delay, is a component of energy consumption. The transient analysis waveform of the proposed ternary subtractor 2 design is shown in Fig. 6, the similar waveform is obtained for proposed ternary subtractor1 and proposed ternary subtractor 3. The supply voltage is 0.9 V and the load capacitor is 10ff is used to obtained the performance parameters. The average power consumption, delay, PDP, and EDP of existing and proposed designs are displayed in Table 1. The product of PDP and delay is EDP [19]. All the performance parameters discussed above are collectively demonstrated and compared in the following discussion of this section.

The transient analysis waveform of Fig. 6 verifies that the proposed circuits are capable to handle input with higher transients correctly. Table 1 demonstrates that the proposed subtractor design 2 consumes lest power and demonstrates improvement of 64.94% over the design of [6], however, the improvement in delay is 15.85463%, least among all the proposed designs. As discussed in the introduction section of this paper the input ternary signal converted from ternary to binary by decoder circuit and recovered by encoder. Therfore, these two circuits are responsible for improvement of the performance of a circuit, being the first and last stages of the ternary circuits. In proposed subtractor design 3 the delay is minimum and improvement over [6] is 33.28%. The Encoder 2 design has two more serially connected diode, due to

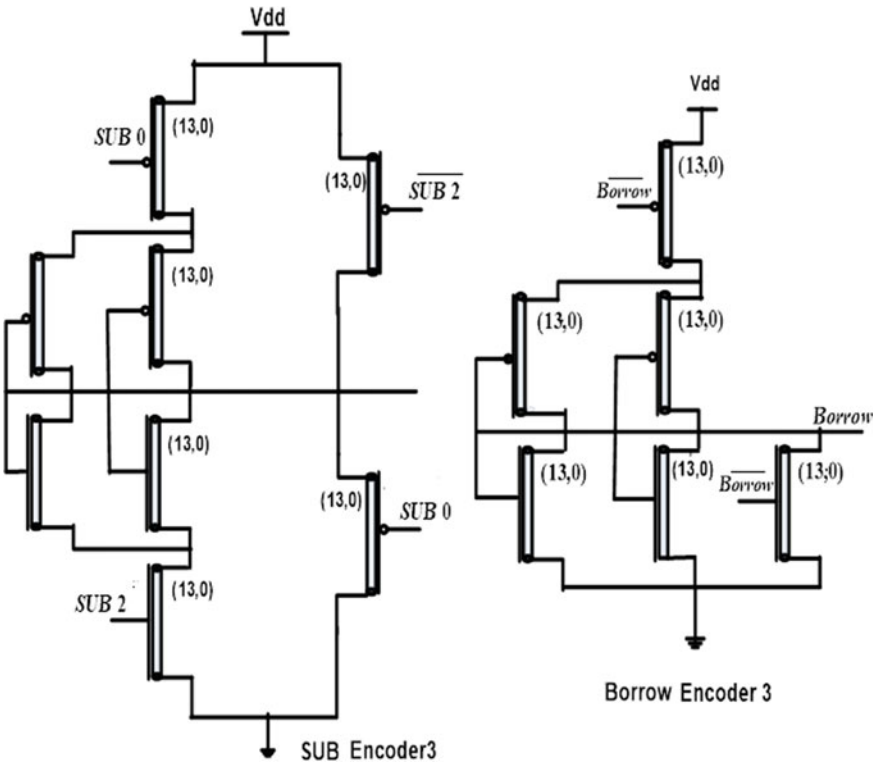

Fig. 5 Encoder design 3

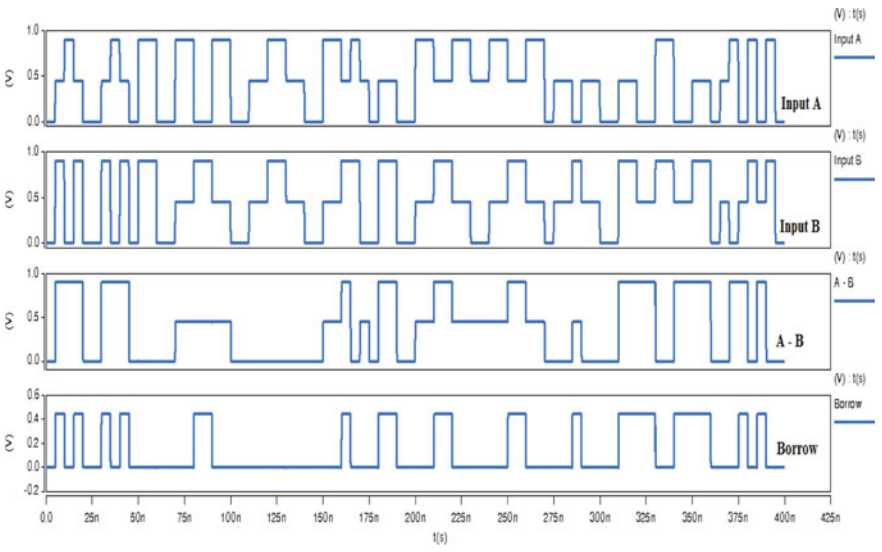

Fig. 6 400 ns computational transient input and output waveforms of subtractor designs

Table 1 Performance comparison of subtractor designs

Type of circuit	Transistor numbers	Consumption of power (nW)	% Power improved over [6]	Delay	% Delay improved over [6]	PDP (aJ)	% PDP improved over [6]	EDP (J s)
Subtractor design of [6]	140	1269.8	–	30.13	–	38.3	–	11.5E−28
Proposed subtractor design 1	62	523.93	58.74	25.2	16.36	13.2	65.53	3.33E−28
Proposed subtractor design 2	66	445.18	64.94	25.353	15.85463	11.3	70.496	2.86E−28
Proposed subtractor design 3	66	817.49	35.62	20.101	33.28	16.4	57.18	3.3E−28

which at the time of ternary logic 1 generation, more impedance is faced by the current flowing between supply voltage and ground, this arrangement reduce the power consumption during the generation of ternary logic 1 in the proposed ternary subtractor design 2. The parallel diode connection in Encoder 3 design reduces the impedence between Vdd and Gnd in proposed ternary subtractor design 3, due to this the delay while generation of logic level 1 is reduced. Therfore, a bargain is observed in proposed subtractor design 2 and proposed subtractor design 3. The proposed subtractor design1 utilizes least transistors and displays compactness among all the proposed and existing designs, this design acquire least area on the die.

4.1 Noise Analysis

Noise immunity curve If the amplitude and width of noise is higher enough to change the output trit (ternary logic digit), the performance of the circuit gets affected. The effect of noise amplitude against pulse width is shown in Noise Immunity Curve (NIC) is shown in Fig. 7. The circuit which obtained the upper most layer in the NIC shown in Fig. 7, is the most noise immune among all the circuits. The NIC of proposed ternary subtrator circuit 2 design has the top layer followed by the proposed ternary subtrator circuit3 designs. This conclude that proposed ternary subtrator circuit 2 is least affected by noise and the ternary subtractor design of [6] is more affected by noise.

Average noise threshold energy: The average noise threshold energy ($ANTE$) is the tolerable amount of noise energy which any circuit could withstand, the $ANTE$ calculation formula is given as

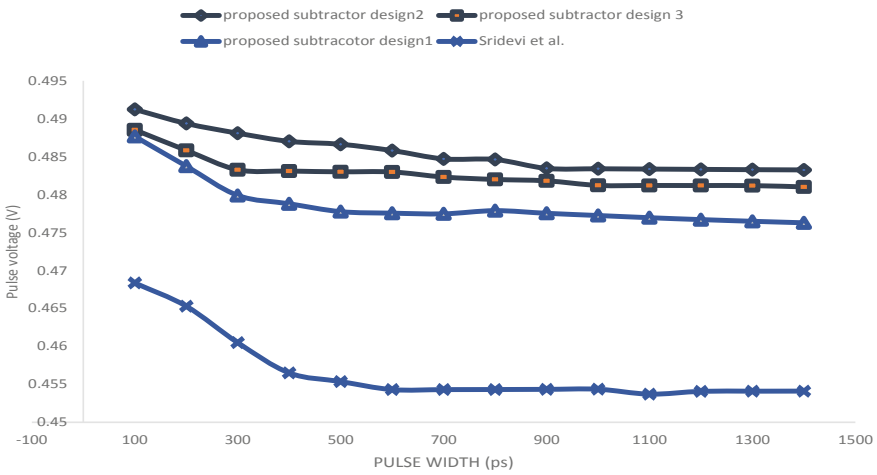

Fig. 7 Noise immunity curve of existing and proposed subtractor designs

Table 2 ANTE of ternary subtractor designs

Circuit type	$ANTE\ (V^2 - ps)$
Proposed subtractor 2	176
Proposed subtractor 3	174
Proposed subtractor 1	171
Sridevi et al. [6]	155

$$ANTE = E(A_n^2 W_n) \tag{1}$$

Here A_n, W_n are the amplitude and width of the input noise pulse, respectively. The average of A_n, W_n is represented by $ANTE$. The NIC is used to calculate A_n and W_n. The calculated values of $ANTE$ is shown in Table 2. The $ANTE$ of proposed subtractor design is highest, which means that this design is more immune to noise among existing and proposed designs.

4.2 Variation in D_{CNT} of the Carbon Nanotube

During the fabrication of CNFET, to acquire the exact D_{CNT} is very difficult, hence it is necessary to observe the effect of D_{CNT} over the existing and proposed design is mandatory [7]. The impact of D_{CNT} variation over existing and proposed ternary subtrcator design is shown in Fig. 8. The analysis of Fig. 8 shows that the proposed subtractor design 1 demonstrates least PDP variation against D_{CNT}.

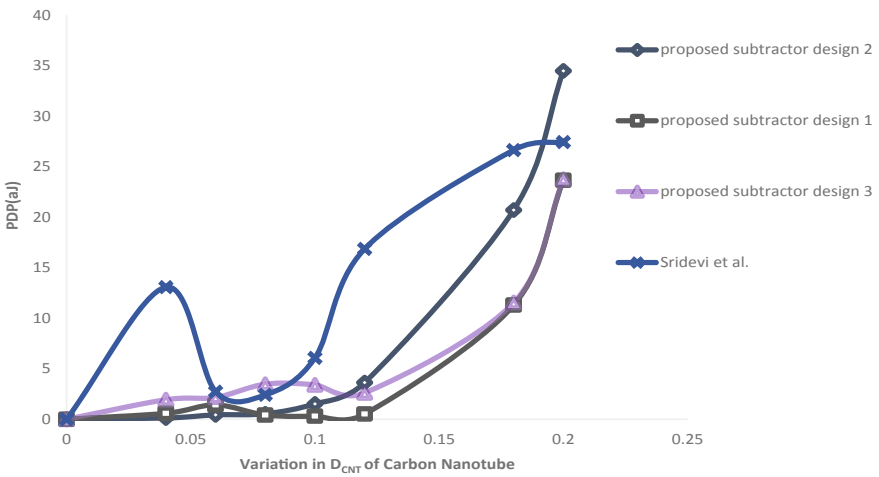

Fig. 8 D_{CNT} variations against PDP of existing and proposed subtractor designs

5 Conclusion

Three ternary subtractor designs has been proposed in this paper. The proposed teranry subtractor design 2 shows least power consumption with least power delay product and Energy delay product. The proposed ternary logic 3 design has displayed improvement in delay. To check the robustness, the proposed and existing designs has undergone the noise analysis by obtaining noise immunity curve and $ANTE$ value. The proposed ternary subtractor design 2 has the upper most layer in noise immunity curve and obtained the highest value of $ANTE$, this proves that the proposed ternary subtractor design 2 is more noise immune among existing and proposed design. The proposed ternary subtractor design1 shows least variation against D_{CNT} variations. The improvement in decoder and encoder stages resulted into improved results of the proposed ternary subtractor circuits. The design topologies of the proposed designs are usefull in obtaining the ALU designs and in designing of other more complex designs.[21–30]

References

1. Porat DI (1969) Three valued digital system. Proceedings 116(6):947–955
2. Butler JT (1995) Multiple-valued logic examining its use in ultra-high speed computation. IEEE Potentials
3. Heung MHT (1985) Depletion/enhancement CMOS for a lower power family of three-valued logic circuits. IEEE J Solid-State Circuits 20(2):609–616
4. Lin S, Kim YB, Lombardi F (2011) Design of a CNTFET-based design of ternary logic gates and arithmatic circuits. IEEE Trans Nanotechnol 10(2):217–225
5. Samadi H, Shahhoseini A, Aghaei-liavali F (2017) A new method on designing and simulating CNTFET based ternary gated and arithmetic circuits. Microelectron J 63:41–48
6. Sridevi V, Jayanthy T (2014) Minimization of CNTFET ternary combinational circuits using negation of literals technique. Arabian J Sci Eng 39:4875–4890
7. Moaiyeri MH, Doostaregan A, Keivan N (2011) Design of energy-efficient and robust ternary circuits for nanotechnology. Circuits Dev Syst IET 5:285–296
8. Panahi T, Naderi S, Heidari T, Nejad EZ, Keshavarzian P (2013) New ternary logic subtractor using carbon nanotube field-effect transistors. Int J Soft Comput Eng 2
9. Murotiya SL, Gupta A (2013) Design of CNTFET-based 2-bit ternary ALU for nanoelectronics. Int J Electron 101:1244–1257
10. Monfared AT, Haghparast M (2017) Designing new ternary reversible subtractor circuits. Microprocess Microsyst 53:51–56
11. Shrivastava Y, Gupta TK (2020) Design of low-power high-speed CNFET 1-trit unbalanced ternary multiplier. Int J Numer Model Electron Netw Dev Fields 33(1)
12. Shrivastava Y, Gupta TK (2021) Design of high-speed low variation static noise margin ternary S-RAM cells. IEEE Trans Dev Mater Reliab 21(1):102–110
13. Shrivastava Y, Gupta TK (2021) Design of compact reliable energy efficient read disturb free 17T CNFET ternary S-RAM cell. IEEE Trans Dev Mater Reliab 21(4):508–817
14. Shrivastava Y, Gupta TK Designing of low power high-speed noise immune CNTFET 1-trit un-balanced ternary subtractor. J Circuits Syst Comput World Sci. https://doi.org/10.1142/S0218126622500827
15. Raychowdhury, Roy K (2008) Stanford University CNTFET model website. Stanford University, Stanford, CA [Online]. Available: http://nano.stanford.edu/model.php?id=23

16. Deng J, Wong H-SP (2007) A compact SPICE model for carbon- nanotube field-effect transistors including nanoidealities and its application—part I: model of the intrinsic channel region. IEEE Trans Electron Dev 54(12):3186–3194
17. Shivashankar HN, Shivaprasad P (1983) Ternary adder and subtractor using ternary multiplexer. Int J Electron
18. Dhande AP, Ingole VT (2005) Design and implementation of 2-bit ternary ALU slice. In: Proceedings international conference IEEE-science electronics, technology information telecommunication, vol 17–21
19. Sahoo SK, Gangishetty A, Sahoo R, Muglikar M (2017) High-performance ternary adder using CNTFET. IEEE Trans Nanotechnol 16(3)
20. Vudadha C, Rajagopalan S, Dusi A, Sai Phaneendra P, Srinivas MB (2018) Encoder-based optimization of CNTFET-based ternary logic circuits. IEEE Trans Nanotechnol 17(2)
21. Rahman A, Guo J, Datta S, Lundstrom M (2003) Theory of ballistic nanotransistors. Subtractor IEEE Trans Electron Dev 50(10):1853–1864
22. Wang B, Poa P, Wei L, Li L, Yang Y, Chen Y (2007) (n, m) Selectivity of single-walled carbon nanotubes by different carbon precursors. J Am Chem Soc 129(29):9014–9019
23. Ohno Y, Kishimoto S, Mizutani T, Okazaki T, Shinohara H (2004) Chirality assignment of individual single- walled carbon nanotubes in carbon nanotube field effect transistors by microphotocurrent spectroscopy. Appl Phys Lett 84(8):1368-1370
24. Bachtold, Hadley P, Nakanishi T, Dekker C (2001) Logic circuits with carbon nanotubes transistors. Science294(5545):1317–1320
25. Lin, Patil N, Ryu K, Badmaev A, De Arco LG, Zhou C, Mitra S, Wong HSP (2009) Threshold voltage and on-off ratio tuning for multiple-tube carbon nanotube FETs. IEEE Trans Nanotechnol 8(1):4–9
26. Raychowdhury, Roy K (1986) Carbon-nanotube-based voltage-mode multiple-valued logic design. IEEE Trans Comput 35(2):99–106
27. Tabrizchi S, Sharifi F, Abdel-Hameed Badawy A (2018) Energy efficient tri-state CNFET ternary logic gates
28. Mirzaee RF, Navi K, Bagherzadeh N (2014) High-efficient circuits for ternary addition. Hindawi VLSI Design
29. Garg S, Gupta TK (2018) Low power domino logic circuits in deep-submicron technology using CMOS. Eng Sci Technol Int J 21(4):625–638
30. Gonzalez-Diaz O, Linares-Aranda M, Mendoza-Hernandez F (2006) A comparison between noise-immunity design techniques for dynamic logic gates. In: 2006 49th IEEE international midwest symposium on circuits and systems, San Juan 4:84–488

Reconfigurable Intelligent Surface as an Access Point: Probability of Error Analysis for Discrete Phase Shifters

B. S. Anjana, Vinoth Babu Kumaravelu, Hindavi Jadhav, Arthi Murugadass, Md. Shohel Sayeed, and Basim Alhadidi

Abstract A fresh line of research for future wireless networks is called reconfigurable intelligent surface (RIS)-aided communication. We developed one-bit and two-bit discrete phase shifter facilitated RIS for access point (AP) scenario in this study. In the AP scenario, RIS is considered as a source and it can transmit the information. When RIS is utilized as an AP, it can generate the phase angles needed for constellation mapping as well as compensate for channel distortion. The proximity of the radio frequency (RF) signal source to RIS minimizes the impact of fading between RIS and AP. The exact phase compensation of each RIS component is very difficult practically. Consequently, we can enhance the system's overall performance using a discrete phase shifter. We are evaluating the effectiveness of one- and two-bit discrete phase shifters over intelligent RIS-AP and blind RIS-AP methods.

Keywords Access point (AP) · Blind communication · Discrete phase shifters · Intelligent communication · Reconfigurable intelligent surfaces (RIS)

B. S. Anjana (✉) · V. B. Kumaravelu · H. Jadhav
Department of Communication Engineering, School of Electronics Engineering, Vellore Institute of Technology, Vellore, Tamil Nadu, India
e-mail: anjanaalakkatt@gmail.com

A. Murugadass
Department of Computer Science and Engineering (AI & ML), Sreenivasa Institute of Technology and Management Studies, Chittoor, Andhra Pradesh, India

Md. S. Sayeed
Faculty of Information Science & Technology (FIST), Multimedia University, Melaka, Malaysia

B. Alhadidi
Department of Computer Information Systems, Prince Abullah Bin Ghazi Faculty of Information and Communication Technology, Al-Balqa Applied University, Salt, Jordan

S. Rawat et al. (eds.), *Proceedings of Second International Conference on Computational Electronics for Wireless Communications*, Lecture Notes in Networks and Systems 554,
https://doi.org/10.1007/978-981-19-6661-3_37

1 Introduction

For future wireless communication systems, RIS-assisted communication is the key enabling technology to improve spectral and energy efficiency. In conventional multiple-input multiple-output (MIMO) systems beamforming can be achieved by complex precoding and RF processing techniques [1]. By reconfiguring the propagation of the electromagnetic wave, information can be beamformed to the intended direction without any RF processing techniques [8]. RIS is a new research direction to manipulate electromagnetic waves. A huge proportion of passive reflector components constructed of meta-materials make up RIS. Regulating each reflector's phase shift in RIS enables for beamforming [4].

When opposed to conventional amplify and forward relay transceiver, RIS technology uses less energy. By altering the phases of each passive reflector for a constructive addition of reflected signals, we can increase the signal strength at the user without using a power amplifier. Because no amplifier is used, RIS-assisted communication is energy efficient. Energy-efficient transmission is aided by regulating the phase shifts of passive reflectors and distributing the transmit power [5].

Meta-surface consists of a sub-wavelength array of meta-atoms. Meta-surface is very thin. There are two types of meta-surfaces, reconfigurable and non-reconfigurable. Non-reconfigurable meta-surfaces have a fixed arrangement of the meta-atoms. After manufacture, changes cannot be made. In RIS, the structural configuration of the meta-atoms can be manipulated. The phase of RIS elements can be reconfigured by using PIN diodes, based on ON/OFF status of the switch [3].

In [10], authors analyzed the minimum quantization levels to obtain diversity. Because of hardware limitation, phase shifts of RIS components has to be quantized to discrete levels. The authors proved that when the quantization level is not less than three, full diversity order is achieved. When the quantization level is three, the outage performance loss is very less. Authors in [2] proposed RIS-assisted intelligent and blind communication schemes. They derived a mathematical framework for symbol error probability of blind and intelligent communication schemes. They introduced a novel method RIS-AP. Average bit error rate (ABER) is analyzed for intelligent and blind communication for both dual- hop and AP scenarios. The remaining portions of the work are structured as follows: Sect. 2 goes into more detail about RIS-assisted transmissions. In Sect. 3, the simulations are examined, and Sect. 4 wraps up the work.

2 RIS-AP-Assisted Communication

The main use cases of RIS-assisted communication are energy focusing and energy nulling based on the constructive reflection and destructive reflection. The energy focusing use case is shown in Fig. 1. When the transmitter sends a signal to a user, the same signal is also reflected through RIS. We get a stronger signal at the user,

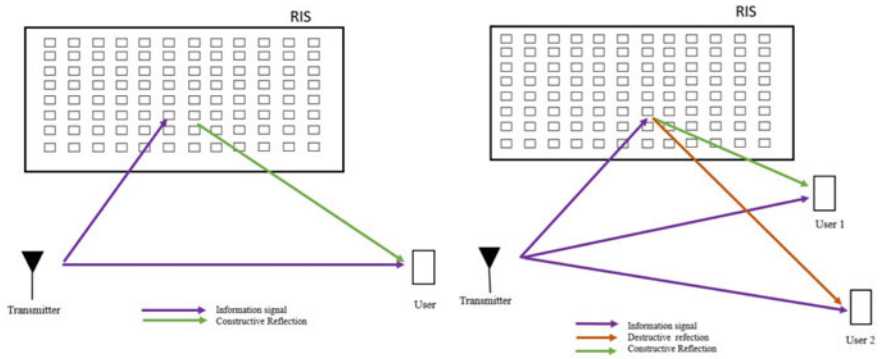

Fig. 1 Energy focusing and energy nulling applications of RIS

if phases of RIS is adjusted for constructive addition of these two signals. Another use case of RIS is energy nulling, which is also shown in Fig. 1. In this case, the transmitter wants to send a signal to user 1, but it also leaks to user 2. By altering the phases of the RIS elements for constructive addition at user 1 and destructive addition at user 2, we may here send the signal to user 1. Therefore, we get a stronger signal at user 1 and user 2 gets zero signal.

The signal can be reflected in the intended direction by a substantial number of passive reflector components that make up RIS. In this work, we consider RIS-AP scenario. RIS can act as a source and it can transmit the information. In the AP scenario, we assume that there is a RF signal generator and it will transmit unmodulated carrier signal toward RIS. The effect of fading is very less because we place the RF signal generator close to RIS. The following describes this work's contributions:

- Implementation of RIS-AP using discrete phase shifters of one- and two-bits.
- ABER comparison of proposed schemes with the conventional intelligent and blind RIS-AP schemes.

2.1 Intelligent RIS-AP Communication

When using an intelligent communications system, RIS is aware of the channel phases. The signal received is represented as [2]

$$y = \left[\sum_{n=1}^{N} c_n e^{-j\phi_n}\right] x + w \tag{1}$$

Data symbol is represented by x with average symbol energy E_S, $w \in \mathbb{C}N(0, N_o)$ is complex Gaussian noise. The n th RIS component's phase adjustment is ϕ_n. The channel between RIS and destination is represented by

$$c_n = \beta_n e^{j\psi_n} \tag{2}$$

Here β_n is the magnitude and ψ_n is phase. For RIS-AP scenario $\psi_n = \phi_n$. The received signal becomes

$$y = \left[\sum_{n=1}^{N} \beta_n\right] x + w \tag{3}$$

where $\sum_{n=1}^{N} \beta_n = B$. The expression for the instantaneous signal to noise ratio (SNR) is [9]

$$\Gamma = \frac{B^2 E_S}{N_o} \tag{4}$$

The channel's magnitude β_n is an independent random variable with a Rayleigh distribution having mean and variance

$$E\left[\beta_n\right] = \frac{\sqrt{\pi}}{2}. \tag{5}$$

$$\text{Var}\left[\beta_n\right] = 1 - \frac{\pi}{4} \tag{6}$$

Since $(N \geq 1)$, according to central limit theorem, the mean and variance of B becomes

$$E\left[B\right] = \frac{N\sqrt{\pi}}{2} \tag{7}$$

$$\text{Var}\left[B\right] = N\left(1 - \frac{\pi}{4}\right) \tag{8}$$

The received SNR's moment generation function (MGF) is written as [6]

$$M_\Gamma\left(t\right) = \left(\frac{1}{1 - \frac{t(4-\pi)NE_S}{2N_o}}\right)^{\frac{1}{2}} \exp\left(\frac{\frac{t\pi N^2 E_S}{4N_o}}{1 - \frac{t(4-\pi)NE_S}{2N_o}}\right) \tag{9}$$

For M-ary phase shift keying (PSK), the average probability of symbol error (APSE) is calculated as [7]

$$p_e = \frac{1}{\pi} \int_0^{\frac{\pi(M-1)}{M}} M_\Gamma\left(-\frac{\sin^2\left(\frac{\pi}{M}\right)}{\sin^2 \mu}\right) d\mu \tag{10}$$

For binary PSK (BPSK), substituting $M = 2$ in (10) results in

$$p_e = \frac{1}{\pi} \int_0^{\frac{\pi}{2}} \left(\frac{1}{1 + \frac{(4-\pi)NE_S}{2\sin^2 \mu N_o}} \right)^{\frac{1}{2}} \exp \left(\frac{-\frac{\pi N^2 E_S}{4sin^2 \mu N_o}}{1 + \frac{(4-\pi)NE_S}{2\sin^2 \mu N_o}} \right) d\mu \tag{11}$$

For $\frac{NE_s}{N_o} \ll 10$, p_e is proportional to exp $\left(\frac{-N^2 \pi E_s}{N_0} \right)$. Hence for the increase in N, p_e decreases exponentially, leading to SNR gains.

2.2 Blind RIS-AP Communication

In this blind communication scheme, the channel phases are unknown to RIS. Therefore SNR maximization is not possible. As a result, the blind RIS-AP communication system performs quite poorly.
The received signal y is obtained by substituting $\phi_n = 0$ in (1).

$$y = \left[\sum_{n=1}^{N} c_n \right] x + w \tag{12}$$

The received SNR's MGF is written as

$$M_\Gamma(t) = \left(\frac{1}{1 - \frac{tNE_S}{N_o}} \right) \tag{13}$$

For blind RIS-AP, the APSE is obtained as

$$p_e = \frac{1}{\pi} \int_0^{\frac{\pi}{2}} \left(\frac{1}{1 + \frac{NE_S}{\sin^2 \mu N_o}} \right) \mathrm{d}\mu \tag{14}$$

2.3 Intelligent Discrete Phase Shifter Integrated RIS-AP

By altering the phase shifts of each RIS passive component, we may guide the signal in the appropriate direction. However, it is quite challenging to actually compensate for each RIS component's phase in practice. Furthermore, the overall performance can be improved by utilizing a discrete phase shifter. We have developed one- and two-bit discrete phase shifters for RIS-AP. The profound discrete phase shifter algorithm is shown below. Follow the steps below for every RIS component:
Step 1: Set up the distinct phase angles that RIS components are capable of producing.

$$\phi_{dis} = \phi_1, \phi_2 \ldots \phi_k$$

where k is the total number of phases that RIS components are capable of producing.
Step 2: Estimate the precise phase that the RIS component could produce in order to maximize SNR.
Step 3: Utilize the minimum mean squared error (MMSE) estimator to determine the angle that a RIS component will generate.

$$\hat{\phi}_{\text{dis}} = \arg\min_{\phi_{\text{dis}}} |\phi - \phi_{dis}|^2 \tag{15}$$

Step 4: At the RIS component, perform the corresponding phase shift.

With a higher k, there are more chances to produce the phase shifts that are necessary to compensate for channel effects.

2.4 Computational Complexity

The computational complexity of the intelligent, blind, one- and two-bit discrete phase shifter supported RIS-AP system is determined by the number of real multiplications necessary. Every complex multiplication necessitates four real multiplications.

For intelligent RIS-AP communication, the maximum-likelihood (ML) detector is given by

$$\hat{x} = \arg\min_{x} \left| y - \left[\sum_{n=1}^{N} c_n e^{-j\phi_n} \right] x \right|^2 \tag{16}$$

4 real multiplications are required for $c_n\, e^{-j\phi_n}$. $\sum_{n=1}^{N} c_n e^{-j\phi_n}$ requires $4N$ real multiplications. By multiplying it with a complex symbol x requires, $4N + 4$ multiplications. The calculation of $\left| y - \left[\sum_{n=1}^{N} c_n e^{-j\phi_n} \right] x \right|^2$ requires, $4N + 6$ multiplications. For a modulation order M, overall complexity of intelligent RIS-AP transmission scheme is given as

$$C_{\text{int}} = (4N + 6)\, M \tag{17}$$

For blind RIS-AP communication, the ML detector is presented by

$$\hat{x} = \arg\min_{x} \left| y - \left[\sum_{n=1}^{N} c_n \right] x \right|^2 \tag{18}$$

For a modulation order M, overall complexity of blind RIS-AP communication scheme is expressed as

$$C_{\text{blind}} = 6M \tag{19}$$

Table 1 Computability of all strategies for BPSK

Strategies	$N=128$	$N=256$	$N=512$
Intelligent	1036	2060	4108
Blind	12	12	12
One-bit	1548	3084	6156
Two-bit	2060	4108	8204

The discrete phase shifter's ML detector is specified as

$$\hat{x} = \arg\min_{x} \left| y - \left[\sum_{n=1}^{N} c_n e^{-j\hat{\phi}_{\text{dis}_n}} \right] x \right|^2 \tag{20}$$

To compute discrete phase shifter for each N, we require k number of real multiplications. The overall complexity of discrete phase shifter is given by

$$C_{dis} = ((4+k)N + 6)\, M \tag{21}$$

The computational complexity of $N=128$, $N=256$, $N=512$ for all schemes is shown in Table 1. As N increases, computational complexity increases as well.

3 Simulation Results

In this work, the potential of a discrete phase shifter is analysed for RIS-AP scenario. Discrete phase shifters are implemented in one-bit and two-bit versions, and their performance is examined for distinct N. Rayleigh fading channel and BPSK is considered for simulation.

Figure 2 shows the ABER analysis of a one-bit discrete phase shifter-aided RIS for $N = 16, 32, 64, 128, 256$ and 512. The SNR required for $N = 16, 32, 64, 128, 256$ and 512 components to achieve an ABER of 10^{-4} is -9 dB, -16 dB, -23 dB, -29 dB, -35 dB and -41 dB respectively. For distinct N, ABER analysis of discrete phase shifter-aided RIS is carried out for two-bit configuration in Fig. 3. The SNR required for $N = 16$, 32, 64, 128, 256 and 512 components to achieve an ABER of 10^{-4} is -7 dB, -19 dB, -27 dB, -34 dB, -42 dB and -48 dB, respectively. The SNR gains increase as N increases. For an ABER of 10^{-4}, Table 2 compares the SNRs of discrete phase shifter-aided RIS for one-bit and two-bit configurations. Observing the table, it is evident that a two-bit system performs better than single-bit system. A discrete phase shifter that uses one-bit is required to have an SNR of -35 dB while a discrete phase shifter that uses two-bits must have an SNR of -42 dB for $N=256$. As a result, the two-bit configuration has a gain of 7 dB over the one-bit configuration.

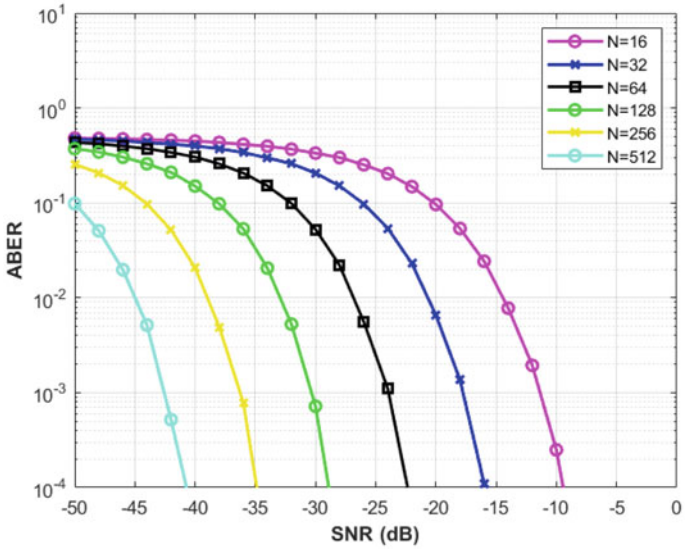

Fig. 2 ABER analysis of single-bit discrete phase shifter-aided RIS-AP

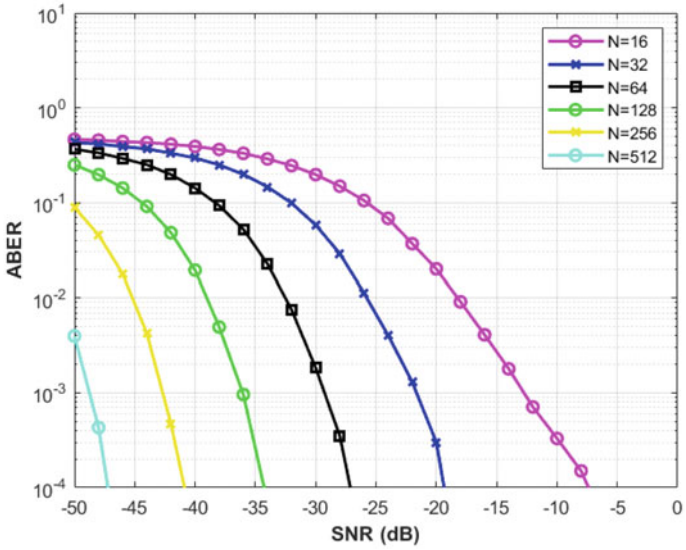

Fig. 3 ABER analysis of two-bit discrete phase shifter-aided RIS-AP

Table 2 SNR requirement analysis for single-bit and two-bit discrete phase shifter-aided RIS-AP

N	One-bit RIS-AP SNR (dB)	Two-bit RIS-AP SNR (dB)	SNR gain
16	−9	−7	2
32	−16	−19	3
64	−23	−27	4
128	−29	−34	5
256	−35	−42	7
512	−41	−48	7

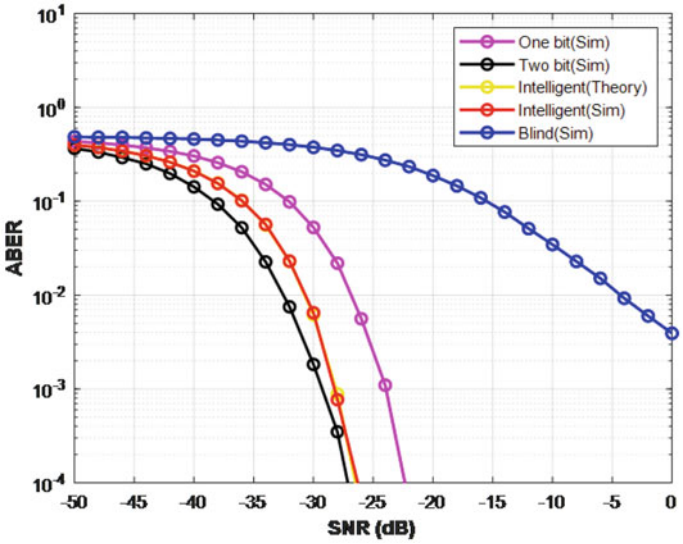

Fig. 4 ABER analysis of all strategies for $N = 64$

ABER analysis of the single-bit, two-bit, intelligent, and blind communication schemes for $N = 64$ is presented in Fig. 4. Blind communication requires a positive SNR, while intelligent communication requires −27 dB to achieve ABER of 10^{-4}. As a result, the intelligent communication system performs better than blind-aided RIS, and the results of the intelligent theoretical and simulation are identical. The SNR requirement for single-bit and two-bit configuration is −23 dB and −27 dB, respectively. Figure 5 compares all RIS-aided communication strategies for $N = 128$. Two-bit discrete phase shifters perform better than the intelligent communication strategy for larger N.

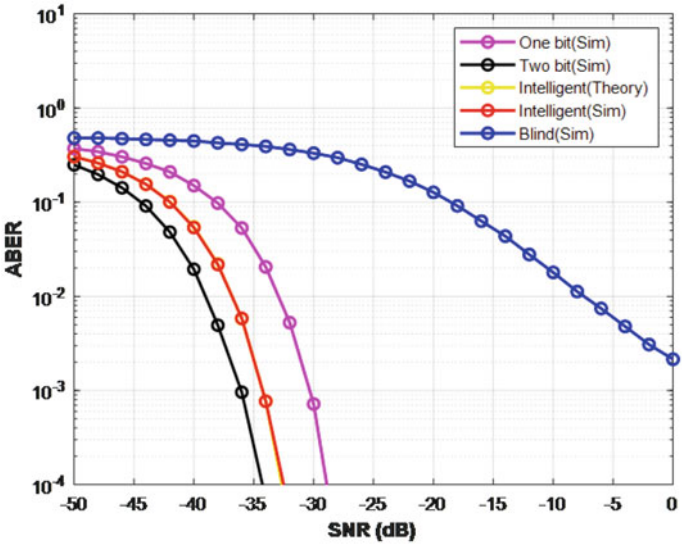

Fig. 5 ABER analysis of all strategies for $N = 128$

4 Conclusions

In this study, we examined the ABER performance of RIS-APs supported by one- and two-bit discrete phase shifters. We can infer from all of the findings that there is a large SNR gain as the prevalence of passive reflector components rises and that two-bit discrete phase shifter configuration outperforms one-bit configuration aided RIS. For intelligent RIS-AP communication, theoretic and simulation curves are almost matching. Because of the less fading effects, the RIS-AP scenario is better suited for next-generation networks than RIS dual-hop communication.

References

1. Albreem MA, Al Habbash AH, Abu-Hudrouss AM, Ikki SS (2021) Overview of precoding techniques for massive mimo. IEEE Access 9:60764–60801
2. Basar E (2019) Transmission through large intelligent surfaces: a new frontier in wireless communications. In: 2019 European conference on networks and communications (EuCNC). IEEE, pp 112–117
3. Di Renzo M, Ntontin K, Song J, Danufane FH, Qian X, Lazarakis F, De Rosny J, Phan-Huy DT, Simeone O, Zhang R et al (2020) Reconfigurable intelligent surfaces vs. relaying: differences, similarities, and performance comparison. IEEE Open J Commun Soc 1:798–807
4. Guo S, Lv S, Zhang H, Ye J, Zhang P (2020) Reflecting modulation. IEEE J Sel Areas Commun 38(11):2548–2561

5. Huang C, Zappone A, Alexandropoulos GC, Debbah M, Yuen C (2019) Reconfigurable intelligent surfaces for energy efficiency in wireless communication. IEEE Trans Wirel Commun 18(8):4157–4170
6. Proakis JG, Salehi M (2008) Digital communications, 4 ed. McGraw-hill
7. Simon MK, Alouini MS (2005) Digital communication over fading channels, 2nd ed
8. Tang W, Dai JY, Chen MZ, Wong KK, Li X, Zhao X, Jin S, Cheng Q, Cui TJ (2020) Mimo transmission through reconfigurable intelligent surface: system design, analysis, and implementation. IEEE J Sel Areas Commun 38(11):2683–2699
9. Wu Q, Zhang R (2018) Intelligent reflecting surface enhanced wireless network: joint active and passive beamforming design. In: 2018 IEEE global communications conference (GLOBECOM). IEEE, pp 1–6
10. Xu P, Chen G, Yang Z, Di Renzo M (2020) Reconfigurable intelligent surfaces-assisted communications with discrete phase shifts: how many quantization levels are required to achieve full diversity? IEEE Wirel Commun Lett 10(2):358–362

Discrete Sine Transform Interpolation-Based Design of 2-D FIR Fractional Delay Digital Filter

Shilpa Garg, Richa Yadav, and Manjeet Kumar

Abstract This study investigates the designing of 2-D FIR fractional delay digital filter. Here, the discrete sine transform-I (DST-I) is used to derive the interpolation formula. Then, it is applied to generate filter coefficients of 2-D FIR fractional delay digital filter exploiting proper index mapping. The design examples are demonstrating that the proposed approach has small absolute magnitude error in comparison with farrow structure and Taylor series expansion method. The simulated results reflect that the proposed method using 2-D DST-I gives absolute magnitude error of 0.0472 and 0.0101 for filter order of (20, 6) and (45, 49), respectively. Further, the calculated coefficients of filter are utilised to design 2-D digital differentiator which is approximating the ideal 2-D digital differentiator.

Keywords Fractional delay · 2-D DST interpolation · FIR filter

1 Introduction

The fractional delay filter delays the sampling time of input signal which is applicable in various digital signal processing systems. The applications of digital fractional delay filters are discrete time modelling [1], conversion of sampling rate [2], software defined radio applications [3], antenna beam forming [4] and fractional order digital differentiator [5, 6] and many more. Until now, many one-dimensional fractional delay FIR filter design approaches are available in the literature. Few of them are

S. Garg · R. Yadav
Department of Electronics and Communication Engineering, IGDTUW, Delhi, New Delhi 110006, India

S. Garg
Department of Electronics and Communication Engineering, JIMSEMTC, Greater Noida, Uttar Pradesh 201308, India

M. Kumar (✉)
Department of Electronics and Communication Engineering, DTU, Delhi, New Delhi 110042, India
e-mail: manjeetchhillar@gmail.com

S. Rawat et al. (eds.), *Proceedings of Second International Conference on Computational Electronics for Wireless Communications*, Lecture Notes in Networks and Systems 554,
https://doi.org/10.1007/978-981-19-6661-3_38

discrete Fourier transform [7], discrete cosine transform [8], power function and least square [6], discrete hartley transform [9], projected least squares (PLS) algorithm [10], weighted least square method [11], B-spline transform [12], comprehensive least square method [13], minimax design method [14, 15] and using optimisation algorithm [16, 17].

Along with one-dimensional approaches, multiple research work is being done to investigate the designing of 2-D FIR fractional delay digital filter. These includes weighted least squares method [18], Taylor series expansion method using 2-D differentiator [19] and farrow structure method [20, 21]. 2-D fractional delay digital filters have found immense range of applications in parallel high speed signal processing [22], image resizing [23], analysis in acoustic spaces [24], wave propagation [25] and wide band beam forming [26]. In general, 2-D fractional delay digital filters can be finite impulse response (FIR) or infinite impulse response (IIR) based on magnitude and phase response to be finite or infinite time. IIR filters are preferred for sharp frequency response, whereas FIR filters find advantageous where inherent stability and linear phase response are the requirement.

This work designs a linear phase 2-D FIR fractional order digital filter catering DST. The ideal equation of frequency response of 2-D FIR fractional delay digital filter is described by

$$H_{id}(\omega_1, \omega_2) = e^{-j\omega_1(I_1+d_1)} e^{-j\omega_2(I_2+d_2)} \tag{1}$$

where I_1 and I_2 are positive delayed integers and d_1 and d_2 are fractional delays in the range from 0 to 1. The 2-D transfer function of a digital filter is stated by

$$H(z_1, z_2) = \sum_{r_1=0}^{Q-1} \sum_{r_2=0}^{S-1} h(r_1, r_2) z_1^{-r_1} z_2^{-r_2} \tag{2}$$

Various widely used applications of discrete sine transform (DST)-based interpolation methods are: image denoising [27], image demosaicking [28] and designing of differentiator [29]. The DST inspite of being similar to discrete Fourier transform (DFT) uses real components with odd symmetry against DFT using imaginary components, which is the beneficial feature of DST. This paper proposes DST-I-based designing of 2-D FIR fractional delay digital filter. It further designs 2-D digital differentiator (DD). The reported approach is found to be useful in computation of coefficients of the filter. The investigation shows that the accuracy of 2-D FIR fractional delayed digital filter is improved with optimal frequency and constant group delay by minimising the integral square magnitude error with respect to farrow structure and Taylor series expansion method.

The paper continues as follows: Sect. 2 considers the details of DST-1 method of designing to examine the optimised coefficients of the 2-D fractional delay digital filter, while simulation outcomes are presented in the Sect. 3 and concluded in Sect. 4.

2 Calculations of Filter Coefficients Using DST-I Method

From the literature survey, it is proven that DST is widely used in image processing specially image denoising [27]. DST has been found as the method which gives accurate results for prediction of noise in comparison with discrete cosine transform and discrete Fourier transform [30]. The discrete sine transform is of eight types: DST (I-VIII). This paper is suggesting a design of 2-D FIR fractional delay digital filter exploiting DST-I.

The 2-D DST-I is explicate by

$$A(q,s) = \sqrt{\frac{2}{(Q+1)}}\sqrt{\frac{2}{(S+1)}}\sum_{n_1=0}^{Q-1}\sum_{n_2=0}^{S-1} a(n_1,n_2) \sin\left(\frac{(n_1+1))(q+1)\pi}{(Q+1)}\right)\sin\left(\frac{(n_2+1)(s+1)\pi}{(S+1)}\right) \tag{3}$$

and inverse DST-I is written as,

$$a(n_1,n_2) = \sqrt{\frac{2}{(Q+1)}}\sqrt{\frac{2}{(S+1)}}\sum_{q=0}^{Q-1}\sum_{s=0}^{S-1} A(q,s) \sin\left(\frac{(n_1+1)(q+1)\pi}{(Q+1)}\right)\sin\left(\frac{(n_2+1)(s+1)\pi}{(S+1)}\right) \tag{4}$$

Here, Q and S are length of the filters in both the dimensions. From Eqs. (3) and (4)

$$a(n_1,n_2) = \sqrt{\frac{2}{(Q+1)}}\sqrt{\frac{2}{(S+1)}}\sum_{q=0}^{Q-1}\sum_{s=0}^{S-1}\left[\sqrt{\frac{2}{(Q+1)}}\sqrt{\frac{2}{(S+1)}} \sum_{m_1=0}^{Q-1}\sum_{m_2=0}^{S-1} a(m_1,m_2)\sin\left(\frac{(m_1+1)(q+1)\pi}{(Q+1)}\right)\sin\left(\frac{(m_2+1)(s+1)\pi}{(S+1)}\right)\right] \sin\left(\frac{(n_1+1)(q+1)\pi}{(Q+1)}\right)\sin\left(\frac{(n_2+1)(s+1)\pi}{(S+1)}\right) \tag{5}$$

$$\Rightarrow a(n_1,n_2) = \sum_{m_1=0}^{Q-1}\sum_{m_2=0}^{S-1} a(m_1,m_2)\left[\frac{4}{(Q+1)(S+1)} \sum_{q=0}^{Q-1}\sum_{s=0}^{S-1}\sin\left(\frac{(m_1+1)(q+1)\pi}{(Q+1)}\right)\sin\left(\frac{(m_2+1)(s+1)\pi}{(S+1)}\right)\right] \sin\left(\frac{(n_1+1)(q+1)\pi}{(Q+1)}\right)\sin\left(\frac{(n_2+1)(s+1)\pi}{(S+1)}\right) \tag{6}$$

It is clear that the interpolated values of $a(n_1, n_2)$ are only the weighted mean of the signal. Furthermore, after interpolation, the sequences n_1 and n_2 can be replaced with $(i_1 + \frac{p_1}{L_1})$ and $(i_2 + \frac{p_2}{L_2})$ using the following relation

$$a(i_1 L_1 + p_1, i_2 L_2 + p_2) = a\left(i_1 + \frac{p_1}{L_1}, i_2 + \frac{p_2}{L_2}\right) \tag{7}$$

where p_1, p_2 varies from 0 to L_1, 0 to L_2 and i_1, i_2 varies from 0 to Q, 0 to S. After replacement, Eq. (6) will become

$$\begin{aligned} a(i_1 + \frac{p_1}{L_1}, i_2 + \frac{p_2}{L_2}) = \sum_{m_1=0}^{Q-1} \sum_{m_2=0}^{S-1} a(m_1, m_2) \Bigg[\frac{4}{(Q+1)(S+1)} \\ \sum_{q=0}^{Q-1} \sum_{s=0}^{S-1} \sin\left(\frac{(m_1+1)(q+1)\pi}{(Q+1)}\right) \sin\left(\frac{(m_2+1)(s+1)\pi}{(S+1)}\right) \Bigg] \\ \sin\left(\frac{((i_1 + \frac{p_1}{L_1})+1)(q+1)\pi}{(Q+1)}\right) \sin\left(\frac{((i_2 + \frac{p_2}{L_2})+1)(s+1)\pi}{(S+1)}\right) \end{aligned} \tag{8}$$

$$= \sum_{m_1=0}^{Q-1} \sum_{m_2=0}^{S-1} a(m_1, m_2) c(m_1, i_1 + \frac{p_1}{L_1}) d(m_2, i_2 + \frac{p_2}{L_2}) \tag{9}$$

where interpolation factors are given by

$$\begin{aligned} c(m_1, i_1 + \frac{p_1}{L_1}) = \frac{2}{(Q+1)} \sum_{q=0}^{Q-1} \sin\left(\frac{(m_1+1)(q+1)\pi}{(Q+1)}\right) \\ \sin\left(\frac{((i_1 + \frac{p_1}{L_1})+1)(q+1)\pi}{(Q+1)}\right) \end{aligned} \tag{10}$$

$$\begin{aligned} d(m_2, i_2 + \frac{p_2}{L_2}) = \frac{2}{(S+1)} \sum_{s=0}^{S-1} \sin\left(\frac{(m_2+1)(s+1)\pi}{(S+1)}\right) \\ \sin\left(\frac{((i_2 + \frac{p_2}{L_2})+1)(s+1)\pi}{(S+1)}\right) \end{aligned} \tag{11}$$

The result of Eq. (8) is utilised to find the coefficients of 2-D FIR fractional delayed digital filter. If an input signal g(n_1 ,n_2) is used at the input of 2-D FIR fractional delayed digital filter, then the output generated intended a weighted average of delayed integer samples of $g(n_1, n_2)$, $g(n_1 - 1, n_2 - 1)$, $g(n_1 - 2, n_2 - 2) \ldots g(n_1 - Q + 1, n_2 - S + 1)$, which is written as

$$y(n_1, n_2) = \sum_{r_1=0}^{Q-1} \sum_{r_2=0}^{S-1} h(r_1, r_2) g(n_1 - r_1, n_2 - r_2) \tag{12}$$

Now, the objective is to determine coefficients of filter h(r_1,r_2) in such a manner that the FIR filter output y(n_1, n_2) approximates with the delayed fractional samples of $g(n_1 - I_1 - d_1, n_2 - I_2 - d_2)$, that is

$$y(n_1, n_2) = g(n_1 - I_1 - d_1, n_2 - I_2 - d_2) \tag{13}$$

So index mapping method is used to achieve the objective, by choosing,

$$\begin{aligned} g(n_1, n_2) &= a(Q-1, S-1) \\ g(n_1 - 1, n_2 - 1) &= a(Q-2, S-2) \\ &\vdots \\ g(n_1 - Q + 1, n_2 - S + 1) &= a(0, 0) \end{aligned} \tag{14}$$

Now, Eq. (16) can be presented as

$$a(m_1, m_2) = g[\{n_1 - (Q-1) + m_1\}, \{n_2 - (S-1) + m_2\}] \tag{15}$$

where

$$0 \le m_1 \le Q-1, 0 \le m_2 \le S-1$$

After this, Eq. (9) can be presented as

$$g[\{n_1 - (Q-1) + i_1 + \frac{p_1}{L_1}\}, \{n_2 - (S-1) + i_2 + \frac{p_2}{L_2}\}] = \sum_{m_1=0}^{Q-1} \sum_{m_2=0}^{S-1} g[\{n_1 - (Q-1) + m_1\}, \{n_2 - (S-1) + m_2\}] c(m_1, i_1 + \frac{p_1}{L_1}) d(m_2, i_2 + \frac{p_2}{L_2}) \tag{16}$$

After substituting interpolation factor $i_1 + \frac{p_1}{L_1}$ and $i_2 + \frac{p_2}{L_2}$ by $(Q - 1 - I_1 - d_1)$ and $(S - 1 - I_2 - d_2)$, the Eq. (16) will become as

$$\begin{aligned} g[\{n_1 - I_1 - d_1\}, \{n_2 - I_2 - d_2\}] \approx \sum_{m_1=0}^{Q-1} \sum_{m_2=0}^{S-1} g[\{n_1 - (Q-1) + m_1\}, \\ \{n_2 - (S-1) + m_2\}] c(m_1, Q - 1 - I_1 - d_1) d(m_2, S - 1 - I_2 - d_2) \end{aligned} \tag{17}$$

After replacing $r_1 = (Q-1) - m_1$ and $r_2 = (S-1) - m_2$, the Eq. (17) changed to

$$g[\{n_1 - I_1 - d_1\}, \{n_2 - I_2 - d_2\}] \approx \sum_{r_1=0}^{Q-1} \sum_{r_2=0}^{S-1} g[n_1 - r_1, n_2 - r_2] \\ c(Q-1-r_1, Q-1-I_1-d_1) d(S-1-r_2, S-1-I_2-d_2) \tag{18}$$

In continuation with the above, taking z transform of both the sides, Eq. (18) becomes

$$z_1^{-(I_1+d_1)} z_2^{-(I_2+d_2)} G(z_1, z_2) \approx \sum_{r_1=0}^{Q-1} \sum_{r_2=0}^{S-1} [c(Q-1-r_1, Q-1-I_1-d_1) \\ d(S-1-r_2, S-1-I_2-d_2) z_1^{r_1} z_2^{r_2}] G(z_1, z_2) \tag{19}$$

here, $G(z_1, z_2)$ is the z-transformation of input signal $g(n_1, n_2)$. After solving the above equation, we have

$$z_1^{-(I_1+d_1)} z_2^{-(I_2+d_2)} \approx \sum_{r_1=0}^{Q-1} \sum_{r_2=0}^{S-1} c(Q-1-r_1, Q-1-I_1-d_1) \\ d(S-1-r_2, S-1-I_2-d_2) z_1^{r_1} z_2^{r_2} \tag{20}$$

According to the results obtained, if the selection of filter coefficients in Eq. (2) is

$$h(r_1, r_2) = c(Q-1-r_1, Q-1-I_1-d_1) d(S-1-r_2, S-1-I_2-d_2) \tag{21}$$

Then the filter coefficients can be achieved by putting Eqs. (10) and (11) within Eq.(21),

$$h(r_1, r_2) = \frac{4}{(Q+1)(S+1)} \sum_{q=0}^{Q-1} \sum_{s=0}^{S-1} \sin\left(\frac{(Q-r_1)(q+1)\pi}{(Q+1)}\right) \sin\left(\frac{(S-r_2)(s+1)\pi}{(S+1)}\right) \\ \sin\left(\frac{(Q-I_1-d_1)(q+1)\pi}{(Q+1)}\right) \sin\left(\frac{((S-I_2-d_2)(s+1)\pi}{(S+1)}\right) \tag{22}$$

From the above method, coefficients of 2-D filter are easily obtained without applying any typical optimisation technique.

3 Simulation Outcomes

The simulation results of a 2-D FIR fractional delay digital filter employing DST-I are presented in this section. To estimate the measurement performance of the suggested 2-D FIR fractional delay filter, simulation results are conferred. The strength of the

given approach is analysed with reference to integral square magnitude error, which is defined as

$$E = \sqrt{\int_0^{\lambda_1\pi}\int_0^{\lambda_2\pi} [|H(\omega_1, \omega_2)| - |H_{id}(\omega_1, \omega_2)|]^2 \, d\omega_1 d\omega_2} \tag{23}$$

All the results are generated with MATLAB.

3.1 As 2-D FIR Fractional Delayed Digital Filter

As a first example DST-I method is used to design 2-D FIR fractional delayed digital filter. Here, the coefficients of 2-D FIR fractional delayed digital filter are computed with the help of Eq. (22). The design requirements are selected as, Q = S = 50, $I_1 = I_2 = 25$, $d_1 = d_2 = 0.5$ and $\lambda_1 = \lambda_2 = 0.9$.

Figures 1 and 2 are showing the normalised magnitude response of the ideal and proposed 2-D FIR fractional delay digital filter. The graph shows the linear range all over the frequencies except at the edges. Figures 3 and 4 show the responses of the ω_1 and ω_2 directional group delay for the proposed 2-D FIR fractional delayed digital filter.

Figure 5 depicts the absolute magnitude error in two dimensions with respect to normalised frequencies for the presented 2-D FIR fractional delayed digital filter. It is evident from the graph that the proposed method gives close match with an average integral square magnitude error of 0.0086 and execution time of 101.58 s.

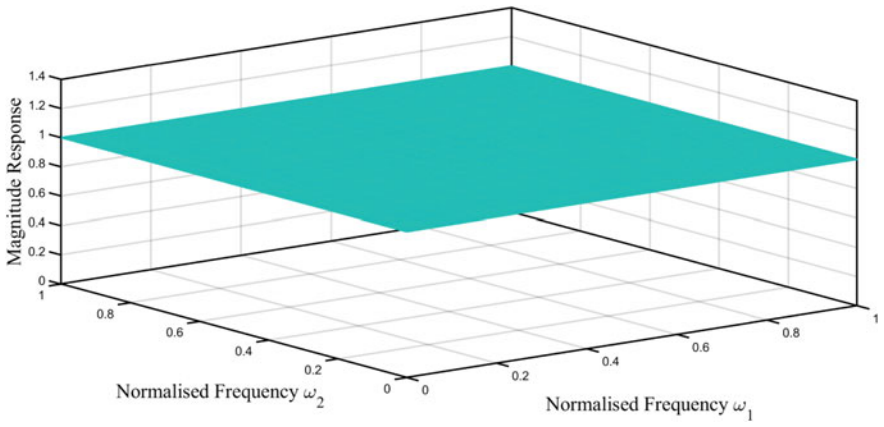

Fig. 1 Normalised magnitude response of ideal 2-D FIR fractional delay digital filter

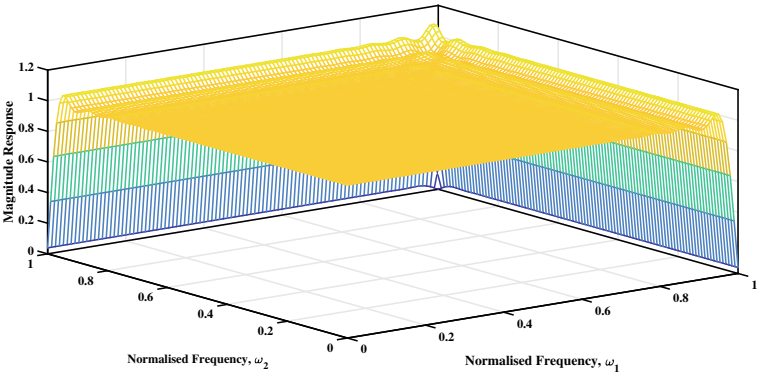

Fig. 2 Normalised magnitude response of 2-D FIR fractional delay digital filter with proposed DST-I method

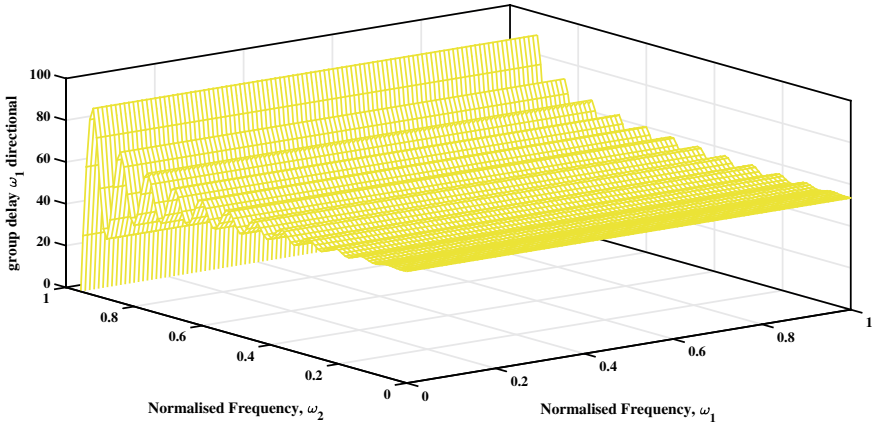

Fig. 3 ω_1 directional group delay response of 2-D FIR fractional delay digital filter with respect to normalised frequencies

3.2 As 2-D Digital Differentiator

In this example, 2-D digital differentiator is designed using the coefficients of proposed 2-D fractional delay digital filter. The motive behind this example is to show that the proposed filter can be used as a component in many applications. After differentiation, the Eq. (1) can be written as,

$$\frac{\partial H_{id}(\omega_1, \omega_2)}{\partial d_1 \partial d_2}\Big|_{d_1,d_2=0} = (j\omega_1)(j\omega_2)e^{-j\omega_1(I_1+d_1)}e^{-j\omega_2(I_2+d_2)}|_{d_1,d_2=0} \tag{24}$$

$$= (j\omega_1)(j\omega_2)e^{-j\omega_1 I_1}e^{-j\omega_2 I_2} \tag{25}$$

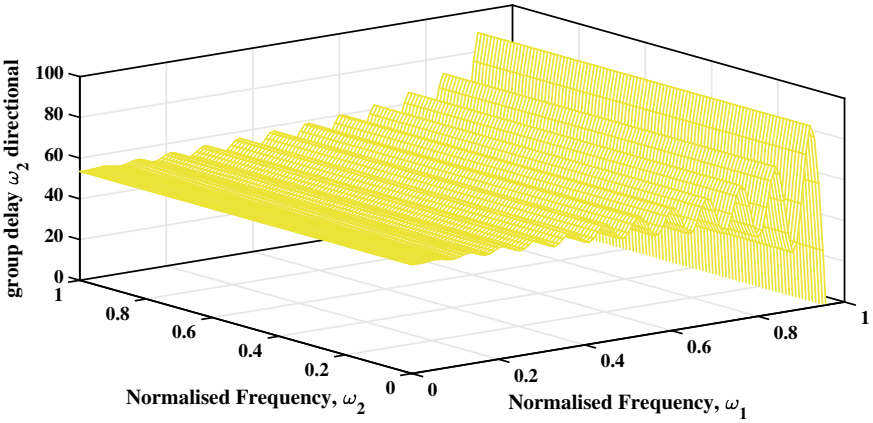

Fig. 4 ω_2 directional group delay response of 2-D FIR fractional delay digital filter with respect to normalised frequencies

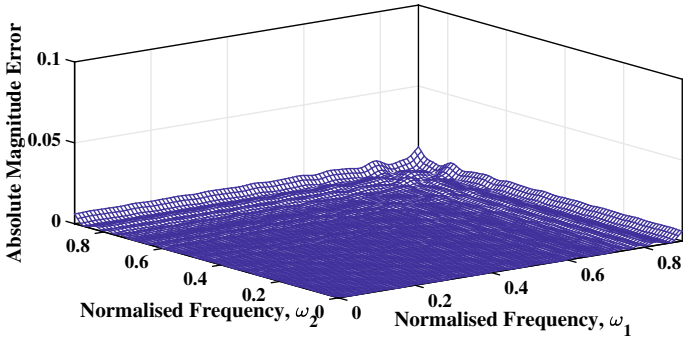

Fig. 5 Absolute magnitude error of proposed 2-D FIR fractional delay digital filter using DST-I method with respect to frequencies

The ideal frequency response of a 2-D digital differentiator is given by Eq. (25). According to the results obtained, the transfer function of proposed 2-D digital differentiator can be achieved. The transfer function of a 2-D digital differentiator is given by

$$U(z_1, z_2) = \sum_{r_1=0}^{Q-1} \sum_{r_2=0}^{S-1} u(r_1, r_2) z_1^{-r_1} z_2^{-r_2} \tag{26}$$

where $u(r_1, r_2)$ is a coefficient of 2-D digital differentiator which can be given as,

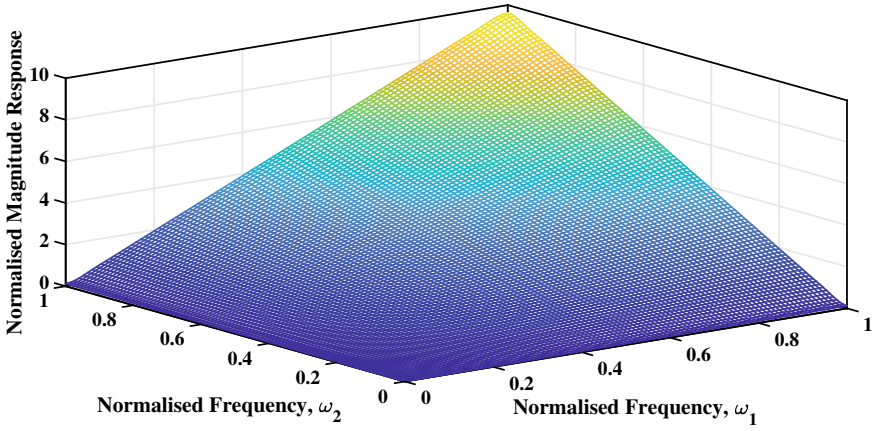

Fig. 6 Normalised magnitude response of 2-D FIR DD with proposed DST-I method

$$u(r_1, r_2) = \frac{4\pi^2}{(Q+1)^2(S+1)^2} \sum_{q=0}^{Q-1} \sum_{s=0}^{S-1} (q+1)(s+1) \sin\left(\frac{(Q-r_1)(q+1)\pi}{(Q+1)}\right)$$
$$\sin\left(\frac{(S-r_2)(s+1)\pi}{(S+1)}\right) \sin\left(\frac{(Q-I_1)(q+1)\pi}{(Q+1)}\right) \sin\left(\frac{((S-I_2)(s+1)\pi}{(S+1)}\right) \tag{27}$$

Figure 6 is showing the normalised magnitude response of designed 2-D digital differentiator for Q = S = 50 and $I_1 = I_2 = 25$. It is clear that the designed filter is approximating the shape of digital differentiator.

3.3 Comparison with Reported Designs

This subsection provides a detailed explanation of the intended work as well as a review of the literature on the design of 2-D FIR fractional delay digital filters to date. Table 1 compares the designed 2-D FIR fractional delay digital filter to the reported designs using farrow structure method [20] and Taylor series expansion [19]. It is depicting absolute integral square magnitude error of proposed method for different fractional delays, for (45, 49), (20, 6) and (21, 6) length 2-D FIR fractional delayed digital filter design. Shyu, Pei and Huang reported absolute integral square magnitude error in pass band and stop band with the design of (20, 6) order and (21, 6) order 2-D fractional delay FIR digital filter using the farrow structure [20]. Tseng applied the Taylor series expansion method [19] for the design of (45, 49) order 2-D fractional delay FIR digital filter and reported various absolute magnitude error for different values of fractional delays. In terms of absolute magnitude error, the results reveal that the suggested strategy outperforms previously published design methods.

Table 1 Performance comparison of 2-D FIR fractional delay digital filter using DST-I interpolation method with existing designs

Design method	Filter length	d_1, d_2 fractional delays	Absolute magnitude error
Farrow structure method [16]	20, 6	0.25, 0.25	Pass band 0.0238 Stop band 0.0331
Farrow structure method [16]	21, 6	0.25, 0.25	Pass band 0.2239 Stop band 0.2781
Taylor series expansion method [15]	45, 49	0.5, 0.25	0.0103
Taylor series expansion method [15]	45, 49	0.5, 0	0.00893
Taylor series expansion method [15]	45, 49	0.25, 0.25	0.0054
Taylor series expansion method [15]	45, 49	0.25, 0	0.0043
Proposed method [DST-I]	45, 49	0.5, 0.25	0.0101
Proposed method [DST-I]	45, 49	0.5, 0	0.0087
Proposed method [DST-I]	45, 49	0.25, 0.25	0.0050
Proposed method [DST-I]	45, 49	0.25, 0	0.0032
Proposed method [DST-I]	20, 6	0.25, 0.25	0.0472
Proposed method [DST-I]	21, 6	0.25, 0.25	0.0452

4 Conclusion

This paper proposes an effective method using DST-I to acquire the optimised coefficients for 2-D fractional delayed digital filter. The method is easy and intuitive to implement. The design examples conclude that it is suitable for the applications where a higher order 2-D fractional delay digital filter is required because absolute magnitude error is decreasing with the increasing order of filter. Its application as a digital differentiator is also explored here. The absolute magnitude error obtained with suggested approach is lesser and comparable to the other reported methods also. Simulation results validate that the proposed method is helpful in minimising the absolute magnitude error. As a future scope, it will be very useful to apply the proposed method for designing of higher dimensional filters.

References

1. Valimaki V (1995) Discrete time modeling of acoustic tubes using fractional delay filters, Doctoral dissertation. Report no. 37, Helsinki University of Technology, Laboratory of Acoustics and Audio Signal Processing
2. Hentschel T, Fettweis G (2000) Sample rate conversion for software radio. IEEE Commun Mag 38(8):142–150
3. Carmona JD, Dolecek GJ, Agundis AR (2010) Frequency-based optimization design for fractional delay FIR filters with software defined radio applications. Int J Digital Multimed Broadcasting 2010:1–6
4. Kumari CK, Babu TN, Siva DS, Sankaracharyulu PVS (2019) Design of variable fractional delay filter using FIR filter approximation. Int J Recent Technol Eng 8(4):8128–8132
5. Tseng CC (2002) Design of variable fractional delay FIR filter using differentiator bank. In: IEEE international symposium on circuits and systems-ISCAS 2002, vol 4, pp 421–424
6. Kumar M, Rawat TK (2016) Fractional order digital differentiator design based on power function and least squares. Int J Electron 103(10):1639–1653
7. Tseng CC, Lee SL (2009) Closed form design of variable fractional delay filter using discrete Fourier transform. In: 17th European signal processing conference-EUSIPCO 2009, pp 426–430
8. Tseng CC, Lee SL (2008) Design of fractional delay FIR filter using discrete cosine transform. In: IEEE Asia Pacific Conference on Circuits and Systems-APCCAS, pp 858–861
9. Tseng CC, Lee SL (2007) Closed-form design of fractional delay FIR filter using discrete Hartley transform. In: IEEE region 10 conference-TENCON 2007, pp 1–4
10. Kwan HK, Jiang A (2009) FIR, All pass, and IIR variable fractional delay digital filter design. IEEE Trans Circuits Syst-I 56(9):2064–2074
11. Huang YD, Pei SC, Shyu JJ (2009) WLS design of variable fractional delay FIR filters using coefficient relationship. IEEE Trans Circuits Syst-II 56(3):220–224
12. Olkkonen JT, Olkkonen H (2007) Fractional delay filter based on the b-spline transform. Signal Process Lett 14(2):97–100
13. Kumar M, Rawat TK (2015) Design of a variable fractional delay filter using comprehensive least square method encompassing all delay values. J Circuits Syst Comput 24(8):1550116–1550129
14. Deng TB (2011) Decoupling minimax design of low complexity variable fractional delay FIR digital filters. IEEE Trans Circuits Syst I 58(10):2398–2408
15. Deng TB (2010) Minimax design of low complexity all pass variable fractional delay digital filters. IEEE Trans Circuits Syst I 57(8):2075–2086
16. Kumar M (2018) Optimal design of fractional delay FIR filter using cuckoo search algorithm. Int J Circuit Theory Appl 46(12):2364–2379
17. Upadhyay K, Kumar M, Rawat TK (2014) Optimal design of weighted least square based fractional delay FIR filter using genetic algorithm. In: International conference on signal propagation and computer technology-ICSPCT 2014, pp 53–58
18. Deng TB, Lu WS (2000) Weighted least squares method for designing variable fractional delay 2-D FIR digital filters. IEEE Trans Circuits Syst-II Analog Digital Signal Process 47(2):114–124
19. Tseng CC (2003) Design of 2-D variable fractional delay FIR filter using 2-D differentiators. In: Proceedings of the 2003 international symposium on circuits and systems-ISCAS 3, IV–IV
20. Shyu J, Pei S, Huang Y (2009) Two dimensional farrow structure and the design of variable fractional delay 2-D FIR digital filters. IEEE Trans Circuits Syst-I 56(2):395–404
21. Bindima T, Elias E (2016) Design of efficient circularly symmetric two-dimensional variable digital FIR filters. J Adv Res 7(3):336–347
22. Den TB, Somab T (1995) Design of 2-D variable digital filters with arbitrary magnitude characteristics. Signal Process 43:17–27
23. Tseng CC (2002) Design of 1-D and 2-D variable fractional delay all pass filters using weighted least-squares method. IEEE Trans Circuits Syst-I 49:1413–1422

24. Savioja L, VaIimiiki V (2000) Reducing the dispersion error in the digital waveguide mesh using interpolation and frequency warping techniques. IEEE Trans Speech Audio Process 8(2):184–194
25. Savioja L (1998) Improving the three dimensional digital waveguide mesh by interpolation. In: Proceedings Nordic acoustic meeting, pp 265–268
26. Ahmad Z, Yaoliang S, Du Q (2016) Adaptive wideband beamforming based on digital delay filter. J Microwaves Opto-electron Electromagn Appl 15(3):261–274
27. Malini S, Moni RS (2014) Use of discrete sine transform for a novel image denoising technique. Int J Image Process 8(4):204–213
28. Zhou X, Wang C, Zhang Z, Fu Q (2018) Interpolation filter design based on all-phase DST and its application to image demosaicking. Information 9:1–17
29. Tseng CC, Lee S (2013) Design of digital fractional order differentiator using discrete sine transform. In: Asia pacific signal and information processing association annual summit and conference, pp 1–9
30. Dhamija S, Jain P (2011) Comparative analysis for discrete sine transform as a suitable method for noise estimation. Int J Comput Sci Issues 8(5):162–164
31. Kumar M, Rawat TK (2017) Design of fractional order differentiator using type-III and type-IV discrete cosine transform. Eng Sci Tech Int J 20(1):51–58

High-Speed Less Area CNTFET Ternary Half Adder Using Pseudologic

Pallepogu Divya, Tattukolla Gowthami, and Sarada Musala

Abstract Ternary logic is used to reduce the chip area and interconnection complexity. Furthermore, in terms of connection complexity, chip size, propagation delay, and energy consumption, multi-valued logic (MVL) circuits outperform binary circuits significantly. Carbon nanotube field-effect transistors (CNTFETs) have properties that make them a good choice for MVL circuit implementation. In this paper, CNTFET-based ternary half adder is proposed using pseudologic with less number of transistors. This proposed pseudo ternary half adder is compared with static ternary half adder. These two logic circuits, such as a static ternary half adder and pseudo ternary half adder, are simulated using Cadence Spectre with CNTFET 32 nm technology. Simulation results show that the propagation delay is reduced in proposed pseudologic ternary half adder when compared to static logic ternary half adder.

Keywords Multiple-valued logic (MVL) · Carbon nanotube (CNT) FET (CNTFET) · Static logic · Pseudologic

1 Introduction

Moore's law states that the number of transistors on a chip has doubled every two years. Over the last two decades, it has roughly doubled every two years. Reduced to a size of around nanometres [1], based on complementary metal oxide semiconductors (CMOS) technology [2–4]. There are many problems regarding CMOS, i.e. effects of short channels, leakage currents, and high costs of lithography. To tackle the issues outlined above, scientists and researchers are looking for alternatives to the classic CMOS method. So to resolve the above problems, CNTFETs are a well-established alternative to CMOS transistor. Due to CNTFETs, area and power will be reduced, and the act also increases.

P. Divya · T. Gowthami · S. Musala (✉)
Vignan's Foundation for Science Technology and Research, Vadlamudi, Andhra Pradesh 522213, India
e-mail: sarada.marasu@gmail.com

S. Rawat et al. (eds.), *Proceedings of Second International Conference on Computational Electronics for Wireless Communications*, Lecture Notes in Networks and Systems 554,
https://doi.org/10.1007/978-981-19-6661-3_39

Multi-valued logic is single suitable approach designed for boosting the rate and information transmit capability in binary systems as compared to typical binary circuits since it minimises the difficulty of interconnections and achieve high-energy efficiency. Because CNTFETs have programmable threshold voltages (Vth), which are proportional to nanotube diameter, they are a great alternative for MVL circuit implementation. This study proposes a method for implementing optimum ternary circuits based on the potential of CNTFET ternary circuits in regard to power usage, transistor count, and delay.

The advantages of CNTFET ternary circuits over CMOS technology are discussed in Sect. 1. Section 2 discusses chiral vectors and threshold voltages, as well as negative, positive, and normal ternary logic. It also provides a brief overview of multi-valued logic. It describes how the decoder and encode circuits are used to create the ternary half adder. Section 3 explains how the suggested method differs from existing methods, as well as the results and conclusions.

2 Back Ground

2.1 CNTFET

Carbon nanotubes have unique structural and electrical properties that enable them to be used in a variety of applications. Carbon nanotubes consist of two types: single-walled carbon nanotubes (SWCNTs) and multi-walled carbon nanotubes (MWCNT). Carbon nanofibers (CNF) [5] are a non-hollow tubular structure. SWCNTs are nanometre sized, 50,000 times smaller than a human hair, and can be several microns long. SWCNTs are made from graphene, a single-atom-thick layer of graphite wrapped into cylinder with open or closed ends. MWCNTs are made up of many concentric layers of grapheme arranged in a tube shape, as their name suggests. Because of their unique features, SWCNTs are employed in important electronic applications like memory, semiconductor components, touch screens, displays, solar cells, sensors, and other gadgets use transparent conducting films. The carbon atom arrangement in the tube sheet is determined by the chiral vector. A new device termed a CNTFET or tube-FET is created by inserting a CNT as a outlet in a electronic transistor.

Equation (1) estimates the distance of the CNTFET tube DCNT using the chiral vector:

$$D_{\mathrm{CNT}} = a\frac{\sqrt{n_1^2 + n_1 n_2 + n_2^2}}{\Pi} \tag{1}$$

where a is the spacing between carbon atoms, which is about 0.249 nm. Equation (2) is used to get the *V*th.

$$V_{\text{th}} = \frac{a V_{\pi}}{\sqrt{3} e D_{\text{CNT}}} \tag{2}$$

V_{th} is inversely proportional to tube diameter, oscillating between n_1 and n_2, and V_{Π} is a constant parameter with a value of 3.033 eV that specifies the carbon-bound energy in tight bonding, and e is the electron charge. CNTFETs are a promising alternative to silicon transistors. In this paper, four chiral vector devices are used, and we get appropriate threshold voltages for these chiral vectors.

2.2 Logic Units of Many Values

When creating a large number of connections in VLSI circuits, problems like rising manufacturing complexity and power consumption must be taken into account. Over the last few decades, it has been demonstrated that MVL [6] ternary logic provides superior qualities over binary circuits. Advanced statistics dealing out capabilities each unit of area, enhanced circuit speed and adaptability, reduced power consumption, reduced connectivity complexity, and a lower the quantity of active devices on a chip are only a few of these qualities.

Systems in the MVL are the most commonly used voltage mode ternary logic system, which has three states of logic corresponding to GND, Vdd/2, and Vdd, respectively. A basic ternary gate (Y_0, Y_1, and Y_2) has one input (x) and three outputs (Y_0, Y_1, and Y_2) that correspond to NTI, STI, and PTI operations.

$$\begin{aligned} Y_0 &= 2, \text{ if } X = 0 \\ &\quad 0, \text{ if } X \neq 0 \\ Y_1 &= 2 - X \\ Y_2 &= 0, \text{ if } X = 2 \\ &\quad 2, \text{ if } X \neq 2 \end{aligned} \tag{3}$$

NTI, STI, and PTI are described in Eq. (3).These are basic for any type of ternary logic to design.

2.3 Previous Works Using Ternary Logic

Linetal [7], Dhande and Ingole [8] all require a significant number of transistors. Circuits with a large number of transistors in digital form consume more energy and are more difficult to build. The decoder and pass transistor approaches were combined to create a ternary half adder. Finally, A_1 Jaber et al. created a ternary half adder employing a multiplexer-based methodology, pass transistor methods, NTI,

Table 1 Ternary half adder truth table

A	B	Sum	Carry	Sum1	Sum2	Carry1
0	0	0	0	0	0	0
0	1	1	0	2	0	0
0	2	2	0	0	2	0
1	0	1	0	2	0	0
1	1	2	0	0	2	0
1	2	0	1	0	0	2
2	0	2	1	0	2	0
2	1	0	0	0	0	2
2	2	1	1	2	0	2

and PTI gates. This half adder has the most transistors and the smallest delay, but it also uses the least power in the previous paper. Equation (4) specifies the technique for generating A_0 and A_1 values (Table 1).

$$\begin{aligned} A_0 &= \mathrm{NTI}(A), \\ A_1 &= \mathrm{PTI}.\overline{\mathrm{NTI}(A)} \end{aligned} \tag{4}$$

Sum_1, Sum_2, and carry of transistor level are illustrated in Fig. 1 using draw up and down networks [10].

$$\begin{aligned} \overline{\mathrm{Sum}_1} &= A_0B_1 + A_1B_0 + A_2B_2, \\ \overline{\mathrm{Sum}_2} &= A_0B_2 + A_1B_1 + A_2B_0 \end{aligned} \tag{5}$$

$$\begin{aligned} \overline{\mathrm{Carry}_1} &= A_1B_1 + A_2B_1 + A_2\ B_2 \\ &= A_1B_2 + A_2(B_1 + B_2) \end{aligned} \tag{6}$$

The transistors are assigned in accordance [11–13] with the preceding formulae, resulting in sum and carry operations.

3 Proposed Design

Executing a half adder sum with sum1, sum2, and pseudologic, which has less time and is therefore more favourable than static logic. Instead of using six transistors in the pull-up network, here in this method, it utilised only one transistor (pseudologic) [14], whose gate is always grounded and whose chirality is (7, 0).

Chiral values for all the transistors in Fig. 2a and b are (10, 0).

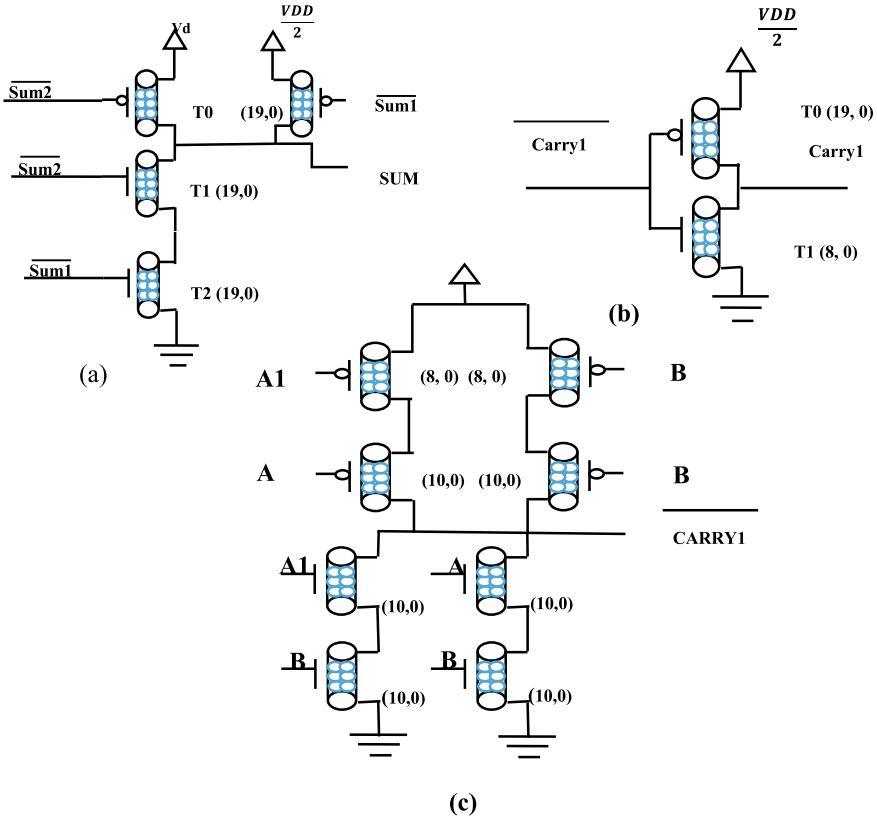

Fig. 1 **a** Sum, **b** carry$_1$, and **c** carry$_1$ transistor levels

4 Simulation Results

Half adder used in the designs [17, 18] is made using two power sources, with the Vdd, Vdd/2 circuit. The circuits' output current and threshold voltage are significantly influenced by CNT diameter and tube count.

CNTFET was used to imitate the decoder, which is a half adder, in 32 nm technology with the different voltages. The outcomes are identical in both cases, with the exception that there are less transistors in the second case. The code is written in CNTFET with chiral vectors in a specific format (Figs. 3 and 4; Table 2).

Static ternary half adder consists of 50 transistors, whereas proposed ternary half adder consists of only 37 transistors. This is the advantage over static ternary logic. So by this, we get less delay in pseudo ternary half adder circuit.

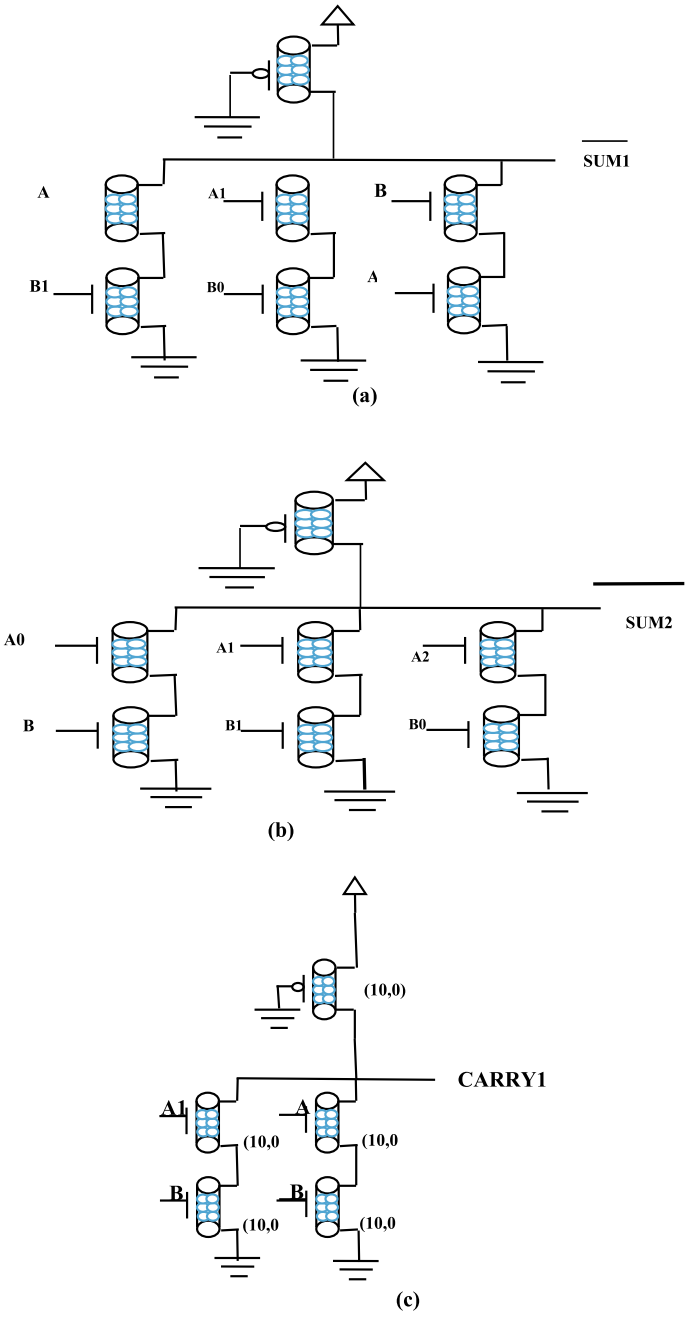

Fig. 2 **a** Pseudo sum$_1$, **b** pseudo sum$_2$ 1 **c** pseudo revised carry$_1$ **d** Pseudo sum (e) Pseudo carry of transistor levels

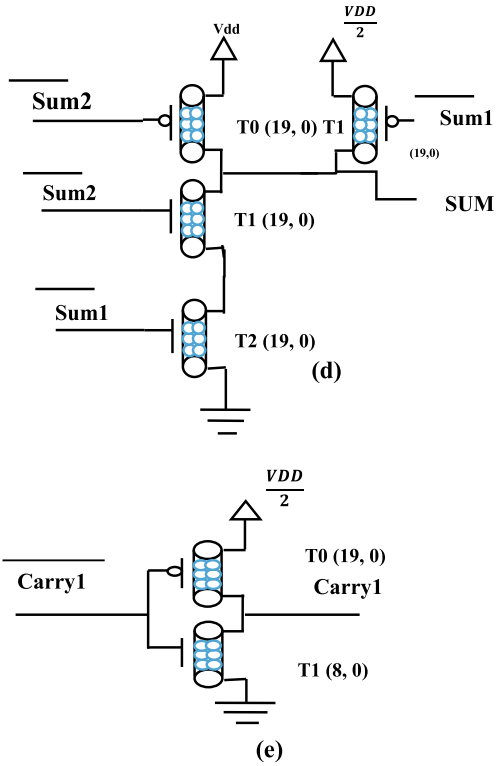

Fig. 2 (continued)

5 Conclusion

MVL circuits have significant advantages in terms of space, device count, interconnections, and as a result, power consumption is low. Because of its capacity to create devices with many threshold voltages, CNTFET technology is a classic choice for creating MVL circuits, as fresh mechanism has proven. In this effort, I have created a half adder by following a methodical circuit design procedure and comparing static CMOS and pseudologic. With the same electrical circumstances in all scenarios, simulation results show a considerable reduction in the shortest delay whilst maintaining a reasonable power consumption and device count. Thus, utilising pseudologic, the area will be lowered, and the delay will be reduced by comparison.

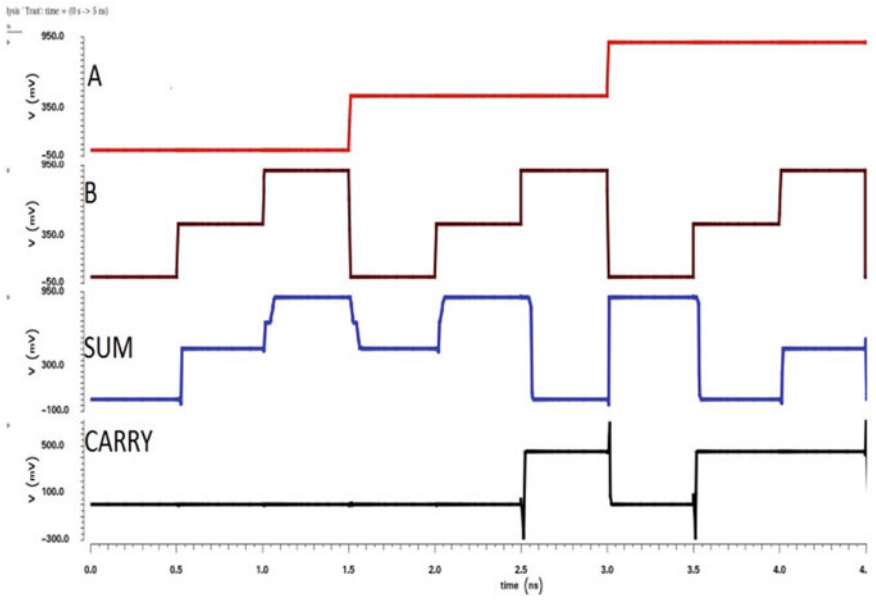

Fig. 3 Simulation of static sum and carry

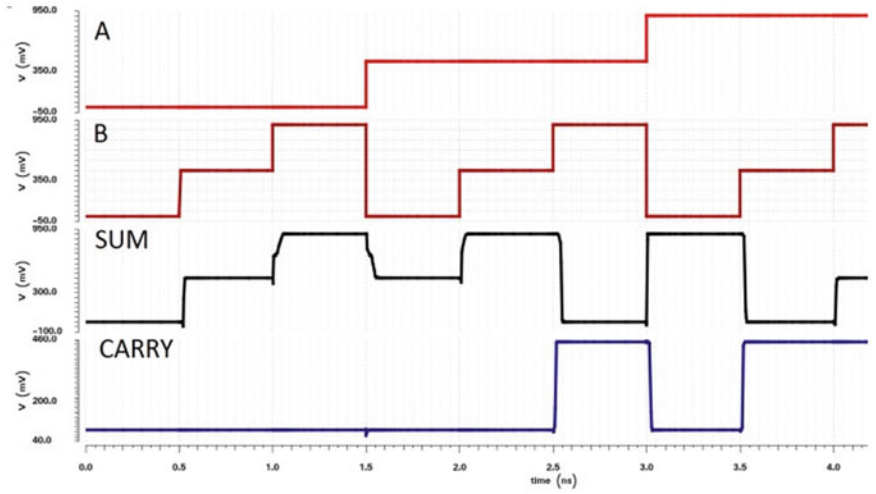

Fig. 4 Pseudo sum and carry simulation

Table 2 Simulation results of ternary half adder

Supply voltage (volts)	Static ternary half adder [19]		Proposed pseudo ternary half adder	
	Power (uw)	Delay (ps)	Power (uw)	Delay (ps)
0.7	299.6	18.35	339.0	12.79
0.8	361.6	13.54	370.3	9.79
0.9	449.4	10.64	450.9	8.36

References

1. Nagulapalli R, Hayatleh K, Barker S, Zourob S, Yassine N, Reddy BNK (2018) A technique to reduce the capacitor size in two stage miller compensated Opamp. In: Proceedings of the 9th international conference on computing, communication and networking technologies (ICCCNT), pp 1–4
2. Sharifi MJ, Ahmadian M (2018) Novel designs for digital gates based on single electron devices to overcome the traditional limitation on speed and bit error rate. Microelectron J 73:12–17
3. AlKaldy E, Majeed AH, Zainal MS, Nor DM (2020) Optimal multiplexer design in quantum-dot cellular automata: says one researcher in Indonesian. J Electr Eng Comput Sci 17(1): 148–155
4. Taheri Tari H, Dabaghi Zarandi A, Reshadinezhad MR (2019) A high- performance CNTFET-based complete adder cell for use in carry ripple, carry choose, and carry skip adders: says the paper. Microelectron Eng 215:110980
5. Davari Shalamzari Z, Dabbaghi Zarandi A, Reshadinezhad MR (2019) The publication describes it as "a high-performance CNTFET-based full adder cell for usage in carry ripple, carry choice, and carry skip adders. Microelectron Eng 215:110980
6. Hills G, Lau C, Wright A, Fuller S, Bishop MD, Srimani T, Kanhaiya P, Ho R, Amer A, Stein Y, Murphy D, Chandrakasan A, Shulaker MM (2019) Modern microprocessor built from complementary carbon nanotube transistors. Nature 572(7771):595–602
7. Lin S, Kim YB, Lombardi F (2011) CNTFET-based design of ternary logic gates and arithmetic circuits. IEEE Trans Nanotechnol 10(2):217–225
8. Dhande A, Ingole V (2005) Design and implementation of 2-bit ternary ALU slice. In: Proceedings international conference IEEE science electronic, technologies, information and telecommunications, 2005, pp 17–21
9. Moaiyeri MH, Rahi A, Sharifi F, Navi K (2017) Design and evaluation of energy-efficient carbon nanotube FET-based quaternary minimum and maximum circuits. J Appl Res Technol 15(3):233–241
10. Hosseini SA, Etezadi S (2020) A novel very low-complexity multi- valued logic comparator in nanoelectronics. Circuits Syst Signal Process 39(1):223–244
11. Shirinabadi Farahani S, Reshadinezhad MR (2019) A new twelve- transistor approximate 4:2 compressor in CNTFET technology. Int J Electron 106(5):691–706
12. Tabrizchi S, Sharifi H, Sharifi F, Navi K (2016) Design of ultra low power ternary half adder and multiplier for nanotechnology. J Nanoelectron Optoelectron 11(6):730–737
13. Soltani M, Charmchi N, Reshadinezhad MR (2016) Optimization of MVL logic gates using carbon nanotube field effect transistors. Proc Int Conf Nanotechnol 1–7
14. Srinivasu B, Sridharan K (2016) Low-complexity multiternary digit multi- plier design in CNTFET technology. IEEE Trans Circuits Syst II Exp Briefs 63(8):753–757
15. Sahoo SK, Akhilesh G, Sahoo R, Muglikar M (2017) High-performance ternary adder using CNTFET. IEEE Trans Nanotechnol 16(3):368–374
16. Kim S, Lim T, Kang S (2018) An optimal gate design for the synthesis of ternary logic circuits. In: Proceedings of the 23rd Asia South Pacific Design Automation Conference (ASP-DAC), Jan 2018, pp 476–481

17. R. A. Jaber, A. Kassem, A. M. El- Hajj, L. A. El-Nimri, and A. M. Haidar :"High-performance and energy-efficient CNFET-based designs for ternary logic circuits" : *IEEE Access*, vol. 7, pp.93871–93886, 2019.
18. Jaber RA, El-Hajj AM, Kassem A, Nimri LA, Haidar AM (2020) CNTFET-based designs of ternary half-adder using a novel 'decoder-less' ternary multiplexer based on unary operators. Microelectron J 96: 104698

A Low Mismatch Current Steering Charge Pump for High-Speed PLL

Subham Roy, Kirankumar H. Lad, S. Rekha, and T. Laxminidhi

Abstract This paper presents the design of a charge pump based on the current steering and positive feedback topology to support application in high-speed PLLs. The primary objective of the design is to counter current mismatch in charging and discharging currents as well as maintain fast operation with the help of positive feedback assisted current steering topology. This charge pump is designed in UMC 65nm CMOS technology and its functionality, characteristics and amount of current mismatch are verified across voltage and temperature variations.

Keywords Charge pump · Current steering · Phase-locked loop · High speed

1 Introduction

As the frontier of electronic device design moves toward higher speeds of operation, the need for high-speed sources of clock becomes paramount. Such signals find their use in data synchronization, as carrier signals in serializer line codes and as primary inputs in all kinds of digital sequential circuits to enumerate a few applications. Charge pump PLL (CP-PLL) is an ubiquitous architecture for PLLs which has a relatively simple design along with the ability to quickly adjust to phase and frequency errors.

A CP-PLL is essentially a control system employing negative feedback. A typical CP-PLL consists of four main components namely a phase-frequency detector (PFD), a charge pump (CP), a passive loop filter (LF) and a voltage controlled oscillator (VCO). Most modern designs of CP-PLL have the charge pump incorporated with phase-frequency detector and a loop filter.

S. Roy (✉) · K. H. Lad · S. Rekha · T. Laxminidhi
Department of Electronics and Communication Engineering, National Institute of Technology Karnataka, Surathkal 575025, India
e-mail: subhamroy1995@gmail.com

S. Rawat et al. (eds.), *Proceedings of Second International Conference on Computational Electronics for Wireless Communications*, Lecture Notes in Networks and Systems 554,
https://doi.org/10.1007/978-981-19-6661-3_40

1.1 Working of a CP-PLL

The purpose of the PFD is to generate error signals based on the phase-frequency error between the output signal generated by the PLL and the reference signal. These signals are often termed as UP and DN signals which then drive the CP which essentially acts as a switchable constant current source whose direction (sourcing or sinking) depends on whether the UP or DN signal is active a certain point of time. The LF bandlimits the output of CP as well as converting the output current signal of the CP to a voltage to drive the VCO, which in turn produces the output frequency. Thus, the loop is setup in such a way to minimize the phase-frequency error. The loop is said to be phase-locked when the output signal phase is equal to the phase of the reference signal. In such a condition, the CP will, ideally, receive no error signal (UP or DN), thus keeping the VCO input control voltage steady [8].

A high-speed charge pump design takes minimum possible time to reach the peak output charging or discharging current $\pm I_{\mathrm{CP}}$.

A conventional charge pump [7] is shown in Fig. 1. It consists of two pairs of transistors of which one pair generally comprises a constant biased MOS (M_{source} and M_{sink}) to generate a fixed current and the other pair (M_1 and M_2) functions as switches in the presence of appropriate signals, namely $\overline{\mathrm{UP}}$ and DN. The load capacitor C_{LF} acts as a simple loop filter.

Since the source and sink currents are produced by two different devices (PMOS and NMOS), there is always a mismatch between the two currents even if the widths of transistors are specifically set to combat it. This is because of variations during the fabrication stage. This mismatch in the two currents results in the resulting PLL system having jitter due to charge pump's lopsided response [6].

This problem is generally tackled by the introduction of a feedback loop that minimizes the current mismatch error. Hwang et al. [4] mention such a technique where two replica bias generation circuits (called compensators) are used to bias the

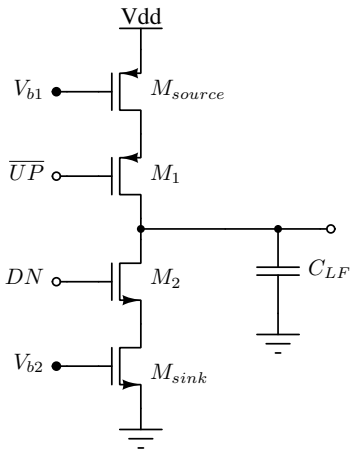

Fig. 1 A conventional charge pump [7]

MOS current sources in the charge pump. These compensators employ op-amps to track error voltage signal at the charge pump output node and generate an appropriate bias voltage accordingly. However, this approach suffers from power as well as area overhead. Also, finite open-loop gain of an op-amp limits the matching between the currents.

Amer et al. [1] propose another topology for charge pump based on current steering technique which performs mismatch cancelation employing only one op-amp. The design only adjusts I_{DN} according to I_{UP}. An op-amp is used to generate the bias voltage for the tail transistors for the DN current steering branches, based on an error signal between charge pump output and current signal value of I_{UP}. The current signal value of I_{UP} is obtained from one of the branches of the UP current steering network.

2 Proposed Charge Pump Design

The proposed design is an amalgamation of current steering and current mismatch cancelation techniques. The aim of the design is to obtain improvement on the following fronts:

1. High current output slew rate or low transition times.
2. Independence of output slew rate with respect to the transition time of the UP and DN signals.
3. Equal charging and discharging currents.

The proposed design is depicted in Figs. 2 and 3.

To achieve the above-mentioned improvements, the conventional CP circuit is added with several subcircuits, which are as follows.

2.1 Current Steering Branches

Current steering architectures are a popular way of designing high-speed switching circuits where maintaining low power consumption is not a priority. Current steering circuits generally have two or more branches, of which at least one always remains conductive through a tail current source. Since the tail current source always remains on irrespective of the state of the rest of the circuit, the switching transition times become independent of the tail current source, thus increasing switching speed.

For the proposed design, two pairs of current steering branches are employed each for UP and DN subcircuits. These branches are composed of the transistors M_3-M_7-M_9, M_6-M_8-M_9 and M_{10}-M_{14}-M_{16}, M_{13}-M_{15}-M_{16}. Since each of the branch is driven by complimentary inputs (either UP/DN or $\overline{\text{UP}}/\overline{\text{DN}}$), only one leg of each branch will be conducting at any point of time. Additional tail capacitors C_{tail1} and

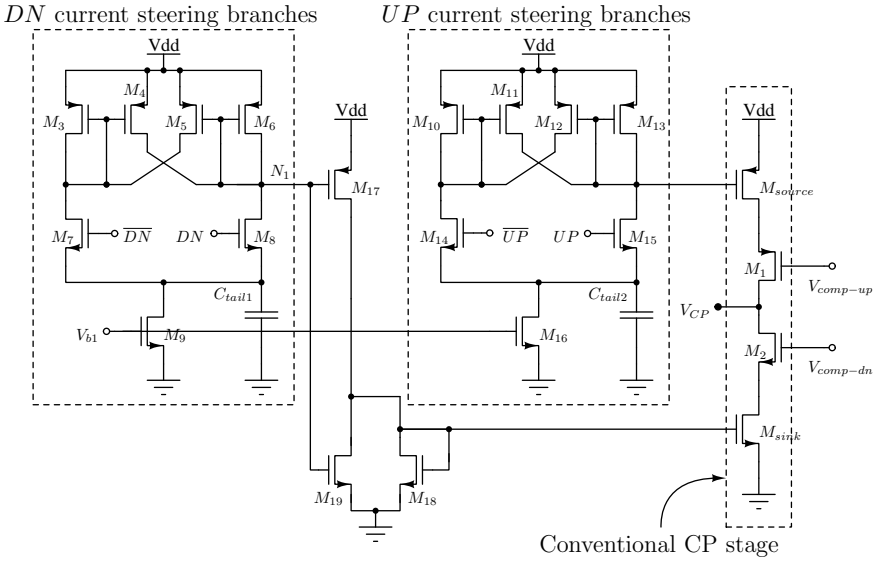

Fig. 2 Proposed charge pump schematic

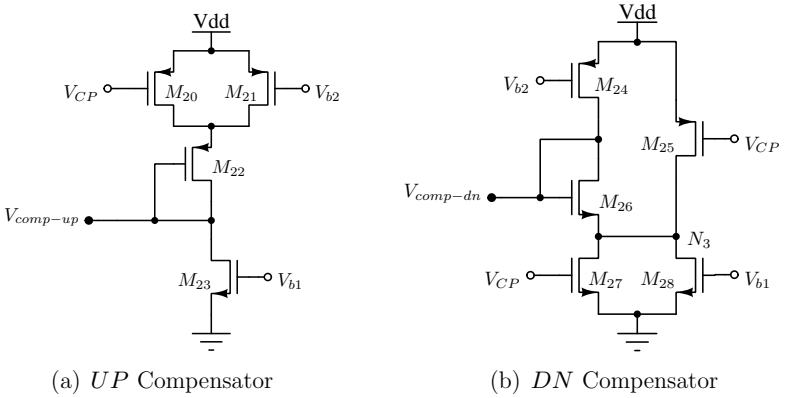

Fig. 3 Compensator subcircuits

C_{tail2} are added to support high-speed operation. The purpose of these capacitors is to hold the tail voltage constant during transition phase of the current steer action.

An additional effect of the current steering branches is that the output transition time becomes fairly independent of the input signal transition time. According to simulations, an order of increase in the input signal transition times only produces about 1.5 times increase in the output signal transition time.

Since both current steering networks' outputs is the V_{SG} voltages of PMOS transistors, this current steering network output can be directly provided to the PMOS gate input (of the transistor M_{source}) at the CP output stage. However, for the NMOS

gate input (of the transistor M_{sink}), the same is not possible. Drive for M_{sink} is derived from the DN current steering branch output using a network comprised of transistors M_{17}, M_{18} and M_{19}. M_{17} and M_{18} form an inverter and M_{19} acts as a weak pull-down element. M_{19} is used to decrease the fall transition time of the voltage at the gate of M_{sink}.

Transistors M_4,M_5 and M_{11}, M_{12} add positive feedback to UP and DN branches, respectively. The resulting regenerative mechanism helps in increasing the speed of switching [5].

Without positive feedback transistors M_4 and M_5, diode-connected transistors M_3 and M_6 are solely acting as pull-up devices providing a slow path. With the introduction of transistor M_4 and M_5, when transistor M_7 turns ON, M_4 also turns ON to act as a pull-up device for node N_1 along with transistor M_6, thus improving the rise transition time of the current steering branches.

2.2 Compensator Subcircuits

Two compensator circuits [4] are employed to generate the gate voltages for the transistors M_1 and M_2. The compensator circuits are depicted in Fig. 3a, b. Each of the compensator circuit works in negative feedback with the help of the V_{CP} voltage signal.

Each compensator subcircuit consists of a MOSFET constant current source (M_{23} and M_{24}) along with MOSFET variable current sources which are dependent on the CP output voltage signal V_{CP}. Thus, as V_{CP} varies, the bias voltages for transistors M_1 and M_2 ($V_{\text{comp-up}}$ and $V_{\text{comp-dn}}$) vary accordingly. The amount of sensitivity is determined by the dimensions of feedback transistors M_{20} and M_{27}.

According to Fig. 6b, I_{UP} decreases and I_{DN} increases when V_{CP} changes by a small positive value. Consequently, at the UP compensator, source-drain current for M_{19} will show a small negative change, thus total current passing through M_{21} will decrease causing a decrease in the gate bias voltage of transistor M_1. This causes an increase in the source-gate voltage of M_1. Hence, source-drain current through M_1 or I_{UP} will increase, thus counteracting the current mismatch of the conventional charge pump. Similar counteractive action is performed by the DN compensator as well, thus maintaining both I_{UP} and I_{DN} equal.

This phenomenon can be verified mathematically as well using small signal analysis for the UP compensator. Figure 4 depicts the UP compensator transistors replaced with small signal models. For simplicity of analysis, it is assumed that V_{CP} is such that both M_{20} and M_{21} are in saturation mode of operation. Applying KCL at nodes $V_{\text{comp-up}}$ and N_4 in Fig. 4, following expressions can be obtained.

$$g_{m20}(V_{\text{DD}} - V_{\text{CP}}) + g_{m21}V_{\text{DD}} = V_{N_4}(r_{20}||r_{21}) + \left(g_{m22} + \frac{1}{r_{22}}\right)(V_{N_4} - V_{\text{comp-up}}) \tag{1}$$

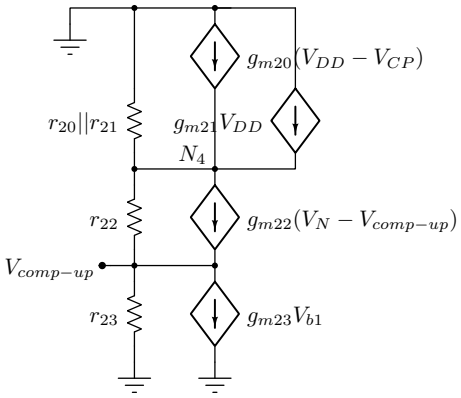

Fig. 4 Small signal model for UP compensator

$$\left(g_{m22} + \frac{1}{r_{22}}\right)(V_{N_4} - V_{\text{comp-up}}) = \frac{V_{\text{comp-up}}}{r_{23}} + g_{m23}V_{b1} \tag{2}$$

Using above expressions

$$V_{\text{comp-up}} = \frac{r_{23}\left(g_{m22} + \frac{1}{r_{22}}\right)\left[V_{\text{DD}}(g_{m20} + g_{m21}) - \mathbf{V_{CP}} \cdot \mathbf{g_{m20}}\right]}{g_{m22} + \frac{1}{r_{22}} + \frac{1}{r_{20}||r_{21}}} - V_{b1}g_{m23}r_{23} \tag{3}$$

Thus, for a small change in V_{CP}

$$\delta V_{\text{comp-up}} = -\delta V_{\text{CP}} \cdot \left[\frac{r_{23}g_{m20}\left(g_{m22} + \frac{1}{r_{22}}\right)}{g_{m22} + \frac{1}{r_{22}} + \frac{1}{r_{20}||r_{21}}}\right] \tag{4}$$

Thus, when V_{CP} rises, the compensator tries to decrease $V_{\text{comp-up}}$, thus forcing I_{UP} to increase and vice versa for I_{DN}. This behavior is also verified by simulation output for $V_{\text{comp-up}}$ w.r.t V_{CP} which is depicted in Figs. 5, 6 and 7.

In order to increase the voltage headroom available at the output, the DN compensator employs a weak pull-up transistor M_{25}. The effect of transistor M_{25} is evident at low V_{CP} voltages when the transistor turns ON slightly pulling the voltage at node N_3 up. Consequently, $V_{\text{comp-dn}}$ is increased slightly more than the value and it would have been with only M_{27} turning off at low V_{CP} voltage. Thus, even at low V_{CP}, voltages transistor M_2 can provide the same amount of drain-source current. The effect of adding the weak pull-up M_{25} on the CP characteristic is depicted in Fig. 8. Further increase in the voltage headroom has been obtained by using the low threshold voltage variants of transistors for M_{20} and M_{27}.

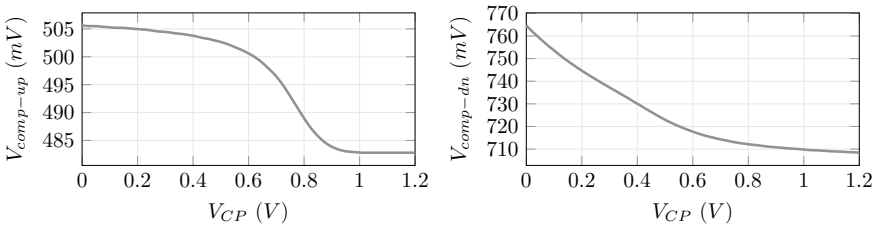

Fig. 5 Compensator subcircuit output voltage w.r.t V_{CP}

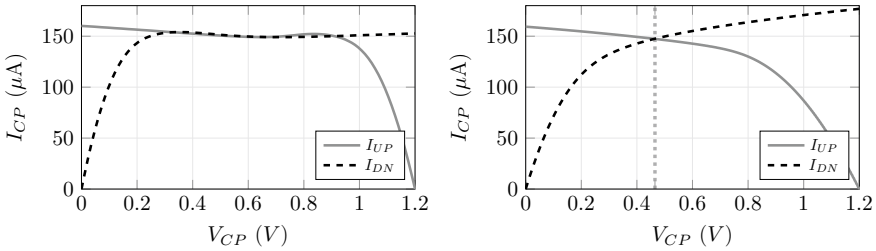

Fig. 6 Comparison of IV characteristics of proposed and conventional designs

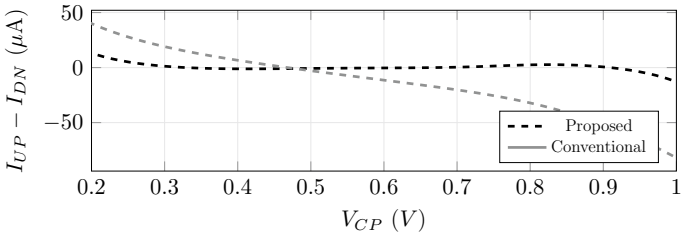

Fig. 7 Mismatch I for proposed and conventional design

The variation of output voltages of the compensator subcircuits with respect to V_{CP} is depicted in Fig. 5. The compensator subcircuits and output CP stage have been designed in such a way that the variation in $V_{comp\text{-}up}$ and $V_{comp\text{-}dn}$ can provide varying bias to the output CP stage to minimize charging and discharging current mismatch.

3 Results

Simulation was done for both the proposed design and the conventional design using Cadence ADE L Simulation Suite using UMC 65 nm technology.

IV characteristics of the proposed design and the conventional design are depicted in Fig. 6a, b respectively (Table 1).

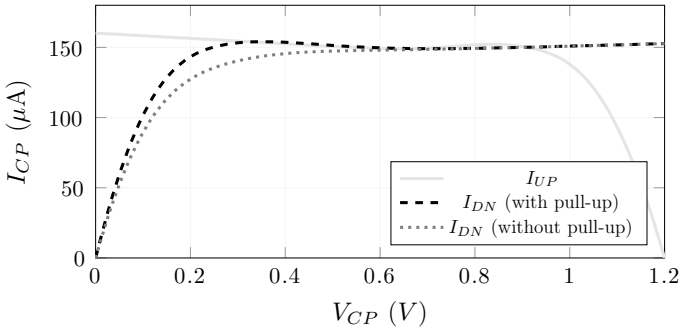

Fig. 8 Effect of addition of weak pull-up transistor M_{25} in Fig. 3b

Table 1 Comparison of proposed design with the conventional design

	Proposed design	Conventional
Designed I_{CP} (μA)	150	150
Compliance range (V)	0.31–0.92	0.3–0.65
Typical I mismatch	0.13–1.77%	$\approx$ 10%

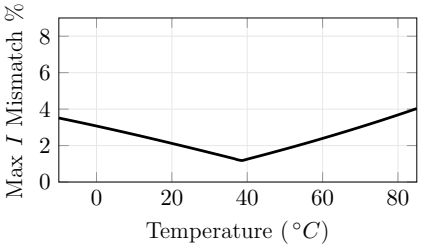

(a) Variation of Max I Mismatch % (in the designed compliance range) with Temperature

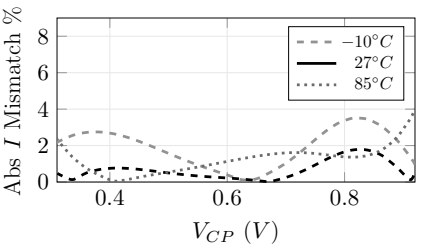

(b) I Mismatch at different temperatures within the designed compliance range of V_{CP}

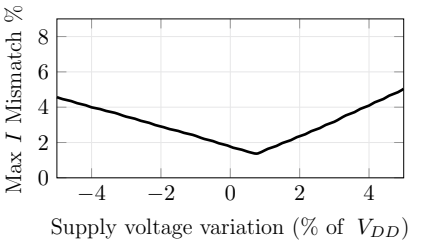

(c) Variation of Max I Mismatch % (in the designed compliance range) with supply voltage variation

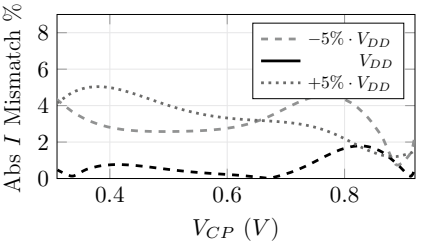

(d) I Mismatch at different supply voltages within the designed compliance range of V_{CP}

Fig. 9 Variation of I mismatch at various operating corners

From the IV characteristics, it can be observed that the charging and discharging currents are matching for a substantial span of the output voltage (V_{CP}). This is due to the effect of the compensator circuits.

An additional effect of using compensator circuits is that they provide a fair amount of gain boosting [2] at the output node of CP which manifests as the CP showing a considerably higher output resistance compared to conventional design as evident from Fig. 6.

Figure 9a, c shows the percentage of Maximum I Mismatch w.r.t the designed charge pump current. For the proposed design, Absolute I mismatch percentage and Max I mismatch percentage are defined as

$$\text{Abs } I \text{ Mismatch } \% = \frac{|I_{UP} - I_{DN}|}{150\,\mu\text{A}} \times 100\% \tag{5}$$

$$\text{Max } I \text{ Mismatch } \% = \frac{\underset{V_{CP}\in[0.31,0.92]}{\text{Max}}(|I_{UP} - I_{DN}|)}{150\,\mu\text{A}} \times 100\% \tag{6}$$

4 Conclusion

It was observed from the data obtained from simulations that the proposed design shows significant improvements over conventional CP design, without the use of operational amplifiers. Thus, unlike CP designs employing operational amplifiers [3], using dynamic mismatch compensator circuits a CP with a considerably less area requirement and a substantially low current mismatch can be obtained.

However, at extremely low and high temperatures (around −10 and 85 °C), mismatch in currents may be slightly more due to higher thermal sensitivity variation among both of the compensation subcircuits. This can be tackled by fine-tuning the sizes of compensation network transistors, but this is often limited by the choice of technology or process node.

References

1. Amer AG, Ibrahim SA, Ragai HF (2016) A novel current steering charge pump with low current mismatch and variation. IEEE Int Symp Circ Syst (ISCAS). https://doi.org/10.1109/ISCAS.2016.7538887
2. Boon CC, Krishna MV, Do MA, Yeo KS, Do AV, Wong TS (2012) A 1.2 v 2.4 GHz low spur CMOS PLL synthesizer with a gain boosted charge pump for a batteryless transceiver. In: IEEE international symposium on radio-frequency integration technology (RFIT). https://doi.org/10.1109/RFIT.2012.6401667
3. Cheng S, Tong H, Silva-Martinez J, Karsilayan AI (2006) Design and analysis of an ultrahigh-speed glitch-free fully differential charge pump with minimum output current variation and

accurate matching. IEEE Trans Circ Syst II Express Briefs 53. https://doi.org/10.1109/TCSII.2006.879100
4. Hwang MS, Kim J, Jeong DK (2009) Reduction of pump current mismatch in charge-pump PLL. Electron Lett 45(3). https://doi.org/10.1049/el:20092727
5. Juarez-Hernandez E, Diaz-Sanchez A (2002) A novel CMOS charge-pump circuit with positive feedback for PLL applications. In: ICECS 2001, 8th IEEE international conference on electronics, circuits and systems. https://doi.org/10.1109/ICECS.2001.957751
6. Lad Kirankumar H, Rekha S, Laxminidhi T (2021) Low mismatch high-speed charge pump for high bandwidth phase locked loops. Microelectron J 114:105156
7. Razavi B (2020) Design of CMOS phase-locked loops, from circuit level to architecture level. Cambridge University Press
8. Rogers J, Plett C, Dai F (2006) Integrated circuit design for high-speed frequency synthesis. Artech House, London

An Ultralow-Power CMOS Integrated and Fire Neuron for Neuromorphic Computing

Md. Nazmul Haque, Samiur Rahman Khan, Md. Tarikul Islam, Jatoth Deepak Naik, AlaaDdin Al-Shidaifat, Sandeep Kumar, and Hanjung Song

Abstract Very large-scale integration (VLSI) implementations of spiking neurons are vital for a range of applications, from high-speed modeling of large neural systems to real-time behavioral systems and bidirectional brain-machine interfaces. The circuit solution utilized to implement the silicon neuron is determined by the application's needs. This paper describes an ultralow-power analog circuit for realizing a leaky integrate and fire neuron model. The suggested circuit comprises parts for executing spike-frequency adaptation and modifying the neuron's threshold voltage, in addition to being designed for low-power consumption.

Keywords Neuromorphic computing · Silicon neuron circuit · Neural network · Artificial neuron · Integrated and fire neuron

1 Introduction

Spike-based models of neurons have lately gained popularity as a tool for both researching the purpose of signal in cognitive neuroscience and developing neuromorphic engineering event-driven computing techniques. In this context, spike-driven neuromorphic simulations have been investigated, and lot of study has focused

Md. N. Haque (✉) · S. R. Khan · Md. T. Islam · J. D. Naik · A. Al-Shidaifat · H. Song
Department of Nanoscience and Engineering, Inje University, Gimhae 50384, Korea
e-mail: nazmul@oasis.inje.ac.kr

S. R. Khan
e-mail: samikhan@oasis.inje.ac.kr

Md. T. Islam
e-mail: tarikul@oasis.inje.ac.kr

H. Song
e-mail: hjsong@inje.ac.kr

S. Kumar
Department of Electronics and Communication Engineering, NITK, Surathkal, Mangaluru, India
e-mail: sandeep@nitk.edu.in

S. Rawat et al. (eds.), *Proceedings of Second International Conference on Computational Electronics for Wireless Communications*, Lecture Notes in Networks and Systems 554,
https://doi.org/10.1007/978-981-19-6661-3_41

on methods and software tools for simulating spiking neural networks [1]. The inquiry into the topic of neuromorphic engineering began with the discovery that the brain functions on analog methods of the mechanics of neural computation, which are fundamentally distinct from digital ideas in classical computing (Mead 1989) [2, 3]. Large-scale spiking neural network array [2] has been proposed for mimicking the brain. Silicon neurons (SiNs) are VLSI circuits that are hybrid analog/digital and mimic the electrophysiological behavior of biological neurons and conductances [4, 5].

They are perfect for real-time, extensive brain simulations since they consume far less power than general-purpose computer simulations [6]. SiN circuits, on the other hand, are inappropriate for rigorous quantitative study since they only provide a qualitative estimate of the actual functioning of digitally replicated neurons. SiN circuits provide a clear advantage when exploring issues concerning the device's exact real-time interaction with its surroundings. These real-time, less-power neuromorphic devices can be made with technology that can also be used to develop computational methods for practical problems [6].

Small currents are frequently integrated onto a capacitor in integrate and fire circuits until a minimal voltage level is achieved [7]. A transient digital signal is produced, signaling the presence of a spike, whenever the voltage here on capacitor reaches the limit, and the capacitor is then restored. These circuits are generally found in large arrays on neuromorphic circuits that implement layers of spiking neurons or on neuromorphic systems that use spiking components to transmit sensory inputs to other neuromorphic functional units. With spike-frequency adaptability, refractory length, and voltage cutoff modulation capabilities, we provide an amazingly low leaky integrate and fire circuits model to achieve this. For the implementation using integrate and fire (I&F) cell models, a number of circuits have been created [8–10]. Implementation of a large-scale neural modeling for a neuromorphic hardware system [8]. Highly accelerated integrated and fire neurons synaptic plasticity [9] is implemented. A VLSI one dimensional array of I&F neurons [10] and adaptive plastic synapses network have been developed. The circuit's features are described in depth, and experimental data from cadence virtuoso utilizing conventional 1.8 um CMOS technology is presented.

2 Circuit Implementation

Figure 1 shows the suggested circuit diagram for an I&F neuron. A current integrator M2–M5, a source follower M9–M10, an inverter with positive feedback M6–M7 and M11–M13 is used to reduce the energy uses of circuits, an inverter with adapting slew-rate M14–M16, an inverter M17–M18 being used generate digital signals, an integrating capacitor C_{mem}, and a transistor M1 are used to regulate the leak current.

C_{mem} integrates the input current I_{inj} onto V_{mem}. C_{mem} is 100 F in the current implementation. Injection currents are typically in the tens of picoamperes range. $V_{\text{in}} = k(V_{\text{mem}}–V_b)$ is produced by the source follower M9–M10, where k is the

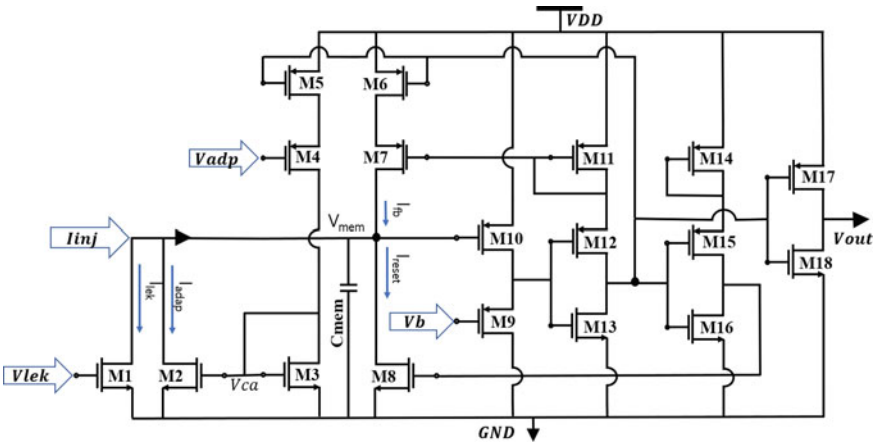

Fig. 1 Schematic diagram of ultralow-power integrate and fire neuron

sub-threshold gradient coefficient, and V_b is a constant sub-threshold bias voltage [11]. The feedback current I_{fb} starts to flow across M6–M7, rising and accelerating as V_{mem} increases, and V_{in} gets closer to the switching voltage of the first inverter. Positive feedback causes the inverter M11–M13 to switch very quickly, resulting a significant decrease in power losses. The voltage is increased to V_{DD}, membrane capacitor C_{mem} is swiftly discharged to zero by resetting transistor M8, and V_{out} is reset to zero voltage. During the upswing, emission period, a current with an amplitude specified by V_{adap} is delivered to the gate to source capacitance of M2 on node V_{ca} (when V_{out} is high). As a result, the voltage V_{ca} rises with each spike, but when no spiking activity occurs, V_{ca} steadily falls to zero due to leakage currents. The input is removed as V_{ca} increases by a negative adjusting current I_{adap} that is exponential inverse to V_{ca}, and the neuron's firing rate gradually lowers. When V_{mem} is passed to ground, it is pushed back to $V_{\text{DD,}}$ which fully activates M10. Voltage from inverter M15–M16 discharged across the route M8. The reset transistor M8 is operational, and V_{mem} is clamped to ground. The neuron cannot spike during this "refractory" period because M8 absorbs all of the input current I_{inj}, which is normally smaller than the reset current.

3 Measuring the Sub-Threshold Behavior of Neurons

The overall current integrated by C_{mem} is $I_{\text{inj}} - I_{\text{lek}} + I_{\text{fb}} - I_{\text{adap}}$, where I_{adap} is the adaptation current produced by the pulses adaptation mechanism, I_{lek} is a leakage current determined by a fixed gate voltage V_b, I_{fb} is the positive reaction current, and I_{inj} is the external input current. Weak-inversion formulas for the transistor are used for calculating the adaption curve [10].

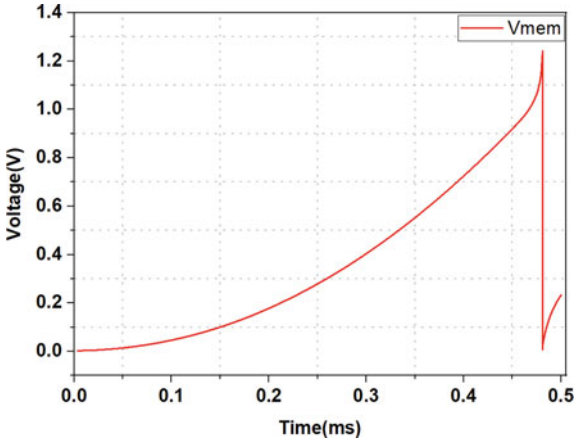

Fig. 2 Measurement results depicting a typical spike shape of integrate and fire neuron

$$I_{\text{adap}} = I_0 e^{\frac{kV_{\text{ca}}}{U_T}} \left(1 - e^{-V_{\text{mem}}/U_T}\right) \tag{1}$$

where U_T, thermal voltage and $I_{0,}$ low current of the transistor (12) (Fig. 1).

4 Simulation Results

This circuit is simulated in cadence using 1.8 μM CMOS process. The graph depicts the input current which is denoted by I_{in}. V_{out} is the artificial neuron's output. The membrane capacitor's voltage is V_{mem}. When the membrane voltage crosses the threshold voltage, then neuron fires. The input current is denoted by I_{in}. V_{out} is the artificial neuron's output (Fig. 3). The membrane capacitor's voltage is V_{mem} (Fig. 2).

5 Power Consumption

The primary sources of power attenuation are the DC current flowing through the source follower M9–M10 times when $V_{\text{mem}} > (V_b + 4U_T)$, where U_T is the electric potential, and V_b is the bias or biased influence of the source follower, and the short-circuit currents flowing through inverters during switching period (Fig. 1). When there is no input current applied, the leakage current causes V_{mem} to be zero (under resting conditions). In this case, there is no power dissipation. When input current is supplied, the firing rate, V_b, and the power supply voltage, V_{DD}, determine how much power is dissipated. In Fig. 1, we introduced input currents of increasing amplitude while setting V_b to 0.45 V and V_{DD} to 1.8 V. The graph depicts how the current that flows through V_{DD} node grows the neuron's firing rate does (switching frequency).

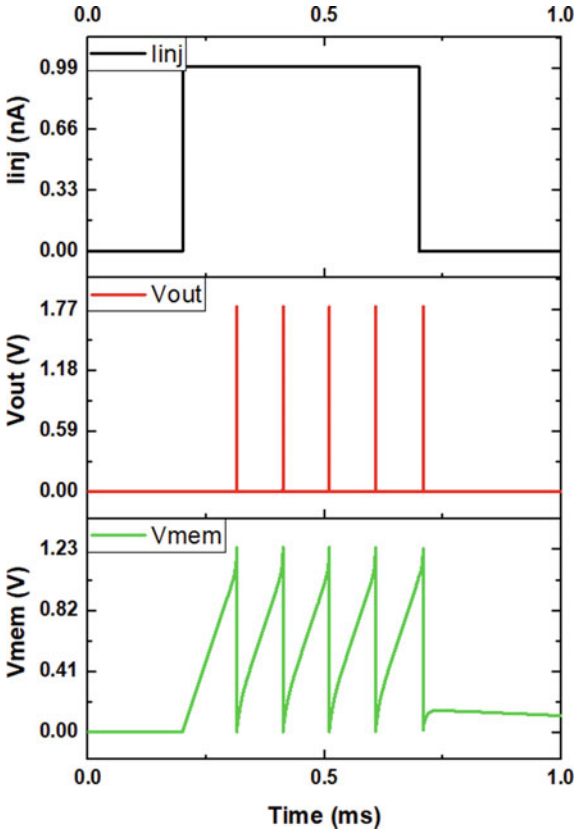

Fig. 3 Findings of neural circuits' transient simulations

We controlled the injection current so that the neuron's firing rate stayed constant at 200 Hz while gradually increasing V_b from 0.4 to 0.65 V in order to show how V_b influences power dissipation. The spike-frequency regulation mechanism is often used to maintain the neuron's mean firing rate below 10 Hz, while the refractory period is used to preserve the neuron's optimum firing rate below 200 Hz.

The average power consumption of the neuron under these settings, with V_{DD} set to 1.8 V and V_b set to 0.45 V, is 58 nW, with a high of 62 nW as shown in Fig. 4.

6 Conclusions

We developed an ultralow-power neuron circuit cell for constructing a leaky integrate and fire neuron prototype having a spike-frequency adaptation mechanism. Spike-frequency adaptation is effective ways to restrict and reduce the circuit's power usage only 60 nW that is highly efficient. For comparison, our proposed circuit minimum 10 times efficient than Axon-Hillock circuit. Circuit schematics and experimented

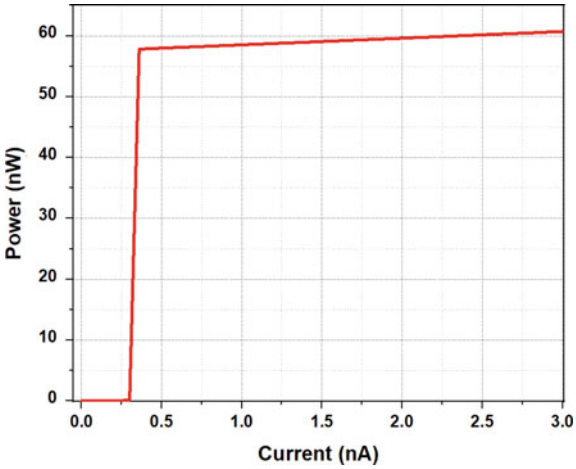

Fig. 4 Power consumption of LIF neuron

data that characterized all aspects of suggested circuit. In order to build neuromorphic multi-chip systems, goals to incorporate the I&F circuit in chips with vast arrays of neural network circuits.

Acknowledgements This research was supported by the Basic Science Research Program through the National Research Foundation of Korea (NRF) funded by the Ministry of Education, Science and Technology (NRF-2019R1F1A1056937). This research was also supported by the KOREA–INDIA joint program of cooperation in science and technology through the National Research Foundation of Korea (NRF) funded by the Ministry of Education, Science and Technology (NRF-2020K1A3A1A19086889). The chip fabrication and EDA tool were supported by the IC Design Education Center (IDEC), Korea.

References

1. Indiveri G et al (2011) Neuromorphic silicon neuron circuits. Front Neurosci 5:73
2. Thakur CS et al (2018) Large-scale neuromorphic spiking array processors: a quest to mimic the brain. Front Neurosci 891
3. Haque MN et al (2021) Analysis of analog neuron circuit using 180nm CMOS process for Brain-Inspired Neural Networks, pp 399–401
4. Serb A et al (2020) Memristive synapses connect brain and silicon spiking neurons. Sci Rep 10(1):1–7
5. Khan SR et al (2021) A study on different memristor model for neuromorphic applications, pp 402–404
6. Furber S (2016) Large-scale neuromorphic computing systems. J Neural Eng 13(5):051001
7. Wang Z et al (2018) Fully memristive neural networks for pattern classification with unsupervised learning. Nat Electron 1(2):137–145
8. Schemmel J et al (2010) A wafer-scale neuromorphic hardware system for large-scale neural modeling. In: 2010 IEEE International symposium on circuits and systems (ISCAS)
9. Schemmel J et al (2007) Modeling synaptic plasticity within networks of highly accelerated I&F neurons. In: 2007 IEEE International symposium on circuits and systems

10. Indiveri G, Chicca E, Douglas R (2006) A VLSI array of low-power spiking neurons and bistable synapses with spike-timing dependent plasticity. IEEE Trans Neural Networks 17(1):211–221
11. Ueno K et al (2009) A 300 nW, 15 ppm/°C, 20 ppm/V CMOS voltage reference circuit consisting of subthreshold MOSFETs. IEEE J Solid State Circuits 44(7):2047–2054

Logic Gates Using Memristor-Aided Logic for Neuromorphic Applications

Samiur Rahman Khan, Md. Nazmul Haque, Md. Tarikul Islam, Jatoth Deepak Naik, AlaaDdin Al-Shidaifat, Hanjung Song, and Sandeep Kumar

Abstract Data transfer rate has been a hornets' nest for modern systems memory and CPU. One of the more appealing potentials to overcome the limits is to combine memory and processing at the same site where the data is stored. Memory processing has been exhibited using memristor-aided logic (MAGIC) operations in memristor. In this paper, Ag/AgInSbTe/Ta (AIST)-based memristor has been used to implement the memristor-based logic design. A memristor-only logic family referred to as MAGIC technique is used to perform logic gates such as AND, OR, NOT, and NAND. The logical operations were executed using Verilog-A model, and the figures of those operations are shown.

Keywords Memristor · MAGIC · Crossbar · Ag/AgInSbTe/Ta-based memristor

1 Introduction

The performance of computer systems has dramatically improved over the previous few decades to meet the need of information technology enterprises. Computing processing efficiency and capability are regarded as a new standard in the big data environment, i.e., Internet of things (IoT) [1]. Electronic devices must be scalable to

S. R. Khan (✉) · Md. N. Haque · H. Song
Department of Nanoscience and Engineering, Inje University, Gimhae 50384, Korea
e-mail: samikhan@oasis.inje.ac.kr

Md. N. Haque
e-mail: nazmul@oasis.inje.ac.kr

H. Song
e-mail: hjsong@inje.ac.kr

Md. T. Islam · J. D. Naik · A. Al-Shidaifat · S. Kumar
Department of Electronics and Communication Engineering, NITK, Surathkal, Mangaluru, India
e-mail: tarikul@oasis.inje.ac.kr

S. Kumar
e-mail: sandeep@nitk.edu.in

S. Rawat et al. (eds.), *Proceedings of Second International Conference on Computational Electronics for Wireless Communications*, Lecture Notes in Networks and Systems 554,
https://doi.org/10.1007/978-981-19-6661-3_42

reduce manufacturing costs, boost speed, and minimize power consumption in order to improve computing efficiency. So far CMOS technology improvement has been fulfilling the requirement. This technology has already reached its limit. As things are becoming smaller and smaller, new problems and challenges emerge, making the creation of smaller technology harder. Current leakage, high-power densities, reliability testing [2], and expensive calibration and production costs are among these issues. A variety of novel electrical elements have been investigated until now to fulfill the demand. A novel two-terminal device called memristor has a variety of appealing qualities among them. Non-volatile memory and low-power consumption [3] are anticipated to be its primary applications thanks to the memristor's ability to store values without a power source, and memristors can also be used to conduct logic operations. Different resistive states of the memristor are used to express logic values [4–6]. Most of the researches are aimed at leveraging them to develop a coherent and effective memory system that will eventually replace existing flash and CMOS-based memories [3–7]. Memristors' versatility creates new opportunities for avoiding the area, execution time, and energy consumption costs associated with reconfigurable hardware solutions. It paves the door for a slew of exciting new applications in this field. Substantial revisions are being explored to the present paradigms of computation, storage, and data access due to the features of memristive devices. A memristor is a two-terminal component whose resistance value is permanently switched between two states (non-volatile) by applying a voltage of a certain polarity, level, and duration. Other new technologies of non-volatile memory have been theoretically related to memristors; hence, the idea of memristor has been broadened to memristive devices [8].

1.1 Modeling of Memristor

The memristor was proposed as the 'missing circuit element' by Chua et al. [9] in 1971. The other three circuit elements were naturally the resistor, capacitor, and inductor. This novel element with hysteresis behavior acts as a resistor and connects flux and electrical charge. The equations that follow formalize this.

$$M(q) = \frac{d\Phi}{dq} \tag{1}$$

The memristance function can be used to illustrate how quickly flux changes (φ) with charge (q) in Eq. (1). A memristive device, commonly known as a memristor, is an 'analog memory' [10] having an analog state w that can be read out by measuring the device's conductance. Figure 1a shows the relationship of different elements between each other. Stanley Williams successfully created the first memristor in 2008 along with his colleagues at HP lab. It had two layers: the TiO_2 x layer, which was doped with oxygen vacancies, and the TiO_2 layer was not doped and had insulating qualities. Figure 1b shows the diagram of a memristor according to [11]. The

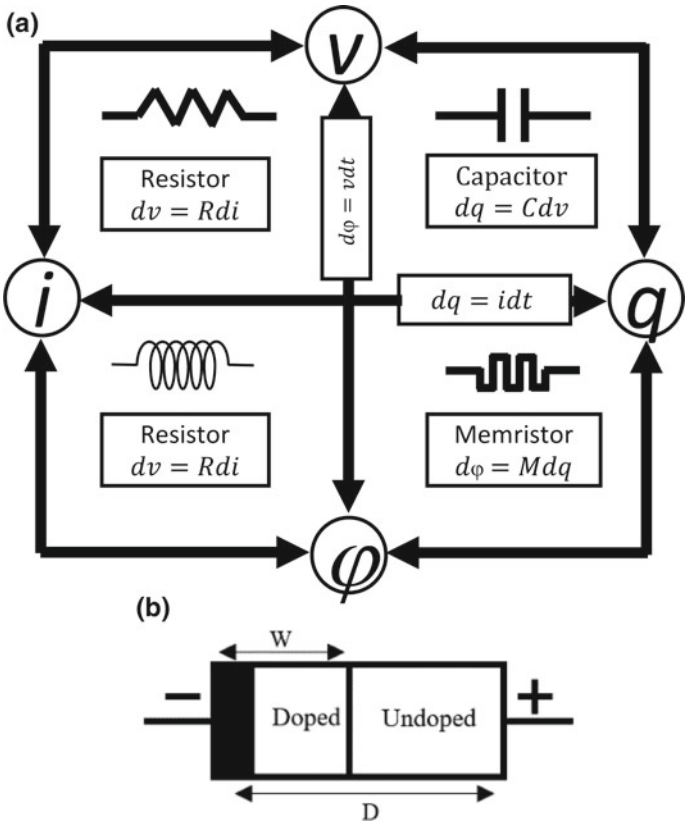

Fig. 1 **a** Four basic components of a two-terminal circuit, **b** HP memristor model

mathematical model that explains the operation of the memristor implies that the field is constant throughout the device. The formula in Eqs. (2) and (3) below is utilized to measure the device's resistance and voltage.

$$V(t) = R(t) * i(t) \tag{2}$$

$$R(t) = R_{\mathrm{ON}} \frac{w(t)}{D} + R_{\mathrm{OFF}} \left(1 - \frac{w(t)}{D}\right) \tag{3}$$

R_{ON} and R_{OFF} are, respectively, the memristor resistance limiting values for $w = D$ and $w = 0$.

An appropriate voltage can modify the resistive state of a memristors. Set pulses are positive voltage pulses that progressively force the memristor into the ON state. Lower voltage pulses over the memristor are known as reset pulses since they gradually turn the device off. Various circuit models for memristors have been presented for

studying memristor-based circuits. This enables a designer to model circuit designs and examine their performance using typical circuit simulation tools. The popular mathematical models are the linear ion drift model [11], the Simmons tunnel barrier model [12], the threshold adaptive memristor model (TEAM) [13], and the voltage threshold adaptive memristor model (VTEAM) [14].

With just a few extra volts, the device can produce a powerful electric field with nanoscale dimensions, and it causes a significant non-linearity in the ionic drift–diffusion. This impact is not considered in the preceding formulas. Various attempts to incorporate nonlinear behavior into the state equation have been made to tackle this problem. To get around this constraint, the initial solution suggested multiplying the state equation's second component by a 'window function', f(x). Various window functions, such as Joglekar's window function [15], Biolek's window function [16], and others, have been proposed to create nonlinearities in ion drift.

1.2 AIST Model

The memristors mentioned above cannot describe the synaptic characteristics of a memristor that can be used in artificial neural network for weight regulation. This work employs a voltage-controlled regulated threshold memristive model, which was compared with the analytical information of the Ag/AgInSbTe/Ag memristor (AIST memristor) [17]. Because of its synaptic behavior, it is somewhat logical to use AIST-based memristor for crossbar array of memristive neural networks. AIST memristors can be used to implement associative memory [18]. The resistance of the memristor continuously reduces as the voltage input crosses the threshold voltage V_{T+}, and consequently, if the voltage input is less than V_{T-}, the memristor's resistance will gradually increase. The numerical model of the Ag/AgInSbTe/Ag memristor is characterized by Eq. (4)

$$\frac{dw(t)}{dt} = \begin{cases} u_v \frac{R_{\mathrm{ON}}}{D} \frac{i_{\mathrm{off}}}{i(t)-i_0} f(w(t)), & v(t) > V_{T+} > 0 \\ 0, & V_{T-} \leq v(t) \leq V_{T+} \\ u_v \frac{R_{ON}}{D} \frac{i(t)}{i_{on}} f(w(t)), & v(t) < V_{T-} < 0 \end{cases} \tag{4}$$

This model is going to add a nonlinear ion drift phenomenon, with a Joglekar's window function [15] in Eq. (5)

$$f(w(t)) = 1 - \left(\frac{2w(t)}{D} - 1\right)^{2p} \tag{5}$$

This window assures no drift at the edges. Nonlinear drift is also imposed throughout the full active region D, and the model mimics linear dopant drift for high values of p.

1.3 Parameter of the Memristor

This simulated memristor has a maximum resistance of 450 (conductance 2.22 Ω^{-1}) and a minimum resistance of 20° (Conductance 50 Ω^{-1}).

The resistance value of the memristor will shift between 20 Ω and 450 Ω when the input voltage amplitude is beyond the positive threshold voltage (0.6 V) and the negative threshold voltage (− 0.20 V), respectively.

Here, i_{off}, $i_{0,}$ and i_{on} are constant. V_{T+} and V_{T-} are threshold voltages of opposite polarity and the migration rate of impurity layer. For this paper, $D = 3$ nm, $R_{\text{on}} = 20\ \Omega$, $R_{\text{off}} = 450\ \Omega$, $V_{T+} = 0.6\,\text{V}$, $V_{T-} = -0.20\,\text{V}$, $uv = 1.6\,\text{pm}$, $i_{\text{on}} = 1\,\text{A}$, $i_{\text{off}} = 10\,\text{uA}$, $i_0 = 1000\,\text{uA}$.

Figure 2a and b show gradual conductance and resistance change, respectively, after input voltage stimuli were given. The initial resistance for Fig. 2a was given 450 Ω (2.222 Ω^{-1})), therefore the memristor value starts from that region. For Fig. 3b, the initial resistance was given 340 Ω, and hence, the memristance started from that region and gradually increased because of the negative voltage given.

1.4 Applications

The resistance values indicate the logic states in MAGIC [4], a sort of memristive logic. Separate memristors are used to store the input bits in this logic family which can be indicated as In_1 and In_2. These two memristors, which will operate as inputs, are coupled in a parallel or series configuration. An additional memristor connected in series is employed as an output memristor, which will be used to store the result of the logic operation.

The logic state will be recorded as the output memristor's high or low resistance, a logical 'zero' will be a high resistance, and a logical 'one' will be a low resistance. Initially, the output memristor has to be programmed to high or low resistance. The logical state of the two input memristors, output memristor, and switches regulates the memristance of the output memristor once voltage stimuli are given. It is set to 0 for non-inverting gates such as AND/OR and 1 for inverting gates such as NOT/NOR/NAND. When both the inputs are on high resistance and the output memristor is on low resistance, the voltage across the two input memristors is substantially higher than that of the output memristor, therefore switching from low resistance to high resistance requires more voltage across the output memristor. The total memristance of the two input memristors will be much less if at least one of the inputs is initialized at low resistance.

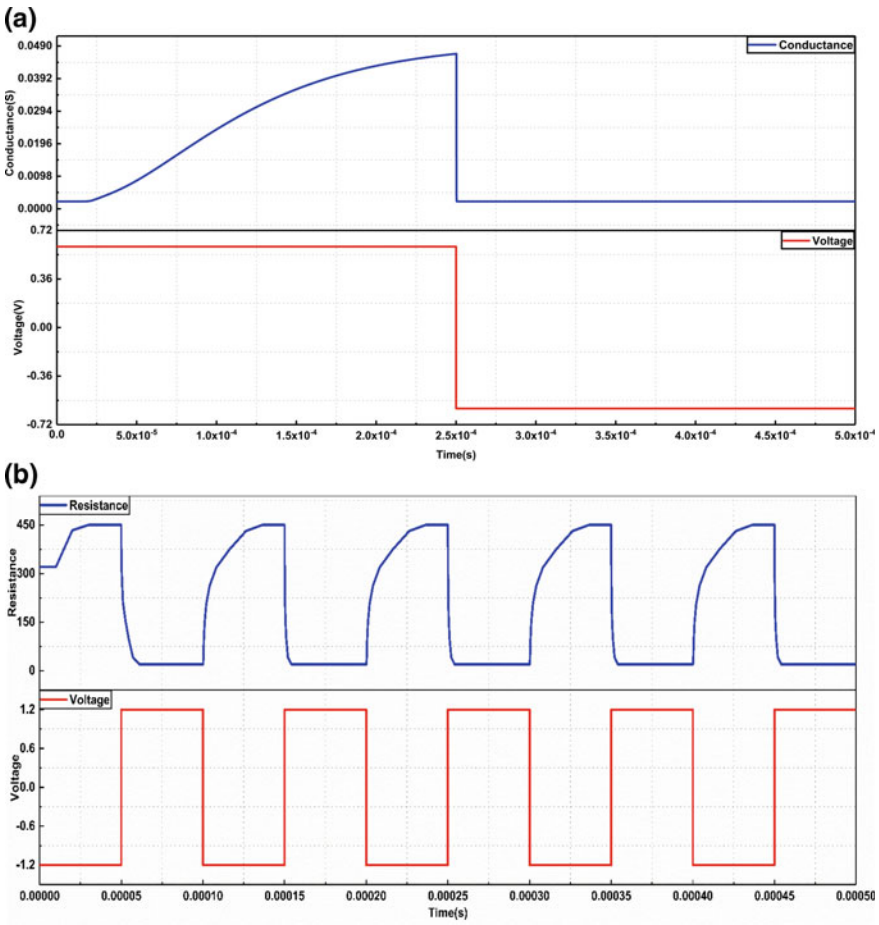

Fig. 2 **a** Change of conductance, **b** change of resistance

The voltage across the output memristor will therefore be high enough to change it to a high resistance. NOR gate comprises of two reverse polarity input memristors in parallel which are with a direct polarity memristor in series. A low resistance *R* is saved in the output memristor, and two input resistors are programmed as resistance R1 and R2 according to the logical input values. When a voltage pulse is provided to the input, the resistance of the output memristor depends on the resistance of the input values. The input memristors are in reverse polarity and parallel with each other, and the output memristor connects with them in series. NAND gate has two input memristors programmed with high resistance R1 and R2 and the output memristor with low resistance *R*. The input memristors are in reverse polarity with series connection, and the output memristor is connected with them in series. And gate has three memristors, including two input memristors and an output memristor.

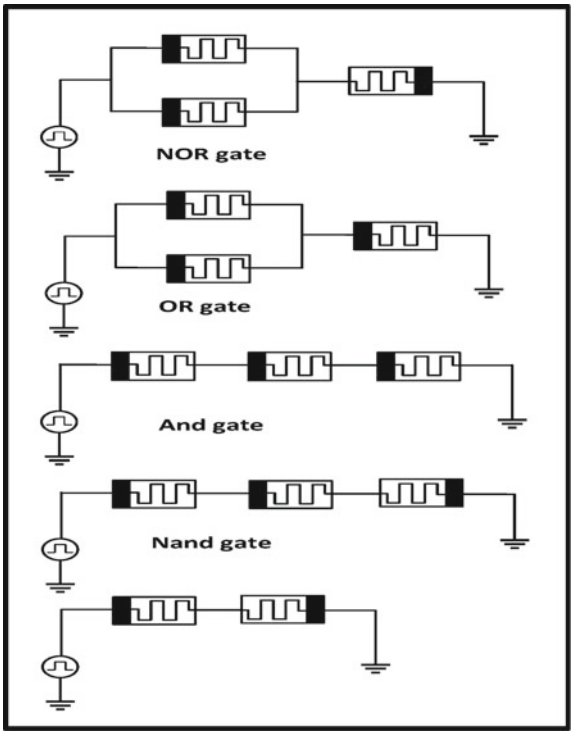

Fig. 3 Logic gates

All of these memristors are in series and reverse polarity. The NOT gate includes one input (reverse polarity) and one output (direct polarity) memristor in series. For high resistance R1, the voltage across the input memristor is high, and hence, there are limitations of given the voltage (Figs. 3–5).

Operation of a MAGIC logic gate can be harmful when resistance for input memristor is low (high) and the resistance switch to high (low) during the execution of the process. The limitations of input voltages are given in Table 1 (Figs. 6 and 7).

Take up the example of a memristor having V_{T+} and V_{T-} threshold voltages. For cases, where the voltage has to be greater or lower than threshold voltages to switch the resistance of the output memristor, galvanize a design limitation to the applied voltage to the input. Compared to the previous works [4], which was implemented using the VTEAM model, this work shows design limitation in the negative scale, which can give different dimension while designing a complex system, especially system such as memristive neural networks, which involves changing conductance in the network to yield the required current to drive the next load. Table 1 shows a comparison of voltage limitation of two models (Figs. 8 and 9).

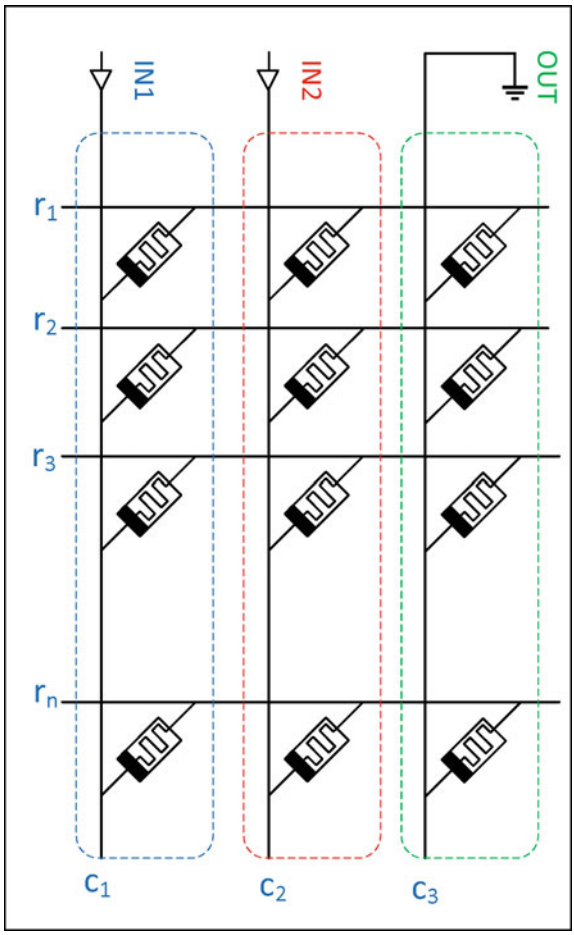

Fig. 4 MAGIC NOR in crossbar

1.5 Crossbar Array

Though the MAGIC design style can be used to build any gate, memristor crossbar mapping is limited to the NOR and NOT gates. Crossbars connect the memristors at the intersections of horizontal and vertical nanowires. Figure 4 illustrates the crossbar mapping for the NOR gate. For synthesizing complex Boolean functions, gates are first mapped to crossbars using various mapping techniques [19, 20]. This model has been applied in several crossbar applications [21–23].

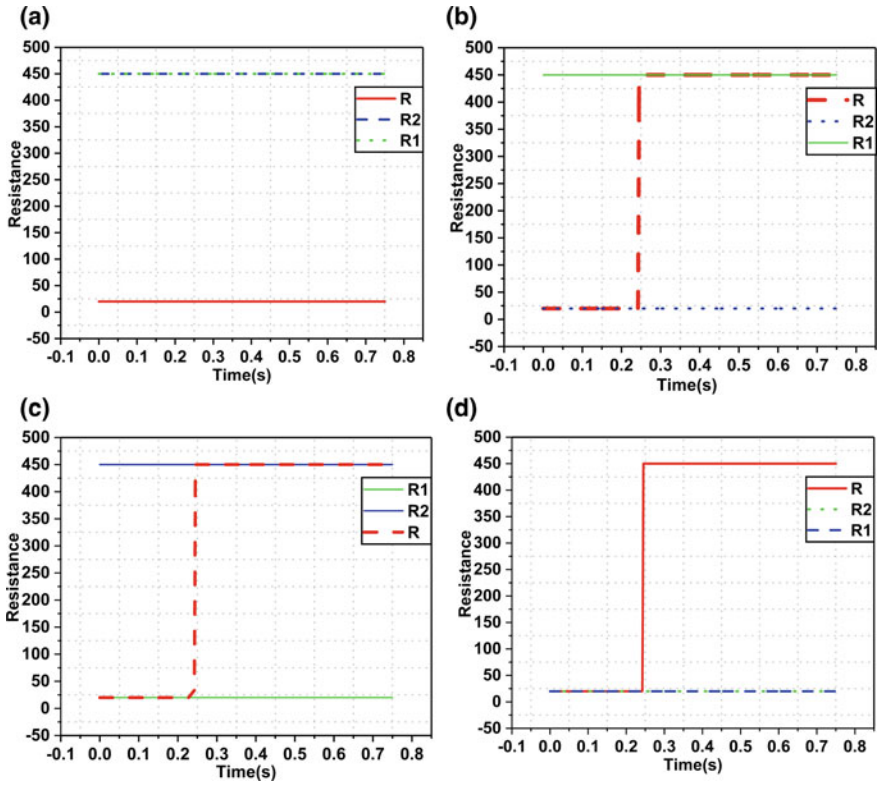

Fig. 5 **a** NOR '0' '0', **b** NOR '0' '1', **c** NOR '1' '0', **d** NOR '1' '1'

Table. 1 Voltage limitation

Function	Design limitations (AIST model)	Design limitations (Vteam model)
NOR	$-V_{T+} < v(t) < -2V_{T-}$	$2V_{T,\mathrm{OFF}} < v(t) < \lvert V_{\mathrm{TON}}\rvert$
NAND	$-V_{T+} < v(t) < -3V_{T-}$	$3V_{T,\mathrm{OFF}} < v(t) < \lvert V_{\mathrm{TON}}\rvert$
OR	$-1.5V_{T+} < v(t) < -V_{T+}$	$V_{T,\mathrm{ON}} < v(t) < 1.5V_{\mathrm{TON}}$
AND	$-2V_{T+} < v(t) < -V_{T+}$	$V_{T,\mathrm{ON}} < v(t) < 2V_{\mathrm{TON}}$

2 Conclusions

AIST-based memristor models are more accurate and can be applied in a variety of situations to simulate the function of biological synapses. In addition to matching the I-V traits of sinusoidal and periodic sweeping stimuli, this model can also accommodate variations in the memristance caused by power supply. Therefore, it was necessary to implement logic gates to find the feasibility of the model. This study shows how AIST-based memristors can be used to create MAGIC gates. It is apparent that

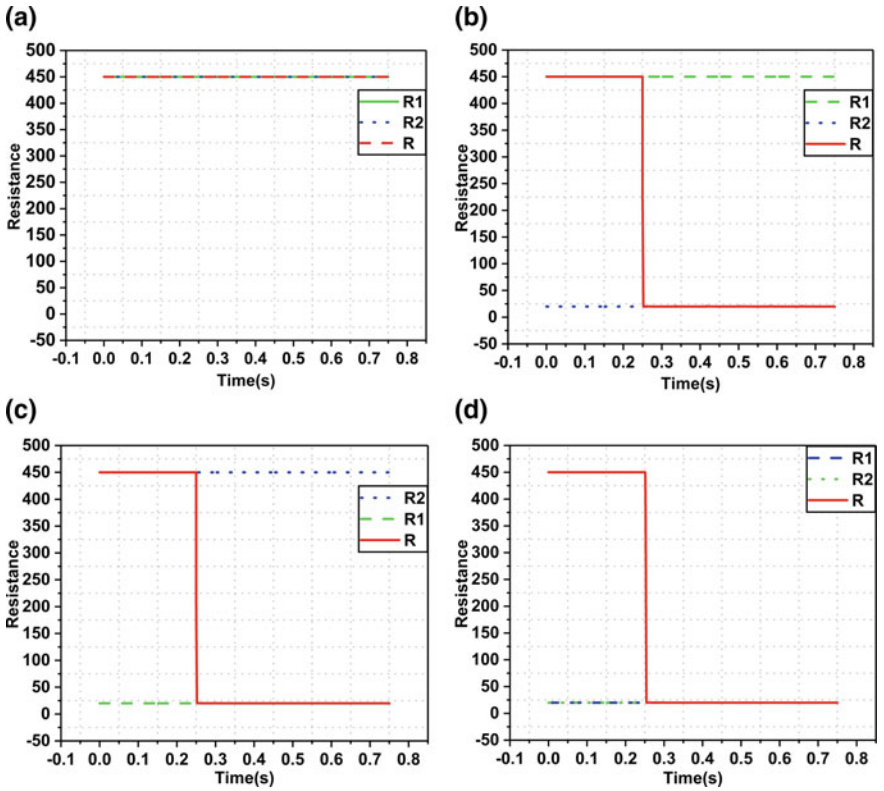

Fig. 6 **a** OR '0' '0', **b** OR '0' '1', **c** OR '1' '0', **d** OR '1' '1'

the output memristor's response to a logic modification is competent. Furthermore, the design limitations beyond which the logically stored input data in the input memristor can be destroyed are demonstrated. In future work, we plan to work with more complex system and their application in a crossbar array.

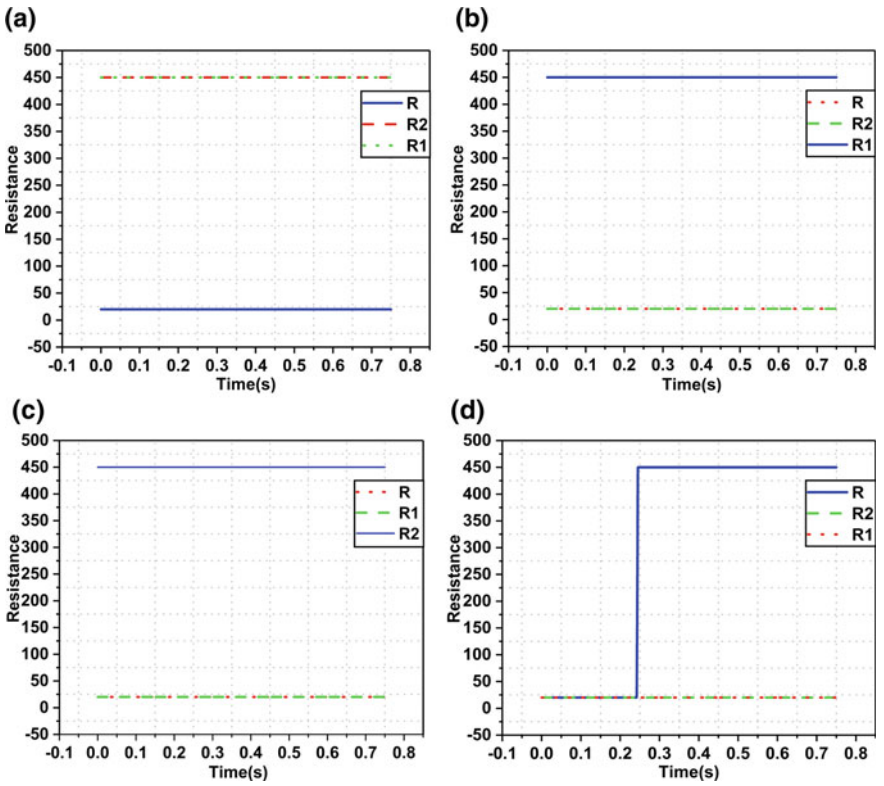

Fig. 7 **a** NAND '0' '0', **b** NAND '0' '1', **c** NAND '1' '0', **d** NAND '1' '1'

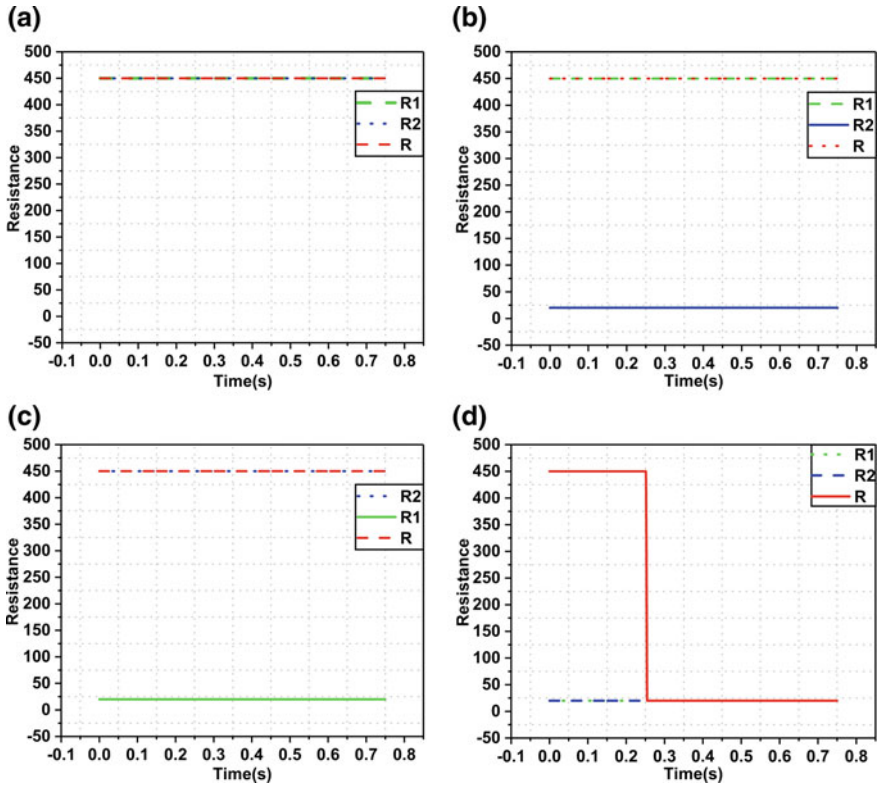

Fig. 8 **a** AND ‘0’ ‘0’, **b** AND ‘0’ ‘1’, **c** AND ‘1’ ‘0’, **d** AND ‘1’ ‘1’

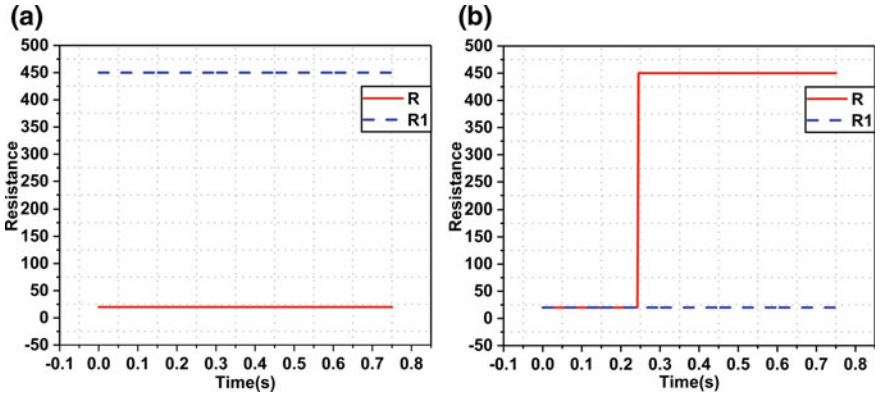

Fig. 9 **a** NOT with inputs ‘0’, **b** NOT with inputs ‘1’

Acknowledgements This research was supported by the Basic Science Research Program through the National Research Foundation of Korea (NRF) funded by the Ministry of Education, Science and Technology (NRF-2019R1F1A1056937). This research was also supported by the KOREA–INDIA joint program of cooperation in science and technology through the National Research Foundation of Korea (NRF) funded by the Ministry of Education, Science and Technology (NRF-2020K1A3A1A19086889). The chip fabrication and EDA tool were supported by the IC Design Education Center (IDEC), Korea.

References

1. Premsankar G, Di Francesco M, Taleb T (2018) Edge computing for the Internet of Things: a case study. IEEE Internet Things J 5(2):1275–1284
2. Radamson HH et al (2020) State of the art and future perspectives in advanced CMOS technology. Nanomater 1555
3. Jeong DS, Thomas R, Katiyar RS, Scott JF, Kohlstedt H, Petraru A, Hwang CS (2012) Emerging memories: resistive switching mechanisms and current status. Rep Prog Phys 75(7):076502
4. Kvatinsky S, Belousov D, Liman S, Satat G, Wald N, Friedman EG, Kolodny A, Weiser UC (2014) MAGIC—memristor-aided logic. In: IEEE 61(11):895–899
5. Kvatinsky S, Satat G, Wald N, Friedman EG, Kolodny A, Weiser UC (2014) Memristor-based material implication (IMPLY) logic: design principles and methodologies. In: IEEE 22(10)
6. Lehtonen E, Laiho M (2009) Stateful implication logic with memristors. In: IEEE
7. Meena JS, Sze SM, Chand U, Tseng T-Y (2014) Overview of emerging non-volatile memory technologies. Nanoscale Res Lett 9(1):526
8. Chua L (2011) Resistance switching memories are memristors. Appl Phys A 102(4):765–783
9. Chua L (1971) Memristor-the missing circuit element. IEEE Trans Circuit Theory 18(5):507–519
10. Snider GS (2008) Spike-timing-dependent learning in memristive nanodevices. In: 2008 IEEE International symposium on nanoscale architectures, pp 85–92
11. Williams R et al (2008) The missing memristor found. Nat 453(7191):80–83
12. Simmons JG (1963) Electric tunnel effect between dissimilar electrodes separated by a thin insulating film. J Appl Phys 34(9):2581–2590
13. Kvatinsky S, Friedman EG, Kolodny A, Weiser UC (2013) TEAM: threshold adaptive memristor model. IEEE Trans Circuits Systems I 60(1):211–221
14. Kvatinsky S, Ramadan M, Friedman EG, Kolodny A (2015) VTEAM: a general model for voltage-controlled memristors. IEEE Trans Circuits Syst II 62(8):786–790
15. Joglekar YN, Wolf SJ (2009) The elusive memristor: properties of basic electrical circuits. Eur J Phys 30(4):661
16. Biolek D, Biolkova V, Biolek Z (2009) SPICE model of memristor with nonlinear dopant drift. Radioeng
17. Zhang Y, Wang X, Li Y, Friedman EG (2017) Memristive model for synaptic circuits. IEEE Trans Circuits Syst II Express Briefs 64(7):767–771
18. Wang L, Zou H (2020) A new emotion model of associative memory neural network based on memristor. Neurocomput 410:83–92
19. Talati N, Gupta S, Mane P, Kvatinsky S (2016) Logic design within memristive memories using memristor-aided logic (MAGIC). IEEE Trans Nanotechnol 15(4):635–650
20. Thangkhiew PL, Gharpinde R, Chowdhary PV, Datta K, Sengupta I (2016) Area efficient implementation of ripple carry adder using memristor crossbar arrays. In: IEEE International design and test symposium (IDT), pp 142–147
21. Haque MN, Khan SR, Jooq MK, Al-Shidaifat A, Song H (2021) Analysis of analog neuron circuit using 180nm CMOS process for brain-inspired neural networks 399–401

22. Li Y et al (2015) Associative learning with temporal contiguity in a memristive circuit for large-scale neuromorphic networks. Adv Electron Mater 1(8):1500125
23. Hong Q, Li Y, Wang X (2020) Memristive continuous Hopfield neural network circuit for image restoration. Neural Comput Appl 32(12):8175–8185

A Low-Power Highly Efficient DC–DC Buck Converter Using PWM Technique

Md. Tarikul Islam, Md. Nazmul Haque, Samiur Rahman Khan, Jatoth Deepak Naik, AlaaDdin Al-Shidaifat, Sandeep Kumar, and Hanjung Song

Abstract Integrated digital circuits (IDCs) have become a popular option for DC–DC buck converters. This article describes a novel CMOS DC–DC buck converter architecture that leverages pulse-width modulation (PWM) for low-power technology. Double delay lines are used in the PWM power consumption which is minimized throughout design and improve unstable voltage while increasing resolution. The functioning of PWM is described using an algorithm developed. Under the working frequency of 100 kHz, the promising findings suggest that the power consumption is reduced to 1.17 W while taking up less space. With a current, the DC–DC buck converter using PWM has a high efficiency of 92.2% across a power range of 4–10 mA. Compared to traditional converters, our PWM approach reduces ripple voltage by 48% and allows in order to create within a DC–DC converter in a smaller chip area.

Keywords CMOS DC · DC buck converter · Digital logic gate · PWM technique for low-power circuit

Md. T. Islam (✉) · Md. N. Haque · S. R. Khan · J. D. Naik · A. Al-Shidaifat · H. Song
Department of Nanoscience and Engineering, Inje University, Gimhae 50384, Korea
e-mail: tarikul@oasis.inje.ac.kr

Md. N. Haque
e-mail: nazmul@oasis.inje.ac.kr

S. R. Khan
e-mail: samikhan@oasis.inje.ac.kr

H. Song
e-mail: hjsong@inje.ac.kr

S. Kumar
Department of Electronics and Communication Engineering, NITK, Surathkal, Mangaluru, India
e-mail: sandeep@nitk.edu.in

S. Rawat et al. (eds.), *Proceedings of Second International Conference on Computational Electronics for Wireless Communications*, Lecture Notes in Networks and Systems 554,
https://doi.org/10.1007/978-981-19-6661-3_43

1 Introduction

Electronic power converters are utilized in electromechanical systems as actuators [1]. In these fields such as wireless sensor networks, the network of things, and medical applications, there is a lot of focus on the power supply. Reducing the energy consumption of digital systems is one of the most critical concerns. For low-voltage operation, numerous DC–DC buck converters on the analogy approaches there have been documented previously [2]. Unfortunately, due to restrictions such as threshold voltage changes, analog designers must work with digital controller approaches in current sophisticated CMOS technology. This has a direct impact on electricity efficiency. However, contemporary researchers are looking for converters that are ultra-low power, which might be useful for charging up those devices. The voltage level (VDD) needs to be very low to achieve low-power usage. Digital circuits' minimal operating voltage, the past, described is a potential for applications requiring a lot of energy [3]. The smallest power point, according to definition, the voltage where overall power required per intended function of a digital circuit using the expansion technique is the smallest. Traditionally, digitally and analog control techniques utilized devices which include analog-to-digital converters (ADCs) to regulate the switching of DC–DC converters. Because of their excessive energy usage and increased chip size, these controllers do not suit for low-power DC–DC converters. A smart controller to low-power DC–DC converters is still being developed, which does not involve static power like such an amplifier [4]. However, for DC–DC converter performance, these electronic devices for controlling require an increase thus in secure area. Increasing the delay line might improve the power consumption of the digital controller. To address these challenges, my research focuses on an effective pulse-width modulation (PWM) technique need for an ADC while consuming less power [5]. The buck converter for DC–DC maximum efficiency is 92.2%.

1.1 Circuit Architecture

The circuit design based on a DC–DC buck converter CCM and its block parts are discussed in this section [6]. The PWM is represented in Fig. 1 as a conspicuous block DC–DC buck converter with CCM diagram. When using a DC–DC converter, there are two blocks [7]: one is the power block and another one the all-digital block. Capacitor (C), inductor (L), and power MOSFETs are all parts of the power stage (MN, MP). The power stage's LC components operate as a filter. The power MOSFETs are optimized with a 1.5 mA for the output current. L, C, and switching frequency are significant critical parameters of the power stage (f_s).

The DC–DC converter's input voltage in the battery has 0.8–1 V, whereas 0.47 V is the output voltage. f_s is set to 100 kHz to a low frequency to decrease digital PWM's power consumption [6]. The digital control side is the buck converter for low-power apps, and required output current is 10 mA or less. As a result, a low

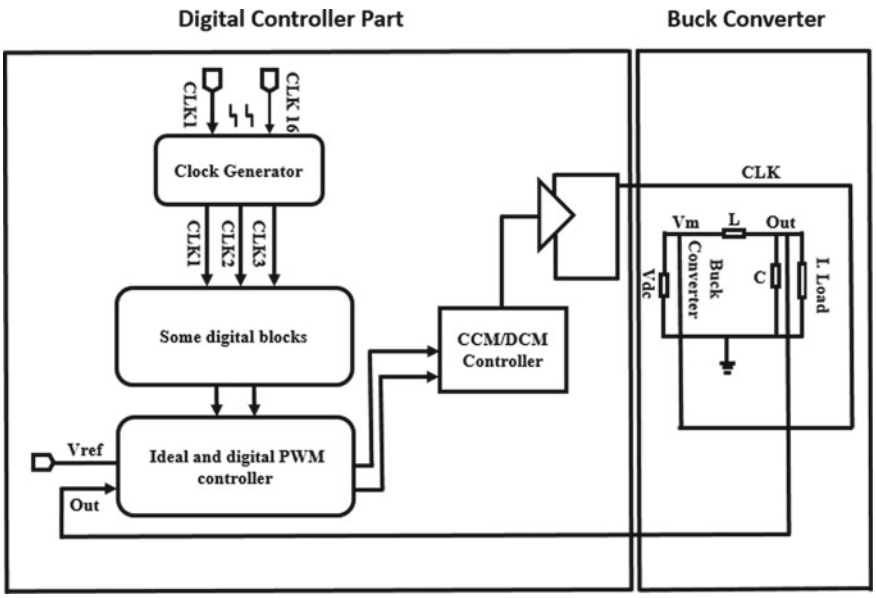

Fig. 1 Diagram of CCM DC–DC converter

switching frequency is aimed to deliver high efficiency by reducing digital control waste and line losses. A long time period necessitates a large inductor size to support low current in the inductor. For this reason, the value of the inductor (L) is taken to 228 H [7]. For limited operation and CCM operation, this inductor ripple current (ΔIL) should be not more than 38% of peak load current of 10 mA (CCM). The output capacitor is often computed using variables like the converter's input voltage in the battery 0.8–1 V, whereas 0.47 V is the output voltage. f_s is set to 100 kHz, a low frequency for decreasing digital PWM's power consumption [6]. The digital control side of buck converter for low-power apps requires an output current below 10 mA. As a result, a low switching frequency is aimed to deliver high efficiency by reducing digital control waste and line losses. Big inductor size is required to support inductor current which is not very high throughout a lengthy clock period. Consequently, this inductor's value (L) is set to 227 H [8]. For limited operation and CCM operation, this inductor ripple current (ΔIL) should be less than 38% of the peak load current of 10 mA (CCM). The output capacitor is often computed using variables like (ΔIL), f_s, and ΔV_{out}.

$$C_{\min} = \frac{\Delta \text{IL}}{8 * f_s * \Delta V_{\text{out}}} = 167 \text{ nF} \tag{1}$$

where ΔV_{out} is the undesirable output ripple, which is set to 25 mV. It is crucial to take note of the over model that does not account for its output capacitor ESR, as it introduces few ripple voltage, as well as the need to drop the cutoff frequency is a

very little frequency from the switching f_s; hence, a high value of 1.2F was selected for the output capacitor (C) [9]. The LC filter's cutoff frequency is estimated to be 10.9 kHz. The proportion of f_s/f_{cutoff} is 9.1.

1.2 PWM Controller

This circuit has A 16-bit delay circuit, an 8-bit delay circuit, a 16-bit bidirectional SR circuit, and logic gates based on CMOS that make up PWM [6]. The 16-bit delay circuit has 15 D flip-flops, whereas the 8-bit delay circuit has 8 D flip-flops. The functioning of the clock CLK1's switching rate on the 16-bit delay circuit uses 100 kHz, whereas 1.6 MHz for clock CLK2. For the functioning of the 8-bit delay line SR, clock CLK3 switches at a frequency of 12.8 MHz (CLK2 frequency 8), and CLK1 and CLK2 combine to form CLK3 [6]. CLK4 determines duty changing frequency and clocks the SR. CLK4 is further reduced and determined at 6.25 kHz or lowers the switching power of shift register and increases the light load efficiency, and the duty ratio was split into 16-bit and 8-bit SR in the PWM employing cells of 16-bit and 8-bit SR delay lines, resulting in a virtual 128-bit delay line. Conventional ADCs are prevented by the 16-bit and 8-bit shift register delay line circuit that make up the 128-bit digital delay line. As a result, when compared to a traditional circuit, the PWM can minimize power consumption (Fig. 5).

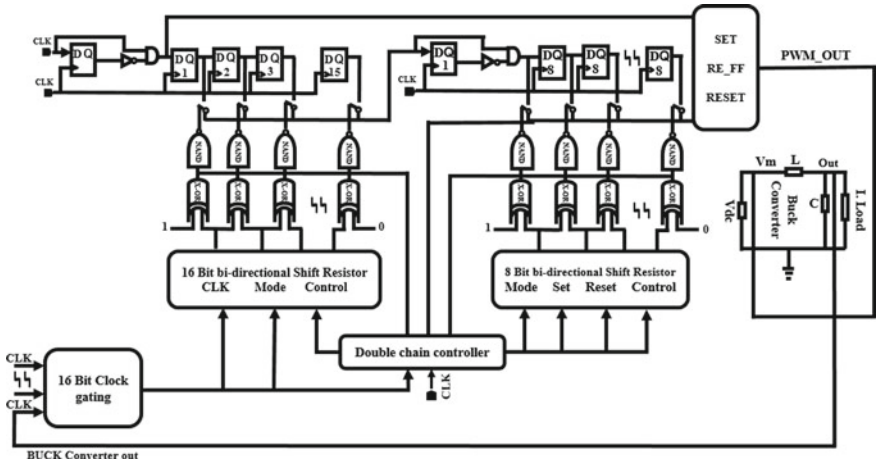

Fig. 2 Ordinary PWM controller and buck converter structure

1.3 Result

In DC–DC buck converter also, a PWM control is discussed here. That circuit design is implemented using conventional 180-nm CMOS technology. Figure 3 shows 16-bit left shift output, same it is work right shift. Figure 4 displays the 8-bit SR left, respectively, right.

Multiple voltage outputs for digital PWM controllers are in this design. The functioning of digital PWM output voltages in accordance with the timing scheme is shown in the preceding section. PWM processors and whole circuits of DC–DC buck converter are compared to standardized ones to verify design performance [10]. The buck converter for DC–DC is run in CCM mode and performs at $V_{DD} = 0.8$ V, $V_{ref} = 0.8$ V, and $I_{load} = 3$ mA.

The total power usage of the PWM is estimated using the CLK3 and CLK4 frequency ranges, which modify the duty ratio on a periodic basis. The DC–DC buck converter and PWM controller were measured for their transient responsiveness [11].

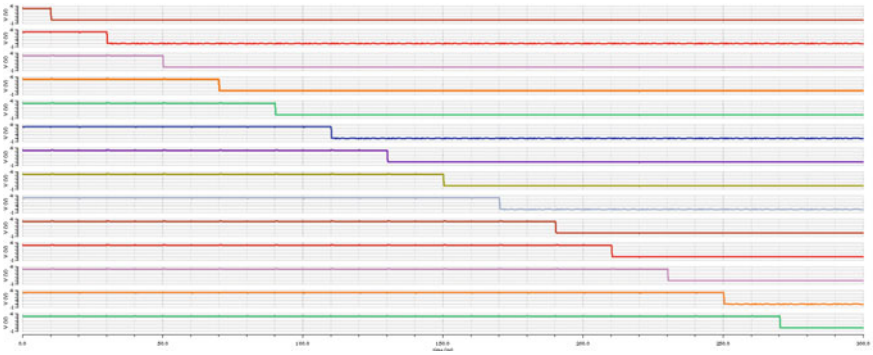

Fig. 3. 16-bit SR left

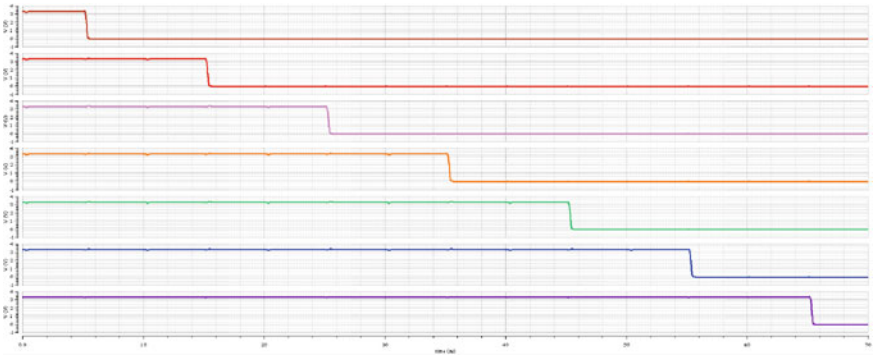

Fig. 4 8-bit SR left

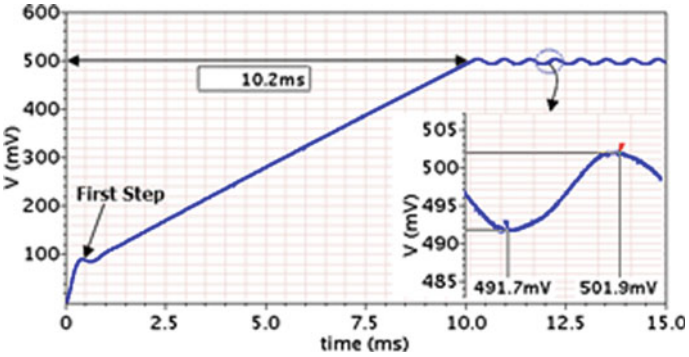

Fig. 5 DC–DC buck converter transient response using PWM method

With PWM, the time it takes for the out voltage of the buck converter to achieve 500 mV is almost 10.2 ms. In the typical architecture, it takes almost 1 ms buck converter out voltage achieving 100 mV (Fig. 5).

As a result, under a 100 kHz switching frequency, this circuit was able to reduce power spent by 59% and ripple 50%. The PWM technique was the whole controller and operates in continuous conduction mode [12]. The 0.52 V output voltage is achieved using a 0.8–1 V as the input voltage, which is the lowest in comparison with prior efforts.

2 Conclusions

In this paperwork, for applications requiring low voltage and low power, we follow a DC–DC buck converter that uses PWM [13]. The 8-bit SR and 16-bit SR delay lines are efficiently connected to build a digital SR 128-bit delay line. PWM approaches increase resolution by employing smaller delay line cells when compared to traditional ideal PWM and digital PWM techniques [14]. The PWM controlled maximum efficiency of a DC–DC converter of 92.2% with a load current range of 4–10 mA. The DC–DC converter's smaller load current range and PWM's low power consumption make it an appealing alternative for low-power applications.

Acknowledgements Fundamental Scientific Research Project of the National Research Foundation of Korea (NRF), which is financed by the Ministry of Education, Science, and Technology, provided funding for this study (NRF-2019R1F1A1056937). Additionally, the National Research Foundation of Korea (NRF), which is sponsored by the Ministry of Education, Science, and Technology, provided funding for this research as part of the collaborative science and technology collaboration between Korea and India (NRF-2020K1A3A1A19086889). The IC Design Education Center (IDEC), Korea, provided support for the EDA tool and chip manufacturing.

References

1. Guldemir H (2011) Study of sliding mode control of DC-DC buck converter. Energy Power Eng 3(04):401–406
2. Walker GR, Pierce JC (2006) Photovoltaic DC-DC module integrated converter for novel cascaded and bypass grid connection topologies—Design and optimization. In: 2006 37th IEEE Power electronics specialists conference. IEEE
3. Ramadass YK, Chandrakasan AP (2008) Minimum energy tracking loop with embedded DC–DC converter enabling ultra-low-voltage operation down to 250 mV in 65 nm CMOS. IEEE J Solid-State Circuits 43(1):256–265
4. Zhu Q et al (2017) A digital polar transmitter with DC–DC converter supporting 256-QAM WLAN and 40-MHz LTE-A carrier aggregation. IEEE J Solid State Circuits 52(5):1196–1209
5. Handbook E (2019) Engineers Handbook. Retrieved from reference tables—coefficient of friction, http://www.engineershandbook.com/Tables/frictioncoefficients.htm
6. Kumar S, Choi J, Song H (2017) An ultra-low power CMOS DC–DC buck converter with double-chain digital PWM technique. Analog Integr Circ Sig Process 92(1):141–149
7. Rosyadi F et al (2016) Power drive system product development for electric vehicle in PT Len Industri. In: 2016 3rd Conference on power engineering and renewable energy (ICPERE). IEEE
8. Kang TK (2010) Specific absorption rate reducer, mobile terminal using the same and method therefor. U.S. Patent No. 7,672,698
9. Schindler G, Zitnick L, Brown M (2008) Category recognition. In: CVPRW'08: IEEE computer society conference on computer vision and pattern recognition workshops, Anchorage. Link to official URL (if available)
10. Kim SY et al (2017) Design of a high efficiency DC–DC buck converter with two-step digital PWM and low power self-tracking zero current detector for IoT applications. IEEE Trans Power Electron 33(2):1428–1439
11. Poon NK, Li CP, Pong MH (2001) A low cost DC-DC stepping inductance voltage regulator with fast transient loading response. In: APEC 2001. Sixteenth annual IEEE applied power electronics conference and exposition (Cat. No. 01CH37181), vol 1. IEEE
12. Tan SC, Lai YM, Tse CK (2006) A unified approach to the design of PWM-based sliding-mode voltage controllers for basic DC-DC converters in continuous conduction mode. IEEE Trans Circuits Syst I Regul Pap 53(8):1816–1827
13. Chen YT, Chen CH (2009) A DC-DC buck converter chip with integrated PWM/PFM hybrid-mode control circuit. In: 2009 International conference on power electronics and drive systems (PEDS). IEEE
14. Patella BJ et al (2003) High-frequency digital PWM controller IC for DC-DC converters. IEEE Trans Power Electron 18(1):438–446

A High-Sensitive High-Input Impedance CMOS Front-End Amplifier for Neural Spike Detection

Jatoth Deepak Naik, Pradeep Gorre, AlaaDdin Al-Shidaifat, Sandeep Kumar, and Hanjung Song

Abstract Neural spikes detection and monitoring for neuro-prosthetic applications require an efficient and robust front-end amplifier (FEA), which regulates the fidelity of the neural signal. This paper presents neutralization and bootstrapping techniques to overcome the input leakage currents produced by amplifiers of the input bias network. In addition, a pseudo-resistor technique ensures the FEA maintains a high-input impedance. The CMOS-based FEA architecture is executed in the advanced design system with the design kit of the CMOS process. The proposed design achieves a high-input impedance of 0.5 TΩ with a maximum simulation gain of 66.2 dB. The overall power consumption of the topology is observed as 2.6 μW with a power supply voltage of 0.9 V. The simulated noise performance of 6 nV/$\sqrt{}$Hz at 1 kHz demonstrates a high-sensitive design compared to the previous works. It is highly recommended for succeeding neuro-prosthetic applications.

Keywords Neuro-prosthetic · Bootstrapping · Front-end amplifier · CMOS technology · Pseudo-resistor

1 Introduction

GROWING investigation toward neuro-prosthetic applications demands highly accurate and robust data acquisition systems that simultaneously monitor millions of neuron spike activities [1]. The slight DC offset due to electrochemical properties at the electrode-tissue interface could result in gain saturation, affecting the sensitivity of the neural spikes monitoring. In addition, the electrical signals like local field potential (LFP) and action potential (AP) generated by electrodes are weak in

J. D. Naik · A. Al-Shidaifat · H. Song (✉)
Department of Nano Science and Engineering, Inje University, Gimhae 621-749, Korea
e-mail: hjsong@inje.ac.kr

P. Gorre · S. Kumar
Department of Electronics and Communication Engineering, National Institute of Technology Karnataka, Surathkal, Mangaluru, India
e-mail: sandeep@nitk.edu.in

S. Rawat et al. (eds.), *Proceedings of Second International Conference on Computational Electronics for Wireless Communications*, Lecture Notes in Networks and Systems 554,
https://doi.org/10.1007/978-981-19-6661-3_44

amplitude ranging from 5 to 50 μVpp over a low-frequency of 100 Hz to 7.5 kHz [2]. Hence, the neural spike characteristics require a high-sensitive and wideband electronic circuitry at the electrode-tissue interface [3]. The front-end amplifier (FEA) is the most critical component, whose performance decides the neural activity monitoring systems [4]. Hence, designing an FEA with high gain, large bandwidth, low noise, and less power consumption is a challenging task for neuro-researchers to simultaneously record and detect a substantial amount of employing many electrodes to collect brain signals [5, 6]. A suggested neuro-prosthetic diagnostic is displayed together with the brain activity's bi-directional signal flow. Before the brain spikes approach the transmitter part, their electrical information is first detected by electrodes and then amplified by FEA. The present work emphasizes the CMOS-based high-sensitive FEA for signal amplification in systems that track brain activity.

Due to its high-input impedance (usually 50 GHz) and variable gain mechanism using an external resistor, an instrumentation amplifier is frequently utilized for RF board designs in neurological monitoring applications, as shown in Fig. 1a. Nevertheless, instrumentation amplifiers' significant form factor and area expense are not feasible for body implantation [7].

The advancements in device technology (CMOS integrated circuits) enable a small yet dense number of sensors, paving a path for accurate implantable neural monitoring [8, 9]. The area penalty of resistors in conventional FEA is overcome by employing capacitive feedback (CF) topology, as shown in Fig. 1b, where the DC offset is mitigated by its variable gain mechanism [10]. In order to reduce signal attenuation at low frequencies, a high-input impedance FEA is realized by choosing a small value of C_1 in CF topology. Operational amplifier input gate leakage current limits the CF topology's high-input impedance. Accordingly, a high-input gate size is required for a low-noise Op-amp design since the flicker noise ($1/f$) of the transistor is inversely proportional to its area. High-leakage current results from large parasitic capacitance produced by large gate dimensions. In investigations [10–12], various techniques are reported to overwhelm the trade-off between the FEA's low-noise and

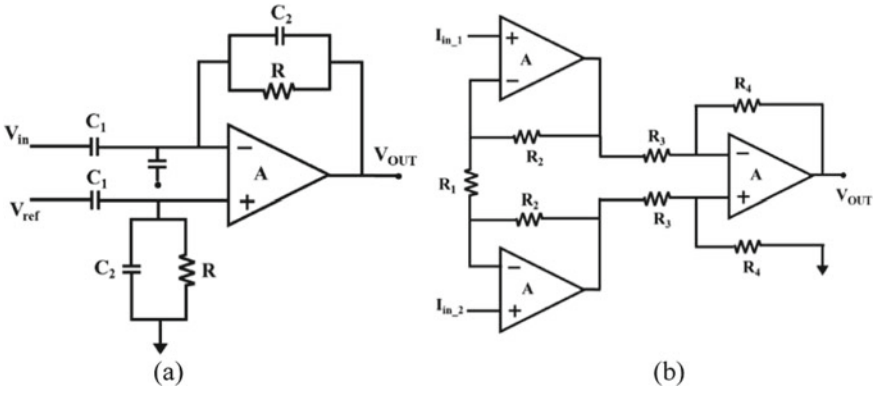

Fig. 1 **a** Capacitive feedback biasing circuit architecture, **b** Amplifier for traditional instruments

high-input impedance. Auto zeroing [1] employs a two-state sample and hold circuit where the amplifier is operated in the cut-off region during the hold phase to nullify the input leakage current. The noise contributed by the sample and hold circuit is reduced by integrating a chopper stabilization (CS) circuit [11, 12] with the sample and hold technique. The modulation and demodulation of the input signal in the CS technique help in reducing the flicker noise but result in narrowband operation. In [13], authors proposed a feedback loop-controlled (FLC) technique to compensate narrow band operation and input leakage currents occur due to low-noise amplifiers. A custom designed contactless sensor FEA [14] is proposed with FCN technique which fully bootstraps the parasitic impedances without any external resistances by ensuring low-leakage and high-input impedance. However, for simultaneous detecting and recording of a large number of neural signals, a wideband (>10 kHz) FEA is required for neuro-prosthetic applications. This work proposes a pseudo-resistor bootstrap neutralization (PRBN) technique to achieve a high impedance and wideband band operation. A feedback loop-control scheme is employed to avoid external digital blocks, which reduces chip area. The significant leakage current reduction suppresses external noise while achieving high-input impedance. The proposed FEA achieves a high-sensitive, wideband, and low-noise electronic circuitry for neural monitoring applications.

2 Circuit Design

The proposed FEA architecture consists of two-stage complementary metal-oxide semiconductor (CMOS) amplifiers with two feedback mechanisms, one for neutralization and the other for bootstrapping, as shown in Fig. 2. The design also includes a pseudo-resistor comprising two metal–oxide–semiconductor field-effect transistors (MOSFETs) connecting them back-to-back to offer a high resistance in a compact design. The current entering PR_2 is reduced by introducing a bootstrapping loop across O2 and PR_2. The signal current through PR_2 is expressed as Eq. (1)

$$I_2 = \frac{V_1 - V_a}{P_2} \tag{1}$$

where V_a is the bootstrapping voltage supplied by V_0 through capacitor C_a. The lower cut-off frequency of this closed-loop feedback is determined by the product of PR_3 and C_a, as shown in Fig. 2.

$$V_O = V_1 \left(\frac{A_O}{A_O + 1} \right)^2 \tag{2}$$

$$V_a = V_O * \left(\frac{P_3}{P_3 + \frac{1}{j\omega a}} \right) \tag{3}$$

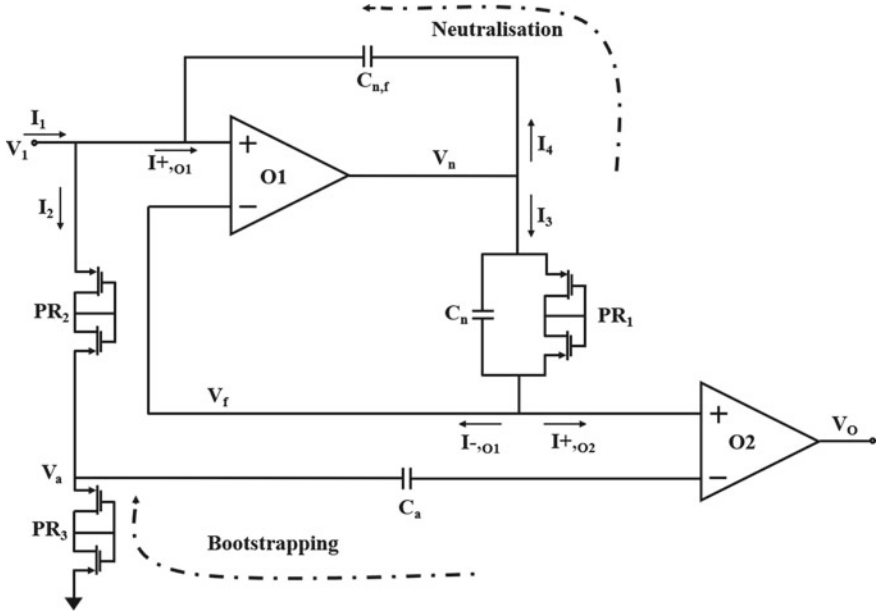

Fig. 2 Suggested FEA design's circuit architecture includes a neutralization loop and bootstrapping

where A_O represents the open-loop gain of amplifiers O1 and O2. V_O is buffered twice to V_1. Due to the current flowing through PR_2. The nearer V_a will be to V_1, and the less signal current is pulled into the bias circuit, as shown in Eq. (1).

"Neutralization" is a current feedback method that transfers a significant portion of the leakage current through amplifier O1 ($I+$, O1). The parasitic gate capacitance of the input transistor is primarily responsible for this leakage current. Raising the gain of O1 and O2 might result in a greater FEA input impedance. The use of PR evolves the primary current at the input stage of the IC after bootstrapping. The voltages V_a, V_1, and Vo are close to one other in Fig. 2, guaranteeing that the gate leakage currents at all terminals are equivalent ($I+$, O1≈$I+$, O1≈$I+$, O2). The leakage currents for the two amplifiers' terminals, " + " of O2 and " − " of O1, will be delivered by O1's output voltage, V_n. The current flowing across the capacitor C_n (while disregarding PR_1's significantly higher impedance).

The current through the capacitor C_n is equivalent to the sum of I, O1, and $I+$, O2 (disregarding the higher impedance of PR_1, which was included to create a DC feedback line). The present I_3 is twice $I+$, O1 since O1 and O2 have the same topological form and are set out using well-known matching procedures.

This current-controlled voltage loop is linked to the input by a capacitor. $C_{n,f}$ has half the capacitance of C_n. As a result, I_3 is twice of I_4 and is roughly equal to the leakage current of the amplifier, as described in Eq. (5). The input current may be described as

$$I_1 = I_2 + I_{+O1} - I_4 \tag{4}$$

$$I_4 = \frac{I_3}{2} = \frac{1}{2} * \frac{V_n}{Z_{C_n} || P_1} = \frac{1}{2}(I_{-O1} + I_{+O1}) \tag{5}$$

The current-mirror OTA employed in the bio-amplifier is schematically shown in Fig. 3. Conventional circuits were used to create the bias current with cascode bias voltages. Despite the fact that the circuit architecture is a conventional one for controlling capacitive loads, the transistor size is crucial for attaining minimal noise at minimal current value. The I_{bias} current is set at 8 μA, resulting in drain currents of 4 μA for the devices. Relying on its (W/L) ratio, each transistor at this current level can function in mild, medium, or strong inversion.

The input devices M3 and M4 have the same size, their transconductance is denoted by g_{m3}, and the ratio of width and length is denoted by $(W/L)_3$. Transistors M5–M10 are of the identical size $(W/L)_5$ and have the equivalent transconductance g_{m5}. The dimensions $(W/L)_9$ and transconductance g_{m9} of the pMOS current-mirror transistors M9 and M10 are the same. The thermal noise power at the input is given by

$$V_n^2 = \left[\frac{16\ \text{kT}}{3g_{\text{m3}}}\left(1 + 2\frac{g_{\text{m5}}}{g_{\text{m3}}} + \frac{g_{\text{m9}}}{g_{\text{m3}}}\right)\right]\Delta f \tag{6}$$

We can reduce the noise of transistors M5–M10 by sizing transistors so that g_{m5}, $g_{\text{m9}} \ll g_{\text{m3}}$. This is done by driving transistor M5–M10 into strong inversion, where their absolute transconductance g_m/I_D drops as $1/\sqrt{I_D}$. We get a large g_m/I_D

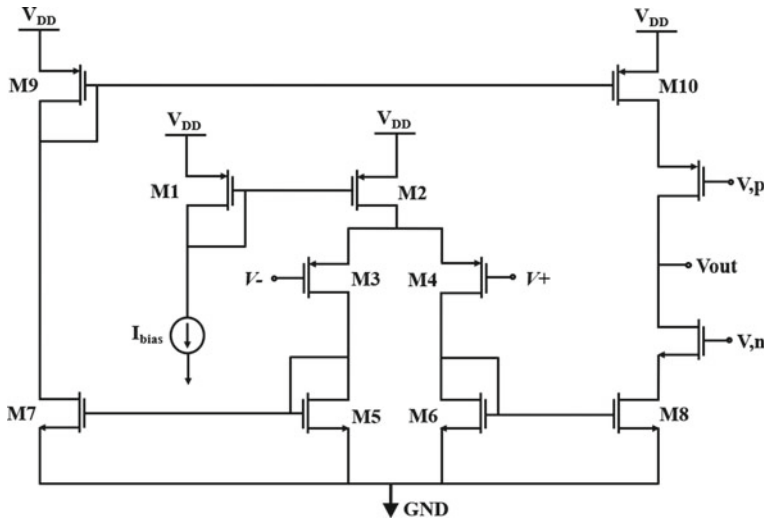

Fig. 3 OTA schematic for a neural amplifier

Table 1 Performance of the proposed FEA in comparison with relevant works

Parameters	Mohseni and Najafi [10]	Harrison and Charles [1]	Song et al. [11]	Zhou and War [13]	Chi et al. [14]	This work
Technology/Process	0.35 μm CMOS	0.18 μm CMOS	0.18 μm CMOS	0.35 μm CMOS	0.5 μm CMOS	90 nm CMOS
Biasing technique	CF	2-stage S&H	CS	LCN	FCN	NL+BS with PR
Supply voltage (V)	1	3	1	3.3	3.3	0.9
Power (μW)	12.1	93	13	3.1	4.95	2.6
Gain (dB)	75	6–47	44.5	75	–	66.2
Bandwidth (Hz)	0.05 ~ 10 K	100 ~ 12 K	0.3 ~ 10 K	22.8 M	800 K	10 K
Input impedance (Ω)	4 M	–	–	42G	> 50 T	0.5 T
Input-referred noise (V/$\sqrt{}$Hz)	2 μ	0.68 μ	4.4 μ	18.2 n	28 n	3.9 n

proportion by controlling M3 and M4 within the subthreshold region, as indicated in Table 1, g_{m3} is substantially bigger than g_{m5} and g_{m9}.

Low-noise systems: A serious issue is low-frequency design noise, sometimes known as flicker noise. To minimize the effects of flicker noise, we employ devices with broad gate areas and pMOS transistors as input devices. As soon as |VGS| does not substantially surpass the threshold voltage and flicker noise is inversely related to the gate area, flicker noise in pMOS transistors is generally one to two orders of magnitude smaller than flicker noise in nMOS transistors. To reduce 1/*f* noise, each transistor must be as wide as allowed. However, when devices M3–M8 becomes larger, resulting in a decreased phase margin. The OTA input capacitance C_{IN} rises when M3 and M4 are increased. To reduce 1/*f* noise, an optimal gate area for M3 and M4 may be identified. For low-frequency operations, lateral p-n-p transistors may be made in regular CMOS technology and have reduced 1/*f* noise than MOS devices.

3 Results and Discussion

The proposed FEA with integrated loop techniques with PR section is simulated using advanced design system (ADS) software v. 20. Figure 4 shows the simulation and post-layout simulation plot for the proposed FEA where a simulation plot results in a maximum flat gain of 66.2 dB over 3-dB frequency of 12.5 kHz. The post-layout simulation results show a gain drop of 3-dB due to parasitic present in the layout design. A high-input impedance (Zin) of 0.5 TΩ is achieved by employing PR technique as shown in Fig. 5. The input leakage current is avoided by the suggested FEA's high value of Zin, which reduces the form factor at the electrode-tissue contact.

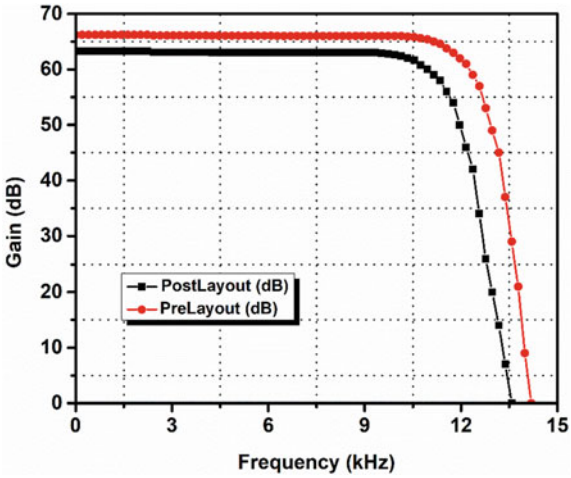

Fig. 4 Pre-layout and post-layout simulations of the FEA

Figure 6 shows the simulation plot of input-referred noise (IRN) for the proposed FEA where a value of 6 nV/$\sqrt{}$Hz is achieved at 1 kHz frequency. It is observed that the IRN is reducing as frequency is increasing, and a minimum value of 3.9 nV/$\sqrt{}$Hz is achieved at 10 kHz. Figure 7 shows a MATLAB simulated plot for noise performance, where the influence of the mobility of the carrier and frequency on IRN is observed. When the carrier's mobility or operating frequency is raised separately, the noise curve grows steadily; however, when both are increased at once, the noise curve grows more quickly. The performance comparison of the proposed work with other recently reported works is shown in Table 1. The current work demonstrates better performance in terms input impedance while bandwidth and gain parameters are considerable.

4 Conclusion

This study suggests an unique FEA with PRNLBP approach for recording and monitoring brain spikes. The suggested FEA is based using CMOS technology, resulting in an input impedance of 0.5 T and low-input-referred noise of 3.9 nV. The present work shows better performance in input impedance and noise compared with the conventional capacitor neutralization technique. A gain of 66.2 dB is reported with a fractional bandwidth of 125% with a power consumption of 2.6 μW. Additionally, the suggested FEA design has steady performance since it is immune to changes in process and temperature. The presented work with these parameter improvements could benefit neural spikes monitoring in implanted bio-medical applications.

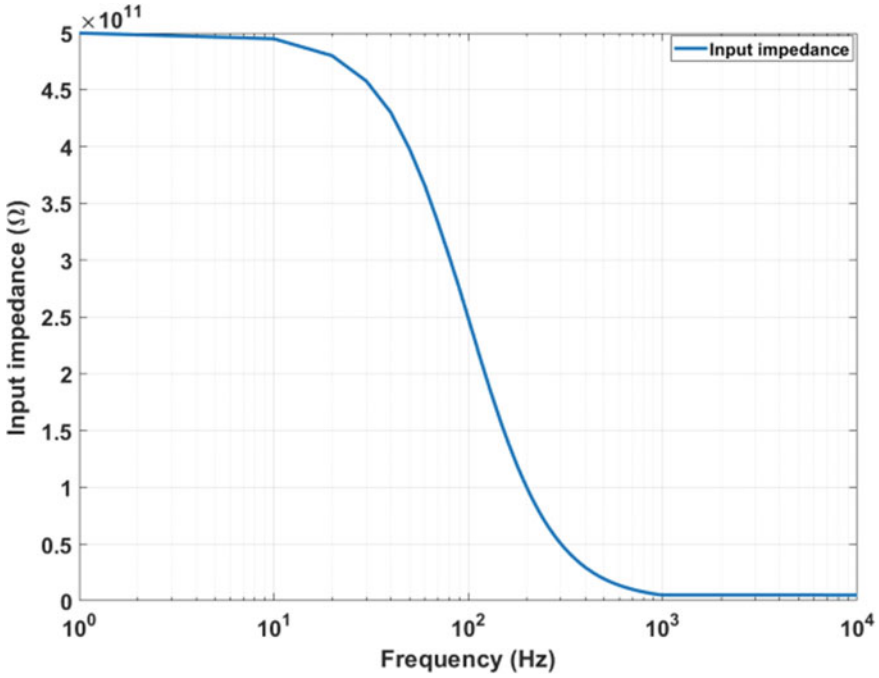

Fig. 5 Simulation plot of input impedance versus frequency of the FEA

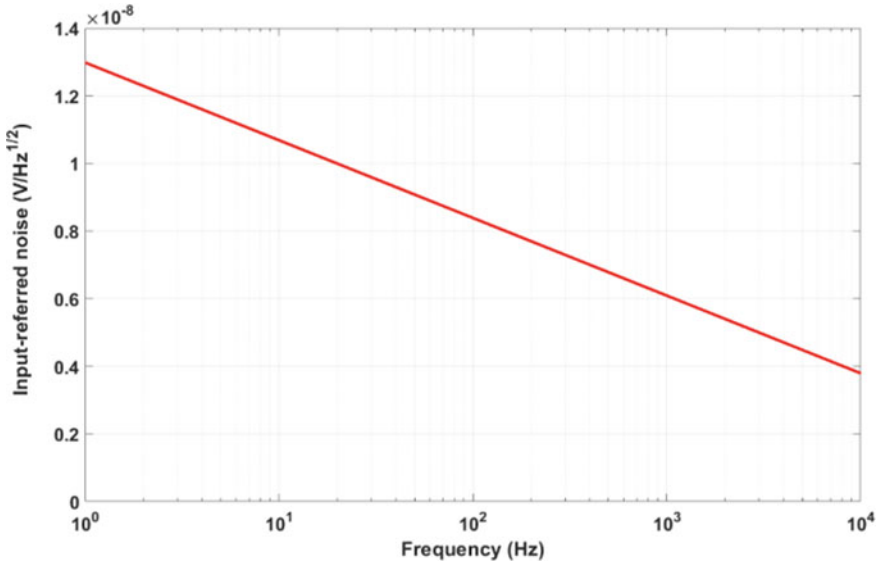

Fig. 6 Input-referred noise versus frequency of the proposed FEA

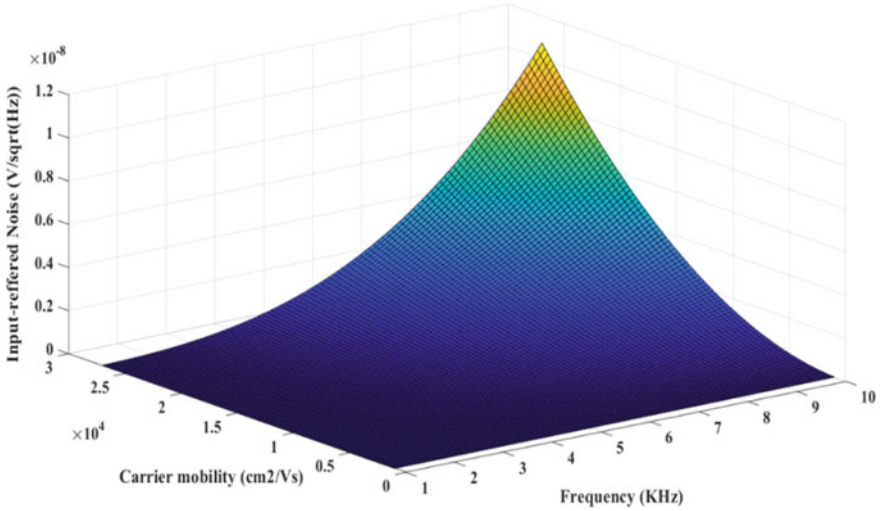

Fig. 7 3D attractor plot showing total input-referred noise as a function of mobility

Acknowledgements The Basic Scientific Research Program of the National Research Foundation of Korea (NRF), which is financed by the Ministry of Education, Science, and Technology, provided funding for this study (NRF-2019R1F1A1056937). Additionally, the National Research Foundation of Korea (NRF), which is sponsored by the Ministry of Education, Science, and Technology, provided funding for this research as part of the collaborative science and technology collaboration between Korea and India (NRF-2020K1A3A1A19086889). The IC Design Education Center (IDEC), Korea, provided support for the EDA tool and chip manufacturing.

References

1. Harrison R, Charles C (2009) A low-power low-noise CMOS amplifier for neural recording applications. IEEE J Solid State Circuits 38(6):958–965
2. Jiraseree-Amornkun A, Worapishet A, Klumperink EA, Nauta B, Surakampontorn W (2008) Theoretical analysis of highly linear tunable filters using switched-resistor techniques. IEEE Trans Circuits Syst I Regul Pap 55(11):3641–3654
3. Barsakcioglu D, Liu Y, Bhunjun P, Navajas J, Eftekhar A, Jackson A, Quiroga Q, Constandinou T (2014) An analogue front-end model for developing neural spike sorting systems. IEEE Trans Biomed Circuits Syst 8(2):216–227
4. Teng S, Rieger R, Lin Y (2014) Programmable ExG biopotential front-end IC for wearable applications. IEEE Trans Biomed Circuits Syst 8(4):543–551
5. Fatoorechi M, Parkinson J, Prance RJ, Prance H, Seth AK, Schwartzman DJ (2015) A comparative study of electrical potential sensors and Ag/AgCl electrodes for characterising spontaneous and event related electroencephalagram signals. J Neurosci Methods 251:7–16
6. Guermandi M, Cardu R, Scarselli E, Guerrieri R (2015) Active electrode IC for EEG and electrical impedance tomography with continuous monitoring of contact impedance. IEEE Trans Biomed Circuits Syst 9(1):21–33

7. Lopez C, Andrei A, Mitra S, Welkenhuysen M, Eberle W, Bartic C, Puers R, Yazicioglu R, Gielen GG (2014) An implantable 455-active-electrode 52-channel CMOS neural probe. IEEE J Solid State Circuits 49(1):248–261
8. Steyaert M, Sansen W (1987) A micropower low-noise monolithic instrumentation amplifier for medical purposes. IEEE J Solid State Circuits 22(6):1163–1168
9. Akin T, Najafi K, Bradley R (1998) A wireless implantable multichannel digital neural recording system for a micromachined sieve electrode. IEEE J Solid State Circuits 33(1):109–118
10. Mohseni P, Najafi K (2004) A fully integrated neural recording amplifier with DC input stabilization. IEEE Trans Biomed Eng 51(5):832–837
11. Song S, Rooijakkers M, Harpe P, Rabotti C, Mischi M, van Roermund A, Cantatore E (2015) A low-voltage chopper-stabilized amplifier for fetal ECG monitoring with a 1.41 power efficiency factor. IEEE Trans Biomed Circuits Syst 9(2):237–247
12. Toth L, Tsividis Y (2003) Generalization of the principle of chopper stabilization. IEEE Trans Circuits Syst I Fundam Theory Appl 50(8):975–983
13. Zhou Z, Warr PA (2016) A high input impedance low noise integrated front-end amplifier for neural monitoring. IEEE Trans Biomed Circuits Syst 10(6):1079–1086
14. Chi Y, Maier C, Cauwenberghs G (2011) Ultra-high input impedance, low noise integrated amplifier for noncontact biopotential sensing. IEEE J Emerg Sel Top Circuits Syst 1(4):526–535

Design and Performance Analysis of Quaternary GNRFET Storage Cell

Tulasi Naga Jyothi Kolanti and K. S. Vasundara Patel

Abstract This paper presents an efficient design of multiple-valued logic (MVL) storage cell using graphene nanoribbon field-effect transistor (GNRFET) and their performance analysis. In this work, storage cell is designed using three inverters having different power supplies to generate different outputs for same input. The designs are simulated using Synopsys HSPICE simulation tool, using the 32-nm MOS like GNRFETs technology node and 0.9 V as the maximum supply voltage. It is observed that the proposed designs are showing optimized delay and better noise margin as compared to existing carbon nanotube field-effect transistor (CNTFET) and CMOS-based designs. Compared to CNTFET SRAM, it is observed that the proposed design exhibits 15 and 58% improved SNM and dynamic power consumption, respectively.

Keywords GNRFET · Quaternary logic · Quaternary storage cell · Noise margin

1 Introduction

GNR is a promising technology to reduce the chip area because of their no alignment and transfer-related problems when compared with CNT circuits. Basically, a static memory circuit requires more than half of the chip area and inflicts the major share of power consumption [1]. Field-effect transistors designed using nanomaterials CNTFET and GNRFET-based SRAM circuits designs are available in the literature [2–5] which are mostly designed using the cross-coupled inverters. To increase the stability, instead of traditional 6t, many were designed 8 and 9 t-based SRAMs. In this work, we proposed a novel quaternary storage cell.

T. N. J. Kolanti (✉) · K. S. V. Patel
B.M.S. College of Engineering, Bengaluru, India
e-mail: tulasinj@bmsce.ac.in

K. S. V. Patel
e-mail: vasu.ece@bmsce.ac.in

S. Rawat et al. (eds.), *Proceedings of Second International Conference on Computational Electronics for Wireless Communications*, Lecture Notes in Networks and Systems 554,
https://doi.org/10.1007/978-981-19-6661-3_45

The rest of the paper is arranged as follows: The GNRFET structure is described in Sect. 2. In Sect. 3, the quaternary voltage logic signals are explained. In Sect. 4, the design of proposed quaternary storage cell is discussed. Simulations and analysis are explained in Sect. 5. Finally, Sect. 6 concludes the proposed work.

2 Graphene Nanoribbon Field-Effect Transistors (GNRFET)

The structure of graphene material consists of a regular hexagon monolayer lattice and carbon atoms at each corner. The width of graphene nanoribbon (W_{ch}) is defined as follows [6]:

$$W_{\text{ch}} = (N-1)\sqrt{3}\frac{dcc}{2} \tag{1}$$

Here N indicates the dimer lines count, the bond length between one carbon atom to another carbon atom is represented by dcc, and its value is 0.144 nm. Electronic properties of armchair nanoribbon depends on the total number of atoms in nanoribbon edge of armchair structure. All the armchair GNRs (AGNRs) that satisfy the conditions N = 3p + 1 or N = 3p and N = 3p + 2 are considered as semiconductors and metallic, respectively, where P represents a positive integer [7, 8].

GNRFET can be realized in two ways, firstly, by connecting Schottky metal contacts at both sides of the channel, this type transistor is called Schottky barrier GNRFET (SB-GNRFET). And in other type of transistors, the heavily doped GNRs as source and drain regions are obtained to get the ohmic contact. Hence, the transistors will work similar to MOSFET. Basically, high ON/OFF current is the property of MOSFET-type GNRFETs, compared to SB-type one. Hence, MOS-GNRFET is appropriate for high-performance applications, and for low-power applications, SB-GNRFET is suitable. Therefore, MOSFET-type GNRFET is inspected to show it has better performance practically.

Threshold voltage is a very important parameter to concentrate while designing the MVL digital circuit. By changing the dimer lines of GNRFET (N), one can get specific threshold voltage values.

The following formula is used to calculate the threshold voltage mathematically

$$\begin{aligned} V_t &= \frac{E_g}{3e} \\ E_g &= 2|\propto|\Delta E \\ \Delta E &= \frac{hV_f\pi}{W} \end{aligned} \tag{2}$$

where E_g and W are the band gap and GNR width, respectively. e is electron charge, h is Planck's constant, V_f is the Fermi velocity, and $\propto$ is the carbon to carbon bond

Table 1 General HSPICE parameters of GNRFET

Device parameters	Parameter descriptions	Default value
L	Channel length of gate	15.0 nm
T_{ox}	Top dielectric material thickness of gate	0.95 nm
2*sp	Two adjacent GNRs space	2.0 nm
nRib	Total GNR numbers in a transistor	6
P	The device edge roughness percentage	0
D_{op}	Doping fraction of drain and source	0.001
T_{ox2}	The oxide thickness between substrate and channel	20 nm
Gates tied	Is gate or substrate hold the same voltage?	0

distance. In this work, Synopsys HSPICE tool is used for simulations, and 32-nm channel length transistor and supply voltage of 0.9 V are used at room temperature with different ranges of N. The important GNRFET HSPICE parameters are listed in Table 1.

3 Quaternary Voltage Logic Signal

Well ahead, MVL is familiarized which uses multiple logic levels to define a signal voltage levels. The logic 0 and 1 (binary) are popularly used in digital calculations to symbolize low and high logic voltages, respectively. As the name suggests, in quaternary voltage logic, digital calculations are performed by four logic levels which consists of low, high and two intermediate logic levels. Quaternary voltage logic attracted a lot of scholars due to its unique advantages over the binary such as less chip area and low interconnect complexity. The voltage levels of any MVL can be found using below formula:

$$0, \frac{Vdd}{N-1}, \frac{2Vdd}{N-1}, \ldots, \frac{(N-1)Vdd}{N-1} \tag{3}$$

where N signifies the number of logics used. In quaternary, N value is taken as 4. All the basic digital gates such as NOT, AND, OR can be implemented using the quaternary voltage logic. As for the NOT gate, four different inverters can be implemented based on the functionality, namely negative inverter (NINV), positive inverter (PINV), in-between inverter (IINV) and standard inverter (SINV). These inverters explained using the Eq. (4) represent the relationship between inputs and outputs of the inverters. Table 2 represents the truth table for each inverters.

$$\text{NINV} = \begin{cases} 3 \text{ if } \text{in} = 0 \\ 0 \text{ if in } \neq 0 \end{cases}$$

Table 2 Quaternary inverter truth table

Input	Output			
	NINV	IINV	PINV	SINV
3	0	0	0	0
2	0	0	3	1
1	0	3	3	2
0	3	3	3	3

$$\begin{aligned} \text{IINV} &= \begin{cases} 3 \text{ if in} = 0 \text{ or } 1 \\ 0 \text{ if in} = 2 \text{ or } 3 \end{cases} \\ \text{PINV} &= \begin{cases} 3 \text{ if in} \neq 3 \\ 0 \text{ if in} = 3 \end{cases} \\ \text{SINV} &= 3 - \text{in} \end{aligned} \tag{4}$$

4 Proposed Quaternary Storage Cell

This section talks through the proposed graphene transistor-based quaternary storage cell with much better performance. Instead of using multi-threshold voltage transistors, this work considered a different approach which uses multiple supply voltages.

The proposed quaternary storage cell is designed using three GNRFET inverters that switches at different voltage levels, a pair of transmission gates (TG) and pass transistors. The two TGs are operated using a non-concurrent control signals to device the hold and write functionalities. Unlike other quaternary storage cell which uses complex cross-coupled inverter to store the data, proposed cell uses simple GNRFET inverters with different supply voltages shown in Fig. 1.

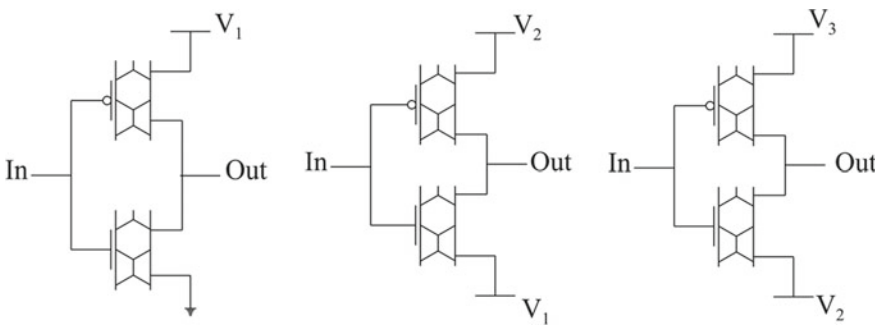

Fig. 1 GNRFET inverters with different supply voltages

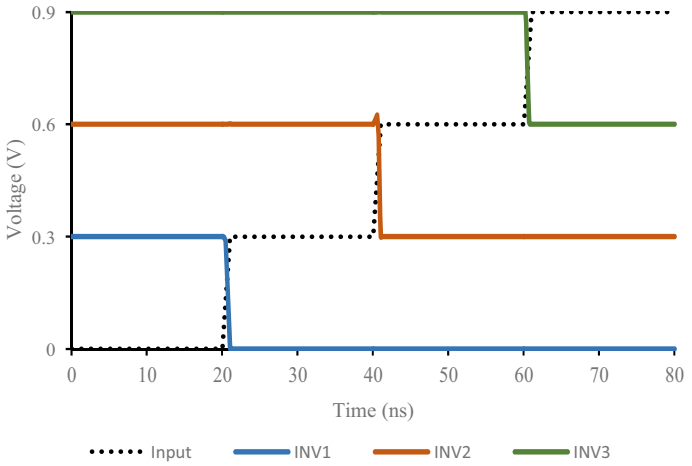

Fig. 2 Inverter responses for quaternary input signal

The threshold voltages of P-type and N-type GNRFET device are derived by the number of dimer line value "*N*". The first inverter works with supply as 0.3 and 0 V. However long 0 < in < 0.15 V, the P-type GNRFET is ON and N-type GNRFET is OFF. Subsequently, out = 0.3 V. Then again when 0.15 < in < 0.3 V, the P-type GNRFET is OFF and N-type GNRFET is ON. Subsequently, out = 0 V. Similarly, the second and third inverters work with supply 0.6–0.3 V and 0.9–0.6 V, respectively. The transient analysis of the inverter with different supply voltages is shown in Fig. 2.

Later, the quaternary storage cell is designed with the help of above three inverters driven by a quaternary input signal Din through the TG which is shown in the circuit diagram in Fig. 3. The proposed storage cell can be used for both read and write operations. Ground (GND), voltage1 (V_1), voltage2 (V_2) and voltage3 (V_3) are the quaternary voltage levels; in the event that input Din is 0 V, Inv1 drives the pass transistor and consequently storing the data. Similarly, the circuit stores all the other voltages.

With the help of TG1, data is written in to the storage cell. The TG2 is used to interrupt the internal feedback to generate distinct input and output nodes. The other TG1 rules the input data with reference to the control (cnt) and control bar (cntb) signals.

5 Simulation Results

The 32-nm MOS-GNRFET model is used for the proposed quaternary storage cell design and simulations on industry standard HSPICE simulation tool. The supply voltages of 0.9, 0.6, 0.3 and 0 V are used to represent the voltages at the nodes V_3,

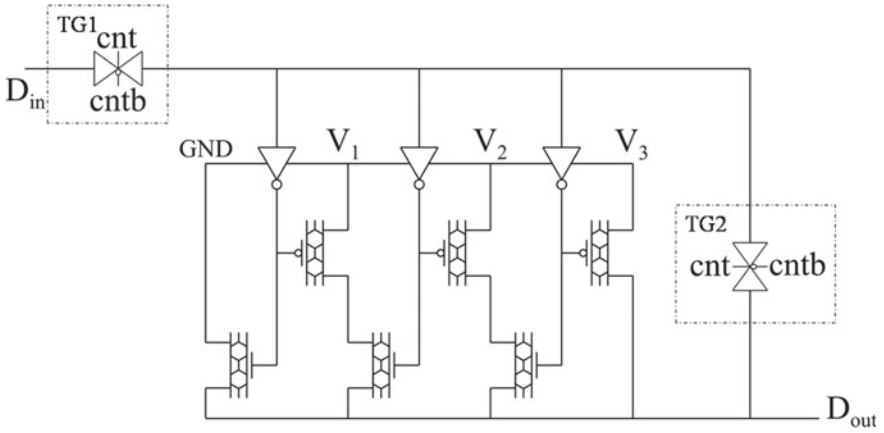

Fig. 3 Quaternary storage cell

V_2, V_1 and GND, respectively. Figure 4 shows the hold and write waveforms of the proposed cell.

During write operation, TG1 is enabled through control signals and data is written in to the storage cell. Cell enters to hold mode when TG1 is disabled and stores previous data until the cnt signal switches back to high. When the cnt signal is 1, the connection is established between Din and main circuit through TG1 and read or write operations can be performed. The condition for write operation is that both the input signals are nonzero. As long as cntrl is 1, data available in input signal Din will be written in to the circuit and it is available at Dout node. The proposed storage cell performance is analyzed by comparing with 8 T SRAM cell proposed in [4]. The performance comparison of proposed circuit is shown in Table 3.

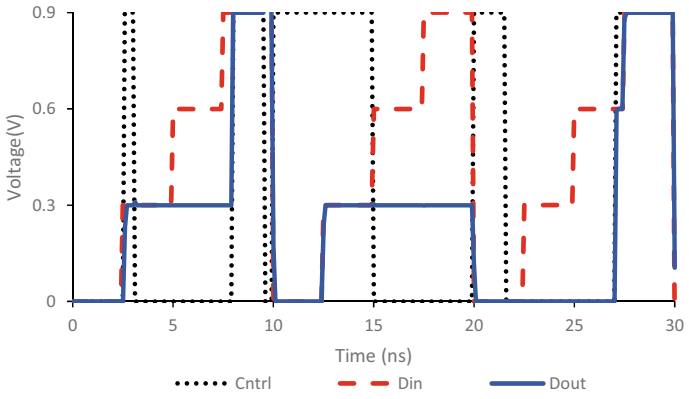

Fig. 4 Storage cell hold and write operation

Table 3 Performance comparison of proposed circuit

	Proposed design	CMOS [4]	CNTFET [4]
Dynamic power (W)	1.27E–06	1.98E–06	1.602E–06
Leakage power (nW)	92.3	110	107.64
Read delay (ps)	3.86	34.0	32.54
Write delay (ps)	1.05	23.87	22.37
SNM (mv)	164	120	141.76

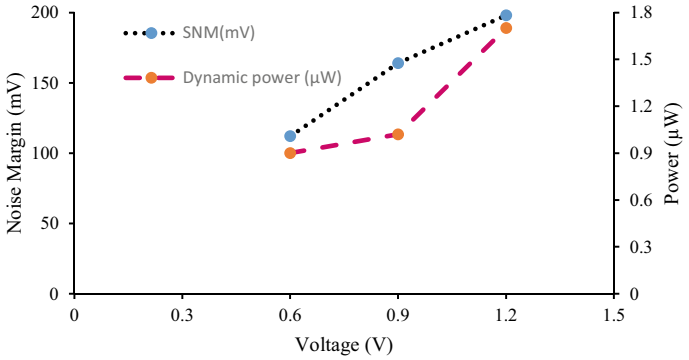

Fig. 5 Dynamic power and SNM consumption with V_{dd} variation

From Table 3, it is observed that the proposed storage cell shows better performance compared with CMOS and CNTFET SRAM cell proposed in [4].

Furthermore, dynamic power and SNM are calculated for three different V_{dd}, i.e., 0.6, 0.9 and 1.2 V. It is observed that both dynamic power and SNM are increasing with increased power supply, and the variation is shown in Fig. 5.

6 Conclusion

Due to the advantages over CMOS and CNTs, the GNRFET has a unique place while developing digital systems. The multiple supply voltage-based memory cell has less complexity as it avoids multi-threshold circuit design. This article introduces a novel GNRFET-based quaternary storage cell circuit. The use of different supply voltages helps to obtain different output voltage levels for the inverters without using the concept of multi-threshold circuits. The designs are simulated using Synopsys HSPICE tool, using 32-nm MOS-GNRFETs and 0.9, 0.6 and 0.3 V as supply voltages for three inverters. The proposed circuit has shown better power improvement, delay optimization and best SNM.

References

1. Gholipour M, Chen YY, Sangai A, Masoumi N, Chen D (2016) Analytical SPICE-compatible model of Schottky-barrier-type GNRFETs with performance analysis. IEEE Trans Very Large Scale Integr Syst
2. Mohammed MU, Nizam A, Ali L, Chowdhury MH (2019) A low leakage SRAM bitcell design based on MOS-type graphene nano-ribbon FET. In: 2019 IEEE International symposium on circuits and systems (ISCAS), pp 1–4. https://doi.org/10.1109/ISCAS.2019.8702461
3. Patel PK, Malik MM, Gutpa TK (2020) A read-disturb-free stable low power and high-density GNRFET 6T SRAM with multi-VT technology. Circuit World 46(3):203–214. https://doi.org/10.1108/CW-06-2019-0054
4. Selvan ST, Sundararajan M (2019) Comparison analysis of three value logic 8T CNTFET SRAM CELL with 6 CMOS SRAM CELL at 32nm technology. Int J Reconfigurable Embed Syst 8(2):107–113. https://doi.org/10.11591/ijres.v8.i2.pp107-113
5. Mohammed MU, Chowdhury MH (2019) Design of energy efficient SRAM cell based on double gate Schottky-barrier-type GNRFET with minimum dimer lines. In: IEEE International symposium on circuits and systems (ISCAS), pp 1–4. https://doi.org/10.1109/ISCAS.2019.8702422
6. Rabieefar F, Dideban D (2019) Utilizing graphene Nano-ribbon transistor in data converters: a comparative study. ECS J Solid State Sci Technol 8(3):M30–M37. https://doi.org/10.1149/2.0161903jss
7. Jiao L, Wang X, Diankov G, Wang H, Dai H (2010) Facile synthesis of high-quality graphene nanoribbons. Nat Nanotechnol 5(5):321–325
8. Zoghi M, Goharrizi AY, Saremi M (2017) Band gap tuning of armchair graphene nanoribbons by using antidotes. J Electron Mater 46(1):340–346

Data Format Heterogeneity in IoT-Based Ambient Assisted Living: A Survey

M. Sandeep, Sagar Khatri, and B. R. Chandavarkar

Abstract Ambient Assisted Living (AAL) has become a significant component of the lives of the elderly in the present decade, allowing them to live independently by assisting their daily activities with automation. Different sensors from various manufacturers with proprietary data formats to detect environmental changes and monitor a person's health metrics. These data formats are the root cause of the data Heterogeneity issue in AAL and, in turn, contribute to data interoperability challenges. In this paper, we have presented a survey on currently available state-of-the-art solutions to address data heterogeneity challenges in AAL and made a comparative study of suggested methods to overcome the data interoperability.

Keywords Ambient assisted living · Internet of Things · Data heterogeneity · Data interoperability · Data aggregation · Data format

1 Introduction

In the recent past, the health sector has seen much advancement and an increase in the cost of health care. The aging ones want to live a healthy and independent life. Old people's vital data should be monitored periodically to ensure good health. People over the age of 60 face many difficulties performing daily activities. Due to people's hectic schedules and the need to commute far from their homes for employment, the elderly must take care of themselves [1]. Automated assistance with health and daily activity will positively affect their social, mental, and physical well-being [2]. As IoT is trending these days, there has been much development in maintaining house ambiance, energy management, and monitoring body vitals of people. This activity was attained with the help of smart devices developed by various organizations. Persons with less medical knowledge can also take care of their health by measuring their body vitals and following the response from an intelligent

M. Sandeep (✉) · S. Khatri · B. R. Chandavarkar
National Institute of Technology Karnataka, Surathkal, India
e-mail: maxniroop@gmail.com

S. Rawat et al. (eds.), *Proceedings of Second International Conference on Computational Electronics for Wireless Communications*, Lecture Notes in Networks and Systems 554,
https://doi.org/10.1007/978-981-19-6661-3_46

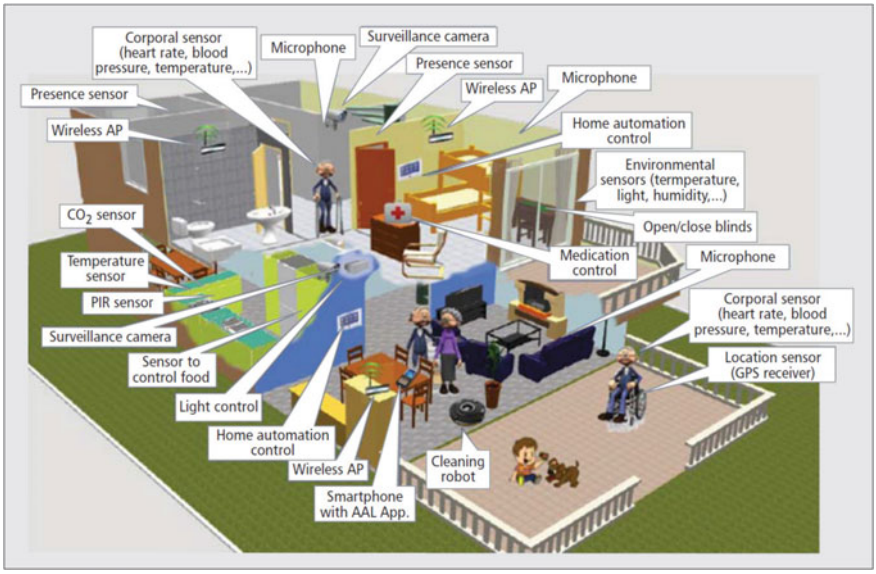

Fig. 1 Smart home with AAL [5]

interactive system. These smart devices include wearable smartwatches, smart bands to monitor heartbeat, electrocardiogram (ECG) patches, etc.

People over the age of 60 suffering from chronic disease are primarily dependent on their caretakers for the Activities of Daily Life (ADL). In order to build a fully-fledged system to automate daily life activities for the elderly and decrease their dependency on the caretaker, Ambient Assisted Living (AAL) based on IoT is an emerging trend. AAL must provide the solution for all age groups, from kids to the elderly, living in the environment. A recent study shows that nearly 68% of the entire population would be living in intelligent homes enabled by IoT devices by 2050 [3]. AAL is defined as the combination of IoT-AAL is defined as the combination of IoT-based automated and semi-automated applications. The solutions in a person's living environment that can communicate and interact with one another to improve a person's health and well-being, quality of life, and independence in the context of their interactions with such environments [4].

Smart home with AAL is shown in Fig. 1 is from article [5] is corporal sensors, the smartphone with an AAL app, medication control, presence sensor, a location sensor, and many more to help the elderly and younger kids live without much manual help from caretakers.

Things that can be achieved by AAL are [6]

- Notifying about the things a person needs to perform, for example, taking medication, health checkup alerts, etc.
- Controlling environment according to the personalized setup by person or caretaker depending on his health condition.

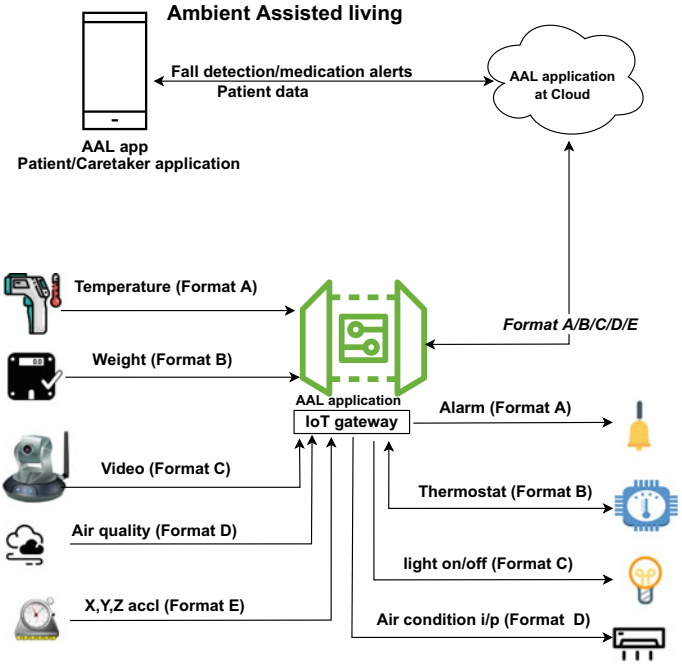

Fig. 2 AAL architecture

- Response based on the context like if the person had left the stove on and no cooking then turning it off etc.
- Predicting future health conditions based on a person's health metric and respond accordingly [7].

A specific scenario in AAL implementation with different components like sensors, actuators, data sink, application processing area, and data visualization is shown in Fig. 2. Further, it specifies multiple sensors and actuators with heterogeneous values and data formats.

The most frequent and valuable topic in AAL is event detection; fall detection is the most concerning. The fall detection must accurately differentiate between a fall and daily life activities [8]. We need to integrate more than one sensor data to detect the fall more accurately, avoiding false detection, which faces the challenge of heterogeneous data. Similarly, the next concerning diagnosis is to assist the elderly in a respiratory emergency, which requires respiration rate, oxygen saturation level in the blood, body temperature, and ambient temperature. The integration of these data will help us to detect and predict the health emergency of the patient more accurately and take appropriate action to stabilize the patient. Even this scenario is affected by heterogeneous data format from the sensor.

The rest of the paper is structured as below. Section 2 contains details of work related to solutions currently available. Section 3 concludes the paper.

2 Related Work

This section concentrates on the causes of AAL's data interoperability issues and solutions to overcome them.

2.1 Data Interoperability

Data interoperability is one of the vital components required to implement the AAL system effectively. Interoperability in IoT is the ability of components and devices in IoT to communicate and exchange information for further use. The most significant reason for the data interoperability challenge is that the device or sensor in the AAL systems is from various manufacturers with their proprietary data structures.

Further, the IoT industry is branched from the perspective of IoT solution providers because of various services, applications, data formats, devices, and communication protocols. The lack of device and data standardization in IoT is another major cause. Because of the above reasons, consumers are encouraged to use devices and software from a single manufacturer. This compound interoperability problem raises the possibility of operational expenditure and product performance. Existing IoT systems are built using application-specific APIs, making cross-platform operation difficult. Interoperability among platforms is not yet achieved due to a lack of support for programs that run on them [9]. Integration of data at data origin is impossible as there is a compatible issue with different data formats [10].

Other categories for interoperability in IoT are:

1. Device-level Interoperability [11]: To establish connection and exchange of data among devices and software components, with communication protocols [12] such as Zigbee, Message Queuing Telemetry Transport (MQTT), and Constrained Application Protocol (CoAP).
2. Network interoperability [13]: Need to deal with device communication over multiple networks smoothly.
3. Semantic interoperability [14]: Unambiguous exchange of data with same meaning and context between communicating device or process.
4. Platform interoperability [15]: Uninterrupted data exchange between IoT platforms with various operating systems, programming languages, and data access protocols.

2.2 Possible Data Formats in IoT are

Text, Binary, Extensible Markup Language (XML), Comma Separated Values (CSV), JavaScript Object Notation (JSON), and Radio Frequency Identification (RFID) are the most common data formats adopted by IoT sensors and applications. The sensor determines the type of data in IoT and the developer's interest [16].

The device metadata with device status or data sensed from the environment are examples of IoT data. As the data provided by IoT is heterogeneous, it is not easy to have a single data representation for all applications [17].

2.3 Solutions Available for Data Interoperability Issue

Publications related to AAL data interoperability are referred to between 2015 and 2021, and solutions are listed. A comparative analysis is made for solutions with different criteria as follows:

- Solution level: cloud, edge, and device.
- Interoperability level: Technical, syntactic, and semantic

Cedillo et al. [18] proposed a solution to solve heterogeneity concerning protocols and data format by middleware at the fog layer before forwarding it to the cloud. The implementation collects data from web services, brokers, and raw data directly from devices. The data from different devices in multiple formats are stored in a generic database with middleware format. The proposed solution has only reduced cloud usage by collecting, storing, and integrating the data. The solution does not have real-life implementation. Data interoperability is not solved.

Gonzalez-Usach et al. [19] specified that the federation of applications like Ambient Assisted Living (AAL) and active and healthy aging (AHA) would benefit together well compared to individual performance. The hindrance to this effort is interoperability, as the system follows different standards, data formats, semantic models, and representations. As a solution, ACTIVAGE architecture enables the Semantic Interoperability Layer (SIL) to provide semantic interoperability among the different platforms. Inter-MW block for syntactic interoperability and Inter-Platform Semantic Mediator (IPSM) for semantics are part of the SIL. Inter-MW interacts with varying platforms through bridges built for every unique platform separately. Syntactic interoperability is achieved by translating the format of every interacting platform into JavaScript Object Notation-Linked Data (JSON-LD) format through these bridges. IPSM performs semantic translation on common data formats depending on the semantic alignment of data. A formulation is used to map the ontologies or models that describe the alignment. Real-time semantic translation is difficult as data models will be in non-resource description framework (RDF) format. A centralized ontology will be maintained, and data will move from platform to platform via two

stages: a platform to central ontology mapping and the next stage to receiver ontology translation. The solution in SIL can provide interoperability between platforms, for example, smart homes AHA cluster using the INTER-IoT project framework. The proposed solution requires bridges to be developed for every new platform to integrate new services. A two-stage mechanism with an intermediate format is necessary for syntactic interoperability, and central ontology needs to be maintained and updated to achieve semantic interoperability.

Modoni et al. [20] had tried to solve CasAware an Ambient Assisted Living platform interoperability challenge. CasAware needs to interact with other IoT implementations for the best living experience and minimize energy usage. The platforms use the heterogeneity of data models, and the lack of a common standard has hindered the smooth data exchange between CasAware and other IoT platforms. An Inter-IoT approach has been adopted to integrate the CasAware application and other IoT platforms. Appropriate bridges have been implemented with the alignment of ontology using INTER-IoT IPSM-AF.

Zgheib [21] proposed interoperability in IoT-based Ambient Assisted Living (AAL) can be handled by software architecture by Semantic Message-Oriented Middleware (SeMoM). In a Cognitive Semantic Sensor Network (CoSSN) ontology for semantic interoperability issues, a high-level semantic knowledge like human activity is inferred using a decision module with rules. Semantic Sensor Network (SSN) ontology is used for handling sensor data. The components can flexibly exchange data as the architecture is loosely coupled with Message-oriented Middleware (MoM) with the publish-subscribe model. The proposed approach tried to achieve interoperability through a new ontology, CoSeOn ontology, where semantics usage in middleware has helped have interoperable IoT applications.

Negesh et al. [22] provided a solution for the Web of Virtual Things (WoVT) server, which can be implemented at both the fog and cloud layers to solve the interoperability challenge. The proposed layer model provides a REST-like uniform interface that can help integrate devices syntactically at the bottom layer. All incoming messages will be formatted uniformly into a virtual representation in the memory, and the virtual model will represent physical devices always. Through RESTful API, the WoVT servers at fog and cloud integration with the devices (virtual things) and achieve semantic interoperability.

Yacchirema et al. [23] have proposed a system that enables IoT Interoperability in AAL, allowing for the monitoring of physiological (heart rate) and environmental (temperature, humidity, CO_2) factors, as well as the tracking of old persons, to support AHA scenarios. A Smart IoT Gateway is proposed to achieve interoperability by performing conversion of protocols between different WSNs (such as Wi-Fi, ZigBee, 802.15.4, and 6LoWPAN) and data from heterogeneous sources are processed, stored, and delivered in a standard format and protocol. The responses are developed for a variety of real-world scenarios. The proposed method can detect and report

caretakers about the activity in elderly care and produce actuate controls depending on input data. In the real-world system, the data are heterogeneous concerning data type, format, and meaning, which is not considered in the experiment.

According to Aloi et al. [25] in AAL systems, gateways play a critical role in enabling IoT interoperability. Through a unified smartphone-centric application, they tried to build a Multi-Technology Gateway for integrating and compatibility of WiFi, Bluetooth Smart, and ZigBee communication protocols. The performance findings show that this technology can be integrated into an IoT infrastructure and used in AAL scenarios. The smartphone's battery capacity, however, limits this approach.

Author	Proposed method	Interoperability level	Advantages	Disadvantages
Gonzalez-Usach et al. [19]	• ACTIVAGE architecture enables Semantic Interoperability Layer (SIL) • Translate data format of interacting platform into JSON-LD format • IPSM to perform semantic translation mapping the ontologies	Syntactic semantic and cloud	Good interoperability solution for volunteered applications	Not suitable for non-web-based applications
Modoni et al. [20]	• INTER-IoT project approach, data format conversion into JSON-LD for syntactic interoperability • IPSM-AF tool is used for mapping the ontologies for semantic interoperability	• Syntactic semantic • Cloud	Good interoperability solution for volunteered applications	Not suitable for Non-web-based applications
Cedillo et al. [18]	• Heterogeneity with protocols and data format handled by middleware at fog layer	• Syntactic, semantic • Fog, and cloud	Middleware store multiple data formats from different devices	Not applied for heterogeneous application
Negash et al. [22]	• Web of Virtual Things (WoVT) server can be implemented at both fog and cloud layers • Interoperability solved by virtual representation of devices	• Syntactic, semantic • fog, cloud	Interoperability solution at fog and cloud	Does not consider heterogeneous application data
Zgheib [21]	• Software architecture by SeMoM • A CoSSN ontology for semantic interoperability	• Semantic • Middleware	Semantics solution in middleware	Syntactic not solved
Yacchirema et al. [23]	• Smart IoT gateway to achieve interoperability	Technical and syntactic, edge	Protocol interoperability solved	Data interoperability not solved
Palma et al. [24]	• WSNs and IPv6 for device interconnection and interoperability	• Technical, syntactic, network	Real-time implementation through a web interface	Data interoperability not addressed
Aloi et al. [25]	• Multi-technology gateway for the integration	• Technical • Gateway at network	Integration of multiple communication protocols through the application	Limited to smartphone capabilities

Garai et al. [26]	• Cloud-based approach for consumer electronics interoperability	• Semantic syntactic • Cloud	Healthcare data through telemedicine interoperability hub	Incomplete syntactic interoperability
Lubamba et al. [27]	• Cyber healthcare cloud with data sink normalize the data by converting it from plain text to XML and then to HL7-CDA standards	• Syntactic, cloud	Interoperability at health record level	Double data translation and complex processing
Rahman et al. [28]	• Semantic interoperability using the fog-based approach by detecting the ontology of the devices and converting the data into RDF format based	• Semantic, fog	Implemented semantic-based model closer to IoT devices	Same RDF for heterogeneous data is a complex issue
Deshmukh et al. [29]	• API or metadata can provide the devices' ontology to help transition between data models, data structure, and data formats to solve data interoperability	• Syntactic, semantic, edge	Provides digital infrastructure and tool for bridging data transfer	Solutions not addressed for different applications and platforms

Palma et al. [24] offer a method for device connectivity and interoperability in AAL systems based on WSNs and IPv6. This concept makes it possible to integrate hardware with constrained computational and memory capabilities.

Aloi et al. [25] in AAL systems, gateways play a critical role in enabling IoT interoperability. Through a unified smartphone-centric application, they tried to build a Multi-Technology Gateway for integrating and compatibility of WiFi, Bluetooth Smart, and ZigBee communication protocols. The performance findings show that this technology can be integrated into an IoT infrastructure and used in AAL scenarios. The smartphone's battery capacity, however, limits this approach.

Garai et al. [26] established the Open Telemedicine Interoperability Hub, a cloud-based platform that defines a centralized data flow and illustrates, maps, converts, and aggregates the data for syntactic and semantic interoperability using middleware. It serves as a link between the architecture of the traditional healthcare system and trending eHealth electronics technology. Here, the method proposed by the author uses the APIs of each device provided by the manufacturer, which gives the format of how data is represented in that device and then included in the hub to process and displays the output requested by the web clients.

Author [27] showed that the devices' data formats are heterogeneous here. The author proved that instead of converting each record in HL7, a process known as normalization, conversion at the data sink resulted in more significant resource usage and fewer overheads. However, most current solutions for interoperability of heterogeneous formats operated devices depend on central resource normalization (translation from source to sink formats). Here, data mapping is to be done from text to XML and then from XML to the standards of HL7. This author calculates the overhead of implementing HL7 and integrating it with lightweight data transmission protocol in the cloud-based environment. It provides proof that the interoperability of the data can be achieved but with overheads of consuming more storage, time, and processing.

Rahman et al. [28] focus on achieving semantic interoperability by converting the raw data from the different sensors into the RDF format based on the ontology of each device. The proposed fog-based semantic model consists of all the cloud functionalities and can implement the frequently used functions of the semantic model closer to the IoT devices. The author performs a comparative study between the other available solution like OpenIoT and IoT-SIM. OpenIoT focuses on interoperable IoT deployments by combining cloud computing and semantic approaches. It employs the semantic sensor network (SNN) ontology to achieve the semantics of raw sensory data. Before sending data to the cloud, OpenIoT performs data aggregation at the gateway device. However, all other semantic processing, such as data modeling, data harmonization, and linking, is done in the cloud, creating a burden for essential IoT applications. While in IoT-SIM, physicians can communicate with their patients using IoT-SIM to check their present status by exchanging valuable information. Some semantic processes, like aggregation and modeling, are performed closer to the IoT devices. In contrast, other procedures are performed on the cloud. The fog-based solution performs better regarding service delay, power utilization, network bandwidth, and the cost of all operations.

Deshmukh et al. [29] proposed the method to solve the data level interoperability by using the devices' ontologies. They use the services and API metadata to capture the specifications of that API. It allows the user to provide its data model of the used format, which can cover the interoperability gap at the data level. The Data Spine provides the essential digital infrastructure and tools to transition between specific services' message formats, data structures, and data models, bridging data transfer interoperability gaps.

The survey indicates there were many attempts from many researchers to solve the data interoperability challenges, as shown in Table ??. Significant efforts were at the cloud level by storing the data in the cloud and representing the sematic in central ontology to solve the semantic interoperability. Another method is by middleware implementation at Fog or cloud level. Here the middleware tries to solve syntactic interoperability by converting the heterogeneous data format into common data format JSON and providing this data for achieving semantic interoperability at cloud. Many are at the gateway to achieve through protocol interoperability or smart gateway to represent the connected devices as virtual objects. The most feasible solutions are at the cloud, a solution at the cost of delay and quality of service (QoS). No attempt is made to solve the issue closer to the data generation, which avoids the data transmission and delays in processing the data in AAL. The creation and understanding of Ontology to achieve semantic interoperability are complex and non-standard. Every IoT application demands its ontology for mapping; as IoT is still in the nascent stage, standard ontology creation should not be hurried. The INTER-IoT IPSM-AF editor tool used for mapping the ontologies is still in the development stage.

3 Conclusion

As Ambient Assisted Living evolving in the recent years, there is much scope for advancement in this field. By increasing the work accuracy of the device and process of the system, data analysis and prediction will be more accurate to help the individual with his living and keep them socially active. However, significant work is yet to be done in this area, considering the actual home environment conditions, analysis, and the challenges involved in the implementation. The survey has shown significant efforts to overcome critical data interoperability hindrances among IoT devices, platforms, and applications with AAL. The interaction will help us exploit the hidden knowledge about the person's activities and environment, which suggests a new and improved system design to make elderly and needy people's lives safe and better.

References

1. Sun H, Florio VD, Gui N, Blondia C (2009) Promises and challenges of ambient assisted living systems. In: 2009 sixth international conference on information technology: new generations, pp 1201–1207. https://doi.org/10.1109/ITNG.2009.169
2. Marques G (2019) Ambient assisted living and internet of things. Harnessing the Internet of everything (IoE) for accelerated innovation opportunities, pp 100–115. https://doi.org/10.4018/978-1-5225-7332-6.ch005
3. United Nation (2018) United nations 68% of the world population projected to live in urban areas by 2050. Says UN
4. Patro SP, Padhy N, Chiranjevi D (2021) Ambient assisted living predictive model for cardiovascular disease prediction using supervised learning. Evol Intell 14(2):941–969. https://doi.org/10.1007/s12065-020-00484-8
5. Cicirelli G, Marani R, Petitti A, Milella A, D'Orazio T (2021) Ambient assisted living: a review of technologies, methodologies and future perspectives for healthy aging of population. Sensors 21(10):3549
6. AAL Association et al (2018) Active and assisted living programme–ICT for ageing well. www.aal-europe.eu
7. Monekosso D, Florez-Revuelta F, Remagnino P (2015) Ambient assisted living [guest editors' introduction]. IEEE Intell Syst 30(04):2–6. https://doi.org/10.1109/MIS.2015.63
8. Malasinghe LP, Ramzan N, Dahal K (2019) Remote patient monitoring: a comprehensive study. J Ambient Intell Human Comput 10(1):57–76. https://doi.org/10.1007/s12652-017-0598-x
9. Noura M, Atiquzzaman M, Gaedke M (2017) Interoperability in internet of things infrastructure: classification, challenges, and future work. In: International conference on internet of things as a service. Springer, pp 11–18. https://doi.org/10.1007/978-3-030-00410-1_2
10. Amjad A, Azam F, Anwar MW, Butt WH (2021) A systematic review on the data interoperability of application layer protocols in industrial iot. IEEE Access 9:96528–96545. https://doi.org/10.1109/ACCESS.2021.3094763
11. Bharamagoudra M, Konduru V (2017) Challenges and solutions of interoperability on IoT how far have we come in resolving the IoT interoperability issues. In: International conference on smart technology for smart nation. LNCS Homepage. https://doi.org/10.1109/SmartTechCon.2017.8358436
12. Babun L, Denney K, Celik ZB, McDaniel P, Uluagac AS (2021) A survey on IoT platforms: communication, security, and privacy perspectives. Comput Netw 192:108040. https://doi.org/10.1016/j.comnet.2021.108040

13. Wan J, Tang S, Shu Z, Li D, Wang S, Imran M, Vasilakos AV (2016) Software-defined industrial internet of things in the context of industry 4.0. IEEE Sens J 16(20):7373–7380. https://doi.org/10.1109/JSEN.2016.2565621
14. Rahman H, Hussain MI (2020) A comprehensive survey on semantic interoperability for internet of things: State-of-the-art and research challenges. Trans Emerg Telecommun Technol 31(12):e3902. https://doi.org/10.1002/ett.3902
15. Rana B, Singh Y, Singh PK (2020) A systematic survey on internet of things: energy efficiency and interoperability perspective. Trans Emerg Telecommun Technol. https://doi.org/10.1002/ett.4166
16. Kenda K, Kažič B, Novak E, Mladenić D (2019) Streaming data fusion for the internet of things. Sensors 19(8):1955. https://doi.org/10.3390/s19081955
17. Mahanthappa S, Chandavarkar B (2021) Data formats and its research challenges in IoT: a survey. In: Evolutionary computing and mobile sustainable networks. Springer, pp 503–515. https://doi.org/10.1007/978-981-15-5258-8_47
18. Cedillo P, Riofrio X, Prado D, Orellana M (2020) A middleware for managing the heterogeneity of data provining from IoT devices in ambient assisted living environments. In: 2020 IEEE ANDESCON, pp 1–6. https://doi.org/10.1109/ANDESCON50619.2020.9272163
19. Gonzalez-Usach R, Julian M, Esteve M, Palau C (2021) Federation of AAL & AHA systems through semantically interoperable framework. In: 2021 IEEE international conference on communications workshops (ICC workshops), pp 1–6 (2021). https://doi.org/10.1109/ICCWorkshops50388.2021.9473503
20. Modoni G, Caldarola EG, Mincuzzi N, Sacco M, Wasielewska K, Szmeja P, Ganzha M, Paprzycki M, Pawlowski W (2020) Integrating IoT platforms using the inter-IoT approach: a case study of the CasAware project. J Ambient Intell Smart Environ **12**. https://doi.org/10.3233/AIS-200578
21. Zgheib R (2017) SeMoM, a semantic middleware for IoT healthcare applications. Ph.D. thesis
22. Negash BS, Westerlund T, Tenhunen H (2018) Towards an interoperable internet of things through a web of virtual things at the fog layer. Future Gener Comput Syst 91. https://doi.org/10.1016/j.future.2018.07.053
23. Yacchirema DC, Palau CE, Esteve M (2017) Enable IoT interoperability in ambient assisted living: active and healthy aging scenarios. In: 2017 14th IEEE annual consumer communications & networking conference (CCNC). IEEE, pp 53–58. https://doi.org/10.1109/CCNC.2017.7983081
24. Palma L, Pernini L, Belli A, Valenti S, Maurizi L, Pierleoni P (2016) Ipv6 WSN solution for integration and interoperation between smart home and AAL systems. In: 2016 IEEE sensors applications symposium (SAS). IEEE, pp 1–5. https://doi.org/10.1109/SAS.2016.7479840
25. Aloi G, Caliciuri G, Fortino G, Gravina R, Pace P, Russo W, Savaglio C (2016) A mobile multi-technology gateway to enable iot interoperability. In: 2016 IEEE first international conference on internet-of-things design and implementation (IoTDI). IEEE, pp 259–264. https://doi.org/10.1109/IoTDI.2015.29
26. Garai Á, Adamkó A (2017) Comprehensive healthcare interoperability framework integrating telemedicine consumer electronics with cloud architecture. In: 2017 IEEE 15th international symposium on applied machine intelligence and informatics (SAMI), pp 000411–000416. https://doi.org/10.1109/SAMI.2017.7880344
27. Lubamba C, Bagula A (2017) Cyber-healthcare cloud computing interoperability using the hl7-CDA standard. In: 2017 IEEE symposium on computers and communications (ISCC), pp 105–110. https://doi.org/10.1109/ISCC.2017.8024513
28. Rahman H, Hussain MI (2019) Fog-based semantic model for supporting interoperability in IoT. IET Commun 13(11):1651–1661. https://doi.org/10.1049/iet-com.2018.6200
29. Deshmukh RA, Jayakody D, Schneider A, Damjanovic-Behrendt V (2021) Data spine: a federated interoperability enabler for heterogeneous IoT platform ecosystems. Sensors 21(12):4010. https://doi.org/10.3390/s21124010

Index Modulation-Based Non-orthogonal Multiple Access (IM-NOMA): Spectral Efficiency Analysis

H. M. Shwetha and S. Anuradha

Abstract Next generations of wireless communication networks are likely to satisfy the emerging demands of high data rate, spectral efficiency and massive connectivity. The present orthogonal multiple access (OMA) schemes cannot meet these requirements. In OMA schemes such as TDMA/FDMA/CDMA/OFDMA, resources are allocated in orthogonal manner to each user. In non-orthogonal multiple access (NOMA), available resources can be shared among all users simultaneously. Thus, NOMA is the next-generation multiple access technology which satisfies demands like high data rate, spectral efficiency and massive connectivity. Using index modulation, information is conveyed to users through both constellation symbols and index symbols. The proposed index modulation-based NOMA scheme, i.e. IM-NOMA, exhibits high performance compared to the other schemes.

Keywords Non-orthogonal multiple access · Orthogonal multiple access · Index modulation · Spectral efficiency · Energy efficiency

1 Introduction

The evolution of wireless communication technology has led to a high demand for massive connectivity as well as data rate. For example, estimated connectivity density of 6G is 10^7 devices/km^2 and data rate is 1 Gb/sec which is ten times greater than 5G [1]. Multiple access techniques which use frequency/time/code in 1G, 2G and 3G, respectively, and OFDMA in 4G come under OMA technique [2]. In OMA, the resources like frequency, time and code are assigned orthogonally to each user [3].

The number of users that OMA technology supports is dependent on the available resources. The evolution of 5G is resulted in the increased demand for data rate,

H. M. Shwetha (✉) · S. Anuradha
Department of Electronics and Communication Engineering, National Institute of Technology, Warangal 506004, India
e-mail: shwethahmutt@gmail.com

S. Anuradha
e-mail: anuradha@nitw.ac.in

S. Rawat et al. (eds.), *Proceedings of Second International Conference on Computational Electronics for Wireless Communications*, Lecture Notes in Networks and Systems 554,
https://doi.org/10.1007/978-981-19-6661-3_47

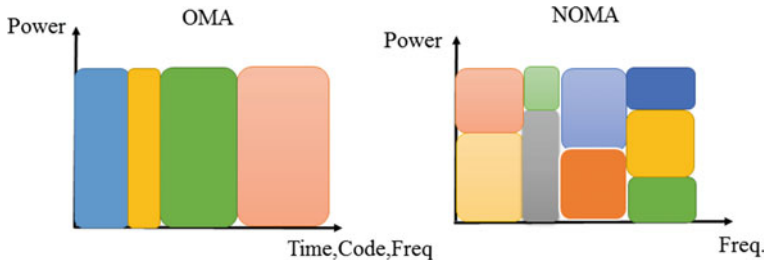

Fig. 1 Graphic comparison of NOMA and OMA

high spectral efficiency and massive connectivity [4]. The OMA-based networks cannot meet the demands since maximum users in which network can support are highly reliant on the available orthogonal resource blocks. Hence, limited users are supported in OMA which in turn reduces the spectral efficiency (SE) and connectivity. NOMA technology encounters the demands that have emerged with the growth of wireless communication technology [5]. NOMA increases the spectral efficiency, connectivity and data rate compared to conventional OMA techniques since NOMA users can use same frequency and time resources [6, 7]. 5G network capacity and sum rate can be significantly enhanced by considering NOMA instead of OMA technology [8]. The illustrative evaluation of NOMA and OMA is given in Fig. 1.

NOMA is basically divided into the following types—code domain and power domain. In NOMA, power domains and code domains are used in multiplexing so that the more number of users can use the available limited resources which in turn improves the capacity of 5G networks. In PD-NOMA, users are assigned with dissimilar powers so that all users in the network can use the alike time/frequency/code resource blocks. In CD-NOMA, different users are allotted with different codes so as to use the same available resource blocks. The basic techniques used in NOMA are at the transmitter—superposition coding (SC) and at the receiver—successive interference cancellation (SIC). Superposition coding process allots power coefficients to users at the transmitter on the basis of their channel state and transmits the information of all users. SIC decodes all user's information on the basis of channels conditions of users at the receiver. SIC decodes strong users signal and eliminates the decoded signal from the received signal; the process is continued until the user receives its own signal. Thus, SIC removes interference from other user's signals and makes detection more efficient.

This paper discussed the IM-NOMA for downlink. Two users' network is considered to realize the proposed system. The results demonstrate that the IM-NOMA SE is better than the OMA system. The energy efficiency and spectral efficiency are discussed in brief.

Index modulation is the promising technique for the upcoming days since it provides high spectral and energy efficiency compared to traditional communication systems. SE and EE are the important metrics in wireless networks. IM is the simple digital modulation technique that conveys additional information bits through

indices of corresponding communication system's building blocks. Index modulation transmits the information in an innovative way by considering subcarriers along with the conventional M-ary signal constellations [9]. The advantages of IM aided NOMA compared to orthogonal methods are high SE and high EE.

The rest of the paper is arranged in this manner—Sect. 2 elaborates the IM-NOMA system, energy efficiency and spectral efficiency. The simulation results of SE and EE are presented and studied in Sect. 3. Section 4 concludes the paper.

2 System Model

Consider a NOMA system in Fig. 2 that includes a single base station (BS) serving NT users. The total bandwidth BT is divided into LT orthogonal subcarriers. Each subcarrier is of bandwidth Bc. The users' $N \leq N$T are served by L adjacent subcarriers. Each user receives P number of bits. According to index modulation concept, each user transmits P bits, and these bits are divided into following blocks: the indices of the combination of active subcarriers as well as M-ary constellation symbols. The first block consists of $\log 2M$ bits and the second block consists of $[\log_2((\frac{L}{K}))]$, where $1 \leq K \leq L$ together makes total P bits to be delivered to each user. The first block is modulated using conventional modulation techniques like QAM/PSK. The second block is considered for selecting an active subcarrier's combination to transmit the corresponding modulated complex symbol C_n. Hence, a total of $(\log_2 M + [\log_2((\frac{L}{K}))])$ bits enter the transmitter of the system in each transmission interval.

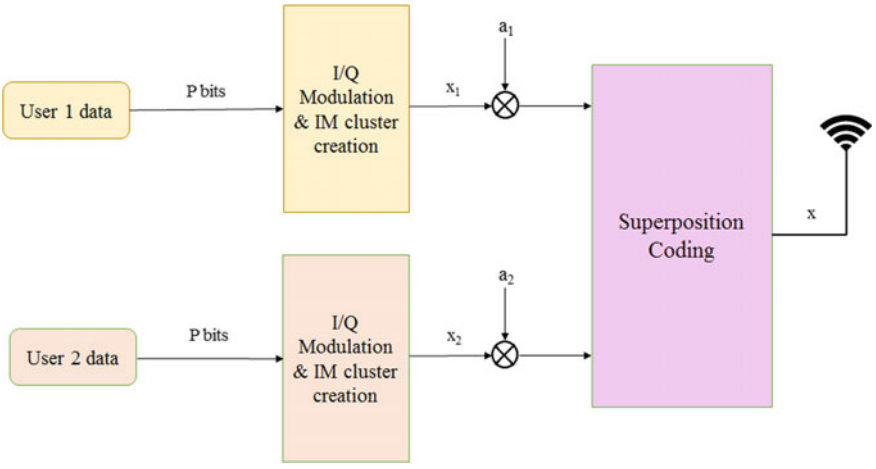

Fig. 2 Downlink IM-NOMA system model

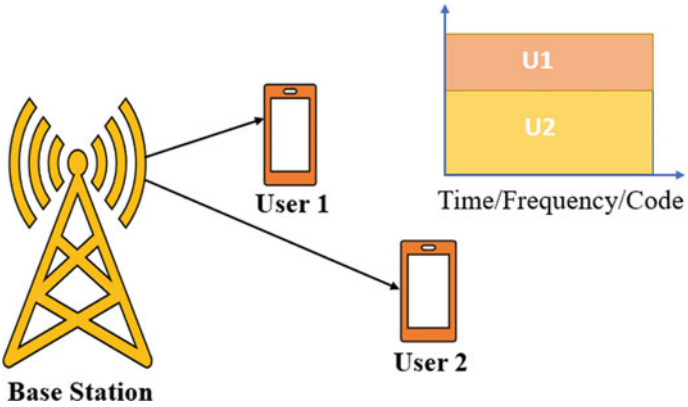

Fig. 3 Two user downlink NOMA network

Specifically, for the nth user, the signal transmitted over subcarrier l is represented by

$$s_{nl} = \begin{cases} c_n, & \text{if } l \in \widehat{l_n} \\ 0, & \text{if } l \in \widehat{l_n} \end{cases}$$

where $\widehat{l_n}$ denotes the nth user's indices of selected active subcarriers. Hence, each user follows the same process for selecting the complex symbol and active subcarriers which carries the symbols. As in conventional power domain NOMA systems shown in Fig. 3, the signals to be transmitted are multiplexed over all active subcarriers and simultaneously transmitted to the different users. According to the superposition coding principle, additional power is apportioned to the far user which has weak channel coefficient compared to the near user.

x_l is the superimposed signal transmitted over subcarrier l is represented as,

$$x_l = \sum_{n=1}^{N} \sqrt{\rho_n} s_{nl}$$

At the user n, the signal received over subcarrier l is given by,

$$y_{nl} = \sqrt{P_{r,n}} h_{nl} x_l + w_{nl}$$

where

$P_{r,n} = P_{\text{tdn}} - \eta$—the user n's received power,
η—the path loss exponent,
P_{t}—transmitted power,
h_{nl}—the channel experienced by user n over subcarrier l,
$w_{\text{nl}} \sim \text{CN}(0, \sigma 2)$—the additive white Gaussian noise.

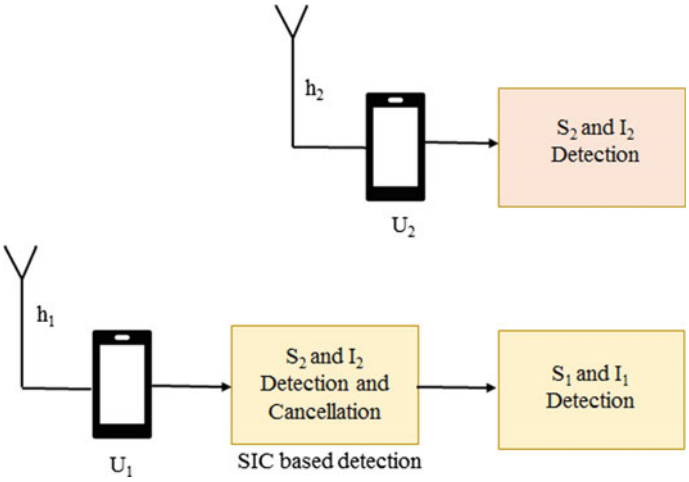

Fig. 4 SIC detection of IM-NOMA

The channel coefficients are assumed to be independent and identically distributed (i.i.d) Rayleigh fading channels between the BS and different users.

SIC Detection:
According to the superposition coding, near user with good channel conditions is allotted with less power coefficient than that of far user. In SIC, each user nearer to the base station (BS) detects and removes the signals that are far from the BS compared to that user and treats all other user's signal as noise.

The decoded signal will be removed from the received signal, and the same process continues till it decodes its own signal. Figure 4 represents the downlink NOMA network's SIC receiver. All user's signals are allotted with power coefficients by the BS according to the SC technique [10].

3 Performance Analysis

Spectral efficiency: SE is the ratio between the total sum rate of the user to the bandwidth used [11].

$$\text{SE} = \frac{R_{\text{T}}}{w} \text{ (bps/Hz)}$$

In orthogonal multiple access technology, each user is assigned with the single channel. The spectral efficiency is $\log_2(M)$ per user. In OMA, SE is independent of L [12].

In NOMA, all channels are used by all users of the network. The spectral efficiency for NOMA is $L^*\log_2(M)$.

In IM-NOMA, per-user spectral efficiency is

$$\left(\log_2 M + \left[\log_2\left(\binom{L}{K}\right)\right]\right) \quad \text{[bpcu]}$$

where $K \leq L$—number if active channels. Only active channels will carry symbols so that trade-off between BER and SE can be made through flexible set-ups. [bpcu] stands for bits per channel use.

Energy efficiency (EE) is the ratio between the sum rates to the base station's power. The message signal power and the circuit power represent the total power consumption at the transmitting side [13].

$$\begin{aligned} \text{EE} &= \frac{\text{R}_T}{\text{P}_T} = \text{SE}\frac{W}{\text{P}_T} \quad \text{(bits/Joule)} \\ P_{\text{T}} &= P_{\text{s}} + P_{\text{Static}} \end{aligned} \tag{1}$$

PT—total power at the BS, P_{s}—signal power and P_{static}—circuitry power.

According to Shannon's theory, the relationship between EE and SE will not consider the power consumption of the circuit, so it is monotonic. SE and EE are inversely proportional to each other, i.e. EE increases for lesser SE region and EE decreases for higher SE region. Peak of the curve denotes the EE at its maximum value. EE-SE relationship is linear for the positive slope of the curve. SE increases with the rise in EE.

4 Results and Discussion

4.1 IM-NOMA Spectral Efficiency

The spectral efficiency of IM-NOMA is compared with the OMA for different values of available channels L, $N = L$ and modulation order of $M = 2$. Three values assigned for active subcarriers are given by $k = 1, 2, 3$. From Fig. 5, we can observe that for a given M and L, the per-user spectral efficiency increases with the increase in the number of active subcarriers.

Figure 6 shows the SE per user versus the number of active subcarriers K for different values of L with the modulation order $M = 4$. For a given value of L, the spectral efficiency increases with the increase in active subcarriers K. The graph indicates that when $K = L/2$, spectral efficiency attains its maximum point. Once the SE attains the maximum value, for the next values of K, the spectral efficiency decreases with the increase in K.

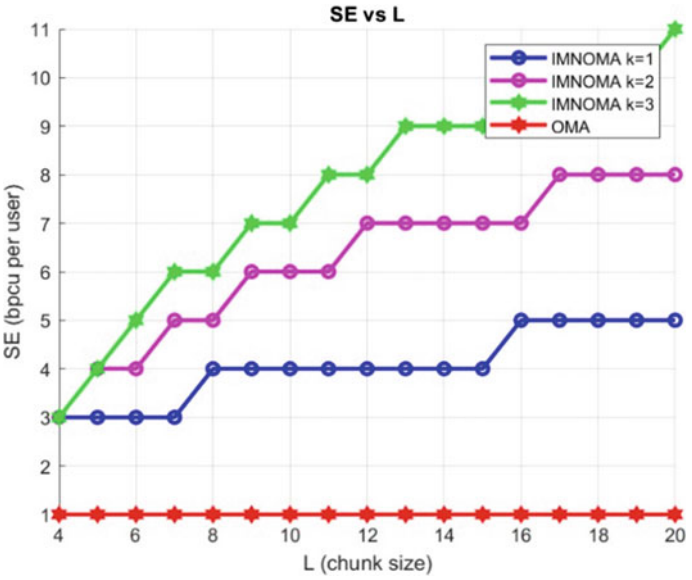

Fig. 5 Per-user spectral efficiency versus L for different values of K

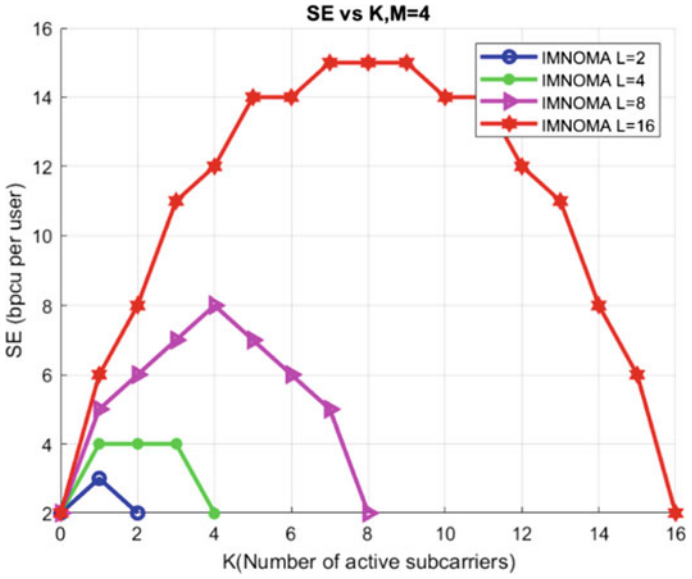

Fig. 6 Per-user spectral efficiency versus K for different values of L

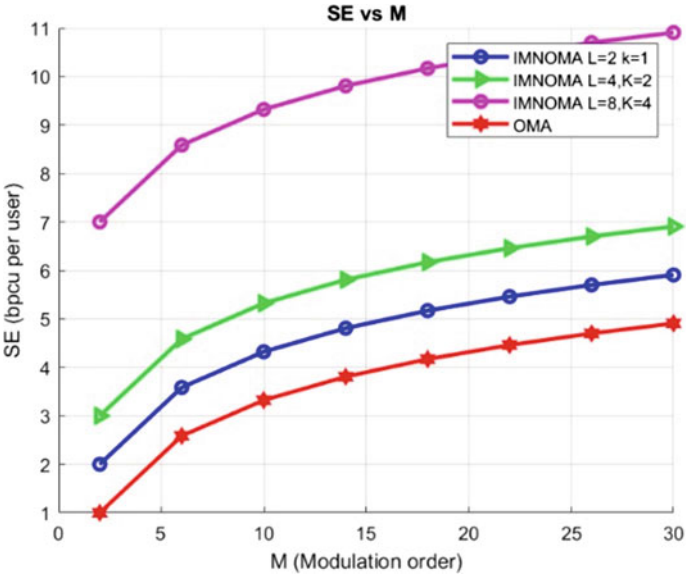

Fig. 7 Per-user spectral efficiency versus M for different values of L and K

Figure 7 indicates the per-user spectral efficiency of IM-NOMA scheme versus the modulation order M for different values of K and L. OMA and IM-NOMA spectral efficiency results are compared. In OMA system, the spectral efficiency is $\log_2 M$ which is independent of L, and hence, there is no enhancement in SE. However, for IM-NOMA, the SE $= [\log_2((\frac{L}{K}))] + \log_2(M)]$. IM-NOMA has additional $[\log_2((\frac{L}{K}))]$ bps/Hz compared to OMA system. In Fig. 8, IM-NOMA achieves additional 1 bps/Hz compared to OMA irrespective of the modulation order for $L = N = 2$.

4.2 NOMA Energy Efficiency

Figure 8 shows the energy efficiency versus the transmit power in dBm for different values of L and K. Circuit power is assumed to be 60 W. Modulation order $M = 2$ is considered. From the figure, we can observe that when P is smaller than or equal to a certain threshold, the graph indicates the same energy efficiency value. Once P reaches the threshold value, the EE begins to decline. Hence, the optimal energy-efficient systems work at the exact value of P when the power crosses the threshold value. The trade-off between EE and SE can be accomplished by adjusting the power. Since OMA system is independent of L, IM-NOMA outperforms the OMA as shown in Fig. 8.

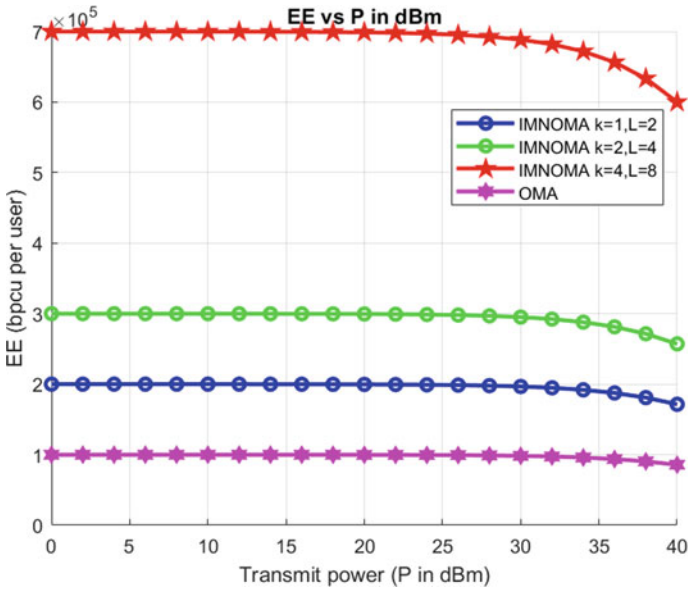

Fig. 8 Energy efficiency versus transmit power P for different values of L and K

5 Conclusion

The downlink IM-NOMA system is analysed by considering SE and EE parameters. SIC is verified for two user networks. Simulation results show that IM-NOMA provides a higher spectral efficiency than OMA. For a given M and L, the per-user spectral efficiency increases with the increase in the number of active subcarriers. When $K = L/2$, spectral efficiency attains its maximum point. As long as P is smaller than or equal to a certain threshold, the graph indicates the same energy efficiency value. IM-NOMA offers higher performance in terms of spectral efficiency and energy efficiency compared to OMA.

References

1. Zhang Z et al (2019) 6G wireless networks: vision, requirements, architecture, and key technologies. IEEE Veh Technol Mag 14(3):28–41. https://doi.org/10.1109/MVT.2019.2921208
2. Liaqat M, Noordin KA, Abdul Latef T, Dimyati K (2020) Power-domain non orthogonal multiple access (PD-NOMA) in cooperative networks: an overview. Wirel Netw 26(1):181–203. https://doi.org/10.1007/s11276-018-1807-z
3. Dai L, Wang B, Ding Z, Wang Z, Chen S, Hanzo L (2018) A survey of non-orthogonal multiple access for 5G. IEEE Commun Surv Tutor 20(3):2294–2323. https://doi.org/10.1109/COMST.2018.2835558

4. Cai Y, Qin Z, Cui F, Li GY, McCann JA (2018) Modulation and multiple access for 5G networks. IEEE Commun Surv Tutor 20(1):629–646. https://doi.org/10.1109/COMST.2017.2766698
5. Aldababsa M, Toka M, Gökçeli S, Kurt GGK, Kucur OL (2018) A tutorial on nonorthogonal multiple access for 5G and beyond
6. Irfan M, Kim BS, Shin SY (2015) A spectral efficient spatially modulated non-orthogonal multiple access for 5G. In: 2015 Internationalsymposium intelligence signal processing, communication systems, ISPACS 2015, pp 625–628. https://doi.org/10.1109/ISPACS.2015.7432847
7. Makki B, Chitti K, Behravan A, Alouini M-S (2020) A Survey of NOMA: current status and open research challenges. IEEE Open J Commun Soc 1(February):179–189. https://doi.org/10.1109/ojcoms.2020.2969899
8. Dai L, Wang B, Yuan Y, Han S, Wang CLIZ (2015) Non-orthogonal multiple access for 5G: solutions, challenges, opportunities, and future research trends. IEEE Commun Mag 53(9):74–81. https://doi.org/10.1109/MCOM.2015.7263349
9. Basar E, Wen M, Mesleh R, Di Renzo M, Xiao Y, Haas H (2017) Index modulation techniques for next-generation wireless networks. IEEE Access 5(August):16693–16746. https://doi.org/10.1109/ACCESS.2017.2737528
10. Ding Z, Yang Z, Fan P, Poor HV (2014) On the performance of non-orthogonal multiple access in 5G systems with randomly deployed users. IEEE Signal Process Lett 21(12):1501–1505. https://doi.org/10.1109/LSP.2014.2343971
11. Ruano P et al (2016) We are IntechOpen, the world's leading publisher of Open Access books Built by scientists , for scientistsTOP 1%. Intech Tourism 13. [Online]. Available: https://www.intechopen.com/books/advanced-biometric-technologies/liveness-detection-in-biometrics
12. Althunibat S, Mesleh R, Qaraqe KA (2019) IM-OFDMA: a novel spectral efficient uplink multiple access based on index modulation. IEEE Trans Veh Technol 68(10):10315–10319. https://doi.org/10.1109/TVT.2019.2937
13. Liu Q, Tan F, Lv T, Gao H (2017) Energy efficiency and spectral-efficiency tradeoff in downlink NOMA systems. In: 2017 IEEE International conference on communication work. ICC Work, 2017, pp 247–252. https://doi.org/10.1109/ICCW.2017.7962665

Fully Quadrature Spatial Modulation Performance with Imperfect Channel Information

Kiran Gunde and Anuradha Sundru

Abstract "Quadrature spatial modulation (QSM)" uses the in-phase and quadrature components to convey the information, which improves the data rate of the system. A fully QSM (F-QSM) scheme is developed to increase the spectral efficiency (SE) of QSM. The SE of the most space modulation techniques (SMTs) is restricted to being logarithmic proportional to number of transmitting antennas. F-QSM scheme uses a novel transmission method to provide a linear proportionality between the SE and number of transmitting antennas. This paper presents the "bit error rate (BER)" performance of F-QSM under imperfect channel conditions and compares the F-QSM scheme with various SMTs. We use maximum-likelihood (ML) detection approach to evaluate the BER of F-QSM and compares it with the QSM scheme. Additionally, it compares the computational complexity of the F-QSM to the RC-mGQSM.

Keywords SM · QSM · F-QSM · Imperfect channel

1 Introduction

A novel and energy efficient scheme for the "multiple input multiple output (MIMO)" transmission system is called "spatial modulation (SM)" [1–3]. SM is proposed to increase the SE of single antenna system without changing the system bandwidth. Unlike conventional MIMO schemes, this scheme can use an additional spatial dimension to convey more information. At every time instant, SM transmits the data using only one transmit antenna. The hardware complexity of the SM system reduced since, it only uses a single "radio frequency (RF)" chain. The input bits in SM processing through two mapping blocks, the first block map the antenna using spatial bits and the second block map the data symbol using data bits. With this transmission mechanism, SM improves the data rate without changing the system

K. Gunde (✉) · A. Sundru
National Institute of Technology Warangal, Warangal, Telangana 506004, India
e-mail: kirangunde4u@gmail.com

A. Sundru
e-mail: anuradha@nitw.ac.in

S. Rawat et al. (eds.), *Proceedings of Second International Conference on Computational Electronics for Wireless Communications*, Lecture Notes in Networks and Systems 554,
https://doi.org/10.1007/978-981-19-6661-3_48

bandwidth. In [4], the authors studied the SM performance with imperfect "channel state information (CSI)". In [5], the authors discusses the recent uses of different SM systems and provides research direction towards 5G wireless networks. The SE of SM is given as, $R_{\mathrm{SM}} = \log_2(N_T) + \log_2(M)$ "bits per channel use (bpcu)" with N_T transmitting antennas and Mth order of M-QAM constellation. For data transmission, the $\log_2(N_T)$ bits choose the transmitting antenna and $\log_2(M)$ bits select data symbol. SM is free of "inter-channel interference (ICI)" and "inter-symbol interference (ISI)", since only one antenna is active at any time instant. Generalised SM (GSM) [6] was developed by removing the constraints of SM, such as N_T is limited to integer powers of 2 and the RF chains are limited to one. GSM scheme use several RF-chains to transmit same data on different antennas. Hence, the SE of GSM is more than SM.

"Quadrature SM (QSM)" [7] is a variant technique of SM transmission. In QSM, the real ($\Re\{\cdot\}$) and imaginary ($\Im\{\cdot\}$) coefficients of complex data symbol are separated and transmitted independently over "in-phase (I)" and "quadrature (Q)" dimensions, respectively. Therefore, the SE of QSM is more than SM by considering an extra spatial dimension. This scheme also avoids ICI, since the orthogonality of I and Q dimensions. The effect of imperfect channel information of the QSM performance was examined in [8], and QSM is studied over correlated fading with imperfect CSI conditions [9]. The modified generalised QSM (mGQSM) [10] is introduced to increase the SE of QSM. In mGQSM, several RF chains are used to convey the data on multiple active antennas. The "reduced codebook mGQSM (RC-mGQSM)" is a mGQSM method with a lower complexity. The mGQSM is studied under channel imperfections over Nakagami [11] and Weibull [12] fading channels.

Fully GSM (F-GSM) [13] scheme was proposed to improve the SE of SM and GSM. To improve data rate, a new transmission mechanism is developed that enables the linear proportionality between data rate and N_T, whereas all other SMTs use logarithmic proportionality between data rate and N_T. Fully grouped generalised SM scheme is introduced in [14], the transmitting antennas are partitioned into number of groups and each group considered as F-GSM scheme. Fully QSM (F-QSM) [15] scheme was developed to further improve the QSM data rate. Like F-GSM, F-QSM scheme employs a novel transmission mechanism in order to attain the linear proportionality between the SE and N_T. However, F-QSM scheme transmits $\Re\{\cdot\}$ and $\Im\{\cdot\}$ parts independently. The complexity of F-QSM is compared to QSM with different N_T. The F-QSM performance is analysed under Rician channels [16]. In [17], the authors presented the comprehensive study of different SMTs and provide the general mathematical framework for SMTs.

In this paper, we study the F-QSM scheme under imperfect channel conditions. The performance of F-QSM scheme is compared to that of several SMTs. We use ML detection to present the BER performance of F-QSM and compare it to the QSM scheme. Additionally, it compares the computational complexity of the F-QSM to the RC-mGQSM.

The rest of the paper is follows as. Section 2 presents the F-QSM system model and illustrated using an example. Section 3 describes the F-QSM performance with an imperfect CSI. Section 4 discusses the results and computational complexity, and the paper concludes in Sect. 5.

2 F-QSM System Model

The transmission diagram of F-QSM is shown as [13, Fig. 1]. The input bits split into 3 blocks, the first block consists of bits which are equal to $\log_2 M$ bits. Using these bits, the data symbol S is selected from the QAM modulation. Furthermore, the symbol S is separated as real $S_{\Re}$ and imaginary $S_{\Im}$ symbols. The remaining two blocks consists of spatial bits which are equal to $(N_T - 1)$ bits per each block. Using these spatial bits, the transmit antenna selection (TAS) is selected. The first $(N_T - 1)$ bits choose a TAS to transmit the $S_{\Re}$, and remaining $(N_T - 1)$ bits choose a same or different TAS to transmit the $S_{\Im}$. Therefore, the SE of F-QSM scheme can be given as [15],

$$R_{\text{F-QSM}} = 2(N_T - 1) + \log_2 M \quad \text{bpcu} \tag{1}$$

From Eq. (1), we can observe that the SE of F-QSM is linearly proportional with N_T, while the conventional SMTs data rate is logarithamically proportional with N_T. Hence, F-QSM scheme provides higher data rates over SM and QSM with fewer N_T values. For example, let $N_T = 4$ and $M = 4$, then the SE of F-QSM becomes 8 bpcu. To attain the SE of 8 bpcu, SM and QSM schemes require $N_T = 64$ and $N_T = 8$, respectively.

Let us consider the input bits [1 1 0 0 0 0 1 1] for F-QSM scheme with 8 bpcu transmission. Where the first, two bits [1 1] map the M-QAM data symbol S. Furthermore, the data symbol S is separated as $S_{\Re}$ and $S_{\Im}$. Remaining, spatial bits split into 2 equal blocks, the first block of bits [0 0 0] choose the transmit antenna T_{x1} and second block of bits, [0 1 1] choose the transmit antenna T_{x4} from Table 1. Finally, the symbols, $S_{\Re}$ and $S_{\Im}$, are transmitted by the antennas T_{x1} and T_{x4}, respectively. Hence, the $N_T \times 1$ dimension transmission vector is given as, $\mathbf{S} = [S_{\Re}\ 0\ 0\ jS_{\Im}]^T$. Similarly, for the other possible transmitted vectors are given in Table 2.

Consider $N_R \times N_T$ system being N_R receiving and N_T transmitting antennas. Let the Rayleigh channel, $\mathbf{H} \in \mathbb{C}^{N_R \times N_T}$ and the noise, $\mathbf{n} \in \mathbb{C}^{N_R \times 1}$. The entries of $\mathbf{H}$ and $\mathbf{n}$ follow "independent and identically distributed (i.i.d.)" Gaussian random variables with mean 0 and variance of unity and σ_n^2, respectively, i.e. $h_{N_R,N_T} \sim \mathcal{CN}(0, 1)$ and $n_{N_R,1} \sim \mathcal{CN}(0, \sigma_n^2)$. The received signal is given by,

Table 1 Transmit antenna selection (TAS) to transmit $S_{\Re}$ or $S_{\Im}$ for $N_T = 4$

Possible bits	Transmit antenna selection (TAS)
000	T_{x1}
001	T_{x2}
010	T_{x3}
011	T_{x4}
100	T_{x1}, T_{x2}
101	T_{x1}, T_{x3}
110	T_{x1}, T_{x4}
111	T_{x2} , T_{x3}

Table 2 Example for the F-QSM transmission with $N_T = 4$ and $M = 4$

i/p bits		Transmission data			
Data bits	Spatial bits	T_{x1}	T_{x2}	T_{x3}	T_{x4}
$b_1 b_2$	000000	S	–	–	–
$b_1 b_2$	000001	$S_{\Re}$	$S_{\Im}$	–	–
$b_1 b_2$	000010	$S_{\Re}$	–	$S_{\Im}$	–
$b_1 b_2$	000011	$S_{\Re}$	–	–	$S_{\Im}$
$b_1 b_2$	111100	$S_{\Im}$	S	$S_{\Re}$	–
$b_1 b_2$	111101	$S_{\Im}$	$S_{\Re}$	S	–
$b_1 b_2$	111110	$S_{\Im}$	$S_{\Re}$	$S_{\Re}$	$S_{\Im}$
$b_1 b_2$	111111	–	S	S	–

$$\begin{aligned} \mathbf{y} &= \mathbf{H}\mathbf{S} + \mathbf{n} \\ &= \mathbf{h}_{l_{\Re}} S_{\Re} + j\mathbf{h}_{l_{\Im}} S_{\Im} + \mathbf{n} \end{aligned} \tag{2}$$

and

$$\mathbf{h}_{l_{\Re}} = \sum_{p=1}^{N_c} \mathbf{h}_p, \quad \mathbf{h}_{l_{\Im}} = \sum_{q=1}^{N_c} \mathbf{h}_q \tag{3}$$

where $\mathbf{h}_p$, $\mathbf{h}_q$ denote the p^{th} and q^{th} columns of $\mathbf{H}$, respectively, and $N_c = 1, 2, \cdots, \lceil \frac{N_T}{2} \rceil$. $\lceil . \rceil$ denotes the ceiling function.

At the receiver, we use the ML detection algorithm by assuming perfect channel information and it is given by,

$$[\widehat{l_{\Re}}, \widehat{l_{\Im}}, \widehat{S_{\Re}}, \widehat{S_{\Im}}] = \underset{l_{\Re}, l_{\Im}, S_{\Re}, S_{\Im}}{\arg\min} \|\mathbf{y} - (\mathbf{h}_{l_{\Re}} S_{\Re} + j\mathbf{h}_{l_{\Im}} S_{\Im})\|^2 \tag{4}$$

where $\widehat{l_{\Re}}$ and $\widehat{l_{\Im}}$ are the detected antenna indices of $\widehat{S_{\Re}}$ and $\widehat{S_{\Im}}$.

3 F-QSM System with Imperfect Channel Knowledge

This section presents the F-QSM performance under imperfect channel knowledge. To illustrate the performance of F-QSM with imperfect channel $(\mathbf{H} + \delta\mathbf{H}) \in \mathbb{C}^{N_R \times N_T}$, the error channel $\delta\mathbf{H} \in \mathbb{C}^{N_R \times N_T}$ is employed along with Rayleigh channel $\mathbf{H} \in \mathbb{C}^{N_R \times N_T}$. The entries of $\delta\mathbf{H}$ follow i.i.d. $\mathcal{CN}(0, \sigma_e^2)$, where σ_e^2 defines the variance of $\delta\mathbf{H}$. Accordingly, the entries of imperfect channel follows i.i.d. $\mathcal{CN}(0, 1 + \sigma_e^2)$. In this paper, we consider two distinct scenarios, 1). fixed σ_e^2: to determine the performance of F-QSM, the value of σ_e^2 is constant for different "signal to noise ratio (SNR)" values, and 2). variable σ_e^2: where the σ_e^2 is changes with

different SNR values as $\sigma_e^2 = 1/(\gamma N)$, where the average SNR, $\gamma = E\left\{|S|^2\right\}/\sigma_n^2$ and N is the number of pilot symbols which are used to estimate the error channel [4].

The ML detection method makes a decision with imperfect channel $\mathbf{H} + \delta\mathbf{H}$. The ML detection for input signal $\mathbf{S}$ can be given as,

$$\hat{\mathbf{S}} = \arg\min_{\mathbf{S}} \|\mathbf{y} - (\mathbf{H} + \delta\mathbf{H})\mathbf{S}\|^2 \tag{5}$$

where, $\hat{\mathbf{S}}$ is the estimated signal of $\mathbf{S}$.

4 Results and Computational Complexity

4.1 Results

This subsection discusses the BER performance of F-QSM scheme with perfect and imperfect channel scenarios. We compare the F-QSM scheme with QSM under imperfect CSI conditions. Consider the entries of Rayleigh channel $\mathbf{H}$ and $\mathbf{n}$ are observed as i.i.d. $\mathcal{CN}(0, 1)$ and $\mathcal{CN}(0, \sigma_n^2)$, respectively. To compute BER, we utilise 10^5 data symbols. For all the computer simulations, assume 4×4 system with $N_T = 4$ and $N_R = 4$ and compare all the schemes at BER of 10^{-4}.

BER comparison of F-QSM, RC-mGQSM, QSM, and SM under uncoded Rayleigh channel is shown in Fig. 1. These schemes are compared with the same SE of 8 bpcu.

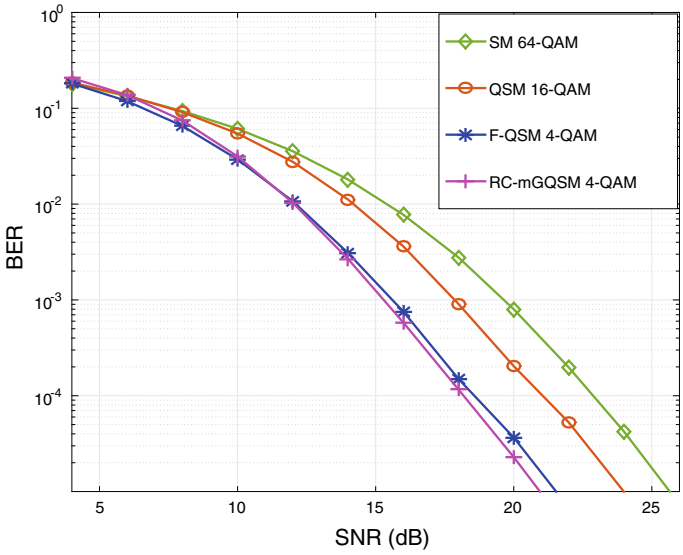

Fig. 1 BER versus SNR of F-QSM, RC-mGQSM, QSM, and SM schemes with 4×4 system over the Rayleigh channel with same SE of 8 bpcu

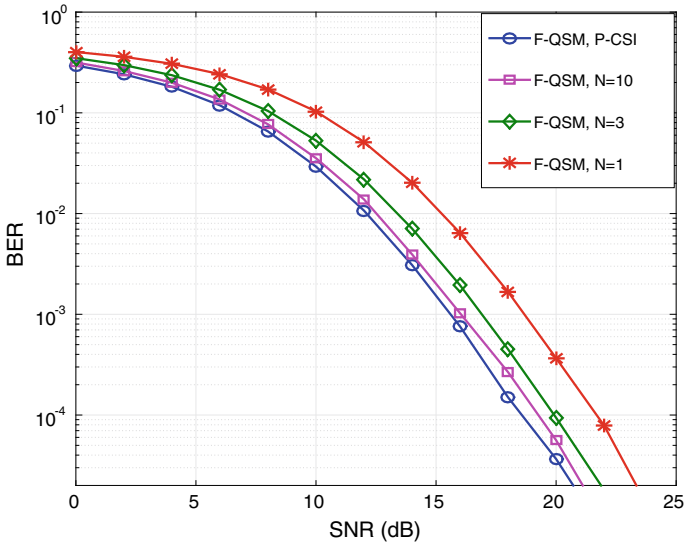

Fig. 2 BER versus SNR of F-QSM with 4×4 system model under imperfect channel with variable σ_e^2 and $N = \{1, 3, 10\}$ and $R_{F-QSM} = 8$ bpcu

The F-QSM scheme outperforms by ~ 2.5 dB SNR of QSM and ~ 4.5 dB SNR of SM. There is a small degradation of ~ 0.5 dB SNR over RC-mGQSM. By comparing these schemes, F-QSM can deliver more spatial bits for a smaller number of transmitting antennas and lower order modulation, and this mechanism decreases the complexity of F-QSM scheme.

Figure 2 presents the BER versus SNR of F-QSM scheme under imperfect channel with variable σ_e^2. We compare the F-QSM performance with perfect channel state information (P-CSI) to F-QSM with imperfect channel and number of pilot symbols N equal to 1, 3, and 10. The BER of F-QSM scheme degrades by ~ 3.5 dB, ~ 1.5 dB, and ~ 0.5 dB SNRs with $N = 1, 3,$ and10 values, respectively. The performance of F-QSM with an imperfect channel approaches that of a perfect channel when N is increased.

The performance of F-QSM and QSM schemes under imperfect channel conditions is shown in Figs. 3 and 4, respectively. We compare the BER of both the schemes at SNR values of 16, 18, and 20 dB which is given in Table 3. We assume the values of error variance σ_e^2 as 0, 0.003, 0.005, and 0.007. However, the value $\sigma_e^2 = 0$ becomes the perfect channel. At SNR of 16 dB, we observed the BER values for F-QSM and QSM schemes are 0.0014 and 0.0051, respectively, and at 20 dB, the BER values are 0.0001 and 0.0005, respectively, for $\sigma_e^2 = 0.005$. Hence, the F-QSM scheme performance better than QSM scheme under imperfect channel conditions. In F-QSM, the data can be transmitted through a variable number of antennas.

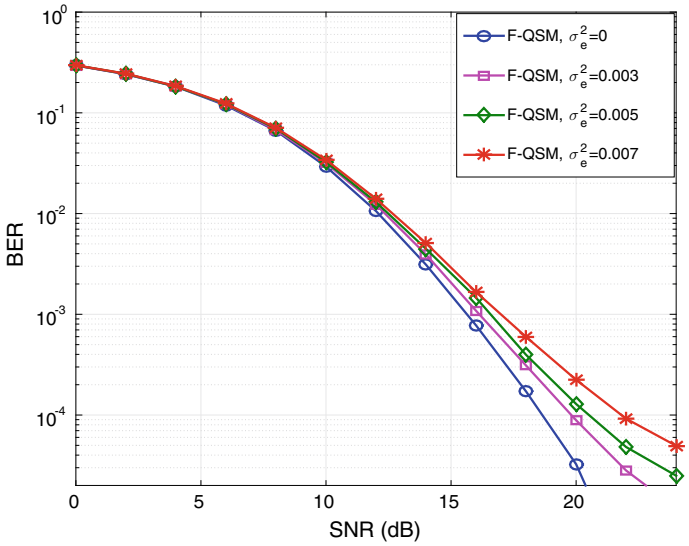

Fig. 3 BER versus SNR of F-QSM with 4×4 system model under imperfect channel with fixed error variance, $\sigma_e^2 = \{0, 0.003, 0.005, 0.007\}$ and $R_{\text{F-QSM}} = 8$ bpcu

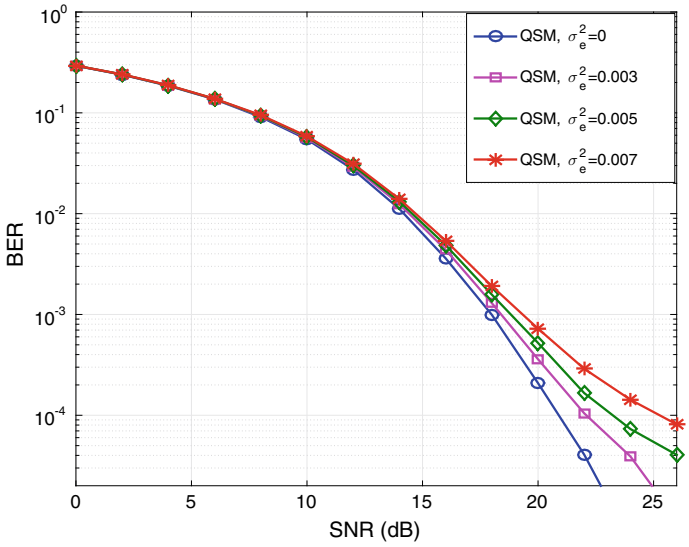

Fig. 4 BER versus SNR of QSM with 4×4 system model under imperfect channel with fixed error variance, $\sigma_e^2 = \{0, 0.003, 0.005, 0.007\}$ and $R_{\text{QSM}} = 8$ bpcu

Table 3 BER versus SNR for perfect CSI ($\sigma_e^2 = 0$) and imperfect CSI ($\sigma_e^2 \neq 0$) of F-QSM & QSM schemes over Rayleigh fading channel

SNR (dB)	**F-QSM** (BER)				**QSM** (BER)			
	$\sigma_e^2 = 0$	$\sigma_e^2 =$ 0.003	$\sigma_e^2 =$ 0.005	$\sigma_e^2 =$ 0.007	$\sigma_e^2 = 0$	$\sigma_e^2 =$ 0.003	$\sigma_e^2 =$ 0.005	$\sigma_e^2 =$ 0.007
16	0.0007	0.0010	0.0014	0.0016	0.0036	0.0043	0.0051	0.0054
18	0.0001	0.0003	0.0004	0.0005	0.0009	0.0012	0.0015	0.0019
20	3.25E−05	8.87E−05	0.0001	0.0002	0.0002	0.0003	0.0005	0.0007

4.2 Computational Complexity

We calculate the computational complexity in terms of real valued multiplications. The computational complexity of the F-QSM and RC-mGQSM is calculated as $8N_R 2^{R_{\text{F-QSM}}}$ and $10N_R 2^{R_{\text{RC-mGQSM}}}$ [10], respectively. For 4×4 system and 4-QAM symbol, the complexity of RC-mGQSM is computed as 10240. Whereas, the complexity of F-QSM is 8092, which is approximately 21% less compared to the complexity of RC-mGQSM.

5 Conclusion

The BER performance of F-QSM is studied under imperfect channel conditions, and the F-QSM performance is compared to that of RC-mGQSM, QSM, and SM. Considered two different imperfect error variance scenarios to present the performance of F-QSM. We described F-QSM scheme with a suitable example and provided a table for all the possible combination of bits. ML detection algorithm is used to study the BER performances via simulations. The F-QSM scheme is compared to RC-mGQSM in terms of computational complexity.

References

1. Mesleh RY, Haas H, Sinanovic S, Ahn CW, Yun S (2008) Spatial modulation. IEEE Trans Veh Technol 57(4):2228–2241
2. Jeganathan J, Ghrayeb A, Szczecinski L (2008) Spatial modulation: optimal detection and performance analysis. IEEE Commun Lett 12(8):545–547
3. Di Renzo M, Haas H, Ghrayeb A, Sugiura S, Hanzo L (2014) Spatial modulation for generalized MIMO: challenges, opportunities, and implementation. Proc IEEE 102(1):56–103
4. Basar E, Aygolu U, Panayirci E, Poor HV (2012) Performance of spatial modulation in the presence of channel estimation errors. IEEE Commun Lett 16(2):176–179
5. Wen M et al (2019) A survey on spatial modulation in emerging wireless systems: research progresses and applications. IEEE J Sel Areas Commun 37(9):1949–1972

6. Younis A, Serafimovski N, Mesleh R, Haas H (2010) Generalised spatial modulation. In: 2010 IEEE 44th Asilomar conference on signals, systems and computers, pp 1498–1502
7. Mesleh R, Ikki SS, Aggoune HM (2015) Quadrature spatial modulation. IEEE Trans Veh Technol 64(6):2738–2742
8. Mesleh R, Ikki SS (2015) On the impact of imperfect channel knowledge on the performance of quadrature spatial modulation. In: 2015 IEEE wireless communications and networking conference (WCNC), pp 534–538
9. Badarneh OS, Mesleh R (2016) Performance of quadrature spatial modulation with imperfect channel information over correlated $\alpha - \mu$ fading channels. In: 2016 IEEE wireless communications and networking conference (WCNC), pp 1–5
10. Gunde K, Hari KVS (2019) Modified generalised quadrature spatial modulation. In: 2019 IEEE national conference on communications (NCC), pp 1–5
11. Gunde K, Sundru A (2021) Modified generalized quadrature spatial modulation performance over Nakagami-m fading channel. Int J Commun Syst 34(16):e4944
12. Gunde K, Sundru A (2021) Modified generalised quadrature spatial modulation performance over Weibull fading channel. In: 2021 proceedings of international conference on communication and computational technologies (ICCCT). Springer, Singapore, pp 79–88
13. Elsayed M, Hussein HS, Mohamed US (2018) Fully generalised spatial modulation. In: 2018 IEEE 35th national radio science conference (NRSC), pp 274–282
14. Shaalan IE, Dawod S, Abuelenin SM (2021) Fully generalized spatial modulation utilizing transmit antenna grouping. Port-Said Eng Res J 25(1):49–58
15. Hussein HS, Elsayed M (2018) Fully-quadrature spatial modulation. In: 2018 IEEE international black sea conference on communications and networking (BlackSeaCom), pp 1–5
16. Hussein HS, Elsayed M, Mohamed US (2018) Fully-quadrature spatial modulation over Rician fading channels. In: 2018 IEEE international Japan-Africa conference on electronics, communications and computations (JAC-ECC), pp 39–42
17. Hussein HS, Elsayed M, Mohamed US, Esmaiel H, Mohamed EM (2019) Spectral efficient spatial modulation techniques. IEEE Access 7:1454–1469

Some Investigations on Path Protection Schemes in Next Generation Optical Wireless Converged Networks

Abhishek Gaur and Vibhakar Shrimali

Abstract A novel path protection scheme is being proposed in this research paper. The main focus in this research paper is to avoid equipment redundancy, increasing channel utilization and bandwidth of the network. The proposed architecture proves to be a better solution as compared to conventional schemes. As customer needs resiliency and reliability, fast restoration of the network is a crucial aspect. In order to achieve this, a dynamic traffic re-routing scheme has been proposed so that faster restoration and resiliency in the network may be achieved, thereby increasing the overall performance of the network in terms of channel utilization and bandwidth.

Keywords Passive optical networks (PON) · Ethernet-based passive optical network (EPON) · Long-term evolution (LTE) · Optical ADD/DROP multiplexer (OADM) · Optical line terminal (OLT) · Optical network unit (ONU) · Long-term evolution-advanced (LTE-a)

1 Introduction

The Internet became a fundamental element of everyday life since web browsing. The key needs of today's digital world are as follows: VOIP, online LAN gaming, online banking, etc. Researchers and network engineers always endeavor to improve bandwidth, robustness and increased transmission speed access more reliable [1]. The Internet is available via wired networking, e.g., via a physical media, or via a wireless network employing smart antennas. One such project is the deployment of fiber optic technology, which has entirely replaced the standard copper wires, coaxial cables and torn pair cables for communications reasons, as the speed and bandwidth requirements of Internet users continuously increase. Applications such as HD video

A. Gaur (✉)
USICT, Guru Gobind Singh Indraprastha University, New Delhi, India
e-mail: abhishek.usict.010164@ipu.ac.in

V. Shrimali
ECE Department, GB Pant Government Engineering College, Government of NCT of Delhi, New Delhi, India

S. Rawat et al. (eds.), *Proceedings of Second International Conference on Computational Electronics for Wireless Communications*, Lecture Notes in Networks and Systems 554,
https://doi.org/10.1007/978-981-19-6661-3_49

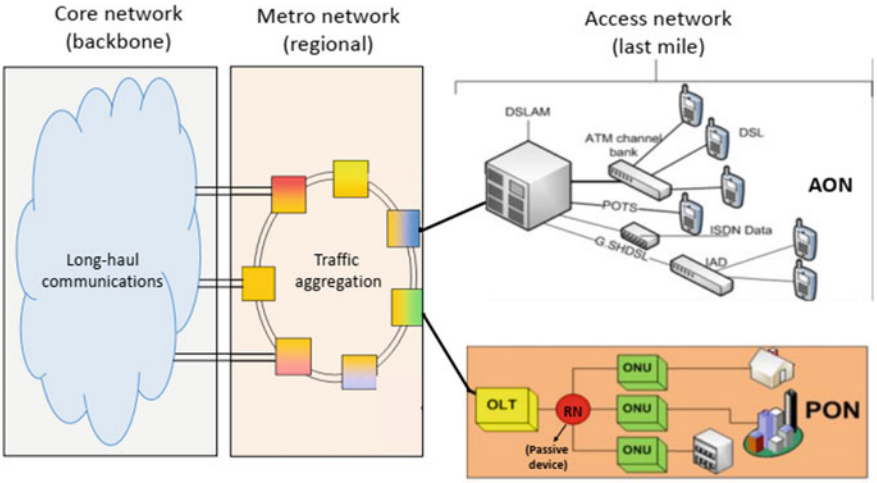

Fig. 1 Telecom infrastructures

streaming on platforms such as YouTube and Facebook require a 100 mbps Internet connectivity. It is therefore necessary that our Internet services should be able to provide larger bandwidth, particularly at the end of the subscriber [2] (Fig. 1).

2 Basics of PON Technology

Passive Optical Networks (PON)

The objective of PON technology is to deliver cost-effective, higher bandwidth and uninterrupted client service. A typical PON consists of a single mode fiber cable, an OLT and ONU connecting units in the distributed network. The distributed network may be time multiplexed based (TDM) or wavelength multiplexed based (WDM) depending upon the end-user requirement (Fig. 2).

Ethernet-based Passive Optical Network (EPON)

The reasons why EPON is developed are the present requirements for stable Internet connection, more bandwidth and high end-user performance requirements. PON's service capacity is substantially higher than standard coaxial cabling, twisted wire pair, etc. A typical PON may service approximately 1250 users on a fiber cable of 0.5 m and can speed from 10 to 100 Gbps, depending on the PON variation (10 GEPON or 100 GEPON). LTE and LTE-A backhaul networks are one of the PON's most essential uses. The EPON is a backbone of mobile technology 4G and 5G. The EPON standards under the subsection of 802.3av protocols and ITU-T are overseen and managed by IEEE 802.11 LAN. The OLT is connected and administered by the local service provider who monitors the upstream and downstream broadcast

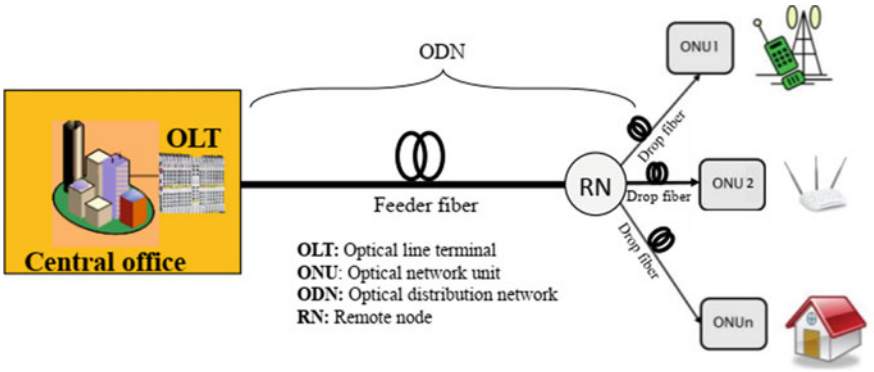

Fig. 2 PON technology

continuously. During downstream transmission, OLT shall supply the concerned ONUs a preset time or bandwidth request for the frames utilizing filtering mechanism and during upstream transmission [3].

TDM-based PON

As the demand for more bandwidth among clients continues to climb, PON technology is without a doubt recognized to be a good choice for the next-generation communication networks. Backhauling of next-generation wireless broadband access designs is required by the service provider. Traffic may be effectively handled by using this architecture. Standard technologies like circuit switching, packet switching and wire line employed in conventional 3G network architecture are not required enough to meet the current 5G user demands. An upgrading of current telecoms infrastructures is therefore necessary. Therefore, NG PONs, due to their enhanced capacity, wider range and economical installation, are considered to be a trustworthy way to establish mobile backhaul networks. Because all network units of the optical network units (ONUs) share the same wavelength in upstream transmission utilizing the TDMA's optical line terminal technology, TDM-based EPONs are proved to be more reliable than other PON schemes (OLT). 10 GEPONs have been suggested and recently standardized for capacity improvement. NG-PON topologies can be regarded more efficient in new deployments [4]. Mobile WiMax and LTE are two viable technologies for next-generation wireless broadband access networks (NG-WBANs) that offer higher data speeds. Furthermore, up to 1 Gbit/s data rates may be delivered by LTE-A with a latency of less than 10 ms. LTE operates the current telecommunications infrastructure utilized by most mobile operators [5]. Therefore, it may not be advisable to create a new network architecture which makes LTE technology universally accepted. Future convergent architectures can handle LTE base stations' communication. The wavelength division multiplexing–passive optical network is a converged design based on ring topology that supports Wi-Fi communication [6].

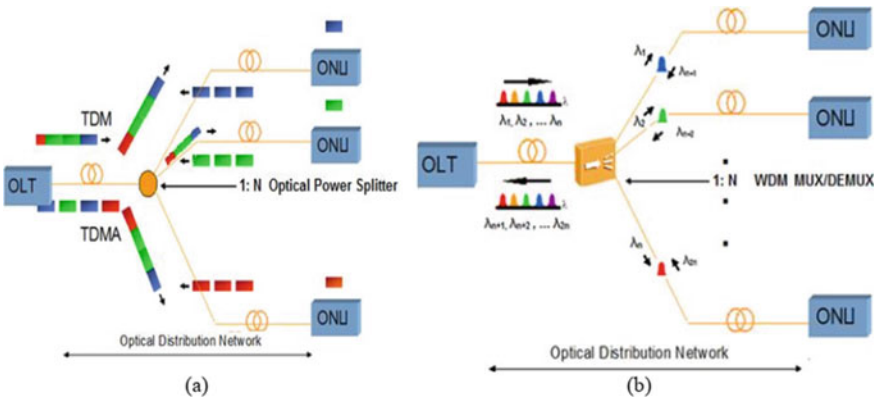

Fig. 3 **a** TDM-PON **b** WDM-PON

WDM-based PON

The time division has been upgraded. A simple option is a multiplexed–passive optical network (TDM-PON) that uses a separate wavelength channel between the OLT and each ONU [7]. This setup provides a topological point-to-point link in PON architecture between OLT and each UNO termed as the WDM-PON [8, 9]. Although WDM-PON in terms of bandwidth, security, rigidity and scalability is considered considerably superior to TDM-PON, the implementation cost and complex installations are a major challenge [11, 12]. Network engineers therefore work best to design the low-cost, less complex WDM-PON (Fig. 3).

3 Path Protection in EPON

Path protection switching in complex PON deployments is a crucial aspect. In order to do this, an EPON must be added a redundant path by offering alternate routed paths. PON network access environments may require different protection systems. Redundancy can be partly or entirely implemented to PON (Fig. 4).

The crucial aspect is to ensure reliability in the network and replacement of faulty equipments. For these purposes, network service providers intend to replace the failed OLTs quickly with spare equipment. However, this technique cannot be implemented every time since using spare equipment for shorter duration may not be preferable [10].

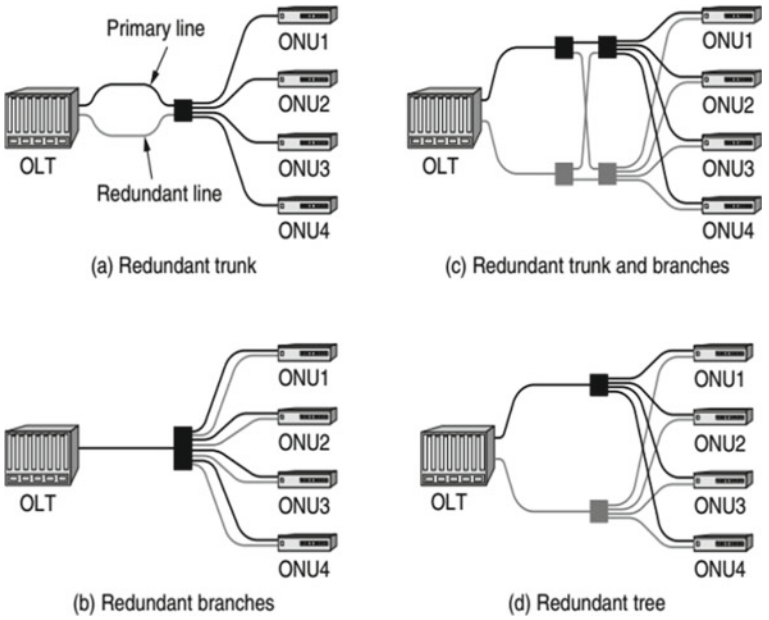

Fig. 4 Redundancy shown in PON topology

4 Proposed Ring Architecture

A protection scheme (Fig. 5) in the form of ring architecture has been proposed. In the proposed scheme, rescheduling of time slots has been done for providing protection. During the failure time, the available bandwidth may be shared. Information like PON ID and ranging interval of ONUs may be provided by control unit of protection scheme. It may also be used for controlling the installed optical switch at central office. On receiving the information of signal lost, protection control unit will identify the faulty OLT or OLT of lowest traffic rate. Then, signal is re-routed for ONUs served by failed OLT to the selected working OLT's network. The main principle of the proposed scheme consists of fault detection, synchronization and switching. A simulation has been on NS-2 simulator for four OLTs with each one serving only three ONUs. All OLTs have traffic rate of approximately 80%. Whenever an OLT fails in the network, a working and redundant OLT is supposed to support the failed OLTs. A bandwidth of 1 Gbps is providing by non-participating OLTs to their respective ONUs. So, the proposed protection scheme is proven to be more reliable particularly during failure time in overall EPON network to ensure that at least one OLT will work in the network.

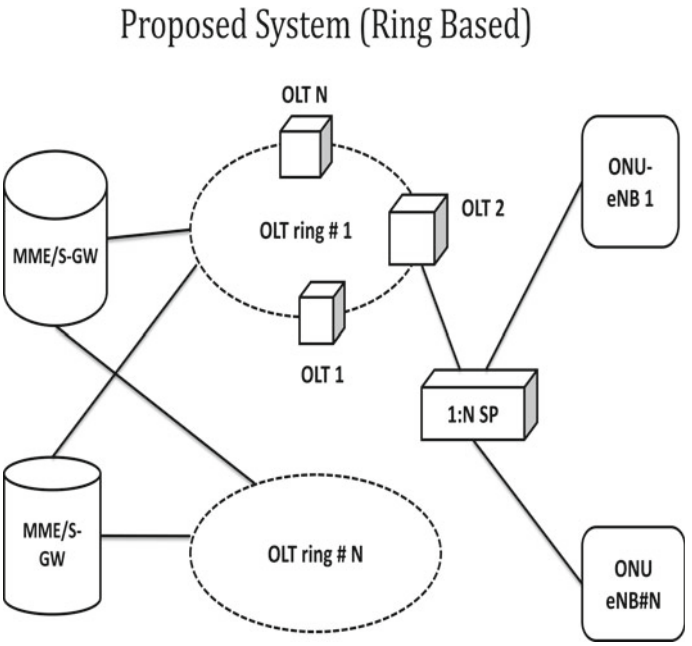

Fig. 5 Ring-based converged architecture

5 Proposed Protection Algorithm

1. Obtain data from all connected ONUs.
2. Check for node failure.
3. Choose the path having with least traffic rate.
4. Reschedule time slot allocation and guard time.
5. Add failed node data to selected working node using OADM.
6. Switch failed node to selected working node.
7. Add failed node data to selected working node.
8. Return to start.

6 Simulated Results

An event-driven simulation has been done in NS-2 simulation software for the proposed ring-based architecture, and an observation has been done in real-time traffic for analyzing the overall traffic performance in terms of channel utilization and bandwidth. It has been observed that when there are failed OLTs participating in the network, the performance in terms of channel utilization and bandwidth is decreasing with the number of failed OLTs which can be improved by removing

failed OLTs from the ring network using OADM, and overall network performance may be enhanced due to increase in channel utilization and bandwidth of the network (Figs. 6, 7, 8 and 9).

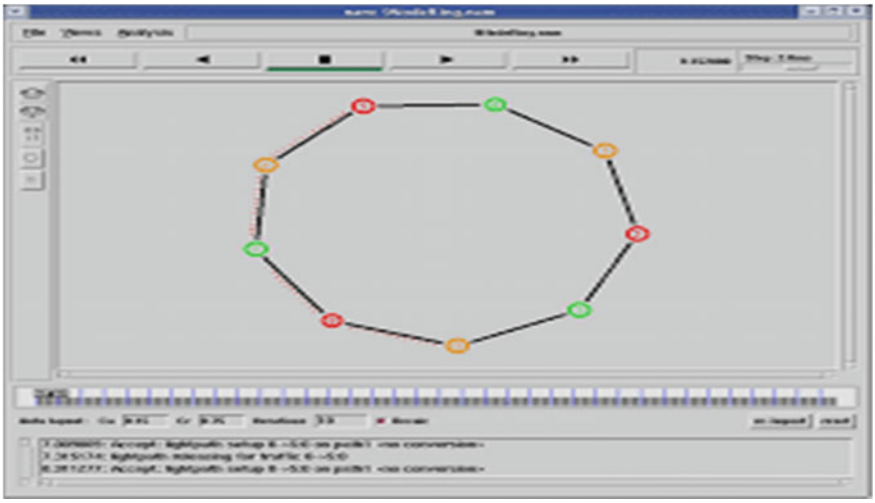

Fig. 6 Simulation of ring-based architecture

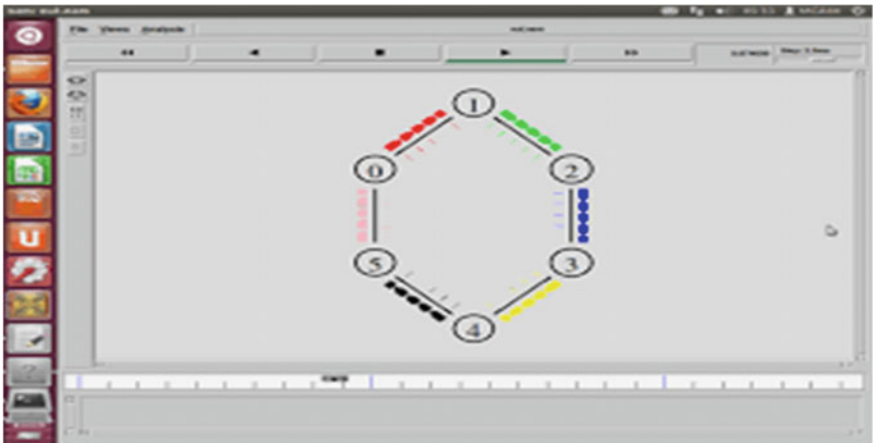

Fig. 7 Sending of data packets in ring-based architecture

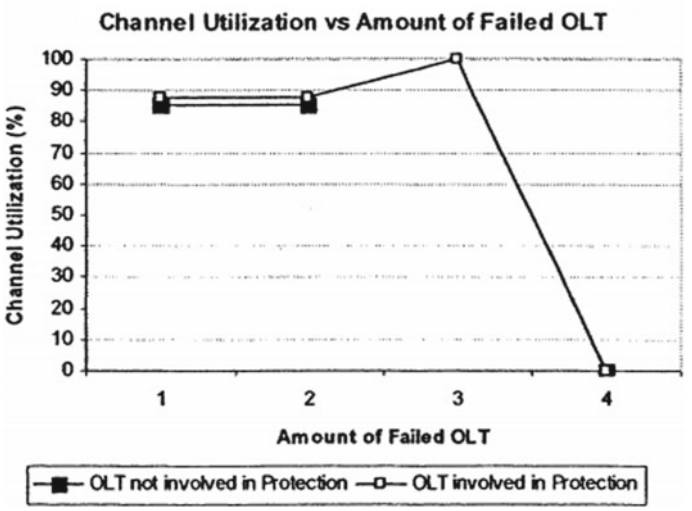

Fig. 8 Utilization of available channel versus No. of failed OLTs

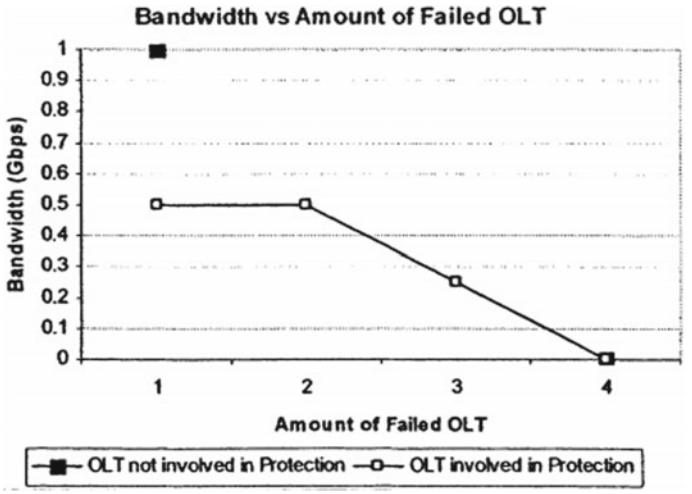

Fig. 9 Bandwidth utilization versus No. of failed OLTs

7 Conclusion and Future Scope

Hub is managing the signals coming from different channel using optical add and drop multiplexer (OADM). In case of node failure, the nearby OADM will manage the fault thereby re-routing the signal through a different path. After restoration of the fault, the ring network will return in the normal path. A new protection scheme

has been proposed for preventing the whole network in case of intermediate node failure. In this protection scheme, equipment redundancy may also be avoided. The converged architecture gives better bandwidth coverage and connectivity solution in such environment. The devices, like OADM, manage the re-routing technique more efficiently and intelligently. As customer needs resiliency and reliability, fast restoration of the network is a crucial aspect.

References

1. IEEE 802.3ah (2004) Ethernet in the first mile
2. Kramer G, Mukherjee B, Pesavento G (2002) IPACT: a dynamic protocol for an ethernet PON (EPON). IEEE Commun Mag, pp 74–80
3. Assi CM et al (2003) Dynamic bandwidth allocation for quality-of-service over ethernet PONs. IEEE JSAC 3(9):1467–1477
4. IEEE 802.16e/D12 (2005) Air interface for fixed and mobile broadband wireless access systems
5. Nair G et al (2004) IEEE 802.16 medium access control and service provisioning. Intel Tech J 8(3):213–28
6. WiMAX Forum (2006) Mobile WiMAX—part I: a technical overview and performance evaluation
7. Vrdoljak M, Vrdojak SI, Skugor G (2007) Fixed-mobile convergence strategy: technologies and market opportunities. IEEE Commun Mag, pp 116–21
8. Nirmalathas A et al (2001) Wavelength reuse in the WDM optical interface of a millimetre-wave wireless antenna base station. IEEE Trans Microwave Theory 49(10):2006–2012
9. IEEE 802.1D (2004) Media access control (MAC) bridges
10. IEEE 802.1Q (2006) Virtual bridged local area networks
11. Gangxiang S et al (2007) Fixed mobile convergence architectures for broadband access: integration of EPON and WiMAX. IEEE Commun Mag 45:44–50
12. Sarkar S et al (2007) Hybrid wireless-optical broadband-access network (WOBAN): a review of relevant challenges. J Lightwave Tech 25:3329–3340

Modification of Automotive HVAC Systems to Automatically Control Vehicular Cabin CO_2 Concentration

Eshan Sabhapandit, P. Prarthana, Soumya Suresh, and Sumit Kumar Jindal

Abstract Automobiles have become a major part of the lifestyle of many households across the world. For day to day commute or long distance travel purposes, vehicles are a common sight on streets. But with the increase in use of vehicles, the number of road accidents has also gone up. There are various causes of road accidents but one of the significant reasons contributing to road accidents all over the world is drivers losing their focus and making mistakes during critical situations while driving. Fatigue, drowsiness and lethargy are worse enemies of drivers, and the common cause is suffocation due to accumulation of CO_2 inside the vehicle cabin. A novel method to modify existing heating, ventilation and air conditioning (HVAC) systems present in most commercial automotive vehicles is proposed that can regulate the concentration of CO_2 inside the vehicle cabin so that the passengers experience a comfortable and safe journey. The new design is experimented both on simulation and with hardware. Reliable and convincing results were obtained.

Keywords CO_2 · HVAC · Fractional recirculation · 8051 microcontroller · PID

1 Introduction

Most commercial vehicles have two modes of operation in their AC systems, namely the fresh air mode and recirculation mode. In recirculation mode, the vehicle inlets are shut close so that the air inside the vehicle can recirculate. This makes the cooling process much faster and saves engine energy. But since the same air is being recirculated, the amount of CO_2 exhaled by the passengers starts accumulating, increasing its concentration. In fresh air mode, the vehicle inlets are completely open. Using the AC in fresh air mode will bring fresh air from outside but it makes the cooling process slower, consumes more energy and can bring pollutants.

E. Sabhapandit · P. Prarthana · S. Suresh · S. K. Jindal (✉)
School of Electronics Engineering, Vellore Institute of Technology, Vellore, Tamil Nadu 632014, India
e-mail: sumitjindal08@gmail.com

S. Rawat et al. (eds.), *Proceedings of Second International Conference on Computational Electronics for Wireless Communications*, Lecture Notes in Networks and Systems 554,
https://doi.org/10.1007/978-981-19-6661-3_50

The average outdoor concentration of CO_2 is 400 PPM, and the average indoor concentration of CO_2 is 800 PPM. At this meager range of 0.04–0.08% of CO_2 in air, the effects of CO_2 gas in our bloodstream are almost negligible [1]. Vehicles have smaller dimensions and volume than indoor spaces. In the limited amount of air trapped inside the vehicular cabin, the concentration of the metabolic CO_2 that the passengers exhale increases with time. Another study [2] concluded that the accumulated CO_2 level in a vehicle with four passengers using recirculation mode for one hour was 9000 PPM. At such high concentrations, it can affect the respiratory system, CNS—central nervous system and can cause symptoms like rapid breathing and increased heart rate, fatigue, emotional imbalances and mainly poor hand-eye coordination. According to the Indian government database [3], 25 out of 100 road accidents happen due to driver fatigue and drowsiness. This is another major symptom along with lethargy. Both of these are recurring patterns observed in road accidents. The inhalation of CO_2 at such levels has also been determined to influence the cognitive abilities of the passengers [4].

2 Related Work

Research has been done that justifies the success of the concept of fractional recirculation where a fraction of air is allowed to enter instead of completely switching to fresh air mode of operation. This is done by slightly opening the inlet flaps or gates of the vehicle such that air is able to enter partially to replenish the gasses present inside. As the rate at which air is allowed to enter is much less in this mode, sufficiently less energy is consumed compared to fresh air mode of operation [5]. Performance of this concept was tested for different values of AC fan speed, number of passengers and vehicle speed by manually varying the percentage recirculation of air. This was achieved by controlling the opening of the inlet flap to pre-calculated angles by providing specific voltage to the flap motor. The results of this research showed a drastic decrease in cabin CO_2 concentration by increasing the inlet flap angle letting more air to enter, i.e., decreasing percentage of recirculation as seen from Fig. 1.

3 Proposed System

Similar experiments were carried out by Jung et al. [6] and Grady et al. [7] under different test conditions, vehicle and location. The results obtained were similar, hence serving as the basis of the proposed work. Previous works have been experimented by manually controlling the inlet flaps, which is not a feasible option when implemented on commercial automobiles. The proposed system is a novel and effective way of automatically controlling the inflow of air through the inlet flaps based

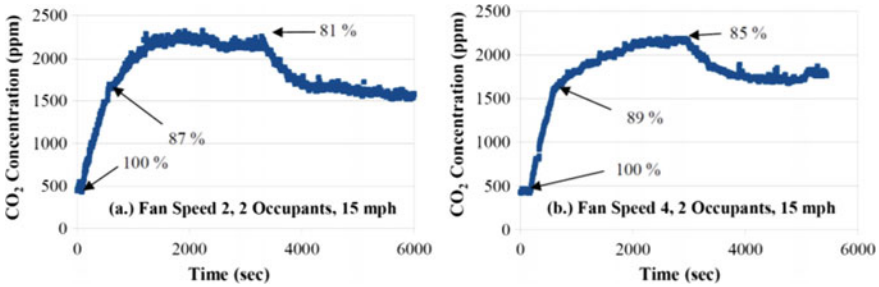

Fig. 1 Performance results of fractional recirculation implemented for various test cases [5]

on the concentration of CO_2 inside the vehicle cabin. It utilizes the HVAC flap actuators present in the inlet of the majority of commercially available automobiles. The typical design of an automobile HVAC system is shown in Fig. 2.

The HVAC inlet flap actuator controls the rotation of the inlet flap which influences the air inflow through the vehicle [9]. This can be automatically controlled by involving a microcontroller. Figure 3 shows the hardware block diagram presenting the modifications to be done in existing HVAC systems. The microcontroller shown can be the HVAC controller or a separate microcontroller interfaced to the HVAC controller.

A vehicle inlet generally leads to a pipe which has a circular cross-section. The modified flap actuator system consists of a servo motor connected to the inlet flap. The rotation of the servo motor directly translates to the rotation of the inlet flap,

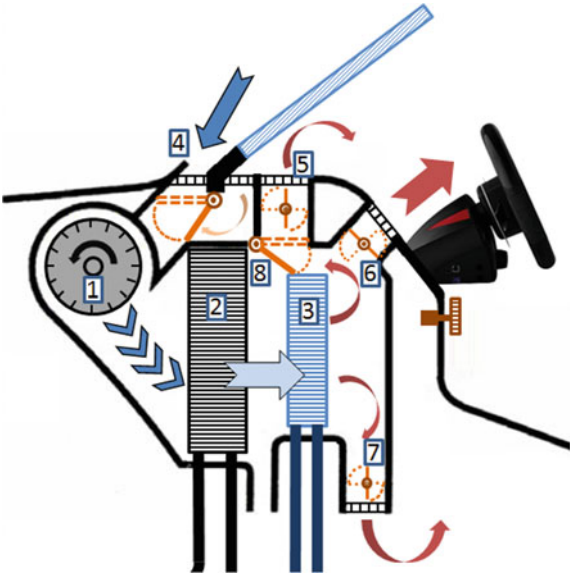

Fig. 2 Typical HVAC system in a vehicle, label '4' highlights the inlet flap [8]

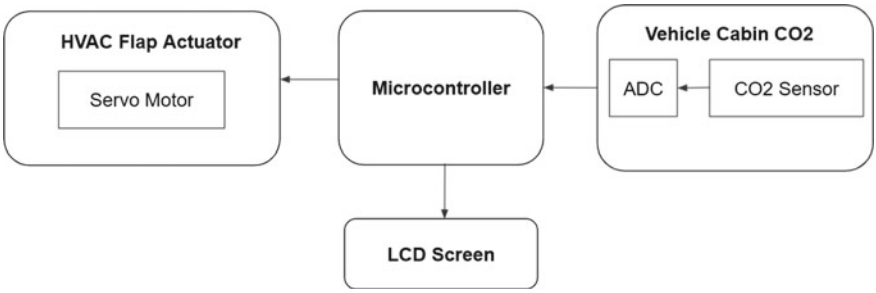

Fig. 3 Hardware block diagram of the proposed system

hence controlling the inflow of air through the cross-section of the pipe. The flap itself needs to be a circular disk. A servo motor is selected because its angle of rotation can be very precisely controlled through a microcontroller, generally by feeding a PWM signal to the servo motor input.

Figure 4 shows how the mode of operation of AC is controlled by the rotation of the circular flap placed at the cross-section of the HVAC pipe. During recirculation mode, the flap completely covers the cross-section area of the pipe, hence not allowing air to pass through at all. While in fresh air mode, the flap is perpendicular to the cross-section allowing maximum air to pass through. By controlling this angle of rotation, fractional recirculation is achieved. To automatically control the angle of rotation of the flap, a closed loop control system employing a PID controller is designed.

The design of an effective PID controller requires the knowledge of the system transfer function which is governed by the actuator and the plant model. In this case, the actuator is the modified HVAC flap actuator while the plant is the vehicular cabin CO_2 mass balance model. To automate the process of controlling the extent of recirculation, the mathematical relation between the actuator and the CO_2 concentration is laid out. The vehicular cabin CO_2 concentration model is derived from its mass balance equation as shown below [10]

$$Vc.\frac{\mathrm{d}Cc}{\mathrm{d}t} = n.Cex.Qex + Ql.(Co - Cc) \tag{1}$$

Cc Cabin CO_2 concentration
Ql Air flow rate from inlet pipe
Qex Air flow rate from human lungs
Co CO_2 concentration in atmosphere
n Number of passengers
Vc Vehicle cabin volume
Cex CO_2 conc. exhaled by human.

The left hand side of the equation shows the change in mass of CO_2 inside the vehicle. The two terms in the right hand side of the equation represent the change in mass of CO_2 inside the vehicle cabin due to the exhalation by passengers and airflow

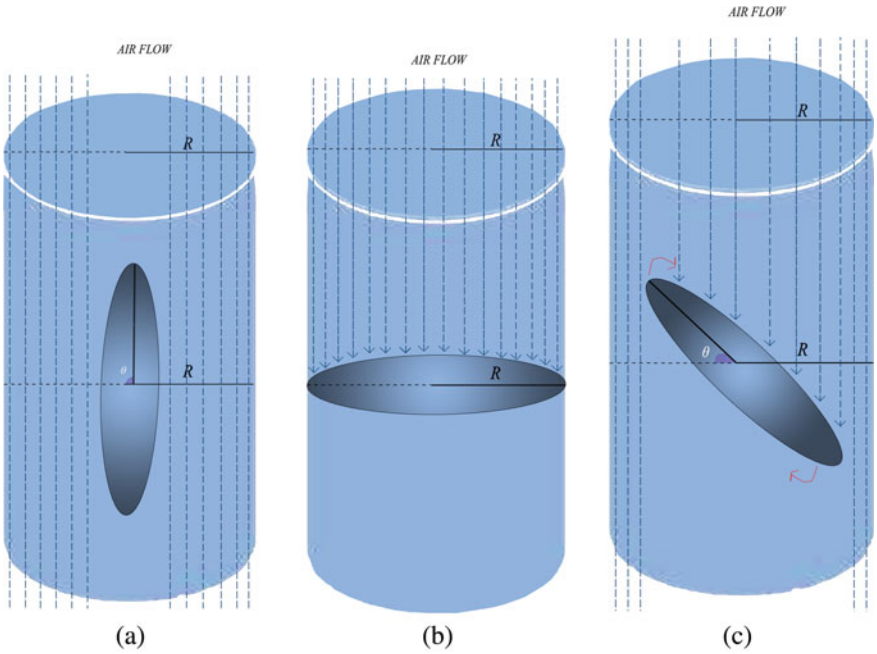

Fig. 4 The two modes of operation of AC controlled by the rotation of flap **a** $\theta = 90°$ (Fresh air mode) **b** $\theta = 0°$ (Recirculation mode) **c** Effective airflow when flap is rotated by an angle 'θ'

from vehicle inlet pipe, respectively. This mass balance equation assumes that air can only enter or exit through the HVAC inlet, i.e., there is no leakage in the vehicle. An inference that can be made from the equation is the fact that if the change in mass of CO_2 due to exhalation by passengers is considered constant for a period of time, then the vehicular cabin CO_2 concentration (Cc) can be controlled by varying the air flow rate from inlet pipe (Ql). For any pipe, the airflow rate is given by the following equation

$$Ql = A.v \tag{2}$$

A Area of cross-section of pipe
v Air flow velocity in pipe.

The airflow velocity inside a pipe with uniform cross-section is given by the following equation.

$$v = 4005.\sqrt{\Delta P} \tag{3}$$

where ΔP is the differential pressure measured in the inlet pipe and this differential pressure is affected by the AC fan speed, car velocity and wind speed. The inlet pipe can be seen as a cylinder with inner radius 'R'. The flap is a circular disk of the same

radius as the inner radius of the pipe. The effective airflow through the pipe will depend on the angle by which the flap is rotated. The total area of the cross-section of the air flow inlet pipe with a radius of R is

$$A_{\text{cross-section}} = \pi.R^2 \tag{4}$$

The effective area covered by the flap when it is rotated by an angle 'θ' is

$$A_{\text{covered}} = \pi.R^2.\text{Cos}\theta \tag{5}$$

The angle 'θ' is referred to as the flap angle or the angle by which servo is rotated. The angle of rotation, i.e., 'θ' can be varied between 0° and 90°. The effective area through which air can flow in the pipe can be understood by Fig. 4c. The effective area of the cross-section can be calculated.

$$A = A_{\text{cross-section}} - A_{\text{covered}} \tag{6}$$

Substituting from Eqs. (4) and (5) we get

$$A = \pi.R^2.(1 - \text{Cos}\theta) \tag{7}$$

On substituting the results of Eqs. (3) and (7) with Eq. (2), the following equation for airflow rate in inlet pipe is obtained.

$$Ql = \pi.R^2.(1 - \text{Cos}\theta).4005.\left(\sqrt{\Delta P}\right) \tag{8}$$

Equation (8) shows how airflow rate can be changed by controlling the rotation angle of the servo motor. This in turn influences the concentration of the carbon dioxide concentration inside the vehicle's cabin as seen from Eq. (1).

4 Controller Design

Simulink, which is a MATLAB-based graphical modeling software, is used to model the system and design the PID controller for it. Figure 5 shows the open loop system where Eq. 8 is modeled as the first block and Eq. 1 is modeled as the second block. The input to the system is the angle of rotation of the flap, while the output is the CO_2 concentration resulting from the rotation of the flap.

For the current experimentation, an average mid-sized commercial car with cabin volume of 3.25 m^3 is considered with four passengers occupying it. To model the human exhalation, the normal minute ventilation in humans of 0.0065 m^3/min and average CO_2 exhalation per breath of 35,000 PPM is considered [11]. Also an average atmospheric concentration of CO_2 of 400 PPM is used for the simulations. The inlet pipe radius is taken as 40 mm. The differential pressure generated inside the inlet

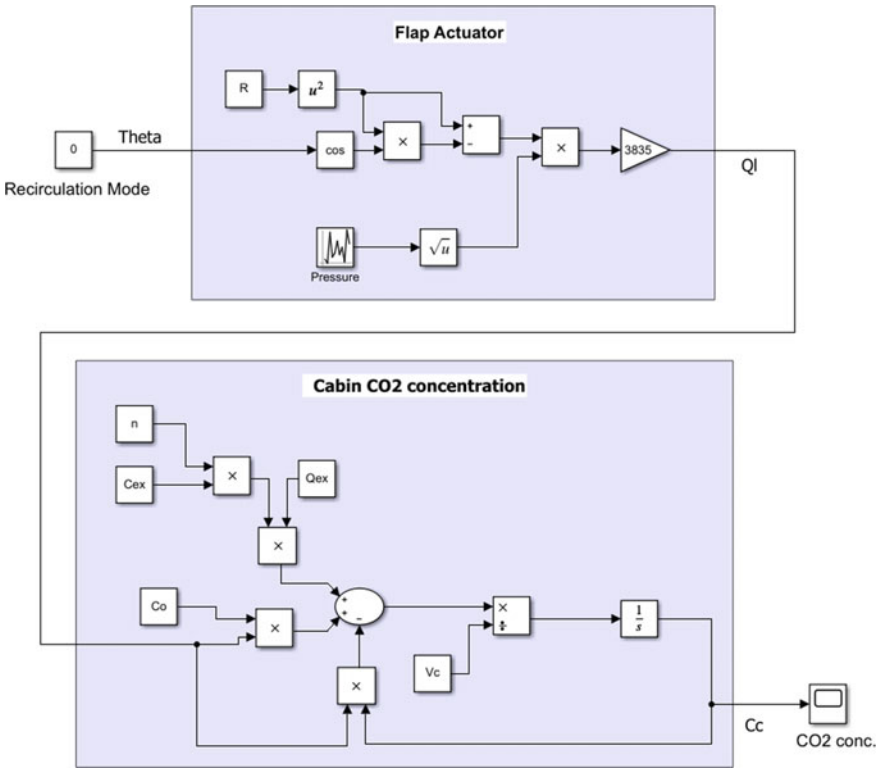

Fig. 5 Open loop block diagram

pipe depends on the vehicle speed, the AC fan speed, the wind speed and the direction of flow of air inside the pipe. It is a very dynamic quantity which is very complicated to model with simple equations. Hence, a random number generator with a suitable range of values is used to represent the differential pressure inside the pipe. The input given to the system in Fig. 5 represents the recirculation mode of operation, i.e., a flap angle of 0°. The open loop response at recirculation shows the linear increase in CO_2 concentration with time. The CO_2 concentration reaches a dangerous level of 4200 PPM within 15 s as seen in Fig. 6.

To model the closed loop system and tune a PID controller, knowledge on the overall system's transfer function is required. Since this system is nonlinear in nature, the transfer function cannot be derived using mathematical transformations. Hence, the System Identification Tool provided by MATLAB is used to estimate a transfer function that can suitably approximate the system response. The System Identification Tool uses simulation data to generate a model response. A transfer function with one pole, one zero and an integrator component has shown to fit the model response. The estimated transfer function is as follows.

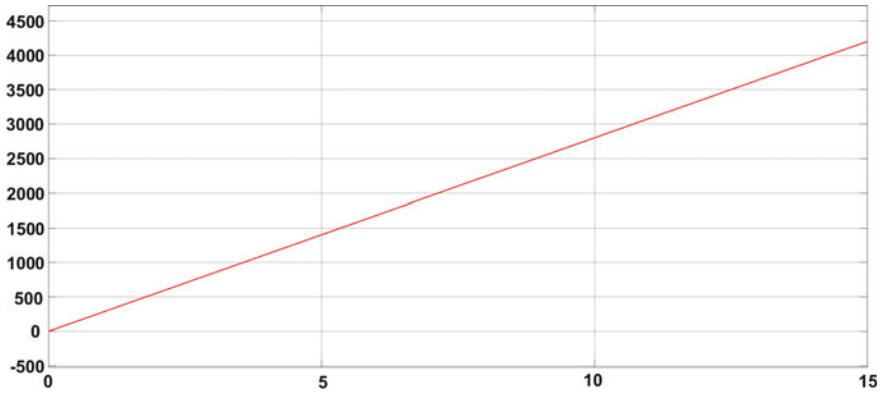

Fig. 6 Simulation of the open loop response (CO_2 (PPM) vs. Time (s))

$$\text{Transfer Function} = \frac{-0.2798(-4515s + 1)}{s(0.1744s + 1)} \tag{9}$$

PID controllers use a closed loop feedback mechanism to control process variables and are the most accurate and stable controller. A PID controller's response is controlled by tuning three gain values namely proportional gain, integral gain and derivative gain. These gain values act on the input error, i.e., the difference between the reference input, i.e., set point and the obtained output value measured from the sensor. The controller attempts to minimize the error where each of the gain values plays a distinctive role to achieve that. The proportional gain acts on the magnitude of error, the integral gain acts upon the error accumulated over time, and the derivative gain acts on the rate at which the error is varying.

CO_2 being a gas is a very dynamically varying quantity, so it is almost impossible to completely bring it down to a fixed concentration unless in laboratory conditions. Using the integrator aspect of a PID controller in such scenario can lead to integrator windup which is a situation where the error value keeps on accumulating due to the dynamic nature of the gas, hence the integrator would end up generating a signal beyond the flap actuator's capability to actuate. This would lead to wastage of energy, completely contradicting the purpose of the proposed design. Hence, a PD controller is adopted and is tuned to have low peak overshoot and sufficiently appreciable settling time. The response observed a peak overshoot of just 0.896% and a settling time of 7.07 s. Such a settling time is appreciable for a gaseous quantity like CO_2. It's the prolonged exposure to high concentrations of CO_2 which has adverse effects. ASHRAE standards recommend an indoor CO_2 level under 1000 PPM so the reference set point of the closed loop controller is set to 1000 PPM. The controller is able to regulate the concentration under 1000 PPM as seen from Fig. 7. The system achieves steady state output within 10 s but this model assumes no leakage in the vehicle, i.e., air can only enter or exit through the HVAC inlets. The response in a real vehicle scenario would be slightly different due to the contribution

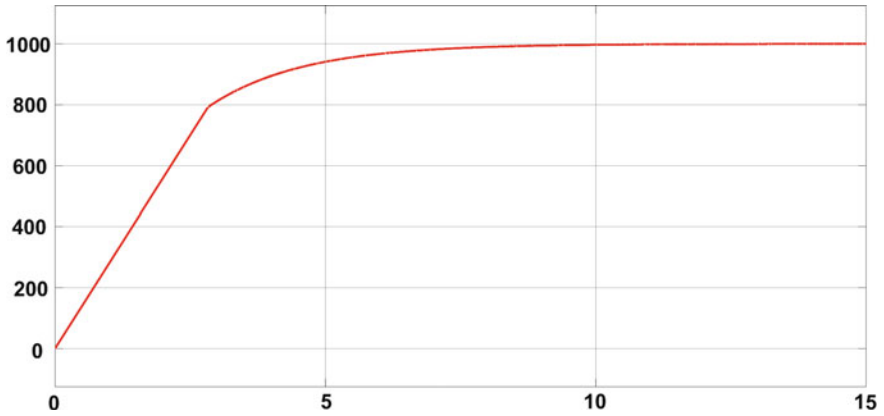

Fig. 7 Simulation of the close loop response (CO_2 (PPM) vs. Time (s))

from the leakage spots, especially in old cars. But CO_2 is not a toxic gas so its effect on humans is only significant when the person is exposed to its high concentration for a long duration. Hence, the achieved simulation results show the capability of the controller to prevent CO_2 from reaching and staying in high concentrations.

5 Hardware Setup

The tuned PD controller is implemented on a microcontroller which is interfaced to the associated sensors and actuators. The controller attempts to bring CO_2 concentration below 1000 PPM every time the concentration increases beyond 1500 PPM. The hardware components are assembled and tested as shown in Fig. 8. The AT89S52 development board which has a 8051-based microcontroller is used for communication between the sensors and actuators. The 8051 microcontroller has 4 kilobytes of on-chip ROM memory and 128 bytes of on-chip RAM memory [12]. ADC0809, an analog to digital converter (ADC) is used to convert the analog readings from the CO_2 sensor to digital data for the microcontroller. A SG90 servo motor is used as an actuator that rotates according to the change in the CO_2 concentration. A 16×2 LCD is used to display the CO_2 concentration and the angle of rotation of the servo motor. The program is written in embedded C language, and the programming environment used is Keil µVision. To simulate the vehicular cabin environment, air is exhaled near the CO_2 sensor to increase the ambient CO_2 concentration, the behavior of the servo motor is observed and reflected on the LCD screen as the CO_2 concentration starts to come down.

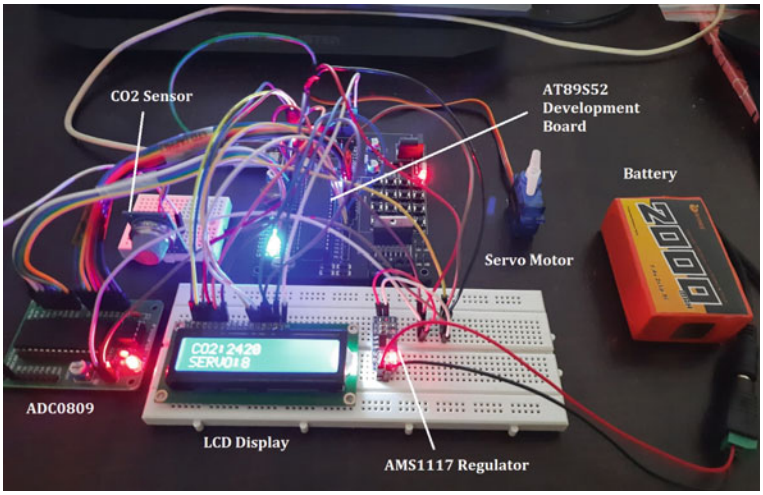

Fig. 8 Experimental setup of the proposed mode

6 Results and Discussion

The hardware experimentation showed that according to the CO_2 concentration in the vehicle's cabin, the servo is rotated to allow the air to flow through the inlet pipe. It is observed that once the CO_2 concentration in the cabin reaches very high concentration, the servo motor rotates by a large angle. As CO_2 concentration decreases, the servo motor angle gradually decreases and becomes zero when the CO_2 concentration reaches below 1000 PPM. For a small decrease in the CO_2 concentration, the flap is rotated by a small angle. The effective area of airflow through the inlet air duct is controlled by rotating the flap actuator which brings down the CO_2 concentration inside the car cabin.

When the CO_2 concentration is observed to be well within the safe limits, the flap actuator is completely closed which brings it back to the initial mode that is recirculation mode. In Fig. 9, a graph is plotted and it is observed that the angle of rotation of the servo motor almost linearly decreases with the decrease in the concentration of the CO_2. This limits the inflow of fresh air into the vehicle cabin as CO_2 concentration starts to decrease. The benefit of this approach lies in the fact that the engine energy consumed to cool down fresh warm air entering the vehicle depends on the CO_2 concentration in the vehicle cabin.

7 Conclusion

The proposed system illustrates a novel method to automate the fractional recirculation process that regulates the concentration of CO_2 inside the vehicle's cabin by

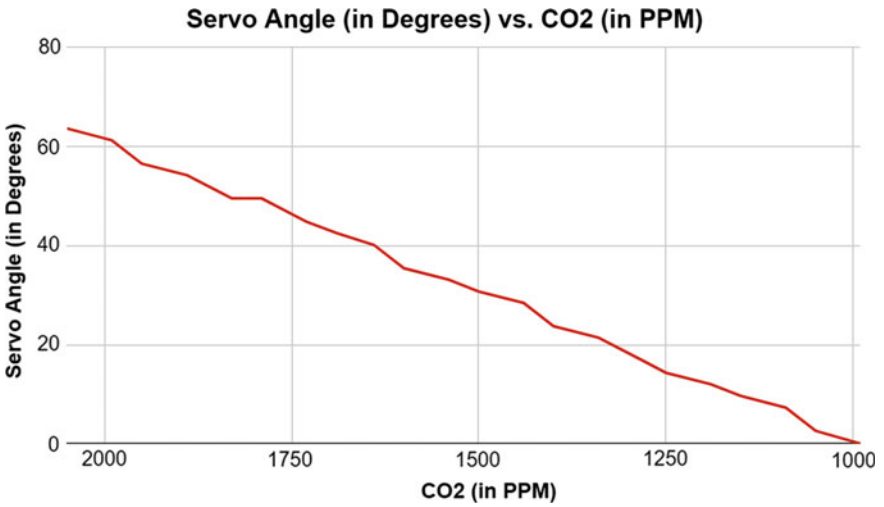

Fig. 9 Servo rotation angle versus CO_2 concentration

changing the angle of rotation of the servo motor accordingly. Implementing the concept of fractional recirculation mode using a PD controller, fresh intake of warm air is regulated to not put unnecessary load on the vehicle engine and AC. During long car journeys, fresh air enters periodically at controlled rates to provide a smooth and safe journey experience for the passengers. The system protects passengers from being exposed to high CO_2 concentrations for prolonged durations.

References

1. Cha Y (2019) In-cabin carbon dioxide and health effects. Blueair Cabin Air AB (2018)
2. Torres C (2014) A study on the levels of CO_2 in vehicle cabins. Breathe Easy
3. Persons injured in road accidents. https://data.gov.in/keywords/indian-road-accident-data
4. Constantin D, Mazilescu CA, Nagi M, Draghici A, Mihartescu AA (2016) Perception of cabin air quality among drivers and passengers. Sustainability 8:1–14
5. Grady M, Jung H, Kim Y, Park J, Lee BC (2013) Vehicle cabin air quality with fractional air recirculation. SAE Technical Paper
6. Jung HS, Grady ML, Victoroff T, Miller AL (2017) Simultaneously reducing CO_2 and particulate exposures via fractional recirculation of vehicle cabin air. Atmos Environ 160:77–88
7. Grady M (2013) On-road air quality and the effect of partial recirculation on in-cabin air quality for vehicles. UC Riverside Electronic Theses and Dissertations (2013)
8. Understanding flap actuators and what drives them in automotive HVAC systems. https://e2e.ti.com/blogs_/b/behind_the_wheel/posts/understanding-flap-actuators-and-what-drives-them-in-automotive-hvac-systems
9. Vatankhah AR, Ghaderinia H (2018) Semi-Circular flap gate as a flow metering structure in circular channels. Flow Meas Instrum 64:28–38

10. Jung H (2013) Modeling CO_2 concentrations in vehicle cabin. SAE Technical Papers
11. Mishra AK, Schiavon S, Wargocki P, Tham KW (2021) Respiratory performance of humans exposed to moderate levels of carbon dioxide. Indoor Air 31(5):1540–1552
12. Mazidi MA, Mazidi JG, McKinlay RD (2006) The 8051 microcontroller and embedded system. Pearson Prentice-Hall Inc., New Jersey

Performance Evaluation of Throughput for CB-CSS in Cognitive Radio Network Over Hoyt Fading Channel

Yashaswini Sharma, Ritu Sharma, and K. K. Sharma

Abstract This paper evaluates the performance of throughput over Hoyt fading channel. The number of cognitive radio users and fusion rule are some parameters that influence throughput for cooperative spectrum sensing. This paper compares centralized cooperative spectrum sensing and cluster-based cooperative spectrum sensing using different fusion rules in terms of throughput metric. An optimum fusion rule is found at which throughput is maximum. It is observed that highest throughput is attained for OR-AND fusion rule against other fusion rules investigated. Under Hoyt fading condition, OR-AND fusion rule attains maximum throughput which increases by 4.07% compared to OR fusion rule and increases by 6.94% compared to AND fusion rule. Further, the impact of number of cognitive radio users and number of clusters over throughput is investigated.

Keywords Cognitive radio · Throughput · Cluster-based cooperative spectrum sensing · Hoyt fading

1 Introduction

Cognitive radio technology was proposed to optimize spectrum utilization by permitting the secondary users (SUs) to access the spectrum bands unused by the primary users (PUs) in a way that no interference is caused between PUs and SUs [1]. In order to detect PU in the spectrum, a non-coherent technique known as energy detection (ED) is the frequently used for spectrum sensing (SS) [2]. Nevertheless, its

Y. Sharma (✉) · R. Sharma · K. K. Sharma
Department of Electronics and Communication, Malaviya National Institute of Technology, Jaipur, Rajasthan, India
e-mail: 2018rec9058@mnit.ac.in

R. Sharma
e-mail: rsharma.ece@mnit.ac.in

K. K. Sharma
e-mail: kksharma.ece@mnit.ac.in

S. Rawat et al. (eds.), *Proceedings of Second International Conference on Computational Electronics for Wireless Communications*, Lecture Notes in Networks and Systems 554,
https://doi.org/10.1007/978-981-19-6661-3_51

performance degrades when single cognitive radio user (SU) faces hidden terminal problem or due to multipath fading [2]. Cooperative spectrum sensing (CSS), in which numerous users collaborate to conduct SS, was used to tackle this problem [3]. But CSS has certain constraints such as channel bandwidth, reporting delay due to a greater number of users [4]. The issue is mitigated by splitting up SUs into clusters and selecting cluster heads (CHs) which gathers local SS information [5, 6].

With an aim to maximize throughput, sensing-throughput trade-off is examined in [7]. Throughput performance is studied for given fusion rule in CSS [8]. In [9], it is analysed over κ–μ and η–μ fading channels. Throughput is investigated over Rayleigh fading for CSS in [10]. In [11], threshold selection scheme is applied to improve throughput for CSS. Optimal number of cognitive radio (CR) users at which throughput is maximum are investigated in [12]. In [13], improved energy detection scheme is considered to improve throughput performance for CSS.

In this paper, throughput performance evaluation is investigated over Hoyt fading channel. Hoyt distribution also known as Nakagami-q distribution is considered for modelling random attenuation in terrestrial links and some of the satellites [14]. In wireless transmissions, it is used to model short-term fading conditions [15]. It is a generalized fading channel as it accounts for Rayleigh fading when Hoyt fading parameter $q = 1$ and for one sided Gaussian fading when $q = 0$ [15]. Lately, Hoyt fading is considered for accounting wireless channels in various fading conditions. This paper investigates throughput over Hoyt fading channel for CB-CSS and centralized cooperative spectrum sensing. Optimum fusion rule at which throughput is utmost is determined. The impact of number of CR users in a cluster and number of clusters on throughput over Hoyt fading channel is also studied.

The following sections make up the paper: In Sect. 2, the system model is briefly defined, and in Sect. 3, the results are discussed and conclusion is presented in Sect. 4.

2 System Model

Let's consider K CR users in a network, along with one PU and one base station (or fusion centre). SUs use energy detection to perform local spectrum sensing. Energy detector (ED) input is the PU signal, and the ED output is monitored as following two hypotheses:

$$W_j(n) = \begin{cases} v_j(n); & H_0(PU \text{ absent}) \\ m_j w(n) + v_j(n); & H_1(PU \text{ present}) \end{cases} \tag{1}$$

The signal $W_j(n)$ is received at the jth SU, $w(n)$ represents primary user signal, m_j gives the complex channel gain, and Gaussian noise is represented by $v_j(n)$. A comparison is made between the energy gathered at the output of ED (ζ_j) and threshold value (λ) to find out the status of the PU. The false alarm probability (P_{fj}) and detection probability (P_{dj}) for non-fading environment are given as [16]

$$P_{fj} = \text{prb}\left[\left|\left|\zeta_j\right|\right| > \lambda_j | H_0\right] = \frac{\Gamma\left(u, \lambda_j\right)}{\Gamma(u)}, \tag{2}$$

$$P_{dj} = \text{prb}\left[\left|\left|\zeta_j\right|\right| > \lambda_j | H_1\right] = Q_u\left(\sqrt{2\gamma_j}, \sqrt{\lambda_j}\right), \tag{3}$$

$$P_{mj} = 1 - P_{dj}, \tag{4}$$

Here, signal-to-noise ratio (SNR) received at SU is γ_j, P_{mj} is the probability of missed detection, incomplete gamma function is $\Gamma(.,.)$ [16], $Q_u(.,.)$ denotes the generalized Marcum-Q function and u denotes the time-bandwidth product [16]. Taking the average of Eq. (3) and substituting the probability density function (PDF) of SNR under fading conditions yields the detection probability for fading channels [14]. For fading environment, the average detection probability ($\tilde{P}_d$) [17] and PDF of SNR ($F_\gamma(\gamma)$) under Hoyt fading channel are given as [15]

$$\tilde{P}_d = \int_0^\infty Q_u\left(\sqrt{2\gamma}, \sqrt{\lambda}\right) F_\gamma(\gamma) \mathrm{d}\gamma, \tag{5}$$

$$F_\gamma(\gamma) = \frac{1+q^2}{2q\overline{\gamma}} e^{-\frac{\left(1+q^2\right)^2}{4q^2\overline{\gamma}}\gamma} I_o\left(\frac{1-q^4}{4q^2\overline{\gamma}}\gamma\right), \tag{6}$$

where $0 \leq q \leq 1$ is the Hoyt fading parameter.

$\tilde{P}_d^{\text{Hoyt}}$ is calculated by putting Eq. (6) in Eq. (5) [15]

$$\tilde{P}_d^{\text{Hoyt}} = 1 - \sum_{l=0}^{\infty}\sum_{i=0}^{\infty}\sum_{j=0}^{\infty} \frac{2^{1-u+l-j}(-1)^j \lambda^{u+j}\left(q^2\overline{\gamma}\lambda\right)^l}{j!(i!)^2\left(4q^2\overline{\gamma} + \left(1+q^2\right)^2\right)^{1+l+2i}} \times \frac{\left(1-q^2\right)^{2i}\left(1+q^2\right)^{1+2i}\Gamma\left(\frac{1+l}{2}+i\right)\Gamma\left(\frac{2+l}{2}+i\right)}{(u+l+j)\Gamma(u+l)\Gamma\left(\frac{1+l}{2}\right)\Gamma\left(\frac{2+l}{2}\right)}. \tag{7}$$

2.1 Centralized Cooperative Spectrums Sensing (CCSS)

In CCSS, all SUs in the network perform local SS to identify primary user signal and forward their result to the common fusion centre (FC) as shown in Fig. 1a. The data is forwarded to FC in form of binary result $D_i \varepsilon [0\ 1]$ where free state of the channel is depicted by bit '0' and busy state of the channel is depicted by bit '1'. FC fuses this received information on the basis of given logic rule [18]

$$S = \sum_{i=1}^{K} D_i \begin{cases} \geq k; & H_1 \\ < k; & H_0 \end{cases} \tag{8}$$

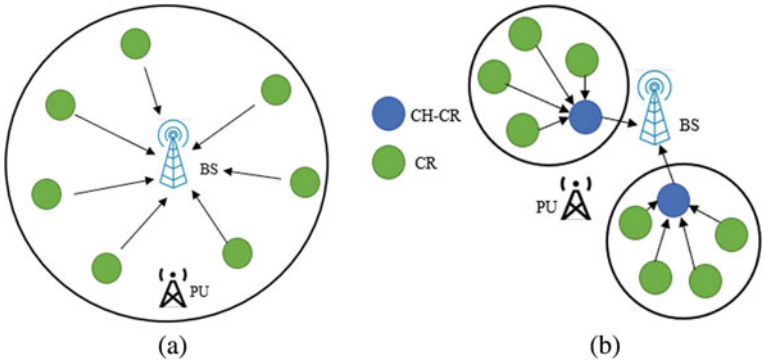

Fig. 1 **a** Concept of CCSS. **b** Concept of CB-CSS

The overall probabilities for k-out-of-K voting rule are given as [19]

$$Q_{f'} = \sum_{j=k}^{K} \binom{K}{j} (P_f)^j (1 - P_f)^{K-j}, \tag{9}$$

$$Q_{d'} = \sum_{j=k}^{K} \binom{K}{j} (P_d)^j (1 - P_d)^{K-j}, \tag{10}$$

Also, $Q_{m'} = 1 - Q_{d'}$. OR fusion rule is achieved when $k = 1$, AND fusion rule is achieved when $k = K$.

2.2 *Cluster-Based Cooperative Spectrums Sensing (CB-CSS)*

Its conceptualization is shown in Fig. 1b. The SUs are aggregated into clusters, and a suitable user is chosen as cluster head (CH) depending upon certain criteria [20]. CHs are responsible for data collection, information exchange [21]. Let's consider the number of clusters 'C' and the number of CR users 'U' within each cluster; consequently, the total number of users in the network is $C \times U = K$. SUs perform local SS and transfer their decision to CH of that cluster. CHs then report this information to the FC. There are following rules for CB-CSS [22].

OR-OR fusion. In this case, OR rule is used by SUs within a cluster to report information to CH. Similarly, by applying OR rule, CHs combine this result with FC. The following are the probabilities for the OR-OR fusion rule:

$$Q_{f,\text{OR-OR}} = 1 - \prod_{j=1}^{C} \left(1 - Q_{f'}^{\text{OR}(j)}\right), \tag{11}$$

$$Q_{m,\text{OR-OR}} = \prod_{j=1}^{C} \left(1 - Q_{d'}^{\text{OR}(j)}\right), \tag{12}$$

Here, C are the number of clusters.

OR-AND fusion. In this case, OR rule is used by SUs within a cluster to report information to CH. CHs combine this result with FC by applying AND rule. The following are the probabilities for the OR-AND fusion rule:

$$Q_{f,\text{OR-AND}} = \prod_{j=1}^{C} \left(Q_{f'}^{\text{OR}(j)}\right), \tag{13}$$

$$Q_{m,\text{OR-AND}} = 1 - \prod_{j=1}^{C} \left(Q_{d'}^{\text{OR}(j)}\right), \tag{14}$$

AND-OR fusion. In this case, AND rule is used by SUs within a cluster to report information to CH. CHs combine this result with FC by applying OR rule. The following are the probabilities for the AND-OR fusion rule:

$$Q_{f,\text{AND-OR}} = 1 - \prod_{j=1}^{C} \left(1 - Q_{f'}^{\text{AND}(j)}\right) \tag{15}$$

$$Q_{m,\text{AND-OR}} = \prod_{j=1}^{C} \left(1 - Q_{d'}^{\text{AND}(j)}\right), \tag{16}$$

AND-AND fusion. In this case, AND rule is used by SUs within a cluster to report information to CH. CHs combine this result with FC by applying AND rule. The following are the probabilities for the AND-AND fusion rule:

$$Q_{f,\text{AND-AND}} = \prod_{j=1}^{C} Q_{f'}^{\text{AND}(j)}, \tag{17}$$

$$Q_{m,\text{AND-AND}} = 1 - \prod_{j=1}^{C} Q_{d'}^{\text{AND}(j)}, \tag{18}$$

2.3 Average System Throughput

This segment presents analysis of the system throughput following [23]. Let us denote probability of spectrum being free as p_{H_o} and probability of spectrum being occupied as p_{H_1}. Thus, $p_{H_o} + p_{H_1} = 1$. Depending upon the result of SS and status of the channel, three probabilities are considered: SU accurately detects PU presence when spectrum is actually busy, the probability is considered as $p_{H_1}(Q_{d,l})$ (l is the type of fusion rule); SU misses the detection of the PU presence even though it is present in the spectrum, $p_{H_1}\ (1 - Q_{d,l})$; SU successfully identifies PU absence when spectrum is indeed unoccupied, $p_{H_o}\left(1 - Q_{f,l}\right)$. If H_p and $\tilde{H}_p$ are considered as primary network throughput when SU is absent and present, respectively, and H_s and $\tilde{H}_s$ are considered as secondary network throughput when PU is absent and when it is present, respectively, then, average system throughput (H_{avg}) is evaluated as

$$H_{\text{avg}} = p_{H_1} Q_{d,l} H_p + p_{H_1}\left(1 - Q_{d,l}\right)\left(\tilde{H}_p + \tilde{H}_s\right) + p_{H_0}\left(1 - Q_{f,l}\right)H_s, \tag{19}$$

Equation (19) can be expanded as

$$H_{\text{avg}} = p_{H_1} Q_{d,l}(H_p - \tilde{H}_p - \tilde{H}_s) + p_{H_1}\left(\tilde{H}_p + \tilde{H}_s\right) + p_{H_0} H_s - p_{H_0} Q_{f,l} H_s, \tag{20}$$

Let us put $p_{H_1}\left(\tilde{H}_p + \tilde{H}_s\right) + p_{H_0} H_s = \vartheta_0$, $p_{H_1}(H_p - \tilde{H}_p - \tilde{H}_s) = \vartheta_1$ and $p_{H_0}(H_s) = \vartheta_2$, then Eq. (20) can be written as

$$H_{\text{avg}} = \vartheta_0 + \vartheta_1 Q_{d,l} - \vartheta_2 Q_{f,l}. \tag{21}$$

3 Results and Discussion

The following simulation parameters are used to evaluate the performance of throughput over Hoyt fading channel using various fusion schemes: $H_p = 30$ bits, $H_s = 20$ bits, $\widetilde{H_p} = 10$ bits, $\widetilde{H_s} = 5$ bits, SNR = 10 dB, $u = 1$ and $p_{H_o} = 0.75$. Hoyt fading parameter, $q = 0.6$. The channels between FC and SUs, i.e. the reporting channels are supposed as ideal. For simplicity, number of clusters are taken as $C = 2$ and number of CR users within each cluster are $U = 5$.

Effect of centralized CSS and cluster-based CSS on throughput $\left(H_{\text{avg}}\right)$ versus detection threshold plot over Hoyt fading channel is shown in Fig. 2. Initially, throughput increases for all the fusion rules with increase in detection threshold because of decrease in false alarm probability. False alarm probability causes less CR user transmission leading to inadequate usage of the spectrum. Thus, when false alarm probability reduces, throughput increases. But H_{avg} reduces with further increase in

detection threshold, because detection probability (Q_d) is less at higher values of threshold. CR users cannot transmit unless correct detection takes place. At very low threshold value about $\lambda = 1$, highest throughput is attained for AND-AND fusion rule as compared to other fusion rules. It is because Q_f for AND-AND fusion rule is lowest, as all clusters and users have to communicate their verdict about PU existence in the spectrum then only FC decides PU's presence. As the detection threshold values increase, H_{avg} for AND-AND fusion rule degrades because of very low Q_d. At comparatively higher values of threshold, about $\lambda = 10$, throughput for OR-OR fusion rule is highest. Reason being, OR-OR fusion rule achieves maximum detection probability as single user and single cluster decision is required for FC to decide PU's existence. It can be observed, OR-AND fusion rule outdid all the others rules and achieves maximum throughput because it exhibits trade-off between high Q_d due to OR fusion inside clusters and low Q_f due to AND fusion between CH and FC. Maximum throughput achieved for OR-AND (CB-CSS) fusion rule is 4.07% greater than OR fusion rule and 6.94% greater than AND fusion rule, i.e. centralized CSS.

In Fig. 3, OR-AND fusion rule is considered and impact of different number of users in a cluster on H_{avg} over Hoyt fading channel is shown. C is kept constant and taken as $C = 2$. It can be observed, initially throughput is more for less number of users. It is because with OR fusion applied inside the clusters, more users result in high Q_f at low threshold values. But as value of detection threshold rises, false alarm probability for OR-AND fusion rule decreases even with the greater number of users, also, Q_d for OR rule applied inside the clusters will increase with increase in number of users. Thus, throughput for $U = 6$ is comparatively higher than other values of U at high detection threshold.

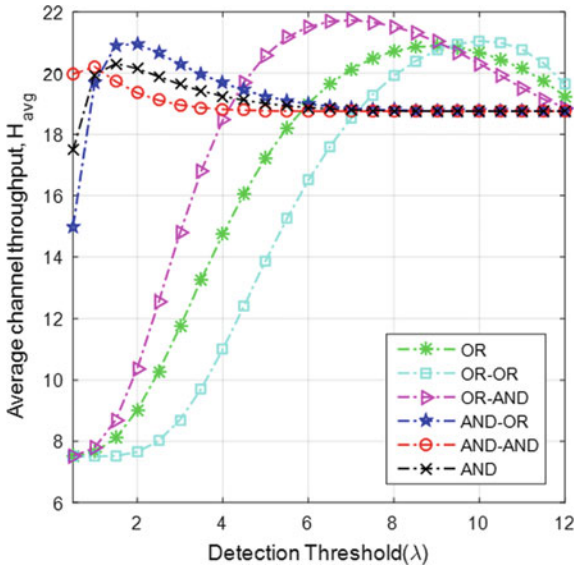

Fig. 2 Performance evaluation of throughput over Hoyt fading channel using different fusion schemes

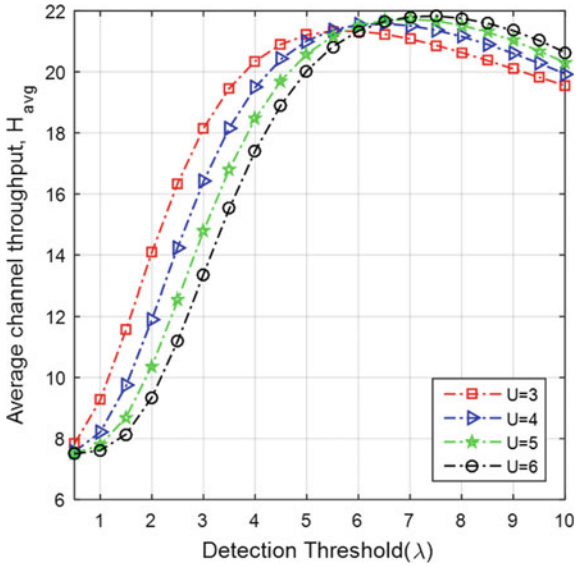

Fig. 3 Impact of different number of users on throughput over Hoyt fading channel. OR-AND fusion rule is applied, $C = 2$

In Fig. 4, impact of different number of clusters on H_{avg} over Hoyt fading channel is shown. Number of users are kept constant; $U = 2$, OR-AND fusion rule is applied. Initially, more clusters result in better throughput. It is because AND fusion applied between CH and FC will reduce false alarm with increase in clusters. However, AND fusion results in decrement of Q_d at high values of threshold, therefore, more clusters result in lower throughput later. Hence, H_{avg} for $C = 2$ is comparatively higher than other values of C at high threshold. The nature of graphs in Figs. 3 and 4 is similar to the one observed in Fig. 2 for OR-AND fusion rule.

Figure 5 shows throughput against number of CR users for various values of SNR considering OR-AND fusion rule and $P_f = 0.05$. Under noisy environment, i.e. when SNR is small, probability of detection falls down resulting in lower throughput.

4 Conclusion

In this paper, the impact of various fusion schemes on throughput in the case of the Hoyt fading channel is investigated. For centralized CSS, two fusion rules are considered. For cluster-based CSS, four different fusion rules are applied. It is analysed that CB-CSS for OR-AND fusion rule outweighs all the other rules in terms of throughput achieved over Hoyt fading channel. Further, it is investigated that throughput for OR-AND rule increases with an increase in the number of CR users at high detection threshold values. Also, for this rule, throughput is high for a greater number of clusters at low detection threshold and it is high for smaller number of clusters at high

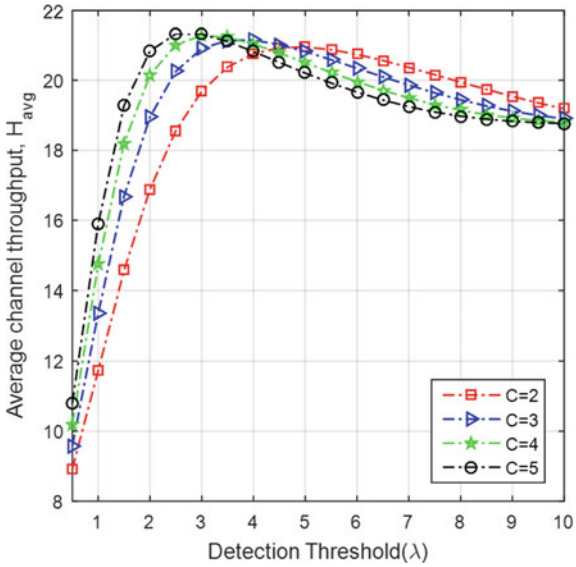

Fig. 4 Impact of different number of clusters on throughput over Hoyt fading channel. OR-AND fusion rule is applied, $U = 2$

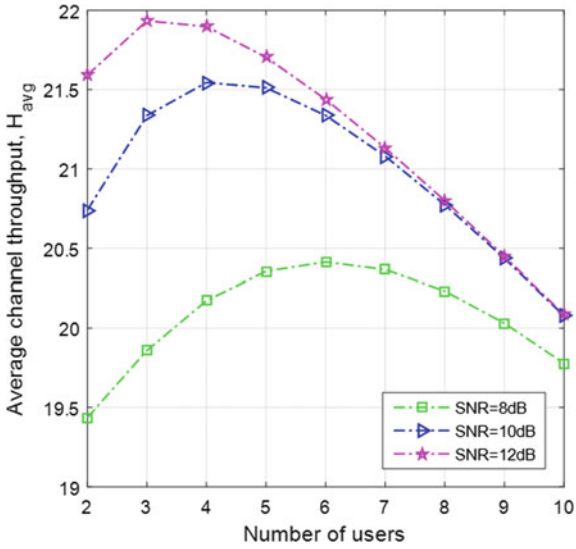

Fig. 5 Effect of SNR on throughput versus number of users for OR-AND fusion rule

detection threshold. With an increase in values of SNR, the throughput of the system under the Hoyt fading condition also improves.

Acknowledgements The authors are greatly thankful to the Department of Electronics & Communication Engineering, Malaviya National Institute of Technology (MNIT) Jaipur for their support in performing this research work.

References

1. Haykin S (2005) Cognitive radio: brain-empowered wireless communications. IEEE J Sel Areas Commun 23(2):201–220
2. Liu Y, Zeng C, Wang H, Wei G (2010) Energy detection threshold optimization for cooperative spectrum sensing. In: 2010 2nd international conference on advanced computer control, vol 4. IEEE, Shenyang, China, pp 566–570
3. Liang YC, Chen KC, Li GY, Mahonen P (2011) Cognitive radio networking and communications: an overview. IEEE Trans Veh Technol 60(7):3386–3407
4. Akyildiz IF, Lo BF, Balakrishnan R (2011) Cooperative spectrum sensing in cognitive radio networks: a survey. Phys Commun 4(1):40–62
5. Bai Z, Wang L, Zhang H, Kwak K (2010) Cluster-based cooperative spectrum sensing for cognitive radio under bandwidth constraints. In: 2010 IEEE international conference on communication systems. IEEE, Singapore, pp 569–573
6. Guo C, Peng T, Xu S, Wang H, Wang W (2009) Cooperative spectrum sensing with cluster-based architecture in cognitive radio networks. In: VTC spring 2009-IEEE 69th vehicular technology conference. IEEE, Barcelona, Spain, pp 1–5
7. Peh ECY, Liang YC, Guan YL, Zeng Y (2009) Optimization of cooperative sensing in cognitive radio networks: a sensing-throughput tradeoff view. IEEE Trans Veh Technol 58(9):5294–5299
8. Banavathu NR, Khan MZA (2016) On the throughput maximization of cognitive radio using cooperative spectrum sensing over erroneous control channel. In: 2016 Twenty second national conference on communication (NCC). IEEE, Guwahati, India, pp 1–6
9. Balam SK, Siddaiah P, Nallagonda S (2019) Throughput analysis of cooperative cognitive radio network over generalized κ–μ and η–μ fading channels. Wireless Netw 25:4625–4638
10. Choi YJ, Pak W, Xin Y, Rangarajan S (2012) Throughput analysis of cooperative spectrum sensing in Rayleigh-faded cognitive radio systems. IET Commun 6(9):1104–1110
11. Kumar A, Thakur P, Pandit S, Singh G (2020) Threshold selection and cooperation in fading environment of cognitive radio network: consequences on spectrum sensing and throughput. AEU-Int J Electron Commun 117:153101
12. Bhowmick A, Das MK, Biswas J, Roy SD, Kundu S (2014) Throughput optimization with cooperative spectrum sensing in cognitive radio network. In: 2014 IEEE international advance computing conference (IACC). IEEE, Gurgaon, India, pp 329–332
13. Nallagonda S, Bhowmick A, Prasad B (2021) Throughput performance of cooperative spectrum sensing network with improved energy detectors and SC diversity over fading channels. Wireless Netw 27:4039–4050
14. Nallagonda S, Chandra A, Roy SD, Kundu S, Kukolev P, Prokes A (2016) Detection performance of cooperative spectrum sensing with hard decision fusion in fading channels. Int J Electron 103(2):297–321
15. Bagheri A, Sofotasios PC, Tsiftsis TA, Ho-Van K, Loupis MI, Freear S, Valkama M (2016) Energy detection based spectrum sensing over enriched multipath fading channels. In: 2016 IEEE wireless communications and networking conference. IEEE, Doha, Qatar, pp 1–6
16. Digham FF, Alouini MS, Simon MK (2003) On the energy detection of unknown signals over fading channels. In: IEEE international conference on communications, 2003. ICC'03, vol 5. IEEE, Anchorage, AK, USA, pp 3575–3579
17. Ghasemi A, Sousa ES (2005) Collaborative spectrum sensing for opportunistic access in fading environments. In: First IEEE international symposium on new frontiers in dynamic spectrum access networks, 2005. DySPAN 2005. IEEE, Baltimore, MD, USA, pp 131–136
18. Letaief KB, Zhang W (2009) Cooperative communications for cognitive radio networks. Proc IEEE 97(5):878–893
19. Banavathu NR, Khan MZA (2017) Optimal number of cognitive users in k-out-of-m rule. IEEE Wireless Commun Lett 6(5):606–609
20. Olawole AA, Takawira F, Oyerinde OO (2019) Fusion rule and cluster head selection scheme in cooperative spectrum sensing. IET Commun 13(6):758–765

21. Joshi GP, Kim SW (2016) A survey on node clustering in cognitive radio wireless sensor networks. Sensors 16(9):1465
22. Sharma G, Sharma R (2018) Performance evaluation of distributed CSS with clustering of secondary users over fading channels. Int J Electron Lett 6(3):288–301
23. Hu H, Zhang H, Yu H, Chen Y, Jafarian J (2015) Energy-efficient design of channel sensing in cognitive radio networks. Comput Electr Eng 42:207–220

Design of Energy-Efficient Wireless Sensor Network for Smart Mobility

Ramandeep Gill and Tarun Kumar Dubey

Abstract A large number of sensor nodes are deployed in the wireless sensor network (WSN) to sense physical or environmental conditions such as humidity, pressure, sound, temperature, and mobility. WSN has an extensive span of applications in the military, biodiversity, agriculture, machine surveillance, and smart city (Zhao and Guibas, Wireless sensor networks, an information processing approach. Morgan Kaufmann Publishers, pp 9–15, 2004 [1]). This paper focuses on smart mobility, which is one of the important features of smart cities. In WSN, there are various limitations and challenges such as limited battery life, limited bandwidth for communication, less space for processing and storage of data, and QoS provisioning (Akyildiz and Vuran, Wireless sensor networks, 1st edn. Wiley, New York, pp 37–40, 2010 [2]). In this paper, an energy-efficient network is designed by considering the battery level of sensor nodes the shortest route is found between the source node and destination node to overcome a few above-mentioned problems in WSN. The technique used is adaptive Dijkstra's algorithm which is simulated in CupCarbon U-One 4.2 simulator (CupCarbon Homepage, http://www.cupcarbon.com/cupcarbon_ug.html [3]).

Keywords WSN · Sensor node · Smart mobility · Battery level

1 Introduction

WSN consists of spatially distributed sensors or IoT nodes that can gather different types of data such as temperature, pressure, humidity, and motion from their surroundings. Sensor nodes are capable of storing and processing the data [4]. The processed data can be sent to the end-user (mobile or stationary) or a system via a gateway. The WSN has an extensive span of applications such as military applications, smart buildings, biodiversity, disaster relief applications, precision agriculture,

R. Gill · T. K. Dubey (✉)
Department of Electronics and Communication Engineering, Manipal University Jaipur, Dahmi Kalan, Jaipur, Rajasthan 303007, India
e-mail: tarunkumar.dubey@jaipur.manipal.edu

S. Rawat et al. (eds.), *Proceedings of Second International Conference on Computational Electronics for Wireless Communications*, Lecture Notes in Networks and Systems 554,
https://doi.org/10.1007/978-981-19-6661-3_52

and smart city [5]. The focus of this paper is to work on one of the features of a smart city called smart mobility. WSN can change the conventional city services to smart cities with the help of sensors or IoT nodes. A smart city has various features such as smart governance, smart security, smart education, smart healthcare, smart energy, and smart mobility [6]. The area of interest in this paper is smart mobility which can further be extended in two directions, i.e., mobility of data and mobility of vehicles.

Sensor node consists of six main components as shown in Fig. 1. The sensing unit consists of sensors to collect data from the environment, and an analog-digital converter (ADC) converts the available analog data to digital form. Data is sent to the processing unit for processing if required or to storage. The processed data is communicated via the transceiver either to neighboring nodes or to the user. Position finding system is used to find the latitude and longitude of the neighboring nodes or a mobile node and a mobilizer is used if the sensor node is used as a mobile node to move on an allocated route. The power unit is the battery that provides energy to all the other components [7].

Sensor nodes have inadequate battery life such as the capacity of the *smart dust mote* is 33 mAh [8]. For MicaZ and Mica2 nodes [9], which use two AA batteries, the node capacity is limited to 1400–3400 mAh. Similarly, the recent SunSPOT platform uses a 750 mAh lithium-ion battery [10]. Sensor node consumes energy to carry out various functions such as sensing of data, storage of data, data processing, and sending and receiving of data. The main constraint in WSN is energy consumption. In most cases, it is not possible to replace the power unit of sensor nodes, especially where sensor nodes are randomly deployed. In a multi-hop WSN, the sensor node plays two important roles: first is as a data provider where it collects data from the surroundings and processes it before transmitting it to neighboring nodes, and second is as a data router where it relays the information provided by its neighboring nodes [2]. The energy consumption is affected by the operations involved in both roles. If any node in the network fails to operate due to low battery, then it changes the overall topology of the network. In such a case network, reorganization and data

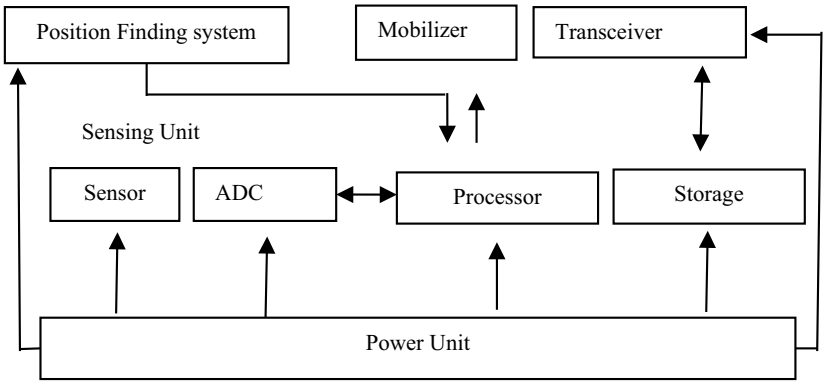

Fig. 1 Basic architecture of a sensor node

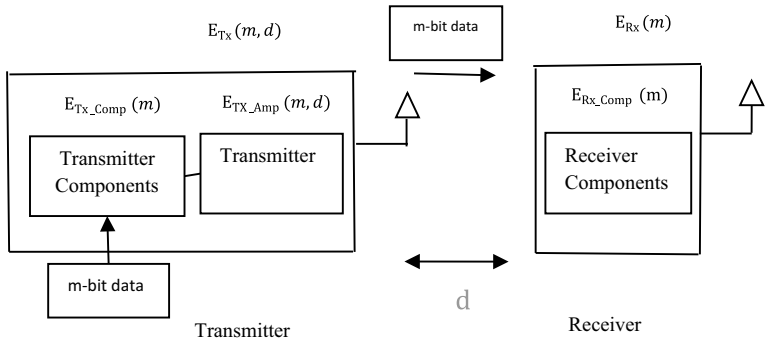

Fig. 2 Energy model for transmitter-receiver in WSN

rerouting are required. So, the design of energy-efficient protocols and algorithms is very important for WSN. One such technique is designed in this paper which is discussed in detail in the next section.

The consumption of energy in WSN depends on various factors such as the type of hardware used, the size of the data packets, the power level of transmission, and the distance between the transmitter and receiver [11]. A simple transmitter-receiver model is considered to determine the energy consumption as shown in Fig. 2.

The energy consumption between transmitter and receiver is given in Eqs. (1) and (2)

$$E_{Tx}(m,d) = E_{Tx\_\text{Comp}} \times m + E_{Tx\_\text{Amp}} \times m \times d^n \tag{1}$$

$$E_{Rx}(m) = E_{Rx\_\text{Comp}} \times m \tag{2}$$

where E_{Tx_Comp} and E_{Rx_Comp} are the consumption of energy per bit for the transmitter and receiver circuit, respectively, and E_{Tx_Amp} is the consumption of energy per bit per distance for the amplifier circuit [2].

Equation (1) shows that a large distance leads to large energy consumption. If the transmitter finds the shortest route to reach the receiver or to send data to the receiver, then a large amount of energy can be saved and will enhance the overall lifetime of the network. Based on this concept, a network of six sensor nodes is designed in CupCarbon U-one 4.2 simulator as shown in Fig. 3. Where $S_1, S_2, \ldots, S_6$ denote the IDs of the nodes and $v_1, v_2, \ldots, v_6$ are the codes assigned to each sensor node, respectively. In this network, S_1 is considered the transmitter node and S_6 is considered the receiver node. All the sensor nodes lie within the radio range of each other and can send or receive messages. Distance between pair of sensor nodes is shown with the help of the "distance button" available in the simulator. The simulator shows the map view of a city where this network is designed.

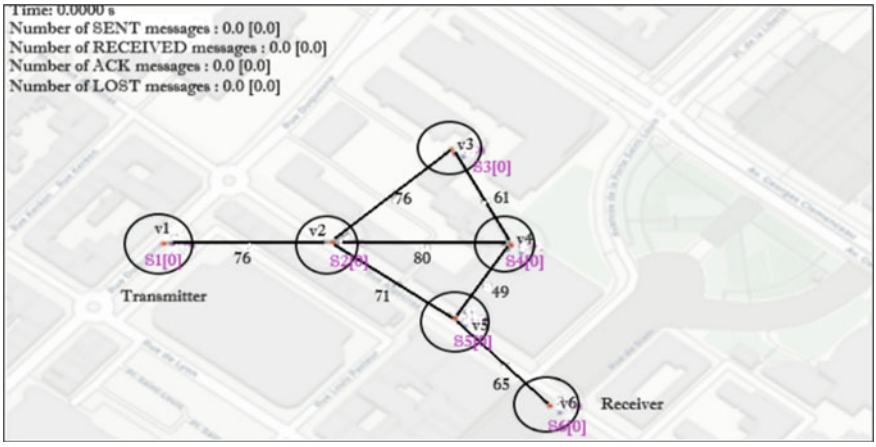

Fig. 3 Random WSN designed in CupCarbon U-One 4.2

Distance between pair of nodes is represented with cost matrix in Table 1, and possible routes between transmitter node and receiver node are represented with path matrix in Table 2.

Adaptive Dijkstra's algorithm is used to find the shortest route between the transmitter and receiver. The algorithm is explained in the next section in detail.

Table 1 Cost matrix of the designed network

	Receiver node IDs					
Transmitter node IDs	S_1	S_2	S_3	S_4	S_5	S_6
S_1	0	76	0	0	0	0
S_2	76	0	76	80	71	0
S_3	0	76	0	61	0	0
S_4	0	80	61	0	49	79
S_5	0	71	0	49	0	58
S_6	0	0	0	79	58	0

Table 2 Path matrix of the designed network

Paths	1	2	3	4	5	6	Distance (in meters)
1	1	2	3	4	5	6	320
2	1	2	4	5	6	0	263
3	1	2	4	6	0	0	235
4	1	2	5	6	0	0	205

Adaptive Dijkstra's Algorithm

Dijkstra's algorithm uses the greedy method to calculate the minimum distance between the transmitter and receiver [12]. In this paper, a new technique is proposed called adaptive Dijkstra's algorithm which will calculate the shortest distance between transmitter and receiver node by considering the battery level of sensor nodes. The step-by-step process of adaptive Dijkstra's algorithm is explained in Fig. 4.

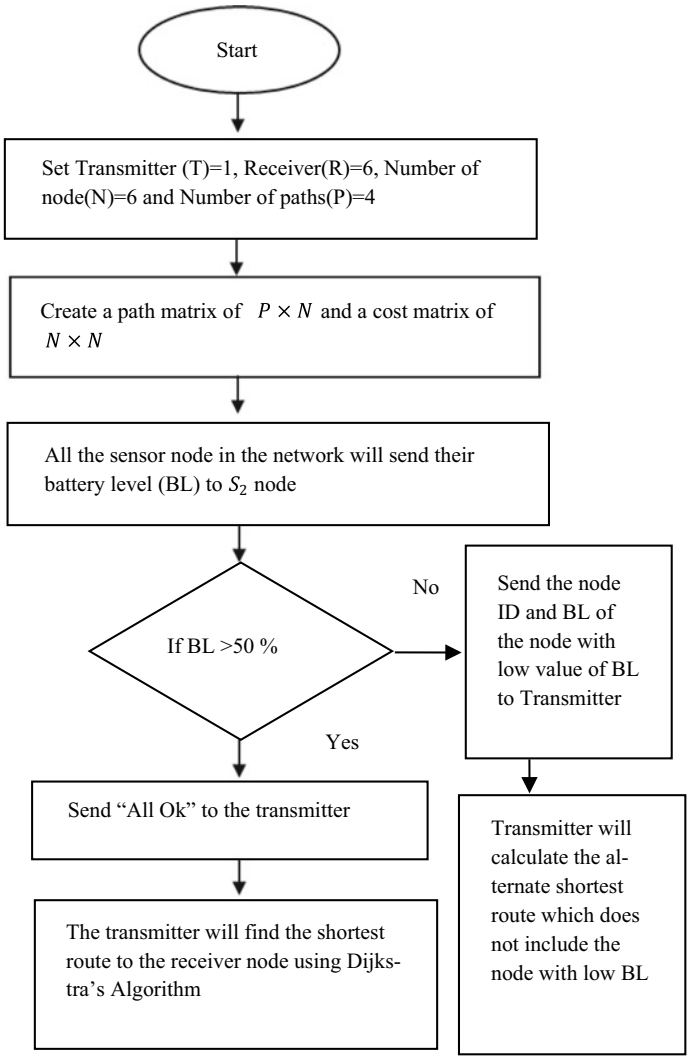

Fig. 4 Flow diagram of adaptive Dijkstra's algorithm

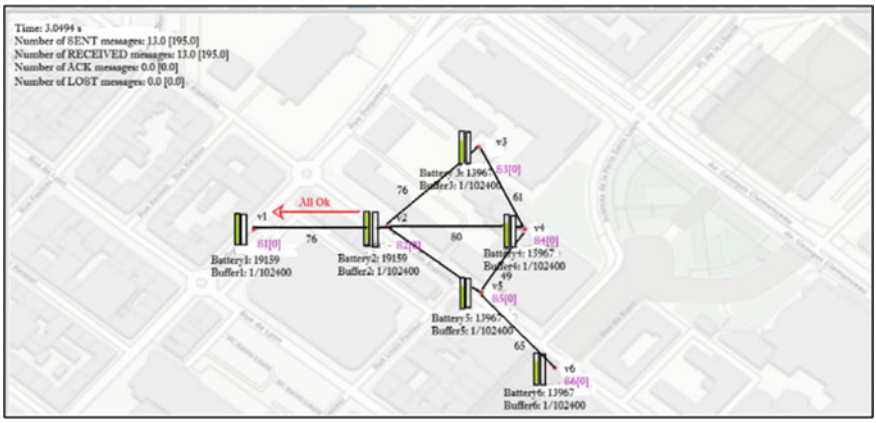

Fig. 5 Simulation of Case 1

2 Simulation and Result Analysis

Adaptive Dijkstra's algorithm is simulated using CupCarbon U-One 4.2 simulator. Two cases are considered which are discussed in detail.

2.1 Case1: Battery Level of Sensor Nodes is More Than 50%

In this case, battery level of S_3, S_4, S_5 and S_6 will vary for three levels. At each level, 10% of the battery level will be reduced and for each level sensor nodes will send their changed BL values to S_2 node. S_2 will store all three sets of values and at the end, it will check the BL level of individual nodes. If the BL level of each node is above 50%, then S_2 will send an "All Ok" message to S_2 node as shown in Fig. 5.

Figure 6 shows the output obtained after simulation of Case 1. The output shows that the BL value of the sensor nodes is more than 50% so the transmitter will choose the shortest path to reach the receiver nodes and the nodes traversed are $S_1 \rightarrow S_2 \rightarrow S_5 \rightarrow S_6$ and the total distance of the route is 205 m. Figures 7 and 8 show the battery level variation with respect to time and energy consumption with respect to time for all the sensor nodes, respectively.

Case 2: Battery Level of sensor nodes is less than 50%

In this case, battery level of S_3, S_4, S_5 and will vary for three levels. At each level, battery level of S_3, S_4 and S_6 will be reduced by 10% and S_5 will be reduced by 40%. The sensor nodes will send their changed BL values to S_2. S_2 will store all three sets of values and at the end, it will check the BL level of individual nodes. If the BL value of any node is below 50%, then S_2 will send the low value of BL value along with the node ID of the sensor node to S_1 node as shown in Fig. 9.

Fig. 6 Results obtained in the Console window of CupCarbon U-One 4.2

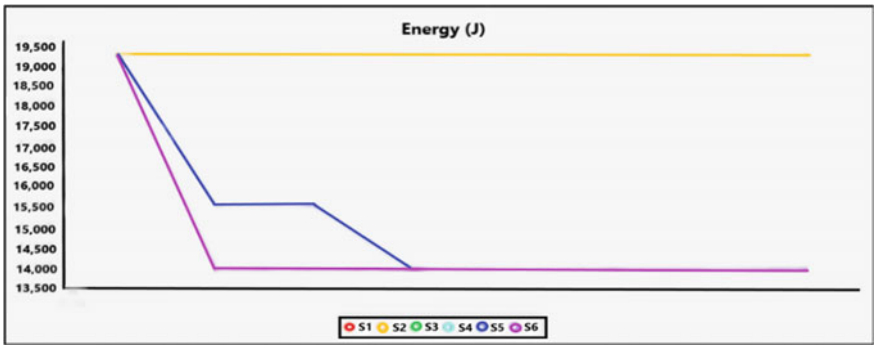

Fig. 7 Battery level of sensor nodes in Case 1

S_1 will check the node ID and BL value, and it will search for the alternate shortest route from transmitter to receiver node in the path matrix which does not include a node S_5 having a low value of BL. The results obtained after simulation are shown in Fig. 10. The nodes traversed in this case are $S_1 \rightarrow S_2 \rightarrow S_4 \rightarrow S_6$, and the total distance of the route is 235 m.

Figures 11 and 12 show the battery level variation with respect to time and energy consumption with respect to time for all the sensor nodes, respectively.

Results obtained in the two cases are shown in Table 3.

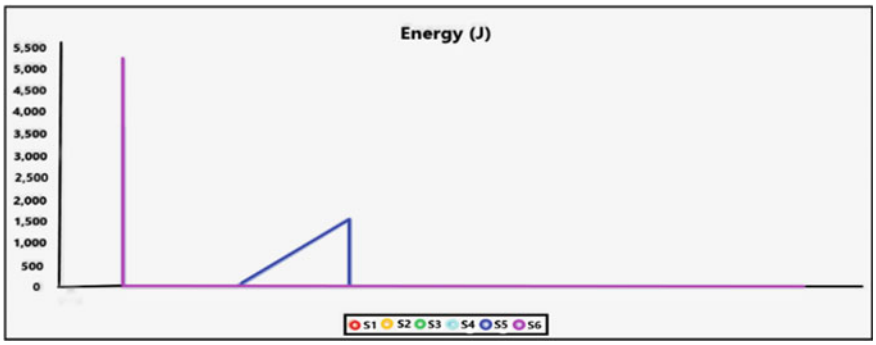

Fig. 8 Energy consumption of sensor nodes in Case 1

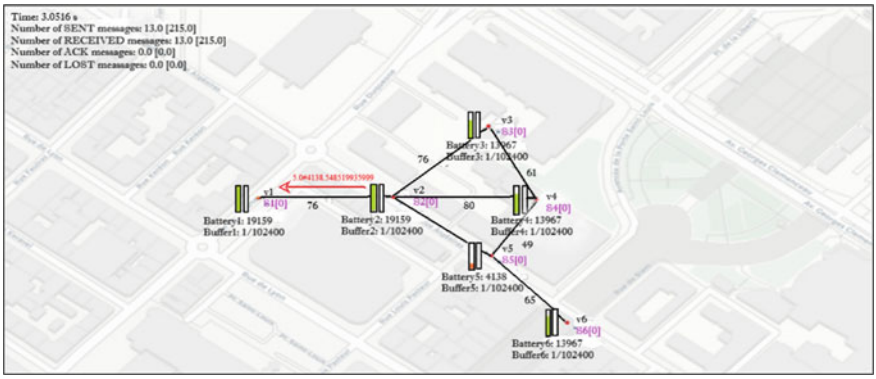

Fig. 9 Simulation of Case 2

Table 3 shows that the number of messages sent and received in both cases is the same, so energy consumption for communication is the same. The distance traveled in Case 2 is 30 m longer as compared to Case 1 and the additional delay to reach the receiver node is 0.0022 s which is negligible. So, the designed network will work efficiently even in the case of node failure. This will enhance the lifetime of sensor nodes and hence enhance the lifetime of the network.

3 Conclusion

A WSN consists of spatially distributed sensor nodes that can be deployed in a planned or random fashion. In this paper, a random network is designed and simulated in CupCarbon U-One 4.2 simulator. The designed network will find application in the field of smart mobility which is one of the important features of a smart city. A small network is designed where two cases are considered to find the shortest route

Fig. 10 Result obtained in Console window of CupCarbon U-One 4.2

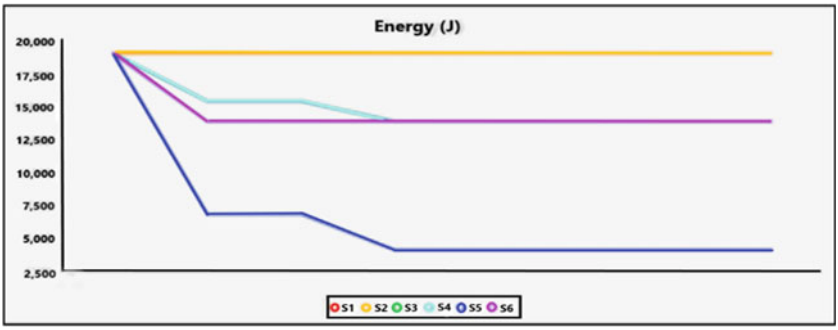

Fig. 11 Battery level of sensor nodes in Case 2

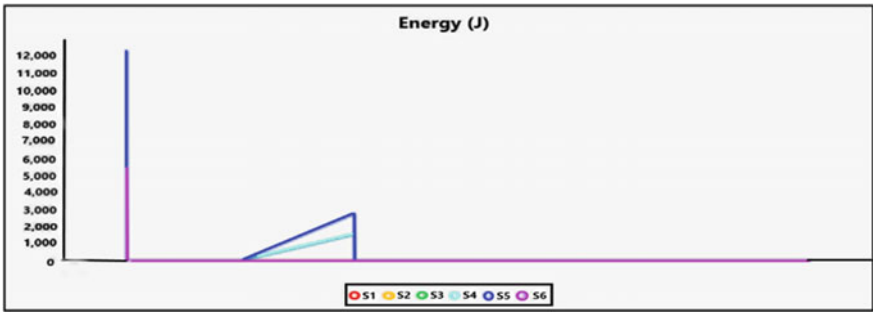

Fig. 12 Energy consumption of sensor nodes in Case 2

Table 3 Result analysis of Case1 and Case 2

Title	Case 1	Case 2
Simulation time	3.0494 s	3.0516 s
Route	$S_1 \rightarrow S_2 \rightarrow S_5 \rightarrow S_6$	$S_1 \rightarrow S_2 \rightarrow S_4 \rightarrow S_6$
Total distance covered	205 m	235 m
Number of sent messages	13	13
Number of received messages	13	13

between transmitter and receiver node using adaptive Dijkstra's algorithm. In Case 1, all the sensor nodes have a battery level of more than 50% where the shortest route is calculated, and in Case 2, one of the nodes has a battery level of less than 50% so to enhance the lifetime of the network an alternate shortest route is calculated which does not include the node with low battery. The results obtained show that the alternate route is 30 m longer as compared to the shortest route but the delay in reaching the receiver node is 0.0022 s which is negligible. This network is energy efficient and can find applications in transmitting data to any node in the network even in case of node failure. Also, it can be implemented to find the shortest route between two locations on a map and can be communicated to a mobile node.

References

1. Zhao F, Guibas L (2004) Wireless sensor networks, an information processing approach. Morgan Kaufmann Publishers is an imprint of Elsevier, pp 9–15
2. Akyildiz F, Vuran M (2010) Wireless sensor networks, 1st edn. Wiley, New York, pp 37–40
3. CupCarbon Homepage. http://www.cupcarbon.com/cupcarbon_ug.html. Last accessed 11 Feb 22
4. Lee S, Bae M, Kim H (2017) Future of IoT networks: a survey. Appl Sci 7:1072–1097
5. Belli L, Clifone A (2020) IoT-enabled smart sustainable cities: challenges and approaches. Sensors 3:1039–1–71
6. Kantarci B, Oktug S (2018) Special issue: wireless sensor and actuator networks for smart cities. J Sensor Actuator Networks 7:71–75
7. Wang S, Chen Y (2021) Optimization of wireless sensor network architecture with the security system. Sensors 1:1–11
8. Pottie GJ, Kaiser WJ (2000) Wireless integrated network sensors. Commun ACM 43:51–58
9. Crossbow MicaZ Mote Specifications. http://www.xbow.com
10. SunSPOT Mote Specifications. http://www.sunspotworld.com
11. Elshrkawey M, Elsherif SM, Wahed ME (2017) An enhancement approach for reducing the energy consumption in wireless sensor networks. J King Saud Univ- Comput Inform Sci 30:259–267
12. Goyal M, Kumar V, Dahiya A (2015) Performance measurement of wireless sensor network using Dijkstra's algorithm. Int J Comput Sci Manage Stud 18:2231–5268

Electricity Theft Detection System for Smart Metering Application Using Bi-LSTM

Ranbirjeet Kaur and Garima Saini

Abstract Power theft is big issues in the field of electricity because it harms transmission lines and results in financial losses. So, it is important to detect electricity theft effectively. A unique method is developed for detecting electricity theft that is based on the bidirectional long short-term memory (Bi-LSTM), which is compared with the exiting techniques like logistic regression (LR), support vector machine (SVM), and convolution neural network and long short-term memory (CNN-LSTM). Main objective of the proposed Bi-LSTM model is to reduce the complexity of electricity theft detection systems and also identify power theft in different scenarios effectively. A real-time dataset has been used in the proposed network. The performance of suggested Bi-LSTM model is evaluated in the MATLAB environment. The efficiency of Bi-LSTM model is assessed and contrasted with LR, SVM, and CNN-LSTM in terms of accuracy, precision, recall, and *F*-score and achieved better results in every parameter.

Keywords Electricity theft detection · Bi-LSTM · Non-technical losses · Power theft

1 Introduction

The architecture of every power station is divided into three stages, the first is electricity generation, second is its transmission, and the third is distribution. The power generation systems produce high voltage electricity that is delivered via transmission lines. This high voltage electricity in power lines is then stepped down to obtain an optimum voltage level that is later on transmitted to residential customers through the distribution system. Customers are usually linked to a low voltage power system. The utility provider can keep track of how much electricity a customer is using

R. Kaur (✉) · G. Saini
Department of Electronics and Communication, National Institute of Technical Teacher's Training and Research Chandigarh, Chandigarh, India
e-mail: ranbirjeetkaur88@gmail.com

S. Rawat et al. (eds.), *Proceedings of Second International Conference on Computational Electronics for Wireless Communications*, Lecture Notes in Networks and Systems 554,
https://doi.org/10.1007/978-981-19-6661-3_53

by installing smart meters at customers' houses. The transmitted electricity experiences certain undesired losses while going through these three phases are technical losses or TLs and non-technical losses or NTLs [1]. Technical losses mainly occur because of the joules effect, when there is a breakdown in a transmission line or transformer during energy transmission. On the other hand, non-technical losses are mainly caused by delays, electricity theft, altering with smart meters, billing and unpaid debts, and so on.

Out of all the NTLs, electricity theft is one of the most common problems that have detrimental effects on revenue in the energy market and the country's GDP [2]. Any illegal consumption of power from energy stations without any contract or legal authorization to modify or update its measurements is called electricity theft [3]. As per the report conducted worldwide, it is assumed that there will be around a $25 billion per year loss of energy due to unauthorized energy use. In India only, utility providers lost up to $4.5 billion per year due to the theft of electricity [5]. For this purpose, smart meters are installed at customer's premises through both, i.e., the customer and electricity providers can regulate and manage their domestic electric usage [6].

1.1 Role of Smart Meters in Power Grids

Smart meters are intelligent instruments that analyze the total energy consumption of customers and send this data to the utility provider confidentially. This bidirectional communication allows utility providers to gather data from customer homes about electricity transferred back to the power grid. In the context of protected communication, smart meters can transmit command messages both virtually and physically. As a result, smart meters can be utilized solely at the customer's premises to track and monitor all household equipment and gadgets. Usually, data exchanged by a smart meter is a mixture of attributes such as a specific meter code, timestamp, and instantaneous quantities of energy use. Smart meters can regulate the maximum consumption of energy. Also smart meter integration enables utilities to detect illegal use and energy theft to increase the efficiency of distribution and power quality [7].

1.2 Identifying Illegal Customers of Electricity

Over the years, several engineering-based monitoring and controlling schemes have been developed and simulated on the high performance computing (HPC) to enhance their performance outcomes. Algorithms used to conduct power engineering tasks have recently become more complicated and computer-intensive due to the emergence of smart grids [8]. A variety of methods have been used to identify illegal consumers. Tool-based classification models for support vector (SVM) machine, rule engine, and neural network pattern recognition (NNPR) are examples of such

classification methods. A thorough literature survey is conducted in the next section of this paper in which different methods for detecting electricity theft are analyzed.

1.3 Literature Review

Over the years, a significant number of electricity theft detection models have been proposed by various researchers, some of them are discussed here; Hasan et al. [9] suggested an electricity theft detection (ETD) model that was based on CNN and LSTM techniques. The CNN was used for automating the features extraction and classification process. Also, the authors utilized the convolution neural network along with long short-term memory (CNN-LSTM) model for categorizing data in SGs. Punmiya et al. [10] introduced a gradient boosting theft detecting model wherein extreme gradient boosting, categorical boosting, and light gradient boosting were used as gradient boosting classifiers (GBCs). Zheng et al. [11] developed a large and deep CNN approach comprising of the broad module and deep CNN module for detecting electricity theft. Gupta et al. [12] suggested a clustering-based technique for monitoring the electricity theft that can occur in real-time energy systems. Ballal et al. [13] developed a real-time approach named electricity theft detection and prevention scheme (ETDPS) that can determine the location or pilferage and computes the total amount of power stolen. Zheng et al. [14] proposed a model where maximum information coefficient (MIC) was used to measure thefts in shapes and clustering by rapid scanning and locating density peaks (CFSFDP) identified fraudulent customers. Gao et al. [15] suggested a new physically inspired data-driven approach for detecting electricity theft in smart meters. Li et al. [16] introduced a hybrid convolutional neural network random forest (CNN-RF) framework for automatic electricity theft detection to aid utility firms in resolving challenges such as poor energy monitoring and erratic power use. Chandel et al. [17] developed a CNN, recurrent neural network (RNN), and Bi-LSTM-based framework for addressing the various challenges that were faced while detecting electricity theft in smart meters. Qu et al. [18] suggested a technique for detecting theft in electricity that was based on enhanced synthetic minority oversampling technique (SMOTE) and improved RF method so that the auditing performance of grid companies can be increased. Commonly used are random forest, decision tree, and support vector machine (SVM). Here, the author used SVM along with a decision tree Jindal et al. [19]. In Hodge et al. [20], Jokar et al. [21] and Nagi et al. [22] clustering and classification using SVM irregularities were found in the dataset. This technique was made more effective by applying clustering for both the primary and secondary steps to get unit consumption Martino et al. [23]. The collaboration of 1-class SVM, decision tree, and optimum path forest is used. Fuzzy logic and SVM [24], also generic algorithm and support vector machine, i.e., GA-SVM is used, which is effective to enhance accuracy for detection of theft of electricity. Toma et al. [25] support vector (SVM) machine, a commonly used machine learning technique is used in the analysis of the training data which is collected from (SM) smart meters and accuracy of predictions data is measured. Then, grid search

method is applied to find the most accurate meta-parameters in SVM are selected where approximately 90% accuracy, 89% precision, 90% recall, and 89% $F1$-score are reached [26]. The author developed a theft detection device called the smart energy theft system (SETS) which uses machine learning and mathematical models. The algorithm achieves an accuracy of 99.89% which improves a smart home based on IoT security Ullah et al. [27]. Here, the author proposed HDNN that is hybrid deep neural network for this project, in which convolution neural network (CNN) is combined with gated recurrent unit (GRU) and particle swarm optimization (PSO), the combination is known as CNN-GRU-PSO-HDNN.

From the literature survey conducted above, it is observed one of the major problems with these systems was that they were highly complex and time-consuming because theft recognition was done at different levels. In addition to this, the techniques used in the traditional models had lower learning rates which had a direct impact on the classification accuracy of the system while detecting electricity theft. Another major drawback of these systems is that the techniques used are not recommended when dealing with sequential data or pattern identification that also resulted in performance degradation.

2 Present Work

To overcome the limitations of the traditional electricity theft detection models, a new model is proposed in this paper that is based on bidirectional long short-term memory (BI-LSTM). The proposed Bi-LSTM technique mainly focuses on two areas, firstly the complexity of the system is reduced by using a Bi-LSTM classifier, and secondly, a real-time dataset is used to make the system more effective and accurate, and capable to handle real data. The main objective of using Bi-LSTM in the suggested approach is that it is bidirectional that means; data can be accessed and retrieved on either side. Moreover, the ability of Bi-LSTM to track longer contexts particularly in noise-robust tasks serves as another motivation to use it. In addition to this, the Bi-LSTM is specially designed for analyzing and producing results for sequential classification data. It is also able to solve the gradient vanishing problem that occurs in most of the recurrent neural network (RNN) systems.

3 Methodology

Proposed electricity theft detection model is shown in Fig. 1.

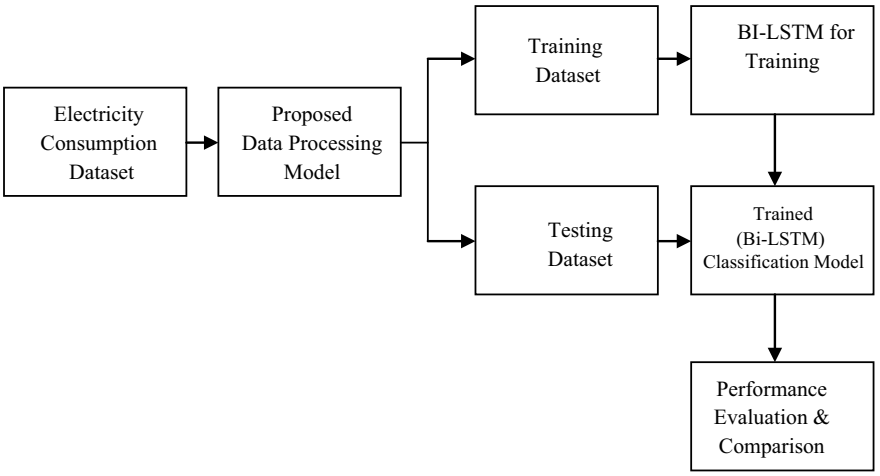

Fig. 1 Block diagram of proposed ETD model

3.1 Data Collection

The first and foremost step is acquiring data from the available datasets. In the proposed work, a real-time dataset has been used in which information of consumers with single or multiple registers with KWH, Kvah, and Kva readings and unique IDs are available. Every register consists of monthly data readings of each customer. In addition to this, the dataset also contains information about the theft cases that were observed during random visits. Data is taken in an excel sheet which is read in MATLAB.

3.2 Pre-processing

After collecting the dataset, the next step is to process it. Here, the pre-processing of the data is done under four stages that are given below;

- **Data cleaning**: In this step, the raw data is cleaned by removing the redundant and duplicate data from it. Also, the missing values, outliers are filled and eliminated, respectively in the dataset to make it more effective and reliable.
- **Maintain data continuity**: The next step of pre-processing is to maintain data continuity. In this process, the cells in which readings are zero, representing that meter has been changed are filled by adding the reading of the next cell to the previous one sequentially so that pattern can be created.
- **Normalization**: The next step is a normalizing dataset in which the total readings of the single customer are divided by its maximum reading so that the reading scale is normalized between 0 and 1.

- **Data balancing**: Once the data is normalized, it needs to be balanced to avoid biases because, in the real world, only a few samples of the data are available in which the consumer is fraudulent. For this, grouping is done in which four entries are incorporated. Data is divided into two categories for training and testing purposes.

3.3 Network Initialization

Once the data is processed and normalized, the next phase is to initialize the proposed network which works on multi-layers. Table 1 shows the parameters with their respective value.

- A sequence input layer inputs the data that is in the form of readings and consumption of the consumers, to the network.
- A bi-LSTM learns bidirectional long-term dependencies between time steps of time series or sequence data that is given through input layer.
- A fully connected layer multiplies the input by a weight matrix and then adds a bias vector.
- A classification layer computes weighted classification tasks with mutually exclusive classes. The layer infers the number of classes from the output size of the previous layer.
- Epochs indicates the number of passes of the entire training dataset the machine learning algorithm has completed. The whole dataset is passed once and forward pass and backward pass is counded as single pass.
- The rate at which the weights are updated is called learning rate. Here, we use Adam optimizer for which we set the value 0.025.
- And we get best results with 100 hidden layers.

Table 1 Network initialization parameters

S. No.	Parameters	Values
1	InputLayer	Sequence
2	HiddenLayer	Bi-LSTM
3	ConnectedLayer	Fully connected
4	OutputLayer	Classification
5	max epoch	200
6	InitialLearnRate	0.025
7	GradientThreshold	1
8	Hidden Units	100

Table 2 Cases of confusion matrix

Actual/predicted	Predicted positive	Predictive negative
True positive	TP	FN
True negative	FP	TN

3.4 Training and Testing

In the next phase of the model, training and testing are done. To do so, the training data is provided to the proposed Bi-LSTM classifier for a total of 200 iterations. The suggested Bi-LSTM model gets trained, and then, its efficiency is evaluated based on this training, bypassing the testing data to it.

3.5 Performance Analysis

The performance of the suggested ETD approach is analyzed and compared with previous approaches while considering various dependency factors like accuracy, precision, recall, sensitivity, specificity, and *F*-score.

4 Results and Discussions

To evaluate the efficiency of the proposed Bi-LSTM electricity theft detection model, its performance is analyzed in MATLAB software. The simulation outcomes were obtained and later on compared with the various electricity theft detection models as per their accuracy, *F*-score, precision, recall, sensitivity, and specificity.

4.1 Evaluation Matrix

After data balancing, the dataset is divided into four cases that is False Positive (FP), True Positive (TP), False Negative (FN), and True Negative (TN), these indices are used to form a confusion matrix, which is shown in Table 2 and different parameters are defined in Table 3 along with their formulas.

5 Performance Evaluation

The performance of the proposed Bi-LSTM electricity theft detection model is firstly analyzed by its training progress graph that is shown in Fig. 2. The blue-colored line

Table 3 Formulae for different parameters

Parameter	Definition	Formula
Accuracy	The accuracy of the system implies computing an exact value A =. It can also be described as the degree to which the estimated value resembles a true or standard value	$\frac{TP+TN}{(TP+FP+TN+FN)}$
Sensitivity	Sensitivity or true positive rate (TPR) can be defined as the percentage of people who has positive test results out of those that have the ailment	$TP = TP + FN$
Specificity	Specificity or true negative rate represents the percentage of people who did not have the ailment but had a negative outcome on this examination	$TN = TN + FP$
Precision	It can be defined as the proportion of relevant or accurate instances among the recovered examples. Precision can be evaluated by the below formula	$P = \frac{TP}{TP+FP}$
Recall	It's measured as a percentage of similar examples that have been recovered. For memory and precision, relevance is essential	$R = \frac{TP}{TP+FN}$
F-score	The F-score, also called the $F1$-score, is a metric to find how precise a model is on a particular dataset	$FM = \frac{2\times P\times R}{(P+R)}$

in the graph depicts the accuracy progress while the red-colored line depicts the loss reduced in the proposed model. It is observed that initially, the accuracy graph is low because the model is not trained properly yet. But, as soon as the number of iterations is increasing, the accuracy of the systems is also increasing. On the contrary, the loss curve is initially high when the model is not trained but decreases gradually to a large extent when a model is trained properly.

Figure 3 illustrates the confusion matrix of the suggested Bi-LSTM scheme that is classified into four sections, namely True Positive (TP), False Positive (FP), True

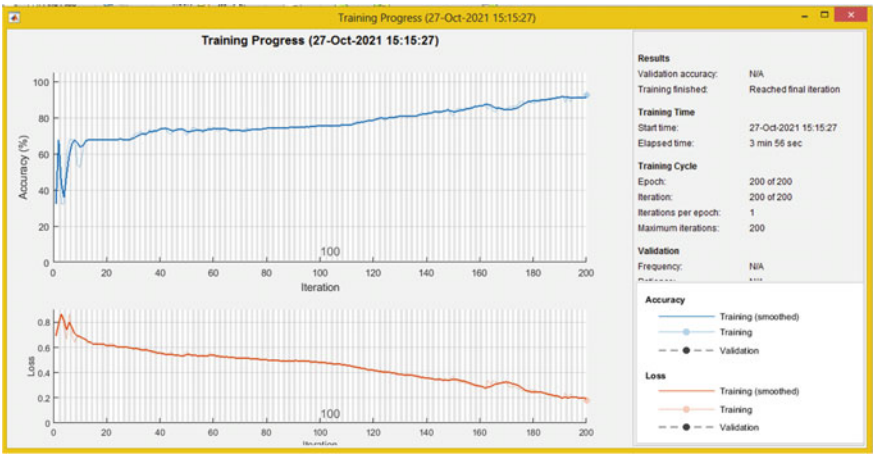

Fig. 2 Training progress in the proposed model

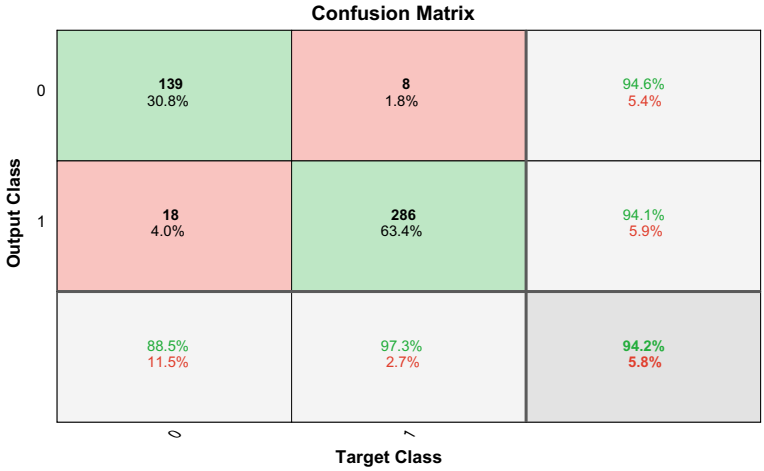

Fig. 3 Confusion matrix of proposed model

Negative (TN), and True Positive (TP). The first column indicates that the accuracy of proposed BI-LSTM model in detecting the thefts of 0 class which came out to be 88.5%. The second column of the figure shows that the accuracy in predicting the thefts of 1 class which is 97.3%, as out of 286 entries only eight entries are predicted wrong as the 0 class which actually belong to 1 class category.

The efficacy of the suggested Bi-LSTM-based ETD method is also analyzed as per their accuracy, recall, *F*-score, precision, sensitivity, and specificity and is shown in Fig. 4. From the graph, it is observed that the value of accuracy attained in the suggested Bi-LSTM technique is mounted to 94.24%. While the value of sensitivity and specificity came out to be around 94% for each. In addition to this, the effectiveness of the suggested Bi-LSTM approach is also assessed in terms of precision, recall, and *F*-score, whose respective values came out to be 97.28%, 94.56%, and 95.65%.

The effectiveness of the proposed Bi-LSTM framework is also compared with the previously proposed electricity theft detection models, and the graph obtained for the same is given in Fig. 5.

The specific values obtained for each parameter are recorded in tabular format and are given in Table 4.

6 Conclusion

An enhanced electricity theft detection model that is based on the Bi-LSTM technique is developed in this paper. The simulation results were determined and compared with traditional ETD systems in terms of various performance parameters like accuracy, recall, *F*-score, sensitivity, precision, and specificity. The classification accuracy

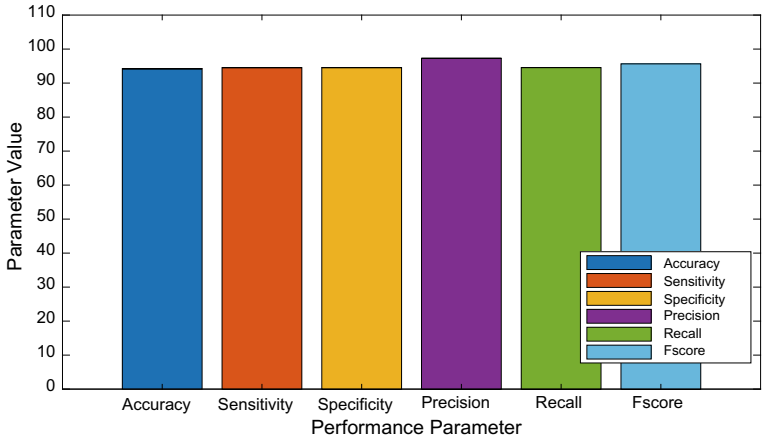

Fig. 4 Different parameters of the proposed model

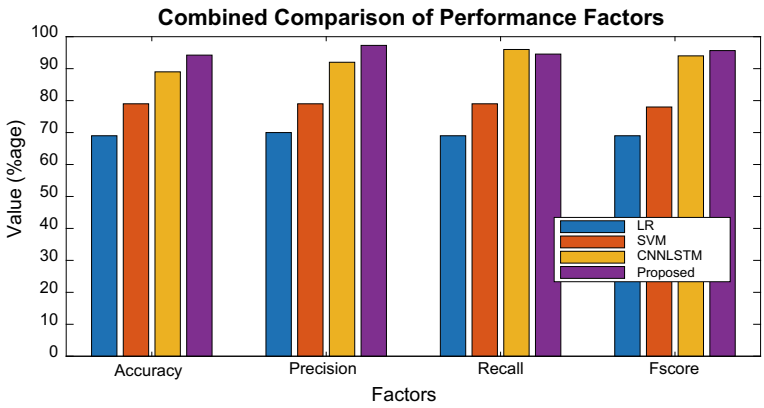

Fig. 5 Comparison graph for different parameters

Table 4 Specific values of each parameter

Parameter/model	LR [9] (%)	SVM [9] (%)	CNN-LSTM [9] (%)	Proposed (%)
Accuracy	69	79	89	94.24
Precision	70	79	92	97.28
Recall	69	79	96	94.56
F-score	69	78	94	95.65

rate attained by the proposed Bi-LSTM model is 94.23%, while its value came out to be just 69%, 79%, and 89% in conventional LR, SVM, and CNN-LSTM models. Moreover, the effectiveness of the proposed Bi-LSTM model is also observed under precision, recall, and *F*-score factors which came out to be 97%, 94%, and 95%, respectively. While as, the precision value in the traditional LR model came out to be 70%, followed by 79% and 92% in CNN-LSTM models. In addition to this, the value obtained in traditional LR in terms of recall and *F*-score is 69% each, 79% and 78% for SVM, and 96% and 94% for the CNN-LSTM model. The values obtained from the results prove that the suggested Bi-LSTM model outperforms the traditional model almost in every parameter and hence is more effective and convenient to use for theft detection.

7 Future Scope

In the future, we can use data for different regions to make the model more stable and reliable. We use the data from industrial category, which include Time of Day (TOD) readings. Along with that can work on UUE part which means unauthorized use of electricity. In addition to this, we can use generative adversarial networks (GANs) to handle the data unbalancing problems by obtaining data from minority classes. Moreover, more work can be done on reinforcement learning for future predictions, as it is capable of learning from its trials and errors.

References

1. Munawar S, Kabir B, Asif M, Ullah A, Javaid N (2021) Electricity theft detection in smart meters using a hybrid bi-directional GRU bi-directional LSTM model
2. Dick AJ (1995) Theft of Electricity—how UK electricity companies detect and deter. In: Proceedings European convention security and detection, Brighton, UK, May 1995, pp 90–95
3. Smith TB (2003) Electricity theft- comparative analysis. Energy Policy 32:2067–2076
4. World electricity distribution losses. International Energy Annual 2006, U.S. Energy Information Administration. http://www.eia.doe.gov. Last accessed 12 Dec 2021
5. Overview of power distribution. Ministry of Power, Govt. of India. http://www.powermin.nic.in. 14 Dec 2021
6. Chebbo M (2007) EU smart grids framework: electricity networks of the future 2020 and beyond. In: Proceedings of IEEE power engineering society general meeting, Tampa, FL, June 2007, pp 1–8
7. Depuru SS, Wang L, Devabhaktuni V (2010) A conceptual design using harmonics to reduce pilfering of electricity. In: Proceedings of IEEE PES general meeting, Minneapolis, MA, July 2010
8. Green RC, Wang L, Alam M (2011) High-performance computing for electric power systems: applications and Trends. In: IEEE PES general meeting, Detroit, MI, July 2011, pp 1–8
9. Hasan MN, Toma RN, Nahid A, Manjurul Islam MM, Kim J-M (2019) Electricity theft detection in smart grid systems: A CNN-LSTM based approach. Energies 12:3310. https://doi.org/10.3390/en12173310

10. Punmiya R, Choe S (2019) Energy theft detection using gradient boosting theft detector with feature engineering-based preprocessing. IEEE Trans Smart Grid 10(2):2326–2329. https://doi.org/10.1109/TSG.2019.2892595
11. Zheng Z, Yang Y, Niu X, Dai H, Zhou Y (2018) Wide and deep convolutional neural networks for electricity-theft detection to secure smart grids. IEEE Trans Industr Inf 14(4):1606–1615. https://doi.org/10.1109/TII.2017.2785963
12. Gupta A, Chakraborty N, Mondal S (2017) CETD: an efficient clustering-based energy theft detection technique in smart grid. In: 2017 IEEE region 10 symposium (TENSYMP), Cochin, 2017, pp 1–5.https://doi.org/10.1109/TENCONSpring.2017.8070055
13. Ballal MS, Suryawanshi H, Mishra MK, Jaiswal G (2020) Online electricity theft detection and prevention scheme for smart cities. IET Smart Cities 2(3):155–164
14. Zheng K, Chen Q, Wang Y, Kang C, Xia Q (2019) A novel combined data-driven approach for electricity theft detection. IEEE Trans Industr Inf 15(3):1809–1819. https://doi.org/10.1109/TII.2018.2873814
15. Gao Y, Foggo B, Yu N (2019) A physically inspired data-driven model for electricity theft detection with smart meter data. IEEE Trans Industr Inf 15(9):5076–5088
16. Li S, Han Y, Yao X, Yingchen S, Wang J, Zhao Q (2019) Electricity theft detection in power grids with deep learning and random forests. J Electr Comput Eng 2019, Article ID 4136874, 12 p
17. Chandel P, Thakur T (2019) Smart meter data analysis for electricity theft detection using neural networks. Adv Sci Technol Eng Syst J 4(4):161–168
18. Qu Z, Li H, Wang Y, Zhang J, Abu-Siada A, Yao Y (2020) Detection of electricity theft behaviour based on improved synthetic minority oversampling technique and random forest classifier. Energies 13(8)
19. Jindal A, Dua A, Kaur K, Singh M, Kumar N, Mishra S (2016) Decision tree and SVM-based data analytics for theft detection in smart grid. IEEE Trans Ind Inform 12:1005–1016
20. Hodge V, Austin J (2004) A survey of outlier detection methodologies. Artif Intell Rev 22:85–126
21. Jokar P, Arianpoo N, Leung VC (2015) Electricity theft detection in AMI using customers' consumption patterns. IEEE Trans Smart Grid 7:216–226
22. Nagi J, Mohammad A, Yap KS, Tiong SK, Ahmed SK (2008) Non-technical loss analysis for detection of electricity theft using support vector machines. In: Proceedings of the 2008 IEEE 2nd international power and energy conference, Johor Bahru, Malaysia, 1–3 December 2008. IEEE, Piscataway, NJ, USA, pp 907–912
23. Di Martino M, Decia F, Molinelli J, Fernández A (2012) Improving electric fraud detection using class imbalance strategies. In: Proceedings of the international conference on pattern recognition applications and methods (ICPRAM), Vilamoura, Portugal, 6–8 February 2012, pp 135–141
24. Nagi J, Yap KS, Tiong SK, Ahmed SK, Nagi F (2011) Improving SVM-based nontechnical loss detection in power utility using the fuzzy inference system. IEEE Trans Power Deliv 26:1284–1285
25. Toma RN, Hasan MN, Nahid A, Li B (2019) Electricity theft detection to reduce non-technical loss using support vector machine in smart grid. In: 2019 1st international conference on advances in science, engineering and robotics technology (ICASERT), Dhaka, Bangladesh, 2019, pp 1–6. https://doi.org/10.1109/ICASERT.2019.8934601
26. Li W, Logenthiran T, Phan V-T, Woo WL (2019) A novel smart energy theft system (SETS) for IoT based smart home. IEEE Internet Things J 6:5531–5539. https://doi.org/10.1109/JIOT.2019.2903281
27. Ullah A, Javaid N, Samuel O, Imran M, Shoaib M (2020) CNN and GRU based deep neural network for electricity theft detection to secure smart grid. In: 2020 International wireless communications and mobile computing (IWCMC). https://doi.org/10.1109/IWCMC48107.2020.9148314

Opportunistic Underwater Routing Protocols: A Survey

Ketan Bhujange, Afrah Nayeem, Anusha P. Das, B. R. Chandavarkar, and Pradeep Nazareth

Abstract Underwater Acoustics Sensor Networks (UASNs) play a significant role in the different underwater applications. Some underwater applications include underwater environment monitoring, mine detection, pollution monitoring, etc. UASNs exhibit several challenges like node movement, changes in link quality between nodes, low bandwidth, high bit-error rate, and high energy consumption. These challenges in UASNs make data delivery unreliable during routing. One of the solutions to achieve better performance during routing is using an opportunistic routing approach. In the opportunistic routing, the sender will forward the data to the set of neighbors so that at least a neighbor can receive and forward the data. Evaluating the neighboring nodes, selecting the set of the neighbors, and coordinating among the selected nodes to forward the received data is the significant steps in opportunistic routing. Thus, we consider the Technique for Order of Preference by Similarity to Ideal Solution (TOPSIS) approach to select the best next-hops during routing. Therefore, we are making a detailed survey on protocols that apply TOPSIS to evaluate neighboring nodes' multiple attributes. Then we discuss various clustering techniques used in the selection of the best next-hops. Finally, we discuss methods used to compute hold time to achieve coordination between cluster nodes.

1 Introduction

The majority of the earth's surface is covered by water. Underwater Acoustic Sensor Networks (UASNs) enable exploring underwater in the fields like underwater monitoring, detecting mining resources, underwater environment, etc. However, in the perspective of underwater networking, there are several challenges like node mobility, high energy consumption, low bandwidth, the highly dynamic link between nodes [1–3].

K. Bhujange · A. Nayeem · A. P. Das · B. R. Chandavarkar · P. Nazareth (✉)
Wireless Information Networking Group (WiNG), Department of Computer Science and Engineering, National Institute of Technology Karnataka, Surathkal, Mangalore, India
e-mail: pradeep.nitk2017@gmail.com

S. Rawat et al. (eds.), *Proceedings of Second International Conference on Computational Electronics for Wireless Communications*, Lecture Notes in Networks and Systems 554,
https://doi.org/10.1007/978-981-19-6661-3_54

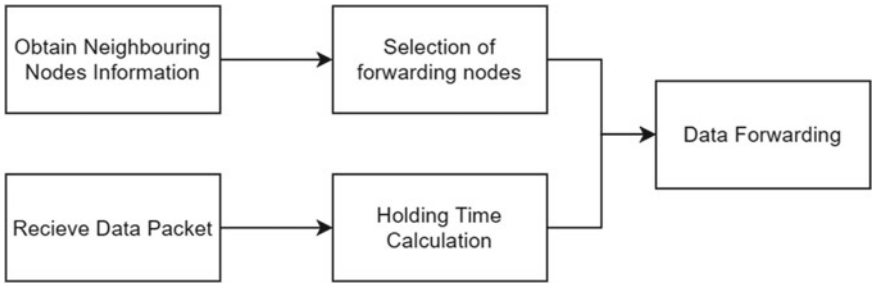

Fig. 1 Basic flow of OR protocols

The dynamic links between nodes impact the routing performance, resulting in poor communication reliability. One of the solutions to improve communication reliability is using opportunistic routing (OR). Instead of a single next-hop forwarder node selected in traditional routing, Opportunistic routing chooses a set of neighboring nodes called candidate forwarding. Further, the packet will be forwarded to the candidate forwarding set.

In the forwarding set, nodes forward the packets in a prioritized way; upon overhearing transmission by other nodes, they suppress the forwarding of the same packet. The opportunistic routing increases the chances of delivering the packet to at least one of the next-hop present in the candidate forwarding set. Thereby OR increases the communication reliability. The nodes in the candidate forwarding set are prioritized by determining hold time. The hold time determines how long a candidate node can hold the received packet before releasing it before forwarding it. Hold time can be determined based on different criteria like depth distance with other nodes in the candidate forwarding set [4, 5].

The flowchart in Fig. 1 represents the overall flow of the OR protocols. Neighboring nodes are chosen for the forwarding set based on the attribute values. The paper focuses on cluster formation and picking the optimal cluster to forward data to. The nodes coordinate by calculating the holding time for each node.

The paper is organized as follows: Sect. 2 elaborates the usage of the TOPSIS in finding the suitability of neighboring nodes, Sect. 3, elaborates existing clustering techniques in opportunistic underwater routing protocols, Sect. 4 discusses holding time calculation methods in existing OR underwater routing. The paper is concluded with the conclusion in Sect. 5.

2 Usage of Topsis in Underwater Routing

Hwang and Yoon [6] introduced a technique for multi-criteria decision making called TOPSIS. TOPSIS chooses the best alternative from many alternatives based on its similarity to the ideal solution. It selects the alternative farthest from the worst solution and nearest to the best solution. In the following subsections, we discuss the applications of the TOPSIS technique in WSNs.

2.1 *Fuzzy-TOPSIS-Based Cluster Head Selection in Wireless Sensor Networks*

Bilal and Young [7], proposed a cluster head selection scheme based on fuzzy TOPSIS. This scheme mainly aims to extend the network lifespan. In this scheme, some nodes are selected as cluster heads, while other nodes form the cluster members. The cluster heads collect the packets from their respective cluster members, aggregate the data and send it to the sink. The five main criteria considered to choose the cluster head are the residual energy of the node, the energy consumption rate, distance between the node and the sink, the node density and the average of distances to each neighbor.

Every sensor node broadcasts a 'Hello' message carrying the five attributes. All sensor nodes update their neighborhood tables after receiving the 'hello' packets from their neighbors. The fuzzy TOPSIS algorithm returns the rank of every node, and the node with the highest rank is selected as the cluster head. The cluster heads broadcast advertisements to their neighbors. The nodes choose to associate with the closest cluster head. Re-clustering is performed only if the threshold value is smaller than the neighbors to avoid overhead. The protocol uses a threshold-based multi-hop communication protocol.

2.2 *Cluster Head Selection in Wireless Sensor Networks Under Fuzzy Environment*

Azad and Sharma [8] proposed a new cluster head selection scheme based on fuzzy TOPSIS. The sensor nodes are assigned to clusters, and cluster heads are selected for every cluster. The cluster heads collect the packets from their respective cluster members using TDMA, aggregate the data and forward it to the base station. The best candidate for cluster head is the one that has the highest residual energy, the neighbor node density, and the least distance to the base station. The three criteria of a node considered are,the residual energy of the node, distance from the node to the base station and the node density.

The TOPSIS algorithm is implemented to rank the nodes. The nodes with the higher TOPSIS ranks announce themselves as cluster heads. The sensor nodes choose to associate with the closest cluster head. If the node is nearer to the base station than the cluster head, it communicates directly to the base station. The cycle of re-clustering and data transmission repeats until the death of all the nodes. The number of clusters keeps on changing along with the node density. If nodes start dying, the smaller clusters merge with the larger ones, thus reducing the number of clusters.

2.3 RODENT: A Flexible TOPSIS-Based Routing Protocol for Multi-technology Devices in WSN

Brandon and Mitton [9] proposed a new routing protocol for multi-technology networks by using a lightweight TOPSIS method. WSNs are limited by the capabilities of the Radio Access Technology used in the network. An MTN overcomes these limitations by supporting several RATs. The nodes can switch between different RATs at each hop. RODENT is mainly designed to support multiple RATs in an MTN. The RODENT protocol dynamically selects the best route and the best RAT at each hop based on the data requirement by using the TOPSIS algorithm.

RODENT accesses the link and route matrices of a node. The Link matrix consists of the attributes of every link between the node and its neighbors. A node constructs its route matrix from its link matrix and the routes received from neighboring nodes. The routing matrix contains the attributes of all the available routes of the node. The requirement vector contains the attribute weights based on the data requirements. The lightweight TOPSIS takes as input the routing matrix of a node and a requirement vector for the use case and outputs the route ranking. The top route is selected for the use case.

2.4 A Novel Approach for Smart Cities in Convergence to Wireless Sensor Networks

Jain and Rani [10], proposed a novel ring-based cross-layer routing model for the IoT in smart cities. The effectiveness of an IoT application depends on how fast the information is relayed from the sensors to the base station. This paper proposes a WSN-IoT protocol designed for real-time applications. The focus is on delivering the information with minimum delay through multi-hop routing.

Routing is performed based on the shortest path, using the TOPSIS algorithm. The nodes follow a ring system in which every node has a ring number. The base station is assumed to be located at the center of the field. The next-hop candidates must be from the next ring or within the same ring in the transmission range. At each hop, the best node is selected using the TOPSIS algorithm. The optimal node is chosen based on the four criteria: shortest distance of selected nodes from the base station, residual Energy, minimum Euclidean distance between mth selected node and next optimum nth node in the transmission range and the number of neighbors. The packet is transferred from the source node to the base station from the outermost ring nodes following the shortest path. The proposed scheme achieves a balance between energy consumption and performance.

2.5 Multi-criteria Decision-Based Path Planning for Data Collection in Fuzzy-Cluster-Based Large Sensor Networks

Sunil and Prabhat [11] propose a fuzzy-logic-based cluster head selection and TOPSIS-based path planning of the mobile sink. The nodes closest to the sink send out more data than the rest of the network and hence use up more power. The hotspot problem reduces the network's lifetime. The mobile sink is employed to deal with this issue. Every node discovers its coordinates using localization and keeps track of its neighbors. Fuzzy logic selects the cluster head based on residual energy and the node degree. The nodes associate themselves with the closest cluster head.

The base station is uninformed of the new cluster heads. So, the mobile sink will traverse in circular paths to learn about all the cluster heads. The cluster heads send information to the mobile sink whenever they fall within the communication range. Thus, the mobile sink now has information about all the cluster heads' residual energy, node degree, and edge cost. The mobile sink will have to decide the order in which it should visit the cluster heads, so the TOPSIS method is used to rank all the cluster heads based on the three criteria: residual energy, node degree, and edge cost. The mobile sink visits the cluster heads according to the sorted order. When the mobile sink approaches a cluster head, it broadcasts a beacon message. The cluster head will acknowledge the beacon message before sending the data it gathered.

Remarks From the Sect. 2.1 through 2.5 discussed usage of the TOPSIS for routing in wireless sensor networks (WSNs) for terrestrial applications. In the above subsections, TOPSIS selects the best neighbor by considering various attributes of neighboring nodes to forward the data. TOPSIS is not used in any of the underwater routing protocols to the best of our knowledge. Thus in the future, we can consider the usage of TOPSIS in underwater routing decision making.

3 Cluster Formation

Clustering is the process of grouping sensor nodes together to forward the received packets. One of the fundamental objectives of clustering is to eliminate duplicate data transmission by the receiving nodes and overcome the hidden-node problem [12, 13]. In the following subsections, the methods of cluster formation used in different routing protocols are discussed.

3.1 HydroCast

Noh et al. [12], proposed HydroCast, a hydraulic pressure-based anycast routing protocol. For selecting a candidate forwarding set, for a node, the Normalized Advance-

ment (NADV) to a neighbor node n having the packet delivery probability, p_n and the progress to the destination d_n^p, in meters, is:

$$\text{NADV}_n = d_n^p \times p_n \tag{1}$$

Packet delivery probability, p_n, is dependent on the frequency, the distance between sender and receiver, and the size of the packet [14]. Thereafter, to form the cluster, sender S will select the neighboring node C, which has the highest NADV. The node S will identify common nodes in its own neighboring set and neighbors of C at a distance $< 0.5 \times R$, where R is the maximum communication range of the node. The highest NADV value is considered among the nodes that are not clustered. In this way, all nodes must be clustered. Finally, one among multiple clusters must be selected as a candidate forwarding set by considering the highest Expected Packet Advancement (EPA). Nodes in the Cluster_k are ordered as $n_1 > n_2 > n_3, \cdots > n_k$, based on their priorities. The EPA of the cluster is computed by Eq. (2).

$$\text{EPA}(\text{Cluster}_k) = \sum_{i=1}^{k} d_{n_i} P_{n_i} \prod_{j=0}^{i-1} (1 - P_{n_j}) \tag{2}$$

Another routing protocol, Geographic and opportunistic routing with Depth Adjustment-based topology control for communication Recovery over void regions (GEDAR), employs a similar cluster formation strategy [13].

3.2 Opportunistic Void Avoidance Routing (OVAR)

OVAR selects the cluster that maximizes the probability of packet delivery and packet advancement [15]. EPA is the expected advancement of each packet if a given cluster forwards it. The EPA for a cluster ϕ created by R_i :

$$\text{EPA}(\phi_z) = \sum_{k=1}^{l} \beta_{ik} P_{ik} \prod_{y=0}^{k-1} (1 - P_{iy}) \tag{3}$$

The forwarding node calculates the EPA for each cluster, and the cluster with the highest EPA value is chosen as the relaying set. When j nodes engage in packet forwarding, let $\text{EPA}(F, j)$ and $E(F, j)$ be the expected packet advancement and energy consumption of the forwarding set, respectively. By incorporating all of the nodes in the forwarding set, $\text{EPA}(F, r)$ and $E(F, r)$, where $r = |F|$, the highest value for EPA and energy ($\text{EPA}_{\max}$ and $E_{\max}$, respectively) may be determined. Thus, taking μ and ρ as the weighting coefficients for EPA and energy, respectively, EEPA may be defined by picking j forwarding candidates from F:

$$\text{EEPA}(F, j) = \mu \frac{\text{EPA}(F, j)}{\text{EPA}_{\max}} - \rho \frac{E(F, j)}{E_{\max}} \tag{4}$$

To obtain the highest value for EEPA, the forwarding set should be checked for different numbers of members by looking through EEPA for $j = 1, 2, 3, \ldots, r$ and then selecting the set with the highest value; after that, removing other extra nodes from the forwarding set. Finally, the best set is chosen to relay the packet.

3.3 Energy-Efficient Void Avoidance Geographic Routing (EVAGR)

EVAGR is an opportunistic routing protocol that uses a similar method to select the forwarding set as discussed in the HydroCast. For a node n_i, its candidate set FC_i is obtained from its neighboring node N_i. For all nodes in the candidate set FC_i, the link reliability (packet reception ratio) of a node n_i to its neighboring node n_j is determined using the following formula:

$$\text{Link}R_{ij} = \mu \frac{N_{\text{succ}}}{N_{\text{total}}} + (1 - \mu)\text{Link}R_{ij} \tag{5}$$

Normalize advance (NADV) [16] is used to choose the neighbors who are making the most progress toward the sonobuoy. The estimation of this metric is based on a proposal in the literature [16, 17]. NADV of each node n_j in forwarding candidate set FC_i is:

$$\text{NADV}(n_j) = \text{Link}R_{ij} \times \text{ADV}(n_j), \tag{6}$$

where $\text{Link}R_{ij}$ is calculated in step 2 and $\text{ADV}(n_j)$ is the packet advancement measure of node n_j, given by:

$$\text{ADV}(n_j) = \text{Dist}(n_i, S_i) - \text{Dist}(n_j, S_j), \tag{7}$$

wherein $\text{Dist}(a, b)$ is the Euclidean distance between two nodes a and b, with b being the sonobuoy nearest to a. The expected packet advance (EPA) of each cluster of FC_i is defined using the following equation where P_{n_k} is delivery probability of packets to node n_k [15, 17].

$$\text{EPA}(\text{FC}_i) = \sum_{l=1}^{i} \text{NADV}(n_l) \prod_{k=0}^{n-1} (1 - P_{n_k}) \tag{8}$$

The cluster with the highest EPA calculated in the previous step is selected as the forwarding set F. If none of the nodes of F receives the packet, the packet will be resent.

3.4 *Energy-Efficient Clustering Algorithm for Underwater Acoustic Sensor Networks*

The paper [18] describes a solution for underwater sensor networks that uses a low-energy clustering structure. When a member node chooses a cluster to join, it takes into account the cluster head's location, as well as energy intake and consumption between member nodes and the cluster head. The cluster head is chosen at random during the initial step of the LEACH algorithm [19]. When a cluster grows too large, the nodes at the network's edge are separated from the cluster head and may consume significantly more energy. The energy-efficient clustering algorithm incorporates two modifications to compensate for the lack of the LEACH procedure; these are, the cluster head's position range should be limited and a new standard for selecting the heads of member nodes has been devised. The simulation results [18] show that the proposed algorithm efficiently balances the size of the cluster and lowers the network's energy usage.

4 Holding Time Computation

Holding time is the time for which the receiving node needs to wait before forwarding the packet. When a candidate node successfully transmits a packet, neighboring nodes overhear the packet and stop the transmission of the same packet. This mechanism contributes to the elimination of duplicate packets and overcrowding.

4.1 *HydroCast*

HydroCast uses distance-based prioritization [12]. When a node receives the packet, the node sets its timer to have a similar approach, but it requires information regarding two-hop connectivity and its distance from neighboring nodes [12]. The calculation of holding time is done by using a linear function which is directly dependent on the distance of the node from the sender node. The timer function for the receiving node x is considered as follows:

$$f(d_x^P) = \alpha(R - d_x^P) \tag{9}$$

Where R is the transmission range, and d_x^P is the progress toward the surface for the given node x. Equation (9) ensures that the node having higher depth progress must have lower hold time. Thus α must guarantee that nodes in the vicinity of the high priority node must overhear the transmission of the packet. The α is given as

$$\alpha > \frac{t_{ci} - t_{cj} + t_{ij} + t_{\text{ack}}}{d_i^P - d_i^P} \tag{10}$$

where t_{ack} is the ack transmission delay and the other term is to cover propagation delay over the distance $d_{ic} - d_{jc} + d_{ij}$ where i, j, and c are the nodes.

4.2 Geographic and Opportunistic Routing with Depth Adjustment-Based Topology Control for Communication Recovery (GEDAR)

In the paper GEDAR [13], they maintain a list of the candidate forwarding nodes. Each node sets itself a timer for when the node will be forwarding the data. Based on the priority, the holding time is set as:

$$T_w^i = T_p + \sum_{k=1}^{i} \frac{D(n_k, n_{k+1})}{s} + i * T_{\text{proc}} \tag{11}$$

where, s is speed of sound underwater, T_{proc} is the packet processing time, T_p is the remaining propagation time given as,

$$T_p = \frac{(R_c) - D(n_a, n_b)}{s} \tag{12}$$

where n_a is current node, and n_b is the node which broadcasts the packet. The summation in the holding time equation provides the propagation delay for all the high priority nodes.

4.3 Inherently Void-Aware Routing (IVAR)

Inherently Void Avoidance Routing Protocol [20] uses equation (13) to schedule forwarding of the received packet.

$$T_{\text{hold}} = \frac{1}{2}(1 - \alpha)T_{\text{Delay}} + \frac{R - |\,\mathbf{SC}\,|}{v_{\text{sound}}} \tag{13}$$

where T_{Delay} is the predefined delay, α is the fitness factor, which is nothing but normalized depth difference between sender and receiver, and given in the Eq. (14), $|\,\mathbf{SC}\,|$ is the distance between sender and receiving candidate node, R communication range and v_{sound} is the speed of the sound in the water.

$$\alpha = \frac{D_s - D_r}{R},\ H_s > H_r, \alpha \in [-1, 1] \tag{14}$$

In Eq. (14), D_s and D_r are the depth of the sender and receiver, respectively.

Opportunistic void avoidance routing (OVAR) [15] is another routing protocol which uses the same equations (13) and (14).

Table 1 Comparison of various opportunistic underwater routing protocols

Protocol	Type	Parameters used in hold time computation	State
HydroCast	Sender-based	Progress from neighbor, distance between clustered nodes	Soft
GEDAR	Sender-based	Priority of neighbor	Soft
IVAR	Receiver-based	Progress, distance between sender and candidate node	Soft
DVOR	Receiver-based	Hop-count	Stateful

4.4 Distance-Vector Based Opportunistic Routing (DVOR)

Distance-Vector based Opportunistic Routing for Underwater Acoustic Sensor Networks [21], in this paper, the nodes have a waiting time that is used to solve the problem of multiple nodes receiving the packet and attempting to forward it. The waiting time is given as follows:

$$t = 2 * [N_i - n_p + 2]^+ * t_0 + \text{rand}(0, \text{CW}) * t_{\text{slot}} * [N_i - n_p + 2]^+ \tag{15}$$

where t_0 is the propagation time for the maximum transmission range, CW being the size of backoff window, unit time for backoff, and the $[.]^+$ is for max(.,0) meaning only positive values. The equation is divided into two parts: the first deals with different hop count in the link, and the second considers using a backoff mechanism to overcome forwarding nodes with the same hop count. Table 1 compares various underwater protocols in terms of type of the protocol in terms of sender or receiver-based, parameters used in the holding time computation , and state.

Remarks In this section, holding time computation methods for various opportunistic underwater routing protocols are discussed. Holding time is used to coordinate the data forwarding among multiple nodes of a cluster. Hold time is potential in suppression of transmission of duplicate packets. All the above-explained holding time computations require identifying the distance between the nodes in the cluster or identifying the hop-count. However, finding distance among nodes or hop-count of nodes increases the complexity of finding holding time. Thus, by considering maximum communication range or based on the priority of nodes, hold time can be computed.

5 Conclusion

In this paper, we discussed the usage of the TOPSIS in routing for wireless sensor networks and found that it has not been used to select the forwarding nodes in underwater networks. Further, elaborated about clustering approaches are used in

opportunistic underwater routing protocols. Existing clustering approaches require clustering of all neighboring nodes, which requires increases the computation complexity. This can be overcome by clustering only the required number of nodes. In last, we analyzed the holding time computations used in various opportunistic underwater routing protocols. Further, there is a scope to simplify hold time computation by eliminating the need to find the distance among nodes in the cluster.

Acknowledgements The authors thank the Science and Engineering Research Board (SERB), Govt. of India, for providing financial support (Ref. No. EEQ/2018/001036).

References

1. Sendra S, Lloret J, Jimenez JM, Parra L (2015) Underwater acoustic modems. IEEE Sensors J 16:4063–4071
2. Liou EC, Kao CC, Chang CH, Lin YS, Huang CJ (2018) Internet of underwater things: challenges and routing protocols. In: 2018 IEEE international conference on applied system invention (ICASI). IEEE, New York, pp 1171–1174
3. Khan A, Ali I, Ghani A, Khan N, Alsaqer M, Rahman AU, Mahmood H, Routing protocols for underwater wireless sensor networks: taxonomy, research challenges, routing strategies and future directions. Sensors 18:1619
4. Coutinho RW, Boukerche A, Vieira LF, Loureiro AA (2016) Design guidelines for opportunistic routing in underwater networks. IEEE Commun Maga 54:40–48
5. Luo J, Chen Y, Wu M, Yang Y (2021) A survey of routing protocols for underwater wireless sensor networks. IEEE Commun Surv Tutorials 23:137–160
6. Hwang CL, Yoon K (1981) Methods for multiple attribute decision making. Multiple attribute decision making. Springer, Berlin, pp 58–191
7. Khan BM, Bilal R, Young R (2018) Fuzzy-TOPSIS based cluster head selection in mobile wireless sensor networks. J Electr Syst Inform Technol, vol. 5. Elsevier, pp 928–943
8. Azad P, Sharma V (2013) Cluster head selection in wireless sensor networks under fuzzy environment. In: International scholarly research notices, vol 2013, Hindawi
9. Foubert B, Mitton N (2021) RODENT: a flexible TOPSIS based routing protocol for multi-technologies devices in wireless sensor networks. ITU J Future Evolv Technol
10. Jain B, Brar G, Malhotra J, Rani S (2017) A novel approach for smart cities in convergence to wireless sensor networks. Sustain Cities Soc 35:440–448
11. Singh SK, Kumar P, Multi-criteria decision-based path planning for data collection in fuzzy-cluster based large sensor networks. https://doi.org/10.21203/rs.3.rs-631721/v1
12. Noh Y, Lee U, Lee S, Wang P, Vieira LF, Cui JH, Kim K (2015) Hydrocast: pressure routing for underwater sensor networks. IEEE Trans Veh Technol 65:333–347
13. Coutinho RW, Boukerche A, Vieira LF, Loureiro A (2015) Geographic and opportunistic routing for underwater sensor networks. IEEE Trans Comput 65:548–561
14. Domingo MC (2008) Overview of channel models for underwater wireless communication networks. Phys Commun 1:163–182
15. Ghoreyshi SM, Shahrabi A, Boutaleb T (2016) A novel cooperative opportunistic routing scheme for underwater sensor networks. Sensors 16:297
16. Lee S, Bhattacharjee B, Banerjee S (2005) Efficient geographic routing in multihop wireless networks. In: Proceedings of the 6th ACM international symposium on Mobile ad hoc networking and computing. ACM, pp 230–241
17. Zeng K, Lou W, Yang J, Brown DRI (2007) On geographic collaborative forwarding in wireless ad hoc and sensor networks. In: International conference on wireless algorithms, systems and applications (WASA 2007). IEEE, New York, pp 11–18

18. Li X, Wang Y, Zhou J, An energy-efficient clustering algorithm for underwater acoustic sensor networks. In: 2012 International conference on control engineering and communication technology, pp 711–714
19. Alhazmi AS, Moustafa AI, Aldosari FM, Energy aware approach for underwater wireless sensor networks scheduling: UMOD_LEACH. In: 21st Saudi Computer Society national computer conference (NCC), pp 1–5
20. Ghoreyshi SM, Shahrabi A, Boutaleb T (2015) An inherently void avoidance routing protocol for underwater sensor networks. In: 2015 International symposium on wireless communication systems (ISWCS). IEEE, New York, pp 361–365
21. Guan Q, Ji F, Liu Y, Yu H, Chen W (2019) Distance-vector-based opportunistic routing for underwater acoustic sensor networks. IEEE Internet Things J 6:3831–3839

Noise Reduction Through Thresholding Process Over the Space of Orthogonal Polynomials

Parul Saini, L. K. Balyan, A. Kumar, and G. K. Singh

Abstract Generally, noise contamination occurs during the acquisition, transmission, and storage processes. Due to these noisy components, the approximated data suffer from the dynamic synthesis of oscillatory patterns that reduces the overall data quality. In this paper, a new discretization technique is employed over the orthogonal basis functions to suppress noise components from the corrupted signal. Also, the acceleration into the error decay rate is done by including a thresholding function into the spectral methods. The efficiency of proposed method is demonstrated in terms of exponential convergence, signal-to-noise ratio, percentage root mean square difference, mean square error, and maximum error.

Keywords Gibbs phenomenon · Filtering · Threshold function · Chebyshev collocation method

1 Introduction

The noise occurs into the data during the acquisition, transmission, and storage process. The noise components cause the dynamic rings of Gibbs phenomenon in resynthesizing process [1]. Mathematically, when a discontinuous function is approximated by series expansion, the approximation is affected by oscillatory patterns of Gibbs phenomenon [2]. Consequently, the actual information of input data is interrupted, and even increasing the resolution will have no impact on the enhancement of reconstructed data [2]. Therefore, the accuracy of reconstructed data is damaged in terms of non-uniform convergence [3]. To the author's best knowledge, first time,

P. Saini (✉) · L. K. Balyan · A. Kumar
PDPM-Indian Institute of Information Technology Design and Manufacturing, Jabalpur, Madhya Pradesh 482005, India
e-mail: iniaslurap1212@gmail.com

G. K. Singh
Department of Electrical Engineering, Indian Institute of Technology Roorkee, Roorkee 247667, India

S. Rawat et al. (eds.), *Proceedings of Second International Conference on Computational Electronics for Wireless Communications*, Lecture Notes in Networks and Systems 554,
https://doi.org/10.1007/978-981-19-6661-3_55

Wilbraham noticed this behavior in 1848 [4–6], and thereafter J. W. Gibbs noticed the same behavior in 1898 [5, 6]. In general, appearance of Gibbs phenomenon has been found in numerous problems in science and engineering field. However, over the past few decades, several techniques have been developed for the minimization of Gibbs phenomenon. In mathematics, the impact of oscillations has been reduced by using Legendre polynomials [7, 8], Chebyshev polynomials [8–12], and Fourier series approximation [12], cubic spline interpolation [13], Gegenbauer polynomial [14], radial basis functions [15, 16].

On the other hand, these oscillations have been reduced by denoising the corrupted signal using Fourier transform [1, 17, 18], wavelet transform in seismic exploration [19], initial condition excitation technique in time-domain spectral analysis [20], and fractional Fourier series [21] in signal processing. Moreover, these oscillations have also been dealt in oscilloscopes in radar processing [22] and wavelet in image processing [23]. In the study of magnetic resonance imaging (MRI), Gibbs phenomenon has been reduced by using Gegenbauer interpolation method in [24]. Also, appearance and restraining of Gibbs phenomenon can be seen in stability and vibration of complex beams study by Fourier series expansion [25], in physics optics by discontinuous basis functions [26] and many more.

The key contribution of this work is to use thresholding procedure in conjunction with spectral methods to reduce the noise particles. The expansion of spectral methods has been employed to discretize the data in terms of Chebyshev polynomials with proposed filter function and threshold function. The proposed method is comprised of new developed filter function, which has already been discussed by authors in the previous work using hard and soft threshold functions [27]. In this work, authors present a threshold filtered Chebyshev collocation method (TFCCM), based on a different threshold function discussed in [19]. Chebyshev spectral method has been widely used because of its simple implementation and low computational cost.

Spectral methods are highly accurate and achieve spectral convergence provided functions are sufficiently smooth. However, the method's performance is not up to the mark for irregular functions because these functions may contain discontinuities or sharp gradients in the source data. Therefore, approximation tends to be smeared by Gibbs oscillations. Due to these reasons, smoothing process has been implemented. In this work, filter function has been considered as a smoothing factor in order to suppress the dynamic synthesis of oscillatory patterns and accelerates the convergence rate of approximation series of discontinuous functions as well as noisy signals. Also, TFCCM is comprised of thresholding process and filtered approximation over Chebyshev polynomials. Second process of thresholding strategy is introduced, which is a novel concept in spectral methods. The key idea behind thresholding is an adaptive selection of approximation coefficients for resynthesizing of signal. The performance evaluation has been demonstrated through numerical analysis. The input signal has been corrupted by additive white Gaussian noise first, and then, the technique has been employed on the corrupted signal. The reconstructed signal has shown the efficiency of proposed technique. Furthermore, numerical analysis has been done in terms of signal-to-noise ratio (SNR), percentage root mean square difference (PRD), mean square error (MSE), and maximum error (ME) [28, 29].

The rest of the paper is organized as follows: In Sect. 2, mathematical background associated with Chebyshev spectral method and proposed filter function has been explained. In Sect. 3, thresholding process with adaptive choice of threshold parameter is discussed. Numerical analysis has been done in Sect. 4. Final concluding remarks are given in Sect. 5.

2 Introduced Methodology

In this section, formulation of the proposed method has been described with approximation series and resolution error estimate. The following procedure facilitates the formulation of interpolated series over the space of Chebyshev polynomials with finite resolution limit N.

2.1 Formulation of Approximation Procedure

The Chebyshev polynomials are given as [30, 31]:

$$\Psi_\nu(\xi_j) = \cos(\nu \cos^{-1} \xi_j), \tag{1}$$

where $\nu = 0, 1, 2, ...$, with ξ_j's Gauss–Lobatto grid nodes:

$$\xi_j = -\cos\left(\frac{\pi j}{N}\right), \qquad j = 0, 1, ..., N. \tag{2}$$

Defining interpolation operator $\mathfrak{I}_N$, the interpolating polynomial of $u(\xi)$ is expressed in the following way [30, 31]:

$$\mathfrak{I}_N u_N(\xi) = \sum_{\nu=0}^{N} \hat{u}_\nu \, \Psi_\nu(\xi), \tag{3}$$

where the expansion coefficients are defined as:

$$\hat{u}_\nu = \frac{1}{\beta_\nu^d} \sum_{j=0}^{N} u(\xi_j) \, \Psi_\nu(\xi_j) w(\xi_j). \tag{4}$$

and the normalization constant is given in terms of resolution:

$$\beta_\nu^d = \begin{cases} \pi, & \text{if } \nu = 0, N, \\ \frac{\pi}{2}, & \text{if } \nu \in [1, 2, ..., N-1]. \end{cases} \tag{5}$$

The discrete closed form of corresponding weight function $w_j = w(\xi_j)$, is explicitly given as:

$$w_j = \begin{cases} \frac{\pi}{2N}, & \text{if } j = 0, N, \\ \frac{\pi}{N}, & \text{if } j \in [1, 2, ..., N-1]. \end{cases} \tag{6}$$

For an analytical function, Chebyshev interpolation error can be obtained as [30–32]:

$$\|\mathfrak{I}_N u_N(\xi) - u(\xi)\|_{L^2_w(\Omega)} \leq \frac{A}{N^p} \|u^p\|_{L^2_w(\Omega)}, \tag{7}$$

where $L^2_w(\Omega)$ is a space of integrable function under Chebyshev weight function [31], and A is a constant value. The term u^p denotes the pth derivative of u function.

2.2 Filtering Process

Filter function smooths out the high-frequency oscillations of Gibbs phenomenon. Filter function $\rho(\varsigma)$ is a real and even function of order p with $(p > 1)$, which satisfies the following axioms [7, 30]:

$$\begin{cases} \rho(0) = 1, \rho(\varsigma) = 0, \text{ for } |\varsigma| > 1, \varsigma = 1, \\ \rho^n(\varsigma) = 0, \text{ with } \varsigma = 0, 1, \forall n \in [1, 2, ..., p-1]. \end{cases}$$

Using filter function, the approximated finite sum can be further modified as:

$$\mathfrak{I}_N u_N^{\rho}(\xi) = \sum_{\nu=0}^{N} \rho\left(\frac{\nu}{N}\right) \hat{u}_\nu \cos(\nu \cos^{-1} \xi). \tag{8}$$

Introducing new filter function:

- Proposed filter function [27]

$$\rho(\varsigma) = \frac{3}{8}(\kappa_0 + \kappa_1 \cos(\pi\varsigma) + \kappa_2 \cos(2\pi\varsigma)), \tag{9}$$

where $\kappa_0 = 1$, $\kappa_1 = \frac{4}{3}, \kappa_2 = \frac{1}{3}$.

For smooth problems, it guaranties the preservation of convergence [7]. On the other hand, in case of non-smooth problems, filter function confirms the closeness of filtered series expansion to original function. But, if noise is introduced in continuous signal, performance of the filtered Chebyshev spectral method becomes unstable. Therefore, a factor must be introduced to remove the un-stability of numerical procedure.

3 Thresholding Process

In this section, a thresholding process is presented. In general, hard and soft thresholding functions are frequently used thresholds in signal processing to control the patterns of Gibbs artifacts, which had been proposed by Donoho et al. [33]. Here, a threshold function has been discussed that was proposed by Zhang et al. in [19]. The expression of threshold function is given as:

$$\hat{u}_i^T = \begin{cases} \text{sign}(\hat{u}_i)\left(|\hat{u}_i| - \frac{\alpha\lambda}{\alpha + \sqrt{|\hat{u}_i|^2 - \lambda^2}}\right), & |\hat{u}_i| \geq \lambda, \\ 0, & |\hat{u}_i| < \lambda, \end{cases} \tag{10}$$

where $\hat{u}_i$, λ, and α are the expansion coefficients, threshold parameter, and limiting parameter, respectively. The $\hat{u}_i^T$'s are the refined expansion coefficients. The threshold is designed in such a manner that the function approaches to soft threshold function as $\alpha \to \infty$ and approaches to hard threshold as $\alpha \to 0$. The main concept behind thresholding process is to pass only those components that have high absolute value than a specific threshold parameter. Extraction of true coefficients is dependent on the threshold value that leads to reconstruction of signal. Therefore, an appropriate selection of threshold value λ must be obtained in such a manner that it can maximize the accuracy of reconstructed signal. In this work, the value of threshold parameter has been taken empirically.

After introducing threshold function, Eq. (8) can be further modified as:

$$\mathfrak{I}_N u_N^{T\rho}(\xi) = \sum_{\nu=0}^{N} \rho\left(\frac{\nu}{N}\right) \hat{u}_\nu^T \cos(\nu \cos^{-1} \xi), \tag{11}$$

where $\hat{u}_\nu^T$'s are the refined expansion coefficients after thresholding, ρ is a filter function.

4 Numerical Analysis

In this section, TFCCM has been employed on a noisy signal to eliminate high-order frequency component in the approximation series.

4.1 Illustration

Illustration 1 A corrupted signal is considered as:

$$y(t) = \cos(2\pi f_1 t) + \sin(2\pi f_2 t) + \text{noise} \tag{12}$$

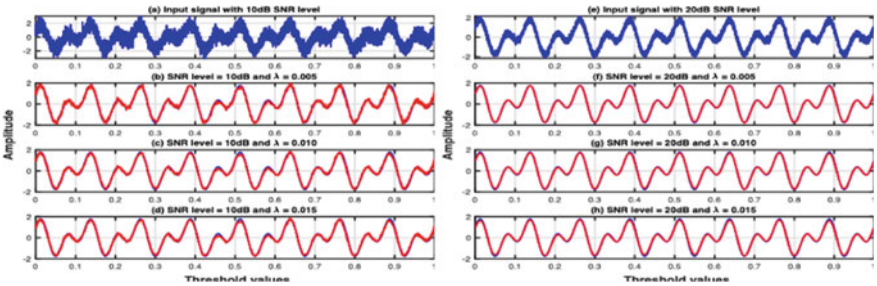

Fig. 1 In noisy rows, blue color shows noise-corrupted signal Eq. (12). In reconstruction rows, blue color represents original signal, and red color displays proposed reconstruction

In this illustration, t is time, and additive white Gaussian noise is added to a continuous signal with zero mean and variance σ^2. The noise is considered at 10 and 20 dB input SNR level. Statistical distribution has been used to extract the Gaussian noise, which has normal distribution as its probability density function. The power spectral density is a constant function with σ^2 height over the entire region. The frequencies f_1 and f_2 have been taken 8 Hz, 16 Hz, respectively.

TFCCM algorithm has been employed to eliminate the noise component using aforementioned threshold function in Eq. (10). The output data are depicted at three different threshold values of λ such as: 0.005, 0.010, and 0.015 with two different SNR levels: 10 and 20 dB. The input signal has been approximated using resolution limit $N = 2^{11}$, which can be seen in Fig. 1. Graphs (a) and (e) (noisy rows) show the corrupted signals with 10 dB and 20 dB SNR level, respectively, while other graphs (b)–(d), (f)–(h) (reconstruction rows) show reconstructed signal. From these graphs, one can see out performance of the proposed method. Apart from this, performance parameters also show the efficiency of proposed method that can be seen in Table 1 for 10 dB SNR level and in Table 2 for 20 dB SNR level. In these tables, nine threshold values have been taken for numerical analysis.

4.2 Comparison Analysis

This section demonstrates a comparison analysis using numerical simulations and estimator parameters. The results of existing Chebyshev collocation (CCM) and filtered Chebyshev collocation method (FCCM) have been used to analyze the efficiency of proposed method. The output results of CCM and FCCM are depicted in Figs. 2 and 3, respectively. In addition, the estimator parameters are shown in Tables 3 and 4, which compares CCM, FCCM, and TFCCM. It is clear that the performance of CCM and FCCM is inferior to the proposed method.

Table 1 Evaluation parameters for 10 dB SNR level

Parameter	λ_i	SNR	PRD	MSE	ME
$m_1 = 5$	0.005	18.9548	11.2847	1.4592e−02	0.3925
	0.010	19.1404	11.0495	1.4099e−02	0.3734
	0.015	20.2041	9.7901	1.0967e−02	0.3372
	0.020	22.3435	7.6668	6.6168e−03	0.3150
	0.025	23.6206	6.6236	4.2721e−03	0.2692
	0.030	**25.1319**	**5.5694**	3.4353e−03	0.1979
	0.035	24.8382	5.7643	3.1450e−03	**0.1779**
	0.040	23.8360	6.4744	**3.0546e−03**	0.2036
	0.045	23.8360	6.4744	3.6855e−03	0.2036
$m_1 = 10$	0.005	19.1281	11.2469	1.2185e−02	0.3663
	0.010	19.2978	11.0319	1.1770e−02	0.3788
	0.015	20.2965	9.8468	9.0350e−03	0.3376
	0.020	21.6009	8.4843	6.7085e−03	0.2596
	0.025	23.3228	6.9669	3.5791e−03	0.1999
	0.030	24.6197	6.0044	2.1029e−03	0.1815
	0.035	**25.0157**	**5.7377**	2.0888e−03	**0.1564**
	0.040	24.4867	6.1017	**1.9515e−03**	0.1722
	0.045	24.4867	6.1017	3.1286e−03	0.1722

Table 2 Evaluation parameters for 20 dB SNR level

Parameter	λ_i	SNR	PRD	MSE	ME
$m_1 = 5$	0.005	31.4476	2.7240	7.7141e−04	0.0900
	0.010	**31.7335**	**2.6359**	**7.2336e−04**	**0.0750**
	0.015	31.1477	2.8201	8.5848e−04	0.0794
	0.020	31.1477	2.8201	8.5848e−04	0.0794
	0.025	31.1477	2.8201	8.5848e−04	0.0794
	0.030	29.2202	3.5220	1.2729e−03	0.0942
	0.035	29.2202	3.5220	1.2729e−03	0.0942
	0.040	29.2202	3.5220	1.2729e−03	0.0942
	0.045	26.4924	4.8260	2.3265e−03	0.1333
$m_1 = 10$	0.005	32.1120	2.5186	6.1500e−04	0.0793
	0.010	32.5110	2.4054	5.6092e−04	0.0651
	0.015	**32.5220**	**2.4023**	**5.5950e−04**	**0.0636**
	0.020	31.5570	2.6852	6.9886e−04	0.0757
	0.025	29.6370	3.3503	1.0873e−03	0.0875
	0.030	29.6370	3.3503	1.0873e−03	0.0875
	0.035	29.6370	3.3503	1.0873e−03	0.0875
	0.040	29.6370	3.3503	1.0873e−03	0.0875
	0.045	26.5900	4.7621	2.1931e−03	0.1224

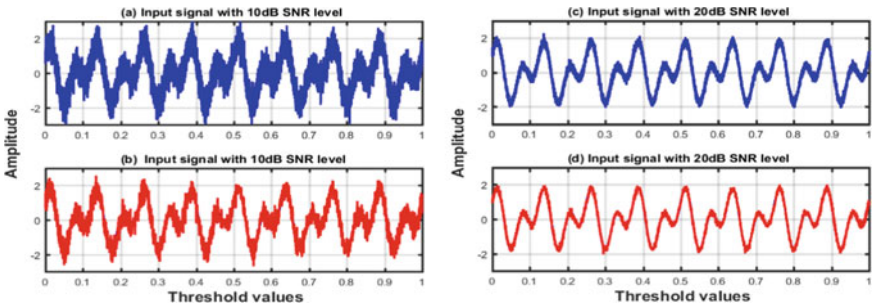

Fig. 2 **a**, **c** Shows the noisy signal. **b**, **d** Shows output results of CCM

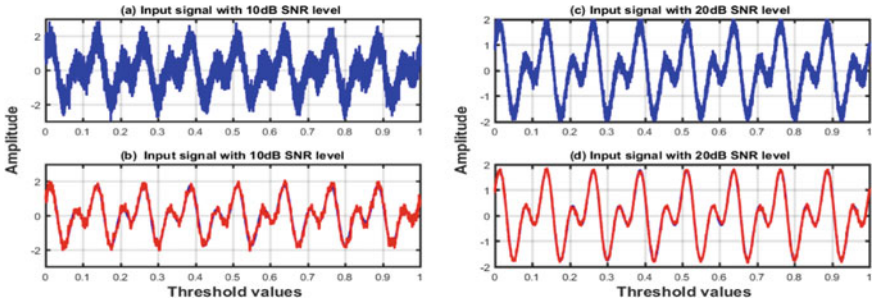

Fig. 3 **a**, **c** Shows the noisy signal. **b**, **d** Shows output results of FCCM

Table 3 Comparison of evaluation parameters for 10 dB SNR level

Parameter		SNR	PRD	MSE	ME
TFCCM	$m_1 = 5$	25.1319	5.5694	3.4353e−03	0.1979
	$m_1 = 10$	25.0157	5.7377	2.0888e−03	0.1564
FCCM		15.5561	16.4717	2.7801e−02	0.6147
CCM		10.0564	30.0513	9.8770e−02	1.565

Table 4 Comparison of evaluation parameters for 20 dB SNR level

Parameter		SNR	PRD	MSE	ME
TFCCM	$m_1 = 5$	31.7335	2.6359	7.2336e−04	0.0750
	$m_1 = 10$	32.5220	2.4023	5.5950e−04	0.0636
FCCM		25.7633	5.1428	2.7901e−03	0.2121
CCM		19.6204	10.4379	1.0927e−02	0.3792

Indeed, the proposed technique works effectively on the noisy signals using thresholding procedure in the spectral methods. All the implementation of proposed work has been done on MATLAB.

5 Conclusion

The key contribution of this work is the integration of threshold function into spectral methods to enhance the quality of reconstructed signal by reducing the Gibbs phenomenon. The discretization method was used that is based on a filtering process, in which the expansion coefficients are refined by thresholding. In the course of action, a new proposed filter function is utilized for filtering process. One of the main advantage of this method is the recovery of global spectral accuracy. In future, work with the real-time denoising problems will be carried out.

References

1. Pan C (2001) Gibbs phenomenon removal and digital filtering directly through the fast Fourier transform. IEEE Trans Sign Process 49(2):444–448
2. Hewitt E, Hewitt RE (1979) The Gibbs-Wilbraham phenomenon: an episode in Fourier analysis. Archive History Exact Sci 21(2):129–160
3. Lin CC, Segel LA (1988) Mathematics applied to deterministic problems in the natural sciences, classics in applied mathematics, vol I. SIAM, Philadelphia, pp 138–143
4. Wilbraham H (1848) On a certain periodic function. Cambridge Dublin Math J 3:198–201
5. Ustina F (1974) Henry Wilbraham and Gibbs phenomenon in 1848. Historia Math 1(1):83–84
6. Jerri AJ (1998) The Gibbs phenomenon in Fourier analysis. Splines and Wavelet Approximations
7. Hesthaven J, Kirby R (2008) Filtering in Legendre spectral methods. Math Comput 77(263):1425–1452
8. Saini P, Balyan LK, Kumar A, Singh GK (2022) Comparative analysis of post-processing on spectral collocation methods for non-smooth functions. SIViP
9. Occorsio D, Themistoclakis W. Some remarks on filtered polynomial interpolation at Chebyshev nodes. arXiv preprint arXiv:2101.04551. 2021 Jan 12
10. Ray S, Saha S (2020) A reconstruction-base Chebyshev-collocation method for the Poisson equation: an accurate treatment of the Gibbs-Wilbraham phenomenon on irregular interfaces. J Comput Phys 1(418):109559
11. De Bonis MC, Occorsio D, Themistoclakis W (2021) Filtered interpolation for solving Prandtl's Integro-differential equations. Numer Algorithms 88(2):679–709
12. Gottlieb D, Hestaven JS (2001) Spectral methods for hyperbolic problems. J Comput Appl Mathematics 128:83–131
13. Zhang Z, Martin CF (1997) Convergence and Gibbs' phenomenon in cubic spline interpolation of discontinuous functions. J Comput Appl Math 87(2):359–371
14. Gottlieb D, Shu CW, Solononoff A, Vandeven H (1992) On the Gibbs phenomenon I: recovering exponential accuracy from the Fourier partial sum of a non-periodic analytical function. J Comput Appl Math 43:81–98
15. Jung JH, Gottlieb S, Kim SO, Bresten CL, Higgs D, Recovery of high order accuracy in radial basis function approximations of discontinuous problems. J Sci Comput 45(1):359–381

16. De Marchi S (2020) Mapped polynomials and discontinuous kernels for Runge and Gibbs phenomena
17. Proakis JG, Manolakis DG (1988) Introduction to digital signal processing. Macmillan Publishing Company, New York, pp 551–559
18. Occorsio D, Themistoclakis W, Uniform weighted approximation by multivariate filtered polynomials. In: International conference on numerical computations: theory and algorithms 2019 Jun 15. Springer, Cham, pp 86–100
19. Zhang QS, Jiang JJ, Zhai JH, Zhang XY, Yuan YJ, Huang XW (2016) Seismic random noise attenuation using modified wavelet thresholding. Ann Geophys 59(6):S0647
20. Li Q, Chen Y (2000) Pseudo-spectral time-domain analysis using an initial-condition excitation technique for elimination of Gibbs phenomenon. Chin J Electron 9(1):92–95
21. Zhu H, Ding M, Li Y, Gibbs phenomenon for fractional Fourier series. IET Sign Process 5(8):728–738
22. Körner TW (1989) Fourier analysis. Cambridge University Press, Cambridge, pp 62–66
23. Chang SG, Yu B, Vetterli M (2000) Adaptive wavelet thresholding for image denoising and compression. IEEE Trans Image Process 9(9):1532–1546
24. Archibald R, Gelb A (2002) A method to reduce the Gibbs ringing artifact in MRI scans while keeping tissue boundary integrity. IEEE Trans Med Imaging 21(4):305–319
25. Fan SC, Zheng DY, Au FTK (2001) Gibbs-phenomenon-free Fourier series for vibration and stability of complex beams. AIAA J 39(10):1977–1984
26. Chen PY, Sivan Y (2021) Resolving the Gibbs phenomenon via a discontinuous basis in a mode solver for open optical systems. J Comput Phys 15(429):110004
27. Saini P, Balyan LK, Kumar A, Singh GK (2022) Modification of Chebyshev Pseudospectral method to minimize the Gibbs oscillatory behaviour in resynthesizing process. Circuits, Systems, and Signal Processing 41(11):6238–6265
28. Kumar A, Singh GK, Anand RS (2011) A simple design method for the cosine-modulated filter banks using weighted constrained least square technique. J Franklin Inst 348(4):606–621
29. Balyan LK, Dutt P, Rathore RKS (2012) Least squares h-p spectral element methods for elliptic eigenvalue problems. Appl Math Comp 218(19):9596–9613
30. Hesthaven JS, Gottlieb S, Gottlieb D (2007) Spectral methods for time-dependent problems, vol 21. Cambridge University Press, Cambridge
31. Canuto C, Hussaini MY, Quarteroni A, Zang TA (1988) Spectral methods in fluid dynamics. Springer, New York, p 162
32. Tadmor E (1986) The exponential accuracy of Fourier and Chebyshev differencing methods. SIAM J Numer Anal 23:1–10
33. Donoho DL, Johnstone IM (1995) Adapting to unknown smoothness via wavelet shrinkage. J Am Stat Assoc 90(432):1200–1224

BER Performance Analysis of Optical Wireless Communication System over Weak and Strong Underwater Turbulence Channels

Ramavath Prasad Naik, U. Shripathi Acharya, L. Bhargava Kumar, Prabu Krishnan, and Wan Young Chung

Abstract In this paper, we have investigated the performance of an underwater wireless optical communication (UWOC) link employing single-input and single-output (SISO) and selection combining (SC) as receiver diversity for varying link-ranges. As the the link-range increases, then strength of turbulence between the underwater optical entities also increases. It is assumed that the distribution of light propagation in weak and strong turbulence UWOC channel as log-normal (LN) and gamma-gamma (GG) density functions, respectively. The analytical bit error rate (BER) equations of on–off keying modulated UWOC link have been derived for SISO and SC receiver diversity using hyperbolic tangent distribution for LN and power series for GG density functions. The analytical BER results are validated with the Monte Carlo simulations.

Keywords Underwater wireless optical communication · Log-normal distribution function · Gamma-Gamma distribution function · Selection combining

1 Introduction

About 71% of the earth is covered with water, in that, around 97% of water holds by the oceans. So, a lot of ventures present in the oceans. Monitoring such conditions is challenging due to harsh channel conditions. The construction of different forms

R. P. Naik
Research Institute of Artificial Intelligence Convergence, Pukyong National University, Daeyeon 3-dong, Nam-gu, Busan 48513, Republic of Korea

U. S. Acharya · L. Bhargava Kumar · P. Krishnan
Department of Electronics and Communication Engineering, National Institute of Technology Karnataka, Surathkal, Karnataka 575025, India

W. Y. Chung (✉)
Department of Electronic Engineering, Pukyong National University, Daeyeon 3-dong, Nam-gu, Busan 48513, Republic of Korea
e-mail: wychung@pknu.ac.kr
URL: http://aiotlab.pknu.ac.kr/01/01.php

S. Rawat et al. (eds.), *Proceedings of Second International Conference on Computational Electronics for Wireless Communications*, Lecture Notes in Networks and Systems 554,
https://doi.org/10.1007/978-981-19-6661-3_56

of AUVs, such as underwater robots and underwater sensor networks to monitor the marine surfaces, has been the focus of recent study. The monitoring tools have grown to include human-occupied submersibles, remote-controlled vehicles, autonomous, and towed robots. AUVs with high-speed communication mechanisms can identify any unnatural things occurring inside oceans and convey information to the related centers to prevent from any unnatural stuff happens.

Exploring, utilizing, and monitoring such powerful resources for underwater wireless optical communication (UWOC) applications are demanding one in this 21st century. Recently, the amount of human activity in the aquatic environment has significantly grown. The data rate and bandwidth of RF and acoustic underwater communication methods are restricted. UWOC, on the other hand, has several benefits, including a high bandwidth and transmission capacity, unlicensed visible spectrum, ease of installation, low latency and energy consumption, and high data transmission speed. As a result, UWOC piques the research community's curiosity and emerges as a feasible alternative potential key-enabling technology [1]. The UWOC adopted in various potential applications such as underwater scientific data collection, communications between submarines and with off-shore ships, marine archeology, environmental monitoring of mineral stores, fish tracing, port security, and tactical surveillance [2].

Despite the various advantages of UWOC over RF and acoustic communications, establishing a UWOC link is difficult owing to the larger level of beam attenuation in underwater channels. The amount of attenuation varies depending on the wavelength of the LASER source. When compared to other wavelength sources, LASER sources with wavelength ranges of 450–530 nm have the least degree of attenuation in an underwater environment [3]. The scintillation index changes due to changes in salt and temperature in ocean environment, which drastically affects the operation of UWOC link. The fluctuation of the scintillation index with temperature, salinity, and other conditions as stated in [4]. Oubei et al. [5] describe an experimental examination of the distribution of irradiance fluctuations with turbulence, air bubbles, temperature, and salinity. The log-normal (LN) density function [6] and the gamma-gamma (GG) density function [7] are used to fit the distribution of received intensity (irradiance) across mild turbulence. Optical beam fluctuation can be caused by unpredictable motions of the marine surface, which impairs system performance. Optical amplification, MIMO, transmit/receiver diversity, coding scheme, relaying, and efficient modulation techniques, among others, are well-known mitigation strategies [8–10].

In this paper, we have investigated the simulation and analytical bit error rate (BER) performance of an on–off keying (OOK) modulated UWOC system under weak turbulence and strong turbulence crises for link-ranges $L = 250$ and 400 m at a transmission speed of 500 Mbps. The variation in link-range changes the strength of turbulence between the source and destination [4]. The strength of turbulence (scintillation index) for varying link-ranges 250 and 400 m link-ranges are given in Sect. 3, which shows weak for $L = 250$ m and strong $L = 400$ m, respectively. BER of simulation and analytical single-input single-output (SISO) UWOC system under weak and strong turbulence obtained. Presence of turbulence can fluctuate the optical

strength from higher into lower intensities, which causes errors in the transmitted data; to mitigate the turbulence-induced errors, we have used M number PD's at the receiver. The PD with the maximum received intensity among all PD's received intensity will be considered as less affected turbulent path (selection combining), and this intensity further used to estimate of transmitted data. The gain in transmit power from SISO to SC ($M = 2, 3, 4$) scheme at BER of 10^{-5} is used to determine the performance improvement. Under weak and strong turbulence crises, we were able to establish closed-form analytical equations for the SISO and SC UWOC systems.

2 System Model

Assume that the binary data are communicated to the LASER source with P_t watts of power for binary '1' and 0 W of power for binary '0' for a time of T_b s. The average power for equiprobable 1's and 0's is $P_t/2$. Data obtained at photo-detector (PD) when OOK modulated data transmitted by LASER source is,

$$Y = \eta\sqrt{P_t T_b} s\, I + n \tag{1}$$

where η is PD responsivity (A/W), P_t is transmit power per bit (mW), $s \in (0,\ 1)$ is transmitted data, I is received irradiance and n is additive Gaussian noise with zero mean and σ^2 variance. Here, we have considered thermal noise is the source of noise (variance due to shot noise and background noise are negligible compared with the thermal noise variance), so the noise variance is $\sigma^2 = 4K_b T_e B/R_L$, K_b is Boltzmann's constant, T_e receiver temperature and it is measured as 256 K, load resistor of detector $R_L = 100\ \Omega$ and B is electrical bandwidth.

3 Channel Model

Optical signal can be distorted due to the presence of underwater turbulence. These turbulence are categorized as weak, moderate, and strong based on the strength of turbulence present in the medium. Strength of turbulence characterized with the Scintillation Index (SI, known as channel variance σ_I^2), for weak turbulence $\sigma_I^2 < 1$ and > 1 for strong turbulence. Expression for the SI is given as [4],

$$\sigma_I^2 = 8\pi^2 k^2 L \int_0^1 \int_0^\infty \mathcal{K}\Phi_n(\mathcal{K}) \left(1 - \cos\left(\frac{L\xi\mathcal{K}^2}{k}\right)\right) \mathrm{d}\mathcal{K}\mathrm{d}\xi \tag{2}$$

where $k = 2\pi/\lambda$ is wave-number, source wavelength is λ, Eq. (3) represents oceanic turbulent power spectrum, where ϵ turbulence kinetic energy dissipation rate, χ_t dissipation rate temperature and salinity, ξ length of Kolmogorov micro-cell, and rel-

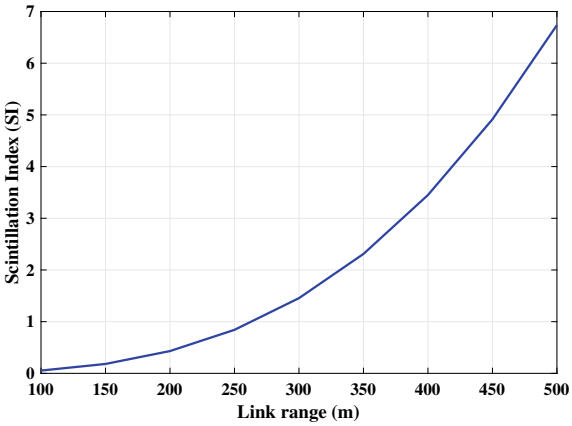

Fig. 1 SI variation with respect to Link-range

ative variable temperature-salinity parameter fluctuation with regard to ocean depth is referred to as *omega*. The parameters A_T, A_S, A_{TS} and δ are considered same as mentioned in [11].

$$\Phi_n(\mathcal{K}) = \frac{0.388 \times 10^{-8} \epsilon^{-1/3} \mathcal{K}^{-11/3} \chi_T}{\omega^2} \left[1 + 2.35(\mathcal{K}\xi)^{2/3}\right] \left(\omega^2 e^{-A_T \delta} + e^{-A_S \delta} - 2\omega e^{-A_{TS} \delta}\right) \quad (3)$$

The scintillation Index (SI) for varying link-range is shown in Fig. 1. SI values for link-range 250 and 400 m links are 0.85 (weak) and 3.50 (strong), respectively. Underwater weak and strong turbulence are model with LN and GG density functions, respectively.

3.1 Weak Underwater Turbulence

The LN probability density function (PDF) characterized by underwater weak turbulence channel model is given as [12],

$$f_I^l(I) = \frac{1}{2I\sqrt{2\pi\sigma_X^2}} \exp\left(-\frac{(\ln(I) - 2\mu_X)^2}{8\sigma_X^2}\right), \quad I \geq 0 \quad (4)$$

where I is received irradiance, μ_X and σ_X^2 are mean and variance of Gaussian distributed random variable $X = 0.5 \ln I$. nth moment of Eq. (4) is $\mathbb{E}(I^n) = \exp\left(2n\mu_X + 2\sigma_X^2 n^2\right)$. $\mathbb{E}(I) = 1$ to obtain normalize PDF given in Eq. (4), which leads $\mu_X = -\sigma_X^2$. SI is depended on the log-amplitude Gaussian variance σ_X^2 and is given as, $\sigma_I^2 = \exp(4\sigma_X^2) - 1$.

3.2 Strong Underwater Turbulence

The PDF characterized by strong turbulence with GG density function is given as,

$$f_I^g(I) = \frac{2(ab)^{(a+b)/2}}{\Gamma(a)\Gamma(b)} I^{\frac{a+b}{2}-1} K_{a-b}\left(2\sqrt{abI}\right), \quad I \geq 0 \tag{5}$$

where a and b are large and small scale turbulence eddies, $K_{a-b}(\cdot)$ is modified Bessel function of the second type of order $(a-b)$, and its representation in power series is as follows [13],

$$K_{a-b}(2\sqrt{abI}) = \frac{\pi}{2\sin(\pi(a-b))} \sum_{j=0}^{\infty} \left(C_{j,I}^{(a,b)} - C_{j,I}^{(b,a)}\right) \tag{6}$$

where $C_{j,I}^{(a,b)} = \frac{(abI)^{\frac{(2j-a+b)}{2}}}{\Gamma(j-a+b+1)j!}$. Substituting Eq. (6) in Eq. (5) yields as,

$$f_I^g(I) = C \sum_{j=0}^{\infty} \left(C_j^{(a,b)} I^{j+b-1} - C_j^{(b,a)} I^{j+a-1}\right) \tag{7}$$

where $C = \frac{(ab)^{(a+b)/2}}{\Gamma(a)\Gamma(b)} \frac{\pi}{\sin(\pi(a-b))}$. The nth moment is $\mathbb{E}(I^n) = \frac{\Gamma(a+n)\Gamma(b+n)}{\Gamma(a)\Gamma(b)}(ab)^{-n}$. The SI given as, $\sigma_I^2 = 1/a + 1/b + 1/(ab)$.

4 Analytical BER Evaluation

Analytical BER equations for OOK modulated SISO and SC schemes are evaluated in this section. For ease of computation, we have considered $\mathbb{Q}(x) \approx 1/12\exp(-x^2/2) + 1/4\exp(-2x^2/3)$ from [14].

4.1 SISO Link

Let $\mathscr{P}_0$ is probability of estimated data when $s = 0$, i.e., $\mathscr{P}_0 = P\left(\hat{s}/s = 0\right)$ and $\mathscr{P}_1$ is probability of estimated data when $s = 1$, i.e., $\mathscr{P}_1 = P\left(\hat{s}/s = 1\right)$, where estimated data $\hat{s} = \mathbb{E}(Y) = \eta I\sqrt{P_t T_b}[\mathbb{E}(s)]$. Probability of error associated with OOK modulated SISO for equiprobable bits is,

$$P_S = \frac{1}{2}\int_0^{\infty}\left(\sum_{i=0}^{1} P\left(\frac{\hat{s} = 1-i}{s = i, I}\right)\right) f_I(I)\mathrm{d}I \tag{8}$$

where $P(\hat{s} = 1/s = 0)$ Gaussian PDF with mean 0 and variance σ^2 and $P(\hat{s} = 0/s = 1)$ also Gaussian PDF with mean $\eta I\sqrt{P_t T_b}$ and variance σ^2, respectively. Integrating Eq. (8) with the threshold $T = \left(\mathbb{E}(Y)\Big|_{s=0} + \mathbb{E}(Y)\Big|_{s=1}\right)\Big/2 = \eta I\sqrt{P_t T_b}/2$, leads the BER of SISO as,

$$P_S = \int_0^\infty \mathbb{Q}\left(\zeta I\right) f_I(I)\mathrm{d}I \tag{9}$$

where $f_I(I)$ is LN/GG PDF for weak/strong turbulence conditions, respectively, and $\mathbb{Q}(x) \triangleq (1/\sqrt{2\pi})\int_x^\infty \exp(-y^2/2)\mathrm{d}y$ and $\zeta = \eta\sqrt{\frac{P_t T_b}{4\sigma^2}}$.

Weak turbulence: BER of SISO for weak turbulence can be modified as,

$$P_S^w = \int_0^\infty \mathbb{Q}\left(\zeta I\right) \frac{\exp\left(-\frac{(\ln I - 2\mu_X)^2}{8\sigma_X^2}\right)}{2I\sqrt{2\pi\sigma_X^2}}\mathrm{d}I \tag{10}$$

Exact solution to Eq. (10) does not exist. Closed-form solutions can be obtained by use of Gauss–Hermite quadrature [15] and power series method proposed in [16]. For ease of computation in this paper, LN PDF modified into algebraic form using the hyperbolic tangent distribution (HTD) family. The LN PDF using HTD is given by,

$$f_I^l(I) \approx \frac{b\exp(2a)I^{b-1}}{\left(1+\exp\left(2a\right)I^b\right)^2} \tag{11}$$

A detail information about LN PDF obtained using HTD is given in [17, 18]. Substituting Eq. (11) in Eq. (10) and then Q-function is approximation is used to compute Eq. (11) from is $\left(\text{i.e., } \mathbb{Q}(x) \approx 1/12\exp(-x^2/2) + 1/4\exp(-2x^2/3)\right)$, which yields as,

$$P_s^w \approx b\exp(2a)\left(\frac{\mathscr{T}_1}{12} + \frac{\mathscr{T}_2}{4}\right) \tag{12}$$

where $\mathscr{T}_1 = \int_0^\infty I^{b-1}\exp(-\frac{\zeta^2 I^2}{2})\left(1 + I^b\exp(2a)\right)^{-2} dI$ and $\mathscr{T}_2 = \int_0^\infty I^{b-1}\exp(-\frac{2\zeta^2 I^2}{3})\left(1 + I^b\exp(2a)\right)^{-2} dI$, which are evaluated, by substitute $\frac{\zeta^2 I^2}{2}$ with t_1 in $\mathscr{T}_1$ and $\frac{2\zeta^2 I^2}{3}$ as t_2 in $\mathscr{T}_2$ then computed using Eq. (21) of [19] as,

$$P = \left(\frac{b}{2\pi}\right)^{\frac{b+1}{2}}\exp(2a)\left[\frac{\mathscr{C}_1}{12} + \frac{\mathscr{C}_2}{4}\right] \tag{13}$$

where $\mathscr{C}_1 = 2\left(\frac{\sqrt{2}}{\zeta}\right)^b G_{2+b,2}^{2,2+b}\left(\begin{matrix}-\frac{1}{2}, 0\frac{t-\frac{b}{2}}{b} \\ 0, \frac{1}{2}\end{matrix}\Big| b^b\mathscr{P}_1^2\right), i = 1, 2, \ldots, b;\ \mathscr{P}_1 = \exp(2a)\left(\frac{\sqrt{2}}{\zeta}\right)^b, \mathscr{C}_2 = 2\left(\sqrt{\frac{3}{2\zeta^2}}\right)^b G_{2+b,2}^{2,2+b}\left(\begin{matrix}-\frac{1}{2}, 0\frac{t-\frac{b}{2}}{b} \\ 0, \frac{1}{2}\end{matrix}\Big| b^b\mathscr{P}_2^2\right), \mathscr{P}_2 = \exp(2a)\left(\sqrt{\frac{3}{2\zeta^2}}\right)^b.$

Strong turbulence: BER of SISO for strong turbulence is,

$$P_S^g = C \sum_{j=0}^{\infty} \int_0^{\infty} \mathbb{Q}(\zeta I) \left(C_j^{(a,b)} I^{j+b-1} - C_j^{(b,a)} I^{j+a-1} \right) dI \tag{14}$$

Invoking Q-function approximation in Eq. (14) yields,

$$P_S^s \approx C \sum_{j=0}^{\infty} \int_0^{\infty} \left(\frac{1}{12} \exp\left(-\frac{\zeta^2 I^2}{2} \right) + \frac{1}{4} \exp\left(-\frac{2\zeta^2 I^2}{3} \right) \right) \times \left(C_j^{(a,b)} I^{j+b-1} - C_j^{(b,a)} I^{j+a-1} \right) \mathrm{d}I \tag{15}$$

Eq. (15) is simplified using $\int_0^{\infty} I^{\alpha-1} \exp(-\beta I^2) dI = \frac{1}{2} \left(\frac{1}{\beta} \right)^{\alpha/2} \Gamma\left(\frac{\alpha}{2} \right)$, the obtained closed-form BER expression is,

$$P = C \sum_{j=0}^{\infty} \left[\mathscr{M}_1^j C_j^{(a,b)} - \mathscr{M}_2^j C_j^{(b,a)} \right] \tag{16}$$

where $\mathscr{M}_1^j = \left(\frac{1}{24} \left(\frac{2}{\zeta^2} \right)^{(j+b)/2} + \frac{1}{8} \left(\frac{3}{2\zeta^2} \right)^{(j+b)/2} \right) \Gamma\left(\frac{j+b}{2} \right), \mathscr{M}_2^j = \left(\frac{1}{24} \left(\frac{2}{\zeta^2} \right)^{(j+a)/2} + \frac{1}{8} \left(\frac{3}{2\zeta^2} \right)^{(j+a)/2} \right) \Gamma\left(\frac{j+a}{2} \right)$.

4.2 Selection/Superior Combining Scheme

The maximal irradiance among all the irradiance of receivers is chosen via selection combining. Signal received using selection combining is,

$$R_{sc} = \eta \sqrt{P_t T_b} s I_{sc} + n \tag{17}$$

where $I_{sc} = \max(I_1, I_2, \ldots, I_M)$. Maximum irradiance has no bearing on the received signal. The CDF of I_{sc} is given as $F_{I_{sc}}(I) = (F_I(I))^M$ and PDF is $f_{I_{sc}}(I) = M (F_I(I))^{M-1} f_I(I)$.

BER of OOK modulated single source to M PD's selection combining is,

$$P_C = \int_0^{\infty} f_{I_{sc}}(I) \mathbb{Q}(\zeta I) \mathrm{d}I_{SC} \tag{18}$$

Weak turbulence:

$$f_{I_{sc}}(I) = \frac{Mb\exp(2Ma)I^{Mb-1}}{\left(1+I^b\exp(2a)\right)^{M+1}} \tag{19}$$

BER is

$$P \approx \int_0^\infty f_{I_{sc}}(I)\left(\frac{1}{12}\exp\left(-\frac{\zeta^2 I^2}{2}\right)+\frac{1}{4}\exp\left(-\frac{2\zeta^2 I^2}{3}\right)\right)\mathrm{d}I \tag{20}$$

$$P \approx Mb\exp(2Ma)\left[\frac{P_1}{12}+\frac{P_2}{4}\right] \tag{21}$$

where $P_1 = \int_0^\infty I^{Mb-1}\exp(-\frac{\zeta^2 I^2}{2})\left(1+I^b\exp(2a)\right)^{-(M+1)}\mathrm{d}I$, $P_2 = \int_0^\infty I^{Mb-1}\exp(-2\zeta^2 I^2/3)\left(1+I^b\exp(2a)\right)^{-(M+1)}\mathrm{d}I$. Substituting $\mathscr{C}\zeta^2 I^2$ (where, $\mathscr{C} \in (1/2,\ 2/3)$) with t and then integrate, we obtain,

$$P = \frac{M\exp(2Ma)b^{\frac{Mb+1}{2}}}{\Gamma(M+1)\,(2\pi)^{\frac{b+1}{2}}}\left[\frac{\mathscr{D}_1}{12}+\frac{\mathscr{D}_2}{4}\right] \tag{22}$$

where $\mathscr{D}_1 = 2^M\left(\sqrt{2}/\zeta\right)^{Mb} G_{2+b,2}^{2,2+b}\left(\begin{matrix}-\frac{1}{2}, 0\frac{t-\frac{b}{2}}{b} \\ 0,\ \frac{1}{2}\end{matrix}\middle|\, b^b\mathscr{P}_1^2\right)$, $i = 1, 2, \ldots, b$; $\mathscr{R}_1 = \left(\sqrt{2}\exp(2a)/\zeta\right)$, $\mathscr{D}_2 = 2^M\left(\sqrt{2/3\zeta^2}\right)^{Mb} G_{2+b,2}^{2,2+b}\left(\begin{matrix}-\frac{1}{2}, 0\frac{t-\frac{b}{2}}{b} \\ 0,\ \frac{1}{2}\end{matrix}\middle|\, b^b\mathscr{P}_2^2\right)$, and $\mathscr{R}_2 = \left(\exp(2a)\sqrt{3/(2\zeta^2)}\right)$.

Strong turbulence:

$$P_C^s = M\int_0^\infty\left(\frac{1}{12}\exp\left(-\frac{\zeta^2 I^2}{2}\right)+\frac{1}{4}\exp\left(-\frac{2\zeta^2 I^2}{3}\right)\right) f_{I_{sc}}(I)\left(F_{I_{sc}}(I)\right)^{M-1}dI \tag{23}$$

Obtained BER expression is given as,

$$P_e = C^M\sum_{j=0}^{\infty}\sum_{i=0}^{M-1}(-1)^i C(j,i)\left[\mathscr{M}_1^{j,i}C_j^{(a,b)} - \mathscr{M}_2^{j,i}C_j^{(b,a)}\right] \tag{24}$$

where $C(j,i) = \frac{\binom{M-1}{i}\left(C_j^{(a,b)}\right)^{M-i-1}\left(C_j^{(a,b)}\right)^i}{(j+b)^{M-i-1}(j+a)^i}$, $\mathscr{M}_1^{j,i} = \left(\frac{1}{24}\left(\frac{2}{\zeta^2}\right)^{t_1}+\frac{1}{8}\left(\frac{3}{2\zeta^2}\right)^{t_1}\right)\Gamma(t_1)$, $\mathscr{M}_2^{j,i} = \left(\frac{1}{24}\left(\frac{2}{\zeta^2}\right)^{t_2}+\frac{1}{8}\left(\frac{3}{2\zeta^2}\right)^{t_2}\right)\Gamma(t_2), t_1 = (M(j+b)+i(a-b))/2, t_2 = (M(j+b)+(i+1)(a-b))/2$.

5 Results and Discussions

The simulation parameters to evaluate the weak and strong underwater turbulence are presented in Table 1.

This study presents simulation and analytical BER results with respect to transmit power (dB). Figure 2a depicts the simulation and analytical BER results of SISO and SC ($M = 2,\ 3,\ 4$) scheme for weak turbulence UWOC channel, and it is evident that the results obtained from the analytical evaluation are good fit with the simulation results at higher transmit powers. Nearly, 10 dB power improvement from SISO to $M = 2$ SC, 14 dB from $M = 3$ SC to SISO and 17 dB power gain from $M = 4$ SC to SISO at BER of 10^{-5}. Figure 2b shows the simulation and analytical BER results of SISO and SC ($M = 2,\ 3,\ 4$) for strong turbulence UWOC channel. The simulated findings reflect the analytical results well. A power gain of at least 70 dB from SISO to $M = 2$ SC, 100 dB gain from $M = 3$ SC to SISO, and 120 dB gain from $M = 4$ SC to SISO at BER of 10^{-5}.

Table 1 Simulation parameters

Turbulence	Scheme	Parameter
		$a,\ b$ or $\alpha,\ \beta$
Weak turbulence	SISO	2.15, 4
	$M = 2$	0.8489, 3
	$M = 3$	0.1306, 2
	$M = 4$	0.2612, 2
Strong turbulence	SISO, $M = 2, 3, 4$ SC	0.75, 0.6

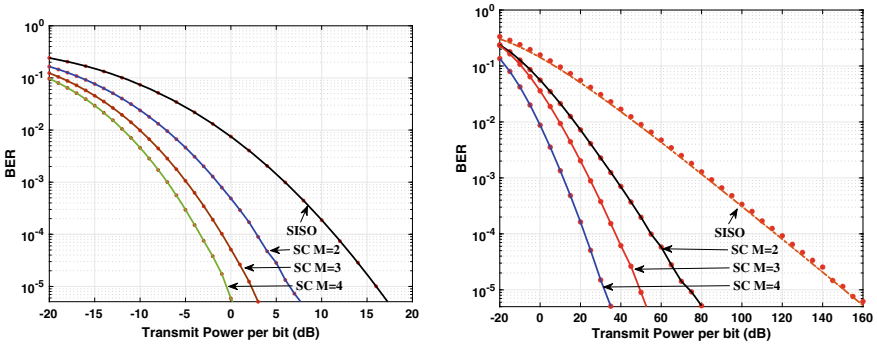

Fig. 2 Bit error rate of **a** Weak turbulence and **b** Strong turbulence

6 Conclusion

We have evaluated the analytical BER expressions of UWOC system under the influence of the weak and strong turbulence scenarios. In order to enhance the UWOC system performance, we have employed selection combining schemes with the two, three, and four number of detectors. This scheme enhances the system BER performance by 14 dB of transmit power using the $M = 2$ SC scheme. The numerical BER results are corroborated with the simulation results.

Acknowledgements This work was supported by a research grant funded by National Research Foundation (NRF) of Korea grant (No. 2020R1A4A1019463).

References

1. Zeng Z, Fu S, Zhang H, Dong Y, Cheng J (2016) A survey of underwater optical wireless communications. IEEE Commun Surveys Tutorials 19(1):204–238
2. Gussen CM, Diniz PS, Campos ML, Martins WA, Costa FM, Gois JN (2016) A survey of underwater wireless communication technologies. J Commun Inf Sys 31(1):242–255
3. Smart JH (2005) Underwater optical communications systems part 1: variability of water optical parameters. In: MILCOM 2005–2005 IEEE military communications conference. IEEE, New York, pp 1140–1146
4. Korotkova O, Farwell N, Shchepakina E (2012) Light scintillation in oceanic turbulence. Waves Random Complex Media 22(2):260–266
5. Oubei HM, Zedini E, ElAfandy RT, Kammoun A, Abdallah M, Ng TK, Hamdi M, Alouini M-S, Ooi BS (2017) Simple statistical channel model for weak temperature-induced turbulence in underwater wireless optical communication systems. Opt Lett 42(13):2455–2458
6. Gerçekcioğlu H (2014) Bit error rate of focused Gaussian beams in weak oceanic turbulence. JOSA A 31(9):1963–1968
7. Elamassie M, Sait SM, Uysal M (2018) Underwater visible light communications in cascaded gamma-gamma turbulence. In: IEEE Globecom workshops (GC Wkshps). IEEE, New York, pp 1–6
8. Ramavath PN, Kumar A, Shashikant Godkhindi S, Acharya US (2018) Experimental studies on the performance of underwater optical communication link with channel coding and interleaving. CSI Trans ICT 6(1):65–70
9. Prasad Naik R, Shripathi Acharya U, Suyan NK (2020) Experimental evaluation of reliable underwater optical communication in the presence of turbulence and blockage. In: Optical and wireless technologies. Springer, Berlin, pp 75–83
10. Zhang H, Dong Y, Hui L (2015) On capacity of downlink underwater wireless optical MIMO systems with random sea surface. IEEE Commun Lett 19(12):2166–2169
11. Korotkova O, Farwell N, Shchepakina E (2012) Light scintillation in oceanic turbulence. Waves Random Complex Media 22(2):260–266
12. Ramavath PN, Udupi SA, Krishnan P (2020) Experimental demonstration and analysis of underwater wireless optical communication link: design, BCH coded receiver diversity over the turbid and turbulent seawater channels. Microwave Opt Technol Lett 62(6):2207–2216
13. Bayaki E, Schober R, Mallik RK (2009) Performance analysis of MIMO free-space optical systems in gamma-gamma fading. IEEE Trans Commun 57(11):3415–3424
14. Chiani M, Dardari D, Simon MK (2003) New exponential bounds and approximations for the computation of error probability in fading channels. IEEE Trans Wireless Commun 2(4):840–845

15. Peppas KP, Boucouvalas AC, Ghassemloy Z (2017) Performance of underwater optical wireless communication with multi-pulse pulse-position modulation receivers and spatial diversity. IET Optoelectron 11(5):180–185
16. Yang F, Cheng J, Tsiftsis TA (2014) Free-space optical communication with nonzero boresight pointing errors. IEEE Trans Commun 62(2):713–725
17. Ramavath PN, Udupi SA, Krishnan P (2020) High-speed and reliable underwater wireless optical communication system using multiple-input multiple-output and channel coding techniques for iout applications. Opt Commun 461:125229
18. Naik RP, Udupi SA, Krishnan P (2020) Co-operative RF-UWOC link performance over hyperbolic tangent log-normal distribution channel with pointing errors. Opt Commun 469:125774
19. Adamchik V, Marichev O (1990) The algorithm for calculating integrals of hypergeometric type functions and its realization in reduce system. In: Proceedings of the international symposium on symbolic and algebraic computation. ACM, pp 212–224

Comparative Study of Power Optimization Technique for M2M Communication Node Under 5G (NR)

Vipin Sharma, Rajeev Kumar Arya, Sandeep Kumar, and Krishna Pandey

Abstract The direct Fourier transform-spread OFDM (DFT-s-OFDM) and cyclic prefix orthogonal frequency division multiplexing (CP-OFDM) are used for the end-to-end data transmission to support the 5G services and backward compatibility. Improving battery life has always been an important concern in 5G machine-to-machine (M2M) communication nodes. Efficient utilization of power amplifiers (PA) and inferior peak-to-average power ratio (PAPR) is helpful to achieve enhanced battery life. Filter bank multi-carrier (FBMC) multiplexing is an alternative to CP-OFDM that offers low PAPR with the benefits of CP removal. Another way to get low PAPR is single carrier OFDM (SC-FDMA). The transmission requirements between these services are different, which presents a challenge for waveform adaptability to PAPR issues. The DFT-s-OFDM technique is one of the choices to overcome the PAPR that is used in uplink scenarios. Apart from PAPR reduction, DFT-s-OFDM provides optimal use of nonlinear power amplifiers. In addition to PAPR analysis, spectral efficiency is also compared in the simulation results. Using parameters that adjust the cost of spectral efficiency, DFT-s-OFDM provides the extent of improvement in PAPR performance and bit error rate over traditional CP-OFDM, SC-FDMA, and FBMC against the noisy channel.

Keywords M2M · 5G (NR) · PAPR · BER · SNR · OFDM · CP-OFDM · SC-FDMA · FBMC DFT-s-OFDM

V. Sharma (✉) · R. K. Arya · K. Pandey
Department of Electronics and Communication Engineering, National Institute of Technology, Patna 800005, India
e-mail: vipins.phd19.ec@nitp.ac.in

S. Kumar
Department of Electronics and Communication Engineering, National Institute of Technology Karnataka, Surathkal 575025, India

S. Rawat et al. (eds.), *Proceedings of Second International Conference on Computational Electronics for Wireless Communications*, Lecture Notes in Networks and Systems 554,
https://doi.org/10.1007/978-981-19-6661-3_57

1 Introduction

Modern wireless systems, including wireless broadband (WiBro), ultra-reliable low-latency communication, LTE networks, Wi-Fi, and the 5G New Radio (NR), are all based on OFDM [1, 2]. It is more significant on the uplink due to the user equipment's restricted cost and power budget. In the physical layer part, PA is one of the most intensive components [3]. Efficient PA conversion can enhance energy efficiency while also extending the user equipment's battery life. It also increases transmission strength in order to enhance the number of cell-edge users.

The CP-OFDM and DFT-s-OFDM waveforms are still used by the Third Generation Partnership Project (3GPP) as 5G (NR) waveforms [3]. FBMC with offset quadrature amplitude modulation (OQAM) is a promising modulation technology for future wireless networks. OQAM delivers significantly lower out-of-band (OOB) emissions than OFDM [1]. Furthermore, FBMC does not need the CP, resulting in higher throughput. This results in inherent interference, which is centred on the imaginary part of the channel, which makes channel prediction [4] and implementation of multiple-input multiple-output (MIMO) more challenging [5, 6]. Several approaches to addressing these issues have been proposed [2, 7], and [8]. In addition to the inherent interference, nonlinearities such as a limited digital-to-analogue-converter (DAC) resolution or a nonlinear power amplifier pose a challenge in actual systems because they blight FBMC's better spectrum confinement [2, 9]. As a result, FBMC is only beneficial if it is used in a suitably linear manner. This is difficult to achieve in multi-carrier systems because of the poor PAPR. Selective mapping [10] and partial transmit sequences [11] are two ways that have been proposed to reduce the PAPR in OFDM. LTE uses SC-FDMA in the uplink, which is essentially a DFT pre-coded OFDM system. Apart from CP-OFDM, DFT-s-OFDM technology will be used in the uplink of 5G wireless systems. The filter bank multiplexing is utilized in place of DFT for superior performance while this approach lowers the PAPR, it still falls short of SC-FDMA and comes with the added drawbacks of higher overhead and computational complexity. In contrast to traditional FBMC, Na and Choi demonstrated that the phase term has an effect on the PAPR performance of a basic DFT spread FBMC scheme.

1.1 Contributions of the Paper

The comparative performance of PAPR, spectral efficiency, and BER is obtained for CP-OFDM, FBMC, DFT-s-OFDM, and SC-FDMA. The 5G PHY layer model is prepared for M2M node. The simulation performance is obtained on MATLAB. The main highlights of the approach are described as:

1. In M2M PHY (physical) layer model, adaptive modulation and coding (AMC) enabled code-modulation profile is utilized for robust transmission. The polar channel encoding is used as forward error correction (FEC).

2. Parametric analysis is obtained via uplink stream, and channel information is given to the transmitter for the best AMC selection via channel state information (CSI).
3. The multipath channel losses are modelled using the Rayleigh channel model and the AWGN channel model.

1.2 Organization of the Paper

The rest of the paper is laid out in the following manner. Section 2 describes the CP-OFDM system model. Section 3 introduces the SC-FDMA system. The FBMC method is examined in Sect. 4. The use of DFT-s-OFDM for PAPR reduction is explored in Sect. 5. In Sect. 6, we compare the performance of PAPR and bit error rate. Section 6 has the conclusion.

2 CP-OFDM

The frequency spacing of Δf, an OFDM symbol is made up of N subcarriers. As a result, the overall bandwidth B will be partitioned into N subcarriers that are evenly spaced. Within a time interval of length $t = 1/\Delta f$, all subcarriers are orthogonal to one another. The complex modulation symbol $A_{m,k}$, where m is a time index and n is a subcarrier index, can be used to modulate each subcarrier individually. Then Eq. (1) may be used to explain the OFDM symbol inside the time t.

$$a_m(t) = \frac{1}{\sqrt{K}} \sum_{k=0}^{K-1} A_{m,k}\ g_k(t - bT) \tag{1}$$

where $g_k(t)$ is defined through Eq. (2).

$$g_k(t) = \begin{cases} \exp(j2\pi k \Delta f t) & 0 \le t \le T \\ 0, & \text{else} \end{cases} \tag{2}$$

The rectangular pulse $g_k(t)$ is applied to each subcarrier [4]. Equation (3) gives the complete continuous time signal $a(t)$ comprised of all OFDM blocks.

$$a_m(t) = \frac{1}{\sqrt{K}} \sum_{m=0}^{\infty} \sum_{k=0}^{K-1} A_{m,k}\ g_k(t - mT) \tag{3}$$

Now, examine a single OFDM symbol ($m = 0$). This is seen by the lacking of overlap symbols between various OFDM signals. $A_{m,k}$ may be substituted by A_k since $m = 0$. The OFDM signal, on the other hand, may be characterized as follows:

$$\{a(t)\} = \frac{1}{\sqrt{k}} \sum_{k=0}^{K-1} A_n e^{j2\pi k \Delta f t} \tag{4}$$

The OFDM signal is in discrete time form if the bandwidth is $B = K \times \Delta f$ and the signal $k(t)$ is sampled by the sample time of $\Delta t = \frac{1}{B} = \frac{1}{K\Delta f}$ (5).

$$a_m(t) = \frac{1}{\sqrt{K}} \sum_{k=0}^{K-1} A_k e^{2\pi k/K}; k = 0, 1, \ldots\ldots N-1 \tag{5}$$

In the frequency domain, k signifies the index, while A denotes the complex symbol. Additionally, the IFFT [5] can be used to represent Eq. (5). An OFDM system is depicted in Fig. 1 as a typical system block diagram.

The root of the temporal average of the envelope power $\left(\sqrt{\overline{\mathcal{P}}}\right)$, where $\mathcal{P}$ is determined by equation, is the RMS magnitude of the OFDM signal (6).

$$\overline{\mathcal{P}} = \frac{1}{t} \int_{t=0}^{T} |a(t)|^2 \mathrm{d}t = \frac{1}{K} \sum_{k=0}^{K-1} |A(k)|^2 \tag{6}$$

The number of subcarriers K determines the PAPR maximum. Only, M^2 sequences with maximum PAPR, K are available for M-PSK modulation, as

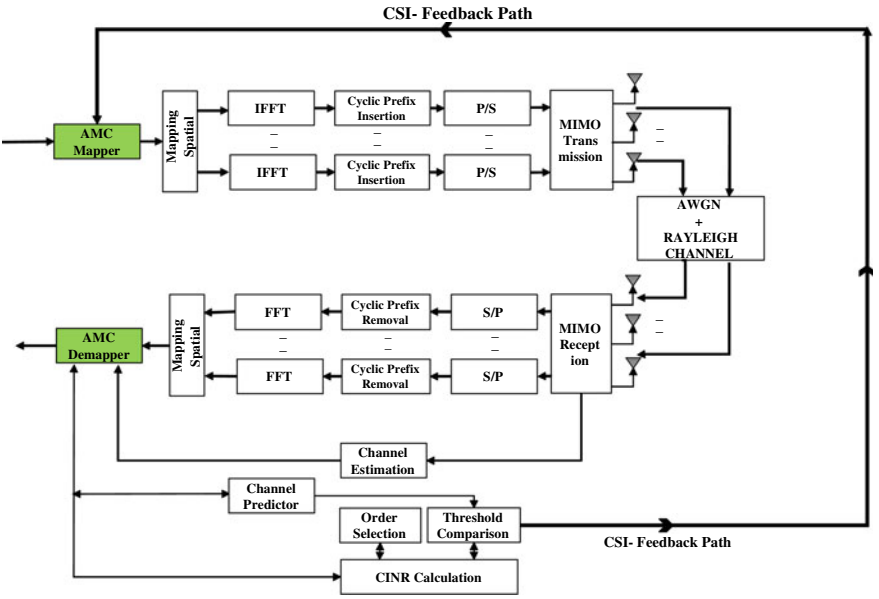

Fig. 1 OFDM-CP simulation model scenario

explained in [6]. The ratio of the sequence that yields a very high PAPR to all different sequences reduces fast as the number of sub-channels grows. The total number of unique sequences in an N-carrier OFDMs system using M-PSK, M^K. As a result, Eqs. (7) and (8) may be used to find the ratio of PAPR.

$$R = \frac{M^2}{M^K} \tag{7}$$

$$R = M^{2-K} \tag{8}$$

3 SC-FDMA

Many PAPR reduction methodologies and selection criteria are documented in the literature [2, 3]. SC-FDMA is an augmentation of the OFDMA system with similar performance and complexity. In terms of PAPR, it provides a major advantage over OFDMA systems due to its inherent multi-carrier structure [4] and high transmission power efficiency. SC-FDMA is a discrete Fourier transform-spread variation of OFDMA in which time domain symbols are transformed into frequency domain before being modulated. Figure 2 shows the PAPR reduction strategy for the recommended SC-FDMA and nonlinear commanding approaches.

The DFT assures that the subcarriers are orthogonal to each other, resulting in a single carrier transmit signal and SC-FDMA. To reduce the system's computational complexity, FFT is employed in place of DFT and IFFT instead of IDFT. There are subcarriers in the subcarrier mapping scheme, with the input data placing subcarriers among them. Let a_m be the modulated data symbols, and the frequency domain samples are A_m when the FFT is performed. Let A_k be the frequency domain samples of time domain a_k samples after subcarrier mapping and IFFT. The following are the frequency domain samples A_k:

$$A_{k=\mathcal{Q}.m} = \begin{cases} A_m, & 0 \le m \le M-1 \\ 0 & \text{Otherwise} \end{cases} \tag{9}$$

$$A_{k=\mathcal{Q}.m} = \begin{cases} A_m, & 0 \le k \le M-1 \\ 0 & M \le k \le N-1 \end{cases} \tag{10}$$

The transfer function for SC-OFDM is defined as follows:

$$f(a) = \begin{cases} \text{sgn(a)} \left(\frac{p+1}{i} \left(1 - e^{\left(-\frac{|a|^2}{\sigma^2} \right)} \right) \right)^{\frac{1}{p+1}}, & |a| \le \alpha \\ \text{sgn(a)} \left(\frac{1 - e^{\left(-\frac{|a|^2}{\sigma^2} \right)}}{i(\text{cA})^{\text{p}}} + \frac{\text{pcA}}{p+1} \right), & |a| > \alpha \end{cases} \tag{11}$$

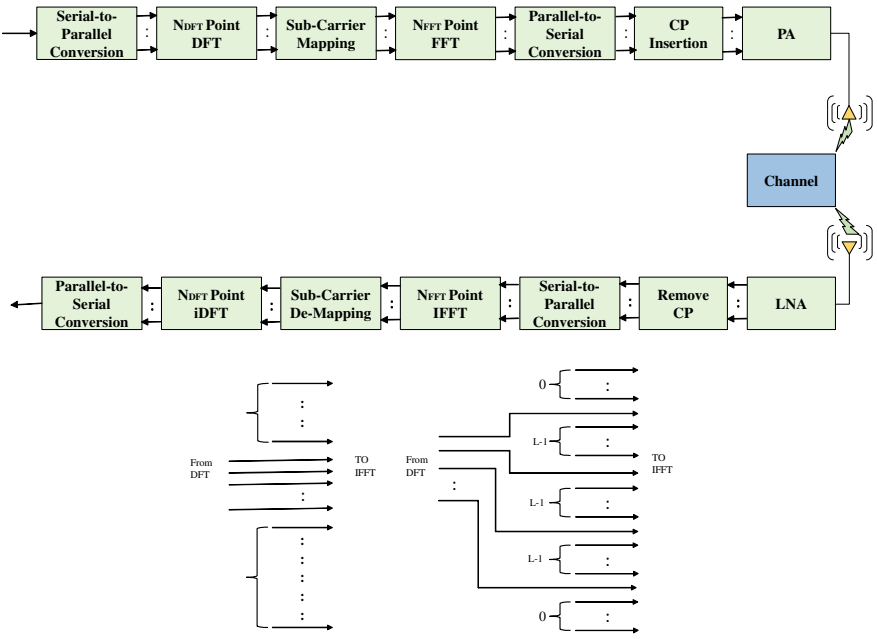

Fig. 2 SC-FDMA simulation scenario

4 FBMC

The amount of multi-carrier symbols overlaps in the temporal domain. The filter's order is 2*N − 1, where N might be 2, 3, or 4, τ_s is the sampling period, and symbols $d[n]$ represent information bits. Figure 3 depicts the FBMC transmitter's block diagram.

$$a[k] = \sum_{m=-\infty}^{+\infty} \Sigma a_R[k] p[k - mK] + a_I[n] p\left[a - mA - \frac{A}{2}\right] \tag{12}$$

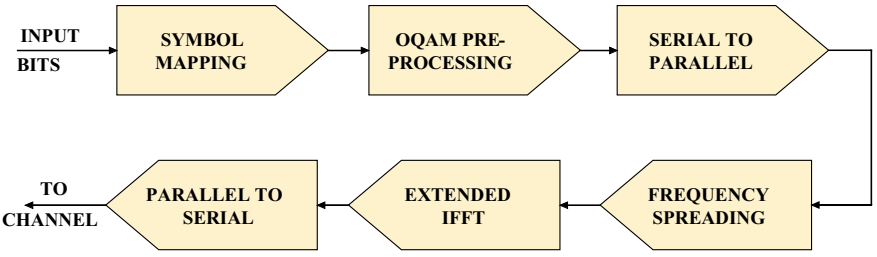

Fig. 3 FBMC transmitter

The real numbers are sent by the overlapping symbols at the transmitting end (13).

$$a_R[n] = \sum_{k=0}^{K-1} \theta_k R\left\{a_{(m,k)}\right\} e^{j\left(\frac{2\pi k}{K}\right)(k-mK)} \tag{13}$$

$$a_I[n] = \sum_{k=0}^{A-1} \theta_{k+1} I\left\{a_{(m,k)}\right\} e^{j\left(\frac{2\pi k}{K}\right)(k-mK)} \tag{14}$$

where θ_k is defined by (15)

$$\theta_k = \begin{cases} \pm 1, \ k \text{ is even} \\ \pm J, \ k \text{ is odd} \end{cases} \tag{15}$$

The orthogonality between the sub-channels can be accomplished by using PHYDYAS filtering (17) with OQAM modulation. Both channel capacity and spectral efficiency are enhanced by FBMC. This is all part of the FBMC-OQAM preprocessing. During transmission, the information stream of 1's and 0's converted from serial to parallel. The frequency spreading H_k and BxK length IFFT symbols are overlay with an interval of $K/2$. OQAM is utilized to achieve full channel capacity. The real and imaginary components of data symbols are not transferred simultaneously, and the imaginary component is half the symbol length behind the real component. The filter coefficients are designed as indicated below. The frequency response equation for m subcarriers is

$$H(f) = \sum_{k}^{K-1} -(k-1) p_k \frac{\sin\left(\pi\left(f - \frac{k}{mk}\right)mk\right)}{mk \sin(\pi(f - k\ mk))'} \tag{16}$$

5 DFT-S-OFDM

Figure 4 shows the basic building block of DFT-S-OFDM that consider the following vector d that is drawn across the mentioned vector

$$q = [\mathcal{S}_h.d.\mathcal{S}_t]^T \tag{17}$$

where $\mathcal{S}_h$ and $\mathcal{S}_t$ are head and tail sequences. A DFT block receives the $K = K_h + K_t + \check{K}$ length, q vector which is subsequently mapped across the subcarriers. The $K_{\text{FFT}} \times 1$, vector h could be expressed as

$$h = F^{-1}_{K_{\text{FFT}}}.m.F_{Kq} \tag{18}$$

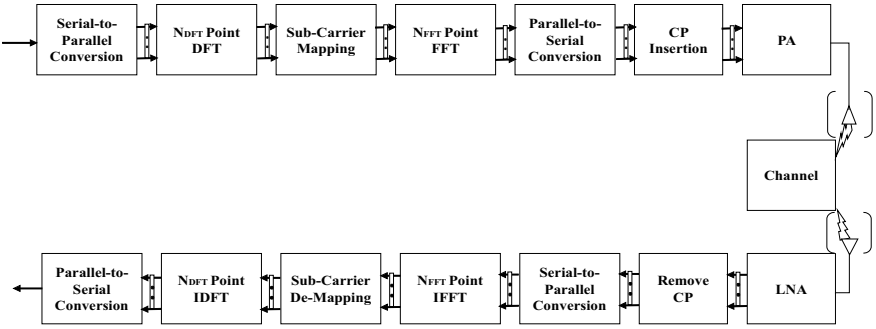

Fig. 4 DFT-S-OFDM scenario

The assumption here is that the localized subcarrier mapping exists [5]. The output signal due to the linearity of the procedures involved can alternatively be represented as $h = h_{\mathcal{S}_h} + h_d + h_{\mathcal{S}_t}$, where $h_{\mathcal{S}_h} = V\left[h_{\mathcal{S}_h} 0_{(K-K_{h'})}\right]^T$, $h_d = V\left[0_{K_{h'}} d 0_{K_t}\right]^T$, and $h_{\mathcal{S}_t} = V\left[0_{(K-K_{h'})} \mathcal{S}_t\right]^T$, with $V = F_{K_{\text{FFT}}}^{-1} \cdot \text{m}F_K$ and 0_x shows a 0 vector with x length. The $\check{h}_{\mathcal{S}_h}, \check{h}_d, \check{h}_{\mathcal{S}_t}$ of the yield vectors are having the vector length $K_{\mathcal{S}_h}, K_d, K_{\mathcal{S}_t}$, respectively. The following relations could be expressed as

$$\sum_{k=0}^{K_{\mathcal{S}_t}-1} \left|\check{h}_{\mathcal{S}_t[k]}\right|^2 \approx \sum_{k=0}^{K_{\text{FFT}}-1} \left|h_{\mathcal{S}_t[k]}\right|^2 \tag{19}$$

$$\sum_{k=K_{\mathcal{S}_t}}^{K_{\mathcal{S}_t}+K_d-1} \left|\check{h}_{d[k]}\right|^2 \approx \sum_{n=0}^{N_{\text{FFT}}-1} \left|h_{d[\text{n}]}\right|^2 \tag{20}$$

$$\sum_{k=K_{\mathcal{S}_t}+K_d}^{K_{\text{FFT}}-1} \left|\check{h}_{\mathcal{S}_h[k]}\right|^2 \approx \sum_{n=0}^{K_{\text{FFT}}-1} \left|h_{\mathcal{S}_h[n]}\right|^2 \tag{21}$$

A small percentage of the samples have enough energy for every vectors that contribute to the output signal. Figure 4 describes the three signal components, also shows how one is influenced by the leakage of the other two. The signal h_d resembles to the ZT DFT-s-OFDM waveform [12] when the two known sequences $\mathcal{S}_h$ and $\mathcal{S}_t$ in Eq. (18) have with zero-vectors.

Non-cyclic inter-symbol interference is reduced in both circumstances to the data part's energy overflow to the following symbol. Instead, because of the cyclicity of the IFFT operation [10], $h_{\mathcal{S}_h}$ is only used to prevent data element to regenerate the power in the last samples of the symbols. When compared to baseline OFDM/DFT-s-OFDM, employing the same head and tail vectors smooths down the abrupt transitions between consecutive time symbols, which should reduce out-of-band signal emissions (Fig. 5).

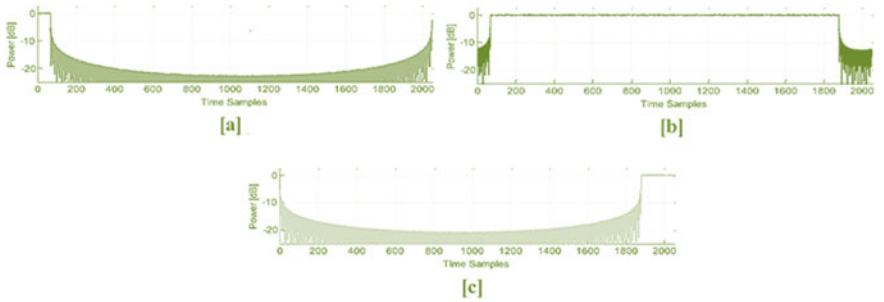

Fig. 5 **a** $h_{\mathcal{S}_h}$, **b** h_d, and **c** $h_{\mathcal{S}_t}$

6 Result and Discussion

Figures 6, 7, 8 and 9 demonstrate the connection between the complementary cumulative distribution function (CCDF) and the PAPR (dB) for a 4-QAM, 8-QAM, 16-QAM, and 64-QAM signal constellation with L = 256 subcarriers, respectively. Whereas Fig. 10 shows the BER performance. Figure 6 shows that DFT-S-OFDM outperforms CP-OFDM, FBMC, and SC-FDMA in terms of PAPR performance. The PAPR of conventional FBMC is the same as that of OFDM. SC-FDMA outperforms OFDM and FBMC by around 3 decibels. Furthermore, by using a frequency CP, the PAPR may be reduced even further, however, at the cost of a poorer spectral efficiency. The overall performance of PAPR degrades as the constellation increases from 4-QAM to 64-QAM, as seen in Figs. 6, 7, 8 and 9. In comparison with FBMC, FBMC demonstrates superior PAPR performance as modulation increases.

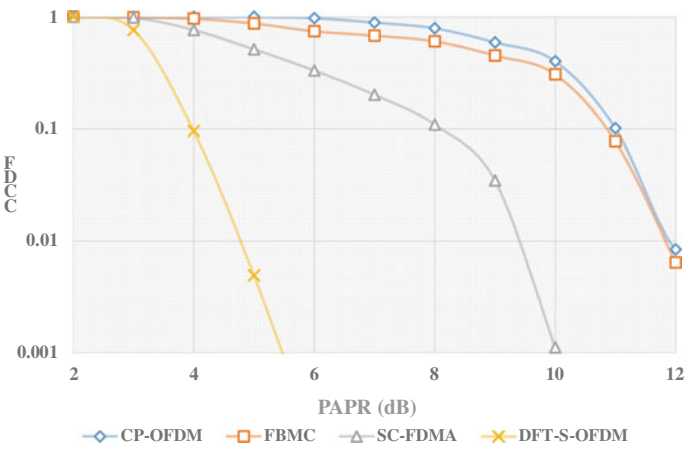

Fig. 6 PAPR performance for 4-QAM

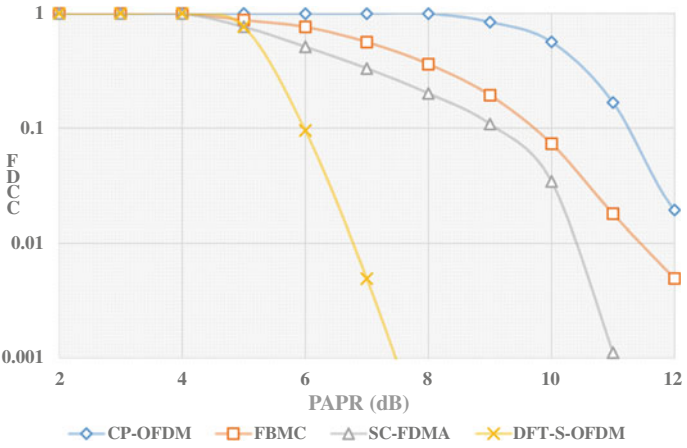

Fig. 7 PAPR performance for 8-QAM

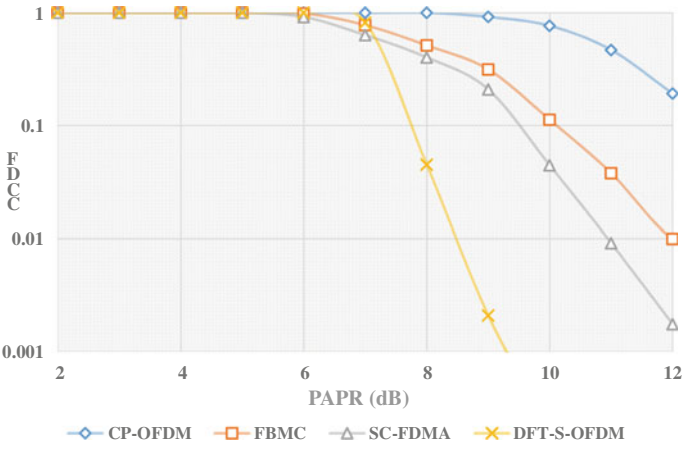

Fig. 8 PAPR performance for 16-QAM

7 Conclusion

In terms of PAPR performance, DFT-s-OFDM surpasses FBMC, SC-FDMA, and CP-OFDM. In a frequency-flat channel, DFT-s-OFDM shows superior performance over FBMC. The M2M nodes potentially utilize DFT-s-OFDM and FBMC over uplink transmissions, where the excellent time–frequency localization eliminates the need for complex synchronization between users. One key point to note is that when a greater modulation profile is used, PAPR increases as well. As a result, a reduced modulation profile indicates good PAPR. DFT-s-OFDM, SC-FDMA, and

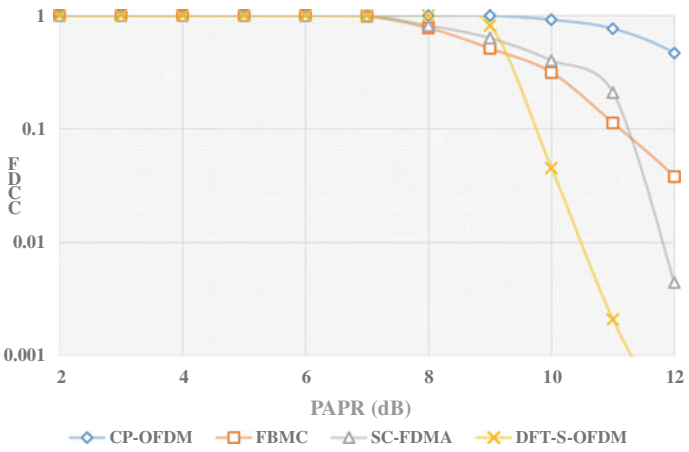

Fig. 9 PAPR performance for 64-QAM

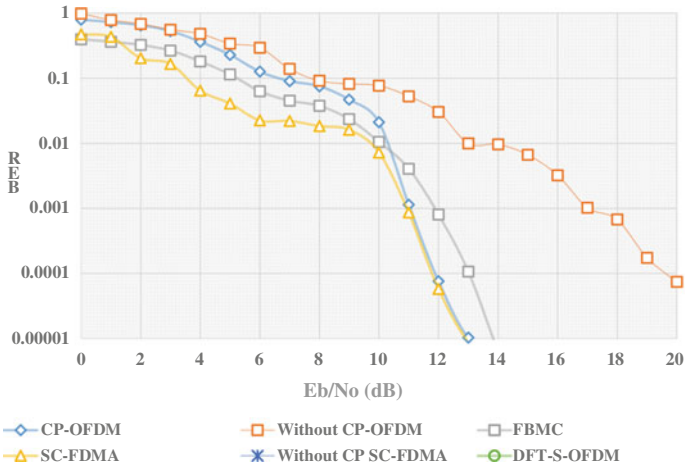

Fig. 10 BER performance for 16-QAM

CP-OFDM have better tolerance to random channel fluctuation than CP-OFDM and FBMC in terms of BER performance.

References

1. Farhang-Boroujeny B, Moradi H (2016) OFDM inspired waveforms for 5G. IEEE Commun Surveys Tuts 18(4):2474–2492. 4th Quart
2. Cases VM, Zaidi AA et al (May 2017) A comparison of OFDM, QAM-FBMC, and OQAM-FBMC waveforms subject to phase noise. IEEE ICC
3. Zhang L, Ijaz A, Xiao P, Tafazolli R (2017) Multi-service system: an enabler of flexible 5g air interface. IEEE Commun Mag 55(10):152–159
4. Rahmatallah Y, Mohan S (2013) Peak-to-average power ratio reduction in OFDM systems: a survey and taxonomy. IEEE Commun Surveys Tuts 15(4):1567–1592. 4th Quart
5. Bauml RW, Fischer RFH, Huber JB (1996) Reducing the peak-toaverage power ratio of multicarrier modulation by selected mapping. Electron Lett 32(22):2056–2057
6. Liu X, Zhang L, Xiong J, Zhang X, Zhou L, Wei J (2020) Peakto- average power ratio analysis for OFDM-based mixed-numerology transmissions. IEEE Trans Veh Technol 69(2):1802–1812
7. Brihuega A, Anttila L, Abdelaziz M, Eriksson T, Tufvesson F, Valkama M (2020) Digital predistortion for multiuser hybrid MIMO at mmWaves. IEEE Trans Signal Process 68:3603–3618
8. Levanen T, Pirskanen J, Pajukoski K, Renfors M, Valkama M (2018) Transparent Tx and Rx waveform processing for 5G new radio mobile communications. IEEE Wireless Commun 26(1):128–136
9. Kongara G, Yang L, He C, Armstrong J (2019) A comparison of CP-OFDM, PCC-OFDM and UFMC for 5g uplink communications. IEEE Access 7:157574–157594
10. Kumar U, Ibars C, Bhorkar A, Jung H (Dec 2015) A waveform for 5g: guard interval DFT-s-OFDM. In: Processing IEEE globecom workshops, pp 1–6
11. Berardinelli G, Frederiksen F, Pedersen K, Mogensen P, Pajukoski K (April 2016) Reference sequence design for zero-tail DFT-spread OFDM. In: Processing IEEE wireless communication network conference (WCNC), pp 1–6
12. Le Goff SY, Al-Samahi SS, Khoo BK, Tsimenidis CC, Sharif BS (2009) Selected mapping without siden information for PAPR reduction in OFDM. IEEE Trans Wireless Commun 8(7)

Outage Probability Analysis of Variable and Fixed Gain Relay-Assisted Dual-Hop RF-FSO Links Using Space–time Block Code Users

Ramavath Prasad Naik, L. Bhargava Kumar, Prabu Krishnan, and Wan Young Chung

Abstract In this paper, we have implemented an analytical study on a relay-assisted dual-hop system using fixed and variable gains for the radio-frequency (RF) and free-space optical communication (FSO). RF and FSO links are realized using the Rayleigh and Malaga distribution functions. Simulation results shows that pointing errors become severe, system performance deteriorates, and conjointly that the RF users exploiting space–time block coding (STBC) will enhance the performance of the end-to-end system. Outage probability of the end-to-end communication link operated with the STBC using the variable and fixed gain system implemented and plotted with respect to average SNR. From the obtained results, fixed gain relay-based communication link performs better efficient than the variable gain relay system.

Keywords RF · FSO · Space–time block coding (STBC) · TDMA

1 Introduction

FSO communication has established a non-inheritable and remarkable presence in the telecommunications industry, owing to its large bandwidth and low-cost transmission capabilities [1]. FSO uses lasers to provide high-speed wireless communication. FSO can be a potent alternative to and complement to existing wireless technology in various applications because to its powerful qualities such as high bandwidth,

R. P. Naik
Research Institute of Artificial Intelligence Convergence, Pukyong National University, Daeyeon 3-Dong, Nam-Gu, Busan 48513, Republic of Korea

L. Bhargava Kumar · P. Krishnan
Department of Electronics and Communication Engineering, National Institute of Technology Karnataka, Surathkal, Karnataka 575025, India

W. Y. Chung (✉)
Department of Electronic Engineering, Pukyong National University, Daeyeon3-Dong, Nam-Gu, Busan 48513, Republic of Korea
e-mail: wychung@pknu.ac.kr
URL: http://aiotlab.pknu.ac.kr/01/01.php

S. Rawat et al. (eds.), *Proceedings of Second International Conference on Computational Electronics for Wireless Communications*, Lecture Notes in Networks and Systems 554,
https://doi.org/10.1007/978-981-19-6661-3_58

low cost, and operation in an unregulated spectrum [2]. However, the environment through which the beam passes has a significant impact on FSO performance. Atmospheric turbulence is the primary and most significant source of fading [3]. Thermal gradient and turbulence along the optical path created by changes in air temperature intensity cause it. Certain systems, such as mixed RF-FSO systems with STBC users, use M-distributed turbulence channels to prevent and mitigate this problem.

The authors in [4–12] describe the FSO system performance with and without any relay under the effects of atmospheric turbulence and pointing error fading. The atmospheric turbulence changes due to differences in the refractive index, produces fluctuations in the received light signal strength and phase. To address this issue, a mathematical model for FSO links that combines beam width and coding rate for FSO channels is being developed. To account for signal intensity fluctuations in fast fading channels, the mathematical formulations for both average and outage capacities for fast and slow fading channels were rigorously applied in [12]. In [13], the authors identified the reduction in performance of the FSO communications system caused by atmospheric turbulence over lengths of 1 km or greater. As a result, a dual-hop relay system was implemented.

With the advancements of FSO over time, it has become an attractive communication technology to mix with RF technology. The researchers started developing a dual-hop RF-FSO communication system that includes a relay that spans asymmetric RF and FSO channels. In [13], using closed-form equations, the authors obtained the outage probability (OP) of the end-to-end RF-FSO system. The outage and channel capacity statistics of a combined RF-FSO system are investigated over the RF and FSO links which are Nakagami-m and gamma–gamma distributed, respectively [14, 15]. The authors analyzed the end-to-end system performance with fixed gain (FG) or variable gain (VG) over gamma-gamma channels.

Space–time block coding (STBC) is a coding method to transmit multiple copies of a data stream over many antennas and exploit the different received data versions to increase data transfer reliability and achieve improved communication performance. In [16], the authors proposed an equalization concept for Alamouti's STBC method. On the other hand, previous research has primarily concentrated on the reliability of hybrid RF-FSO systems having single RF antenna users. It is vital to assess the end-to-end system performance with STBC users in order to fully comprehend the STBC's consequences and characteristics. [17, 18] use Rayleigh fading RF channels and *M*-distributed turbulence FSO channels with pointing errors to find closed-form equations for the end-to-end outage and average symbol error probability. An amplify-and-forward relay schemes investigated in this work for VG and FG relay methods.

The following is a breakdown of the work: The system and channel model that we employed in this research paper is depicted in Sect. 2 and Sect. 3. In Sect. 4, the statistical and OP performance analysis is carried out using the M distribution fading channel using Meijer-G function. Section 5 presents the numerical statistics together with a graphical interpretation. The conclusion is found in Sect. 6.

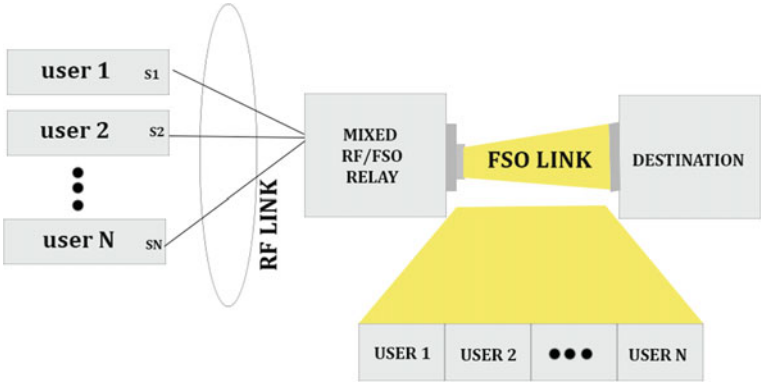

Fig. 1 Dual-hop RF-FSO communication system

2 System Model

Figure 1 shows a dual-hop RF-FSO communication system consisting of N number of RF users, a relay, and a destination node. The relay node converts the RF signals provided as input and converted to optical signals to send them to the alternative end over the FSO link. The N number of RF users employs the TDMA to share optical channel.

Using the STBC technique, we analyze a dual-hop RF-FSO system with a Rayleigh fading RF channel and M-distributed atmospheric turbulence with pointing error. The RF channel uses Rayleigh fading, and the RF link switches when the LOS path is unavailable for the FSO link. This represents the limitation of FSO communication systems. Rayleigh fading works when several indirect paths between source and destination instead of one distinct dominant path. Therefore, when FSO communication is not possible, due to its limitations, we switch to an RF system with Rayleigh fading.

3 Channel Model

3.1 RF Links

In this work, RF users employ Alamouti's STBC method with two transmit antennas [19]. **Alamouti's** STBC is a sole coding method that may reach the full rate (Rate 1 Code). In the first symbol period, antenna 1 sends signal 1 (s_1) and antenna 2 sends signal 2 (s_2), respectively. At the relay node, the expression for the RF signal is

$$y = h_1 s_1 + h_2 s_2 + n_1,$$

where $h_i = a_i e^{j\theta_i}$, $i = 1, 2$ are channel gains of the RF links, a_i and θ_i represent the amplitude and the phase of h_i, and n_i is the AWGN at the relay node with mean zero and N_{o_2} power spectral density.

During the second symbol period, $-s_2{}^*$ and $s_1{}^*$ are transmitted, respectively, in place of s_1 and s_2, , in which * represents the conjugate operator. Then, at the relay, the RF signal is given as

$$y_2 = -h_1 s_2^* + h_2 s_1^* + n_2,$$

where n_2 is similar to n_1. By applying conjugate on y_2, the obtained signal model is given as [19]

$$\begin{bmatrix} y_1 \\ y_2^* \end{bmatrix} = \begin{bmatrix} h_1 & h_2 \\ h_2^* & -h_1^* \end{bmatrix} \begin{bmatrix} s_1 \\ s_2 \end{bmatrix} + \begin{bmatrix} n_1 \\ n_2 \end{bmatrix} \tag{1}$$

Multiplying $\begin{bmatrix} h_1 & h_2 \\ h_2^* & -h_1^* \end{bmatrix}^H$ each side of Eq. (1), we get

$$\begin{bmatrix} z_1 \\ z_2 \end{bmatrix} = \begin{bmatrix} h_1 & h_2 \\ h_2^* & -h_1^* \end{bmatrix} \begin{bmatrix} y_1 \\ y_2^* \end{bmatrix} + \left(a_1^2 + a_2^2\right) \begin{bmatrix} s_1 \\ s_2 \end{bmatrix} + \begin{bmatrix} \tilde{n}_1 \\ \tilde{n}_2 \end{bmatrix} \tag{2}$$

where H represents the conjugate-transpose operator, and $\tilde{n}_i$ represents the AWGN with variance $\left(a_1^2 + a_2^2\right) N_0$. The effective SNR after considering familiar channel knowledge at the relay is provided as [19]

$$\gamma_{RF} = \left(a_1^2 + a_2^2\right) \frac{E_s}{2N_0} = \frac{\gamma_1 + \gamma_2}{2} \tag{3}$$

where E_s is the symbol energy, $\gamma_i = a_i^2 \frac{E_s}{N_0}$ represents the SNR of RF links from the ith antenna. The PDF of the Rayleigh faded RF links is provided as [20]

$$f_{\gamma_{RF}}(\gamma_{RF}) = \frac{4\gamma}{\overline{\gamma}_{RF}^2} exp\left(\frac{-2\gamma}{\overline{\gamma}_{RF}}\right) \tag{4}$$

The CDF of the RF link is given as

$$F_{\gamma_{RF}}(\gamma_{RF}) = 1 - \left[1 + \frac{2\gamma}{\overline{\gamma}_{RF}}\right] exp\left(\frac{-2\gamma}{\overline{\gamma}_{RF}}\right) \tag{5}$$

Table 1 Turbulence associated parameters

α	β	Atmospheric effects
2.4	3	Weak
2.296	2	Moderate
2.04	1	Strong

3.2 FSO Link

The CDF of atmospheric turbulence and misalignment fading is given as [7]

$$F_{\gamma_{FSO}}(\gamma_{FSO}) = \frac{\varepsilon^2 A}{8\pi} \sum_{m=1}^{\beta} y_m 2^{(\alpha+m-1)} G_{3,7}^{6,1} \left[\left(\frac{D^2\gamma}{16\mu_{IMDD}} \right) \middle| \begin{matrix} 1, \\ \frac{\varepsilon^2}{2}, \frac{\varepsilon^2+1}{2}, \frac{\alpha}{2}, \frac{\alpha+1}{2} \end{matrix} \begin{matrix} \frac{\varepsilon^2+1}{2}, \frac{\varepsilon^2+2}{2} \\ \frac{m}{2}, \frac{m+1}{2}, 0 \end{matrix} \right] \tag{6}$$

where the parameters associated to CDF are evaluated from [7] (Table 1).

3.3 End-To-End SNR

The FG relay SNR of the system is given as

$$\gamma_{e2e}^{FG} = \frac{\gamma_{RF}\gamma_{FSO}}{\gamma_{FSO} + C} \tag{7}$$

where C represents the fixed relay gain, which will be treated as a unity. The instantaneous SNR for the VG scheme is [15]

$$\gamma_{e2e}^{VG} = \frac{\gamma_{RF}\gamma_{FSO}}{\gamma_{RF} + \gamma_{FSO} + C} \tag{8}$$

The VG relay SNR of the system can be given as [21]

$$\gamma_{e2e}^{VG} \approx min(\gamma_{RF}, \gamma_{FSO}) \tag{9}$$

4 Outage Performance

OP is the probability of the system where the SNR falls below the threshold SNR beneath which the system communication is not possible and is given as [20]

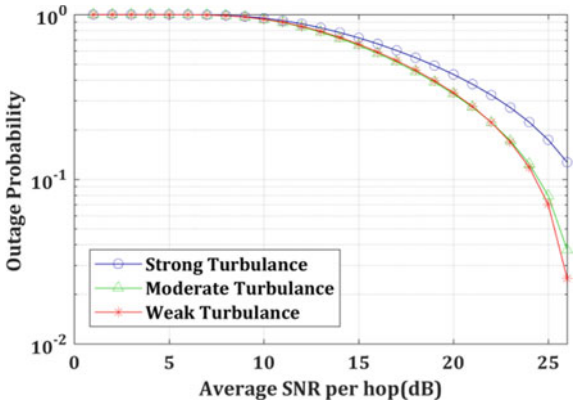

Fig. 2 Outage probability for different values of atmospheric parameters (α and β) with FG relay

$$P_{\text{out}} = P_r\{\gamma \leq \gamma_{TH}\} = F_{e2e}(\gamma_{TH}) \tag{10}$$

where γ_{TH} represents threshold SNR, and $F_{e2e}(\gamma_{TH})$ represents the CDF of the combined RF-FSO system.

5 Numerical Simulation Results

The results obtained for the dual-hop RF-FSO system using FG and VG relay methods are presented in this section. Rayleigh faded RF links are considered, while FSO links are subjected to Malaga turbulence fading in addition to pointing issues. The RF-FSO system performance in various atmospheric turbulence settings is first examined. Then, for both FG and VG relay methods, we compare outage probabilities under various SNR thresholds. The RF and FSO lines' average SNRs are assumed quantitatively equivalent.

In Figs. 2 and 3, OP for FG and VG relay with different values of threshold SNR (γ_{TH}) is analyzed. We vary γ_{TH} from 5 to 15 dB keeping the channel parameters fixed (Fig. 4).

6 Conclusion

We analyze the combined RF-FSO system's outage performance with two antenna STBC users utilizing relays. The results are obtained using the VG and FG with a gain relay factor 0.5. The OP performance of the VG system deteriorates 20 dB of performance with the FG relay at an OP of 10^{-2}.

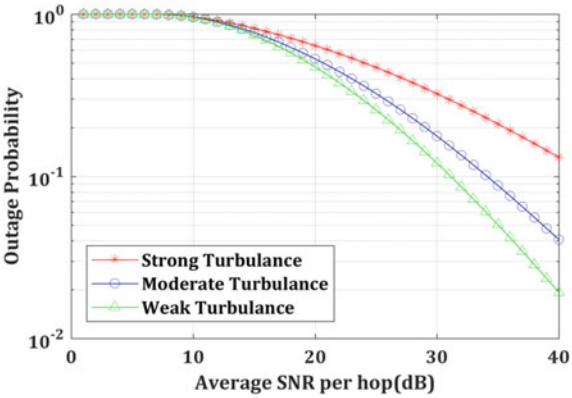

Fig. 3 Outage probability performance for various values of atmospheric turbulence parameters (α and β) with VG relay

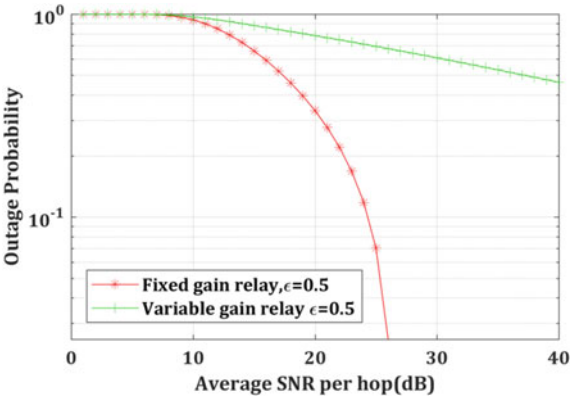

Fig. 4 Outage probability-FG versus VG

Acknowledgements This work was supported by a research grant funded by National Research Foundation (NRF) of Korea grant (No. 2020R1A4A1019463).

References

1. Dubey V, Chadha D, Chandra V (2014) Bit error rate and reliability analysis of cooperative communication in free-space optical systems. Photon Netw Commun
2. Garcia-Zambrana A, Castillo-Vazquez C, Castillo-Vazquez B, Boluda-Ruiz R (2012) Bit detect and forward relaying for FSO links employing equal gain combining over gamma-gamma atmospheric turbulence channels with pointing errors. Opt Express
3. Farid AA, Hranilovic S (2007) Outage capacity optimization for free-space optical links with pointing errors. J Lightwave Technol
4. Zhu XM, Kahn JM (2007) Performance bounds for coded free-space optical communications through atmospheric turbulence channels. IEEE Trans Commun
5. Sejan MAS, Chung W-Y (2021) Security aware indoor visible light communication. In: 2021 IEEE photonics conference (IPC). IEEE pp 1–2

6. Arya S, Chung YH, Chung W-Y, Kim J-J, Kim N-H (2021) Transmit power optimization over low-power poisson channel in multiuser MISO indoor optical communications. ICT Express 7(3):361–365
7. Naik RP, Simha GDG, Krishnan P (2021) Wireless-optical-communication-based cooperative IoT and IoUT system for ocean monitoring applications. Appl Optics 60(29):9067–9073
8. Levidala BK, Ramavath PN, Krishnan P (2021) Performance enhancement using multiple input multiple output in dual-hop convergent underwater wireless optical communication–free-space optical communication system under strong turbulence with pointing errors. Opt Eng 60(10):106106
9. Prabu K, Kumar DS, Srinivas T (2014) Performance analysis of FSO links under strong atmospheric turbulence conditions using various modulation schemes. Optik 125(19):5573–5581
10. Prabu K, Bose S, Kumar DS (2013) BPSK based subcarrier intensity modulated free space optical system in combined strong atmospheric turbulence. Optics Commun 305:185–189
11. Levidala BK, Krishnan P (2020) Asymptotic bit error rate analysis of convergent underwater wireless optical communication-free-space optical system over combined channel model for different turbulence and weather conditions with pointing errors. Optical Eng 59(11):116102
12. Nistazakis HE, Tombras GS, Tsigopoulos AD, Karagianni EA, Fafalios ME (2009) Capacity estimation of optical wireless communication systems over moderate to strong turbulence channels. J Commun Netw
13. Lee E, Park J, Han D, Yoon G (2011) Performance analysis of the asymmetric dual-hop relay transmission with mixed RF/FSO links. IEEE Photon Technol Lett
14. Anees S, Bhatnagar MR (2015) Performance of an amplify-and-forward dual-Hop asymmetric RF-FSO communication system. J Opt Commun Netw
15. Zedini E, Ansari IS, Alouini M-S (2015) Performance analysis of mixed Nakagami-m and gamma-gamma dual-Hop FSO transmission systems. IEEE Photon
16. Gerstacker WH, Obernosterer F, Schober R, Lehmann AT, Lampe A, Gunreben P (2004) Equalization concepts for Alamouti's space-time block code. IEEE Trans Commun 52(7):1178–1190
17. Yang L, Hasna MO, Gao XQ (2015) Performance of mixed RF/FSO with variable gain over generalized atmospheric turbulence channels. IEEE J Sel Area Commun
18. Samimi H, Uysal M (2013) End-to-end performance of mixed RF/FSO transmission systems. J Opt Commun Netw
19. Marvin M-SA, Simon K (2005) Digital communication over fading channels. Wiley, Hoboken, New Jersey
20. Ramavath PN, Udupi SA, Krishnan P (2020) Co-operative RF-UWOC link performance over hyperbolic tangent log-normal distribution channel with pointing errors. Optics Commun 469:125774
21. Li, Sai, Liang Yang (2021) Performance analysis of dual-hop THz transmission systems over α-μ fading channels with pointing errors. IEEE Int Things J

Performance Analysis of Relay-Assisted Free-Space Optical Communication (FSO) Under Gamma-Gamma Atmospheric Turbulence Channels with Pointing Errors

Catherine Protas Tarimo and M. Kulkarni

Abstract The use of infrared and visible spectrum parts in the electromagnetic spectrum has made great changes in communication because of its higher data rate, high security, and larger bandwidth. This technology can be implemented using guided media; that is optic fiber cable or unguided media such as free-space optical communication (FSO). In this work, gamma-gamma distribution with relay-assisted transmission as the main fading mitigation tool for FSO systems under different atmospheric conditions is proposed. The performance was evaluated by considering signal-to-noise ratio (SNR) and BER for a link with different atmospheric conditions using amplify and forward method for the relay transmission, in which geometrical losses and pointing errors were considered. Further, the output power versus distance was analyzed using multiple-input multiple-output (MIMO) technology.

Keywords FSO link · Pointing errors · Gamma-gamma model · Atmospheric attenuation

1 Introduction

FSO is a wireless technology that uses light amplification by stimulated emission (LASER) or light-emitting diode (LED) as a light source and avalanche photodiode (APD), positive-intrinsic-negative (PIN), and positive-intrinsic (PN) as a photo detector to provide a point-to-point connection with higher data rates up to 2.5 gigabytes per second. FSO link consists of three major components as a transmitter, FSO channel, and receiver. A transmitter is the one that converts the electrical signal into an optical signal with the support of LED or LASER as a carrier source.

The transmitter comprises pseudo-random bit sequence (PRBS) generator and modulator, and a receiver consists of a photodiode, an amplifier, and a filter. Although APD, PN, or PIN is the photodiodes used at the receiver, the most preferable photodiode is APD because it has higher internal gain and is highly responsive. The last

C. P. Tarimo · M. Kulkarni (✉)
National Institute of Technology. Karnataka Surathkal, Mangaluru 575025, India
e-mail: mkul@nitk.edu.in

S. Rawat et al. (eds.), *Proceedings of Second International Conference on Computational Electronics for Wireless Communications*, Lecture Notes in Networks and Systems 554,
https://doi.org/10.1007/978-981-19-6661-3_59

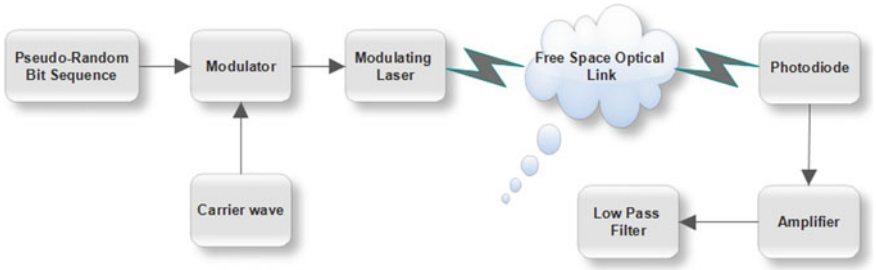

Fig. 1 FSO link

part is the transmitter channel, and this is the free space where the light beam propagates from transmitter to receiver as shown in Fig. 1. As the signal propagates in free space from transmitter to receiver, it encounters different losses due to absorption, scattering, and reflection of the signal.

Despite all listed advantages of this technology, various links in FSO systems are mostly affected by atmospheric conditions that may lead to signal degradation and hence lower SNR while increasing BER. Also, there is a great challenge of distance limitation as it can only transmit at a short distance of around 5 km maximum [1]. Furthermore, if the transmitter and receiver are installed on the top of buildings, they can be affected by the movement of the buildings causing pointing errors in the FSO link [2].

2 Atmospheric Effects

In an FSO link, the signal propagates in free space in the form of the light beam from the transmitter to the receiver. As the signal propagates from the source to the destination, the signal can be distorted due to different effects from the atmosphere. The FSO link is mostly affected by atmospheric instability that affects the performance of the system output. The type of the ground, the effect of the sun, the wind, and a lake nearby are all those elements that will modify the pressure, humidity, and temperature of the air [3]. When temperature, humidity, and pressure change, it makes the refractive index turbulence occur at a very high speed up to kHz. The atmospheric situations such as snow, fog, and rain also affect the operation of the FSO link. Different models have been proposed by many researchers to reduce the effect of atmospheric effects such as K-fading, gamma-gamma model, and log normal.

2.1 Log-Normal Model

Many researchers proposed log-normal model to eliminate weak turbulence in FSO systems. LN can underestimate the peak irradiance value when compared to experimental data. Also, the atmospheric turbulence can be weak, moderate, or strong; therefore, log-normal model cannot work effectively in reducing atmospheric effects, as it is only applicable in weak turbulence [4]. Mathematically, this can be presented as given in Eq. (1).

$$p(I_s|\rho) = \frac{1}{I_s(\rho)\sqrt{2\pi}}\exp\left(\frac{\left(ln\left(\frac{I_s}{I\gamma(\sqrt{\rho})}\right) + \frac{1}{2}\sigma^2(\rho)\right)^2}{2\rho^2(\rho)}\right) \tag{1}$$

where $\sigma^2(\rho)$ is the log-irradiance variance.

2.2 K-Fading PDF Model

Strong turbulence in FSO can be mitigated by using the K distribution fading model [5]. The major weakness of this model (K-fading model) is that it can only deal with strong turbulences in FSO systems. The normalized received beam power in this distribution can be obtained as shown in Eq. (2).

$$P(I) = \frac{2}{\Gamma(\alpha)}\alpha^{(\alpha+1/2)}I^{(\alpha-1)/2}K_{\alpha-1}\left[2(I\alpha)^{1/2}\right] \tag{2}$$

where $\alpha = 2/\left(E\left[I^2\right]\right)$, $K_v(z)$ is the modified Bessel function of the second kind and Γ is the gamma function. The fading PDF in K distribution can be obtained by using conditional exponential distribution as presented in Eq. (3). The given expression is from doubly stochastic theory that assumed that PDF in K is due to the modulation of two stochastic processes.

$$p_1(I/b) = \frac{1}{b}\exp(-1/b)I > 0 \tag{3}$$

where b is the mean value follow the gamma distribution where

$$p_2(b) = \frac{\alpha(\alpha b)}{\Gamma(\alpha)}\exp(-\alpha b), b > 0, \alpha > 0 \tag{4}$$

Therefore,

$$p(I) = \int_0^\infty p_1(I/b)p_2(b)db \tag{5}$$

2.3 Gamma-Gamma Distribution

The gamma-gamma ($\Gamma\Gamma$) distribution attracted many researchers due to its application in communication systems especially in FSO links as it can be used to model weak to strong turbulence. The gamma-gamma model is mostly used for model-independent gamma random variables [6]. Furthermore, the gamma-gamma model in the FSO link can be used to define the variations of the irradiance of optical signals affected by atmospheric turbulence. The gamma-gamma channel model depends on the atmospheric parameters, and it is also used to evaluate fading effects depending on the level of turbulence in the FSO link [6].

$$BER = \frac{2^{\alpha+\beta-3}}{\sqrt{\pi^3}\Gamma(\alpha)\Gamma(\beta)} G_{5,2}^{2,4}\left[\left(\frac{2}{\alpha\beta}\right)^2 x2x\frac{\eta I_o}{\sqrt{2N_o}}\middle| \begin{matrix}\frac{1-\alpha}{2}, \frac{2-\alpha}{2}, \frac{1-\beta}{2}, \frac{2-\beta}{2}, 1 \\ 0, \frac{1}{2}\end{matrix}\right] \tag{6}$$

It assumed small-scale irradiance fluctuations that are modulated by large-scale irradiance fluctuations of the propagating wave. When simple statistical models are considered, it may lower the performance of the link. Also, the channel with correlation under multiple-input single-output (MISO) diversity is modeled by Gaussian distribution, and it is concluded that the operation requires less power at low BER. BER in turbulence channel using gamma-gamma model can be expressed as shown in the given Eq. (6).

3 Pointing Errors

Normally, wide-beam widths with stable and constant information can safely be installed on top of buildings. For narrow beam links installed on buildings, re-adjustment of the transmitting device and receiving device is required due to small movements of the buildings. Most of the FSO links are installed on the top of buildings that are much affected by wind, thermal expansion of building parts, weak earthquakes, and building sway; all of these result in pointing errors [7]. BER in pointing errors and turbulence channel gamma-gamma model for large SNR is given in Eq. (7).

$$ER = \frac{2^{\beta-1}\Gamma\left(\frac{\beta}{2}+\frac{1}{2}\right)\exp\left(-\frac{s^2}{2\sigma_s^2}+\frac{-s^{2\gamma^2}_{\sigma_s^2}}{2\beta-2\gamma^2}\right)\left(\frac{\alpha\beta}{A_0}\right)^{\beta}}{\Gamma(\alpha)\Gamma(\beta)\sin[(\alpha-\beta)\pi]\Gamma\left(-(\alpha-\beta)+1\middle|\gamma^2-\beta\middle|\beta\right)} \times \Gamma\left(\frac{\beta+1}{2}\right)\sqrt{\pi}\gamma^2\left(\frac{\eta I_0}{\sqrt{2N_0}}\right)^{\frac{-\beta}{2}} \tag{7}$$

4 Relay-Assisted FSO Link

Relay-assisted FSO link involves a source node where the signal propagates through several relays to reach the receiving point. The relay nodes can be configured in series or parallel depending on the system [8]. Figure 2 depicts an FSO system that comprises a relay (R), destination (D), and source (S), and they are all separated at a distance of D1, D2, and D3.

The distances from source to destination and source to relay are D1 and D2, respectively, while the relay to signal destination distance is D3. By considering amplify and forward technique, the relay will just amplify the received signal to a certain level required and send it as it is to the destination. Consider the design model diagram as presented in Fig. 2, when the source broadcast symbol x the output can be received by both the relay (R) and destination (D), mathematically this can be expressed as in Eq. (9).

$$y_R = h_{D2}x + n_R$$

$$y_D = h_{D1}x + n_D$$

$$y_{RD} = h_{D3}\beta_{yR} + n_D$$

$$\beta = \sqrt{\frac{P_R}{P_s|h_{D2}|^2\sigma_D^2}} \tag{8}$$

where β= scaling factor

$$y_{RD} = \sqrt{\frac{P_R}{P_s|h_{D2}|^2 + \sigma_D^2}} h_{D3}h_{D2}x + n'_D \tag{9}$$

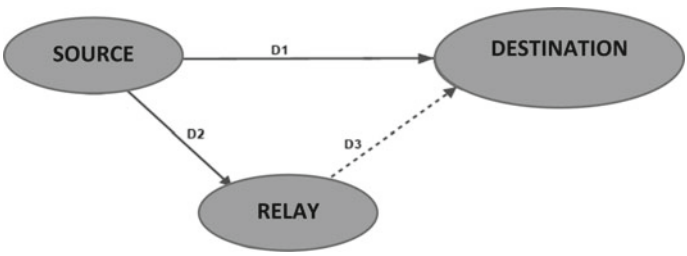

Fig. 2 FSO link block diagram with relay

$$n_D^{'} = \sqrt{\frac{P_R}{P_s|h_{D2}|^2 + \sigma_D^2}} h_{D3} n_R + n_D \tag{10}$$

The destination received two copies of the original signal that is from the relay after amplification (D3) and also from the source to the destination through path the labeled D1. Maxima ratio combining (MRC) was used to combine the signal from the source and the relay at the destination.

$$y_D = W_{D1} y_{D1} + W_{D3} Y_{D3} \tag{11}$$

where W_{D1} and W_{D3} are for maximizing SNR

$$W_{D1} = \frac{h_{D1}^*}{\sigma^2 D} \tag{12}$$

$$W_{D3} = \frac{\sqrt{\frac{P_R}{P_s|h_{D2}|^2 + \alpha_D^2}} h_{D2}^* h_{D3}}{\frac{P_R |h_{D3}|^2 \sigma_R^2}{P_R h_{D3}^2 + \sigma_D^2} + \sigma_D^2} \tag{13}$$

When the signal propagates from one point to another, it encounters different obstacles such as trees and buildings. The transmitted signal may scatter and lead to numerous copies of the transmitted signal at the receiver which is termed multipath fading [9].

$$y_b(t) = hS_b(t) \tag{14}$$

where $h =$ complex function coefficient and S_b is the transmitted signal. The amplitude of this multipath channel follows Rayleigh probability density function, in which the complex fading coefficient can be presented as shown in Eq. (15).

$$h = \sum_{i=0}^{L=1} a_i e^{-j2\pi f \tau_i} = 1 = x + iy = ae^{j\phi} \tag{15}$$

$$f_X(x) = \frac{1}{\sqrt{2\pi\,\partial^2}} e^{-\frac{(x-\pi)^2}{2\partial^2}} \tag{16}$$

X is the Gaussian random variable with mean μ and variance σ, i.e., $\mathcal{N}(\mu, \partial^2)$.

$$f_{A,\phi} = \frac{1}{\pi} e^{-a^2} det(J_{XY}) \tag{17}$$

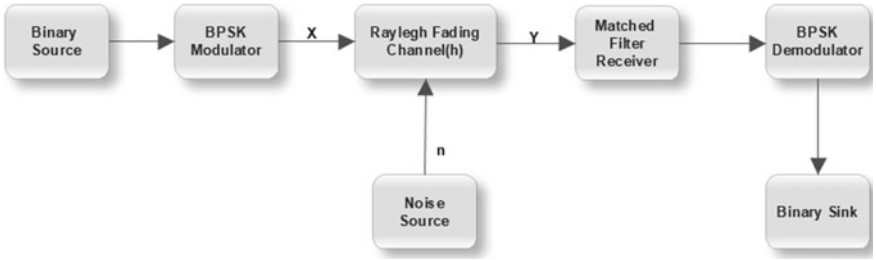

Fig. 3 Wireless communication system model diagram

5 BER Analysis

Bit error rate (BER) expresses the ratio of bits with errors in a given system percentage-wise to the total number of bits received in percentage [10].

As depicted in Fig. 3, the binary source will generate binary codes and send them to the BPSK modulator to add them to a carrier signal, and the output (x) generated will be multiplied by the fading coefficient (h) generated from Rayleigh fading channel. The output vector received combines the additive white noise signal from the external environment and the channel.

$$y = hx + n \tag{18}$$

$$\text{Received power} = PX|h| \tag{19}$$

$$P_{\text{rad}} = PXa^2 \tag{20}$$

Then let:
P = power of the signal and σ_n^2 = noise power

$$\text{Received SNR} = \frac{a^2 P}{\sigma_n^2} \tag{21}$$

6 System Setup Using OptiSystem Software

As depicted in Fig. 4, the proposed system setup consists of a bit sequence generator for generating random bits at 10 Gbits per second, an NRZ pulse generator, and an optical transmitter that can transmit at a frequency of 193.1 THz.

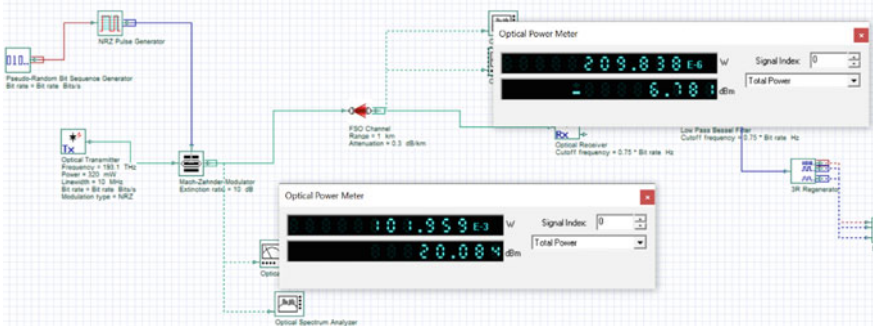

Fig. 4 FSO link at a distance of 1 km (one FSO channel)

Table 1 FSO link 1 design parameters

S. No.	Parameters	Values
1	Transmit power in mW	320
2	Frequency in THz	193.1
3	Transmitter wavelength in nm	1550
4	Link distance in Km	1, 2, 3, 4, 5
5	Transmitter and receiver aperture in cm	10, 20
6	Transmission rate in Gbps	1
7	Attenuation (dB/Km)-clear sky	0.3
8	Beam divergence (mrad)	1
9	Geometrical losses	YES

Additionally, the system consists of a Mach–Zehnder modulator to modulate the message signal and the carrier signal, and an optical amplifier amplifies the signal after modulation.

It also consists of an OWC channel to transmit the optical signal in free space, optical power meter to measure the output power, an optical spectrum analyzer, an optical receiver that is used to convert the received signal into electrical for am, a low-pass filter, and BER analyzer to analyze the output of the system. The parameters of each component are given in Table 1.

7 Results and Discussion

Figure 5 depicts the transmission link of 0.5 km between transmitter and receiver. It shows that there is a minimal difference between the simulated and theoretical results. The performance can be obtained by considering the SNR and BER values, the simulation results give a result of 45.35 for SNR, and BER is 0.0001198.

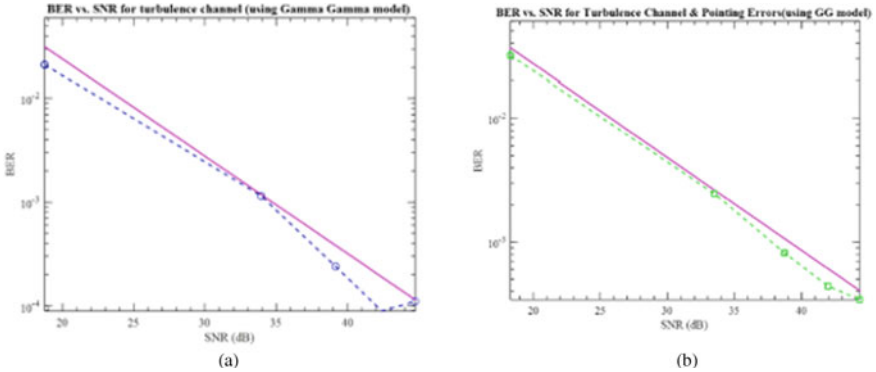

Fig. 5 BER versus SNR at a link distance of 0.5 km in **a** and 0.9 km in **b**

Figure 5b shows the effect of pointing errors and transmitter–receiver distance on the performance of the FSO link. From analysis, the SNR was reduced to 43.9, while BER increased to 0.0006118 as shown in Fig. 5 Likewise, the quality factor was reduced from 1.066 to 1.01. These results imply that the performance of the system was reduced due to the effect of point errors and link distance. As depicted in Fig. 6, the simulation and theoretical values do not indicate a significant difference. Also, the effect of amplifying and forward using relays can be observed.

The effect of FSO channels is depicted here under, where the output power of −3.575 dBm was obtained when two FSO channels were used and −2.095 dBm when four FSO channels were used, both at a distance of 1 km as shown in Fig. 7 and Fig. 8, respectively, implying that the output power improved as the number of

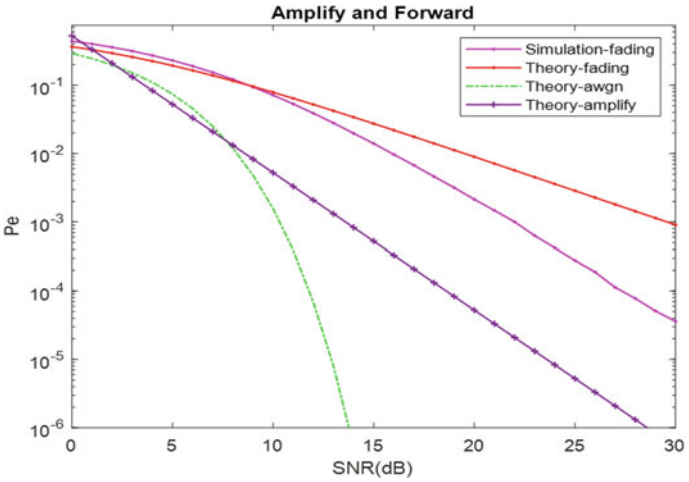

Fig. 6 Pe versus SNR with amplify and forward

FSO channels increased. Similarly, output power using BER analyzer is depicted in Fig. 9.

Table 2 gives the output power FSO link. It is perceived from the results that as the distance increases, the output power is reduced. This is well stated by the Friis transmission equation which describes how output power can be reduced at a distance including the gain of transmitting and receiving antennas.

Figure 10 depicts the three scenarios of using a different number of FSO channels at a distance of 1 km to 5 km. It can be seen that using two FSO channels at a distance of 3 km, the output power is −13.58 dBm, and by using one FSO channel at a distance of 2 km, the output power is −13.029 dBm.

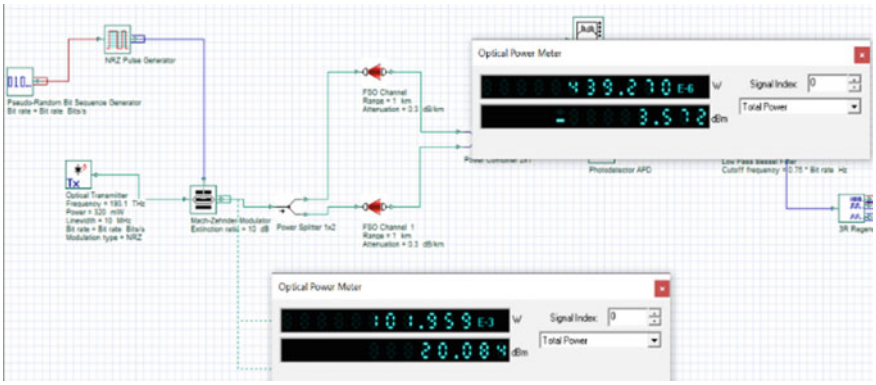

Fig. 7 FSO link at a distance of 1 km (two FSO channels)

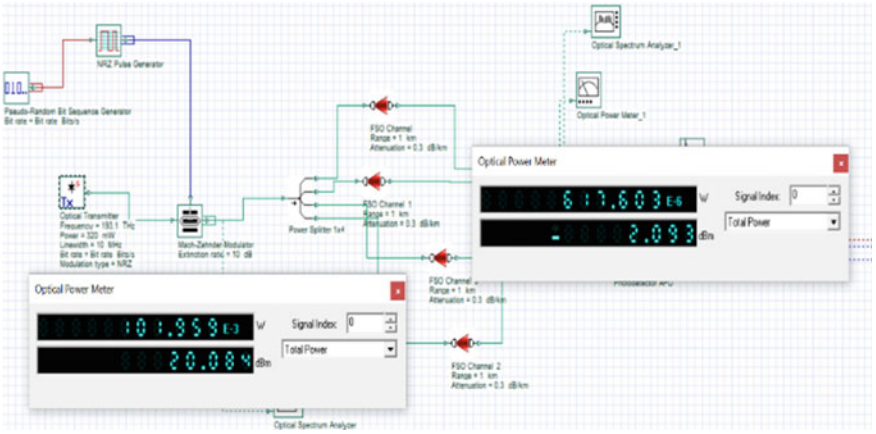

Fig. 8 FSO link at a distance of 1 km (four FSO channels)

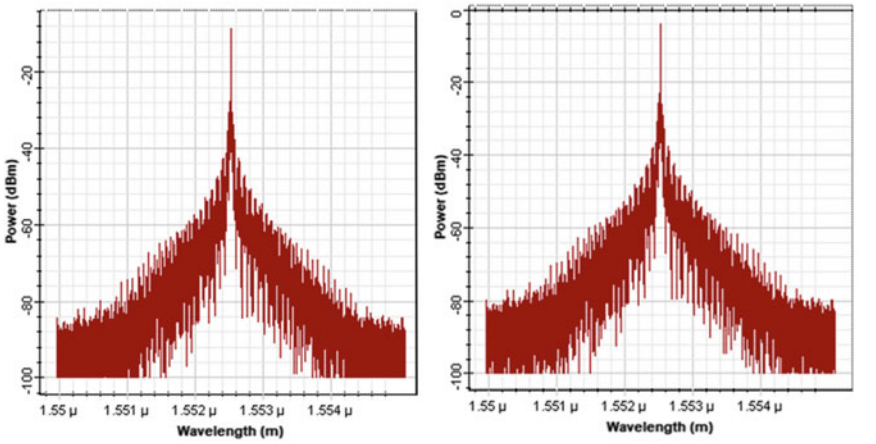

(a) BER Analyzer Output Power (1 FSO Channel) (b) BER Analyzer Output Power (4 FSO Channel)

Fig. 9 BER analyzer

Table 2 FSO link 2 design parameters

Distance (Km)	One FSO channel	Two FSO channels	Four FSO channels
1	−6.701	−3.575	−2.095
2	−13.029	−9.799	−6.573
3	−16.820	−13.580	−10.341
4	−19.614	−16.371	−13.113
5	−21.846	−18.550	−15.335

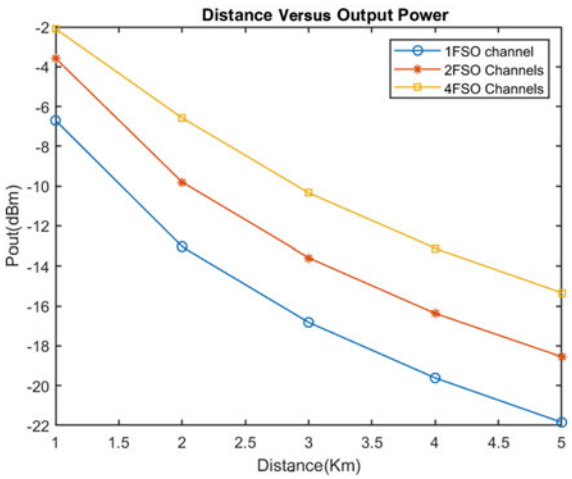

Fig. 10 Output power versus distance in FSO link

The links have approximately the same output power but at a different distance. This means that the use of more than one FSO channel (MIMO) extends the distance coverage with an improvement in system performance.

8 Conclusion

The FSO communication is more important in high-speed data rate and security; it has the best properties which make it more inspiring than radio frequency communication. Different channel models can be used to describe the operation of the FSO system at different levels of turbulence scenarios. Among all studied models, it is concluded that the gamma-gamma model is more efficient and gives out a good performance compared to other models. Also, the use of relay-assisted transmission system is recommended to improve the performance of the system and extend the coverage distance of the FSO link. Through the use of a power combiner and more than one receiving antenna, the analysis shows that the output power of the link can be improved. The results have been presented through simulations using MATLAB software and OptiSystem software. Different parameters were used such as SNR, BER, Q factor, output power, and eye diagram. The results are presented and studied for each case.

References

1. Mohammed NA, El-Wakeel AS, Aly MH (2012) Pointing error in so link under different weather conditions. Fog 15(33.961):84–904
2. Uysal M, Li J, Yu M (2006) Error rate performance analysis of coded free-space optical links over gamma-gamma atmospheric turbulence channels. IEEE Trans Wireless Commun 5(6):1229–1233
3. Sahota JK, Dhawan D (2018) Reducing the effect of scintillation in FSO system using coherent based homodyne detection. Optik 171:20–26
4. Layioye OA, Afullo TJO, Owolawi PA (2017) Performance analysis of FSO communication systems with higher-order spatial diversity schemes using BPSK-sim over log-normal atmospheric turbulence channels. J Commun 12(6):312–327
5. Khanna H, Aggarwal M, Ahuja S (2018) Performance analysis of a variable-gain amplify and forward relayed mixed rf-fso system. Int J Commun Syst 31(1):e3400
6. Chatzidiamantis ND, Sandalidis HG, Karagiannidis GK, Kotsopoulos SA, Matthaiou M (2010) New results on turbulence modeling for free-space optical systems. In: 2010 17th international conference on telecommunications. IEEE, pp 487–492
7. Borah DK, Voelz DG (2009) Pointing error effects on free-space optical communication links in the presence of atmospheric turbulence. J Lightwave Technol 27(18):3965–3973

8. Nor NAM, Ghassemlooy Z, Zvanovec S, Khalighi MA, Bhatnagar MR, Bohata J, Komanec M (2019) Experimental analysis of a triple-hop relay-assisted fso system with turbulence. Opt Switching Networking 33:194–198
9. Jahid A, Alsharif MH, Hall TJ (2022) A contemporary survey on free-space optical communication: potentials, technical challenges, recent advances, and research direction. J Network Comput Appl 103311
10. Alam SJ, Alam MR, Hu G, Mehrab MZ (2011) Bit error rate optimization in fiber optic communications. Int J Mach Learn Comput 1(5):435

An Improved Expectation-Based Multi-attribute Multi-hop Routing (IEM^{2}R) in Underwater Acoustic Sensor Networks

Akhilraj V. Gadagkar and B. R. Chandavarkar

Abstract Underwater Acoustic Sensor Networks (UASNs) uses acoustic signals as a physical layer medium for communication underwater. The distinct characteristics of acoustic communication channel make reliable routing a challenging task in underwater applications. To handle this, an Expectation-Based Multi-Attribute Multi-Hop Routing (EM^{2}R) was proposed, which selects the best next-hop using an expectations-based multi-attribute ranking based on multiple attributes that are node's residual energy and distance. However, in EM^{2}R node mobility was not considered, which is inevitable underwater. Also, fetching the attributes incurs communication overhead and is prone to attacks. Further, it is crucial to optimize the timing of executing expectation-based multi-attribute ranking in deciding the best next hop. To address these issues, this paper proposes an extension to the previous work called an Improved Expectation-Based Multi-Attribute Multi-Hop Routing (IEM^{2}R). The IEM^{2}R introduces node mobility and implements a prediction model which uses distance and predicted energy as attributes and predicts the best next hop. The proposed method implemented in the industry standard underwater network simulator UnetStack3 is described. Additionally, results show the predicted and actual next-hop selection, energy depletion, average end-to-end delay, and throughput.

Keywords Node mobility, Comunnication overhead, Prediction model, Predicted energy, UnetStack3

A. V. Gadagkar (✉) · B. R. Chandavarkar
Wireless Information Networking Group (WiNG), Department of Computer Science and Engineering, National Institute of Technology Karnataka, Surathkal, Mangalore, India
e-mail: gadagkar.akhil@gmail.com

S. Rawat et al. (eds.), *Proceedings of Second International Conference on Computational Electronics for Wireless Communications*, Lecture Notes in Networks and Systems 554,
https://doi.org/10.1007/978-981-19-6661-3_60

1 Introduction

Our planet earth has more than 70% of water in the form of oceans, rivers, and other water bodies. Over the years, Underwater Acoustic Sensor Networks (UASNs) have gained significant attention with its advantage in various underwater applications. some of them are military surveillance, pollution monitoring, offshore exploration, disaster monitoring, marine life study, underwater resource exploration, etc. [1–4]. For most underwater applications, acoustic communication is considered the preferred option. However, the distinct characteristics of the acoustic channel, such as huge propagation delay, limited bandwidth, multipath effects, high bit error rate, and substantial node mobility, make reliable routing in underwater a challenging task [5–7].

To handle the issues mentioned above of underwater communication medium a routing technique named EM^{2}R was proposed in our previous work [8]. The algorithm employed expectation-based multi-attribute ranking in selecting the best next forwarding node, considering the node's left out energy and the distance as multiple attributes. The multi-attribute ranking has the benefits of overcoming the critical limitations of conventional multi-attribute decision making (MADM) methods that are ranking unreliability and rank reversals in decision making [9].

Although the protocol achieved reliable data transfer by effectively choosing the optimal forwarder. However, for applications requiring long-term deployment and containing sensor nodes tethered with cables to the ocean bottom, which makes them quasi-stationary, allowing nodes to drift with water currents [10]. Since mobility was not taken into account in the previous work [8], a selected next-hop can go out of the coverage area during communication. The selected next-hop might become invalid after a short duration affected by the distance if the node floats away from the communication range. Further, the literature states that residual energy and node mobility are vital attributes for deciding an optimal path for routing in sensor networks [11]. However, fetching these attributes is a major concern. Whether the parameters are requested and fetched from neighboring nodes or they are predicted by the source. A severe drawback in fetching attributes is that it incurs communication overhead and is prone to attacks.

Motivated by these factors, this work proposes an Improved Expectation-Based Multi-Attribute Multi-Hop Routing (IEM^{2}R) for UASNs, which incorporates mobility in the network, performs residual energy prediction. Most importantly introduces a prediction model to select the best forwarder. The circular motion mobility model is applied to the source node. The source nodes are typically tethered to the sea bed and restricted to circular motion centered to the anchor. Further, the prediction model uses expectation-based multi-attribute ranking to select the best forwarding node based on the predicted values of the attributes. Thus, significantly reducing the fetching of actual attributes by source from its neighbors, reducing the energy spent by the nodes and the traffic in the network. Additionally, the timing for ranking the node to update the best forwarder is also optimized. The objectives of this paper are as follows:

- Incorporation of node mobility, which brings the dynamic nature of underwater network topology and influences the routing performance.
- Development of Prediction model and neighbor's residual energy prediction
- Implementation and performance analysis of IEM^{2}R through simulation in Unet-Stack3

The remainder of the paper is structured as follows. Section 2 presents a survey on protocols that uses prediction based approach. The design of IEM^{2}R is described in Sect. 3. Section 4 presents the implementation details of IEM^{2}R in Unet-Stack3. Section 5 depicts the results and analysis of IEM^{2}R in terms of predicted and actual next-hop selection, energy depletion, end-to-end delay and throughput. Finally, Sect. 6 draws the conclusion and future work.

2 Literature Survey

This section of the paper presents survey on different protocols that works based on prediction of one or more routing attributes. Prediction can significantly improve the efficiency of protocols. However, the accuracy of the prediction plays a vital role in deciding the efficiency.

The prediction based opportunistic routing(POR) proposed by Wu et. al. [12] for martime search and rescue wireless sensor network. The work focuses on prioritizing best forwarding nodes to send data from source to sink in a highly dynamic martime search and rescue WSN. The authors extend the existing opportunistic routing that uses a combination of geographic location and link quality to prioritize forwarding node and propose a time series based prediction method to cut down the communication overhead incurred by reducing the frequency of location and link quality information exchange between nodes.

Yu et. al [13] proposed a local energy consumption prediction-based clustering protocol (LECP-CP) which uses predicted local energy loss of nodes as an attribute for the selection of cluster head so as to optimize the global energy loss. In addition the authors also propose a routing tree construction method for inter-cluster communication which also uses the local energy loss of the nodes.

A prediction model for the ocean current movement proposed in [14] for optimal routing scheduling strategy in underwater wireless sensor networks. Considering the left out energy, distance to the sink and the predicted path of the nodes, a particle swarm optimization algorithm is used to determine an optimal scheduling scheme. The proposed work aims to address the routing hole and hidden terminal issues caused by the movement of nodes due to ocean currents.

Raj Priyadarshini and Sivakumar [15] proposed a routing protocol for underwater acoustic wireless sensor network with mobility called the modified HH-DAB which is an altered version of existing HH-DAB to increase the network coverage and

connectivity . Their proposed modified HH-DAB is based on energy prediction using Markov Chain Monte Carlo (MCMC) based on water temperature and pressure of water surface.

Zhang et. al. [16] proposed an algorithm to overcome communication overhead by predicting node movement. Their algorithm is designed to work in two stages. First is the mobility prediction and second is localizing the node.

Song et. al. [17] presented a method for estimating node speed and predicting location to overcome challenges in navigation of autonomous underwater vehicles (AUVs).

3 Design of IEM^{2}R

This section of the paper presents the design of the proposed Improved Expectation-Based Multi-Attribute Multi-Hop Routing (IEM^{2}R) protocol. IEM^{2}R is the extensions of one of our published work referred to as EM^{2}R addressing most of its limitations. One of the major limitations of EM^{2}R is the time of its execution for selecting the best next hop, which has been addressed by IEM^{2}R with the inclusion of the prediction model.

Fig. 1 presents the overall relation between EM^{2}R and the prediction model referred to as IEM^{2}R. The initial execution of the EM^{2}R is independent of the prediction model decision. However, the future execution of the EM^{2}R is decided based on the decision of the prediction model. Since the design of the EM^{2}R is limited to the energy and distance, the same is retained in IEM^{2}R as predicted energy and calculated distance.

3.1 Design of the Prediction Model

Figure 2 presents the prediction model of the IEM^{2}R. As shown in Fig. 2, there is regular event of predicting the energy loss of all the probable next hop based on the data transfer rate of the source. Further, the predicted energy of all the probable next hops are updated as follows;

predicted energy ← actual energy
TickerBehavior every data rate interval **do**
  predicted energy ← predicted energy - predicted energy loss
end TickerBehavior

However, the predicted energy loss of all the probable next hop decided by the current status. If a probable next hop is the current best hop, the predicted energy loss will be a function of energy loss due to reception and transmission, otherwise, energy loss due to only over hearing.

Algorithm 1 UnetStack: Prediction model implementation

```
1: function PREDICTIONMODEL
2:     preAttr ← null
3:     preRval ← new Result()
4:     nodeLoc1 ← [ ]
5:     nodeLoc2 ← 3D co-ordinates of relay node1
6:     nodeLoc3 ← 3D co-ordinates of relay node2
7:     TickerBehavior interval do
8:         nodeLoc1[0] ← current x co-ordinate
9:         nodeLoc1[1] ← current y co-ordinate
10:        nodeLoc1[2] ← current z co-ordinate
11:        preDist2 ← getDistance(nodeLoc1,nodeLoc2)
12:        preDist3 ← getDistance(nodeLoc1,nodeLoc3)
13:        preAttr ← preEn2,preDist2
14:        predictionTable.add ← preAttr
15:        preAttr ← preEn3,preDist3
16:        predictionTable.add ← preAttr
17:        preRval ← EBMMR*(predictionTable)
18:        preHop ← preRval.nodeid
19:        if preRval.nodeid != nextNode then
20:            return 1
21:        else
22:            return 0
23:        end if
24:    end TickerBehavior
25: end function
```

When the prediction interval expires, it takes the predicted energy (PE_i) and calculated distance (D_i) of all the neighbors based on the current 3-dimension co-ordinates of the source. As the source node is mobile, the distance between the source and the neighbors changes over time depending on velocity and angle of the source. However, the distance is not calculated at data rate interval since the distance calculation is independent to the data rate. Further, the prediction model executes EM^{2}R*[1] and selects the predicted best hop. Finally, checks if the predicted best hop and actual best hop is same, then outputs a 0, otherwise outputs 1.

4 Implementation of IEM^{2}R in UnetStack

This section provides implementation details on the proposed prediction based routing algorithm (IEM^{2}R) designed for use in UASN routing.

In the implementation of proposed system, excluding the surface node, the relay nodes are engaged either in attribute response or forwarding data to the surface node. The source or sender node is engaged in finding or update its routing table with best

[1] Here, the * indicates that the last stage of EM^{2}R [8] (sending data packets via selected node) is excluded in the prediction model of IEM^{2}R.

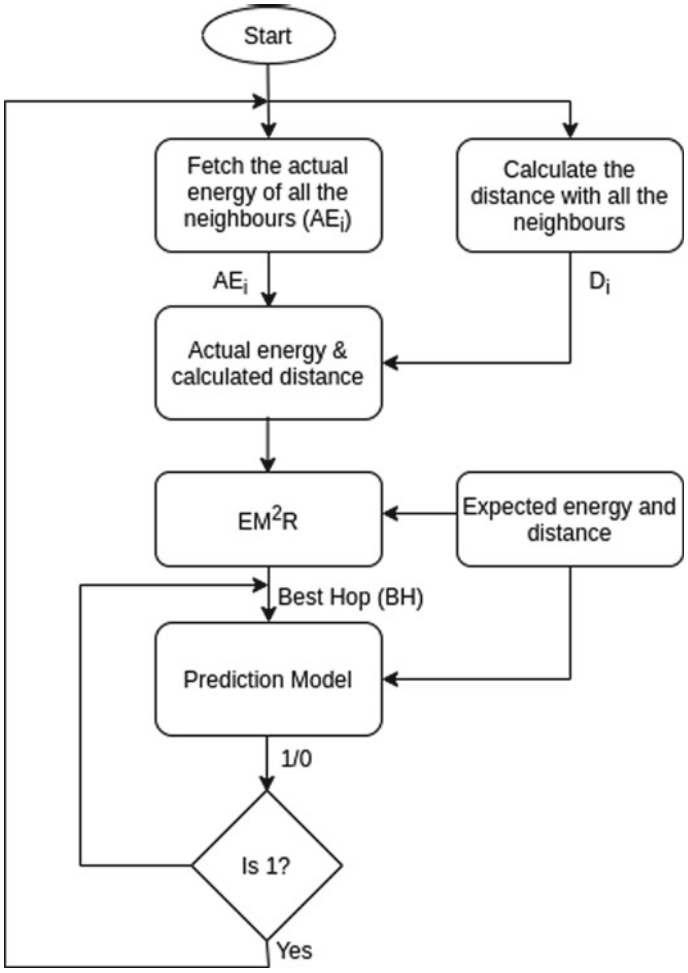

Fig. 1 IEM^{2}R design

forwarder. At the source or sender node, after the initial network and route setup with the existing EM^{2}R. The source or sender node operates in one of the two modes for selection of the best forwarding node. One is the prediction mode, in which, based on the output of the prediction model, the existing forwarder is retained or the routing table is updated with best forwarder switching to the actual mode. In both the modes, the source or the sender node runs the Expectation-Based Multi-Attribute ranking.

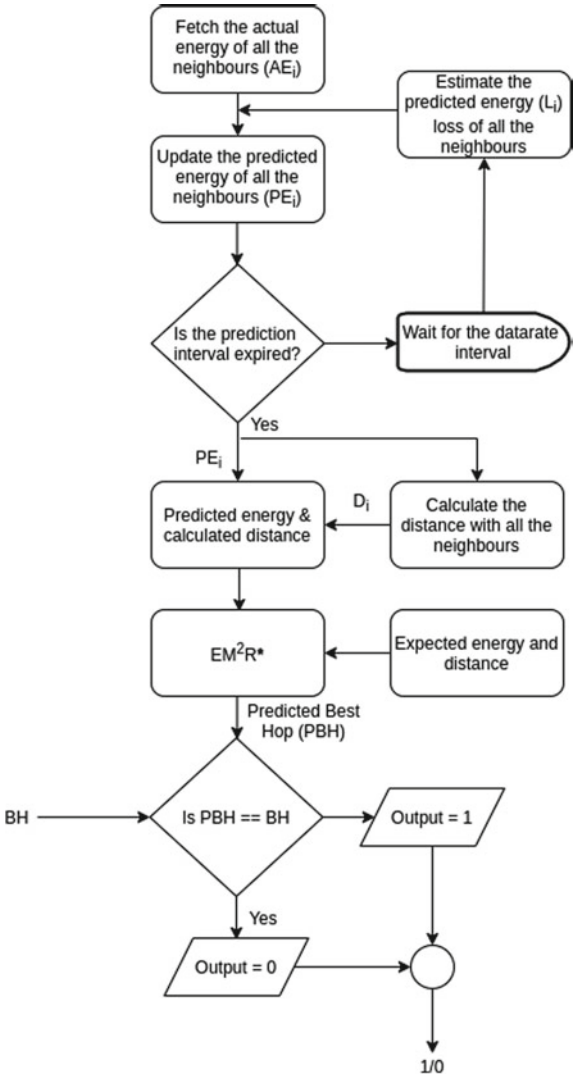

Fig. 2 Prediction model design

4.1 Implementation of Prediction Model in UnetStack

The prediction model runs periodically, it takes multiple attributes as input and outputs either a zero or one. In the proposed work the predicted residual energy of neighboring nodes and the distance to the neighboring nodes are taken as multiple attributes. The prediction of residual energy depends on the data rate, as the energy loss for all the events that occur at the neighbor node has to be predicted for each packet transmitted. In UnetStack, the node is defined as derived agent of UnetAgent.

For the source node, initially, the `startup()` method of UnetAgent is overridden obtaining AgentID of NODE_INFO, PHY and ROUTING services. At next, to send data and to predict energy loss at potential neighbors at the interval of data rate specified. A behavior called `DSBehavior` is defined which is an instance of `TickerBehavior`.[2] The `DSBehavior` handles sending the data via the selected next hop and calculations for the energy loss for the selected next hop and other neighbors in the vicinity.

Further, the source node defines `predictionModel()` method which is invoked in the `startup()` (Ref. Algorithm 1). The `predictionModel()` comprises a `TickerBehavior` to make the model to run periodically. When the model runs it calculates the current distance between the source and its neighbors. As the distance changes overtime with the mobility of the source node. To calculate the distance the model fetches the current 3D co-ordinates of source and of its neighbors using the indexed parameter `location` of the NODE_INFO service. It then calls the `getDistance()` method which returns the calculated distance based on the Euclidean distance. After calculating the distances between the neighbor nodes, the source obtains the predicted residual energy of the neighbors and stores the predicted energy and the distance in the predictionTable. Thereafter, the model invokes expectation-based multi-attribute ranking to get the predicted next hop. Finally, compares the predicted next hop with the current selected next hop and returns its decision.

5 Results and Analysis

This section presents results of IEM^{2}R with changes in the next hop based on predicted attributes and actual attributes ranking, predicted and actual energy depletion at neighbors for transmission, reception and overhearing. Further, the end-to-end packet delay and throughput obtained in the simulation of IEM^{2}R for the topology shown in Fig. 3. As per the topology shown in the figure, the values between the edges of node represents the Euclidean distance, numbers inside the nodes denotes the node address. Node-1 and Node-5 are labelled as Source and Sink respectively. The Sink node is at the water surface, other nodes are submerged in water at different depths. Node-2 and -3 are in the coverage area of Node-1 and thus are the neighbors of Node-1. The Node-4 is in the coverage area of Node-5 (Sink), Node-3, and Node-2, and act as intermediate node between Node-3 and sink with route connecting Node-3 to Sink.

The graph in Fig. 4 shows the actual and predicted energy loss at the neighbor nodes for the transmission event. Depletion of energy at neighbor node for transmission event occurs when that node is selected as next hop by the source. As the selected node has to further forward the data received by the source which is in turn a transmission event. As shown in Fig. 4, mapping with the actual next hop selection made by the source (Node-1). Initially Node-3 is selected as next hop thus, in Fig.

[2] https://fjage.readthedocs.io/en/latest/behaviors.html#ticker-behavior.

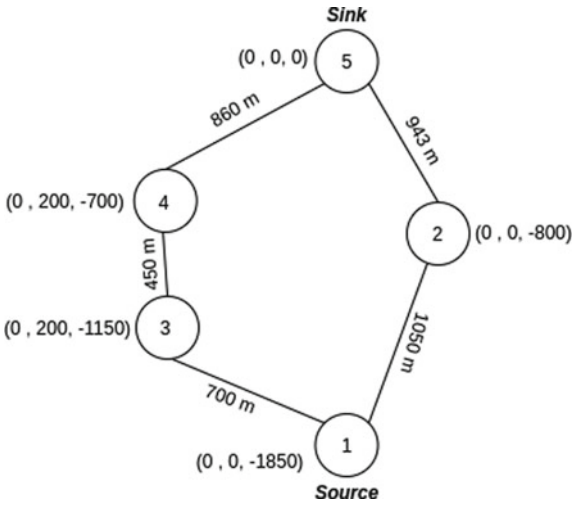

Fig. 3 Topology used for IEM^{2}R simulation

4 depletion can be seen for Node-3, whereas, there is no depletion at Node-2 as it is not involved in forwarding. Later, in Fig. 4 when the source switches the next hop to Node-2 then depletion can be seen at Node-2 and no depletion at Node-3.

Similar to the graph in Fig. 4 depicts the actual and predicted energy depletion at neighbor nodes for reception event. Like in the transmission event, energy depletion at the neighbor node for the reception occurs when the node is acting as selected next hop. The selected node has to receive the data sent from the source. Mapping with the graph in Fig. 4 corresponding to the actual next hop selection, energy depletion can be seen at Node-3 and -2 in Fig. 4.

The graph in Fig. 4 depicts the actual and predicted energy depletion at neighbor nodes for overhearing. Energy depletes for this event occurs when a node involved in overhearing the transmissions or receptions made by other neighbors in the vicinity. In connection with the graph in Fig. 4 and topology shown in Fig. 3 the energy depletion for overhearing can be seen in Fig. 4. When Node-3 is selected as next hop, the Node-2 overhears the transmissions and receptions made by Node-3 for which the energy depletes at Node-2. Further, Node-9 which is next to Node-3, receives data from Node-3 and forwards to sink (Node-9). This causes overhearing at both Node-3 and Node-2 which are in the range of Node-9. Similarly, when Node-2 is selected as next hop, the Node-3 overhears the events that occur at Node-2 for which the energy depletion at Node-3 can be seen.

The graph in Fig. 5 presents the averaged end-to-end packet delay at each interval between Node-1 (Source) and Node-5 (Sink) for the packets sent at the specified data rate. The graph shows variations the delay corresponding to the actual next hop selection in Fig. 4 and the topology shown in Fig. 3. When Node-3 is selected as next hop an increase in the delay can be seen due to the increase in the hop count to reach the sink.

The graph in Fig. 5 presents the throughput estimated at each interval for the packets received at Node-5 (Sink). With reference to the graph in Fig. 4, a slight

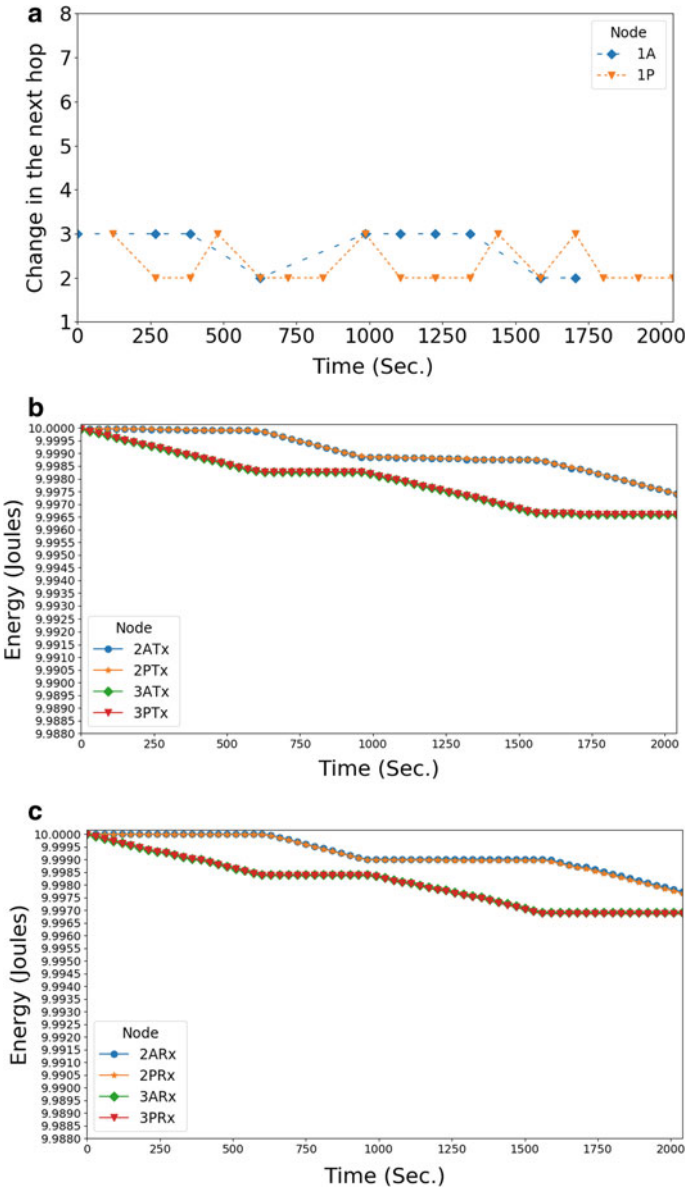

Fig. 4 Predicted and actual next hop selection and energy loss. **a** Next hob selection. **b** Energy loss for transmission. **c** Energy loss for reception. **d** Energy loss for overhearing

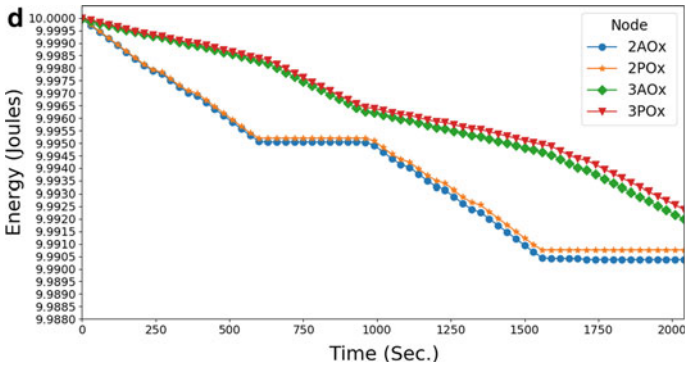

Fig. 4 (continued)

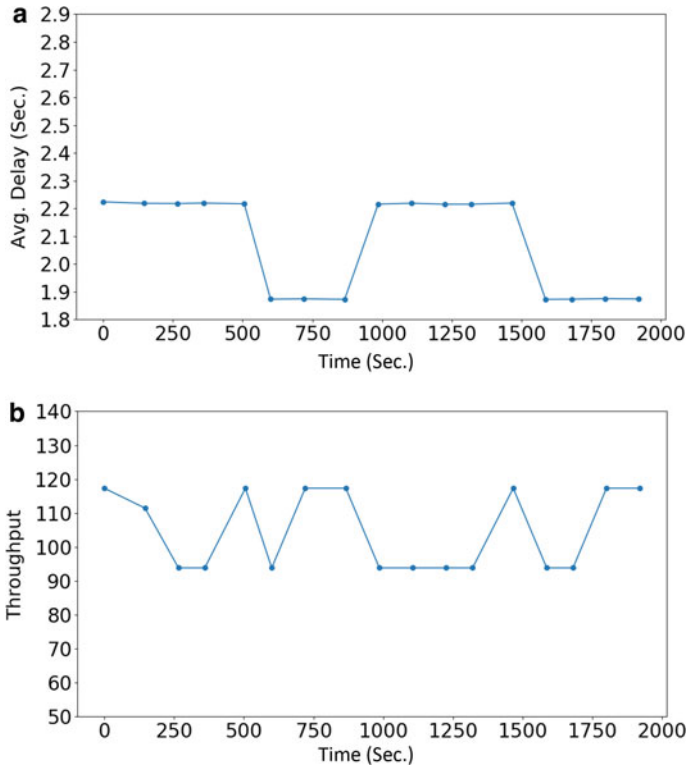

Fig. 5 Average end-to-end delay and throughput at each interval. **a** Delay between Node-1 and 5. **b** Throughput between Node-1 and 5

decrease in the throughput can be observed at the intervals where the actual EM^{2}R is executed. This is due to the collisions that occurs with exchange of attribute request and response between source and the neighbors.

6 Conclusion and Future Work

In this work an Improved Expectation-Based Multi-Attribute Multi-Hop Routing (IEM^{2}R) is proposed for UASNs. In order to improve the performance of Expectation-Based Multi-Attribute Multi-Hop Routing (EM^{2}R) proposed in our previous work [8]. IEM^{2}R introduces node mobility by applying circular motion model to the source nodes, performs residual energy prediction to avoid communication overhead, and introduces a prediction model. The prediction model takes distance and predicted residual energy as multiple attributes and predicts the next hop selection. Based on the output of the prediction model it is decided whether data can be transferred with the current next hop or best next hop should be determined by fetching actual attributes. The proposed work is implemented in UnetStack3 and its performance is presented through predicted and actual next hop selection, predicted and actual energy depletion, average end-to-end delay and throughput.

The proposed IEM^{2}R is not limited for the distance and predicted energy attributes, since our previous work was designed to work with these attributes the same are retained in this work. Further, the timing of the execution of prediction model can be made dynamic depending on the network behavior which is considered as future work. In addition, as the implementation and simulation of proposed work is done in UnetStack3. The same code can be run on an UnetStack compatible modem without the overhead of altering the code. Thus an real-time deployment and analysis of the proposed method can also be done.

Acknowledgements The authors thank the Science and Engineering Research Board (SERB), Govt. of India, for providing financial support (Ref. No. EEQ/2018/001036).

References

1. Akyildiz IF, Pompili D, Melodia T (2005) Underwater acoustic sensor networks: research challenges. Ad hoc networks 3(3):257–279
2. Akyildiz IF, Pompili D, Melodia T (2006) State-of-the-art in protocol research for underwater acoustic sensor networks. In: Proceedings of the 1st ACM international workshop on Underwater networks, pp 7–16
3. Lanbo L, Shengli Z, Jun-Hong C (2008) Prospects and problems of wireless communication for underwater sensor networks. Wirel Commun Mob Comput 8(8):977–994
4. Pompili D, Akyildiz IF (2009) Overview of networking protocols for underwater wireless communications. IEEE Commun Magaz 47(1):97–102

5. Jouhari M, Ibrahimi K, Benattou M, Kobbane A (2016) New greedy forwarding strategy for UWSNs geographic routing protocols. In: International wireless communications and mobile computing conference (IWCMC), IEEE, pp 388–393
6. Ghoreyshi SM, Shahrabi A, Boutaleb T (2015) An inherently void avoidance routing protocol for underwater sensor networks. In: 2015 International symposium on wireless communication systems (ISWCS), IEEE, pp 361–365
7. Coutinho RW, Vieira LF, Loureiro AA (2013) DCR: depth-controlled routing protocol for underwater sensor networks. In: 2013 IEEE symposium on computers and communications (ISCC), IEEE, pp 000453–000458
8. Chandavarkar BR, Gadagkar AV (2020) Expectation-based multi-attribute multi-hop routing (EM2R) in underwater acoustic sensor networks. In: 2020 IEEE 15th international conference on industrial and information systems (ICIIS), IEEE, pp 555–560
9. Chandavarkar BR, Guddeti RMR (2016) Simplified and improved multiple attributes alternate ranking method for vertical handover decision in heterogeneous wireless networks. Comp Commun 83:81–97
10. Nowsheen N, Karmakar G, Kamruzzaman J (2014) MPDF: movement predicted data forwarding protocol for underwater acoustic sensor networks. In: The 20th Asia-Pacific conference on communication (APCC2014), IEEE, pp 100–105
11. Olakanmi OO, Odeyemi KO, Abbas A (2020) Mobility and energy prediction models: approach toward effective route management in mobile wireless sensor networks. Eng Rep 2(3):e12095 (Wiley Online Library)
12. Wu H, Wang J, Ananta RR, Kommareddy VR, Wang R, Mohapatra P (2018) Prediction based opportunistic routing for maritime search and rescue wireless sensor network. J Parall Distrib Comput 111:56–64
13. Yu J, Feng L, Jia L, Gu X, Yu D (2014) A local energy consumption prediction-based clustering protocol for wireless sensor networks. Sensors 14(12):23017–23040
14. Sun B, Li Y, Sun S, Qiao L, Tian K, Li Z, Lu X (2021) Optimal routing scheduling strategy based on prediction of ocean current movement for underwater wireless sensor networks. In: IEEE 21st international conference on communication technology (ICCT), IEEE, pp 549–553
15. Raj Priyadarshini R, Sivakumar N (2020) Enhancing coverage and connectivity using energy prediction method in underwater acoustic WSN. J Amb Intell Human Comput 11(7):2751–2760
16. Zhang W, Han G, Wang X, Guizani M, Fan K, Shu L (2020) A node location algorithm based on node movement prediction in underwater acoustic sensor networks. IEEE Trans Vehic Technol 69(3):3166–78
17. Song S, Liu J, Guo J, Zhang C, Yang T, Cui J (2021) Efficient velocity estimation and location prediction in underwater acoustic sensor networks. IEEE Internet Things J

Author Index

S. Rawat et al. (eds.), *Proceedings of Second International Conference on Computational Electronics for Wireless Communications*, Lecture Notes in Networks and Systems 554,
https://doi.org/10.1007/978-981-19-6661-3